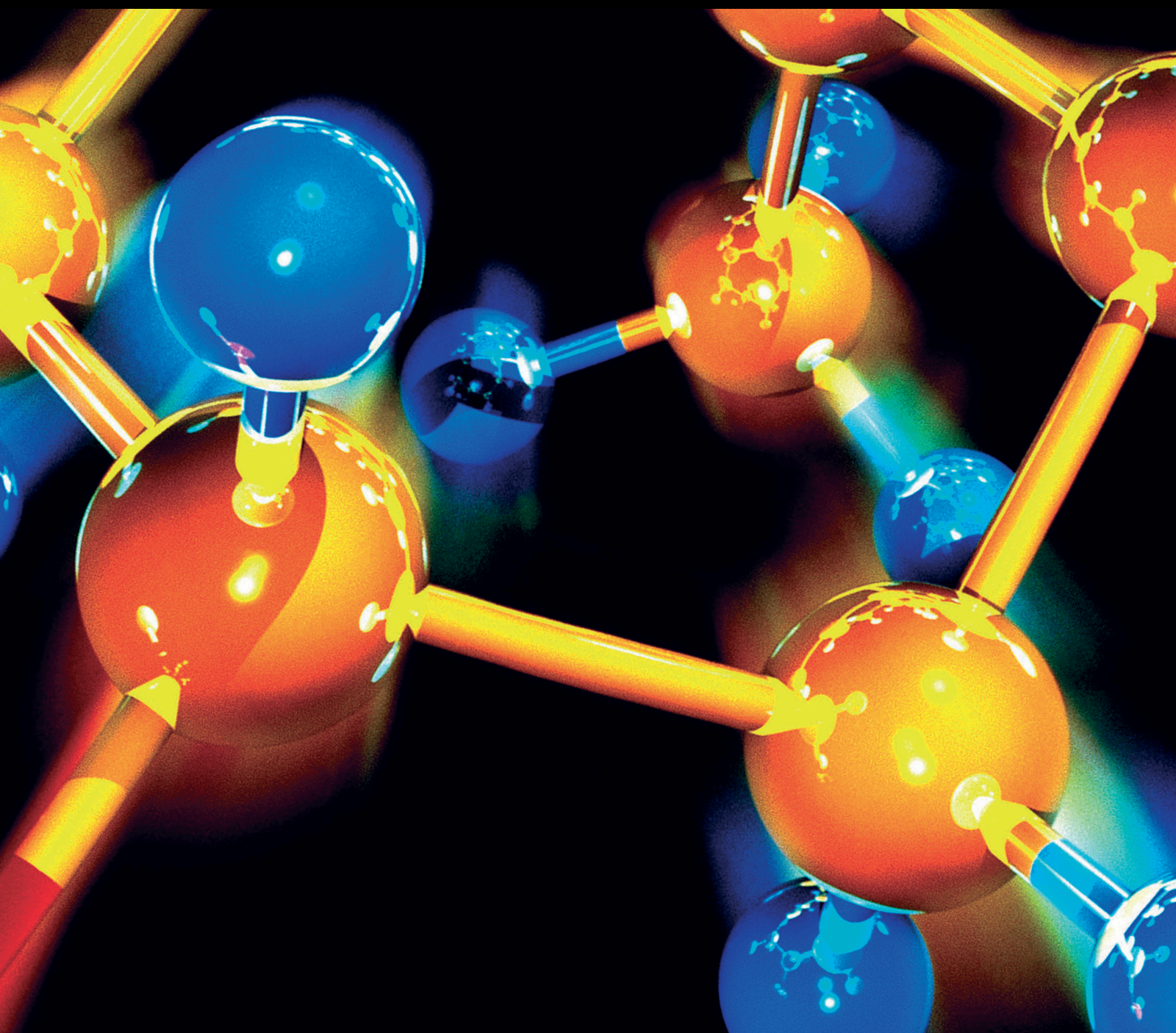


Advanced Nanomaterials for Green Growth

Lead Guest Editor: Thanh-Dong Pham

Guest Editors: Nguayen Van Noi, Ajit Kumar Sharma, and Van Duong Dao





Advanced Nanomaterials for Green Growth

Journal of Chemistry

Advanced Nanomaterials for Green Growth

Lead Guest Editor: Thanh-Dong Pham

Guest Editors: Nguayen Van Noi, Ajit Kumar Sharma, and
Van Duong Dao



Copyright © 2020 Hindawi Limited. All rights reserved.

This is a special issue published in "Journal of Chemistry." All articles are open access articles distributed under the Creative Commons Attribution License, which permits unrestricted use, distribution, and reproduction in any medium, provided the original work is properly cited.

Editorial Board

Luqman C. Abdullah, Malaysia
Daryoush Afzali, Iran
Mohammad A. Al-Ghouthi, Qatar
Shafaqat Ali, Pakistan
Amit Bhatnagar, Finland
Claudio Cameselle, Spain
Zenilda Cardeal, Brazil
Claudia Crestini, Italy
Shayessteh Dadfarnia, Iran
Fatih Deniz, Turkey
Claudio Di Iaconi, Italy
Ludo Diels, Belgium
Yingchao Dong, China
Valdemar Esteves, Portugal
Alberto Figoli, Italy
Andrea Gambaro, Italy
Wenshan Guo, Australia
Ewa Kaczorek, Poland
Mostafa Khajeh, Iran
Woojin Lee, Kazakhstan
Carlos A Martínez-Huitle, Brazil
Mehrab Mehrvar, Canada
Saima Q. Memon, Pakistan
Maurice Millet, France
Kaustubha Mohanty, India
José Morillo, Spain
Khaled Mostafa, Egypt
Pedro Avila Pérez, Mexico
Nicolas Roche, France
Stéphanie Sayen, France
Darren Sun, Singapore
Sedat Yurdakal, Turkey
Minghua Zhou, China

Contents

Advanced Nanomaterials for Green Growth

Thanh-Dong Pham , Nguyen Van Noi, Ajit Kumar Sharma , and Van-Duong Dao 
Editorial (2 pages), Article ID 9567121, Volume 2020 (2020)

Synthesis of Iron-Modified Biochar Derived from Rice Straw and Its Application to Arsenic Removal

Thi Hanh Nguyen , Thi Huong Pham, Hong Tham Nguyen Thi, Thi Nham Nguyen , Minh-Viet Nguyen , Trinh Tran Dinh , Minh Phuong Nguyen , Trung Quang Do , Thao Phuong , Thu Trang Hoang, Thanh Tung Mai Hung, and Viet Ha Tran Thi 
Research Article (8 pages), Article ID 5295610, Volume 2019 (2019)

SiO₂/TiO₂ Composite Coating on Light Substrates for Photocatalytic Decontamination of Water

Hana Bíbová, Lenka Hykrdová , Hiep Hoang , Milan Eliáš, and Jaromír Jirkovský
Research Article (11 pages), Article ID 2634398, Volume 2019 (2019)

Synergistic Adsorption and Photocatalytic Activity under Visible Irradiation Using Ag-ZnO/GO Nanoparticles Derived at Low Temperature

Viet Ha Tran Thi , The Ha Cao , Tri Nhut Pham , Tien Thanh Pham , and Manh Cuong Le 
Research Article (13 pages), Article ID 2979517, Volume 2019 (2019)

Preparation of Manganese Dioxide Nanoparticles on Laterite for Methylene Blue Degradation

Thu-Huong Le, Thu Hong Anh Ngo , Van Thuan Doan, Le Minh Tri Nguyen, and Manh Cuong Le 
Research Article (9 pages), Article ID 1602752, Volume 2019 (2019)

Using Electrode Made of Carbon Nanotubes and Bismuth Oxide for the Determination of Metal Concentration by Anodic Stripping Voltammetry

Thi Thu Phuong Nguyen , Xuan Gian Trinh, and Dao Thi To Uyen
Research Article (7 pages), Article ID 6170967, Volume 2019 (2019)

Structure and Electrochemical Properties of Li₄Ti₅O₁₂ Prepared via Low-Temperature Precipitation

Le Thanh Nguyen Huynh , Cam Thanh Duy Ha, Viet Dung Nguyen, Dinh Quan Nguyen, My Loan Phung Le , and Van Man Tran
Research Article (7 pages), Article ID 1727859, Volume 2019 (2019)

Cellulose Conversion to 5-Hydroxymethyl Furfural (5-HMF) Using Al-Incorporated SBA-15 as Highly Efficient Catalyst

Son Tung Pham, Manh B. Nguyen , Giang H. Le , Trang T. T. Pham, Trang T. T. Quan , Trinh Duy Nguyen , Thanh Le Son , and Tuan Anh Vu 
Research Article (8 pages), Article ID 5785621, Volume 2019 (2019)

Synthesis of SAPO-34 Using Different Combinations of Organic Structure-Directing Agents

Tuan Doan , Khang Nguyen , Phong Dam , Thanh Huyen Vuong, Minh Thang Le , and Huyen Pham Thanh 
Research Article (10 pages), Article ID 6197527, Volume 2019 (2019)

Sonochemical Synthesis and Properties of YVO₄:Eu³⁺ Nanocrystals for Luminescent Security Ink Applications

Chinh Dung Trinh , Phuong Thi Pham Hau, Thi My Dung Dang, and Chien Mau Dang 
Research Article (13 pages), Article ID 5749702, Volume 2019 (2019)

Fast and Effective Route for Removing Methylene Blue from Aqueous Solution by Using Red Mud-Activated Graphite Composites

Ha Xuan Linh, Ngo Thi Thu, Tran Quoc Toan, Do Tra Huong, Bui Thanh Giang, Huynh Ky Phuong Ha , Hong-Tham T. Nguyen, N. T. K. Chung, Tri Khoa Nguyen , and Nguyen Thanh Hai 
Research Article (7 pages), Article ID 2858170, Volume 2019 (2019)

Enhancing Activity of Pd-Based/rGO Catalysts by Al-Si-Na Addition in Ethanol Electrooxidation in Alkaline Medium

Minh Dang Nguyen , Lien Thi Tran, Quang Minh Nguyen, Thao Thi Nguyen, and Thu Ha Thi Vu 
Research Article (13 pages), Article ID 6842849, Volume 2019 (2019)

Enhanced Photocatalytic Degradation of Rhodamine B Using C/Fe Co-Doped Titanium Dioxide Coated on Activated Carbon

Thuy Le Thi Thanh , Lan Nguyen Thi, Trinh Tran Dinh , and Noi Nguyen Van
Research Article (8 pages), Article ID 2949316, Volume 2019 (2019)

Modeling and Optimization of the BSCF-Based Single-Chamber Solid Oxide Fuel Cell by Artificial Neural Network and Genetic Algorithm

Minh-Vien Le, Tuan-Anh Nguyen , and T.-Anh-Nga Nguyen 
Research Article (9 pages), Article ID 7828019, Volume 2019 (2019)

Influence of Organoclay on the Flame Retardancy and Thermal Insulation Property of Expandable Graphite/Polyurethane Foam

Nhung Hac Thi , Duy Linh Pham, Nguyen Thi Hanh , Ho Thi Oanh , Thi Hai Yen Duong, Thanh Nhan Nguyen , Nguyen Duc Tuyen , Dinh Long Phan, Ha Thu Trinh, Ha Tran Nguyen, Tung Ngo Trinh, and Mai Ha Hoang 
Research Article (8 pages), Article ID 4794106, Volume 2019 (2019)

Kinetics, Isotherm, Thermodynamics, and Recyclability of Exfoliated Graphene-Decorated MnFe₂O₄ Nanocomposite Towards Congo Red Dye

Van Thinh Pham, Hong-Tham T. Nguyen, Thuan Van Tran , Duyen Thi Cam Nguyen , Hanh T. N. Le, Thuong Thi Nguyen, Dai-Viet N. Vo, Thi Hong Nhan Le , and Duy Chinh Nguyen 
Research Article (16 pages), Article ID 5234585, Volume 2019 (2019)

Study on Fire Resistance Ability and Mechanical Properties of Composites Based on Epikote 240 Epoxy Resin and Thermoelectric Fly Ash: An Ecofriendly Additive

Tuan Anh Nguyen , Quang Tung Nguyen, Xuan Canh Nguyen , and Van Hoan Nguyen
Research Article (8 pages), Article ID 2635231, Volume 2019 (2019)

Contents

Mechanical Properties and Flame Retardancy of Epoxy Resin/Nanoclay/Multiwalled Carbon Nanotube Nanocomposites

Tuan Anh Nguyen , Quang Tung Nguyen, and Trong Phuc Bach
Research Article (9 pages), Article ID 3105205, Volume 2019 (2019)

Preparation and Characterization of a Hydrophilic Polysulfone Membrane Using Graphene Oxide

Hoan Thi Vuong Nguyen , Thu Hong Anh Ngo , Khai Dinh Do, Minh Ngoc Nguyen, Nu Thi To Dang, Tham Thi Hong Nguyen, Vo Vien , and Tuan Anh Vu 
Research Article (10 pages), Article ID 3164373, Volume 2019 (2019)

Platinum Nanoflower-Modified Electrode as a Sensitive Sensor for Simultaneous Detection of Lead and Cadmium at Trace Levels

Thi Lieu Nguyen , Van Hoang Cao, Thi Hai Yen Pham, and Truong Giang Le 
Research Article (10 pages), Article ID 6235479, Volume 2019 (2019)

An Initial Evaluation on the Adsorption of SO₂ and NO₂ over Porous Fe₃O₄ Nanoparticles Synthesized by Facile Scalable Method

Xuan-Manh Pham , Duy Linh Pham , Nguyen Thi Hanh , Tuyet Anh Dang Thi , Le Nhat Thuy Giang , Hoang Thi Phuong , Nguyen Tuan Anh , Hac Thi Nhung , Giang Truong Le, Mai Ha Hoang , and Tuyen Van Nguyen 
Research Article (7 pages), Article ID 9742826, Volume 2019 (2019)

Synthesis of Acidic Heterogeneous Catalysts with High Stability Based on Graphene Oxide/Activated Carbon Composites for the Esterification of Lactic Acid

Thu Ha Thi Vu , Manh Ha Nguyen , and Minh Dang Nguyen 
Research Article (7 pages), Article ID 7815697, Volume 2019 (2019)

Effect of Silver Nanoparticles on Tropical Freshwater and Marine Microalgae

Thanh-Luu Pham 
Research Article (7 pages), Article ID 9658386, Volume 2019 (2019)

Synthesis of Magnesium Oxide Nanoplates and Their Application in Nitrogen Dioxide and Sulfur Dioxide Adsorption

Thi Hai Yen Duong, Thanh Nhan Nguyen , Ho Thi Oanh , Tuyet Anh Dang Thi, Le Nhat Thuy Giang, Hoang Thi Phuong, Nguyen Tuan Anh , Ba Manh Nguyen , Vinh Tran Quang , Giang Truong Le, and Tuyen Van Nguyen 
Research Article (9 pages), Article ID 4376429, Volume 2019 (2019)

Preparation of Graphene Nanoplatelets by Thermal Shock Combined with Ball Milling Methods for Fabricating Flame-Retardant Polymers

Vinh Q. Tran , Hai T. Doan , Nhiem T. Nguyen , and Cuong V. Do 
Research Article (6 pages), Article ID 5284160, Volume 2019 (2019)

A Facile Synthesis, Characterization, and Photocatalytic Activity of Magnesium Ferrite Nanoparticles via the Solution Combustion Method

Loan T. T. Nguyen , Lan T. H. Nguyen, Nhuong Chu Manh, Dung Nguyen Quoc, Hai Nguyen Quang, Hang T. T. Nguyen, Duy Chinh Nguyen , and Long Giang Bach

Research Article (8 pages), Article ID 3428681, Volume 2019 (2019)

Novel Removal of Diazinon Pesticide by Adsorption and Photocatalytic Degradation of Visible Light-Driven Fe-TiO₂/Bent-Fe Photocatalyst

Nguyen Minh Phuong , Ngoc Chau Chu, Doan Van Thuan, Minh Ngoc Ha, Nguyen Thi Hanh, Huong Do Thi Viet, Nguyen Thi Minh Thu, Pham Van Quan, and Nguyen Thi Thanh Truc 

Research Article (7 pages), Article ID 2678927, Volume 2019 (2019)

A Novel Approach for Fabricating LaMnO₃ Thin Films Using Combined Microwave Combustion and Pulsed Electron Deposition Techniques

Thi Ha Tran, Thi Trung Anh Tang, Nguyen Hai Pham, Thanh Cong Bach, Cong Doanh Sai , Quang Hoa Nguyen, Van Vu Le, Hoang Nam Nguyen , Quoc Khoa Doan, Trong Tam Nguyen, Viet Bau Le, Khac Hieu Ho, and Viet Tuyen Nguyen 

Research Article (8 pages), Article ID 3568185, Volume 2019 (2019)

Metal-Organic Framework MIL-53(Fe) as an Adsorbent for Ibuprofen Drug Removal from Aqueous Solutions: Response Surface Modeling and Optimization

Duyen Thi Cam Nguyen , Hanh Thi Ngoc Le, Trung Sy Do, Van Thinh Pham, Dai Lam Tran , Van Thi Thanh Ho , Thuan Van Tran , Duy Chinh Nguyen , Trinh Duy Nguyen , Long Giang Bach , Huynh Ky Phuong Ha , and Van Thuan Doan 

Research Article (11 pages), Article ID 5602957, Volume 2019 (2019)

Editorial

Advanced Nanomaterials for Green Growth

Thanh-Dong Pham ¹, **Nguyen Van Noi**,¹ **Ajit Kumar Sharma** ², and **Van-Duong Dao** ³

¹Vietnam National University, Hanoi, Vietnam

²Lovely Professional University, Phagwara, India

³Phenikaa University, Hanoi, Vietnam

Correspondence should be addressed to Thanh-Dong Pham; thanhdongpham080808@gmail.com

Received 17 February 2020; Accepted 18 February 2020; Published 16 March 2020

Copyright © 2020 Thanh-Dong Pham et al. This is an open access article distributed under the Creative Commons Attribution License, which permits unrestricted use, distribution, and reproduction in any medium, provided the original work is properly cited.

Green and sustainable development is widely recognized as a concept of the modern society. This concept has appeared as a state of society where living conditions and resource use continue to meet human needs without undermining the integrity and stability of the natural system. Advanced nanomaterials can be applied to produce cleaner, more efficient, and valuable products to address our present environment-related concerns to a more sustainable future. Thus, the main goal of this issue is to highlight recent advances in synthesis and green applications of nanomaterials. The special issue contains twenty-eight selected research articles relating to nanomaterials. These reported nanomaterials present excellent performance and outstanding stability, have environmental benefits, and are cost-effective.

Most of the selected papers in the special issue reported the synthesis of nanomaterials applying for pollutant treatment. N. M. Phuong et al. reported novel activity of Fe-TiO₂/Bent-Fe photocatalysts for removal of diazinon pesticides. T. T. V. Ha et al. presented synergistic adsorption and photocatalytic activity of Ag-ZnO/GO photocatalysts for extremely high removal of methylene blue. L. T. T. Thuy et al. reported high photocatalytic activity of C/Fe codoped TiO₂ coated on activated carbon for degradation of Rhodamine B (Rh B). H. Bibova et al. successfully synthesized SiO₂/TiO₂ composite coating on light substrates for photocatalytic decontamination of oxalic acid and methylene blue in water. L. T. T. Nguyen et al. successfully used the solution combustion method to synthesize MgFe₂O₄ nanoparticles for methylene blue dye degradation under visible light. N. T. Hanh et al. synthesized of Fe-modified biochar derived from rice straw to apply for arsenic removal.

H. X. Linh et al. reported that their synthesized red mud-activated graphite composites fast and effective in removing methylene blue from aqueous solutions. V. T. Pham et al. studied kinetics, isotherm, thermodynamics, and recyclability of exfoliated graphene-decorated MnFe₂O₄ nanocomposites for Congo red dye absorption. T. H. Le et al. successfully synthesized MnO₂ nanoparticles on laterite for degradation of methylene blue. X. M. Pham et al. investigated the adsorption of SO₂ and NO₂ over porous Fe₃O₄ nanoparticles. D. T. C. Nguyen et al. successfully synthesized metal organic framework MIL-53(Fe) as an adsorbent for ibuprofen drug removal from aqueous solutions.

There are four selected papers in the special issue which presented application of nanomaterials as flame retardants. T. A. Nguyen et al. investigated mechanical properties and flame retardancy of epoxy resin/nanoclay/multiwalled carbon nanotube nanocomposites. H. T. Nhung et al. successfully used organoclay to modify expandable graphite/polyurethane foam to use as a flame retardant and thermal insulator. V. Q. Tran et al. successfully used thermal shock combined with ball milling methods to prepare graphene nanoplatelets using flame retardant polymers. T. A. Nguyen et al. studied on fire resistance ability and mechanical properties of composites based on Epikote 240 epoxy resin and thermoelectric fly ash.

There are three selected papers in the special issue which reported catalytic activity of nanomaterials. S. T. Pham et al. reported that Al-incorporated SBA-15 highly efficiently catalyze cellulose conversion to 5-hydroxymethyl furfural (5-HMF). T. H. T. Vu et al. successfully synthesized acidic heterogeneous catalysts with high stability based on

graphene oxide/activated carbon composites for the esterification of lactic acid. M. D. Nguyen et al. reported enhancing activity of Pd-based/rGO modified by Al-Si-Na catalysts in ethanol electro-oxidation in an alkaline medium.

The special issue also presented other useful applications of nanomaterials. C. D. Trinh et al. used the wet chemical method to synthesize $YVO_4:Eu^{3+}$ nanocrystals for luminescent security ink applications. T. T. P. Nguyen used carbon nanotubes and bismuth oxide to make electrodes for determination of metal concentration by the anodic stripping voltammetry method. T. L. Nguyen et al. successfully utilized platinum nanoflowers to modify electrodes to use as a sensitive sensor for simultaneous detection of lead and cadmium at trace levels. H. T. V. Nguyen et al. successfully used graphene oxide to prepare a hydrophilic polysulfone membrane.

These papers in the issue have been properly selected and concerned most recent progresses in the field of nanomaterials for green growth. The editors hope that the presented objectives of the special issue will be useful not only to working nanomaterial researchers but also to interested engineers as well as students and researchers in other fields. We offer many thanks for reading the enclosed papers and our best wishes for your future research.

Conflicts of Interest

The Guest Editor and Guest Co-Editors declare that there are no conflicts of interest or agreements with private companies, which will prevent us working impartially in the editorial process.

Acknowledgments

We are would like to deeply acknowledge all the authors for their contributions to the special issue and appreciate all the reviewers and related editorial board members for critical assessments and valuable comments to improve the quality of these papers.

*Thanh-Dong Pham
Nguyen Van Noi
Ajit Kumar Sharma
Van-Duong Dao*

Research Article

Synthesis of Iron-Modified Biochar Derived from Rice Straw and Its Application to Arsenic Removal

Thi Hanh Nguyen ¹, **Thi Huong Pham**,² **Hong Tham Nguyen Thi**,³ **Thi Nham Nguyen** ^{4,5}, **Minh-Viet Nguyen** ⁵, **Trinh Tran Dinh** ⁵, **Minh Phuong Nguyen** ⁵, **Trung Quang Do** ⁵, **Thao Phuong** ⁵, **Thu Trang Hoang**,⁵ **Thanh Tung Mai Hung**,⁶ and **Viet Ha Tran Thi** ⁷

¹Faculty of Environment, University of Science, Vietnam National University, 334 Nguyen Trai, Thanh Xuan, Hanoi, Vietnam

²Center for Advanced Chemistry, Institute of Research and Development, Duy Tan University, Da Nang, Vietnam

³NTT Hi-Tech Institute, Nguyen Tat Thanh University, Ho Chi Minh City, Vietnam

⁴Center for Analytical Sciences Development and Application, Vietnam National University, Thanh Xuan, Hanoi, Vietnam

⁵Faculty of Chemistry, University of Science, Vietnam National University, Thanh Xuan, Hanoi, Vietnam

⁶Faculty of Chemical Engineering, Ho Chi Minh City University of Food Industry, 140 Le Trong Tan, Ho Chi Minh City, Vietnam

⁷Vietnam-Japan University, Vietnam National University, Hanoi, Vietnam

Correspondence should be addressed to Thi Nham Nguyen; nguyenthinham_t57@hus.edu.vn

Received 14 March 2019; Revised 20 May 2019; Accepted 13 September 2019; Published 16 October 2019

Guest Editor: Ajit Kumar Sharma

Copyright © 2019 Thi Hanh Nguyen et al. This is an open access article distributed under the Creative Commons Attribution License, which permits unrestricted use, distribution, and reproduction in any medium, provided the original work is properly cited.

A novel iron-modified biochar (FMBC) derived from rice straw was synthesized using FeCl₃ modification for efficient As(V) removal from aqueous solution. FTIR and SEM-EDX analyses were carried out to determine the mechanism involved in the removal process and also demonstrated that Fe had loaded successfully on the surface of modified biochar. The iron-modified biochar showed higher arsenic removal ability than the raw biochar. The iron-modified biochar showed a maximum adsorption with an initial solution pH of 5.0. Moreover, for the tested biochar, the As(V) removal kinetics data were well fitted by the pseudo-second-order model. Furthermore, the As(V) removal data upon being well fitted by the Langmuir model showed the maximal removal capacity of 28.49 mg/g. The simple preparation process and high adsorption performance suggest that the iron-modified biochar derived from rice straw could be served as an effective, inexpensive, and environmentally sustainable adsorbent to replace typical granular activated carbon (AC) for As(III) removal from aqueous solution.

1. Introduction

Arsenic is one of the most abundant elements in the biosphere and in the Earth's crust. Arsenic occurs in most natural waters as As(V), As(III), As(0), and As(-III) oxidation states. As-contaminated water affects a large group of population worldwide, particularly in Vietnam, China, and India. Chronic exposure to inorganic arsenic may lead to cancer or noncancer health effects [1]. Arsenic has been classified as a Class A carcinogen by the United States Environmental Protection Agency (USEPA). According to the World Health Organization (WHO) and USEPA, the limitations for As concentration are 10 µg/L

and 0.2 mg/L in safe drinking water and discharge wastewater, respectively [2]. Ingestion of arsenic, even at low concentration, has resulted in various detrimental health issues such as pulmonary disease, cardiovascular disease, nervous system dysfunction, and also cancer of the lung kidney and skin [3].

Coagulation/precipitation, ion exchange, reverse osmosis, and adsorption processes were utilized for arsenic-contaminated water remediation [4–6]. Among the various techniques, adsorption has been considered the most common and effective technology for removing contaminants from groundwater or wastewater [7]. Adsorption is often utilized at the end of a treatment plan for removal of

contaminants because of its low cost, and it does not generate any secondary waste that needs further treatment.

Biochar (BC), a carbon material produced mainly from the pyrolysis process of low-cost biomass residuals such as rice straw, has received much recent attention because of its many potential environmental abilities such as carbon sequestration, soil improvement, water treatment, and environmental remediation [8, 9]. BC can be utilized as an adsorbent because of its porosity, large surface area, and negative surface charge that can be useful for decontaminating water (organic and inorganic pollutants) [10]. Some BCs can be utilized for removal of heavy metal ions or organic polluted compounds in the aqueous solution. However, the lack of adsorption sites and functional group limits its application to As removal [11, 12]. Many researchers have modified BCs to improve their properties such as enhance the surface functional groups for effective adsorption [13, 14]. Several studies have utilized metal oxyhydroxide surfaces and clay minerals containing Fe, Mn, Al, Cu, and Co to remove As in the aqueous solution [15]. Hematite, an abundant and natural Fe mineral, was a good adsorbent for As removal from groundwater [16]. The hematite mineral was activated by the thermal method to enhance its ability to remove aqueous As [17].

Vietnam is the world's fifth largest rice producer all over the world. The total amount of rice straw generated was approximately 67 million dry ton in 2013. In order to reduce the environmental problem from rice straw burning, it is necessary to find a suitable method to remove the excess rice straw. Therefore, biochar derived from rice straw can be an effective, inexpensive, and environmentally sustainable adsorbent for environmental treatment and can reduce atmospheric pollution from rice straw burning.

In the present study, dried rice straw was used for the preparation of biochar by slow pyrolysis and then modified with the mixture of FeCl_3 and FeSO_4 before being applied for the removal of As(V) in aqueous solution.

2. Materials and Methods

2.1. Biochar Production. In this study, the rice straw biomass was collected from a rice farm in the city of Hanoi, Vietnam. It was pyrolyzed at a temperature of 500°C for 1 h using a tube-type electrical furnace under N_2 gas. The biochar was collected from the reactor after being cooled till a room temperature of $25\text{--}30^\circ\text{C}$ inside the muffle furnace. The iron-modified biochar was synthesized by the following procedure. 10 g of the obtained BC was mixed with 500 ml of 7.3 g $\text{FeSO}_4 \cdot 7\text{H}_2\text{O}$ and 7.23 g $\text{FeCl}_3 \cdot 6\text{H}_2\text{O}$ in a glass tube. This mixture was heated at 50°C to form a stable suspension. The pH was raised to 11 by adding 0.05 M NaOH solution, dropwise. After mixing for 60 min, the organic residues were removed by washing with distilled water (H_2O) until the pH of the washing solution reached 7.0. The fine powdered modified biochar (FMBC) was vacuum-filtered and then dried overnight at 50°C in a hot air oven [18].

2.2. Characterization of Biochar (BC). The surface architecture of the synthesized BC (FMBC) was examined using a JED-2300 Analysis Station Plus (JEOL) scanning electron microscope (SEM). Energy-dispersive X-ray (EDX) spectroscopy analyses were carried out using a Quantax instrument (Bruker, USA). The infrared (IR) spectra of synthesized materials (as KBr pellets) were analyzed. The surface functional groups of FMBC were analyzed by using an IR spectrophotometer (PerkinElmer FTIR, USA) with an attenuated total reflectance attachment within the wavelength of $400\text{--}4,000\text{ cm}^{-1}$.

The point of zero charge (PZC) of FMBC was determined by using the pH drift method of 0.01 M NaCl pH interval of 2 and in the range of pH 2 to 12 [19]. The pH values of solutions were adjusted between 2 and 12 by using 0.1 M HCl or 0.1 M NaOH solution. The initial pH values of solutions were measured. A 0.2 g of biochar was added into a beaker with 20 mL of NaCl solution and left undisturbed for 24 h under N_2 bubbles to prevent CO_2 dissolution until the pH value became stable, and then final pH of the solutions was measured. The final pH was measured, and pH_{PZC} was determined as the value at which $\text{pH}_{\text{final}} = \text{pH}_{\text{initial}}$.

2.3. Batch Sorption of Arsenic. Adsorption experiments were conducted to determine the isotherms of arsenic sorption onto the FMBC sample. About 0.2 g of the FMBC was mixed with 100 mL of As(V) solution for each experiment. The mixture was then shaken in a mechanical shaker (120 rpm) at room temperature ($22 \pm 2^\circ\text{C}$). At the end of each experiment, the remaining As concentrations were determined by using inductively coupled plasma mass spectrometry (ICP-MS) after vacuum-filtered. Duplicate sets of samples were taken for the analysis of residual concentration of As, and the difference of two measurements should be smaller than 10%. All chemical reagents used in the experiments were of high purity grade from Sigma-Aldrich.

The amount of As(V) adsorbed onto the FMBC (adsorbent) was calculated by the concentration difference between the initial and final concentrations of the solution by using the following equation:

$$q_e (\text{mg} \cdot \text{g}^{-1}) = [C_o - C_e (\text{mg L}^{-1})] \times V (\text{L}) / W (\text{g}). \quad (1)$$

Hence, q_e is the equilibrium amount of the As(V) adsorbed ($\text{mg} \cdot \text{g}^{-1}$) on the FMBC, C_o and C_e are the initial and equilibrium concentration of As(V) (mg/L), V is the solution volume of the test sample (L), and M is the total mass of Fe-modified BC added (g).

2.4. Adsorption Isotherms and Kinetic Models. The equilibrium adsorption isotherms were utilized to determine the adsorption mechanism. In this study, Langmuir isotherm and Freundlich isotherm models were utilized to analyze the adsorption process of biochar. Langmuir isotherm is valid for monolayer sorption and expressed in the following equation:

$$\frac{c_e}{q_e} = \frac{1}{q_{\max} K_L} + \frac{c_e}{q_{\max}}, \quad (2)$$

where q_{\max} ($\text{mg}\cdot\text{g}^{-1}$) indicates the monolayer adsorption capacity and K_L ($\text{L}\cdot\text{mg}^{-1}$) is the heat of adsorption. The favorability or unfavorability of Langmuir adsorption can be expressed by

$$R_L = \frac{1}{1 + K_L C_0}, \quad (3)$$

where R_L indicates favorable adsorption and has the range between 0 and 1.

A Freundlich isotherm describes the heterogeneous surface energies by multilayer adsorption and is expressed in the following equation:

$$\log q_e = \log K_F + \frac{1}{n} \log C_e, \quad (4)$$

where K_F expresses the adsorption capacity ($\text{mg}\cdot\text{g}^{-1}$) and n is an empirical parameter related to the adsorption intensity, which varies with the heterogeneity of the adsorbent. The increase in $1/n$ enhanced the adsorption favorability.

The adsorption kinetic is an important characteristic influencing the adsorption efficiency. The pseudo-first-order and pseudo-second-order kinetic models express the adsorption process as follows:

$$\ln(q_e - q_t) = \ln q_e - k_1 t, \quad (\text{pseudo - first - order model}),$$

$$\frac{t}{q_t} = \frac{1}{k_2 q_e^2} + \frac{1}{q_e} t, \quad (\text{pseudo - second - order model}), \quad (5)$$

where q_e and q_t ($\text{mg}\cdot\text{g}^{-1}$) are concentrations adsorbed at equilibrium and at different time t and the parameters k_1 (min^{-1}) and k_2 ($\text{g}\cdot\text{mg}^{-1}\cdot\text{min}^{-1}$) are the equilibrium rate constants of pseudo-first-order and pseudo-second-order kinetic models, respectively.

3. Results and Discussion

3.1. Characteristics of BCs. The SEM analysis was investigated for the determination of shape, size, and surface morphological structure of the raw biochar (RB) and FMBC. Figure 1 reveals the surface morphologies of the two samples are distinctly different. The Fe-modified biochar showed more heterogeneous structure than the raw biochar after modification process that can contribute to enhance the sorption of As(V) in the aqueous solution [20].

The FTIR spectrum of RB and FMBC is shown in Figure 2, representing the functional groups on the RB and FMBC material introduced by the chemical modification process. The peaks found in the spectrum of the RB and FMBC show almost similar wavenumbers. Several peaks obtained around wavenumbers 1,605 and 1,379 cm^{-1} , which were assigned to C=O and C-O peaks that were attributed to carboxyl and lactone functional groups, respectively [21]. The peaks at 3,409 and 1094 cm^{-1} correspond to vibration of O-H of the adsorbent [22]. Vibration of the Fe-O peak was

observed on the FMBC at 780 cm^{-1} . These FTIR results indicated that the chemical modification plays an important role in the changing properties of biochar. The modification process enhanced the functional group intensity on the surface of the biochar; thus, these functional groups can be new active sites for the adsorption improvement on the biochar. The EDX spectra of the RB and FMBC (Figure 3) further indicated the increasing Fe content on the biochar surface after modification. It revealed that magnetite was added to the biochar surface after the modification process.

The point of zero charge (PZC) of a biochar determines the pH at which the surface of the biochar has positive or negative charge [23]. In this work, the points of zero charge of RB and FMBC were 5.44 and 6.88, respectively (Figure 4). The acidic value of the FMBC indicated that arsenic removal is feasible below this pH because the net positively charged surfaces are favorable to attract the anions.

3.2. Effect of Initial Solution pH. A pH solution is an important adsorption parameter for the adsorption study because the pH solution demonstrates the H^+ ions of specific functional groups on the biochar surface and varies the form of As in the solution. pH_{PZC} also plays an important role in the adsorption process. At $\text{pHs} < \text{pH}_{\text{PZC}}$, the surface of the FMBC is positively charged and gives a strong electrostatic attraction between surface groups and anion species in the solution that could enhance the adsorption process. The decrease in the adsorption amount observed at pH higher than pH_{PZC} (when the surface of the adsorbent is negatively charged) could lead to increased competition between OH^- and anion species for the adsorption sites [24]. The effect of solution pH on the adsorbent's arsenic sorption (removal) was identified by varying the initial solution pH while keeping other sorption parameter constants. The pH effect on adsorption was determined by mixing 1.0 g of modified BC with 100 ml of a 10 mg/l As(V) solution at various pH values ranging from 2.0 to 8.0 for 120 min.

The pH effect ranging from 2.0 to 8.0, on the adsorption of As(V) on biochar, is shown in Figure 5. The removal of As(V) ions was relatively low in the alkaline solution ($\text{pH} > 6.8$) compared with that at lower pH values, ranging from pH 2.0 to 6.8 (pH_{PZC}), because the OH^- ions at alkaline conditions can compete with As(V) anion for active sites under strong alkaline conditions, resulting in the blocking of As(V) adsorption on the surface of the modified BC. This is because As(V) existed in the aqueous solutions in the form of H_3AsO_4 , H_2AsO_4^- , HAsO_4^{2-} , AsO_4^{3-} , and especially H_2AsO_4^- at the pH range of 2.0–6.0 [25]. Therefore, increasing the initial concentration of proton in aqueous solutions increased the level of As(V) removal under acid conditions, ranging from pH 2.0 to 6.8. The highest removal efficiency was 86.3 and 62.3% for FMBC at the condition of $\text{pH} < 6.0$ and $\text{pH} > 6.0$, respectively. The RB showed lower removal efficiency even under the condition of $\text{pH} < 5.0$. This demonstrates the feasibility of the FMBC for As(V) removal from wastewater with pH values in the range of 4–7.

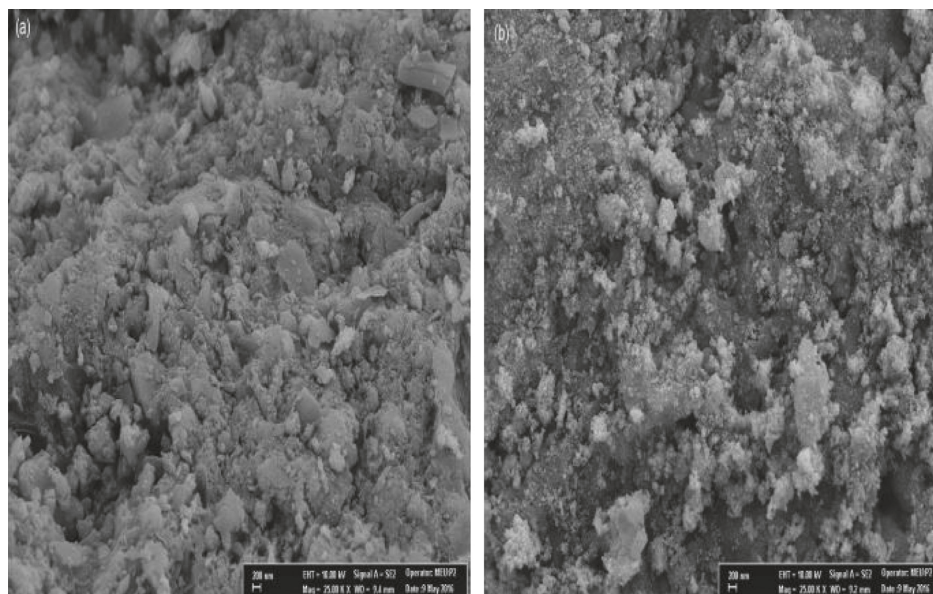


FIGURE 1: SEM images of raw biochar (RB) and iron-modified BC (FMBC).

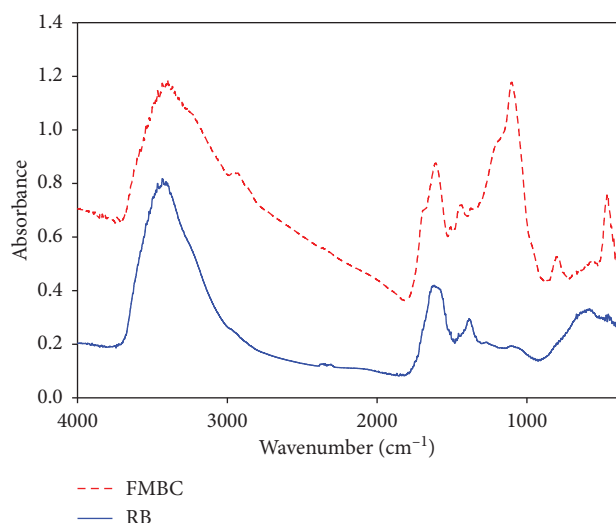


FIGURE 2: FTIR spectra of RB and FMBC.

3.3. Effect of Initial Concentration. Figure 6 shows the effect of initial concentration of As(V) ion solution for removal at a pH of 5.0 and a constant agitation speed of 150 rpm for 120 min. The amount of As(V) adsorbed increased with increasing initial concentration up to 30 mg/l, indicating that As(V) removal is highly concentration dependent. At lower concentrations, the amount of ions available for adsorption by a given amount of BC is less than the available sites on the adsorbent. However, at higher concentrations, the number of available sites for adsorption decreases. These results indicate that the adsorption removal of the As(V) ions depends on the initial concentration. Figure 3 shows the removal efficiency of FMBC decreased from 91.5 to 63.5% when the concentration increased from 4 to 30 mg/L.

3.4. Effect of Phase Reaction Time. The As(V) removal was also controlled by the reaction time. The rapid interaction of the As(V) ions to be removed by BC is desirable and beneficial for practical removal of arsenic anions from aqueous solutions or wastewater. Figure 7 shows the effects of reaction time for arsenic ion removal by the FMBC. For a given concentration of As(V), the amount of adsorbed As(V) ions was almost proportional to the increasing reaction time up to 45 min. The adsorption equilibrium was obtained at a reaction time of 90 min, with an adsorption capacity of 23.57 mg/g. The adsorption rate was relatively fast at the initial adsorption stage but then slowed down gradually after more sites were occupied by the adsorbed As(V) ions. The slower adsorption was due to the gradual decrease in the number of available adsorption sites.

3.5. Adsorption Isotherm. The adsorption isotherm data of FMBC were fitted to the Langmuir and Freundlich isotherms were fitted to the Langmuir adsorption isotherm ($R^2 = 0.9955$) ($p < 0.01$) than the Freundlich isotherm ($R^2 = 0.9360$) (Table 1). The results showed a monolayer As(V) adsorption onto the adsorption sites of the iron-modified biochar. The maximum adsorption capacities (q_{\max}) of As(V) decreased in the order of FMBC ($28.49 \text{ mg}\cdot\text{g}^{-1}$) > RB ($10.3 \text{ mg}\cdot\text{g}^{-1}$). The controls showed that the As(V) adsorption capacity of FMBC was higher than that of RB. The adsorption capacity of FMBC may relate to the increasing number of surface functional groups of the modified material. The maximum adsorption capacity of the FMBC for As(V) ions, based on the Langmuir isotherm, was 28.49 mg/g. Table 2 compares this study's result for the As(V) adsorption capacity of FMBC with values reported from other similar studies. The adsorption capacity of FMBC was much higher than that of other commercial material, and the FMBC can be utilized as a green adsorbent for the removal of As(V) in groundwater.

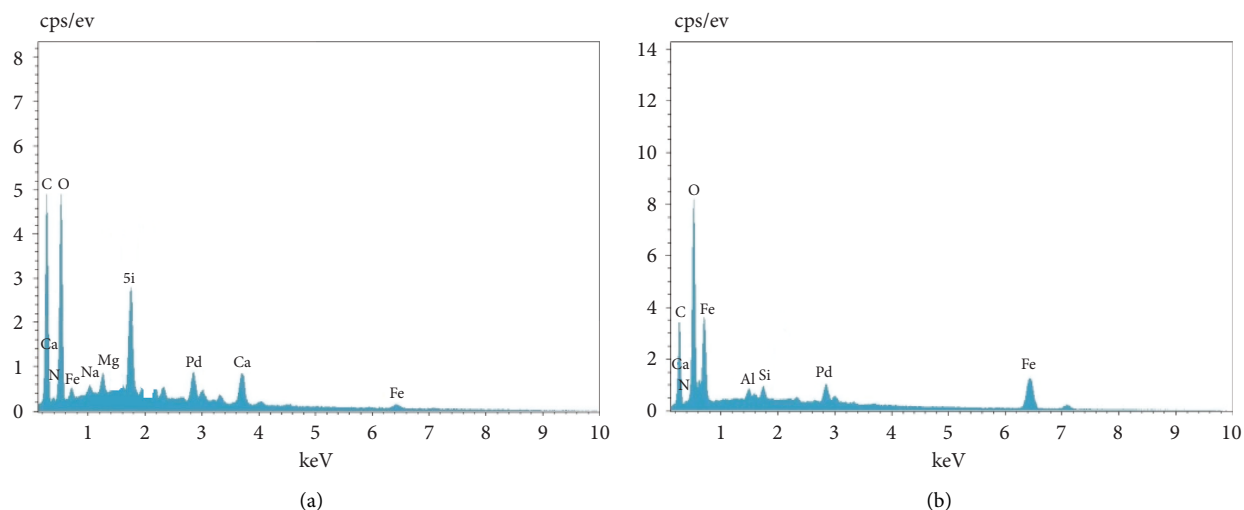


FIGURE 3: EDX spectra of RB (a) and FMBC (b).

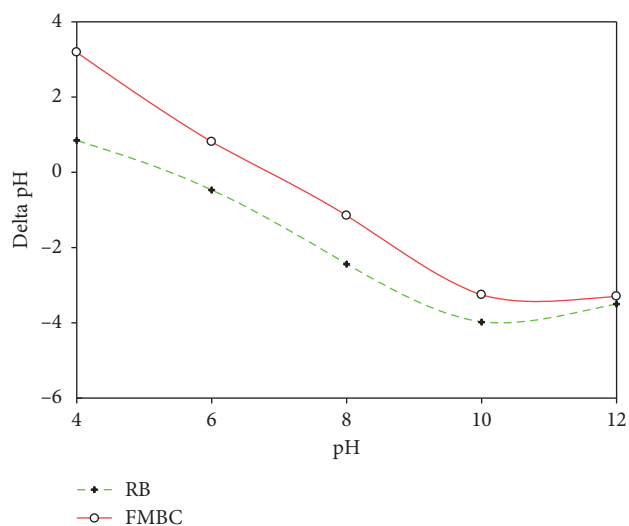


FIGURE 4: pH_{pzc} of RB and FMBC.

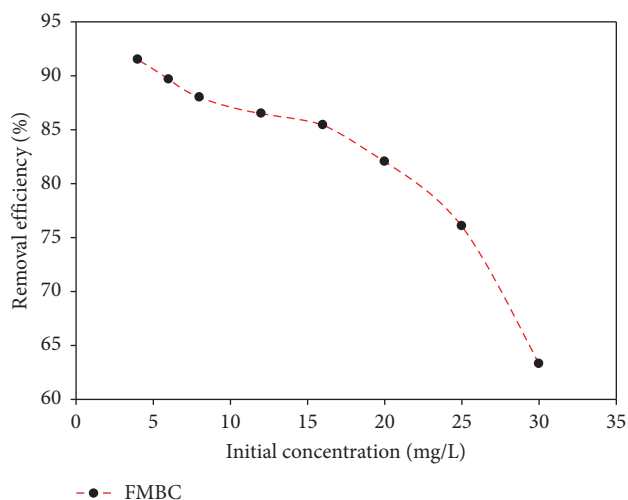


FIGURE 6: Effect of initial concentration for the As(V) removal on FMBC.

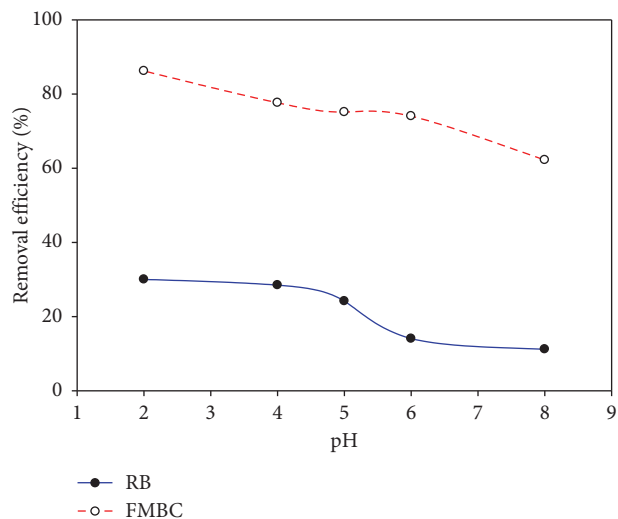


FIGURE 5: Effect of pH for the As(V) removal on RB and FMBC.

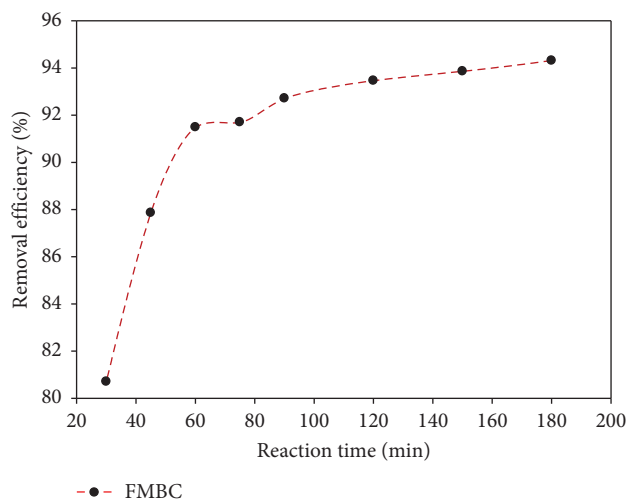


FIGURE 7: Effect of reaction time for the As(V) removal on FMBC.

TABLE 1: Adsorption isotherm of Fe-modified BC.

	Langmuir isotherm			Freundlich isotherm		
	q_{\max} (mg/g)	K_L	R^2	$\ln K_F$	$1/n$	R^2
Fe1-BC	28.49	0.563	0.9955	2.2118	0.5128	0.9360

TABLE 2: Adsorption comparison with other studies.

Material	Adsorption capacity (mg/g)	Reference
TiO ₂ -CNTs	1.8	[26]
Biochar	7.21	[27]
Supported nanoscale zero-valent iron on activated carbon	12.0	[28]
Ascorbic acid-coated Fe ₃ O ₄ nanoparticles	16.56	[29]
Activated carbon	25	[30]
FMBC	28.49	This study
Activated carbon	34.46	[30]
Al ₂ O ₃ /Fe(OH) ₃	36.63	[31]

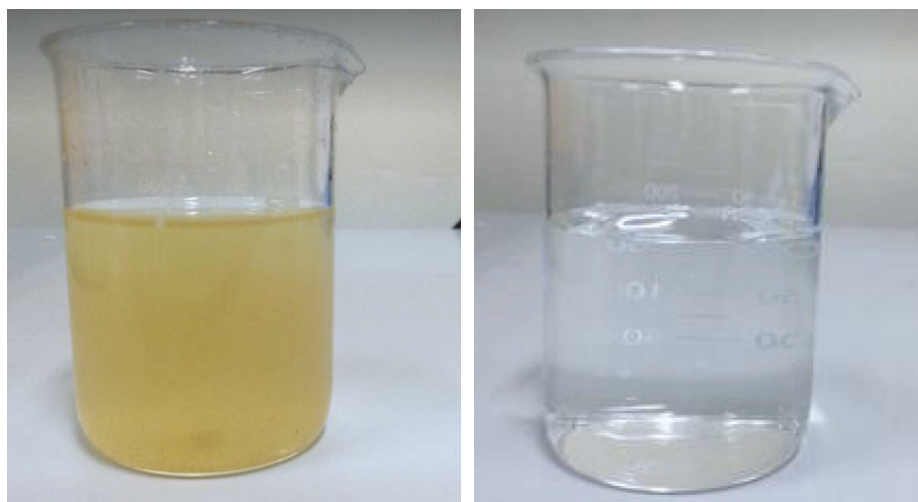


FIGURE 8: Groundwater sample before and after treatment.

The FMBC was applied for the removal of As(V) in the groundwater sample which had the concentration of As(V) 91 $\mu\text{g/L}$. Figure 8 shows the groundwater sample before and after treatment. The testing experiments showed that 1 kg of the Fe-modified BC can treat 278 and 141 m³ of contaminated groundwater to clean water of 50 $\mu\text{g/L}$ and 10 $\mu\text{g/L}$ As(V) based on the regulation of Vietnam for water supply and drinking water, respectively.

3.6. Adsorption Kinetics. Pseudo-first- and pseudo-second-order models were utilized to determine the kinetics of As(V) removal. The kinetic model of FMBC for As(V) in the aqueous solutions is shown in Table 3. The adsorption experimental data were best described by the pseudo-second-order kinetics that was proved by the obtained values of correlation coefficient ($R^2 = 0.988$) to describe the adsorption behavior of As(V) onto the modified BC. The experimentally obtained adsorption capacity ($q_{e(\text{exp})}$) values were close to the calculated data from the pseudo-second-order model, which also showed good evidence to support the

pseudo-second-order model and chemisorption [32]. For the pseudo-first-order kinetic model, the calculated adsorption capacity ($q_{e(\text{cal})}$) was much lower than the experimental value ($q_{e(\text{exp})}$) and the determination coefficient (R^2) was low ($R^2 = 0.844$).

Figure 9 presents the intraparticle diffusion model for sorption by the FMBC. The adsorption processes of As(V) are related by two steps—the first step depicting macropore diffusion and the second micropore diffusion [33]. In the first stage, the sharper portion may be considered as an external surface adsorption or faster adsorption stage. The second phase describes the gradual adsorption stage, where intraparticle diffusion is rate-controlled. These results of As(V) adsorption showed only the pore diffusion adsorption. The rate of uptake might be limited by the size of the adsorbate molecule, the concentration of the adsorbate and its affinity to the adsorbent, the diffusion coefficient of the adsorbate in the bulk phase, the pore-size distribution of the adsorbent, and the degree of mixing [34]. The first and second phases can be attributed to the external mass transfer and intraparticle diffusion mechanisms, respectively [35–

TABLE 3: Kinetic adsorption models.

$q_{e(\text{exp})}$ (mg/g)	Pseudo-first-order model			Pseudo-second-order model		
	$q_{e(\text{cal})}$ (mg/g)	K_1 (g/mg/min)	R^2	$q_{e(\text{cal})}$ (mg/g)	K_2 (g/mg/min)	R^2
28.49	3.238	0.0051	0.844	30.53	0.0892	0.988

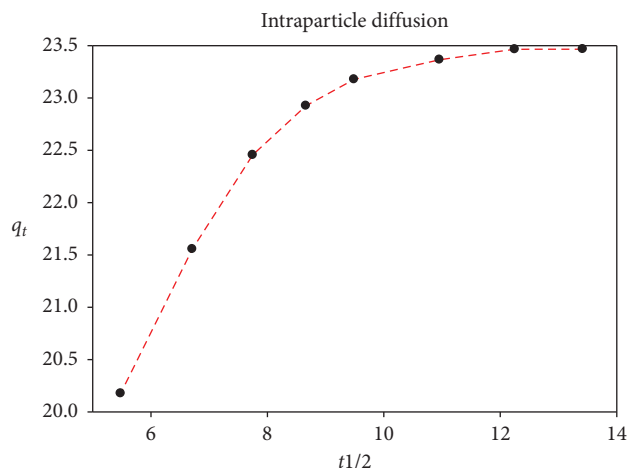


FIGURE 9: Intraparticle diffusion model for As(V) removal by the FMBC.

37]. Furthermore, the regression did not pass through the origin, showing that the intraparticle diffusion is not the only rate-controlling step in the sorption process. Thus, it can be inferred that external mass transfer and intraparticle diffusion occurred simultaneously during the As(V) sorption onto the Fe-modified BC.

The pseudo-second-order model and Langmuir isotherm usually assume that chemisorption of As(V) on FMBC is the rate-limiting step; it is inferred that As(V) was likely adsorbed on the surface of FMBC via chemical interaction. The proposed mechanisms of the removal of As(V) onto the FMBC through the complexation with iron are shown in the following equations:



4. Conclusion

This study investigated the removal of As(V) from aqueous solution using iron-modified biochar (FMBC) produced from the slow pyrolysis of rice straw. The FMBC afforded maximum adsorption at a pH of 5.0. The adsorption data were strongly correlated with the Langmuir adsorption isotherm, indicating surface homogeneity and unilayer adsorption. The equilibrium sorption capacity of 28.49 mg · g⁻¹ for As(V), as determined from the Langmuir isotherm, was very high compared to that of previously reported adsorbents. The As(V) adsorption was well fitted with the pseudo-second-order kinetic model ($R^2 = 0.988$)

which showed good evidence to support the chemisorptions of As(V) onto Fe-modified BC. The arsenic removal capacity of the FMBC is comparable to that of many commercial water treatment agents, including AC. Because the FMBC can be produced from rice straw relatively inexpensively, this simple activation method can also be applied to other thermally produced BCs to create an alternative and value-added sorbent for arsenic removal in groundwater.

Data Availability

The data used to support the findings of this study are available from the corresponding author upon request.

Conflicts of Interest

The authors declare that they have no conflicts of interest.

Acknowledgments

This research was funded by Vietnam National University, Hanoi (VNU), under project no. QG.19.19.

References

- [1] National Research Council (NRC), *Arsenic in Drinking Water*, The National Academies Press, Washington, DC, USA, 1999.
- [2] S. Hu, J. Lu, and C. Jing, "A novel colorimetric method for field arsenic speciation analysis," *Journal of Environmental Sciences*, vol. 24, no. 7, pp. 1341–1346, 2012.
- [3] A. Rana, N. Kumari, M. Tyagi, and S. Jagadevan, "Leaf-extract mediated zero-valent iron for oxidation of Arsenic (III): preparation, characterization and kinetics," *Chemical Engineering Journal*, vol. 347, pp. 91–100, 2018.
- [4] J. Kim and M. M. Benjamin, "Modeling a novel ion exchange process for arsenic and nitrate removal," *Water Research*, vol. 38, no. 8, pp. 2053–2062, 2004.
- [5] M.-C. Shih, "An overview of arsenic removal by pressure-driven membrane processes," *Desalination*, vol. 172, no. 1, pp. 85–97, 2005.
- [6] S. K. Gupta and K. Y. Chen, *Journal (Water Pollution Control Federation)*, pp. 493–506, Wiley, Hoboken, NY, USA, 1978.
- [7] A. H. Sulaymon and K. W. Ahmed, "Competitive adsorption of furfural and phenolic compounds onto activated carbon in fixed bed column," *Environmental Science & Technology*, vol. 42, no. 2, pp. 392–397, 2008.
- [8] Y. Yao, B. Gao, H. Chen et al., "Adsorption of sulfamethoxazole on biochar and its impact on reclaimed water irrigation," *Journal of Hazardous Materials*, vol. 209–210, pp. 408–413, 2012.
- [9] M. Inyang, B. Gao, P. Pullammanappallil, W. Ding, and A. R. Zimmerman, "Biochar from anaerobically digested sugarcane bagasse," *Bioresource Technology*, vol. 101, no. 22, pp. 8868–8872, 2010.
- [10] C. Peiris, O. Nayanathara, C. M. Navarathna et al., "The influence of three acid modifications on the physicochemical

- characteristics of tea-waste biochar pyrolyzed at different temperatures: a comparative study," *RSC Advances*, vol. 9, no. 31, pp. 17612–17622, 2019.
- [11] L. Lin, W. Qiu, D. Wang, Q. Huang, Z. Song, and H. W. Chau, "Arsenic removal in aqueous solution by a novel Fe-Mn modified biochar composite: characterization and mechanism," *Ecotoxicology and Environmental Safety*, vol. 144, pp. 514–521, 2017.
- [12] Z. Qi, T. P. Joshi, R. Liu, Y. Li, H. Liu, and J. Qu, "Adsorption combined with superconducting high gradient magnetic separation technique used for removal of arsenic and antimony," *Journal of Hazardous Materials*, vol. 343, pp. 36–48, 2018.
- [13] X. Hu, Z. Ding, A. R. Zimmerman, S. Wang, and B. Gao, "Batch and column sorption of arsenic onto iron-impregnated biochar synthesized through hydrolysis," *Water Research*, vol. 68, pp. 206–216, 2015.
- [14] M. Zhang, B. Gao, S. Varnosfaderani, A. Hebard, Y. Yao, and M. Inyang, "Preparation and characterization of a novel magnetic biochar for arsenic removal," *Bioresource Technology*, vol. 130, pp. 457–462, 2013.
- [15] B. Mandal and K. T. Suzuki, "Arsenic round the world: a review," *Talanta*, vol. 58, no. 1, pp. 201–235, 2002.
- [16] J. Gimenez, M. Martinez, J. Depablo, M. Rovira, and L. Duro, "Arsenic sorption onto natural hematite, magnetite, and goethite," *Journal of Hazardous Materials*, vol. 141, no. 3, pp. 575–580, 2007.
- [17] K. Ramirez-Muñiz, F. Jia, and S. Song, "Adsorption of As(V) in aqueous solutions on porous hematite prepared by thermal modification of a siderite—goethite concentrate," *Environmental Chemistry*, vol. 9, no. 6, pp. 512–520, 2012.
- [18] A. G. Karunanayake, N. Bombuwala Dewage, O. A. Todd et al., "Salicylic acid and 4-nitroaniline removal from water using magnetic Biochar: an environmental and analytical experiment for the undergraduate laboratory," *Journal of Chemical Education*, vol. 93, no. 11, pp. 1935–1938, 2016.
- [19] M. V. Lopez-Ramon, F. Stoeckli, C. Moreno-Castilla, and F. Carrasco-Marin, "On the characterization of acidic and basic surface sites on carbons by various techniques," *Carbon*, vol. 37, no. 8, pp. 1215–1221, 1999.
- [20] S. Wang, B. Gao, Y. Li, A. E. Creamer, and F. He, "Adsorptive removal of arsenate from aqueous solutions by biochar supported zero-valent iron nanocomposite: batch and continuous flow tests," *Journal of Hazardous Materials*, vol. 322, pp. 172–181, 2017.
- [21] S. Deng and Y.-P. Ting, "Characterization of PEI-modified biomass and biosorption of Cu(II), Pb(II) and Ni(II)," *Water Research*, vol. 39, no. 10, pp. 2167–2177, 2005.
- [22] F. Fu and Q. Wang, "Removal of heavy metal ions from wastewaters: a review," *Journal of Environmental Management*, vol. 92, no. 3, pp. 407–418, 2011.
- [23] A. Mukherjee, A. R. Zimmerman, and W. Harris, "Surface chemistry variations among a series of laboratory-produced biochars," *Geoderma*, vol. 163, no. 3-4, pp. 247–255, 2011.
- [24] M. J. Baniamerian, S. E. Moradi, A. Noori, and H. Salahi, "The effect of surface modification on heavy metal ion removal from water by carbon nanoporous adsorbent," *Applied Surface Science*, vol. 256, no. 5, pp. 1347–1354, 2009.
- [25] K. Henke, *Arsenic in Natural Environments*, John Wiley & Sons, Hoboken, NJ, USA, 2009.
- [26] H. Liu, K. Zuo, and C. D. Vecitis, "Titanium dioxide-coated carbon nanotube network filter for rapid and effective arsenic sorption," *Environmental Science & Technology*, vol. 48, no. 23, pp. 13871–13879, 2014.
- [27] N. K. Niazi, I. Bibi, M. Shahid et al., "Arsenic removal by perilla leaf biochar in aqueous solutions and groundwater: an integrated spectroscopic and microscopic examination," *Environmental Pollution*, vol. 232, pp. 31–41, 2018.
- [28] H. Zhu, Y. Jia, X. Wu, and H. Wang, "Removal of arsenic from water by supported nano zero-valent iron on activated carbon," *Journal of Hazardous Materials*, vol. 172, no. 2-3, pp. 1591–1596, 2009.
- [29] L. Feng, M. Cao, X. Ma, Y. Zhu, and C. Hu, "Superparamagnetic high-surface-area Fe₃O₄ nanoparticles as adsorbents for arsenic removal," *Journal of Hazardous Materials*, vol. 217–218, pp. 439–446, 2012.
- [30] X. Guo and F. Chen, "Removal of arsenic by bead cellulose loaded with iron oxyhydroxide from groundwater," *Environmental Science & Technology*, vol. 39, no. 17, pp. 6808–6818, 2005.
- [31] J. Hlavay and K. Polyák, "Determination of surface properties of iron hydroxide-coated alumina adsorbent prepared for removal of arsenic from drinking water," *Journal of Colloid and Interface Science*, vol. 284, no. 1, pp. 71–77, 2005.
- [32] M.-F. Li, Y.-G. Liu, G.-M. Zeng, N. Liu, and S.-B. Liu, "Graphene and graphene-based nanocomposites used for antibiotics removal in water treatment: a review," *Chemosphere*, vol. 226, pp. 360–380, 2019.
- [33] S. J. Allen, G. Mckay, and K. Y. H. Khader, "Intraparticle diffusion of a basic dye during adsorption onto sphagnum peat," *Environmental Pollution*, vol. 56, no. 1, pp. 39–50, 1989.
- [34] P. Antonio, K. Iha, and M. E. V. Suárez-Iha, "Kinetic modeling of adsorption of di-2-pyridylketone salicyloylhydrazone on silica gel," *Journal of Colloid and Interface Science*, vol. 307, no. 1, pp. 24–28, 2007.
- [35] G. L. Dotto and L. A. A. Pinto, "Analysis of mass transfer kinetics in the biosorption of synthetic dyes onto *Spirulina platensis* nanoparticles," *Biochemical Engineering Journal*, vol. 68, pp. 85–90, 2012.
- [36] G. L. Dotto, M. L. G. Vieira, V. M. Esquerdo, and L. A. A. Pinto, "Equilibrium and thermodynamics of azo dyes biosorption onto *Spirulina platensis*," *Brazilian Journal of Chemical Engineering*, vol. 30, no. 1, pp. 13–21, 2013.
- [37] N. F. Cardoso, E. C. Lima, B. Royer et al., "Comparison of *Spirulina platensis* microalgae and commercial activated carbon as adsorbents for the removal of Reactive Red 120 dye from aqueous effluents," *Journal of Hazardous Materials*, vol. 241–242, pp. 146–153, 2012.

Research Article

SiO₂/TiO₂ Composite Coating on Light Substrates for Photocatalytic Decontamination of Water

Hana Bíbová,^{1,2} Lenka Hykrdová ,¹ Hiep Hoang ,³ Milan Eliáš,^{1,2} and Jaromír Jirkovský¹

¹Department of Electrochemical Materials, J. Heyrovsky Institute of Physical Chemistry of the CAS, v.v.i., 182 23 Prague 8, Czech Republic

²Faculty of Science, Charles University in Prague, 128 43 Prague 2, Czech Republic

³Vietnam National University of Agriculture, Gia Lam, Hanoi, Vietnam

Correspondence should be addressed to Lenka Hykrdová; lenka.hykrdova@jh-inst.cas.cz and Hiep Hoang; hoanghiep@vnua.edu.vn

Received 15 March 2019; Revised 17 June 2019; Accepted 30 July 2019; Published 22 September 2019

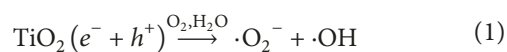
Guest Editor: Ajit Kumar Sharma

Copyright © 2019 Hana Bíbová et al. This is an open access article distributed under the Creative Commons Attribution License, which permits unrestricted use, distribution, and reproduction in any medium, provided the original work is properly cited.

In this study, we describe synthesis and characterization of a floating photocatalyst for water treatment consisting of a light substrate coated by SiO₂/TiO₂ composite. Three supports of natural origin were used: natural cork, expanded clay (Liapor), and volcanic porous glass (Sorbix). The photoactivity of the coated supports was tested in a laboratory photoreactor, with Liapor being the most photoactive support with good mechanical stability. The corresponding rate constant for the degradation of a model pollutant, 4-chlorophenol, was $7.8 \times 10^{-5} \text{ s}^{-1}$. Detail characterization of the coated Liapor was obtained by XRF, SEM/EDX, and UV-Vis diffuse reflectance spectroscopy, and surface area measurements. Outdoor experiments were carried out with calcined Liapor and oxalic acid or methylene blue under sunlight on pilot reactors in the Czech Republic and Vietnam. We demonstrated satisfactory photocatalytic activity, long-term stability, and reusability of the new floating photocatalyst. The photoefficiency to mineralize oxalic acid in water under sunlight was estimated as 6.7% under the applied conditions.

1. Introduction

Procedures for contaminated water treatment are still being developed and optimized. Methods using heterogeneous photocatalysis by TiO₂ represent environmental friendly and economical processes that have been investigated for several decades [1]. They are based on the formation of pairs of charge carriers, electron and hole ($e^- + h^+$), in a semiconductor particle upon interaction with photons of sufficient energy (equation (1) [2]). Hydroxyl groups bound on the semiconductor surface are oxidized by migrating holes to hydroxyl radicals ($\cdot\text{OH}$), oxidizing species powerful to accomplish total mineralization of organic compounds and even of microbes. In the presence of oxygen, electrons are consumed under the formation of superoxide radical anions ($\cdot\text{O}_2^-$).

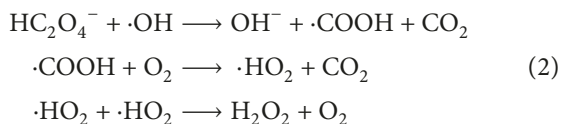


Recently, floating photocatalysts have been increasingly studied due to their advantages, such as easy recovery after the treatment and wide variability of buoyant substrates. Photocatalytic layers were immobilized on various supports, such as graphite [3, 4], perlite [5, 6], vermiculite [7], diatomite powder [8, 9], light-expanded clay aggregate [10, 11], fly ash cenospheres [12–14], palm trunk [15], silica gel beads [16], and others. Besides TiO₂, other metal oxides deposited on a surface were used (e.g., BiVO₄ [14]).

Photocatalytic efficiency of the materials is often tested by means of a model compound degradation. Halogenated hydrocarbons are stable compounds commonly found as water pollutants due to their wide industrial use. They often show low biodegradability and photodegradability. That is why their representatives, such as 4-chlorophenol (4-CP), are selected as model compounds in photocatalytic studies [17–19]. The proposed mechanism of 4-CP degradation initiated by OH radical attack includes reaction pathways

leading both to the formation of hydroxylated benzene derivatives [20] and to the direct opening of aromatic ring [21].

Oxalic acid (OA) represents another model compound, suitable especially for larger scales and pilot experiments. Its oxidation by hydroxyl radical results directly in the formation of carbon dioxide and hydrogen peroxide (equation (2)) [22]. As a model reactant, OA was used in several studies [22–25].

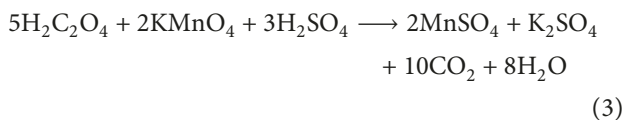


The aim of the presented manuscript is to characterize low-density materials applicable as floating substrates for photocatalytic layers. The required properties of such light supports should include availability, stability, and environmental friendliness. Three different types of supports were selected and used: cork, Liapor, and Sorbix. Photocatalytic efficiency of the supports with immobilized layer of SiO₂/TiO₂ composite was tested both under the laboratory and outdoor conditions, with the use of 4-CP and OA as model pollutants. We accomplished our study by evaluating the photocatalyst performance in a pilot solar reactor.

2. Materials and Methods

4-Chlorophenol (4-CP) (Acros Organics, 99%) was used as a model pollutant in the laboratory-scale experiments. Its concentration was determined by HPLC (Agilent Technology 1200 Series; detection wavelength 254 nm, mobile phase 60 : 40 water/methanol, flow rate 1 mL/min, injection volume 20 μL, column LiChroCART® 125-4 LiChrosphere 100 RP-18 (5 μm)). Prior to injection, the samples were filtered with 0.45 μm HA filter (Millipore). UV-Vis spectra of the irradiated solutions of 4-CP were measured without filtration by spectrophotometer UV/Vis/NIR Lambda 19 (PerkinElmer).

Oxalic acid (g.r., Lachner, 99.6%) was used for the outdoor experiments. Its concentration was determined by manganometric titration with KMnO₄ (Fluka, ≥99.0% p.a.; H₂SO₄ was obtained from Lachner, ≥95% p.a.):



Total organic carbon (TOC) was determined by TOC-Vwp Analyzer (Shimadzu). Prior to injection, the samples were filtered with 0.45 μm HA filter (Millipore).

Methylene blue (MB) (Sigma-Aldrich, 82%) was used as a model compound for the outdoor experiments in Vietnam. Its concentration was measured spectrophotometrically at 665 nm by Spectro UV-2550 (Labomed, Inc.).

Water glass (30% SiO₂, Vodní sklo, a.s.) and TiO₂ P25 (Evonik) were used for the coating of tested floating substrates (experiments in the Czech Republic).

The surface structure and morphology of Liapor and the applied layers were obtained by scanning electron microscopy

coupled with energy dispersive X-ray (SEM/EDX) spectroscopy. SEM Philips XL 30 CP microscope equipped with EDX, Robinson, SE (secondary electron), and BSE (back-scattered electron) detectors were used. Composition of Liapor was measured by X-ray fluorescence (XRF) spectroscopy. The XRF elementary analysis was performed by 4 kW wavelength dispersive X-ray fluorescence spectrometer S4 Pioneer (Bruker AXS) equipped with a rhenium tube operated at 20–60 kV. The samples were prepared and analyzed by the GEO-QUANT method.

Diffuse reflectance spectrum of the SiO₂/TiO₂ composite layer was measured after the deposition of layers (0.5 mL of the solution was spread on the microscopic glass plate; the procedure and concentration of solutions were otherwise kept same as in the case of the coating of supports) by spectrophotometer UV/Vis/NIR Lambda 19 (PerkinElmer) equipped with the integration sphere. The detail procedure of data evaluation is described by Kočí et al. [26].

The BET specific surface area of Liapor and the applied layers was determined from the adsorption isotherms of N₂ at the boiling point of liquid nitrogen using a Micromeritics ASAP 2010 apparatus [27].

Liapor used for the outdoor experiments in Vietnam was coated by the commercially available suspension of photoactive TiO₂ Protectam FN2 according to the procedure recommended by the manufacturer (Advanced Materials-JTJ, Czech Republic). Protectam FN2 is protected by U.S. patent no. 8,647,565 (2009) and consists of about 74% of Aeroxide TiO₂ P25, the remaining part being an inorganic binder.

2.1. Floating Support. In this study, three types of substrates were selected that meet the following criteria: density lower than 1 kg·dm⁻³, large surface area, low cost, easy accessibility, and environmental friendliness (as itself and with regard to possible degradation products) (Figure 1).

As the widely available organic material, raw cork (Korek Jelínek, spol. s.r.o.) was chosen. Inorganic support was represented by expanded volcanic glass perlit “Sorbix” (WB 0/3, Imerys) and expanded clay Liapor (Lias Vintířov). Density and grain size of chosen supports are listed in Table 1.

2.2. Preparation of Coated Floating Substrates. The preparation of the photoactive layers is based on the synthesis of SiO₂/TiO₂ composite described in the utility model [28], modified for the deposition on the studied supports. The synthesis employs general amphoteric properties of solid oxide materials when zero points of charge (pH_{zpc}) of TiO₂ and SiO₂ are different. At the appropriate pH value, TiO₂ particles are dominantly protonated while the particles of SiO₂ are negatively charged. As a result, spontaneous association among them occurs. It was found that colloidal suspensions of such composite are stable in a long-term period.

The coating procedure consisted of the following steps:

1st layer (water glass): cleaned (washed and dried under room temperature) substrates were dipped in the



FIGURE 1: Floating supports (from the left cork, Sorbix, and Liapor) and demonstration of their stability on water surface.

TABLE 1: Properties of the floating substrates.

	Cork	Sorbix	Liapor
Density ($\text{kg}\cdot\text{dm}^{-3}$)	0.15–0.350	0.070	0.25–0.9
Grain size (mm)	0.5–3	<0.125	4–8

suspension of water glass (2 wt.% SiO_2) for 2 hours and then dried at 80°C . This step was performed in order to improve adhesion of the photocatalyst on the support surface.

2nd and 3rd layers (photocatalyst): support with the dried water glass layer was dipped in the suspension of 5 wt.% TiO_2 and 5.99 wt.% SiO_2 for 2 hours and then dried at 80°C .

Liapor samples for the outdoor experiments were further calcined at 250°C for 1 hour (temperature gradient $1^\circ\text{C}/\text{min}$).

The mechanical stability of the deposited layers was tested after washing (5 g) in demineralized water (0.1 dm^3) for 6 hours under stirring, followed by drying at room temperature.

2.3. Photoreactors and the Operating Conditions. Photocatalytic experiments were carried out in the photoreactors of our own design and construction (Figures 2(a) and 2(b)). The laboratory photoreactor (Figure 2(a)) enables to perform series of experiments under the identical conditions, thus reducing random effects. The bottom of the device consists of 6 or 15 magnetic stirrers (Variomag Telesystem) with a cut-out slab to keep the beakers with the tested solutions in constant positions. In the upper part, UV fluorescent lamps are installed that can be switched on/off separately. The inner walls of the photoreactor are covered by the brushed aluminum foil to maximize light reflection and ensure homogeneous irradiation. For the purpose of our study, the photoreactor was equipped with 10 fluorescent black lamps ($\lambda_{\text{max}} = 365 \text{ nm}$, 8 watt, Sylvania), and the flux

density at the probe level was $6.24 \text{ mW}\cdot\text{cm}^{-2}$ measured by UVA probe (ILT 1400-A Photometer, probe UVA #28949).

For the outdoor experiments, solar reactors of a larger scale were used (Figure 2(b)). In the 40 dm^3 plastic basin, the tested solution (25 dm^3) is pumped and circulates through the integrated jet system that causes regular rotation and watering of the floating photocatalyst. The solar reactors were covered by UVA transparent glass sheets ($A_{(300\text{nm})} \leq 0.1$) to prevent evaporation of the tested solution. The weather conditions were monitored by an integrated sensor suite (ISS), the measured data sent to ForVantage Pro2 Plus™ console, and evaluated by WeatherLink software.

During the outdoor experiments in Vietnam, the intensity of the incident sunlight was monitored continuously by quantum meter (Apogee Instruments, Inc.).

The course of photocatalytic degradation of the model compound was formally described by the first-order kinetics. The corresponding rate constants were calculated by a nonlinear curve fitting procedure using the relation $c = c_0 e^{(-kt)}$, where c , t , and k represent concentration of 4-CP, time of irradiation, and rate constant, respectively.

3. Results and Discussion

3.1. Comparison of the Supports. The photoactivity of the supports was monitored by means of 4-CP degradation. Determination of photoactivity of the noncoated substrates was performed with 4-CP ($2 \times 10^{-4} \text{ mol}\cdot\text{dm}^{-3}$, 0.1 dm^3) in the laboratory photoreactor (Figure 2(a)). In the case of Sorbix and Liapor, concentration of 4-CP remains constant during the whole irradiation time, that is, no measurable photoactivity of the floating substrates was found for at least 6 hours under stirring. Cork, on the other hand, releases a small amount of organic matter upon the contact with water. This phenomenon complicates determination of 4-CP concentration due to the high background response detected by UV-Vis spectroscopy and TOC and will be discussed further.

3.2. Photoactivity and Mechanical Stability of the Deposited Layers. The kinetics of 4-CP degradation was followed both by HPLC (Figures 3–5) and by the measurement of the relative change of TOC. Although the former value represents direct decrease of 4-CP concentration resulting from hydroxyl radical attack, the latter reflects mineralization to carbon dioxide that proceeds, due to complex degradation mechanism via various intermediates, much slower.

The course of photocatalytic degradation of 4-CP with coated Sorbix and Liapor follows formally the first-order kinetics (Figures 4 and 5). The values of corresponding rate constants and relative changes of TOC are summarized in Table 2.

In the case of using Sorbix as the floating substrate, the deposition of a stable layer is difficult because of the high hydrophobicity of the support. Low wettability of the prepared floating photocatalyst is thus associated with its low photoactivity (Table 2). At a stirring rate of 200 rpm, negligible degradation of 4-CP is observed and even 500 rpm is not

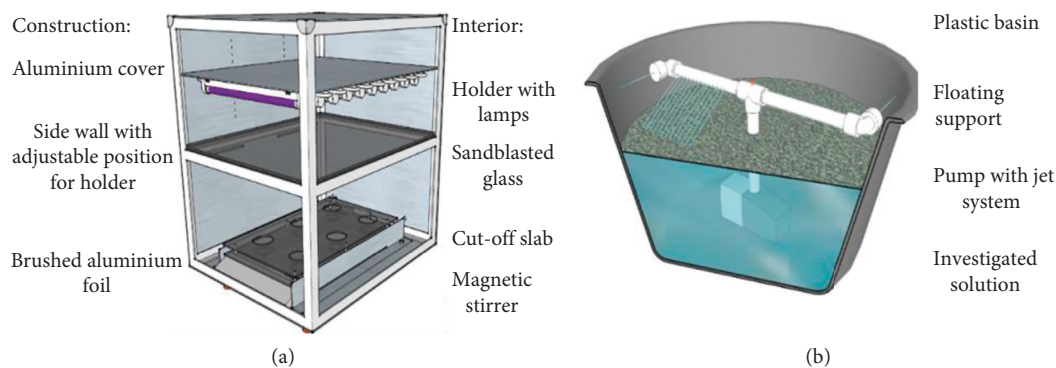


FIGURE 2: Photoreactors of our own design and construction. (a) Laboratory photoreactor. (b) Outdoor photoreactor.

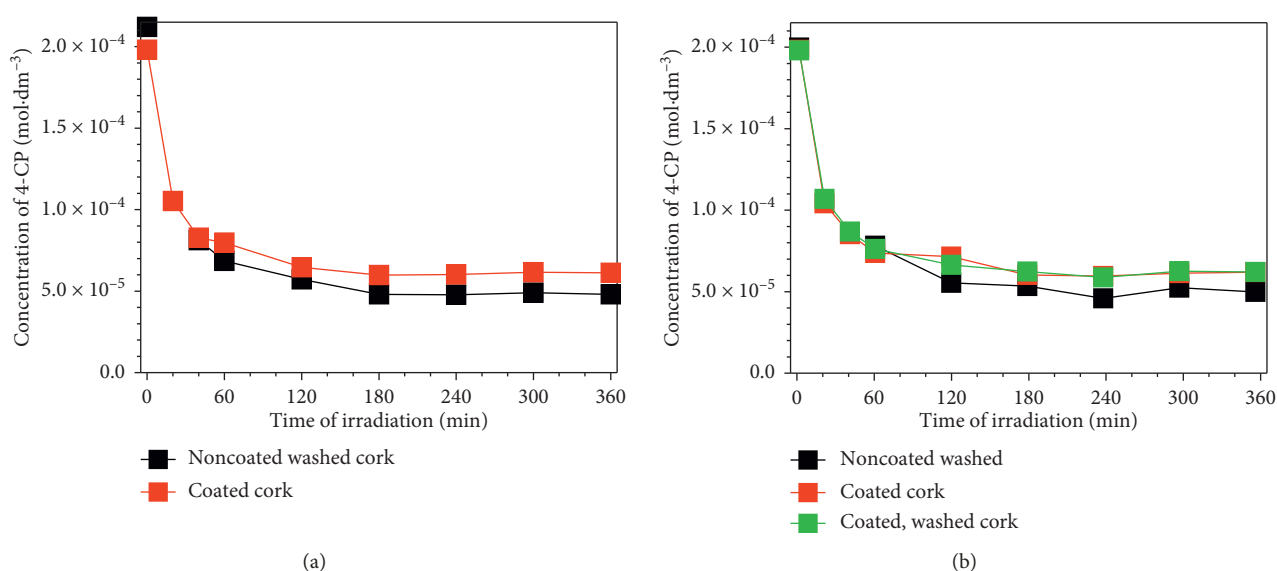


FIGURE 3: (a) Blank—sorption of 4-CP on Noncoated washed cork and coated cork. (b) Photocatalytic degradation of 4-CP (in laboratory photoreactor at a stirring rate of 500 rpm) using noncoated washed, coated, and coated, washed cork.

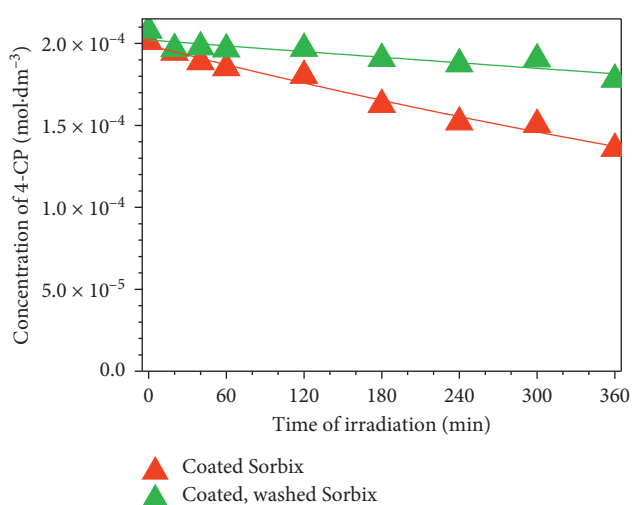


FIGURE 4: Photocatalytic degradation of 4-CP (in laboratory photoreactor at a stirring rate of 500 rpm) using coated Sorbix and coated, washed Sorbix.

sufficient to ensure satisfactory contact with the solution as after 6 hours of the irradiation; the concentration of 4-CP decreased only to 70% of its original value. The mechanical stability of the deposited layer is not satisfactory enough, since by washing, the degradation rate is reduced to one-third and a similar effect is observed in the case of TOC values (Table 2).

The physicochemical properties of Liapor enabled the preparation of a uniform stable layer according to the described procedure (90% of a particle volume was submersed in SiO₂ or SiO₂/TiO₂ aqueous suspensions). The surface of coated Liapor grains is sufficiently wetted during irradiation, and further increase of stirring rate does not alter the course of 4-CP degradation. Neither the adsorption of 4-CP on Liapor particles (both noncoated and coated) nor any other effects that could affect photocatalytic process were observed under the applied laboratory conditions.

The results of 4-CP degradation with coated Liapor are summarized in Table 2. Within 6 hours of the irradiation, concentration of 4-CP decreased approximately to 10% of its original value ($k = 7.80 \times 10^{-5} \text{ s}^{-1}$). Washing has not changed

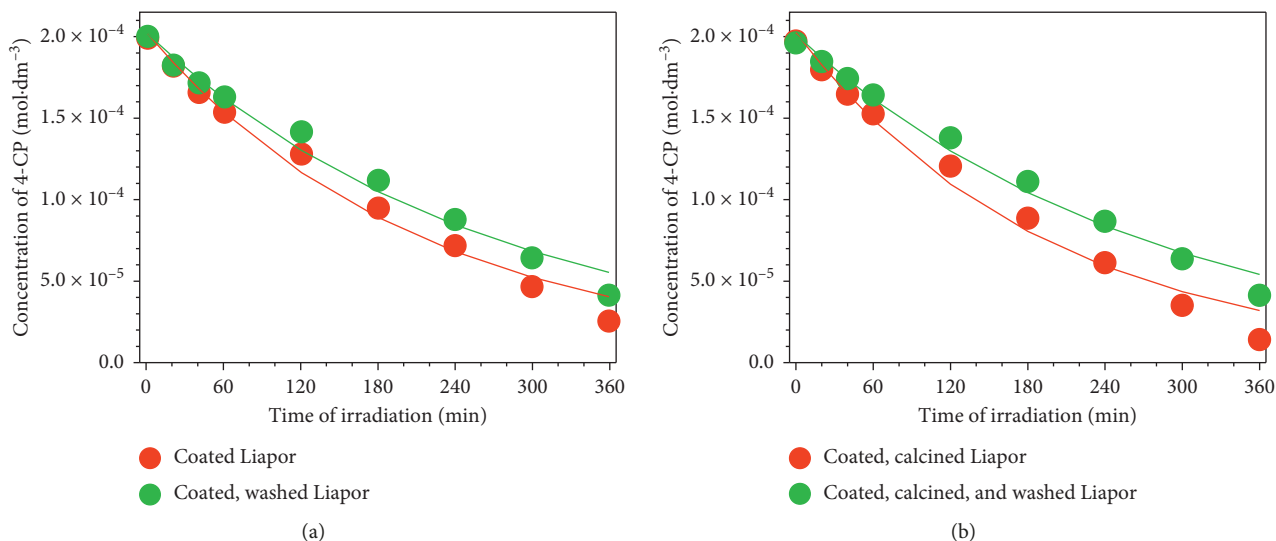


FIGURE 5: Photocatalytic degradation of 4-CP (in laboratory photoreactor at a stirring rate of 500 rpm) using (a) nonwashed and washed Liapor. (b) Calcined, and calcined, washed Liapor.

TABLE 2: Rate constants of 4-CP photocatalytic degradation and relative change of TOC after 6 hours of irradiation.

	Material	Rate constant (10^{-5} s^{-1})	TOC: relative change (%)
Sc	Sorbix: coated	1.72	76.3
Scw	Sorbix: coated and washed	0.50	89.1
Lc	Liapor: coated	7.80	27.0
Lcw	Liapor: coated and washed	6.22	40.1
Lcc	Liapor: coated and calcined	8.53	15.0
Lccw	Liapor: coated, calcined, and washed	6.08	37.2

the photoperformance of coated Liapor markedly (Figure 5(a) and Table 2).

Calcination of coated Liapor at 250°C leads to an increase of 4-CP degradation rate ($8.53 \times 10^{-5} \text{ s}^{-1}$) (Figure 5(b)). After washing, almost the same photoactivity of calcined Liapor and Liapor without the heat treatment is observed ($6.08 \times 10^{-5} \text{ s}^{-1}$). From the comparison of the data in Table 2, it can be concluded that Liapor represents the most appropriate floating substrate for the photocatalyst deposition.

Cork used as a support for the photocatalyst layer shows completely different physicochemical properties. Besides the aforementioned release of an organic matter, marked sorption effects occur when 4-CP is exposed to this floating substrate. Blank experiments without irradiation demonstrate significant adsorption of 4-CP on both noncoated and coated cork (Figure 3(a)). According to the experimental data, sorption processes play dominant role and photocatalytic degradation represents only a minor part under the applied experimental conditions, both before and after washing of the cork substrate (Figure 3(b)). Concentration decrease of 4-CP could not be approximated by the first-order kinetics.

3.3. Characterization of Liapor and the Deposited Layers. Liapor with deposited photocatalyst layer has been further studied in detail. The results of elemental analyses (XRF and EDS) show that this expanded clay consists of silicone oxide

as the main component (41.02%, Table 3), and of aluminum and iron oxides as less abundant components. Titanium dioxide represents approximately 3% of the total oxide content.

Figure 6 shows SEM images of Liapor sample before the deposition of the photoactive layer. Original Liapor has a heterogeneous surface structure (Figure 6(a)). After water glass deposition, fine cracks typical of silicate layer appear on the surface (Figure 6(b)). The coated layer is thin as evidenced by EDS analysis that provides a similar elemental composition for both uncoated and coated samples (Figure 7(a) and Table 4).

Changes of Liapor surface structure due to the particular steps of the photoactive layer preparation, that is, coating and drying (Figure 8(a)), calcination (Figure 8(b)), and washing (Figure 8(c)) were also followed by SEM technique. Observed smooth layer of the photocatalyst copies depressions and protrusions of the support surface. Formed polygons are separated by numerous cracks. Surface mapping scans of samples show that the polygons consist of the deposited photocatalyst with Si, O, and Ti as the main atomic components (Figure 7(b), Table 4) while in the cracks, the original support surface is observed. The composite layers coated on Liapor substrate show high mechanical stability.

The value of bandgap energy was calculated from UV-Vis diffuse reflectance spectrum of the $\text{SiO}_2/\text{TiO}_2$ composite layers deposited on a quartz glass. Original coordinates of

TABLE 3: XRF analysis of Liapor.

Formula	SiO ₂	Al ₂ O ₃	Fe ₂ O ₃	TiO ₂	CaO	K ₂ O	MgO	Others
Concentration (%)	41.02	25.67	12.16	3.334	3.079	2.592	2.072	<0.5

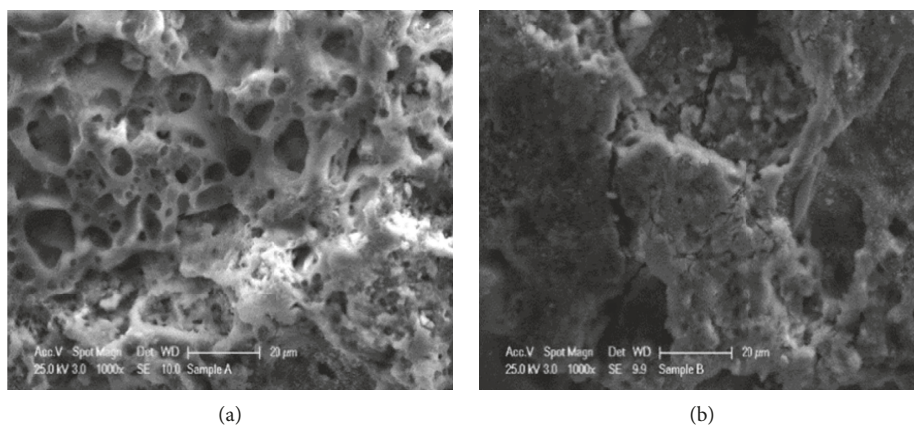
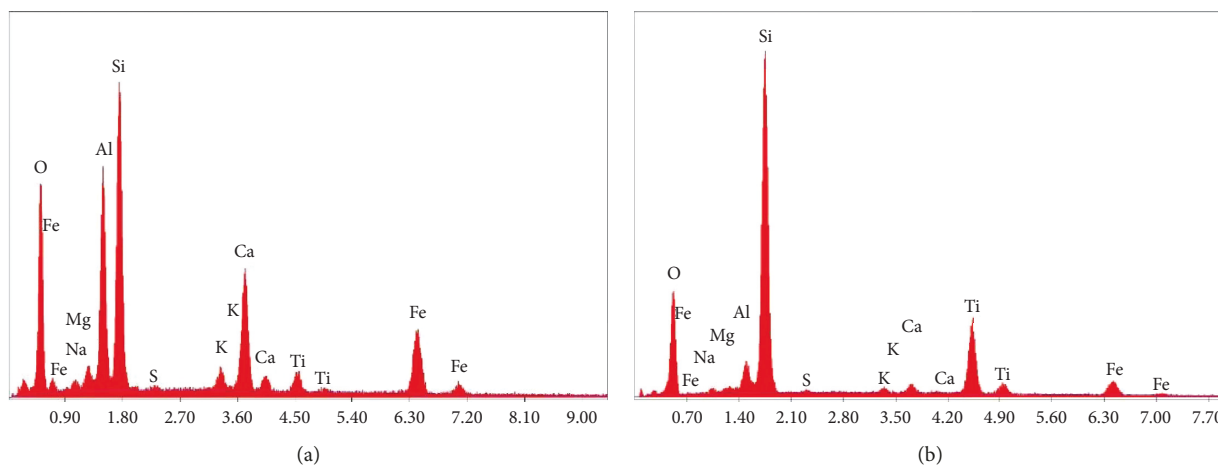
FIGURE 6: SEM images of Liapor. (a) Liapor before coating. (b) Liapor with the first layer of SiO₂.FIGURE 7: EDS analyses of Liapor. (a) Liapor with the SiO₂ layer. (b) Liapor with the first layer of SiO₂ and two composite layers.

TABLE 4: EDS analysis of Liapor.

Element (wt.%)	Liapor	SiO ₂ layer	Composite
O K	41.59	41.59	43.27
Na K	1.14	1.34	1.22
Mg K	2.14	2.08	0.97
Al K	15.13	13.81	3.56
Si K	20.20	19.95	32.54
S K	0.26	0.27	0.34
K K	2.33	1.44	0.63
Ca K	5.41	7.97	1.10
Ti K	1.69	1.76	12.32
Fe K	10.11	9.80	4.04

the spectrum, that is, reflectance vs. wavelength, were transformed to Kubelka–Munk function (K) vs. photon energy ($h\nu$). Bandgap energy is usually estimated by extrapolation of the linear part of the dependence; however, we employed a more precise method based on fitting of the

experimental dependences by Boltzmann symmetrical function using nonlinear regression [26]. Then, the calculated crossing point of the tangent line in the inflection point of the Boltzmann fit with its lower asymptote determines the bandgap energy as 3.04 eV (Figure 9).

The surface area of the support and deposited layers was investigated by the measurement of adsorption isotherms of N₂ at 77 K. While the surface area of Liapor is only 0.15 m²·g⁻¹, a marked increase to 1.2 m²·g⁻¹ is observed after the deposition of SiO₂. Finally, the composite layer shows the largest value, 4.3 m²·g⁻¹. The observed trend suggests that the photocatalyst specific surface area is maintained during its application.

3.4. Outdoor Experiments. The aim of parallel outdoor experiments was to test the photocatalytic activity of coated Liapor under sunlight. The experiments were carried out in the solar reactor depicted in Figure 2(b). Oxalic acid

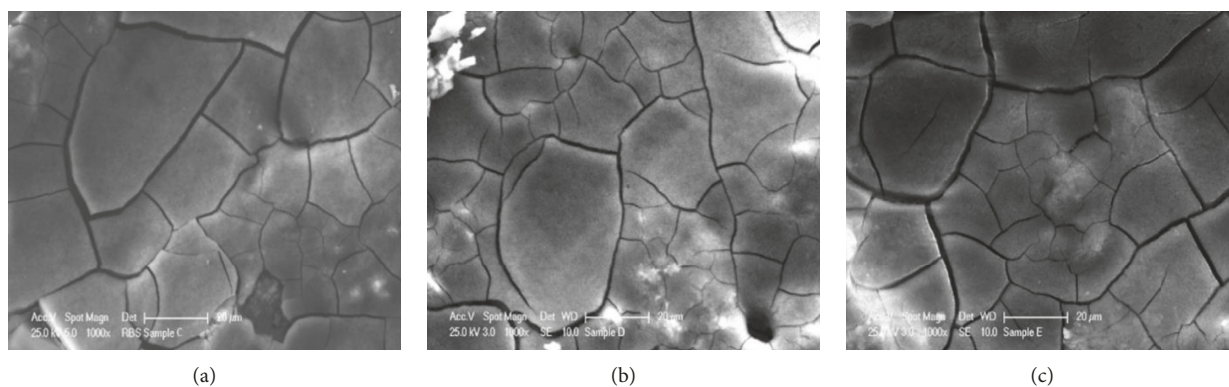


FIGURE 8: SEM images of Liapor coated with SiO₂ layer and two composite layers. (a) Dried at room temperature. (b) Calcined at 300°C. (c) Calcined at 300°C and washed for 6 hours.

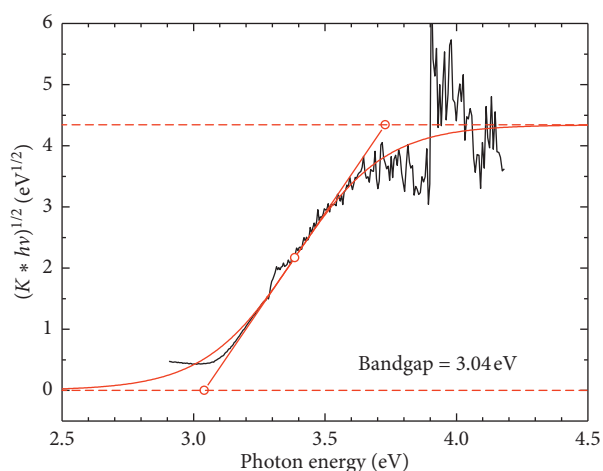


FIGURE 9: Transformed diffuse reflectance spectrum and determination of bandgap energy.

($3.3 \times 10^{-3} \text{ mol} \cdot \text{dm}^{-3}$, 25 dm^3) was chosen as a model compound due to its relative nontoxicity that allows its usage in large amounts. During the irradiation, temperature and UV index were monitored by the ISS probe. It was observed that direct photolysis of OA proceeded in parallel to its photocatalytic degradation, although at a much slower reaction rate. Therefore, the higher amount of the coated support, that is, 200 g (60% of water surface covered) was used in order to reduce the contribution of photolysis to the total photodecomposition.

Concentration changes of OA correlated with the solar radiation intensity (Figure 10(a)). At the end of the fourth day of the irradiation, OA was practically decomposed.

An appropriate initial concentration of OA for the experiments under the applied conditions (200 g of coated support, grain size 4–8 mm) was determined on the basis of another series of experiments (Figure 10(b)). While lower concentrations of OA would be decomposed too fast under sunny weather, high initial concentration would lead to unnecessarily long degradation time.

The size of Liapor grains (1–4 mm, 4–8 mm, and 8–16 mm) was another studied parameter (Figure 11(a)). Small grains (1–4 mm) show a large specific area; however, the

smallest beads of expanded clay tend to immerse, thus resulting in the deceleration of the photocatalytic process. On the other hand, large coated grains (8–16 mm) flow easily on the water surface at the cost of a smaller specific area. Photocatalytic performance of both medium and large support grains is comparable.

The stability of the floating photocatalyst was tested by its repeated use under the otherwise same conditions (Figure 11(b)). No significant changes of the photocatalytic performance after one or two experimental cycles compared with the freshly prepared sample (200 g, grain size 4–8 mm) were observed. This fact signifies good stability and durability of the layer deposited on the Liapor substrate, a parameter important for the practical use of any photocatalyst.

3.5. Pilot Experiments in the Czech Republic and in Vietnam.

To study the performance of the floating photocatalyst in a scale corresponding to its intended use, pilot experiments were performed. The solar reactor in the Czech Republic (Figure 12(a)) was designed to simulate the remediation of contaminated water in rural areas, for example, in the wells that were left after the bomb attacks during the Vietnam War. It consists of the round plastic pool ($V=7 \text{ m}^3$) equipped with a jet system, pump, and filter. The floating photocatalyst (coated, calcined Liapor) covered almost all water surface and was sprinkled by the jet system. As a model compound, oxalic acid (OA; $3.3 \times 10^{-3} \text{ mol} \cdot \text{dm}^{-3}$) was chosen, and instead of distilled water, ordinary tap water was used. This fact shows the importance of such type of experiments, as some cations present in water (Ca^{2+} , Mg^{2+} , and Fe^{3+}) tend to precipitate as insoluble oxalates. Therefore, these cations were initially removed from the solution by a sufficient excess of OA and subsequent filtration. It was found by EDX analysis that the precipitate contained predominantly Fe(III), indicating the presence of iron ions in the used tap water.

A typical course of the pilot solar experiment with OA in the presence of the floating photocatalyst is shown in Figure 12(b). Stepwise decrease of OA concentration, determined by both manganometric titration and TOC analysis, corresponds well to the day and night period. After

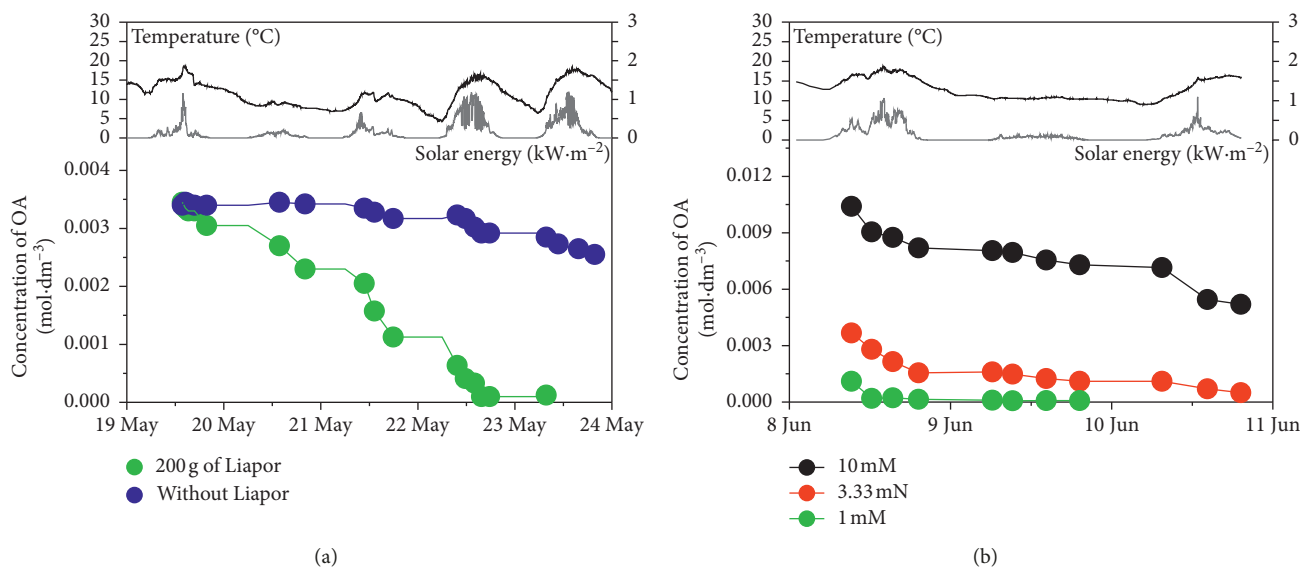


FIGURE 10: Photocatalytic degradation of OA. (a) Without (photolysis) and with coated, calcined Liapor. (b) Influence of OA concentration with coated, calcined Liapor, grain size 4–8 mm.

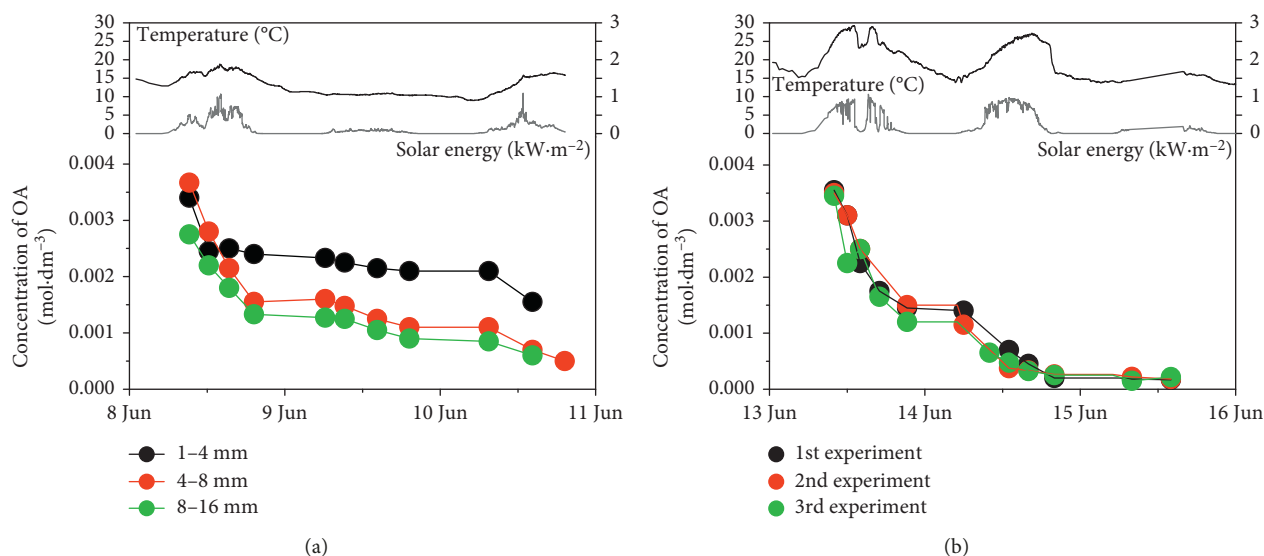


FIGURE 11: Photocatalytic degradation of OA with coated, calcined Liapor. (a) Different grain sizes (1–4 mm, 4–8 mm, and 8–16 mm). (b) Used for the first, second, and third time.

four days of irradiation, no detectable amount of OA remained in the solution and TOC dropped to 11.9% of its original value.

Comparative solar experiments were carried out in Vietnam, employing a special set of batch photoreactors (Figure 13(a)). The device consists of six glass compartments (50 dm³ each) equipped with aeration, stirring, and a system preventing evaporation. About 2 cm below the solution level, metal plates are placed to prevent immersion of the floating photocatalyst. A typical daily course of solar radiation intensity is shown in the inset of Figure 13(b).

The floating photocatalyst was prepared by coating an expanded clay (analogous to the Liapor) with commercially

available TiO₂ suspension with inorganic additives (Protectam FN2). Two grain sizes of the floating support were tested (5 mm and 10 mm).

As a model compound, methylene blue (MB, 3.3×10^{-6} mol·dm⁻³) was used. Two hours before exposing to solar radiation, the tested solution and floating photocatalyst were left in dark to equilibrate adsorption of MB on the photocatalyst surface. Besides adsorption of MB on the photocatalyst surface, no other interaction was observed. Figure 13(b) shows time dependence of MB concentration during 6 days of solar irradiation. The decrease reflects photocatalytic degradation, in contrast to the overnight periods and the blank experiment, during which MB

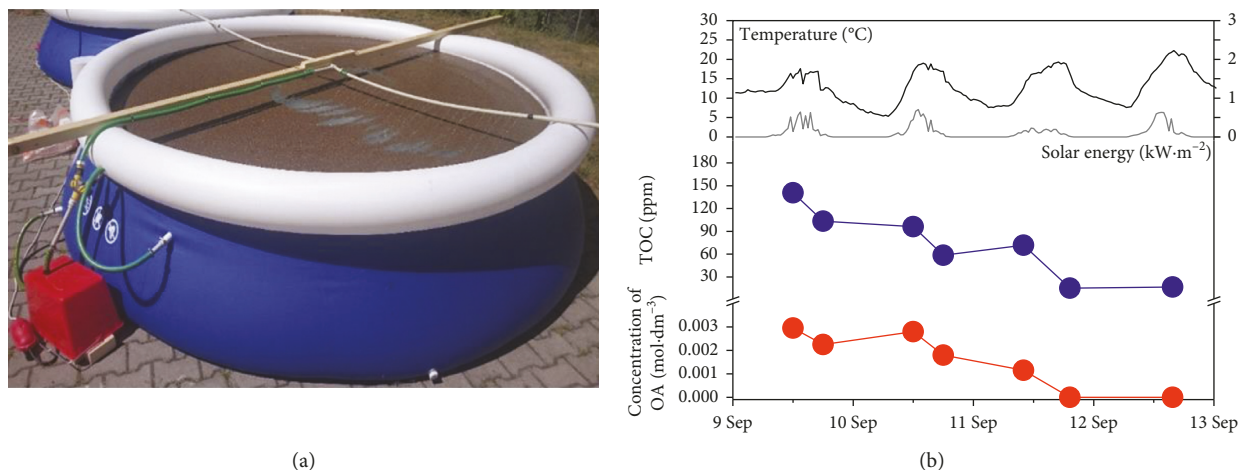


FIGURE 12: Pilot experiments in the Czech Republic. (a) Solar reactor with coated Liapor. (b) Photocatalytic degradation of OA during 4 days of solar irradiation.

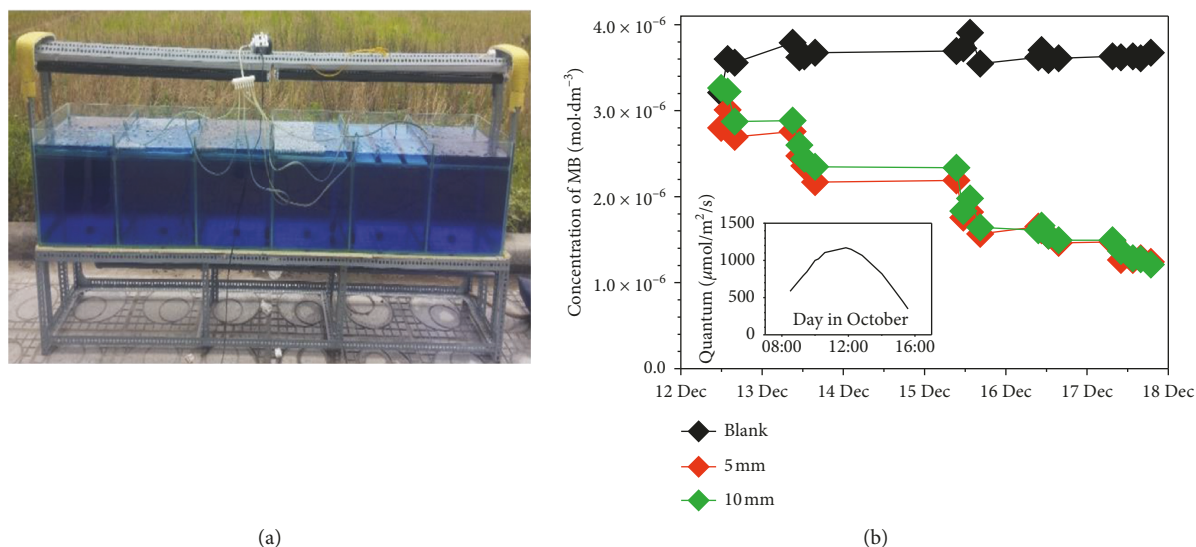


FIGURE 13: Pilot experiments in Vietnam. (a) Set of solar reactors with floating photocatalyst. (b) Photocatalytic degradation of MB during 6 days of solar irradiation.

concentration remained stable. The size of photocatalyst particles did not affect significantly the overall course of the photocatalytic degradation.

3.6. Estimation of the Photocatalyst Performance under Real Environmental Conditions. The intensity of solar radiation was measured and integrated during the whole period of outdoor experiments with oxalic acid. Thus, for example, in the case of the three-day experiment in the batch photo-reactor (Figure 11(b)), the integrated solar radiation reached 13.38 kWh·m⁻², of which 5%, that is, 0.669 kWh·m⁻², represents UVA radiation available for TiO₂ photocatalysis. Considering, for simplification, UVA photons of a “middle” wavelength 380 nm, the value of 0.669 kWh·m⁻² would correspond to 7.62 mol·m⁻² of incident photons in three days (for detail calculation, see Supplementary Material

(available here)). Applied to the parameters of our outdoor solar reactor and assuming the observed decrease of OA concentration, 0.082 moles of OA were mineralized by 1.23 moles of photons, which corresponds to a quantum efficiency 6.67%. This relatively high value might be partially attributed to a strong adsorption of OA on the photocatalyst surface that could cause its efficient oxidation by direct charge transfer mechanism.

The general capacity of the solar photocatalytic treatment of water can be approximately quantified. Provided that the mineralization of one organic carbon atom may require, on average, two subsequent photo-induced oxidative steps, then under the weather conditions typical of the central Vietnam (5.0 kWh·m⁻²·day⁻¹, [29]), up to 0.095 moles of harmful organics can be mineralized by floating photocatalyst (e.g., Liapor with SiO₂/TiO₂ composite coating) covering area of 1 m² of contaminated water

in 1 day, using quantum efficiency calculated above. For a depth of 1 m and the corresponding volume of 1 m^3 , the TOC content of contaminated water would thus be reduced by 1.14 ppm in one sunny day.

This is a promising result implying that solar photocatalysis can represent a method capable to decontaminate not only small water contents in the laboratory scale but also larger surface water amounts intended for cattle watering, fish breeding, etc. Hardly degradable toxic compounds presented in water at extremely low concentrations (such as 2,3,7,8-tetrachlorodioxin and DDT) can thus be successfully mineralized in order of days to weeks.

4. Conclusions

- (i) Photocatalytic performance of $\text{SiO}_2/\text{TiO}_2$ composite deposited on three different floating substrates was tested by means of 4-CP photodegradation
- (ii) Liapor with deposited $\text{SiO}_2/\text{TiO}_2$ composite showed high photoactivity and long-term durability
- (iii) Coated Sorbix was less photoactive due to its high hydrophobicity
- (iv) Cork was experimentally found as a less suitable support due to its strong adsorption properties and release of soluble organic matter
- (v) $\text{SiO}_2/\text{TiO}_2$ composite layer on Liapor was characterized in detail, including atomic composition and surface microscopic images corresponding to each step of the deposition process
- (vi) Pilot solar experiments demonstrated high efficiency, durability, and the ease of use of the new floating photocatalyst necessary for water decontamination
- (vii) The efficiency of the new floating photocatalyst to mineralize organic matter in real contaminated surface water under sunlight was estimated

Data Availability

The data used to support the findings of this study are available from the corresponding authors upon request.

Conflicts of Interest

The authors declare that there are no conflicts of interest regarding the publication of this paper.

Acknowledgments

The authors acknowledge the assistance provided by the Research Infrastructure NanoEnviCz, supported by the Ministry of Education, Youth and Sports of the Czech Republic under Project no. LM2015073. This work was supported by the FIRST project, Subcomponent 1a—Foreign Talents STI Grants (no. 29/FIRST/1a/VNUA), the European Commission's Seventh Framework Programme (FP7) for Research and Technological Development (4G-PHOTO-CAT, 309636), and Project AS CR (VAST-16-05). The

authors would like to thank Dr. Jan Šubrt for SEM-EDS measurements and Dr. Michal Kolář for XRF analyses.

Supplementary Materials

Supplementary Material file contains a calculation procedure for determining the photocatalyst efficiency. (*Supplementary Materials*)

References

- [1] S.-I. Kato and F. Mashio, "Titanium dioxide-photocatalyzed liquid phase oxidation of tetralin," *The Journal of the Society of Chemical Industry, Japan*, vol. 67, no. 8, pp. 1136–1140, 1964.
- [2] O. Legrini, E. Oliveros, and A. M. Braun, "Photochemical processes for water treatment," *Chemical Reviews*, vol. 93, no. 2, pp. 671–698, 1993.
- [3] X. Wang, X. Wang, J. Zhao et al., "An alternative to in situ photocatalytic degradation of microcystin-LR by worm-like N, P co-doped TiO_2 /expanded graphite by carbon layer (NPT-EGC) floating composites," *Applied Catalysis B: Environmental*, vol. 206, pp. 479–489, 2017.
- [4] A. Modestov, V. Glezer, I. Marjasin, and O. Lev, "Photocatalytic degradation of chlorinated phenoxyacetic acids by a new buoyant titania-exfoliated graphite composite photocatalyst," *The Journal of Physical Chemistry B*, vol. 101, no. 23, pp. 4623–4629, 1997.
- [5] H. Joolaei, M. Vossoughi, A. Rashidi Mehr Abadi, and A. Heravi, "Removal of humic acid from aqueous solution using photocatalytic reaction on perlite granules covered by Nano TiO_2 particles," *Journal of Molecular Liquids*, vol. 242, pp. 357–363, 2017.
- [6] Y. Shavisi, S. Sharifnia, S. N. Hosseini, and M. A. Khadivi, "Application of TiO_2 /perlite photocatalysis for degradation of ammonia in wastewater," *Journal of Industrial and Engineering Chemistry*, vol. 20, no. 1, pp. 278–283, 2014.
- [7] L. Jin and B. Dai, " TiO_2 activation using acid-treated vermiculite as a support: characteristics and photoreactivity," *Applied Surface Science*, vol. 258, no. 8, pp. 3386–3392, 2012.
- [8] R. Cherrak, M. Hadjel, N. Benderdouche, S. Bellayer, and M. Traisnel, "Treatment of recalcitrant organic pollutants in water by heterogeneous catalysis using a mixed material (TiO_2 -diatomite of Algeria)," *Desalination and Water Treatment*, vol. 57, no. 36, pp. 17139–17148, 2016.
- [9] R. Zuo, G. Du, W. Zhang et al., "Photocatalytic degradation of methylene blue using TiO_2 impregnated diatomite," *Advances in Materials Sciences and Engineering*, vol. 2014, Article ID 170148, 7 pages, 2014.
- [10] A. Mishra, A. Mehta, and S. Basu, "Clay supported TiO_2 nanoparticles for photocatalytic degradation of environmental pollutants: a review," *Journal of Environmental Chemical Engineering*, vol. 6, no. 5, pp. 6088–6107, 2018.
- [11] Y. Shavisi, S. Sharifnia, M. Zendezhaban, M. L. Mirghavami, and S. Kakehazar, "Application of solar light for degradation of ammonia in petrochemical wastewater by a floating TiO_2 /LECA photocatalyst," *Journal of Industrial and Engineering Chemistry*, vol. 20, no. 5, pp. 2806–2813, 2014.
- [12] J. Song, X. Wang, Y. Bu et al., "Photocatalytic enhancement of floating photocatalyst: layer-by-layer hybrid carbonized chitosan and Fe-N-codoped TiO_2 on fly ash cenospheres," *Applied Surface Science*, vol. 391, pp. 236–250, 2017.
- [13] J. Song, X. Wang, Y. Bu et al., "Preparation, characterization, and photocatalytic activity evaluation of Fe-N-codoped TiO_2 /fly

- ash cenospheres floating photocatalyst,” *Environmental Science and Pollution Research*, vol. 23, no. 22, pp. 22793–22802, 2016.
- [14] J. Zhang, H. Cui, B. Wang, C. Li, J. Zhai, and Q. Li, “Fly ash cenospheres supported visible-light-driven BiVO₄ photocatalyst: synthesis, characterization and photocatalytic application,” *Chemical Engineering Journal*, vol. 223, pp. 737–746, 2013.
- [15] M. Sboui, M. F. Nsib, A. Rayes, T. Ochiai, and A. Houas, “Application of solar light for photocatalytic degradation of Congo red by a floating salicylic acid-modified TiO₂/palm trunk photocatalyst,” *Comptes Rendus Chimie*, vol. 20, no. 2, pp. 181–189, 2017.
- [16] H. Taoda, “Development of TiO₂ photocatalysts suitable for practical use and their applications in environmental cleanup,” *Research on Chemical Intermediates*, vol. 34, no. 4, pp. 417–426, 2008.
- [17] M. Barbeni, E. Pramauro, E. Pelizzetti, E. Borgarello, M. Grätzel, and N. Serpone, “Photodegradation of 4-chlorophenol catalyzed by titanium dioxide particles,” *Nouveau Journal de Chimie*, vol. 8, pp. 547–550, 1984.
- [18] G. Shang, H. Fu, S. Yang, and T. Xu, “Mechanistic study of visible-light-induced photodegradation of 4-chlorophenol by TiO_{2-x}N_x with low nitrogen concentration,” *International Journal of Photoenergy*, vol. 2012, Article ID 759306, 9 pages, 2012.
- [19] B. Palanisamy, C. M. Babu, B. Sundaravel, S. Anandan, and V. Murugesan, “Visible-light active mesoporous ce incorporated TiO₂ for the degradation of 4-chlorophenol in aqueous solution,” *Journal of Nanoscience and Nanotechnology*, vol. 13, no. 4, pp. 2572–2581, 2013.
- [20] J. Theurich, M. Lindner, and D. W. Bahnemann, “Photocatalytic degradation of 4-chlorophenol in aerated aqueous titanium dioxide suspensions: a kinetic and mechanistic study,” *Langmuir*, vol. 12, no. 26, pp. 6368–6376, 1996.
- [21] V.-M. Guérin, R. Zouzelka, H. Bibova-Lipsova, J. Jirkovsky, J. Rathousky, and T. Pauporté, “Experimental and DFT study of the degradation of 4-chlorophenol on hierarchical micro-/ nanostructured oxide films,” *Applied Catalysis B: Environmental*, vol. 168–169, pp. 132–140, 2015.
- [22] M. M. Kosanić, “Photocatalytic degradation of oxalic acid over TiO₂ power,” *Journal of Photochemistry and Photobiology A: Chemistry*, vol. 119, no. 2, pp. 119–122, 1998.
- [23] D. Tomova, V. Iliev, A. Eliyas, and S. Rakovsky, “Promoting the oxidative removal rate of oxalic acid on gold-doped CeO₂/TiO₂ photocatalysts under UV and visible light irradiation,” *Separation and Purification Technology*, vol. 156, pp. 715–723, 2015.
- [24] N. Barka, M. Abdennouri, A. Boussaoud et al., “Full factorial experimental design applied to oxalic acid photocatalytic degradation in TiO₂ aqueous suspension,” *Arabian Journal of Chemistry*, vol. 7, no. 5, pp. 752–757, 2014.
- [25] D. Santoro, F. Crapulli, A. Turolla, and M. Antonelli, “Detailed modeling of oxalic acid degradation by UV-TiO₂ nanoparticles: importance of light scattering and photoreactor scale-up,” *Water Research*, vol. 121, pp. 361–373, 2017.
- [26] K. Kočí, L. Obalová, L. Matějová et al., “Effect of TiO₂ particle size on the photocatalytic reduction of CO₂,” *Applied Catalysis B: Environmental*, vol. 89, no. 3–4, pp. 494–502, 2009.
- [27] T. Pauporte and J. Rathousky, “Growth mechanism and photocatalytic properties for dye degradation of hydrophobic mesoporous ZnO/SDS films prepared by electrodeposition, microporous and mesoporous,” *Microporous and Mesoporous Materials*, vol. 117, no. 1–2, pp. 380–385, 2009.
- [28] J. Jirkovský, F. Peterka, J. Šubrt, and M. Lambrecht, “Colloidal photo-catalytic composition,” U. S. Patent US2013019684 5A1, 2013, <https://patents.google.com/patent/US20130196845A1/es>.
- [29] <https://www.pveducation.org/pvcdrom/properties-of-sunlight/average-solar-radiation>.

Research Article

Synergistic Adsorption and Photocatalytic Activity under Visible Irradiation Using Ag-ZnO/GO Nanoparticles Derived at Low Temperature

Viet Ha Tran Thi ¹, The Ha Cao ^{1,2}, Tri Nhut Pham ^{3,4}, Tien Thanh Pham ⁵,
and Manh Cuong Le ⁶

¹Master's Program in Environmental Engineering, Vietnam Japan University, Hanoi, Vietnam

²Center for Environmental Technology and Sustainable Development (CETASD), Hanoi, Vietnam

³Center of Excellence for Green Energy and Environmental Nanomaterials, Nguyen Tat Thanh University, Ho Chi Minh City, Vietnam

⁴NTT Hi-Tech Institute, Nguyen Tat Thanh University, Ho Chi Minh City, Vietnam

⁵Master's Program in Nano Technology, Vietnam Japan University, Hanoi, Vietnam

⁶Department of Building Materials, National University of Civil Engineering, Hanoi, Vietnam

Correspondence should be addressed to Viet Ha Tran Thi; ttv.ha@vju.ac.vn

Received 7 March 2019; Revised 30 May 2019; Accepted 27 June 2019; Published 18 September 2019

Guest Editor: Nguyen Van Noi

Copyright © 2019 Viet Ha Tran Thi et al. This is an open access article distributed under the Creative Commons Attribution License, which permits unrestricted use, distribution, and reproduction in any medium, provided the original work is properly cited.

Ag-ZnO/graphene oxide (AG-ZnO/GO) nanocomposite was synthesized via facile aqueous solution reactions at low temperature in order to improve the photocatalytic activity for cationic dye removal under visible light irradiation. Analytical techniques were carried out in order to determine the abilities including structure, state of elements, morphology, and surface area of synthesized materials. Ag-ZnO/GO nanocomposite presented an extremely high removal rate of methylene blue (MB) not only under UV light (over 99% removal) but also under visible light (85% removal) during the same irradiation time. In this study, initial process parameters of catalyst dosage, MB concentration, and pH of the solution were also examined for MB removal efficiency effects. The proposed mechanisms for the increased removal of MB by Ag-ZnO/GO nanocomposite under visible irradiation include increased photocatalytic degradation, mainly due to increased charge transfer capacity by lowering band gap energy; minimized recombination of the excited electron-hole pairs of ZnO with the addition of Ag into the ZnO crystal lattice; and an increased adsorption capacity with the addition of GO with high surface area and semiconductor function with zero band gap energy.

1. Introduction

Developing semiconductor photocatalysts has been considered a promising green technology for solving environmental issues. Among various semiconductors, zinc oxide (ZnO) has been considered one of the most promising photocatalysts because of its outstanding properties, such as physical and chemical stability, low cost, and nontoxicity. Thus, ZnO has been widely used for many different applications such as in optical materials, sensors, solar energy conversion devices, and photocatalysts for pollutant treatment. ZnO also has

several advantages over TiO₂—the most popular photocatalyst [1], which includes higher thermal stability and easier and less expensive synthesis [2]. However, the photocatalytic performance of ZnO is reduced because of its wide band gap (theoretical ~ 3.2 eV at room temperature) [3] and high recombination rate between photogenerated electrons from the conduction band (CB) and holes from the valence band (VB) [4]. Such a noble metal modification can also influence the surface properties, in particular, by introducing hydroxyl groups on the surface of the photocatalysts [5–7]. However, these modifications require calcination at high temperature

(400–600°C) and the consequent need for strict control which hinders large-scale production.

Graphene sheets possess a unique two-dimensional layered structure of sp^2 -hybridized carbon atoms, and thus, they can exhibit novel electronic properties as zero band gap semiconductors. Ahmad et al. synthesized graphene-Ag/ZnO nanocomposite via a solvothermal method [8]. However, it is not easy to synthesize due to high levels of impurities with graphene; thus, oxidized forms are usually used as a substitute for graphene in many research studies. In addition, graphene oxide (GO) provides a large scaffold for anchoring various substances owing to its large specific surface area [9] and two-dimensional planar conjugated structure. For example, GO bonding with TiO_2 or WO_3 composites has been widely investigated [10, 11]. Moreover, GO-based photocatalysts can avoid the aggregation of nanoparticles anchored on graphene sheets, which can provide more reactive sites for the photocatalytic degradation process. For instance, Nasrollahzadeh et al. reported on the synthesis and use of graphene oxide/ZnO nanocomposite as a heterogeneous catalyst for the synthesis of various tetrazoles [12]. Easy separation of the GO-based photocatalysts used for organic removal from water systems offers other benefits for repeated catalyst use and wide industrial applications [13, 14]. However, most of the derived nanoparticles need to be calcinated at high temperature; thus, GO can form reduced GO (rGO) or other forms of GO. Raj Pant et al. synthesized Ag-ZnO/rGO nanocomposite in an autoclave at 140°C [15], and Gao et al. synthesized sulfonated graphene oxide-ZnO-Ag photocatalyst at 300°C [13]. Only limited reports are available for different fabrication methods of Ag-ZnO/GO to treat organic pollutants under UV light [16].

Herein, we report a novel fabrication method of Ag-ZnO/GO nanocomposite and its characterizations, and then apply it for use in effective removal of the cationic dye methylene blue (MB) in an aqueous solution. This study also aims to save energy and costs by using a novel synthesis method at low temperature, with visible lamps rather than UV lamps as the light source of the photocatalytic process. A suitable photocatalytic degradation mechanism for enhanced MB removal was also proposed.

2. Materials and Methods

2.1. Preparation of Photocatalysts. Sodium hydroxide (NaOH), silver nitrate ($AgNO_3$), zinc sulfate heptahydrate ($ZnSO_4 \cdot 7H_2O$), ascorbic acid ($C_6H_6O_6$), and MB ($C_{16}H_{18}N_3S$) were purchased from DaeJung Chemicals & Metals Co., Ltd., Korea. GO was purchased from Sigma-Aldrich Co LLC. All purchased chemicals were used without any further purification. Distilled water was used for experiments.

ZnO nanoparticles were prepared by dropwise addition of 25 mL of NaOH 0.4 mol/L into 25 mL of $ZnSO_4$ 0.2 mol/L at an approximate addition rate of 5 mL/min. After stirring with a magnetic stirrer (GLHPS-G, Global Lab., Ltd.) at a speed of 150 rpm for 60 min, the solution was kept at 60°C for 2 h.

The Ag-ZnO composite nanoparticles were prepared by adding 6 mL of ascorbic acid 0.01 mol/L and 13 mL of $AgNO_3$ 0.01 mol/L into the solution of NaOH and $ZnSO_4$, while stirring under the same condition as in the first experiment, and again the solution was kept at 70°C for 2 h.

For the preparation of Ag-ZnO/GO, the steps of the Ag-ZnO synthesis procedure were repeated. At the same time, 50 mg of GO was mixed into 50 mL water in an ultrasonicator (D250H, DAIHAN Scientific, Co., Ltd.) for 30 min at room temperature. The two solutions were then mixed, and the final solution obtained was kept at 70°C for 2 h. In the last step, the synthesized products were centrifuged and washed with deionized water several times and dried in a vacuum at 70°C for 24 h.

2.2. Characterization. The synthesized reaction products were characterized by X-ray diffraction (XRD; Bruker AXS D8 ADVANCE) to identify the structure and phase composition. Wide-angle patterns were recorded from $2\theta = 10^\circ$ to 80° using a step size of 0.1° . Their surface morphologies and microstructures were examined using field emission scanning electron microscopy (FE-SEM; JEOL, JSM-6500F, 10 kV) and transmission electron microscopy (TEM; JEOL, JEM-2100F). Composition mapping of the major elements on the material surface was carried out using energy dispersive X-ray spectroscopy (EDS; JEOL, JSM-6500F). The surface compositions and chemical states were measured by using X-ray photoelectron spectroscopy (XPS; Thermo Fisher Scientific, ESCALAB 250XI). The specific surface areas of the compounds were determined by the Brunauer–Emmett–Teller (BET) method using nitrogen gas adsorption. Room temperature photoluminescence (PL) spectra were recorded using a fluorescence spectrometer.

The visible light absorption of the synthesized products was measured in the range of 400 to 800 nm using a UV-Vis spectrophotometer (GENESYS™ 10S UV-Vis., USA) with integrating sphere accessories. To plot the calibration curve of MB dye, aqueous dye solutions were prepared at a concentration ranging from 1 to 25 mg/L by using distilled water. The concentrations of the MB solutions were determined using the obtained calibration curve. The dye removal efficiency was calculated based on following equation:

$$\text{Removal efficiency (\%)} = \frac{C_0 - C}{C_0} \times 100\%, \quad (1)$$

where C_0 (mg/L) is the concentration of the MB solution at the initial time $t = 0$ (min) and C (mg/L) is the concentration after the treatment reaction in a dark condition or after UV-visible light irradiation.

2.3. Photocatalytic Activity Measurement. The photocatalytic activity of the synthesized materials was estimated by using an illumination system consisting of five lamps [visible lamp (EFTR 20EX-D, Kumho Co., Ltd., Republic of Korea)/UV lamp (AL-2220D1 20W, Alim Co., Ltd, the Republic of Korea)] as irradiation sources. In a typical process, 20 mg of the synthesized photocatalyst was suspended in 20 mL of MB

with a concentration of 15 mg/L in a cylindrical glass reactor. Before starting the photocatalytic reaction, the suspension was stirred for 30 min in a dark condition to obtain an adsorption/desorption equilibrium between the dye and the photocatalyst. Photocatalytic reactions were carried out under a stable condition (stirring speed of 80 rpm at intervals of 3 h under light irradiation).

To clarify the dominant radical or ion on the photocatalysis reaction, the experiments using different radical scavengers were performed. Scavengers including *tert*-butyl alcohol, benzoquinone, ammonium oxalate, and $K_2S_2O_8$ were used for OH^\bullet , O_2^\bullet , holes and electrons, respectively. The experiment was carried out similar to the removal experiment with the added radical scavenger (0.1 mmol).

3. Results and Discussions

3.1. Characterization of Material

3.1.1. XRD Pattern Analysis. Figure 1 showed the XRD patterns of the ZnO and Ag-ZnO/GO samples. The Ag-ZnO/GO spectrum included a diffraction peak at $2\theta = 11.5^\circ$ of pristine GO [17, 18], indicating that the major form of graphene in the synthesized material was GO. In both ZnO and Ag-ZnO/GO spectra, the observed diffraction peaks at $2\theta = 32, 34,$ and 36° confirmed the presence of the hexagonal wurtzite structure of ZnO. In general, the intensity of the diffraction peaks decreases greatly with the increase in doping concentration [19]. Thus, it can be observed that the peak intensity of ZnO in the Ag-ZnO/GO sample was decreased as compared with that of the ZnO sample. Besides, the XRD pattern of Ag-ZnO/GO mainly showed a small silver peak at $2\theta = 38^\circ$ [20–22], and this confirmed the doping activity of Ag onto the structure of ZnO. Simultaneously, a small amount of Ag entered the ZnO crystal structure, as confirmed by the broadening at $2\theta = 32, 34,$ and 36° in the Ag-ZnO/GO peaks compared to ZnO peaks [23, 24]. The value of full width at half maximum (FWHM) of diffraction peak is showed on Table 1.

3.1.2. Morphology and Microstructure by SEM and TEM Analysis. FE-SEM and TEM analyses were used to identify the morphology and microstructure of the synthesized materials. The SEM images of ZnO before addition of Ag and GO exhibited high degree of uniformity in the nanosized ZnO particles (Figures 2(a) and 2(b)). When GO was introduced into the composites, numerous Ag-ZnO nanoparticles were deposited on the GO sheets (Figures 2(c) and 2(d)). In the Ag-ZnO/GO heterostructure, GO sheets were consistently decorated with Ag and ZnO nanoparticles. TEM images revealed a hexagonal shape for ZnO (Figure 2(e)) with a diameter 50–60 nm, which is in good agreement with the diameter of ZnO revealed in SEM images. Figure 2(f) shows the TEM image of Ag-ZnO/GO composite, demonstrating the attendance of few-layered GO sheets decorated with Ag and ZnO particles which may result in better adsorption capacity and electron-hole separation.

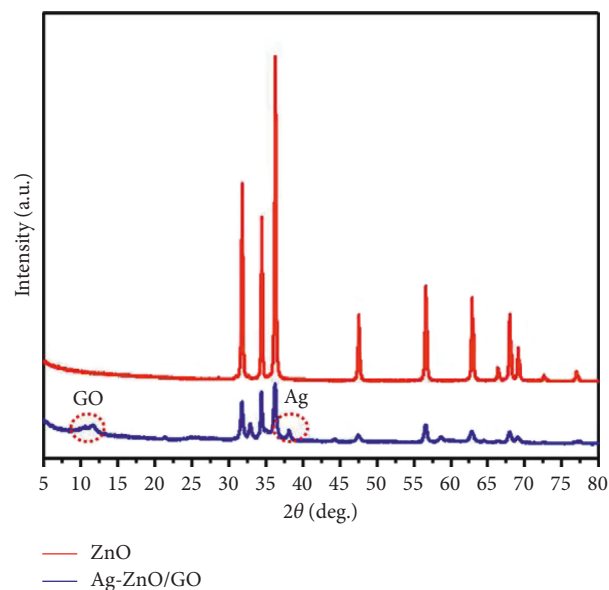


FIGURE 1: XRD patterns of the ZnO and Ag-ZnO/GO samples.

TABLE 1: FWHM in the samples.

Sample	FWHM (cm^{-1})
ZnO	0.2210
Ag-ZnO/GO	0.2377

The chemical compositions of ZnO and Ag-ZnO/GO were analyzed by energy dispersive spectrometry (EDS) and mapping technique in conjunction with SEM (Figure 3). All the peaks were ascribed to Zn, Ag, and O in the ZnO sample, and peak of C elements appeared in the composite sample. The mapping results confirmed the presence and uniform distribution of zinc, silver, and oxygen on the GO surface. In combination, these elemental mapping and SEM and TEM results demonstrate the capability of GO to function as an effective scaffold for ZnO and silver.

3.1.3. XPS Analysis. The surface element composition and chemical state of the as-synthesized samples were analyzed by XPS analysis, as shown in Figure 4. The peaks of Zn $2p_{3/2}$ and Zn $2p_{1/2}$ of the synthesized ZnO and Ag-ZnO/GO were observed at around 1,021.8 eV and 1,045.1 eV, respectively, which are very similar to the peaks of pure ZnO (Figure 4(a)). This finding, therefore, demonstrated the presence of the Zn^{2+} form in both samples [19, 25]. In the C1s spectra of Ag-ZnO/GO (Figure 4(b)), the presence of C was attributed to the GO addition. Compared to ZnO, the C peaks of the Ag-ZnO/GO nanocomposite were shifted toward a slightly lower binding energy. In the ZnO sample, the presence of C originated from the vacuum oil used in the pretreatment system before the XPS testing. The four peaks in the Ag-ZnO/GO sample at 282.4, 284.8, 286.1, and 288.6 eV were ascribed to Zn-C, C-C/C=C, Zn-O-C, and C=O, respectively [26, 27]. The presence of abundant carbon species on the surface of the Ag-ZnO/GO composite increased the photodegradation because it facilitated the

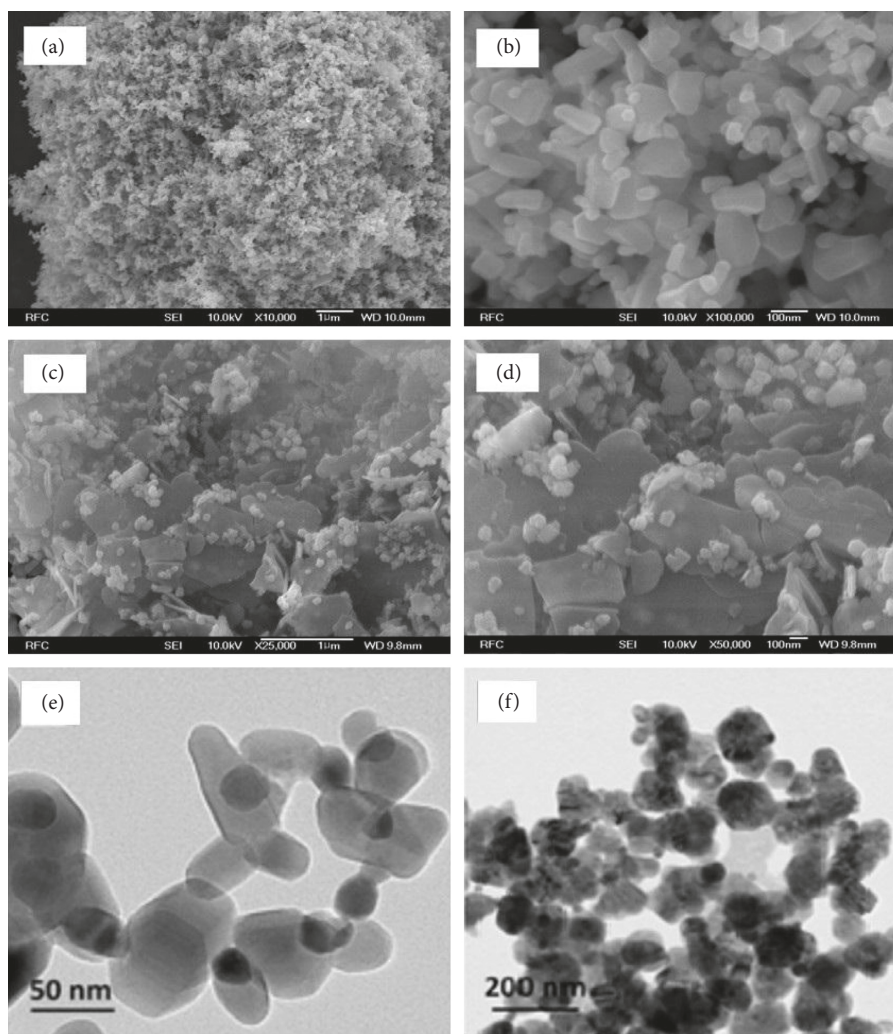


FIGURE 2: FE-SEM and TEM analyses of synthesized materials.

contact with organic pollutant molecules. The high resolution spectra of the strong O1s peak (Figure 4(c)) at 531.3 eV in the ZnO sample was due to the oxygen in the ZnO crystal lattice (Zn-O bonds) [28, 29]. Two O1s peaks at 531.5 and 531.8 eV in the Ag-ZnO/GO composite sample revealed the presence of surface oxygen complexes in the carbon phase [21, 28]. These oxygen-containing groups increased the photocatalytic activities due to their involvement in the production of active radicals, which play an important role in the photodegradation process. The Ag 3d XPS peaks of Ag-ZnO/GO, shown in Figure 4(d) located at 367.7 and 374.0 eV, were ascribed to Ag 3d_{5/2} and Ag 3d_{3/2}, respectively [30, 31]. The XPS results were in good agreement with the aforementioned XRD and EDS results. These observations in Figure 4 further confirmed the successful preparation of Ag-ZnO/GO nanoparticles and viability of Ag-ZnO/GO as a superior nanocomposite material.

3.1.4. UV-VIS Reflectance Spectra and Band Gap. The optical absorption properties of the synthesized nanomaterials were investigated by UV-VIS reflectance spectra (Figure 5). The doping activity induced a shift from the UV light

absorption of ZnO to the visible light absorption of Ag-ZnO/GO. The optical band gaps of the synthesized materials were calculated by using the following Tauc equation:

$$\alpha h\nu = A(h\nu - E_g)^n, \quad (2)$$

where α is the absorption coefficient, E_g is the band gap, A is a constant, and n is an index that characterizes the optical absorption process (for direct band gap semiconductor material $n = 1/2$). By extrapolating the linear region of the plot $(\alpha h\nu)^2$ vs. $h\nu$, the band gap could be estimated. The band gap values for ZnO and Ag-ZnO/GO are given in Figure 5. Band gap of Ag-ZnO/GO (2.92 eV) is smaller than that of synthesized ZnO (3.15 eV). This decreased band gap may have been due to the introduction of silver and carbon as dopants in the ZnO lattice. Similar phenomena have been observed in ZnO-based material systems in other studies [19, 32, 33].

3.1.5. BET Surface Area. The specific surface area of the synthesized materials was measured using the BET method with N₂ adsorption-desorption (Figure 6). The identified surface area of Ag-ZnO/GO was almost 3.6 times larger than

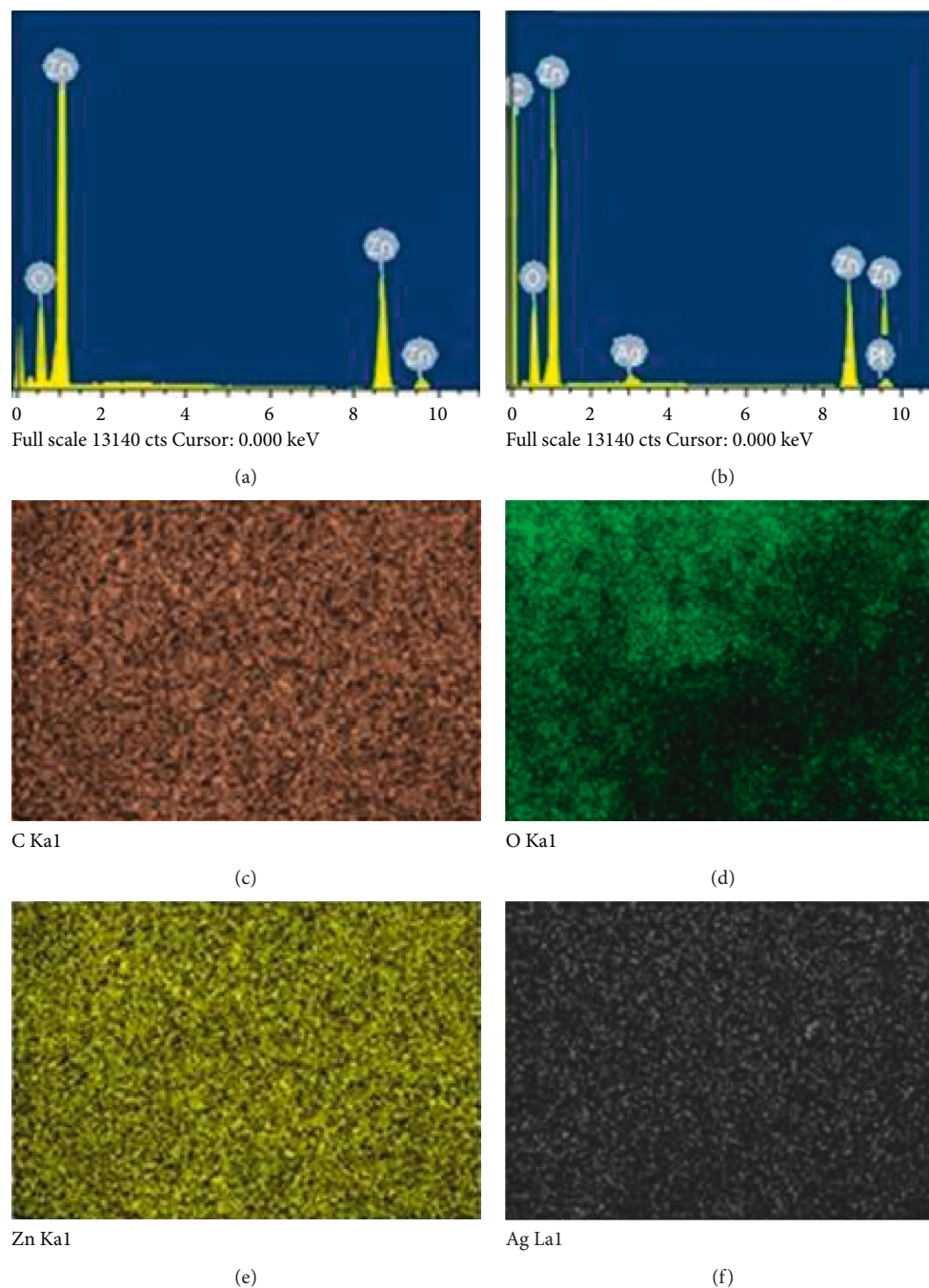


FIGURE 3: EDS and mapping analyses of synthesized materials.

that of ZnO. With Ag-ZnO/GO present in a dark condition, pollutant adsorption is mainly assisted by the increased specific surface area (S_{BET}). In general, graphene has a very high specific surface area [34], and thus, it could provide a high adsorption capacity. GO, the oxidized form of graphene, contains oxygen functional groups on its surface that can become adsorption sites. Therefore, the enhanced degradation capacity under visible light can be attributed to the adsorption power of GO combined as a semiconductor or adsorption substrate [35, 36]. In addition, the increased pore size of Ag-ZnO/GO nanocomposite could lead to the increases in adsorption efficiency.

3.1.6. PL Spectra. The PL spectra of as-prepared ZnO and Ag-ZnO/GO at room temperature are presented in Figure 7. As observed, the PL intensities of the samples increase in the following order: Ag-ZnO/GO and ZnO. The PL intensity of the composite sample is weaker as compared with that of the ZnO sample, indicating that the fluorescence of the composite is quenched more efficiently than that of ZnO. It also indicated that the incorporation of ZnO with Ag and GO can improve the separation of photoinduced electrons and holes. Thus, there is a high agreement with the order of PL intensities when compared with the result from the removal experiments, and the recombination process can be

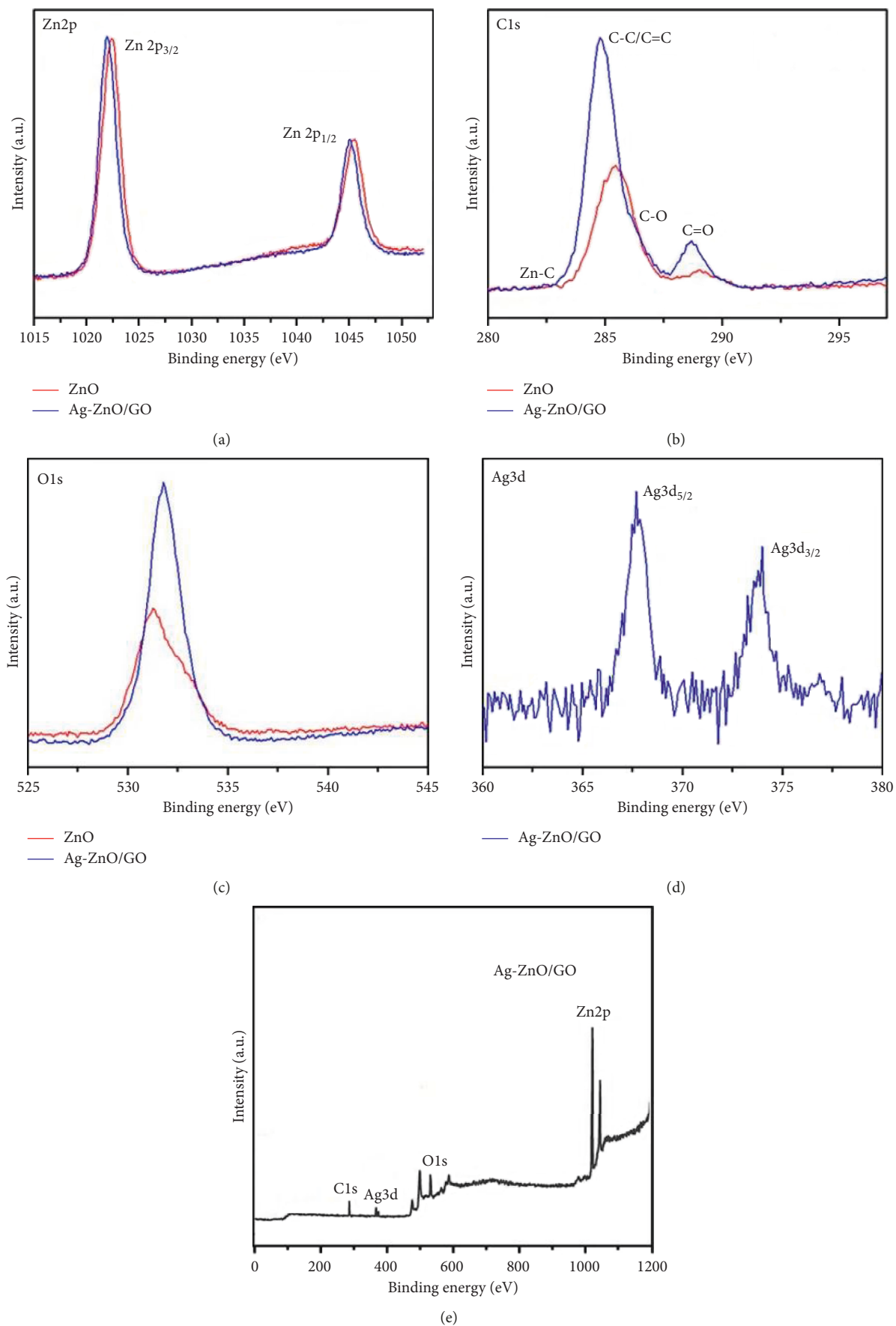


FIGURE 4: XPS analyses of synthesized materials.

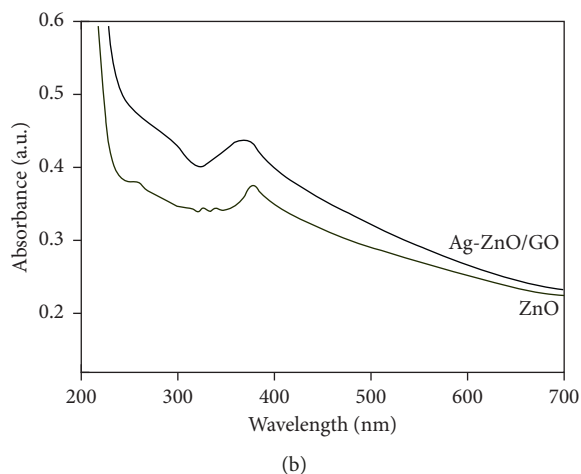
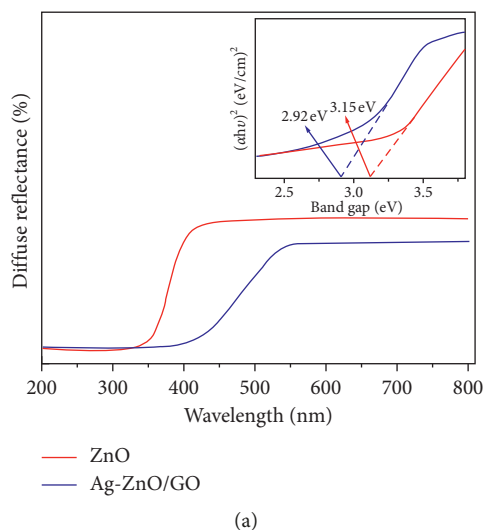


FIGURE 5: UV-VIS reflectance spectra and band gap of synthesized materials.

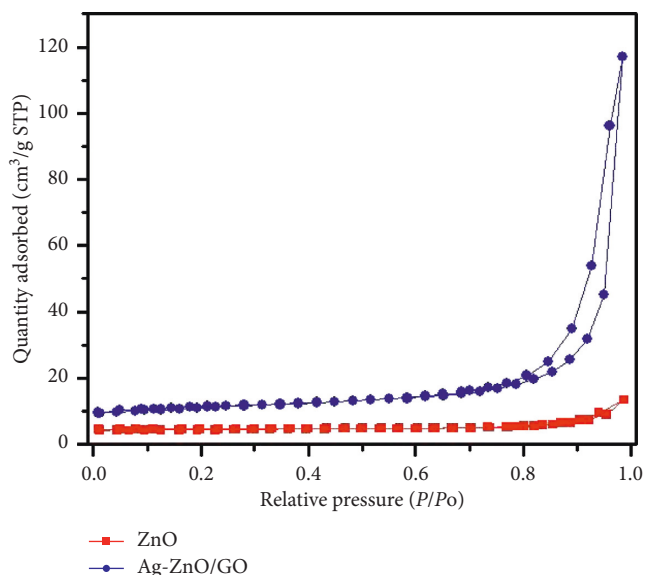


FIGURE 6: BET analysis data of synthesized materials.

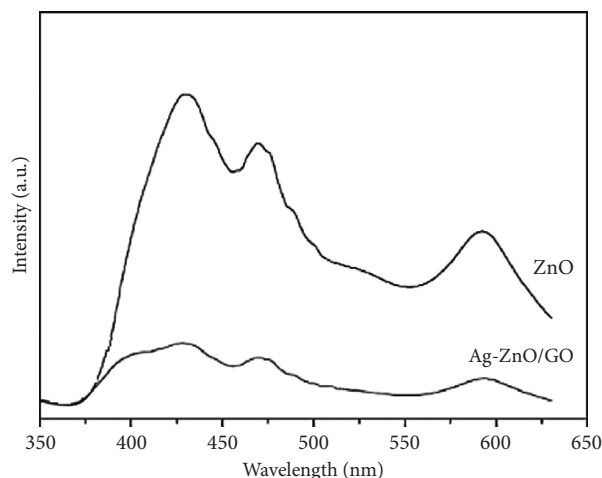


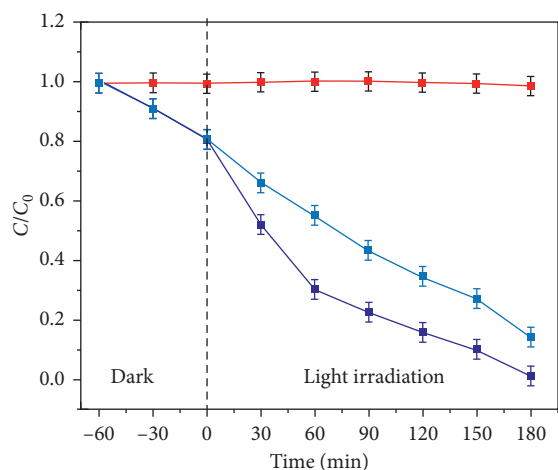
FIGURE 7: PL spectra of synthesized materials.

significantly suppressed through the combination of ZnO with Ag and GO.

3.2. Removal of MB Dye Using Synthesized Materials. It is commonly accepted that most dyes are resistant to biodegradation and direct photolysis, and many N-containing dyes such as MB undergo natural reductive anaerobic degradation to yield potentially carcinogenic aromatic amines [31]. In this study, therefore, MB was chosen as a model contaminant to evaluate the photocatalytic activity of the synthesized photocatalysts.

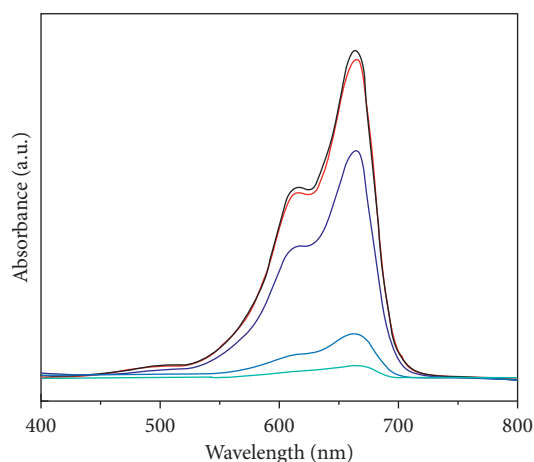
Figures 8(a) and 8(b) show the UV-Vis absorption spectrum and removal efficiency of MB degraded by using synthesized materials under dark and light (visible and UV) irradiation conditions, respectively. ZnO did not show any significant adsorption of MB, when the addition of Ag-ZnO/GO into the MB solution without any light source afforded an MB removal efficiency of around 20%. After the adsorption, visible light or UV light was directed at the MB removal system containing Ag-ZnO/GO added into MB solution as a photocatalyst. The addition of Ag-ZnO/GO into the MB solution under visible light and UV light irradiation increased the MB removal efficiency after 3 h by up to 85% and 99%, respectively. The comparison of the light absorption results between the dark and light irradiation conditions clearly demonstrated that most of the MB removal effects were due to photocatalytic degradation by the Ag-ZnO/GO nanocomposite. Under visible light, MB removal was significantly increased by Ag-ZnO/GO because of the combination effects of the adsorption and photocatalytic degradation. Under UV conditions, removal efficiency reached up to 99% because of the high photon energy in UV light, and so photodegradation could occur more strongly than under the visible light. The photocatalytic activity by Ag-ZnO/GO under visible light is explained in the mechanism section.

To clarify the role of photogenerated radical species in the removal process, different scavengers were used. It is observed from the scavenger tests' result that the degradation level of MB was significantly inhibited when tert-butyl



—■— ZnO
 —■— Ag-ZnO/GO_UV light
 —■— Ag-ZnO/GO_visible light

(a)



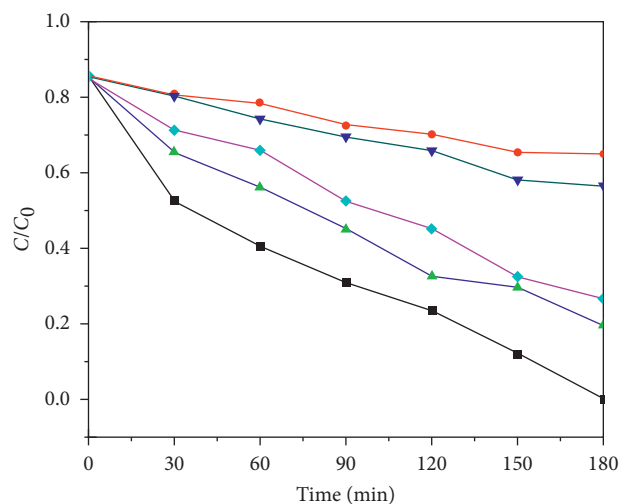
— Initial MB solution — Ag-ZnO/GO-visible
 — ZnO_visible — Ag-ZnO/GO-UV
 — Ag-ZnO/GO-dark

(b)

FIGURE 8: Removal of MB by using synthesized materials.

alcohol and ammonium oxalate were added. Thus, it is clear that most of the reactive radicals responsible for catalytic activity are found to be OH^\bullet and photogenerated holes (Figure 9).

Synthesized composite material have higher surface area and greater numbers of active sites as compared with ZnO, where the photogenerated charge carriers react with absorbed molecules to form hydroxyl and superoxide radicals. A set of experiments was carried out in order to check the reusability and stability of the composite catalysts. The photodegradation experiment was duplicated eight times after the centrifugation and cleaning process. As shown in Figure 10, the photocatalytic activities were almost stable in the first 4 cycles. From the 5th cycle, the removal of MB was decreased; it might be due to the loss of adsorption properties after several centrifugation and cleaning process. The particles readily form aggregates, leading to the loss of the



—■— Without scavenger —▼— Ammonium oxalate
 —●— *tert*-Butyl alcohol —◆— $\text{K}_2\text{S}_2\text{O}_8$
 —▲— Benzoquinone

FIGURE 9: Evaluation of reactive radical species using various scavengers for photocatalytic degradation of MB by using Ag-ZnO/GO.

original structure and active sites, thus decreasing the photocatalytic efficiency.

3.3. Effect of Initial Process Parameter. pH of the solution has been reported as one of the most important factors affecting the removal efficiency of organic pollutants by photocatalytic processes in an aqueous solution [37, 38]. Interpreting the pH effects on the MB dye removal process is a difficult task because it is affected by multiple factors. The effect of pH on the removal of MB dye was investigated in the pH range 3 to 12. The pH of the point of zero charge (pH pzc) of ZnO was about 8.6 [39]. At pH above pH pzc, the surface of the ZnO particles was mostly positively charged. As the solution pH increases from the acidic range up to pH pzc of ZnO (pH < 8.6), the decreased H_3O^+ concentration produces less repulsion of Ag-ZnO/GO with the positively charged MB molecules, resulting in increased adsorption of MB. As the solution pH further increases above pzc (pH > 8.6), the increased OH^- produces more electron repulsion of Ag-ZnO/GO with negatively charged MB molecules, leading to less adsorption. Therefore, pH 8.5–9 was chosen as the optimal pH for MB adsorption (Figure 11(a)).

Figure 11(b) shows the effects of different Ag-ZnO/GO loadings on the MB removal process under visible light irradiation. As the dosage of Ag-ZnO/GO increased up to 1.0 g/L, the MB removal effect also increased. The increased Ag-ZnO/GO dosage led to more active sites for adsorption and thus more moiety availability for photocatalytic degradation of MB molecules. However, even the MB removal efficiency decreased as the dosage loading was increased above 1 g/L. At higher dosages, there was excessive increase in the amount of suspended Ag-ZnO/GO, with excessive addition, disturbing the penetration of visible light into the reaction system. This also led to reduction in the generation

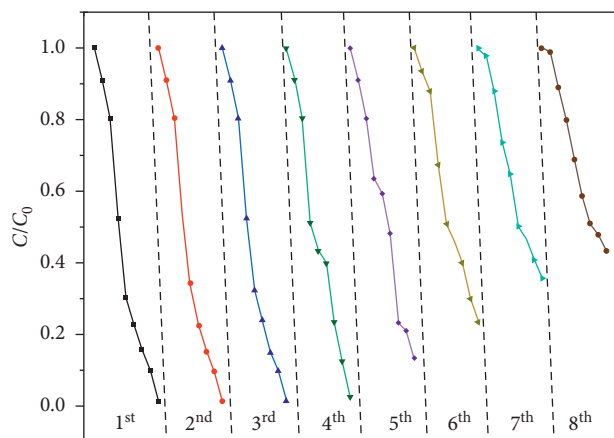


FIGURE 10: Reusability of the synthesized composite material.

of the electron-hole pairs and subsequent reduction in the production of oxy-radicals and hydroxyl radicals [40]. Furthermore, excessive photocatalyst dosage increases the pollutant removal costs. Hence, 1 g/L was determined to be the optimum Ag-ZnO/GO dosage.

Different initial MB solution concentrations, ranging from 1 mg/L to 25 mg/L, were used to evaluate the MB removal effect by Ag-ZnO/GO (Figure 11(c)). The MB removal efficiency decreased when the initial MB concentration was more than 15 mg/L within 3 h of irradiation. When the MB concentration was beyond the limit of 15 mg/L, the MB molecules adsorbed on the adsorbent/photocatalyst surface repulsed further MB molecules from approaching the adsorbent/photocatalyst, thereby decreasing MB removal. In addition, a high initial MB concentration hindered visible light penetration due to increased turbidity, as explained in the previous section, which decreased the light irradiation effect for photocatalytic degradation of MB [41, 42].

3.4. Photocatalytic Mechanism. Three mechanisms proposed to explain the increased photocatalytic degradation of MB dye by Ag-ZnO/GO under visible light irradiation are schematically shown in Figure 12.

The first proposed mechanism for the increased MB removal is associated with GO addition to the photocatalytic system (Figure 12(a)). GO was used as a better substrate for the photocatalytic reaction by increasing the surface area of the photocatalyst. Moreover, the photocatalytic degradation efficiency of MB by Ag-ZnO/GO was improved by combining it with a zero band gap semiconductor, GO [43, 44]. Some previous studies have reported that GO can also enhance the photocatalytic ability of ZnO under visible light irradiation due to

resonance effects, including the increased surface area with added GO and increased formation of π - π^* interactions between the dye molecules [25]. The high surface area of GO can contribute to the effective adsorption of MB molecules on the photocatalyst surface. MB is a sensitive chromophore that absorbs light in a wide range of wavelengths, including the visible region [45, 46], and thus, MB molecules easily enter an excited status. The electrons in the excited MB* can jump to the conduction band (CB) of ZnO through GO [47] and then be transferred to various Ag levels (Figures 12(b) and 12(c)). This series of excited electron transfer can minimize or delay the recombination of electrons with holes. Therefore, the excited electrons can have more delayed recombination, while simultaneously increasing the charge transfer capacity from the valence band (VB) to the CB of ZnO.

The second mechanism for the enhanced photocatalytic degradation of MB could be due to the Ag doping effect into the ZnO crystal lattice (Figure 12(c)). It is well known that band gap is a region of energy with no allowed states. The density of states versus energy depends on the chemical composition of the material, and the state density distribution will be changed if the chemical composition is changed. In this case, Ag dopant is the impurity, so the chemical composition was changed by doping. When the doping density is high enough, the dopant states generate a band. If this band is very close to the valence or conduction band edge, the band gap will decrease. The electrons transferred to the CB of ZnO tend to be transferred to Ag at that time, which prevents delay of the recombination of the excited electrons and holes. Addition of Ag led to the formation of “stairs” that allow the excited electrons to move easily to higher energy levels with visible light irradiation rather than directly moving down to the holes. The minimized recombination of the excited electrons in the CB with the holes in the VB can increase the opportunity for the production of oxy-radicals by reaction with O_2 molecules, leading to the oxidative degradation of MB molecules.

The third proposed mechanism is based on the narrowed band gap of the semiconductor (Figure 12(b)). The major limitation of ZnO is its restriction to UV light irradiation because of its wide band gap. This weakness was improved through Ag doping into the ZnO lattice by narrowing the band gap. Dotted green lines (Figure 12(c)) represent a new band gap for ZnO, which was narrowed by the interaction between ZnO, Ag, and GO during the synthesis of the Ag-ZnO/GO nanocomposite [48]. The major oxidative and reductive processes for the photodegradation of MB by using Ag-ZnO/GO with a narrowed band gap under visible light illumination can be explained as shown in equation (3) to (11).



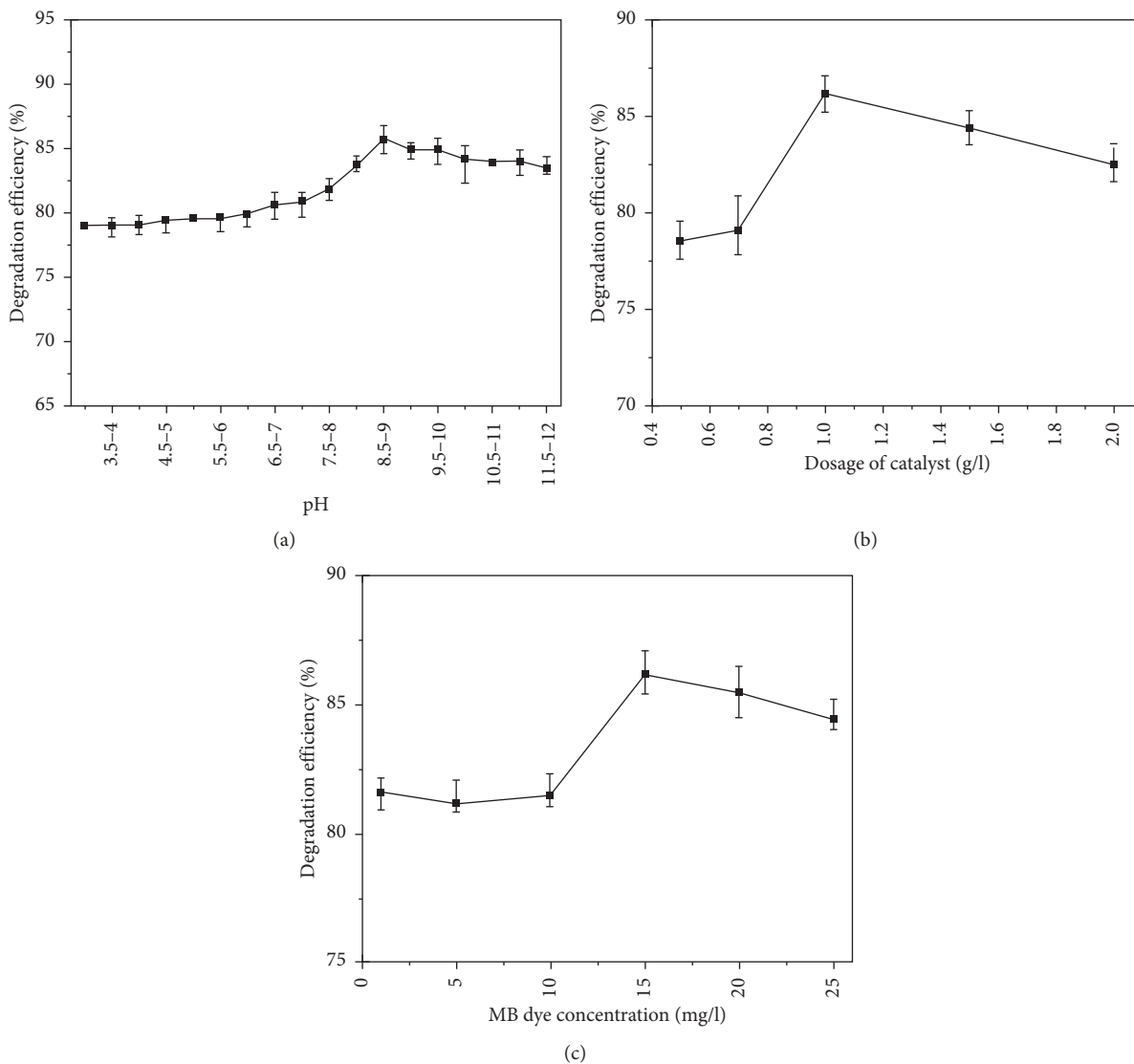


FIGURE 11: Effect of the initial parameter on the MB removal efficiency.

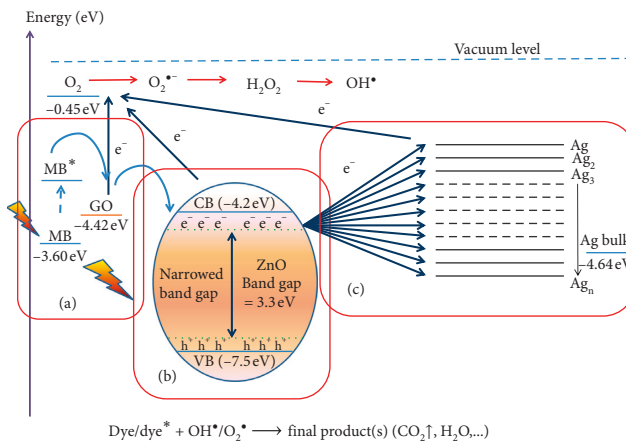
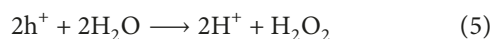


FIGURE 12: Proposed mechanism for MB removal using synthesized material.

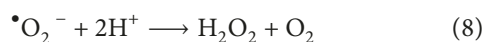
TABLE 2: Comparison between previous and current studies for MB removal using photocatalytic degradation.

Photocatalyst	Chemical ingredients	Calcination temperature	Light source	Adsorption	Photocatalysis	Total removal	Remark	Ref.
Sulphonated GO-ZnO-Ag	Zn(CH ₃ COO) ₂ ·2H ₂ O, HMTA, EG, AgNO ₃ , HCl, ClCH ₂ CH ₂ SO ₃ H, AgNO ₃ , NaNO ₃ , KMnO ₄ , H ₂ O ₂ , H ₂ SO ₄	160	Visible	20%	78%	98%	Sulfonated GO high calcination temperature	[13]
Ag-ZnO/RGO	GO, bis-hexamethylene triamine, Zn(NO ₃) ₂ ·6H ₂ O, AgNO ₃ , ethanol	140, in autoclave	Visible		Not separated	65%	Reduced GO high calcination temperature in autoclave	[15]
Graphene-Ag/ZnO	Graphene, EG, CH ₃ COOAg, Zn(CH ₃ COO) ₂ ·2H ₂ O, NaOH	160	Visible	28.6%	65.6%	94.4%	Graphene expensive high calcination temperature	[8]
Ag/ZnO/GO	Graphite oxide, ZnO, AgNO ₃	55	UV		Not separated	98%	GO UV light high energy safety issue	[16]
Ag-ZnO/GO	Graphene oxide, AgNO ₃ , ZnSO ₄ ·7H ₂ O, C ₆ H ₆ O ₆	70	Visible UV	25% 25%	60% 74%	85% 99%	GO visible light low energy high safety UV light high energy safety issue	This study This study

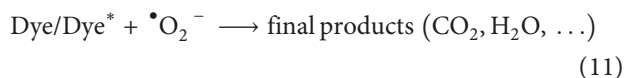
(I) Oxidative reactions with holes



(II) Reduction reaction with O₂



(III) Photocatalytic oxidation with oxy-radicals



3.5. Energy and Cost Issue. Nowadays, the demand and market for the use of nanoparticles or nanocatalysts in pollutant removal are increasing. As discussed above, ZnO nanoparticle is one of the most promising materials for wastewater treatment. Performance of ZnO can be enhanced by adding some ingredients to make better nanocomposite. The methods currently developed for making better ZnO nanomaterials mainly consist of sol-gel template and hydrothermal methods. However, the requirement of high crystallinity is a major problem in ZnO synthesis. With the

sol-gel method, calcination of gels or thermal annealing of emulsions is therefore required to induce crystallization of the nanoparticle, and thus, normally a high temperature of more than 200°C is required. Hydrothermal methods are directly carried out at slightly lower temperatures than sol-gel methods (but not less than 120°C). However, nanocrystals formed with hydrothermal methods agglomerate and thus are insoluble in most solvents, and thus, some stabilizing agents are required to prevent agglomeration. Their characteristics from previous relevant study outcomes are summarized in Table 2 with comparisons.

The search for a simple and economic synthesis method to derive nanoparticles with good size and shape at low temperature is still an open challenge. The ability to produce nanomaterials at lower temperatures is needed for the purpose of saving energy and increasing safety for large-scale production. In this study, we demonstrate that it is possible to cost effectively produce nanomaterials at low temperature in considerable quantities, with increased safety in a wide range of applications. By adding the noble metal Ag as a dopant and GO as a high surface area adsorption substrate, firstly, our nanomaterial can work excellently for adsorption and also as a photocatalyst, even under visible light. Researchers have previously used UV light in their studies to irradiate the photocatalyst, and the removal efficiency of their process was very high. However, the price of a UV lamp is at least two times as high as the price of a visible lamp. Furthermore, UV waves are invisible but very harmful for human eyes. Secondly, for processing our current method, only a calcination temperature of around 70°C is needed without any requirements for complex instruments. From an economical view, such fabrication may offer better opportunities to significantly lower the cost of manufacturing nanomaterials, while bringing environmental advantages such as low energy consumption and reduced CO₂ emissions. Thirdly, the simplicity of the synthesis procedure

would make it safe for workers and easy to apply to industrial manufacturing.

4. Conclusion

Ag-ZnO/GO nanocomposite was successfully synthesized by facile aqueous solution reactions at low temperature. The MB removal efficiency increased up to 99% under the UV light and 85% under visible light. The optimum conditions for maximum removal efficiency of MB were pH 8.5–9, temperature 35°C and dosage 1 g/L at MB concentration 15 mg/L. The significant increase in photocatalytic degradation for MB removal exhibited by Ag-ZnO/GO was due to the combined effects of the two semiconductors, ZnO and GO, and Ag doping into the ZnO crystal lattice. The proposed mechanism for enhanced removal includes an increase in adsorption by adding GO with a high surface area and an increase in photocatalytic activities due to improved charge transfer capacity achieved through lowering the band gap energy of ZnO, thus minimizing the recombination of the excited electrons in the CB with the holes in VB of ZnO, leading to higher removal rate of MB.

Data Availability

The data used to support the findings of this study are available from the corresponding author upon request.

Conflicts of Interest

The authors declare that they have no conflicts of interest.

Acknowledgments

The authors would like to thank Vietnam Japan University Research Fund which is funded by Japan International Cooperation Agency (JICA) to full time lecturer of Vietnam Japan University (Dr. Tran Thi Viet Ha of Master's Program of Vietnam Japan University).

References

- [1] M. Nasrollahzadeh, M. Atarod, B. Jaleh, and M. Gandomirouzbahani, "In situ green synthesis of Ag nanoparticles on graphene oxide/TiO₂ nanocomposite and their catalytic activity for the reduction of 4-nitrophenol, congo red and methylene blue," *Ceramics International*, vol. 42, no. 7, pp. 8587–8596, 2016.
- [2] M. Eskandari, V. Ahmadi, S. Kohnehpoushi, and M. Yousefi rad, "Improvement of ZnO nanorod based quantum Dot (cadmium sulfide) sensitized solar cell efficiency by aluminum doping," *Physica E: Low-Dimensional Systems and Nanostructures*, vol. 66, pp. 275–282, 2015.
- [3] K. Takahashi, A. Yoshikawa, and S. Adarsh, *Wide Bandgap Semiconductors: Fundamental Properties and Modern Photonic and Electronic Devices*, Springer, Heidelberg, Germany, 2007.
- [4] F. Ghorbani Shahna, A. Bahrami, I. Alimohammadi et al., "Chlorobenzene degeradation by non-thermal plasma combined with EG-TiO₂/ZnO as a photocatalyst: effect of photocatalyst on CO₂ selectivity and byproducts reduction," *Journal of Hazardous Materials*, vol. 324, pp. 544–553, 2017.
- [5] X. Li, Q. Wang, Y. Zhao, W. Wu, J. Chen, and H. Meng, "Green synthesis and photo-catalytic performances for ZnO-reduced graphene oxide nanocomposites," *Journal of Colloid and Interface Science*, vol. 411, pp. 69–75, 2013.
- [6] O. Yayapao, T. Thongtem, A. Phuruangrat, and S. Thongtem, "Sonochemical synthesis of Dy-doped ZnO nanostructures and their photocatalytic properties," *Journal of Alloys and Compounds*, vol. 576, pp. 72–79, 2013.
- [7] L. Zhang, N. Li, H. Jiu, G. Qi, and Y. Huang, "ZnO-reduced graphene oxide nanocomposites as efficient photocatalysts for photocatalytic reduction of CO₂," *Ceramics International*, vol. 41, no. 5, pp. 6256–6262, 2015.
- [8] M. Ahmad, E. Ahmed, Z. L. Hong, N. R. Khalid, W. Ahmed, and A. Elhissi, "Graphene-Ag/ZnO nanocomposites as high performance photocatalysts under visible light irradiation," *Journal of Alloys and Compounds*, vol. 577, pp. 717–727, 2013.
- [9] A. Omidvar, B. Jaleh, M. Nasrollahzadeh, and H. R. Dasmeh, "Fabrication, characterization and application of GO/Fe₃O₄/Pd nanocomposite as a magnetically separable and reusable catalyst for the reduction of organic dyes," *Chemical Engineering Research and Design*, vol. 121, pp. 339–347, 2017.
- [10] L.-L. Tan, W.-J. Ong, S.-P. Chai, and A. Mohamed, "Reduced graphene oxide-TiO₂ nanocomposite as a promising visible-light-active photocatalyst for the conversion of carbon dioxide," *Nanoscale Research Letters*, vol. 8, no. 1, pp. 1–9, 2013.
- [11] P.-Q. Wang, Y. Bai, P.-Y. Luo, and J.-Y. Liu, "Graphene-WO₃ nanobelt composite: elevated conduction band toward photocatalytic reduction of CO₂ into hydrocarbon fuels," *Catalysis Communications*, vol. 38, pp. 82–85, 2013.
- [12] M. Nasrollahzadeh, B. Jaleh, and A. Jabbari, "Synthesis, characterization and catalytic activity of graphene oxide/ZnO nanocomposites," *RSC Advances*, vol. 4, no. 69, pp. 36713–36720, 2014.
- [13] P. Gao, K. Ng, and D. D. Sun, "Sulfonated graphene oxide-ZnO-Ag photocatalyst for fast photodegradation and disinfection under visible light," *Journal of Hazardous Materials*, vol. 262, pp. 826–835, 2013.
- [14] B. Jaleh and A. Jabbari, "Evaluation of reduced graphene oxide/ZnO effect on properties of PVDF nanocomposite films," *Applied Surface Science*, vol. 320, pp. 339–347, 2014.
- [15] H. Raj Pant, B. Pant, H. Joo Kim et al., "A green and facile one-pot synthesis of Ag-ZnO/RGO nanocomposite with effective photocatalytic activity for removal of organic pollutants," *Ceramics International*, vol. 39, no. 5, pp. 5083–5091, 2013.
- [16] J. Qin, R. Li, C. Lu, Y. Jiang, H. Tang, and X. Yang, "Ag/ZnO/graphene oxide heterostructure for the removal of rhodamine B by the synergistic adsorption-degradation effects," *Ceramics International*, vol. 41, no. 3, pp. 4231–4237, 2015.
- [17] S. Xu, L. Fu, T. S. H. Pham, A. Yu, F. Han, and L. Chen, "Preparation of ZnO flower/reduced graphene oxide composite with enhanced photocatalytic performance under sunlight," *Ceramics International*, vol. 41, no. 3, pp. 4007–4013, 2015.
- [18] L. Zhang, G. Du, B. Zhou, and L. Wang, "Green synthesis of flower-like ZnO decorated reduced graphene oxide composites," *Ceramics International*, vol. 40, no. 1, pp. 1241–1244, 2014.
- [19] S. Shet, K.-S. Ahn, T. Deutsch et al., "Synthesis and characterization of band gap-reduced ZnO:N and ZnO:(Al, N) films for photoelectrochemical water splitting," *Journal of Materials Research*, vol. 25, no. 1, pp. 69–75, 2010.
- [20] R. S. Patil, M. R. Kokate, D. V. Shinde, S. S. Kolekar, and S. H. Han, "Synthesis and enhancement of photocatalytic activities of ZnO by silver nanoparticles," *Spectrochimica Acta Part A: Molecular and Biomolecular Spectroscopy*, vol. 122, pp. 113–117, 2014.

- [21] Z. H. Ibupoto, N. Jamal, K. Khun, X. Liu, and M. Willander, "A potentiometric immunosensor based on silver nanoparticles decorated ZnO nanotubes, for the selective detection of d-dimer," *Sensors and Actuators B: Chemical*, vol. 182, pp. 104–111, 2013.
- [22] Y.-W. Tseng, F.-Y. Hung, T.-S. Lui, and S.-J. Chang, "Structural and Raman properties of silver-doped ZnO nanorod arrays using electrically induced crystallization process," *Materials Research Bulletin*, vol. 64, pp. 274–278, 2015.
- [23] R. Viswanath, H. S. B. Naik, Y. K. G. Somalanaik, P. K. P. Neelanjenallu, K. N. Harish, and M. C. Prabhakara, "Studies on characterization, optical absorption, and photoluminescence of yttrium doped ZnS nanoparticles," *Journal of Nanotechnology*, vol. 2014, Article ID 924797, 8 pages, 2014.
- [24] S. W. Lu, B. I. Lee, Z. L. Wang et al., "Synthesis and photoluminescence enhancement of Mn²⁺-doped ZnS nanocrystals," *Journal of Luminescence*, vol. 92, no. 1-2, pp. 73–78, 2000.
- [25] S. Vadivel, M. Vanitha, A. Muthukrishnaraj, and N. Balasubramanian, "Graphene oxide–BiOBr composite material as highly efficient photocatalyst for degradation of methylene blue and rhodamine-B dyes," *Journal of Water Process Engineering*, vol. 1, pp. 17–26, 2014.
- [26] H. Ma, X. Cheng, C. Ma et al., "Characterization, and photocatalytic activity of N-doped ZnO/ZnS composites," *International Journal of Photoenergy*, vol. 2013, Article ID 625024, 8 pages, 2013.
- [27] M. Ahmad, E. Ahmed, W. Ahmed, A. Elhissi, Z. L. Hong, and R. N. Khalid, "Enhancing visible light responsive photocatalytic activity by decorating Mn-doped ZnO nanoparticles on graphene," *Ceramics International*, vol. 40, no. 7, pp. 10085–10097, 2014.
- [28] K. Dai, L. Lu, C. Liang et al., "Graphene oxide modified ZnO nanorods hybrid with high reusable photocatalytic activity under UV-LED irradiation," *Materials Chemistry and Physics*, vol. 143, no. 3, pp. 1410–1416, 2014.
- [29] Y. Ji, S.-A. Lee, A.-N. Cha et al., "Resistive switching characteristics of ZnO-graphene quantum dots and their use as an active component of an organic memory cell with one diode-one resistor architecture," *Organic Electronics*, vol. 18, pp. 77–83, 2015.
- [30] J. Xu, Y. Chang, Y. Zhang, S. Ma, Y. Qu, and C. Xu, "Effect of silver ions on the structure of ZnO and photocatalytic performance of Ag/ZnO composites," *Applied Surface Science*, vol. 255, no. 5, pp. 1996–1999, 2008.
- [31] J. Xu, X. Han, H. Liu, and Y. Hu, "Synthesis and optical properties of silver nanoparticles stabilized by gemini surfactant," *Colloids and Surfaces A: Physicochemical and Engineering Aspects*, vol. 273, no. 1–3, pp. 179–183, 2006.
- [32] B. Sankara Reddy, Y. Prabhakara Reddy, S. V. Reddy, and N. K. Reddy, "Structural, optical and magnetic properties of (Fe, Ag) co-doped ZnO nanostructures," *Advanced Materials Letters*, vol. 5, pp. 199–205, 2014.
- [33] R. Rahimi, J. Shokrayian, and M. Rabbani, "Photocatalytic removing of methylene blue by using of Cu-doped ZnO, Ag-doped ZnO and Cu,Ag-codoped ZnO nanostructure," in *Proceedings of the 17th International Electronic Conference on Synthetic Organic Chemistry*, Basel, Switzerland, November 2013.
- [34] Y. Zhu, S. Murali, W. Cai et al., "Graphene and graphene oxide: synthesis, properties, and applications," *Advanced Materials*, vol. 22, no. 35, pp. 3906–3924, 2010.
- [35] P. Fu, Y. Luan, and X. Dai, "Preparation of activated carbon fibers supported TiO₂ photocatalyst and evaluation of its photocatalytic reactivity," *Journal of Molecular Catalysis A: Chemical*, vol. 221, no. 1-2, pp. 81–88, 2004.
- [36] H. Yoneyama and T. Torimoto, "Titanium dioxide/adsorbent hybrid photocatalysts for photodestruction of organic substances of dilute concentrations," *Catalysis Today*, vol. 58, no. 2-3, pp. 133–140, 2000.
- [37] M. R. Hoffmann, S. T. Martin, W. Choi, and D. W. Bahnemann, "Environmental applications of semiconductor photocatalysis," *Chemical Reviews*, vol. 95, no. 1, pp. 69–96, 1995.
- [38] L. N. Lewis, "Chemical catalysis by colloids and clusters," *Chemical Reviews*, vol. 93, no. 8, pp. 2693–2730, 1993.
- [39] J. Wang, Z. Jiang, Z. Zhang et al., "Sonocatalytic degradation of acid red B and rhodamine B catalyzed by nano-sized ZnO powder under ultrasonic irradiation," *Ultrasonics Sonochemistry*, vol. 15, no. 5, pp. 768–774, 2008.
- [40] M. Pera-Titus, V. García-Molina, M. A. Baños, J. Giménez, and S. Esplugas, "Degradation of chlorophenols by means of advanced oxidation processes: a general review," *Applied Catalysis B: Environmental*, vol. 47, no. 4, pp. 219–256, 2004.
- [41] M. M. Ba-Abbad, A. A. Al-Amiery, A. Mohamad, and M. Takriff, "Toxicity evaluation for low concentration of chlorophenols under solar radiation using zinc oxide (ZnO) nanoparticles," *International Journal of Physical Sciences*, vol. 7, no. 1, pp. 48–52, 2012.
- [42] M. M. Ba-Abbad, A. A. H. Kadhum, A. Bakar Mohamad, M. S. Takriff, and K. Sopian, "The effect of process parameters on the size of ZnO nanoparticles synthesized via the sol-gel technique," *Journal of Alloys and Compounds*, vol. 550, pp. 63–70, 2013.
- [43] S. Cao, K. L. Yeung, J. K. C. Kwan, P. M. T. To, and S. C. T. Yu, "An investigation of the performance of catalytic aerogel filters," *Applied Catalysis B: Environmental*, vol. 86, no. 3-4, pp. 127–136, 2009.
- [44] N. Yao, S. Cao, and K. L. Yeung, "Mesoporous TiO₂-SiO₂ aerogels with hierarchical pore structures," *Microporous and Mesoporous Materials*, vol. 117, no. 3, pp. 570–579, 2009.
- [45] J. S. Lee, K. H. You, and C. B. Park, "Highly photoactive, low bandgap TiO₂ nanoparticles wrapped by graphene," *Advanced Materials*, vol. 24, no. 8, pp. 1084–1088, 2012.
- [46] A. Sionkowska, "The influence of methylene blue on the photochemical stability of collagen," *Polymer Degradation and Stability*, vol. 67, no. 1, pp. 79–83, 2000.
- [47] A. Adán-Más and D. Wei, "Photoelectrochemical properties of graphene and its derivatives," *Nanomaterials*, vol. 3, no. 3, pp. 325–356, 2013.
- [48] H. N. Tien, V. H. Luan, L. T. Hoa et al., "One-pot synthesis of a reduced graphene oxide-zinc oxide sphere composite and its use as a visible light photocatalyst," *Chemical Engineering Journal*, vol. 229, pp. 126–133, 2013.

Research Article

Preparation of Manganese Dioxide Nanoparticles on Laterite for Methylene Blue Degradation

Thu-Huong Le,¹ Thu Hong Anh Ngo ,² Van Thuan Doan,^{3,4} Le Minh Tri Nguyen,^{5,6} and Manh Cuong Le ⁷

¹Department of Chemistry and Environment, Thuyloi University, Hanoi 100000, Vietnam

²Faculty of Chemistry, University of Science, Vietnam National University, 334 Nguyen Trai, Thanh Xuan, Hanoi, Vietnam

³NTT Hi-Tech Institute, Nguyen Tat Thanh University, Ho Chi Minh City 700000, Vietnam

⁴Center of Excellence for Green Energy and Environmental Nanomaterials (CEGrEEN), Nguyen Tat Thanh University, Ho Chi Minh City, Vietnam

⁵Laboratory of Advanced Materials Chemistry, Advanced Institute of Materials Science, Ton Duc Thang University, Ho Chi Minh City, Vietnam

⁶Faculty of Applied Sciences, Ton Duc Thang University, Ho Chi Minh City, Vietnam

⁷Faculty of Building Material, National University of Civil Engineering, Hanoi 100000, Vietnam

Correspondence should be addressed to Manh Cuong Le; cuonglekhtn@gmail.com

Received 11 March 2019; Revised 30 May 2019; Accepted 25 June 2019; Published 5 September 2019

Academic Editor: Claudia Crestini

Copyright © 2019 Thu-Huong Le et al. This is an open access article distributed under the Creative Commons Attribution License, which permits unrestricted use, distribution, and reproduction in any medium, provided the original work is properly cited.

The laterite-coating manganese dioxide nanoparticle material (M2) prepared by the immersion method was used for the efficient removal of methylene blue (MB) from aqueous solution. The adsorption and heterogeneous Fenton catalytic oxidation experiments of M2 were investigated by changing the effective factors such as time, pH, amount of M2, and concentration of MB. The adsorption data of M2 showed good fitting with the Langmuir isotherm, suggesting that the adsorption of MB on the surface of M2 is a heterogeneous and physical adsorption process. Degradation of MB was also carried out to evaluate the heterogeneous Fenton catalytic oxidation characterization of a new catalytic oxidation material (M2). The results show that the M2 material has both adsorption and heterogeneous Fenton catalytic oxidation. However, the heterogeneous Fenton catalytic oxidation of the M2 material is the main performance. Hence, our groups have investigated the ability of the catalytic column treatment with high efficiency of 98–100% and the degradation efficiency after the sample running through the column almost does not change much. This proves that heterogeneous Fenton catalytic activity of the catalytic column is completely unaffected and reused many times after oxidizing MB. Specifically, even if the M2 material is reused for five times, the degradation efficiency still reaches 98.86%.

1. Introduction

Methylene blue (MB) is an organic compound which used in the treatment of cyanide poisoning, treatment of impetigo, pyoderma, urogenital antiseptic, and dying tissues in some diagnostic operations (bacterial staining, etc.) [1]. In addition, methylene blue is a chemical that is widely used in the dyeing industry of fabrics, nylon, leather, wood, and ink production. Moreover, a large amount of MB remain is in the wastewater of textile dyeing process [2]. Hence, the removal of MB has attracted considerable attention in the

environmental field. Over the past few years, several physical methods and chemical methods have been employed for removing MB [3]. There are several treatment processes that have been applied for treatment of dye wastewater such as photocatalytic degradation [4, 5], membrane separation [5, 6], adsorption-precipitation processes [7, 8], ultrafiltration [9, 10], chemical-biological degradation [6, 11], Fenton system and heterogeneous Fenton-like catalytic reactions [12–14], and adsorption on activated carbon and electrolysis [15, 16]. However, some of these techniques are rarely used due to insensitivity to a toxic substance, the complexity of

the design, and high cost. Therefore, development of an effective, cheap, and eco-friendly method is of crucial importance for the removal of dye wastewater.

Recently, manganese oxide nanoparticles have been also widely used for dye removal due to the effect of the chemical and physical interactions which occur between the organic (polymer) and inorganic (manganese dioxide nanoparticles) components [17, 18]. Manganese dioxide nanoparticles material is not only nontoxic but also has highly active and strong oxidations because the oxidation number of Mn is +4. In addition, manganese oxide nanoparticles have been used as adsorbents and catalytic materials [19–22]. Hence, most research focus on investigating the ability of Fenton catalytic oxidation of manganese oxide, especially manganese dioxide (MnO_2), for degradation of dye molecules. Dantas et al. [23] studied the ability of catalytic oxidation reaction of methylene blue with H_2O_2 under catalysts of β - MnOOH , α - FeOOH , γ - Mn_3O_4 , and treated methylene blue at 30 mg/L in 40 minutes. In addition, Zhang et al. [24] synthesized β - MnO_2 with size about 30–400 nm and applied β - MnO_2 to form bars and columns, with the surface area of $68.82 \text{ m}^2/\text{g}$, as a catalyst to remove methylene blue. The degradation percentage of methylene blue using β - MnO_2 is 100% in 40 minutes. Furthermore, Liangjie Yuan [1] studied the ability of the catalyst carbon nanometre coated MnO_2 to treat MB by adding H_2O_2 agent. In addition, Yang et al. [2] also studied the ability of the catalysts to remove hexanol of amorphous MnO_2 oxide and pyroluzite (β - MnO_2). The study found that 99% of hexanol was treated in 60 minutes. Han et al. [25] also synthesized $\text{Mn}_3\text{O}_4/\text{SBA-15}$ to treat ethanol with a concentration of 100 ppm under the H_2O_2 agent. The study of Han et al. group and Liangjie Yuan group also demonstrated that manganese oxide nanoparticles are a oxidation catalytic to induce free radicals OH^* , O_2^* , and HO_2^* , leading to potential application of it in heterogeneous Fenton catalytic. Thus, manganese dioxide nanoparticles are not only degradation MB by physical adsorption but also degradation MB by heterogeneous Fenton catalytic oxidation. However, the use of manganese dioxide nanoparticles has several disadvantages due to self-aggregation, difficulty in solid-liquid separation, and leaching of nanoparticles with the treated effluents. These limitations can be avoided by anchoring the particle on the substrates with high sorption capacity of adsorbents and Fenton catalytic activity such as laterite ore. Therefore, manganese oxide nanoparticles were then mixed with denaturated laterite (iron-rich ore, available in Vietnam) to create new high-performance materials because impregnation or coating with nanoparticles enhances the sorption capacity of adsorbents and Fenton catalytic activity. Therein, the manganese oxide nanoparticle is the catalysts effective material, and the laterite is the adsorption efficiency material for degradation MB. Therefore, the combination of these two effective materials can result in the best adsorbent and catalytic oxidation material for MB removal. The objectives of this study are to synthesize colloidal manganese dioxide nanoparticles (MnO_2 NPs), to prepare mixed material by mixing colloidal MnO_2 NPs and denaturated laterite, and to investigate the adsorption and heterogeneous Fenton catalysts of the mixed material for MB removal.

2. Materials and Methods

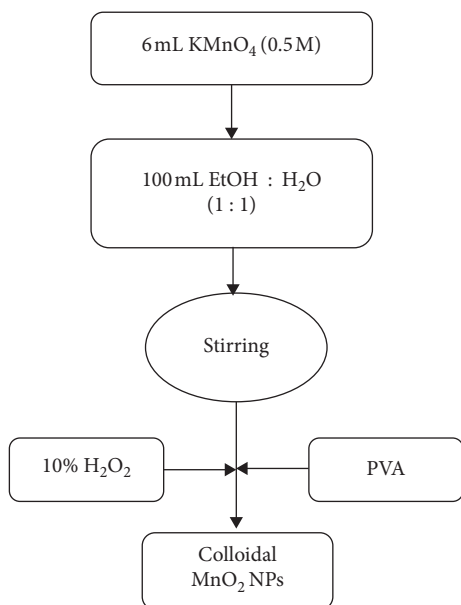
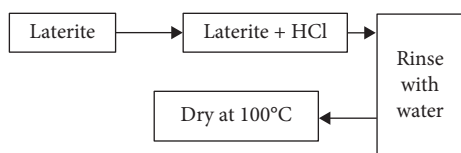
2.1. Chemicals and Characterization. All chemical reagents, including manganese sulfate monohydrate ($\text{MnSO}_4 \cdot \text{H}_2\text{O}$), potassium permanganate (KMnO_4), hydrogen peroxide (H_2O_2), ethanol ($\text{C}_2\text{H}_5\text{OH}$, 99.5%), polyvinyl alcohol (PVA, $M_w \sim 31,000$), and methylene blue, were purchased from Merck. In our experiment, we use laterite ore from Cao Bang Province, VietNam.

X-ray diffraction (XRD) spectra of absorption materials were obtained using D8 Advance (Bruker, Germany) and D5005 (Siemens, Germany). The scanning electron microscopy and energy dispersive X-ray spectroscopy (EDX) were performed with S-4800 (SEM, Hitachi). The transmission electron microscopy (TEM) was performed with a JEOL JEM1010 operated at 80 kV. UV-Vis absorption spectra were obtained on an UV1800, Japan.

2.2. Synthesis of Colloidal Manganese Dioxide Nanoparticles (MnO_2 NPs). The colloidal MnO_2 NPs are synthesized as shown in Scheme1 [26]. 6 mL of the diluted potassium permanganate (KMnO_4 0.5 M) solution was added into 100 mL mixture solvent of EtOH : H_2O (1 : 1) at room temperature. The mixture was stirred, and then 10% H_2O_2 and polyvinyl alcohol (PVA) were added. The polyvinyl alcohol (PVA) was used a coreduction agent to obtain MnO_2 . Soon after adding 10% H_2O_2 and polyvinyl alcohol (PVA), the brown precipitate began to appear. The brown precipitate was collected by centrifugation and washed with ethyl alcohol (three times). To remove polyvinyl alcohol (PVA), the mixture was precipitated with ethanol as a solvent and hexane as an antisolvent. Finally, colloidal MnO_2 NPs were obtained as brown powder.

2.3. Preparation of Laterite-Based Materials. The laterite ore was collected from Cao Bang Province, Vietnam. The laterite ore was crushed and sieved. The fraction small laterite particle is thermally denaturated by following the procedure in Scheme2. 100 g of laterite powder was treated with 40 mL of HCl in a 250 mL beaker. The mixtures were soaked for 2 hours and then decant a liquid. The remaining powder was rinsed with distilled water and dried at 100°C . Finally, we obtained the substrate material, referred to as M1.

2.4. Preparation of Mixed. In the final step, the prepared colloidal MnO_2 NPs were mixed with denaturated laterite by the immersion method. 50 g of the denaturated laterite particle (0.5 mm) was added into the beaker which contained the colloidal MnO_2 NPs. The mixture was impregnated for 12 hours and then dried at 105°C for 8 hours. The power was rinsed by distilled water to remove the remaining salt. Finally, we obtained the mixed adsorbent material symbolized as M2.

SCHEME 1: Synthesis of colloidal MnO₂ NPs.

SCHEME 2: Thermal denaturation of laterite ore.

To determine the shape, phase composition, particle size, particle distribution of colloidal MnO₂ NPs (M1), and M2 materials, we use the transmission electron microscopy (TEM), scanning electron microscopy (SEM), and X-ray diffraction (XRD) pattern (XRD) analysis.

The adsorptive and catalytic activities of the mixed material (M2) were assessed by using methylene blue. The methylene blue concentrations before and after treatment were determined by the absorption intensity of the UV spectrum at the maximum absorption wavelength of 664 nm, which is explained in detail in Supplementary Materials.

2.5. Adsorption Experiments. Adsorption experiments were investigated by changing the effective factors such as time, pH, and concentration of methylene blue (MB). The residual concentration of MB was determined with the help of the calibration plot of MB solution at a fixed wavelength (667 nm) with varying initial ion metal concentration which is explained in detail in Supplementary Materials. The amount of adsorbed MB (C_a mg/L) was found out using the following formula [27]:

$$C_a = C_0 - C_e \text{ (mg/L)}, \quad (1)$$

where C_0 is the initial concentration and C_e is the residual concentration of MB. The adsorption percentage was calculated by the following equation:

$$\text{Adsorption (\%)} = \frac{C_a}{C_0} \times 100, \quad (2)$$

where C_a is the adsorbed concentration (mg/L) of MB and C_0 is the initial concentration of MB.

The equilibrium adsorption capacities of M2 for methylene blue (MB) were calculated by the following equation [27]:

$$q_e = \frac{V_0(C_0 - C_e)}{m}, \quad (3)$$

where q_e is the equilibrium adsorption capacity (mg/g), C_0 and C_e are the initial and residual concentrations (mg/L) of MB solution, respectively, V_0 is the volume of the initial solution (L) use for sorption, and m is the weight of the adsorbent (g).

2.5.1. Determination of Equilibrium Time. The equilibrium time was determined by taking 1.0 g of the adsorbent M2 with 100 mL MB (80 mg/L) solution at pH equal to 7, followed by stirring at room temperature at various time intervals ranging from 0 to 7 h.

2.5.2. Adsorption Isotherm. The adsorption isotherms of MB were investigated by taking 1.0 g of M2 material with 100 mL of MB solution with different initial concentrations (varying from 10 to 300 mg/L) at pH about 7 under room temperature with stirring for 6 hours.

2.5.3. Kinetic Adsorption Experiment. The adsorption kinetic is described by the Langmuir adsorption model and the Freundlich adsorption model. The Langmuir equation is generally expressed as follows [28]:

$$\frac{1}{q_e} = \frac{1}{q_{\max} K_L C_e} + \frac{1}{q_{\max}}, \quad (4)$$

where q_e and q_{\max} are the equilibrium adsorption capacity and a maximum capacity of adsorbent (mg/g), respectively, C_e is the equilibrium MB concentration in solution (mg/L), and K_L is the Langmuir adsorption constant pertaining to the energy of adsorption (L/mg).

The Freundlich equation is generally expressed as follows [28]:

$$\lg q_e = \lg K_F + \frac{1}{n_F} \lg C_e, \quad (5)$$

where $n = 1/n_F$ is the slope of Freundlich isotherm and K_L is the Freundlich adsorption constant.

2.6. Heterogeneous Fenton Catalytic Oxidation Experiments. Degradation of MB was carried out to evaluate the heterogeneous Fenton catalytic oxidation characterization of a new catalytic oxidation material (M2). Sodium hydroxide and hydrochloric acid were used for modifying the pH of the solutions. 30% hydrogen peroxide was used as the oxidation agent to enhance the degradation of MB. The degradation experiments were performed as a function of time, pH of MB

solution, and the amount of 30% hydrogen peroxide under room temperature. The degradation percentage of MB was calculated according to the following equation [1]:

$$\text{degradation (\%)} = \frac{C_0 - C_e}{C_0} \times 100, \quad (6)$$

where C_0 is the initial concentration of MB solution and C_e is the residual concentration of MB solution after treating with the catalyst oxidation material M2.

2.6.1. Effect of Amount of Hydrogen Peroxide. The effect of amount of 30% H_2O_2 on the degradation of methylene blue (MB) was evaluated by stirring 1.0 g M2 material with 100 mL of MB solution (20 mg/L) for various volumes of 30% H_2O_2 solution from 0.2 to 5 mL, at pH 7.0, followed by stirring for 45 min. Then, the MB solutions were separated by centrifugation to determine the methylene blue concentration by using the UV-Vis spectrophotometer.

2.6.2. Effect of Time. The effect of time on the degradation of MB was evaluated by stirring 1.0 g M2 material and adding 1.5 mL 30% H_2O_2 and 100 mL of MB solution (20 mg/L) at various time intervals ranging from 0 to 180 min, at pH 7.0. Then, the MB solutions were separated by centrifugation to determine the methylene blue concentration by using the UV-Vis spectrophotometer.

2.6.3. Effect of pH. The effect of pH of metal ion solutions on degradation of MB was examined. 1.0 g of M2 material was added to 100 mL of MB 20 mg/L solution with varying pH values ranging from 2 to 12, at room temperature, followed by stirring for 45 min. The pH of metal ion solutions was adjusted to the desired value by using HCl 0.1 M or NaOH 0.1 M.

2.6.4. Effect of Catalyst Oxidation Material M2 Mass. The effect of amount of M2 on the degradation of MB was tested by stirring different amounts of M2 (0.2, 1.0, 1.5, 2.0, 2.5, 3.0, 3.5, 4.0, and 5.0 g) and adding 1.5 mL 30% H_2O_2 and 100 mL of MB solution (20 mg/L) at pH 7.0, followed by stirring for 45 min. Then, the MB solutions were separated by centrifugation to determine the methylene blue concentration by using the UV-Vis spectrophotometer.

3. Results and Discussion

3.1. Characterization of Colloidal MnO_2 NPs, Laterite, and Mixed Material (M2). Figure 1 shows the transmission scanning electron microscopy (TEM) image of colloidal MnO_2 NPs. The average sizes of the MnO_2 NPs are about 50 nm. The TEM image clearly shows that the spherical particle of MnO_2 NPs sample is formed, and their size distribution is narrow. Moreover, the TEM results of MnO_2 NPs sample show those particles which aggregate to form a block with a porous structure.

The surface structures of laterite (M1) and mixed material (M2) were analysed by the scanning electron

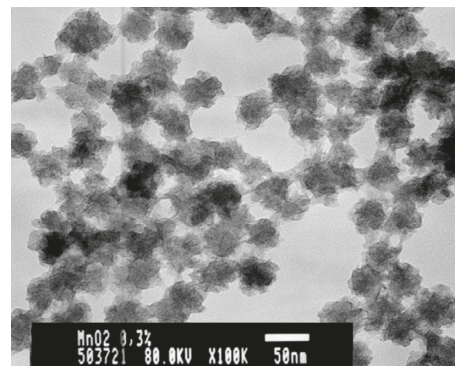


FIGURE 1: TEM micrograph of MnO_2 nanoparticles.

microscopy (SEM) in Figures 2(a) and 2(b). The SEM results show that the surface of the laterite after the immersion process has been coated by the nanoparticle layer. In addition, the average sizes of laterite particles are about 5 μm in Figure 2(a). Therefore, we believe that the nanoparticle layer is MnO_2 NPs, which coats on the laterite surface.

Figure 3 shows X-ray diffraction (XRD) patterns of M1, MnO_2 NPs, and M2 materials. The XRD results of laterite (M1) and laterite after coating with MnO_2 nanoparticle (M2) showed some similar main peaks at 2θ of 24.2, 34.1, 35.8, 54.6, 62.7, 21.0, 26.7, 50.10, and 60° which were associated with hematite and quartz [29]. In addition, the XRD result of MnO_2 NPs does not show any peaks. Thus, these results prove that the MnO_2 NPs layer coats on laterite in an amorphous structure.

The composition of the laterite after coating MnO_2 nanoparticle (M2) is also analysed by energy dispersive X-ray spectroscopy (EDX). Figure 4 shows that these M2 materials are composed of mainly Fe element (from Fe_2O_3), Si element (from the SiO_2), Al element (from the Al_2O_3), O element (from Fe_2O_3 , SiO_2 , and Al_2O_3), and S element. Furthermore, the manganese element is detected in the EDX result which shows that MnO_2 NPs had been coated on the surface of the laterite particle.

3.2. The Adsorption of the Mixed Material (M2)

3.2.1. Effect of Time. The adsorption process is time dependent, as shown in Figure 5 and Table S1 (Supplementary materials). The results of MB showed that when increasing the adsorption time, the adsorption percentage increased. In Figure 5, adsorption occurs rapidly in the first 5 hours, and then the adsorption rate slowed down and almost reached equilibrium at 6 hours. Hence, 6 hours have to be considered as an optimized time for the adsorption of MB.

The adsorption isotherms of MB were investigated by taking 1.0 g of M2 adsorbent material with 100 mL of MB solution with different initial concentrations (varying from 20 to 100 mg/L) at pH of about 7 under room temperature with stirring for 6 hours. The results in Table S4 (Supplementary materials) show that when the concentration of MB gradually increases, the adsorption capacity increases and the percentage decreases.

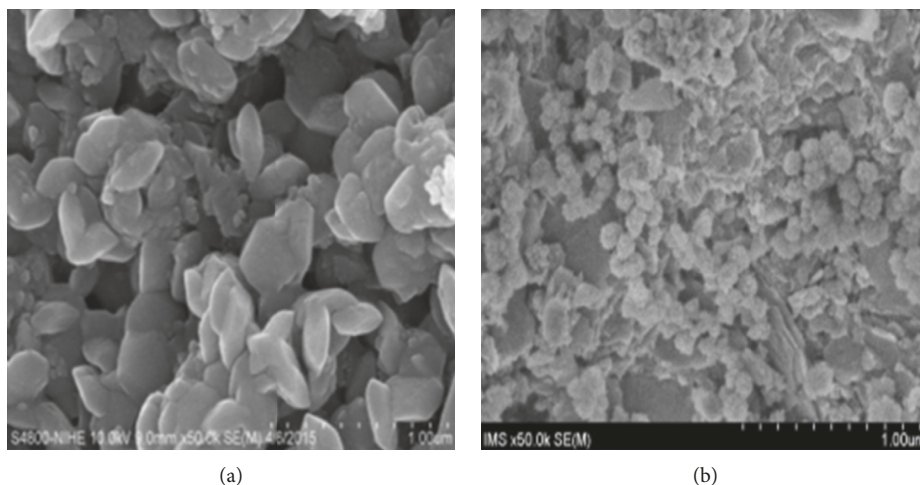


FIGURE 2: SEM micrographs of (a) laterite (M1) and (b) laterite after coating with MnO₂ nanoparticles (M2).

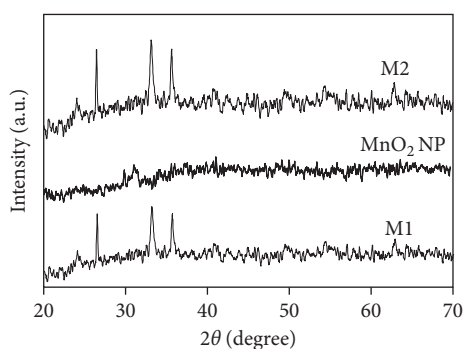


FIGURE 3: Powder X-ray diffraction pattern of M1, MnO₂ NP, and M2 samples.

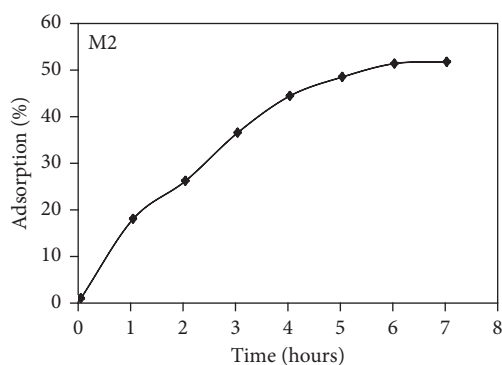


FIGURE 5: Effect of time on the adsorption process of MB.

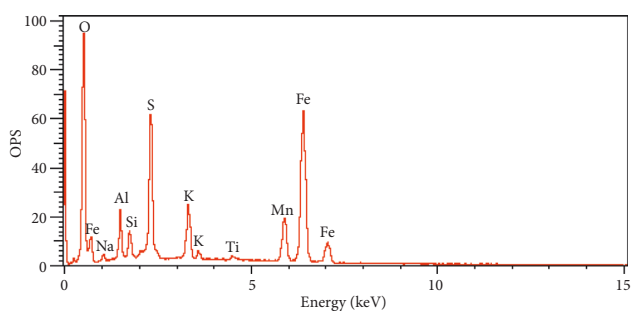


FIGURE 4: Energy-dispersive X-ray (EDX) spectra of the mixed laterite after MnO₂ NP (M2) coating.

3.2.2. Adsorption Isotherm. The adsorption kinetic is described by the Langmuir adsorption model and the Freundlich adsorption model [28]. The linear equation was used to fit the MB adsorption process on M2, as shown in Figures 6(a) and 6(b) and Table S2 (Supplementary materials). The Langmuir adsorption isotherm assumes that the monolayer adsorption occurs on a homogeneous surface of the adsorbent, while Freundlich adsorption isotherm assumes that the multilayer adsorption occurs on a heterogeneous surface of the adsorbent. Results show that the Freundlich model ($R^2 = 0.966$) is better than the Langmuir

model ($R^2 = 0.8717$) in simulating the adsorption experiments. This suggests that the adsorption process is a heterogeneous process. The maximum adsorption capacity for MB was 10.63 mg/g. The n_F value in the Freundlich equation (Table 1) is used to determine adsorption whether it is linear adsorption ($n_F = 1$), chemical adsorption ($n_F < 1$), or physical adsorption ($n_F > 1$) [28]. Moreover, the adsorption of M2 on MB powder is the physical adsorption process due to the n_F value ($n_F = 2.6$) larger than 1 (Table 1).

Moreover, to assess the adsorption performance of laterite after coating MnO₂ NP material (M2) in environmental treatment, our group investigated large-scale survey adsorption performance by preparing one adsorption column with a diameter of 15 cm, height of 15 cm, and weight of M2 material about 50 g. The ability absorption MB of the column was carried out with the initial concentration of methylene blue 40 mg/L and flow rate 2 mL/min. The results of column processing absorption are given in Table 2.

The results of Table 2 show adsorption performance of the laterite-coating MnO₂ NP material (M2). These results suggest the MB adsorption over the laterite after coating MnO₂ NPs (M2) proceeds rather through weak and physical type adsorption than chemical type adsorption. Moreover, the adsorption time reached equilibrium at 6 hours with low adsorption percentage of MB of 50%.

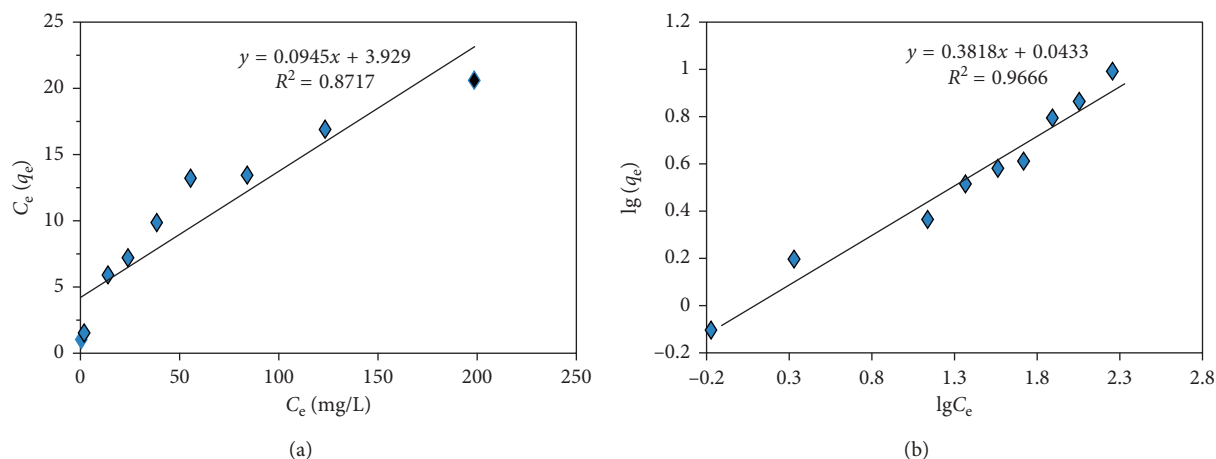


FIGURE 6: Adsorption isotherm of MB: (a) Langmuir isotherm and (b) Freundlich isotherm.

TABLE 1: Kinetic parameter and correlation coefficient of two kinetic equations.

Langmuir			Freundlich		
K_L (L/mg)	q_{max} (mg/g)	R^2	n_F	K_F	R^2
0.024	10.6	0.871	2.6	1.10	0.966

TABLE 2: Results of the large-scale surveys on adsorption performance of M2.

No.	V (mL)	Output concentration of MB (mg/L)
1	2000	—
2	1000	0.2
3	900	0.91
4	800	1.35
5	700	3.79
6	600	5.11
7	400	8.77
8	200	16.66
9	100	27.80
10	50	33.79
11	25	36.84
12	15	38.01
13	10	39.17
14	5	40.00

Amount of methylene blue absorbed on column is 2.51 g

3.3. The Catalytic Oxidation Activity of the Mixed Material (M2)

3.3.1. Effect of H_2O_2 Concentration. As mentioned above, thanks to the outstanding advantage of removing organic pollutants, the highly biodegradable organic matter (POP) enhanced the oxidation process based on free radicals HO^* of H_2O_2 , which is considered a “key gold” to solve the challenging problems of the century for the current water and wastewater treatment industries. Thus, we investigate the effect of H_2O_2 concentration on the degradation of MB in Figure 7. In Figure 7 and Table S3 (Supplementary materials), the effect of hydrogen peroxide concentration on the degradation of methylene blue shows that in the range of 0.2

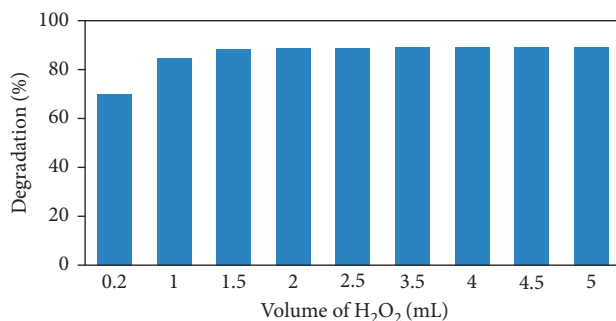


FIGURE 7: Effect of the hydrogen peroxide concentration on the degradation percentage of MB.

to 1.5 mL of 30% H_2O_2 , the degradation percentage increases strongly from 70 to 89.01%. Thus, MB efficiency degradation is proportional to the concentration of H_2O_2 . This result is explained by the increase in the number of free radicals (HO^*) generated from H_2O_2 over the laterite after MnO_2 NP (M2) catalyst coating.

When the amount of H_2O_2 increased over 1.5 mL, the excessive H_2O_2 reacts with the availability of HO^* to release the hydroperoxyl radicals (HOO^*) (Equation (7)). Moreover, the hydroperoxyl radicals (HOO^*) react immediately with HO^* (Equation (8)) to induce H_2O and O_2 (Equation (8)) resulting in a reduction of the availability of HO^* [30].



The consumption of free radical HO^* reduced the catalytic ability, leading to reduction in the efficiency of treatment. Thus, it can be seen that the optimal amount of H_2O_2 for methylene blue treatment is 1.5 mL of 30% H_2O_2 .

3.3.2. Effect of Time. The survey results of the effect of time (Figure 8 and Table S4 (Supplementary materials)) show that

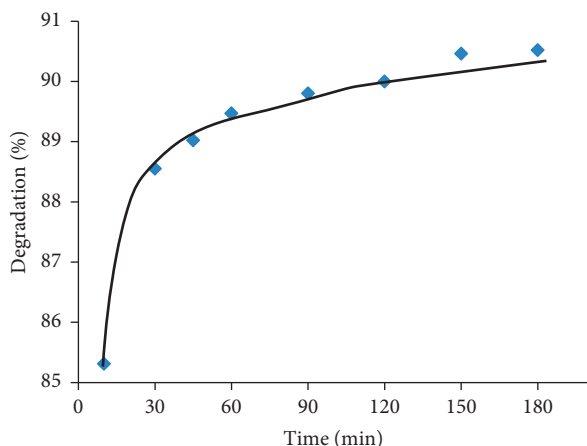
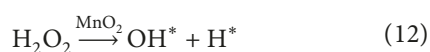
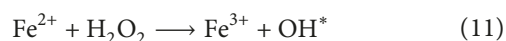
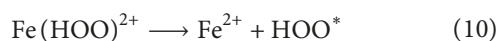
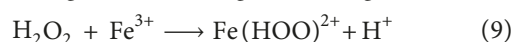


FIGURE 8: Effect of time on the degradation percentage of MB.

the first 45 min of processing speed increased rapidly and reached a quite high efficiency of 89.96% and then increased slowly. Thus, during the next survey, it is recommended to select the optimal time of 45 min.

3.3.3. Effect of pH. The pH of the solution plays an important role in determining the adsorption ability of M2 for methylene blue. The effect of pH on the MB removal was investigated at a pH range of 2–12. The results obtained are presented in Figure 9 and Table S5 (Supplementary materials). The results of surveying the effect of pH show that when the pH was 2–5, the MB degradation efficiency was low. When the pH is from 6 to 8, the degradation efficiencies of MB increase strongly from 80 to 89%. Especially, the maximum degradation efficiency of MB is 100% in the pH region of 9–12. Therefore, we choose pH 7 for further studies.

3.3.4. Effect of Catalyst Dosage. The effect of the amount of the laterite after MnO₂ NP (M2) catalyst coating on the removal of methylene blue is investigated and is shown in Figure 10 and Table S6 (Supplementary materials). The result shows that the degradation efficiency increases with increasing catalyst content, due to the increase in the catalytic active sites on the surface of the catalyst and the associated generated free hydroxyl radicals (equations (9)–(12)) [29, 30]. Especially, the degradation efficiency increases rapidly in the range of 0.5 to 1.5 g of M2 (Figure 10):



However, when the amount of M2 increased over 1.5 g, the degradation efficiency did not change so much. This

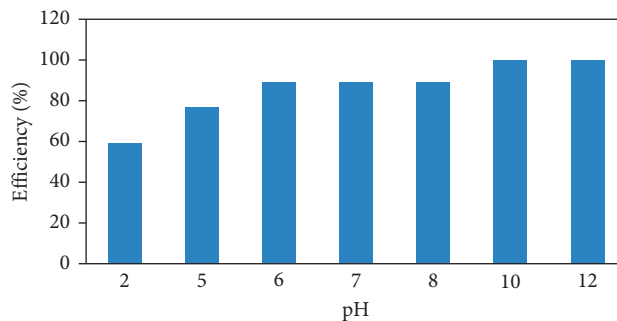


FIGURE 9: Effect of pH on the degradation percentage of MB.

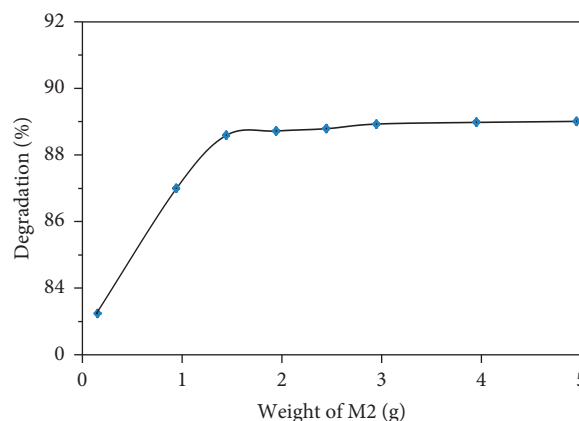
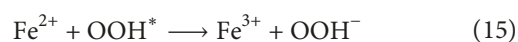
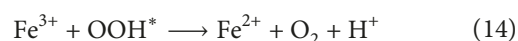
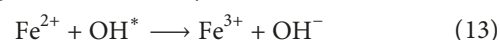


FIGURE 10: The effect of the amount of mixed material M2 on the degradation percentage of MB.

phenomenon is attributed to the scavenging effect of HO* radicals during unwanted side reactions over the catalyst surface M2, resulting in a reduction of the availability of HO* and degradation efficiency [29]:



Thus, in the next survey, we conducted the selection of catalyst amount of about 1.5 g. Moreover, the increase of catalyst dosage should be accompanied by an increase in H₂O₂ concentration, and an optimum concentration ratio has to be maintained.

To assess the heterogeneous Fenton catalytic oxidation performance of laterite after coating MnO₂ NP material (M2) in environmental treatment, our group conducted large-scale surveys by preparing one catalytic column with a diameter of 15 cm, height of 15 cm, and weight of M2 material on the column of about 50 g. The ability degradation MB of the catalytic column was carried out with 3 mL H₂O₂ 30%, the initial concentration of methylene blue of 40 mg/L and flow rate 2 mL/min. The results of columns processing capacity are given in Table 3.

The results in Tables 2 and 3 show that the laterite-coating MnO₂ nanoparticle material (M2) has both

TABLE 3: Results of the large-scale surveys on the heterogeneous Fenton catalytic oxidation performance of M2.

No.	V (mL)	Output concentration of MB (mg/L)
1	1200	—
2	1000	—
3	1000	—
4	1000	0.21
5	900	0.26
6	800	0.27
6	700	0.29
7	600	0.32
8	500	0.34
9	400	0.41
10	300	0.45
11	300	0.48
12	200	0.53
13	200	0.57
14	200	0.62
15	100	0.63
16	100	0.64
17	50	0.65

TABLE 4: The degradation efficiency of MB after reusing the catalyst five times.

No.	1	2	3	4	5
Degradation efficiency (%)	99.85	99.68	99.53	98.92	98.86

adsorption and heterogeneous Fenton catalytic oxidation performances. However, the heterogeneous Fenton catalytic oxidation performance is the domain because the degradation efficiency of MB after the sample running through the catalytic column almost does not change much and is about 96–100% (Table 3). This is consistent with that of the previous studies [1, 25, 31]. Specifically, our group has investigated the possibility of catalytic reuse of M2 material with 3.0 mL of 30% H₂O₂, 10 L of methylene blue of 40 mg/L, and flow rate 2 mL/min. The number of reusing the catalyst (M2) is five as shown in Table 4, the degradation efficiency of MB still reaches 98.86%. Therefore, these results prove that heterogeneous Fenton catalytic oxidation performances of the M2 material with 3.0 mL H₂O₂ 30% is completely unaffected after oxidizing MB and reusing at least five times.

4. Conclusions

In conclusion, the adsorption and heterogeneous Fenton catalytic oxidation experiments of laterite-coating manganese dioxide nanoparticle material (M2) were investigated by changing the effective factors such as time, pH, and concentration of MB. The results show that the laterite-coating MnO₂ NP material (M2) shows both adsorption and heterogeneous Fenton catalytic oxidation performances. However, the heterogeneous Fenton catalytic oxidation performance is the domain. Hence, our groups have investigated the ability of catalytic column treatment with high degradation efficiency after the MB solution running through the column almost does not change much. These results prove that the heterogeneous Fenton catalytic activity

of laterite-coating MnO₂ NP material (M2) is completely unaffected by the number of times the MB solution runs through the column. Moreover, this M2 material can be reused five times with the degradation efficiency still being 98.86%. Based on these catalytic performances, the laterite-coating MnO₂ NP material is worthy to be seriously considered in the design of sustainable and readily affordable wastewater treatment solutions in developing tropical countries.

Data Availability

The data used to support the findings of this study are available from the corresponding author upon request.

Conflicts of Interest

The authors declare that they have no conflicts of interest.

Acknowledgments

This research was supported by the researcher program of National University of Civil Engineering, Viet Nam (VL-2019/01).

Supplementary Materials

Figure S1: the calibration graph of MB solution at λ_{\max} to about 644 nm. Table S1: the effect of time on adsorption percentage of M2 for MB. Table S2: the effect of MB concentration solution on the adsorption capacity. Table S3: the effect of hydrogen peroxide concentration on the degradation percentage of MB. Table S4: the effect of time on the degradation percentage of MB. Table S5: the effect of pH on the degradation percentage of MB. Table S6: the effect of the amount of the M2 on the degradation percentage of MB. (*Supplementary Materials*)

References

- [1] L. Zhang, Y. Nie, C. Hu, and X. Hu, "Decolorization of methylene blue in layered manganese oxide suspension with H₂O₂," *Journal of Hazardous Materials*, vol. 190, no. 1–3, pp. 780–785, 2011.
- [2] Z. Yang, Y. Zhang, W. Zhang et al., "Nanorods of manganese oxides: synthesis, characterization and catalytic application," *Journal of Solid State Chemistry*, vol. 179, no. 3, pp. 679–684, 2006.
- [3] M. Rafatullah, O. Sulaiman, R. Hashim, and A. Ahmad, "Adsorption of methylene blue on low-cost adsorbents: a review," *Journal of Hazardous Materials*, vol. 177, no. 1–3, pp. 70–80, 2010.
- [4] C. Xu, G. P. Rangaiah, and X. S. Zhao, "Photocatalytic degradation of methylene blue by titanium dioxide: experimental and modeling study," *Industrial & Engineering Chemistry Research*, vol. 53, no. 38, pp. 14641–14649, 2014.
- [5] V. K. Gupta and Suhas, "Application of low-cost adsorbents for dye removal—a review," *Journal of Environmental Management*, vol. 90, no. 8, pp. 2313–2342, 2009.
- [6] J.-S. Wu, C.-H. Liu, K. H. Chu, and S.-Y. Suen, "Removal of cationic dye methyl violet 2B from water by cation exchange

- membranes," *Journal of Membrane Science*, vol. 309, no. 1-2, pp. 239-245, 2008.
- [7] Y. Li, Q. Du, T. Liu et al., "Comparative study of methylene blue dye adsorption onto activated carbon, graphene oxide, and carbon nanotubes," *Chemical Engineering Research and Design*, vol. 91, no. 2, pp. 361-368, 2013.
- [8] M.-X. Zhu, L. Lee, H.-H. Wang, and Z. Wang, "Removal of an anionic dye by adsorption/precipitation processes using alkaline white mud," *Journal of Hazardous Materials*, vol. 149, no. 3, pp. 735-741, 2007.
- [9] N. Zaghbani, A. Hafiane, and M. Dhahbi, "Separation of methylene blue from aqueous solution by micellar enhanced ultrafiltration," *Separation and Purification Technology*, vol. 55, no. 1, pp. 117-124, 2007.
- [10] J. Huang, L. Peng, G. Zeng et al., "Evaluation of micellar enhanced ultrafiltration for removing methylene blue and cadmium ion simultaneously with mixed surfactants," *Separation and Purification Technology*, vol. 125, no. 214, pp. 83-89, 2014.
- [11] G. Sudarjanto, B. Keller-Lehmann, and J. Keller, "Optimization of integrated chemical-biological degradation of a reactive azo dye using response surface methodology," *Journal of Hazardous Materials*, vol. 138, no. 1, pp. 160-168, 2006.
- [12] C. L. Hsueh, Y. H. Huang, C. C. Wang, and C. Y. Chen, "Degradation of azo dyes using low iron concentration of Fenton and Fenton-like system," *Chemosphere*, vol. 58, no. 10, pp. 1409-1414, 2005.
- [13] H. Lim, J. Lee, S. Jin, J. Kim, J. Yoon, and T. Hyeon, "Highly active heterogeneous Fenton catalyst using iron oxide nanoparticles immobilized in alumina coated mesoporous silica," *Chemical Communications*, vol. 4, pp. 463-465, 2006.
- [14] S. Yang, H. He, D. Wu et al., "Decolorization of methylene blue by heterogeneous Fenton reaction using $\text{Fe}_{3-x}\text{Ti}_x\text{O}_4$ ($0 \leq x \leq 0.78$) at neutral pH values," *Applied Catalysis B: Environmental*, vol. 89, no. 3-4, pp. 527-535, 2009.
- [15] B. H. Hameed, A. L. Ahmad, and K. N. A. Latiff, "Adsorption of basic dye (methylene blue) onto activated carbon prepared from rattan sawdust," *Dyes and Pigments*, vol. 75, no. 1, pp. 143-149, 2007.
- [16] M. Matheswaran and T. Raju, "Destruction of methylene blue by mediated electrolysis using two-phase system," *Process Safety and Environmental Protection*, vol. 88, no. 5, pp. 350-355, 2010.
- [17] Y. Wang, X. Zhang, X. He, W. Zhang, X. Zhang, and C. Lu, "In situ synthesis of MnO_2 coated cellulose nanofibers hybrid for effective removal of methylene blue," *Carbohydrate Polymers*, vol. 110, pp. 302-308, 2014.
- [18] P. Gómez-Romero and C. Sanchez, "Hybrid materials, functional applications. an introduction," in *Functional Hybrid Materials*, Wiley-VCH Verlag GmbH & Co. KGaA, Weinheim, Germany, 2005.
- [19] D. M. Robinson, Y. B. Go, M. Mui et al., "Photochemical water oxidation by crystalline polymorphs of manganese oxides: structural requirements for catalysis," *Journal of the American Chemical Society*, vol. 135, no. 9, pp. 3494-3501, 2013.
- [20] S. Chakrabarti, B. K. Dutta, and R. Apak, "Active manganese oxide: a novel adsorbent for treatment of wastewater containing azo dye," *Water Science and Technology*, vol. 60, no. 12, pp. 3017-3024, 2009.
- [21] X. Liao, C. Zhang, Y. Liu et al., "Abiotic degradation of methyl parathion by manganese dioxide: kinetics and transformation pathway," *Chemosphere*, vol. 150, pp. 90-96, 2016.
- [22] M. Shaban, M. R. Abukhadra, S. S. Ibrahim, and M. G. Shahien, "Photocatalytic degradation and photo-Fenton oxidation of Congo red dye pollutants in water using natural chromite-response surface optimization," *Applied Water Science*, vol. 7, no. 8, pp. 4743-4756, 2017.
- [23] T. L. P. Dantas, V. P. Mendonça, H. J. José, A. E. Rodrigues, and R. F. P. M. Moreira, "Treatment of textile wastewater by heterogeneous Fenton process using a new composite $\text{Fe}_2\text{O}_3/\text{carbon}$," *Chemical Engineering Journal*, vol. 118, no. 1-2, pp. 77-82, 2006.
- [24] W. Zhang, Z. Yang, X. Wang, Y. Zhang, X. Wen, and S. Yang, "Large-scale synthesis of $\beta\text{-MnO}_2$ nanorods and their rapid and efficient catalytic oxidation of methylene blue dye," *Catalysis Communications*, vol. 7, no. 6, pp. 408-412, 2006.
- [25] Y.-F. Han, F. Chen, K. Ramesh, Z. Zhong, E. Widjaja, and L. Chen, "Preparation of nanosized $\text{Mn}_3\text{O}_4/\text{SBA-15}$ catalyst for complete oxidation of low concentration EtOH in aqueous solution with H_2O_2 ," *Applied Catalysis B: Environmental*, vol. 76, no. 3-4, pp. 227-234, 2007.
- [26] R. S. Dassanayake, E. Rajakaruna, H. Moussa, and N. Abidi, "One-pot synthesis of MnO_2 -chitin hybrids for effective removal of methylene blue," *International Journal of Biological Macromolecules*, vol. 93, pp. 350-358, 2016.
- [27] I. Ahmad, W. A. Siddiqui, and T. Ahmad, "Synthesis, characterization of silica nanoparticles and adsorption removal of Cu^{2+} ions in aqueous solution," *International Journal of Emerging Technology and Advanced Engineering*, vol. 7, no. 8, pp. 439-445, 2017.
- [28] W. Zhu, W. Jingxuan, D. Wu et al., "Investigating the heavy metal adsorption of mesoporous silica material prepared by microwave synthesis," *Nanoscale Research Letter*, vol. 12, no. 1, p. 323, 2017.
- [29] G. M. R. Kpinsoton, H. K. Y. Richardson, B. N. Koffil et al., "New insight into the micro structure of natural calcined laterites and their performance as heterogeneous Fenton catalyst form ethylene blue degradation," *Reaction Kinetics, Mechanisms and Catalysis*, vol. 124, no. 2, pp. 931-956, 2018.
- [30] M. E. Becerra, A. M. Suarez, N. P. Arias, and O. Giraldo, "Decomposition of the methylene blue dye using layered manganese oxide materials synthesized by solid state reactions," *International Journal of Chemical Engineering*, vol. 2018, Article ID 4902376, 11 pages, 2018.
- [31] S. Chou and C. Huang, "Application of a supported iron oxyhydroxide catalyst in oxidation of benzoic acid by hydrogen peroxide," *Chemosphere*, vol. 38, no. 12, pp. 2719-2731, 1999.

Research Article

Using Electrode Made of Carbon Nanotubes and Bismuth Oxide for the Determination of Metal Concentration by Anodic Stripping Voltammetry

Thi Thu Phuong Nguyen ¹, Xuan Gian Trinh,² and Dao Thi To Uyen^{3,4}

¹Faculty of Chemical Technology, Hanoi University of Industry, 298 Cau Dien, Bac Tu Liem, Hanoi, Vietnam

²Institute of Chemistry, Vietnam Academy of Science and Technology, 18 Hoang Quoc Viet, Cau Giay, Hanoi, Vietnam

³Center of Excellence for Green Energy and Environmental Nanomaterials (CEGrEEN), Nguyen Tat Thanh University, 300A Nguyen Tat Thanh, District 4, Ho Chi Minh City 755414, Vietnam

⁴NTT Hi-Tech Institute, Nguyen Tat Thanh University, Ho Chi Minh City 700000, Vietnam

Correspondence should be addressed to Thi Thu Phuong Nguyen; thuphuongdhn@yahoo.com

Received 13 March 2019; Revised 30 May 2019; Accepted 27 June 2019; Published 2 September 2019

Guest Editor: Nguayen Van Noi

Copyright © 2019 Thi Thu Phuong Nguyen et al. This is an open access article distributed under the Creative Commons Attribution License, which permits unrestricted use, distribution, and reproduction in any medium, provided the original work is properly cited.

We have successfully manufactured a new electrode modified with bismuth oxide (Bi_2O_3) using carbon nanotubes (CNTs). The electrode was fabricated to detect cadmium (Cd), lead (Pb), and indium (In) by differential pulse anodic stripping voltammetry (DP-ASV). The electrode surface was studied by scanning electron microscopy (SEM), and the reduction and oxidation processes were studied by cyclic voltammetry (CV) techniques. Operational parameters such as electrode size, bismuth concentration, and electrolytic background were optimized. The DP-ASV method used fabricated electrodes with a linear response range from $1.5\text{--}20\ \mu\text{g}\cdot\text{L}^{-1}$ with Cd(II) and Pb(II) and $2.5\text{--}20\ \mu\text{g}\cdot\text{L}^{-1}$ with In(III); low detection limit (LOD) of $0.22\ \mu\text{g}\cdot\text{L}^{-1}$ with Cd(II), $0.65\ \mu\text{g}\cdot\text{L}^{-1}$ with In(III), and $0.26\ \mu\text{g}\cdot\text{L}^{-1}$ with Pb(II); and good repeatability with relative standard deviations (RSD) of 2.65%, 2.51%, and 3.34% with Cd(II), Pb(II), and In(III), respectively ($n=8$). The electrode can be used to test the content of Cd(II), In(III), and Pb(II) in water.

1. Introduction

The Cd and Pb determination is very important because of their toxic effects to environment and humans [1]. Several compounds of In can cause cancer and are toxic [2]. Some analytical methods such as atomic absorption spectrometry (AAS) [3–8], inductively coupled plasma-mass spectrometry (ICP-MS) [9–11], and inductively coupled plasma-atomic emission spectroscopy (ICP-AES) [12–16] have been applied to analyse Cd(II), In(III), and Pb(II). These techniques have high selectivity and sensitivity, but they are very expensive and time-consuming. The electroanalytical method not only has high accuracy and sensitivity but also is low cost, has good repeatability, and allows in situ measurement [17]. Carbon paste electrodes (CPEs) have been widely applied in analytical chemistry in some recent years [18–21]. Nowadays, CNTs are

also used in CPEs because they have high mechanical strength, electrical conductivity, and surface area [22–25]. The electrochemical analysis methods using various working electrodes (WEs) have been widely used, in which mercury electrodes have been most commonly used. However, mercury is very toxic. Bismuth is less toxic than mercury, and it has some similar electrochemical characteristics of mercury, so it has been used a lot to replace mercury in electrochemical analysis [26–35]. In this study, we manufactured a new modified CNT electrode with Bi_2O_3 as replacement for mercury electrodes, and this electrode is used as a WE in electrochemical analysis equipment for the simultaneous analysis of Cd(II), In(III), and Pb(II). The method was tested successfully on water samples. In addition, the results were compared with those of graphite furnace atomic absorption spectroscopy (GF-AAS). The accuracy of the method is

evaluated by using the sediment certified reference material (CRM) and graphite furnace atomic absorption spectrometry (GF-AAS).

2. Experimental

2.1. Chemicals and Reagents. CH_3COONa , KI, KCl, NaNO_3 , paraffin oil, CH_3COOH (100%, m/v), and HNO_3 (65%, m/v) were purchased from Merck (Germany). Multiwalled carbon nanotubes (MWCNTs 95%, diameter \times length: 10–35 nm \times 1–10 μm). Bismuth oxide (Bi_2O_3 , grain size $< 10 \mu\text{m}$) was provided by Sigma-Aldrich. Working standards for Pb, Cd, and In were prepared using standard solutions supplied by Merck (standard solutions of 1000 ppm for Cd, Pb, and In).

2.2. Apparatus. The Metrohm 797 VA Computrace (Switzerland) with the working electrode (WE) was the CPE modified with Bi_2O_3 using CNTs. For AAS measurements, a PerkinElmer 3300, USA, was used. For SEM measurements, a field emission SEM S-4800, Hitachi, Japan, was used.

2.3. Fabrication of Electrodes. CNTs (heated at 700°C for 15 min) and paraffin oil (6 : 4, w/w) were mixed with an agate mortar and pestle, and then they were transferred into test tubes with the help of ultrasonic agitation for 2 h. By continuous mixing of carbon paste with Bi_2O_3 by mixing similar to the abovementioned method, the modified carbon nanotube paste was obtained. This modified carbon nanotube stuff was packed into a Teflon tube. Electrode surface was cleaned with a filter paper.

2.4. Procedures. The analytical solution was added into the electrolyte beaker. The measurement conditions were as follows: the deposition potential (E_{dep}) -1.2 V , deposition time (t_{dep}) 120 s, speed 15 mV per second, and pulse amplitude (ΔE) $50 \text{ mV}\cdot\text{s}^{-1}$. After a rest time, 20 s, the DP-ASV was saved. The DP-ASV of blank solution was saved with the similar measurement conditions. Before the test, oxygen was removed from the analytical solution by exposing to pure nitrogen gas for 5 minutes.

3. Results and Discussions

3.1. Influence of Electrode Diameters. In stripping voltammetry analysis, all preconcentration and stripping processes happen on the surface of the WE, so the electrode diameter has a great influence on the limit diffusion line. So, we study the influence of different electrode diameters (diameters are 1.8, 2.2, 2.5, 3, 3.5, and 4.0 mm) on the peak (I_p) of metal ions. The results are shown in Figure 1. At 3 mm electrode diameter, I_p of all 3 ions are high, the peak is balanced, and the repeatability is good. Therefore, we chose 3 mm as the optimum electrode diameter.

3.2. Influence of Bi_2O_3 . The simultaneous analysis of Cd(II), Pb(II), and In(III) by DP-ASV using a CPE modified with 1%, 3%, 5%, and 8% (w/w) Bi_2O_3 was researched. The CPE

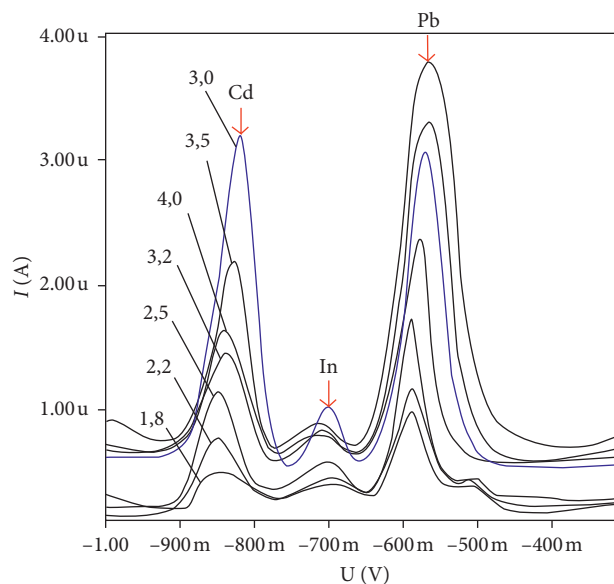


FIGURE 1: Effect of the electrode diameters at a modified CPE with 5% Bi_2O_3 (w/w) in the supporting electrolyte mixture of 0.1 M KI and acetate buffer. Conditions: $E_{\text{dep}} = -1.2 \text{ V}$; $t_{\text{dep}} = 120 \text{ s}$; $\Delta E = 50 \text{ mV}\cdot\text{s}^{-1}$; speed = $15 \text{ mV}\cdot\text{s}^{-1}$.

modified with 5% (w/w) Bi_2O_3 produced the highest Cd, In, and Pb peaks; resolution is high, and repeatability is good. Therefore, the CPE modified with 5% (w/w) Bi_2O_3 was used for the further studies.

3.3. Influence of E_{dep} and t_{dep} . Influence of E_{dep} on the I_p of Cd(II), Pb(II), and In(III) has been investigated with E_{dep} from -0.9 to -1.4 V (Figure 2). The effect of t_{dep} in the range from 30 s to 300 s was also researched (Figure 3). The best stripping signal was obtained at $E_{\text{dep}} -1.2 \text{ V}$ and $t_{\text{dep}} 120 \text{ s}$. From these results, E_{dep} and t_{dep} of -1.2 V and 120 s were selected for the further studies.

3.4. Cyclic Voltammetry (CV). The reduction and oxidation processes were studied by potential scanning from -1.2 to 0.3 V and continuous scanning from 0.3 V to -1.2 V at a speed of 15 mV per second. The results are shown in Figure 4. In Figure 4, the anodic scan resulted in a peak potential of Bi which was -0.12 V that reflects the oxidation of the metallic bismuth.

3.5. Morphological Surface Characterization. Figure 5 shows the scanning electron micrograph (SEM) surface image of the CPE containing 5% Bi_2O_3 (w/w) before and after reduction at $E_{\text{dep}} -1.2 \text{ V}$ with t_{dep} of 120 s. After the electrochemical reduction, the electrode surface was changed because Bi_2O_3 was converted to Bi at -1.2 V for 120 s following the reaction [36]



According to the SEM image, the electrode surface has got a porous structure, and the surface is relatively uniform.

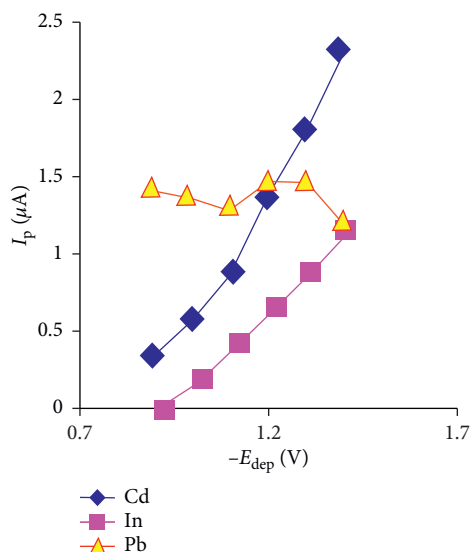


FIGURE 2: DP-ASV of Cd, In, and Pb at different E_{dep} values. Conditions: supporting electrolyte mixture of 0.1 M KI and acetate buffer; $t_{\text{dep}} = 120$ s; $\Delta E = 50 \text{ mV}\cdot\text{s}^{-1}$; speed = $15 \text{ mV}\cdot\text{s}^{-1}$.

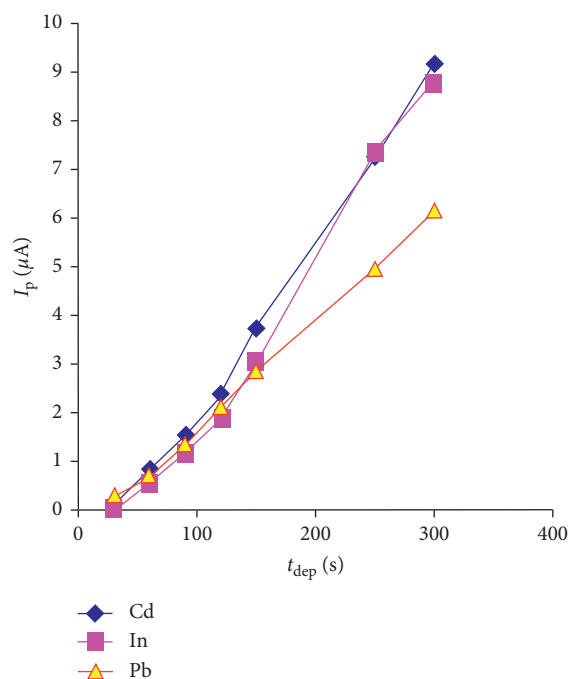


FIGURE 3: DP-ASV of Cd, In, and Pb at different t_{dep} . Conditions: supporting electrolyte mixture of 0.1 M KI and acetate buffer; $E_{\text{dep}} = -1.2$ V; $\Delta E = 50 \text{ mV}\cdot\text{s}^{-1}$; speed = $15 \text{ mV}\cdot\text{s}^{-1}$.

Therefore, it is supposed to be beneficial for the stripping analysis.

3.6. Influence of Supporting Electrolytes. The influence of the background electrolytes, acetate buffer, mixture of NaNO_3 and acetate buffer, KCl and acetate buffer, and KI and acetate buffer, on the I_p of metals were studied. The results are shown in Figure 6. According to [37], simultaneous measurement of

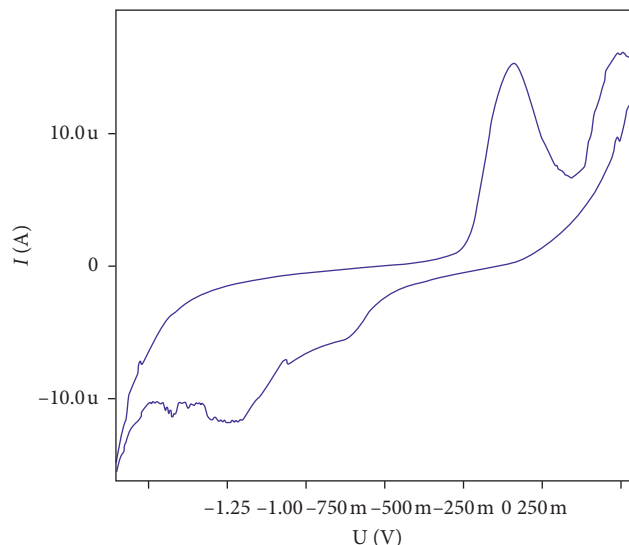


FIGURE 4: Cyclic voltammograms at a modified CPE with 5% Bi_2O_3 (w/w) in the supporting electrolyte mixture of 0.1 M KI and acetate buffer. Conditions: $E_{\text{dep}} = -1.2$ V; $t_{\text{dep}} = 120$ s; $\Delta E = 50 \text{ mV}\cdot\text{s}^{-1}$; speed = $15 \text{ mV}\cdot\text{s}^{-1}$.

Cd(II) , Pb(II) , and In(III) is possible if there is a difference of peak potential of at least 100 mV. In Figure 6(a), the resolution between Cd and In signals in acetate buffer as well as the mixture of NaNO_3 and acetate buffer and KCl and acetate buffer solution is not good. Amongst these mentioned electrolytes, the supporting electrolyte mixture of 0.1 M KI and acetate buffer is the best choice with the best resolution, and largest peak current is for Cd(II) , Pb(II) , and In(III) (Figure 6(b)). Therefore, a medium containing 0.1 M KI and acetate buffer was selected.

3.7. Linear Response Range, LOD, and Reproducibility. The DP-ASV at different concentrations was recorded. The results of linear range are shown in Figure 7(a), and the calibration curves are shown in Figures 7(b)–7(d). The linear response ranges were $1.5\text{--}20 \mu\text{g}\cdot\text{L}^{-1}$ with Cd(II) and Pb(II) and $2.5\text{--}20 \mu\text{g}\cdot\text{L}^{-1}$ with In(III) .

The CPE modified with Bi_2O_3 using MWCNTs also demonstrated LOD ($S/N = 3$) of $0.22 \mu\text{g}\cdot\text{L}^{-1}$ with Cd(II) , $0.26 \mu\text{g}\cdot\text{L}^{-1}$ with Pb(II) , and $0.65 \mu\text{g}\cdot\text{L}^{-1}$ with In(III) (at $t_{\text{dep}} = 120$ s). The method has a fine reproducibility with RSD of 2.65%, 3.34%, and 2.51%, respectively ($n = 8$) (with the concentration of Cd(II) , Pb(II) , and In(III) to be $10 \mu\text{g}\cdot\text{L}^{-1}$).

Various Bi precursor-modified and Bi_2O_3 -modified carbon electrodes for analysis of Cd(II) , Pb(II) , In(III) are shown in Table 1.

3.8. Influence of Ions. The influence of several ions K^+ , Na^+ , Ca^{2+} , Mg^{2+} , Zn^{2+} , Fe^{3+} , and Cu^{2+} at concentration range from 0.1 to $100 \text{ mg}\cdot\text{L}^{-1}$ on the peak of Cd(II) , Pb(II) , and In(III) was examined. No signal changes were observed on the I_p of Cd(II) , Pb(II) , and In(III) (changes in peak currents $< 10\%$). The influence of cetyltrimethylammonium

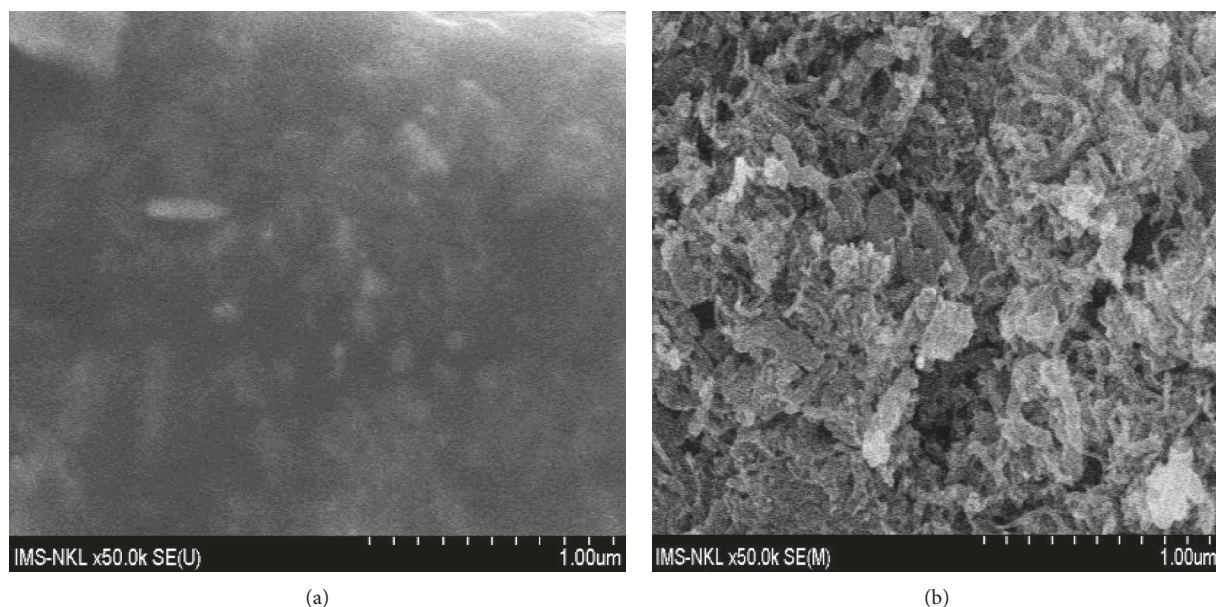


FIGURE 5: Scanning electron micrographs of the CPE modified with 5% Bi₂O₃ (w/w) (a) before and (b) after electrochemical reduction at -1.2 V for 120 s in the supporting electrolyte mixture of 0.1 M KI and acetate buffer solution. Other conditions are as in Figure 1.

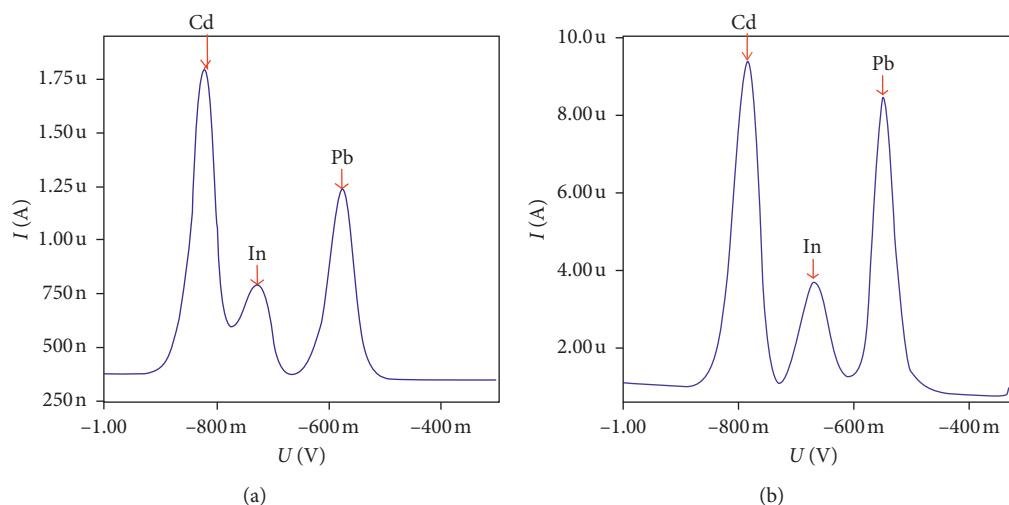


FIGURE 6: DP-ASV of Cd, Pb, and In supporting electrolytes: (a) acetate buffer (pH = 4.5); (b) mixture of 0.1 M KI and acetate buffer (pH 4.5). Conditions: [Cd(II)] = 5 μg·L⁻¹; [Pb(II)] = 5 μg·L⁻¹; [In(III)] = 10 μg·L⁻¹. Other conditions are as in Figure 1.

bromide and Triton X-100 surfactants in range from 0.1 to 10 mg·L⁻¹ concentrations was also studied. A decrease in the I_p value was found for Cd(II), Pb(II), and In(III) determination on increasing the amount of the surfactant. Nevertheless, this surfactant interference was reduced by the UV irradiation with a UV lamp at 254 nm wavelength in 90 min.

3.9. Determination of CRM. The accuracy of the method was studied by analysis of sediment CRM (MESS-2). The results are shown in Table 2. The results of these five trials were not significantly different from the certified values following Student's t test ($t_{\text{exp}} = 2.52$ greater than $t(0.05, 4)$).

3.10. Determination of River Water Samples. Water pollution in some rivers of Hanoi, Vietnam, has been a serious problem, with high concentration of metal ions and other ions [38, 39]. So, we took some river samples in Hanoi to analyse Cd(II), In(III), and Pb(II). The samples were acidified by 10% HNO₃, and then the solution was filtered using the 0.45 μm membrane filter. The sample was treated with UV light for 90 minutes at wavelength 254 nm.

After filtering, 10.0 mL of the solution was taken, and the mixture of 0.1 M KI and acetate buffer was added. Content analysis of Cd, In, and Pb in 3 different river samples by DP-ASV was performed using the manufactured CPE. The content of Pb(II) in the samples ranged from 1.45 ± 0.01 μg·L⁻¹ to 1.93 ± 0.20 μg·L⁻¹. The content of Cd(II)

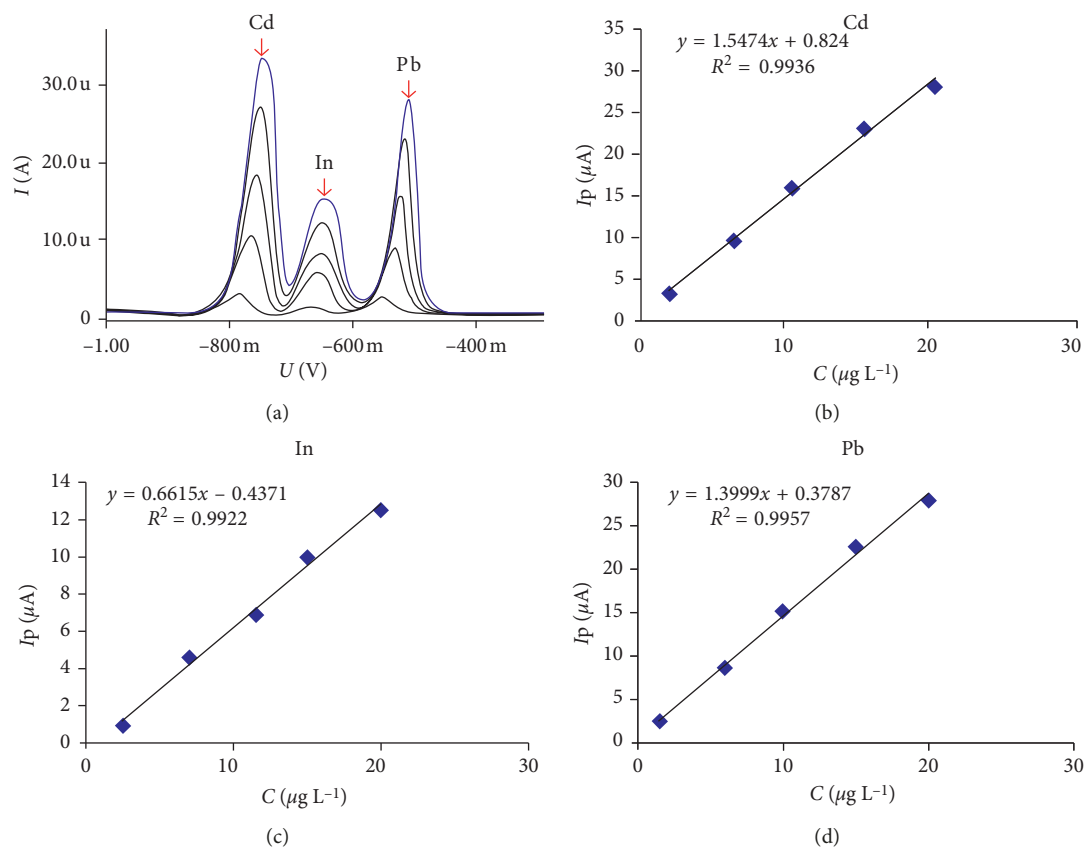


FIGURE 7: (a) DP-ASV of Cd(II), Pb(II), and In(III) and the calibration curve of (b) Cd(II), (c) In(III), and (d) Pb(II). Conditions: [Pb(II)]; [Cd(II)] = 1.5, 6, 10, 15, and 20 $\mu\text{g}\cdot\text{L}^{-1}$; [In(III)] = 2.5, 7, 11.5, 15, and 20 $\mu\text{g}\cdot\text{L}^{-1}$; supporting electrolyte mixture of 0.1 M KI and acetate buffer. Other conditions are as in Figure 1.

TABLE 1: Various Bi precursor-modified and Bi_2O_3 -modified carbon electrodes for analysis of Cd(II), Pb (II), and In(III).

Electrode material	Voltammetric	Studied ions	LOD	Linear range	Reference
$\text{Bi}_2\text{O}_3/\text{SPE}$	SW-ASV	Pb	5 $\mu\text{g}\cdot\text{L}^{-1}$ (at pH = 1.2) 10 $\mu\text{g}\cdot\text{L}^{-1}$ (at pH = 4.5)	5–150 $\mu\text{g}\cdot\text{L}^{-1}$ (at pH = 1.2) 10–150 $\mu\text{g}\cdot\text{L}^{-1}$ (at pH = 4.5)	[28]
		Cd	2.5 $\mu\text{g}\cdot\text{L}^{-1}$ (at pH = 1.2) 5 $\mu\text{g}\cdot\text{L}^{-1}$ (at pH = 4.5)	5–150 $\mu\text{g}\cdot\text{L}^{-1}$ (at pH = 1.2) 10–150 $\mu\text{g}\cdot\text{L}^{-1}$ (at pH = 4.5)	
$\text{Bi}_2\text{O}_3/\text{SPE}$	SW-ASV	Pb	2 $\mu\text{g}\cdot\text{L}^{-1}$	50–300 $\mu\text{g}\cdot\text{L}^{-1}$	[29]
$\text{Bi}_2\text{O}_3/\text{SPE}$	DP-ASV	Pb	1.0 $\mu\text{g}\cdot\text{L}^{-1}$		[30]
$\text{Bi}_2\text{O}_3/\text{SPE}$	SW-ASV	Pb	2.3 $\mu\text{g}\cdot\text{L}^{-1}$	20–100 $\mu\text{g}\cdot\text{L}^{-1}$	[31]
		Cd	1.5 $\mu\text{g}\cdot\text{L}^{-1}$	20–100 $\mu\text{g}\cdot\text{L}^{-1}$	
$\text{Bi}_2\text{O}_3/\text{SPE}$	SW-ASV	Pb	1.1 $\mu\text{g}\cdot\text{L}^{-1}$	0–80 $\mu\text{g}\cdot\text{L}^{-1}$	[32]
		Cd	2.1 $\mu\text{g}\cdot\text{L}^{-1}$	0–160 $\mu\text{g}\cdot\text{L}^{-1}$	
$\text{Bi}_2\text{O}_3/\text{SPE}$	SW-ASV	Pb	5 $\mu\text{g}\cdot\text{L}^{-1}$		[33]
		Cd	5 $\mu\text{g}\cdot\text{L}^{-1}$		
BONPs-IL/CPE	SW-ASV	Pb	0.21 $\mu\text{g}\cdot\text{L}^{-1}$	3–30 $\mu\text{g}\cdot\text{L}^{-1}$	[34]
		Cd	0.15 $\mu\text{g}\cdot\text{L}^{-1}$		
$\text{BiOCl}/\text{MWCNT-GCE}$	SW-ASV	Pb	1.9 $\mu\text{g}\cdot\text{L}^{-1}$		[35]
		Cd	4 $\mu\text{g}\cdot\text{L}^{-1}$		
$\text{Bi}_2\text{O}_3/\text{MWCNT-CPE}$	DP-ASV	Pb	0.26 $\mu\text{g}\cdot\text{L}^{-1}$	1.5–20 $\mu\text{g}\cdot\text{L}^{-1}$	This study
		Cd	0.22 $\mu\text{g}\cdot\text{L}^{-1}$	1.5–20 $\mu\text{g}\cdot\text{L}^{-1}$	
		In	0.65 $\mu\text{g}\cdot\text{L}^{-1}$	2.5–20 $\mu\text{g}\cdot\text{L}^{-1}$	

SPE: screen printed electrode; GCE: glassy carbon electrode; SW-ASV: square wave anodic stripping voltammetry; BONP: bismuth oxide nanoparticle; IL: ionic liquid; BiOCl: bismuth-oxychloride.

TABLE 2: Cd(II), Pb(II), and In(III) determination in CRM by the DP-ASV method (using the CPE modified with Bi₂O₃) and μ value of CRM.

Ion	\bar{X} ($\mu\text{g/g}$)	μ ($\mu\text{g/g}$)
Pb(II)	20.5	21.9
In(III)	<LOD	<LOD
Cd(II)	<LOD	0.24

Note. \bar{X} is the average value of the DP-ASV method (5 measurements).

TABLE 3: Pb(II) content in water samples identified by the DP-ASV method (using the CPE modified with Bi₂O₃ using CNTs) and the GF-AAS method.

Samples	GF-AAS	DP-ASV	Recovery (%)	t_{exp}
1	1.86	1.93	96.37	2.52
2	1.62	1.76	108.64	2.35
3	1.47	1.45	98.64	1.68

Note. All concentrations are expressed in $\mu\text{g}\cdot\text{L}^{-1}$; the result of the DP-ASV method is the average value of 5 measurements.

and In(III) in samples was smaller than the limit of quantitative. The results of Pb(II) in this sample using the DP-AAS method with CPE modified with Bi₂O₃ using MWCNTs were compared with GF-AAS and are shown in Table 3. The results of these five measurements were not significantly different from the certified values.

4. Conclusions

The CPE modified with 5% (w/w) Bi₂O₃, 3 mm diameter, using CNTs was applied for simultaneous analysis of the concentration of Cd(II), Pb(II), and In(III) by the DP-ASV method. The CPE modified with 5% (w/w) Bi₂O₃ are not only easy to make and easy to use, but also environmentally friendly. The method has good accuracy, low detection limit, and good repeatability.

Data Availability

The data used to support the findings of this study are available from the corresponding author upon request.

Conflicts of Interest

The authors declare that they have no conflicts of interest regarding the publication of this paper.

Acknowledgments

The authors gratefully acknowledge the Hanoi University of Industry and Chemical Analysis Laboratory, Institute of Chemistry, Vietnam Academy of Science and Technology, for providing support to this work.

References

- [1] P. Patnaik, *Handbook of Inorganic Chemicals*, McGraw-Hill, New York, NY, USA, 2002.
- [2] Ministry of Health Labour and Welfare (MHLW), "Indium and indium compounds," Initial Risk Assessment Report, Ministry of Health Labour and Welfare (MHLW), Tokyo, Japan, 2010.
- [3] M. Maanan, "Heavy metal concentrations in marine molluscs from the Moroccan coastal region," *Environmental Pollution*, vol. 153, no. 1, pp. 176–183, 2008.
- [4] I. Narin, M. Soylak, L. Elci, and M. Dogan, "Determination of trace metal ions by AAS in natural water samples after preconcentration of pyrocatechol violet complexes on an activated carbon column," *Talanta*, vol. 52, no. 6, pp. 1041–1046, 2000.
- [5] M. Soylak, L. Elci, and M. Dogan, "Flame atomic absorption spectrometric determination of cadmium, cobalt, copper, lead and nickel in chemical grade potassium salts after an enrichment and separation procedure," *Journal of Trace and Microprobe Techniques*, vol. 17, pp. 149–156, 1999.
- [6] N. C. A. Martínez, A. B. Barrera, and P. B. Bermejo, "Indium determination in different environmental materials by electrothermal atomic absorption spectrometry with amberlite XAD-2 coated with 1-(2-pyridylazo)-2-naphthol," *Talanta*, vol. 66, no. 3, pp. 646–652, 2005.
- [7] K. Dash, S. Thangavel, S. C. Chaurasia, and J. Arunachalam, "Determination of indium in high purity antimony by electrothermal atomic absorption spectrometry (ETAAS) using boric acid as a modifier," *Talanta*, vol. 70, no. 3, pp. 602–608, 2006.
- [8] O. Acar, A. R. Türker, and Z. Kiliç, "Determination of bismuth, indium and lead in spiked sea water by electrothermal atomic absorption spectrometry using tungsten containing chemical modifiers," *Spectrochimica Acta Part B: Atomic Spectroscopy*, vol. 55, no. 10, pp. 1635–1641, 2000.
- [9] A. T. Townsend and I. Snape, "Multiple Pb sources in marine sediments near the Australian Antarctic station, Casey," *Science of The Total Environment*, vol. 389, no. 2-3, pp. 466–474, 2008.
- [10] P. Heitland and H. D. Köster, "Biomonitoring of 37 trace elements in blood samples from inhabitants of Northern Germany by ICP-MS," *Journal of Trace Elements in Medicine and Biology*, vol. 20, no. 4, pp. 253–262, 2006.
- [11] F. B. Alkas, J. A. Shaban, A. A. Sukuroglu, M. A. Kurt, D. Battal, and S. Saygi, "Monitoring and assessment of heavy metal/metalloid concentration by inductively coupled plasma mass spectrometry (ICP-MS) method in Gonyeli Lake, Cyprus," *Environmental Monitoring and Assessment*, vol. 189, no. 10, p. 516, 2017.
- [12] B. Mikula and B. Puzio, "Determination of trace metals by ICP-OES in plant materials after preconcentration of 1,10-phenanthroline complexes on activated carbon," *Talanta*, vol. 71, no. 1, pp. 136–140, 2007.
- [13] J.-H. Xie, M.-Y. Shen, S.-P. Nie et al., "Simultaneous analysis of 18 mineral elements in cyclocarya paliurus polysaccharide by ICP-AES," *Carbohydrate Polymers*, vol. 94, no. 1, pp. 216–220, 2013.
- [14] B. Feist, B. Mikula, K. Pytlakowska, B. Puzio, and F. Buhl, "Determination of heavy metals by ICP-OES and F-AAS after preconcentration with 2,2'-bipyridyl and erythrosine," *Journal of Hazardous Materials*, vol. 152, no. 3, pp. 1122–1129, 2008.
- [15] M. Türkmen, A. Türkmen, Y. Tepe, A. Ateş, and K. Gökkuş, "Determination of metal contaminations in sea foods from Marmara, Aegean and Mediterranean seas: twelve fish species," *Food Chemistry*, vol. 108, no. 2, pp. 794–800, 2008.
- [16] I. Boevski, N. Daskalova, and I. Havezov, "Determination of barium, chromium, cadmium, manganese, lead and zinc in atmospheric particulate matter by inductively coupled plasma

- atomic emission spectrometry (ICP-AES),” *Spectrochimica Acta Part B: Atomic Spectroscopy*, vol. 55, no. 11, pp. 1643–1657, 2000.
- [17] R. Segura, K. Díaz, J. Pizarro, A. Placencio, D. Tapia, and Á. Fajardo, “Anodic stripping voltammetric determination of lead using a chemically modified electrode based on AZA crown ether,” *Journal of the Chilean Chemical Society*, vol. 62, no. 4, pp. 3726–3730, 2017.
- [18] U. Injang, P. Noyrod, W. Siangproh, W. Dungchai, S. Motomizu, and O. Chailapakul, “Determination of trace heavy metals in herbs by sequential injection analysis-anodic stripping voltammetry using screen-printed carbon nanotubes electrodes,” *Analytica Chimica Acta*, vol. 668, no. 1, pp. 54–60, 2010.
- [19] J. H. Luo, X. X. Jiao, N. B. Li, and H. Q. Luo, “Sensitive determination of Cd(II) by square wave anodic stripping voltammetry with in situ bismuth-modified multiwalled carbon nanotubes doped carbon paste electrodes,” *Journal of Electroanalytical Chemistry*, vol. 689, pp. 130–134, 2013.
- [20] G. Hwang, W. Han, J. Park, and S. Kang, “Determination of trace metals by anodic stripping voltammetry using a bismuth-modified carbon nanotube electrode,” *Talanta*, vol. 76, no. 2, pp. 301–308, 2008.
- [21] F. Mirrahimi, M. A. Taher, H. Beitollahi, and R. Hosseinzadeh, “Electrocatalytic and selective determination of d-penicillamine in the presence of tryptophan using a benzoylferrocene-modified carbon nanotube paste electrode,” *Applied Organometallic Chemistry*, vol. 26, no. 4, pp. 194–198, 2012.
- [22] A. R. Taheri, A. R. Mohadesi, D. Afzali et al., “Simultaneous voltammetric determination of norepinephrine and folic acid at the surface of modified carbon nanotube paste electrode,” *International Journal of Electrochemical Science*, vol. 6, p. 171, 2011.
- [23] H. Beitollahi, H. Karimi-Maleh, and H. Khabazzadeh, “Nanomolar and selective determination of epinephrine in the presence of norepinephrine using carbon paste electrode modified with carbon nanotubes and novel 2-(4-oxo-3-phenyl-3,4-dihydro-quinazolinyl)-N'-phenyl-hydrazinecarbothioamide,” *Analytical Chemistry*, vol. 81, no. 2, p. 856, 2009.
- [24] M. Siswana, K. Ozoemena, and T. Nyokong, “Electrocatalytic detection of amitrole on the multi-walled carbon nanotube—iron (II) tetra-aminophthalocyanine platform,” *Sensors*, vol. 8, no. 8, pp. 5096–5105, 2008.
- [25] F. Fathirad, D. Afzali, A. Mostafavi, T. Shamspur, and S. Fozooni, “Fabrication of a new carbon paste electrode modified with multi-walled carbon nanotube for stripping voltammetric determination of bismuth(III),” *Electrochimica Acta*, vol. 103, pp. 206–210, 2013.
- [26] A. Economou, “Screen-printed electrodes modified with “green” metals for electrochemical stripping analysis of toxic elements,” *Sensors*, vol. 18, no. 4, p. 1032, 2018.
- [27] N. Serrano, A. Alberich, J. M. Díaz-Cruz, C. Ariño, and M. Esteban, “Coating methods, modifiers and applications of bismuth screen-printed electrodes,” *TrAC Trends in Analytical Chemistry*, vol. 46, pp. 15–29, 2013.
- [28] R. O. Kadara, N. Jenkinson, and C. E. Banks, “Disposable bismuth oxide screen printed electrodes for the high throughput screening of heavy metals,” *Electroanalysis (NY)*, vol. 21, no. 22, pp. 2410–2414, 2009.
- [29] J. C. Quintana, F. Arduini, A. Amine et al., “Part I: a comparative study of bismuth-modified screen-printed electrodes for lead detection,” *Analytica Chimica Acta*, vol. 707, no. 1–2, pp. 171–177, 2011.
- [30] N. Lezia, A. Economou, P. A. Dimovasilis, P. N. Trikalitis, and M. I. Prodromidis, “Disposable screen-printed sensors modified with bismuth precursor compounds for the rapid voltammetric screening of trace Pb(II) and Cd(II),” *Analytica Chimica Acta*, vol. 728, pp. 1–8, 2012.
- [31] G.-H. Hwang, W.-K. Han, J.-S. Park, and S.-G. Kang, “An electrochemical sensor based on the reduction of screen-printed bismuth oxide for the determination of trace lead and cadmium,” *Sensors and Actuators B: Chemical*, vol. 135, no. 1, pp. 309–316, 2008.
- [32] N. Lezi, A. Economou, C. E. Efstathiou, and M. Prodromidis, “A study of Bi₂O₃-modified screen-printed sensors for determination of Cd(II) and Pb(II) by anodic stripping voltammetry,” *Sensing in Electroanalysis*, vol. 6, pp. 219–229, 2011.
- [33] R. Pauliukaite, R. Metelka, I. Švancara et al., “Carbon paste electrodes modified with Bi₂O₃ as sensors for the determination of Cd and Pb,” *Analytical and Bioanalytical Chemistry*, vol. 374, no. 6, pp. 1155–1158, 2002.
- [34] P. JianFeng, W. Jian, and Y. YiBin, “Determination of trace heavy metals in milk using an ionic liquid and bismuth oxide nanoparticles modified carbon paste electrode,” *Chinese Science Bulletin*, vol. 57, no. 15, pp. 1781–1787, 2012.
- [35] C. Sandra, G. Valéria, K. Zoltán et al., “Trace level voltammetric determination of lead and cadmium in sediment pore water by a bismuth-oxochloride particle-multiwalled carbon nanotube composite modified glassy carbon electrode,” *Talanta*, vol. 134, pp. 640–649, 2015.
- [36] V. Sosa, N. Serrano, C. Ariño, J. M. Díaz-Cruz, and M. Esteban, “Sputtered bismuth screen-printed electrode: a promising alternative to other bismuth modifications in the voltammetric determination of Cd(II) and Pb(II) ions in groundwater,” *Talanta*, vol. 119, pp. 348–352, 2014.
- [37] J. F. van Staden and M. C. Matoetoe, “Simultaneous determination of copper, lead, cadmium and zinc using differential pulse anodic stripping voltammetry in a flow system,” *Analytica Chimica Acta*, vol. 411, no. 1–2, pp. 201–207, 2000.
- [38] T. L. H. Nguyen, M. Ohtsubo, L. Y. Li, and T. Higashi, “Heavy metal pollution of the To-Lich and Kim-Nguu River in Hanoi city and the industrial source of the pollutants,” *Journal of the Faculty of Agriculture*, vol. 52, no. 1, pp. 141–146, 2007.
- [39] T. Kikuchi, T. Furuichi, H. T. Hai, and S. Tanaka, “Assessment of heavy metal pollution in river water of Hanoi, Vietnam using multivariate analyses,” *Bulletin of Environmental Contamination and Toxicology*, vol. 83, no. 4, pp. 575–582, 2009.

Research Article

Structure and Electrochemical Properties of $\text{Li}_4\text{Ti}_5\text{O}_{12}$ Prepared via Low-Temperature Precipitation

Le Thanh Nguyen Huynh ¹, Cam Thanh Duy Ha,¹ Viet Dung Nguyen,¹
Dinh Quan Nguyen,² My Loan Phung Le ^{1,3} and Van Man Tran^{1,3}

¹Applied Physical Chemistry Laboratory (APCLAB), VNUHCM-University of Science, 227 Nguyen Van Cu Street, District 5, Ho Chi Minh City, Vietnam

²Biomass Laboratory, VNUHCM-University of Technology, 268 Ly Thuong Kiet street, District 10, Ho Chi Minh City, Vietnam

³Department of Physical Chemistry, Faculty of Chemistry, VNUHCM-University of Science, 227 Nguyen Van Cu street, District 5, Ho Chi Minh City, Vietnam

Correspondence should be addressed to My Loan Phung Le; lmphung@hcmus.edu.vn

Received 3 March 2019; Revised 21 May 2019; Accepted 10 June 2019; Published 25 August 2019

Guest Editor: Nguyen Van Noi

Copyright © 2019 Le Thanh Nguyen Huynh et al. This is an open access article distributed under the Creative Commons Attribution License, which permits unrestricted use, distribution, and reproduction in any medium, provided the original work is properly cited.

This work aimed to prepare the spinel phase $\text{Li}_4\text{Ti}_5\text{O}_{12}$ by a combination of the low-temperature precipitation technique and assisted calcination step. X-ray diffraction (XRD) revealed that the intermediated phase was Li_2TiO_3 , and the spinel phase could be evidently formed at 700°C for 12 to 20 hours. The morphology of spinel powder, determined by SEM and TEM, exhibited a good distribution at the submicrometric scale that promoted a fast kinetic of Li migration and an excellent performance at the high-rate cycling test. The stable performances were achieved in the charge-discharge test at different current densities: 80 mA/g (165 mAh/g), 320 mA (160 mAh/g), and 1600 mA (145 mAh/g) upon 100 cycles. Moreover, we observe a capacity retention of 48% (corresponding 80 mA/g) at a high rate of 5000 mA/g. The cyclic voltammetry measurement displayed a reversible system and revealed the lithium diffusion coefficient of $1.15 \times 10^{-11} \text{ cm}^2/\text{s}$.

1. Introduction

Spinel $\text{Li}_4\text{Ti}_5\text{O}_{12}$ has become an attractive anode material for high-power and fast-charging Li-ion battery because of its excellent cycle performance, structural stability, and little change in the unit cell volume during lithium intercalation/deintercalation. The spinel structure of $\text{Li}_4\text{Ti}_5\text{O}_{12}$ provides a three-dimensional network for Li migration [1, 2]. The process of lithium insertion/extraction occurs as the two-phase mechanism at 1.55 V (vs. Li^+/Li), characterized by a long flat plateau in the voltage profile. The voltage plateau happens to be much above the reduction potentials of most common electrolyte solvents mitigating the formation of the solid electrolyte interface (SEI). In spite of these beneficial properties, $\text{Li}_4\text{Ti}_5\text{O}_{12}$ does not yet meet all the requirements for successful use in fast-charging applications caused by its

poor electrical conductivity and sluggish diffusion of lithium ions. [3, 4].

In the literature, many efforts have been aimed to overcome these disadvantages by doping or carbon coating of particles [5, 6] to enhance the conductivity of LTO particles; or alternative synthesis methods fabricate the nano-size LTO with controlled and regular morphologies aiming to shorten the lithium diffusion pathway. It has been reported that nanocrystalline $\text{Li}_5\text{Ti}_5\text{O}_{12}$ electrode materials have excellent performance even at high charging rate and high temperature; therefore, they are useful when applied in high-rate charge/discharge Li-ion batteries. Different synthesis methods have been investigated such as sol-gel processes, high-temperature annealing treatment, solution-combustion, and hydrothermal to improve the phase purity and electrochemical performance. Hao et al. [7] synthesized

$\text{Li}_4\text{Ti}_5\text{O}_{12}$ particles by a sol-gel method with citric acid as a chelating agent and Li_2CO_3 and tetrabutyl titanate as starting materials. Mixtures of $\text{Li}_4\text{Ti}_5\text{O}_{12}$ and rutile- TiO_2 were observed after heating at 800°C for 20 hours in air, while the pure $\text{Li}_4\text{Ti}_5\text{O}_{12}$ phase with an average particle size of 500 nm was obtained at 850°C for 24 hours. Li et al. [8] prepared $\text{Li}_4\text{Ti}_5\text{O}_{12}$ with nanotubes and nanowires morphology by a hydrothermal lithium exchange processing. XRD analysis showed a trace of anatase- TiO_2 in spinel $\text{Li}_4\text{Ti}_5\text{O}_{12}$ nanotubes calcinated at 350°C for 2 hours. The $\text{Li}_4\text{Ti}_5\text{O}_{12}$ spinel was synthesized by a sol-gel method using titanium isopropoxide, LiOH , and 2-methoxy ethanol and subsequent treatment with high ball milling by Kim et al. [9] It was also notified that a trace of rutile- TiO_2 was observed for the powder annealed at 850°C for 5 hours. According to previous studies, the heat treatment at high temperature in synthesizing the $\text{Li}_4\text{Ti}_5\text{O}_{12}$ spinel obviously led to the formation of rutile or anatase- TiO_2 , and these impurities are detrimental to the electrochemical performance of the spinel phase. Consequently, low-temperature synthesis or minimum heat treatment by employing a suitable aqueous particulate sol-gel route or intermediate precipitate phase has been recently suggested. Chui and coworker [10, 11] utilized the extreme excess ratio of Ti versus Li (Ti:Li = 6:1) to prepare the spinel phase $\text{Li}_4\text{Ti}_5\text{O}_{12}$ through the intermediated phase lithium titanate hydrate $\text{Li}_{1.81}\text{H}_{0.19}\text{Ti}_2\text{O}_5\cdot 2\text{H}_2\text{O}$ (LTH).

Our work aimed to prepare the nanosized spinel $\text{Li}_4\text{Ti}_5\text{O}_{12}$ powder from the intermediated cubic phase Li_2TiO_3 which was obtained from a low-temperature precipitation. The effect of temperature and duration of calcination on the formation of the spinel phase was regarded. The structural and morphological properties were characterized by powder X-ray diffraction, Raman spectroscopy, and scanning/transmission electronic microscopy (SEM/TEM). The high-rate performance through galvanostatic charge-discharge and the diffusion coefficient of lithium ions (D_{Li}) in the host $\text{Li}_4\text{Ti}_5\text{O}_{12}$ were measured and compared with the bulk material.

2. Experimental

2.1. Synthesis of Nanostructured $\text{Li}_4\text{Ti}_5\text{O}_{12}$. Spinel-type $\text{Li}_4\text{Ti}_5\text{O}_{12}$ was prepared via a low-temperature precipitation method combining with the calcining process from 600 to 800°C . Titanium butoxide $\text{Ti}(\text{O}i\text{Bu})_4$ with a normal purity of 97% (Sigma Aldrich, $d = 1.491 \text{ g/mL}$ at 20°C , $M = 340.39 \text{ g/mole}$) and lithium hydroxide monohydrate $\text{LiOH}\cdot\text{H}_2\text{O}$ with a normal purity of 99.95% (Sigma Aldrich) were used as titanium and lithium precursors. 10.50 mg $\text{Ti}(\text{O}i\text{Bu})_4$ was dropped into 25 mL solution of 1 M LiOH solution under vigorous stirring at 5°C with the molar ratio Li:Ti of 1:1.33. Then, the produced powder was collected by centrifugation and washed several times with deionized water to neutral pH to eliminate the excess of LiOH and dried at 120°C for overnight. The as-prepared powder was annealed at 600– 800°C for 12 hours.

2.2. Structural Characterizations. The structure of samples was identified by X-ray diffraction (XRD) in D8-Advance (Bruker) diffractometer using $\text{CuK}\alpha$ radiation ($\lambda = 1.5406 \text{ \AA}$). XRD patterns were collected in the range 10° – 70° with a step of 0.029° per second. Lattice parameters were calculated by software CelRef. Raman spectra were measured with a XploRA Raman microspectrometer (Jobin-Yvon-Horiba), using a He:Ne laser (632.8 nm) as the excitation source. The morphologies and the distribution of grain size were determined by using scanning electron microscope (FE-SEM S4800 Hitachi, Japan) and transmission electronic microscopy (TEM, JEOL 1400, Japan).

2.3. Electrochemical Characterizations. The electrochemical performance, including rate capability and charge/discharge capacity of spinel $\text{Li}_4\text{Ti}_5\text{O}_{12}$, was evaluated at room temperature with the coin-cell type CR-2025 in which a metallic lithium foil was used as the counterelectrode. The composite electrodes were made of the active material (80 wt.%), conducting acetylene black (7.5 wt.%), carbon graphite (7.5 wt.%), and polyvinylidene fluoride (PVdF) binder (5 wt.%) homogeneously dispersed in *N*-methyl-2-pyrrolidone (NMP) solvent. The slurry was coated on an aluminum foil and cut to pieces with diameter of 10 mm (an area surface of 0.785 cm^2) and then dried at 120°C in vacuum for 12 hours. The coin cell was assembled in an argon-filled glove box (M. Braun Co., $[\text{O}_2] < 1 \text{ ppm}$ and $[\text{H}_2\text{O}] < 1 \text{ ppm}$). The employed organic electrolyte was a mixture of 1 M LiPF_6 with ethylene carbonate (EC) and dimethyl carbonate (DMC) at volumetric ratio 2:1.

A constant current protocol in the range of 20 mA/g to 5000 mA/g was used for formation cycles in a potential range of 1–2.5 V (vs. Li^+/Li). The cyclic voltammetry (CV) was performed at different scan rates between the voltage of 10 and $120 \mu\text{V/s}$ to evaluate the lithium coefficient diffusion related to the charge/discharge process.

3. Results and Discussion

3.1. Structure and Morphology. Considering the structure of $\text{Li}_4\text{Ti}_5\text{O}_{12}$, the previous studies [1, 2, 4] demonstrated a cubic spinel (unit cell $a = 8.3557 \text{ \AA}$) with a space group of F3dm. The three ions Li^+ are situated at the tetrahedral 8a site, the other ions Li^+ and ions Ti^+ randomly locate in the octahedral 16d sites with a ratio of 1:5, and the oxygen atoms totally are located at the 32e site; this suggests that $[\text{Li}_3]^{8a}[\text{Li}_1\text{Ti}_5]^{16d}[\text{O}_{12}]^{32e}$ is the probable structure. Figure 1 compares the XRD patterns of the intermediated phase and final samples calcinated at different temperatures from 500°C to 800°C for 12 hours. The intermediate phase can be indexed in the orthorhombic phase Li_2TiO_3 (JSPDS: 00-003-1024). At 500°C , the spinel $\text{Li}_4\text{Ti}_5\text{O}_{12}$ phase was apparently formed, but the transformation was uncompleted; the remaining of the intermediate phase was still observed in the XRD diagram. At 600°C , XRD patterns provided the main peaks of the $\text{Li}_4\text{Ti}_5\text{O}_{12}$ phase (JSPDS: 000-049-0207) [12], indicating the

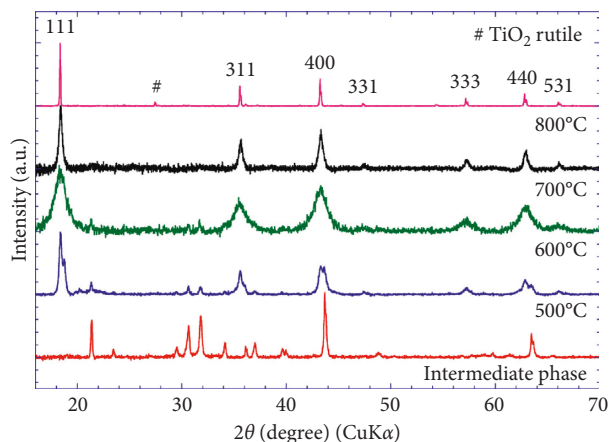


FIGURE 1: XRD patterns of samples at different calcination temperatures.

complete transformation from the intermediated phase to $\text{Li}_4\text{Ti}_5\text{O}_{12}$ phase. However, it was noticed in the samples thermally treated, and $\text{Li}_4\text{Ti}_5\text{O}_{12}$ presents wide peaks, which indicated the formation of the small crystalline material. The pure spinel phase $\text{Li}_4\text{Ti}_5\text{O}_{12}$ was obtained at 700°C and 800°C, and it could be obviously observed that the crystallinity degree of $\text{Li}_4\text{Ti}_5\text{O}_{12}$ improved with increase in calcination temperature. In contrast, the calcination at 800°C led a trace of rutile- TiO_2 . When the calcinating temperature was raised from 600°C to 700°C, the lattice parameter a slightly increased: 8.3477 Å (600°C) to 8.3599 Å (700°C). Colbow et al. [1] reported $a = 8.357$ Å, and Harisson et al. [13] also reported $a = 8.358$ Å which is in good agreement with our value at 700°C. The sample calcinated at 800°C exhibited unexpectedly the high value of the lattice parameter and 8.3716 Å due to the emergence of the TiO_2 rutile phase, respectively.

In order to examine the impact of calcination time, the sample at 700°C was treated at variable scheduling (Figure 2). The remaining intermediate phase was still observed for 4 hours and 8 hours, while the pure phase $\text{Li}_4\text{Ti}_5\text{O}_{12}$ only appeared at the duration from 12 hours to 20 hours. However, with 24 hours of calcination, the TiO_2 anatase phase was merged in the LTO phase. XRD patterns of samples at 12, 16, and 20 hours are identical and indexed to the pure spinel phase. The lattice parameter a can be determined to be 8.3595 Å which is in good agreement with the reported standard values even though the wide XRD peaks indicated the small crystallite of LTO. The crystallite size of the LTO phase was, respectively, calculated from their reflections using the Scherrer equation based on the full width at half maximum (FWHM) of diffraction peaks:

$$d_{hkl} = \frac{k\lambda}{\beta \cos \theta} \quad (1)$$

where d_{hkl} is the average crystallite size, k is the constant depending on the crystalline shape (0.9), λ is the radiation X-ray wavelength of Cu (1.5406 Å), β is the FWHM of the most intense peak, and 2θ is the diffraction angle. The rough estimation of crystallite size is around 40 nm for all three

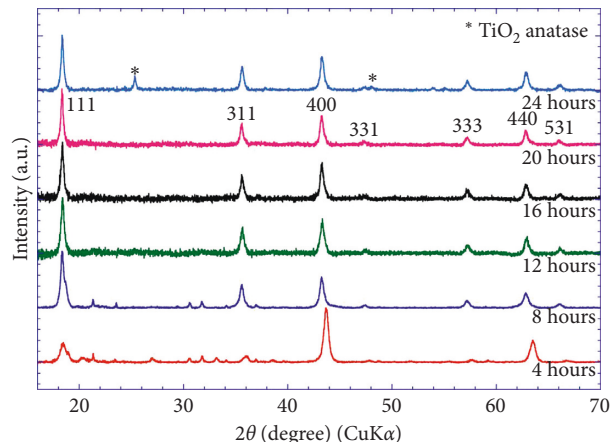


FIGURE 2: XRD patterns of samples at different calcination times at 700°C.

samples. The submicrometric LTO could suggest a fast kinetic of lithium insertion due to shortening of the lithium pathway diffusion.

Raman active modes of spinel $\text{Li}_4\text{Ti}_5\text{O}_{12}$ involve F_{2g} , E_g , and A_{1g} following the calculation of symmetry group O_h^2 , which represented the stretching and bending vibration of Ti-O bonds in $[\text{TiO}_6]$ octahedra and Li-O bonds in $[\text{LiO}_4]$ and $[\text{LiO}_6]$ polyhedra. [14, 15] At high frequency, two vibration modes A_{1g} at 671 cm^{-1} and 740 cm^{-1} were assigned to the vibrations of Ti-O bonds, while the stretching vibrations of the Li-O bonds were attributed by two modes in region medium frequency 430 cm^{-1} and 374 cm^{-1} . The last modes in low frequency (235 cm^{-1}) were attributed to the bending vibrations of O-Ti-O bonds. In brief, we succeeded to produce the pure phase $\text{Li}_4\text{Ti}_5\text{O}_{12}$ treated at 700°C for three schedules (12, 16, and 20 hours) without structural difference.

Figure 3 shows the SEM and TEM morphology of the sample $\text{Li}_4\text{Ti}_5\text{O}_{12}$ treated at 700°C for 16 hours. It can be seen that the sample consists of submicro-scaled primary particles with a homogeneous size distribution, which are in turn composed of larger particles of 100 μm . From the TEM image, the primary particles consist of nanorods of 10 nm in length (Figure 4).

3.2. Electrochemical Performance. The electrochemical performance of the spinel nanosized $\text{Li}_4\text{Ti}_5\text{O}_{12}$ as anode materials for lithium ion batteries has been investigated. Figure 5(a) illustrates the voltage profiles at low current density 20 mA/g of three samples $\text{Li}_4\text{Ti}_5\text{O}_{12}$ calcinated at 700°C for 12, 16, and 20 hours. The samples delivered a first discharge capacity of 178 mAh/g with a cutoff value of 1.0 (vs. Li^+/Li). This is in line with the theoretical capacity of 175 $\text{mAh}\cdot\text{g}^{-1}$ meaning that the excess lithium ions were intercalated into LTO, and no SEI film formed during the first charge which is usually formed in the range 0.2–0.8 V vs. Li^+/Li [8]. In the subsequent cycles, the capacity discharge was stabilized at 167 mAh/g without obvious capacity fading. A flat plateau at 1.65 V vs. Li^+/Li precisely corresponding to the $\text{Ti}^{3+}/\text{Ti}^{4+}$ redox reaction means that is the insertion/

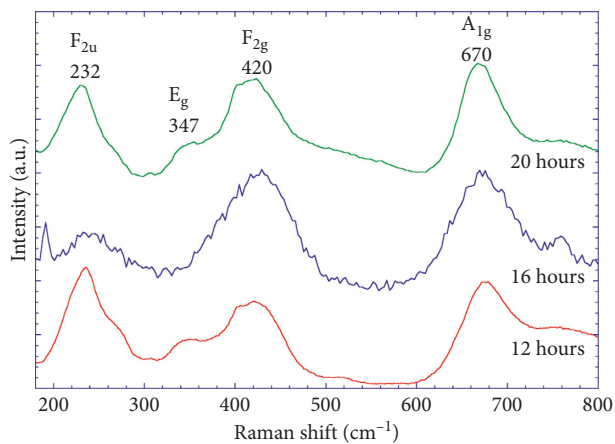


FIGURE 3: Raman spectroscopy of $\text{Li}_4\text{Ti}_5\text{O}_{12}$.

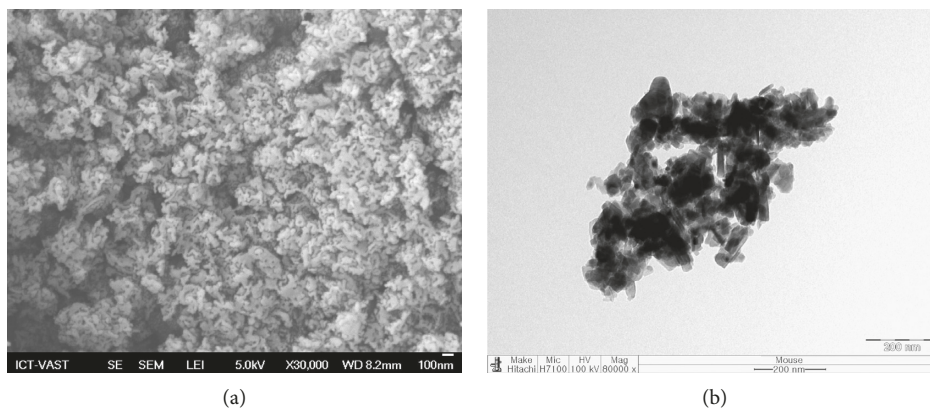


FIGURE 4: SEM images (a) and TEM image (b) of $\text{Li}_4\text{Ti}_5\text{O}_{12}$ treated at 700°C for 16 hours.

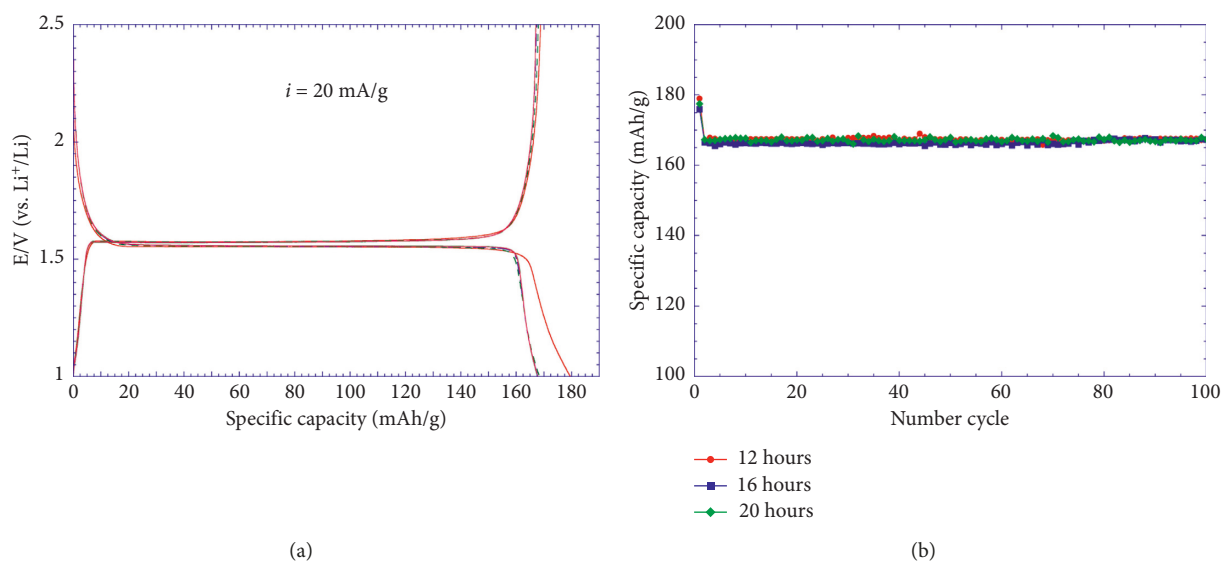


FIGURE 5: (a) Typical charge-discharge curves at current density of 20 mA/g and (b) cycling performance of samples $\text{Li}_4\text{Ti}_5\text{O}_{12}$ calcinated at 700°C for 12 hours, 16 hours, and 20 hours.

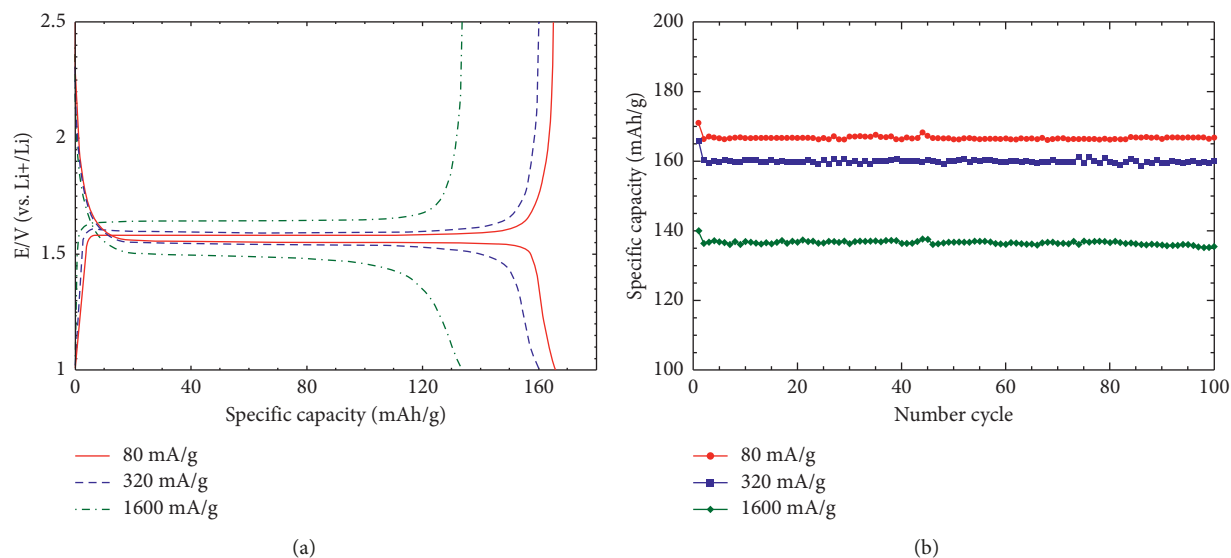


FIGURE 6: (a) Typical charge-discharge curves at current density: 80, 320, and 1600 mA/g and (b) cycling performance of $\text{Li}_4\text{Ti}_5\text{O}_{12}$.

extraction of lithium ions during the charge/discharge process. In addition, a small electrode polarization of about 0.02 V (below 20 mV) is observed between charge and discharge curves indicating the existence of good interparticle electrical contacts and better ion transport owing to the $\text{Li}_4\text{Ti}_5\text{O}_{12}$ nanoparticles and good stability of the spinel structure during Li migration. Furthermore, all three spinel samples exhibited excellent cycling stability with a capacity retention of 100% upon 100 cycles (Figure 5(b)).

Spinel $\text{Li}_4\text{Ti}_5\text{O}_{12}$ is subjected to cycling at different charge-discharge rates such as 80 mA/g, 320 mA/g, and 1600 mA/g to evaluate the capacity-rate relationship (Figure 6(a)). The charge-discharge curve at current 320 mA/g seems to quasi-superimpose on the one at current 80 mA/g without potential difference. The sample exhibited a capacity value of 165 mAh/g (80 mA/g) and 160 mAh/g (320 mA/g), a value close to the theoretical value of 175 mAh/g. At extremely high current of 1600 mA/g, there is a slight drop in capacity values (12.5% decrease) together with a drop in the discharge voltage plateau at 1.5 V (vs. Li^+/Li) which causes high electrode polarization (140 mV). However, the cycling performance upon 100 cycles at all three constant current show an excellent Coulombic efficiency; typically, the capacity retention remained 100% after 100 cycles with the capacity of 165 mAh/g, 160 mAh/g, and 135 mAh/g, respectively.

The rate capability is also important parameter for evaluating an electrode material addressed to the battery as well as supercapacitor application. A constant current discharge test was performed on $\text{Li}_4\text{Ti}_5\text{O}_{12}$ electrodes varying the rate from 20 mA/g to 5000 mA/g during discharge in the voltage range of 1.0–2.5 V, with the voltage profiles visible in Figures 7(a)–7(c). The charge-discharge profiles at rates below 1000 mA/g (Figure 7(a)) show a low polarization from 20 mV (40 mA/g) to 90 mV (960 mA/g) indicating the electron transfer efficiency and lithium diffusion pathway.

Our spinels exhibit the better rate capability than those reported in the literature [16]. A capacity of 145 mAh/g was achieved at current 400 mA/g, and this capacity amounts to 85% of capacity at the low current of 20 mA/g. From the current density above 1200 mA/g, we observe the critical impact of rates on the voltage profiles and the specific capacity. The more the current density applied, the more the discharge plateau shortened. Traditionally, the lithium insertion/extraction into host $\text{Li}_4\text{Ti}_5\text{O}_{12}$ occurred via a two-phase mechanism; herein, it showed a sloping voltage curve similar to that of a one-phase reaction due to the large electrode polarization.

Figure 7(d) illustrates the electrode polarization and specific capacity as function of the C-rate, and the highest current 5000 mA/g corresponds to rate 30°C. In the high current density performance, the electrochemical profiles significantly depended on the electronic conduction, which served as the electrode polarization. The drastic increase of polarization voltage from 100 mV to 350 mV was observed when the currents applied varied from 1200 mA/g to 5000 mA/g. Our spinel $\text{Li}_4\text{Ti}_5\text{O}_{12}$ still shows an impressive performance at such high current densities. At three highest currents 4500 mA/g (26°C), 4750 mA/g (28°C), and 5000 mA/g (30°C), the capacities 90 mAh/g, 85 mAh/g, and 80 mAh/g were achieved, respectively. It is noteworthy that the capacity (80 mAh/g) obtained with nanosized LTO at 30°C rate is much higher than that obtained at the 5°C rate (95 mAh/g) with bulk LTO. Indeed, the morphology of mesoporous and nanoparticle LTO powders provide a short diffusion path for Li and pore fill of electrolytes ensuring a high flux of Li.

Cyclic voltammetry analysis has been carried out to further investigate the electrochemical properties of spinel $\text{Li}_4\text{Ti}_5\text{O}_{12}$. Figure 8(a) shows the cyclic voltammetry curve at different scan rates to determine the kinetic of Li-migration process. The pair of anodic/cathodic peaks of spinel $\text{Li}_4\text{Ti}_5\text{O}_{12}$,

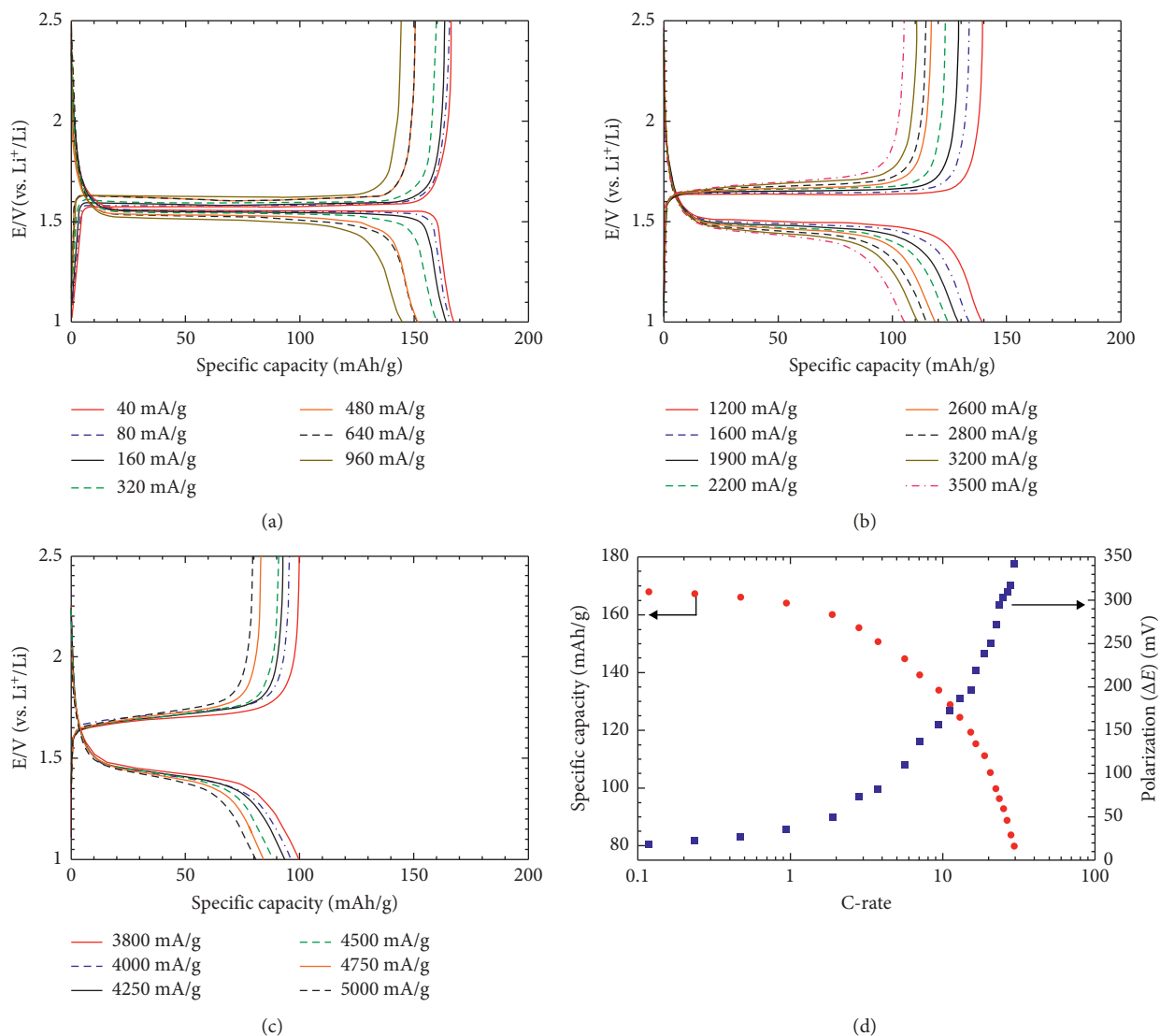


FIGURE 7: (a–c) Charge-discharge profile of $\text{Li}_4\text{Ti}_5\text{O}_{12}$ at various current densities from 40 mA/g to 5000 mA/g and (d) electrode polarization and specific capacity as the function of C-rate.

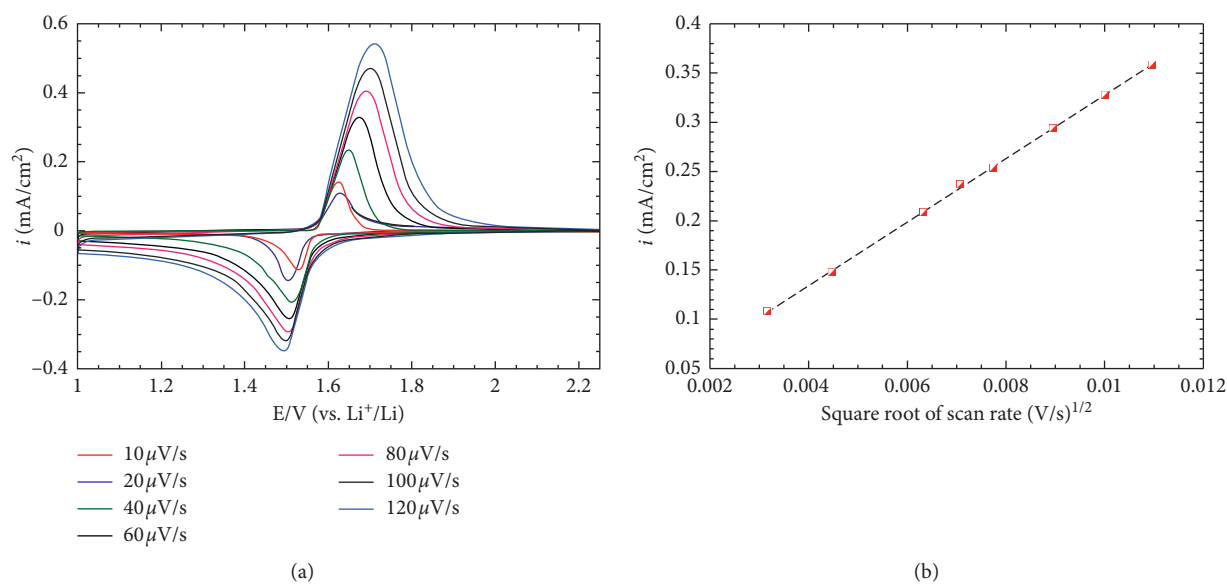


FIGURE 8: (a) CV curves under various scan rates from 10 $\mu\text{V/s}$ to 120 $\mu\text{V/s}$ and (b) current density as a function of the square root of the scan rate $v^{1/2}$.

located at 1.62 V/1.55 V at the scan rate of $10 \mu\text{V/s}$, demonstrate reversible lithium intercalation and deintercalation of host $\text{Li}_4\text{Ti}_5\text{O}_{12}$, respectively. The peak separation increases with the increasing scan rate that indicated the effect of electrode polarization owing to the limited diffusion process. The plot of cathodic peak current density (i_{pc}) as a function of the square root of the scan rate ($v^{1/2}$) in Figure 8(b) shows a good linear relation between i_{pc} and $v^{1/2}$ ($R = 0.9999$). Herein, the equation Randles–Sevcik [17] can be applied to determine the diffusion coefficient of lithium ions (D_{Li}), characterized as the kinetics of the lithium insertion process. The diffusion coefficient of lithium ions was calculated to be $1.15 \times 10^{-11} \text{ cm}^2/\text{s}$.

4. Conclusion

In summary, spinel $\text{Li}_4\text{Ti}_5\text{O}_{12}$ has been successfully prepared through a low temperature precipitation process to obtain a particle-size distribution at the submicrometric scale. The electrochemical measurements show that spinel LTO exhibited the discharge capacity of 178 mAh/g at 0.1°C in the first discharge and favorable cyclic reversibility at different current rates of 20, 80, 320, and 1600 mA/g with a capacity of 167, 165, 160, and 135 mAh/g upon 100 cycles. Furthermore, the spinel samples show an excellent performance at extremely high rate, which is capable of delivering a capacity of 80 mAh/g at current 5000 mA/g.

Data Availability

The data used to support the findings of this study are available from the corresponding author upon request.

Conflicts of Interest

The authors declare that they have no conflicts of interest.

Acknowledgments

This research was funded by the Department of Science and Technology in Ho Chi Minh City (DOST) under contract no. 135/2017/HĐ-SKHCN.

References

- [1] K. M. Colbow, J. R. Dahn, and R. R. Haering, "Structure and electrochemistry of the spinel oxides LiTi_2O_4 and $\text{Li}_{43}\text{Ti}_{53}\text{O}_4$," *Journal of Power Sources*, vol. 26, no. 3-4, pp. 397-402, 1989.
- [2] T. Ohzuku, "Zero-strain insertion material of $\text{Li}[\text{Li}_{1/3}\text{Ti}_{5/3}]\text{O}_4$ for rechargeable lithium cells," *Journal of The Electrochemical Society*, vol. 142, no. 5, p. 1431, 1995.
- [3] D. Li and H. Zhou, "Two-phase transition of Li-intercalation compounds in Li-ion batteries," *Materials Today*, vol. 17, no. 9, pp. 451-463, 2014.
- [4] I. A. Leonidov, O. N. Leonidova, L. A. Perelyaeva, R. F. Samigullina, S. A. Kovyazina, and M. V. Patrakeev, "Structure, ionic conduction, and phase transformations in lithium titanate $\text{Li}_4\text{Ti}_5\text{O}_{12}$," *Physics of the Solid State*, vol. 45, no. 11, pp. 2183-2188, 2003.
- [5] C. H. Chen, J. T. Vaughey, A. N. Jansen et al., "Studies of Mg-substituted $\text{Li}_{4-x}\text{Mg}_x\text{Ti}_5\text{O}_{12}$ spinel electrodes ($0 \leq x \leq 1$) for lithium batteries," *Journal of The Electrochemical Society*, vol. 148, no. 1, pp. A102-A104, 2001.
- [6] K.-S. Park, A. Benayad, D.-J. Kang, and S.-G. Doo, "Nitridation-driven conductive $\text{Li}_4\text{Ti}_5\text{O}_{12}$ for lithium ion batteries," *Journal of the American Chemical Society*, vol. 130, no. 45, pp. 14930-14931, 2008.
- [7] Y.-J. Hao, Q.-Y. Lai, D.-Q. Liu, Z.-U. Xu, and X.-Y. Ji, "Synthesis by citric acid sol-gel method and electrochemical properties of $\text{Li}_4\text{Ti}_5\text{O}_{12}$ anode material for lithium-ion battery," *Materials Chemistry and Physics*, vol. 94, no. 2-3, pp. 382-387, 2005.
- [8] J. Li, Z. Tang, and Z. Zhang, "Controllable formation and electrochemical properties of one-dimensional nanostructured spinel $\text{Li}_4\text{Ti}_5\text{O}_{12}$," *Electrochemistry Communications*, vol. 7, no. 9, pp. 894-899, 2005.
- [9] H.-J. Kim, M.-H. Oh, W.-K. Son, T.-I Kim, and S.-G. Park, "Novel synthesis method and electrochemical characteristics of lithium titanium oxide as anode material for high power device," in *Proceedings of the 2006 IEEE 8th International Conference on Properties Applications of Dielectric Materials*, pp. 464-467, Denpasar, Indonesia, June 2006.
- [10] H.-C. Chiu and G. P. Demopoulos, "A novel green approach to synthesis of nanostructured $\text{Li}_4\text{Ti}_5\text{O}_{12}$ anode material," *ECS Transactions*, vol. 50, no. 26, pp. 119-126, 2013.
- [11] H.-C. Chiu, N. Brodusch, R. Gauvin, A. Guerfi, K. Zaghib, and G. P. Demopoulos, "Aqueous synthesized nanostructured $\text{Li}_4\text{Ti}_5\text{O}_{12}$ for high-performance lithium ion battery anodes," *Journal of the Electrochemical Society*, vol. 160, no. 5, pp. A3041-A3047, 2013.
- [12] D. Tsubone, T. Hashimoto, K. Igarashi, and T. Shimizu, "Electrical characterization of phase changes in lithium titanate," *Journal of the Ceramic Society of Japan*, vol. 102, no. 1182, pp. 180-184, 1994.
- [13] M. R. Harrison, P. P. Edwards, and J. B. Goodenough, "The superconductor-semiconductor transition in the $\text{Li}_{1+x}\text{Ti}_{2-x}\text{O}_4$ spinel system," *Philosophical Magazine B*, vol. 52, no. 3, pp. 679-699, 1985.
- [14] D. Z. Liu, W. Hayes, M. Kurmoo, M. Dalton, and C. Chen, "Raman scattering of the $\text{Li}_{1+x}\text{Ti}_{2-x}\text{O}_4$ superconducting system," *Physica C: Superconductivity*, vol. 235-240, pp. 1203-1204, 1994.
- [15] C. M. Julien, M. Massot, and K. Zaghib, "Structural studies of $\text{Li}_4/3\text{Me}_5/3\text{O}_4$ (Me = Ti, Mn) electrode materials: local structure and electrochemical aspects," *Journal of Power Sources*, vol. 136, no. 1, pp. 72-79, 2004.
- [16] M. V. Tran, N. L. T. Huynh, T. T. Nguyen, D. T. C. Ha, and P. M. L. Le, "Facile solution route to synthesize nanostructure $\text{Li}_4\text{Ti}_5\text{O}_{12}$ for high rate Li-ion battery," *Journal of Nano-materials*, vol. 2016, Article ID 4261069, 7 pages, 2016.
- [17] D. Y. W. Yu, C. Fietzek, W. Weydanz et al., "Study of LiFePO_4 by cyclic voltammetry," *Journal of The Electrochemical Society*, vol. 154, no. 4, pp. A253-A257, 2007.

Research Article

Cellulose Conversion to 5-Hydroxymethyl Furfural (5-HMF) Using Al-Incorporated SBA-15 as Highly Efficient Catalyst

Son Tung Pham,^{1,2} Manh B. Nguyen ,^{1,3} Giang H. Le ,¹ Trang T. T. Pham,^{1,4}
Trang T. T. Quan ,¹ Trinh Duy Nguyen ,⁵ Thanh Le Son ,² and Tuan Anh Vu ^{1,4}

¹Institute of Chemistry, Vietnam Academy of Science and Technology (VAST), 18 Hoang Quoc Viet, Cau Giay, Hanoi, Vietnam

²Hanoi University of Science (HUS), Vietnam National University (VNU), 334 Nguyen Trai, Hanoi, Vietnam

³Institute of Research and Development, Duy Tan University, Da Nang 550000, Vietnam

⁴Graduate University of Science and Technology, Vietnam Academy of Science and Technology, 18 Hoang Quoc Viet Street, Cau Giay, Ha Noi, Vietnam

⁵NTT Institute of High Technology, Nguyen Tat Thanh University, 300A Nguyen Tat Thanh, District 4, Ho Chi Minh City, Vietnam

Correspondence should be addressed to Thanh Le Son; lethanhson@yahoo.com and Tuan Anh Vu; vuanhtuan.vast@gmail.com

Received 14 March 2019; Revised 1 June 2019; Accepted 2 July 2019; Published 7 August 2019

Academic Editor: Elena Gomez

Copyright © 2019 Son Tung Pham et al. This is an open access article distributed under the Creative Commons Attribution License, which permits unrestricted use, distribution, and reproduction in any medium, provided the original work is properly cited.

Al-incorporated SBA-15 samples (xAl/SBA-15) were successfully prepared by “atomic implantation” method. The samples were characterized by X-ray diffraction spectroscopy (XRD), transmission electron microscopy (TEM), energy-dispersive X-ray spectroscopy (EDX), N₂ adsorption-desorption isotherms (BET), and temperature-programmed desorption (NH₃-TPD). In this catalyst, metal oxide species were highly dispersed on the SBA-15 surface and existed as isolated atoms. It was shown that the Al incorporation lead to the formation of medium and strong acid sites. The catalytic activity and selectivity were tested in a mild hydrothermal process for degradation of cotton cellulose to 5-hydroxymethyl furfural (5-HMF). A cellulose conversion of 68.5% and 5-HMF selectivity of 62.1% after 2 h of reaction at 170°C were achieved. The very high 5-HMF yield (42.57%) obtained in this paper is much higher than that was reported in the literature.

1. Introduction

In recent years, the process of biomass conversion to hydrocarbon fuels has received much attention due to the limited fossil fuels resource, demanding the alternatives to obtain biofuels. Biomass is as well known as carbon renewable energy resources for the production of bio-oil by the fast pyrolysis technology. However, bio-oil is composed of different compounds with high oxygen content and low chemical stability and, therefore, cannot be used as biofuels. Recently, great efforts have been made to develop practical pathways to transform biomass-derived carbohydrates into chemicals and fuels. 5-Hydroxymethyl furfural (5-HMF) has a versatile range of applications and can be obtained from the chemical conversion of C₆ carbohydrates. The

conversion of cellulosic biomass to valuable chemicals such as 5-hydroxymethyl furfural, which is often termed the “sleeping giants,” is currently one of the most interests of worldwide research and developments to foster a biobased economy [1]. Therefore, considerable efforts devoted to the depolymerization of cellulose to obtain 5-HMF as a promising bio-oil.

Due to its high degree of crystallinity and stability, hydrolysis of cellulose was often carried out in acidic medium using acids like H₂SO₄, HCl, and HF. In the rigorous reaction condition, the experimental equipment must have high corrosion resistance. Besides, high concentration of inorganic acid used in the reaction can cause extremely negative impacts on surrounding environment. Conversion of cellulose to 5-HMF by using solid acid catalysts under

hydrothermal conditions is an environment-friendly chemical process, and it is easy to separate products by filtration. Interestingly, after the reaction, the catalyst can be easily recovered and reused. The $\text{SO}_4^{2-}/\text{ZrO}_2\text{-Al}_2\text{O}_3$ catalysts were employed in glucose hydrolysis in hot water which led to a 5-HMF conversion 39% [2]. Zhang et al. stated the preparation of $\text{SO}_4^{2-}/\text{ZrO}_2$ on TiO_2 and showed high conversion of glucose into 5-HMF [3]. The combined yield of 5-HMF and levulinic acid reached 28.8% in the presence of $\text{SO}_4^{2-}/\text{ZrO}_2\text{-TiO}_2$ when the Zr:Ti molar ratio was 5:5 after 2 h of reaction at 170°C.

The advantage of the use of SBA-15 material as catalyst support includes its well-ordered hexagonal mesoporous silica structure with high surface-to-volume ratio, high permeability, variable framework compositions, and high thermal stability [4–6]. However, the electrically neutral framework of purely siliceous SBA-15 gives a rise to its lack of functionality. As a result, it normally plays a role of adsorbent, not acidic or redox catalysts [7, 8]. In order to be used as acidic or redox catalysts, SBA-15 should be modified by incorporation of transition metals into framework using direct and/or postsynthesis [9–17]. Aluminium ions (Al^{3+}) insertion into the SBA-15 creates acid sites in the structure which is extremely important for acid-catalyzed reaction. However, the incorporation of aluminium into Al/SBA-15 is difficult because of the difference in hydrolysis rates of Al and Si in low pH medium during the SBA-15 synthesis process [18]. Various synthetic methods have been devoted for the incorporation of higher amounts of aluminium to achieve higher acid sites [14, 16, 17].

In this paper, we report a novel method to incorporate aluminium ion into the SBA-15 framework by atomic implantation and use it as an efficient catalyst for conversion of cellulose to HMF. Effects of reaction temperature and catalyst dosage were also investigated.

2. Experimental Methods

2.1. Preparation of SBA-15. Synthesis of SBA-15 material was done as follows: 1 g of poly (ethylene glycol)-block-poly (propylene glycol)-block-poly (ethylene glycol) (P123) was dissolved in 60 mL of HCl (2 M) and stirred for few hours until a clearly surfactant solution was obtained. Sodium silicate solution ~27% SiO_2 (Sigma-aldrich) was added dropwise into the surfactant solution with vigorous stirring for 2 hours; then, the mixture was further stirred for 24 hours at 45°C, and the obtained mixture was poured into Teflon lined and autoclave hydrothermal treatment was performed in an oven at 100°C for 24 h. Finally, the white solid product was washed, dried at 80°C overnight, and calcined at 550°C for 6 h in air.

2.2. Preparation of xAl/SBA-15. Al incorporate was carried out by atomic implantation method using AlCl_3 (99.99%, Sigma-aldrich) as Al source [19]. In order to obtain 1Al/SBA-15 with different Al loading, we deposited Al by repeating the Al deposition time. AlCl_3 first deposited on SBA-15 which was prepared previously (denoted 1Al/SBA-15 sample). Use of 1Al/SBA-15 as starting material, we

deposited the second Al layer on 1Al/SBA-15 to obtain 2Al/SBA-15 and use of 2Al/SBA-15 as starting material we deposited the third Al layer (denoted 3Al/SBA-15 sample). The reactor was a quartz tube (2 cm × 25 cm) in which amount of AlCl_3 was introduced on one side and an opposite side placed a determined amount of SBA-15.

Reactor was heated to 350°C, and AlCl_3 evaporated and passed through substrate of SBA-15 by flowing carrier gas (N_2). The reaction time was varied between 0.5 h to 1 h. Then the sample was calcined at 500°C to remove chloride.

2.3. Characterization of Materials and Membrane. The morphology characteristics of the materials were analyzed by transmission electron microscopy (HITACHI-H-7500). The pore structure of all resulting solids was determined by nitrogen adsorption-desorption isotherms at 77 K using TriStar Plus II. The powder X-ray diffraction patterns of the samples were recorded on a D8 Advance analyzer with $\text{Cu K}\alpha$ radiation ($l = 1.5417 \text{ \AA}$). The chemical composition of the samples was analyzed by EDX, on JED-2300 analysis Station (JEOL) machine. The acid sites were measured by using $\text{NH}_3\text{-TPD}$ (model: Autochem II). The ammonia concentration in the effluent gases was determined by a thermal conductivity detector.

2.4. Catalytic Test. The investigation of catalytic degradation of cotton cellulose was carried out in a high-pressure batch stainless-steel reactor equipped with a liner of polytetrafluoroethylene (PTFE). The cotton cellulose, solid acid catalysts, and water were thoroughly mixed in the reactor; then, the mixture was heated in the oven. Some effects of operation parameters were mainly investigated such as catalyst type and dosage, reaction temperature, and time on the cellulose saccharification to glucose and the monosaccharide dehydration to 5-HMF. After the reaction, the mixture of solution and solid reactants were separated by filtration.

The cellulose conversion, selectivity, and yield 5-HMF were calculated by the following equation:

$$\text{cellulose conversion (C\%)} = \frac{\text{reacted cellulose}}{\text{initial cellulose}} \times 100\%, \quad (1)$$

$$\text{5-HMF selectivity (S\%)} = \frac{\text{5-HMF}}{\text{reacted cellulose}} \times 100\%, \quad (2)$$

$$\text{5-HMF - Yield (Y\%)} = \text{C(\%)} \times \text{S(\%)}. \quad (3)$$

3. Results and Discussion

3.1. X-Ray Diffraction Spectroscopy (XRD). Figure 1(a) shows the low-angle X-ray diffraction patterns of xAl/SBA-15. In the XRD pattern, the one peak with strong intensity in the 2θ angle of ~1.02°, two peaks with weak intensity at 2θ angle of ~1.6° and 2θ ~1.8°, corresponding to the diffraction of (100), (110), and (200) reflection, respectively, which are characteristic for the structure of 2D hexagonal $p6mm$ symmetry of mesoporous SBA-15 structure [19, 20]. In the

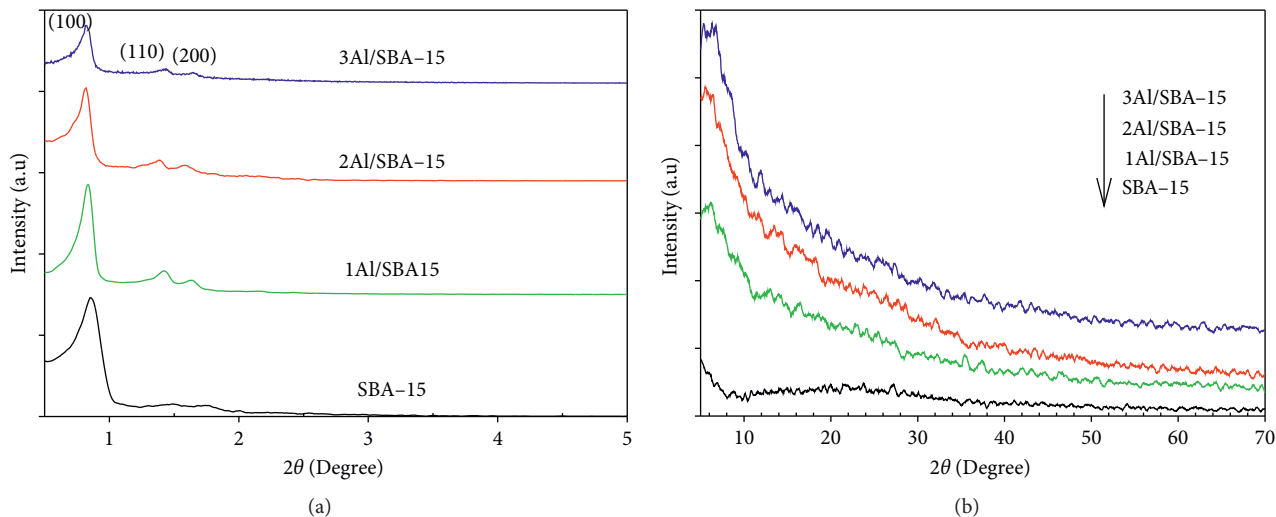


FIGURE 1: Small angle (a) and wide angle (b) XRD patterns of SBA-15 and xAl/SBA-15.

wide angle (Figure 1(b)) XRD pattern of the xAl/SBA-15, no diffraction lines of crystalline Al oxide in xAl/SBA-15 samples were observed. This can be explained by the fact that almost all Al incorporated into SBA-15 framework; therefore, the phase of Al₂O₃ could not be detected by [5].

As shown in Table 1, the Rietveld refined parameter of the crystal structure of these samples was slightly changed with different Al incorporated into SBA-15 framework. This is related to the substitution of metal ions (Al) for Si in the SBA-15 framework. Because the ionic radius of Al³⁺ (0.51 Å) is greater than Si⁴⁺ (0.41 Å), the Al-O bond lengths are longer than Si-O bond, leading to increase in d_{100} and a_0 parameters [7, 17, 21]. This result strongly confirms that Al incorporation into SBA-15 framework.

3.2. N₂ Adsorption-Desorption Isotherms (BET). Figure 2 shows the N₂ isotherms and pore size distribution of calcined SBA-15 and xAl/SBA-15. It can be seen from N₂ isotherms of these samples that the hysteresis loops indicated the typical feature of mesoporous materials owing to the capillary condensation. The increase in N₂ amount adsorbing on the material is clearly observed which is resulted from the multilayer adsorption in the formed mesopore [16, 19]. This indicates that the samples have a large pore size (5.5 nm for SBA-15 and 5.5–5.8 nm for xAl/SBA-15). The high degree of mesopore ordering leads a sharp inflection at relative pressures (P/P_0) between 0.6 and 0.8 which is consistent with well-defined 3 nm mesopores. The BET surface areas of SBA-15 and xAl/SBA-15 (Table 2) were strongly decreased from 668 m²/g to 143 m²/g, respectively. This result can be explained that the new small Al oxides particles were formed and located along to the channels, causing the decrease of surface area. As seen in Table 2, the SBA-15 sample had a pore diameter of 5.50 nm and a wall thickness of 5.51 nm, while xAl/SBA-15 samples showed a slight increase of pore diameter and wall thickness. This result clearly indicated that the new mesopore system

TABLE 1: Characterization of the crystal structure of all samples.

Samples	D_{100} (Å)	a_0 (nm) ($a_0 = 2 \cdot d_{100} / \sqrt{3}$)
SBA-15	95.419	11.01
1Al/SBA-15	100.356	11.58
2Al/SBA-15	101.276	11.69
3Al/SBA-15	102.542	11.84

was formed and located along to the pore SBA-15 system [11, 22].

3.3. Transmission Electron Microscopy (TEM) and Energy-Dispersive X-Ray Spectroscopy (EDX). The transmission electron microscopy (TEM) images of SBA-15 and xAl/SBA-15 samples are illustrated in Figure 3. The TEM image of SBA-15 display well-ordered hexagonal arrays of mesopore with one-dimensional channels, indicating a 2D hexagonal ($p6mm$) mesostructure. The average wall thickness was ~5-6 nm, with similar width pore diameters determined by BET. As seen in Figures 3(b)–3(d), the pore and wall thickness of Al incorporated SBA-15 were not uniform as compared to those of pure SBA-15. Especially, for the Al-incorporated SBA-15 sample with high Al content (3Al/SBA-15), Al oxide particles covered the surface, no pores and wall of SBA-15 were observed.

The results of EDX in Figure 4 and Table 3 show that the Al element contents (5.6, 9.7, and 12.5%) deposited on the xAl/SBA-15 were approximately equal to the value calculated. From Figure 4, it was noted that the Al loading was increasing. Thus, at high Al loading (3Al/SBA-15), the intensity of Al peak was higher than that of medium loading sample (2Al/SBA-15). However, when Al content was too high, Al content determined by EDX is lower than calculated amount. This due to the saturation of Al deposited on SBA-15 surface. The 3Al/SBA-15 sample was prepared by deposition the third Al layer on 2Al/SBA-15 sample. In this case, penetration of Al into SBA-15 is hindered by the two Al

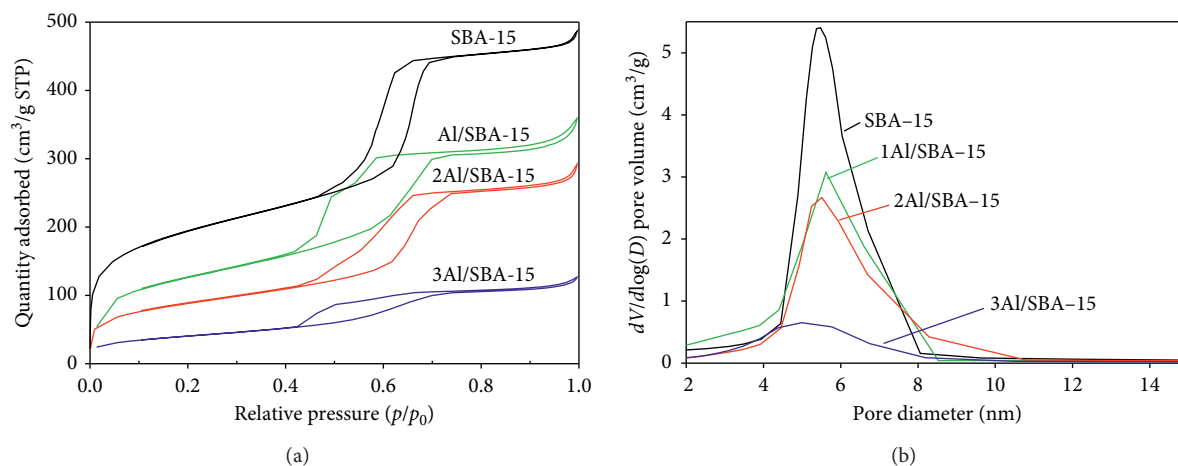


FIGURE 2: BET specific surface area of SBA-15 and $x\text{Al/SBA-15}$ samples (a) and pore size distribution (b).

TABLE 2: Textual characteristics of SBA-15 and $x\text{Al/SBA-15}$ samples.

Samples	S_{BET} (m^2/g)	S_{micro} (m^2/g)	V_{pore} (cm^3/g)	D_{BJH} (nm)	W_t (nm) $W = a_0 - D_{\text{BJH}}$
SBA-15	668.52	182.93	0.70	5.50	5.51
1Al/SBA-15	443.05	127.61	0.55	5.54	5.90
2Al/SBA-15	309.16	87.07	0.44	5.76	5.93
3Al/SBA-15	143.39	43.75	0.19	5.80	6.04

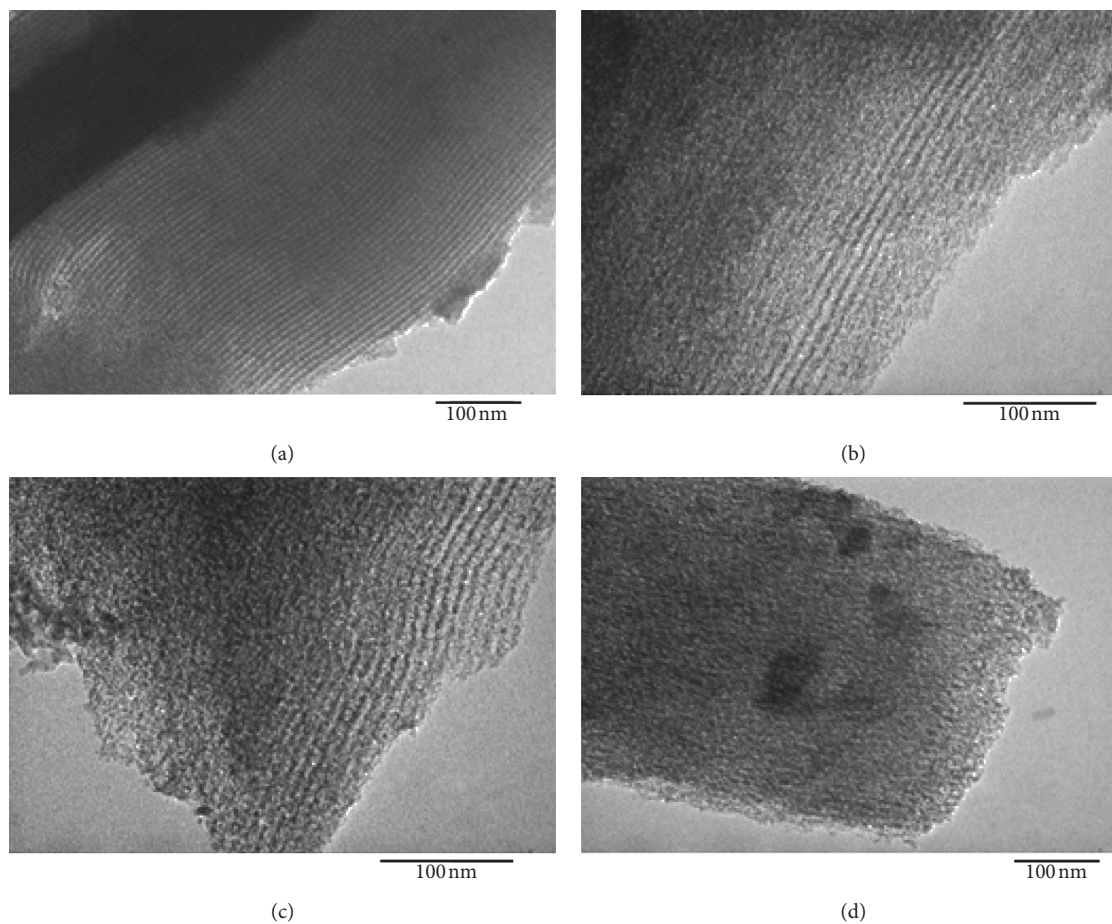


FIGURE 3: TEM images of (a) SBA-15 and (b) $x\text{Al/SBA-15}$, (c) $x\text{Al/SBA-15}$, and (d) $x\text{Al/SBA-15}$.

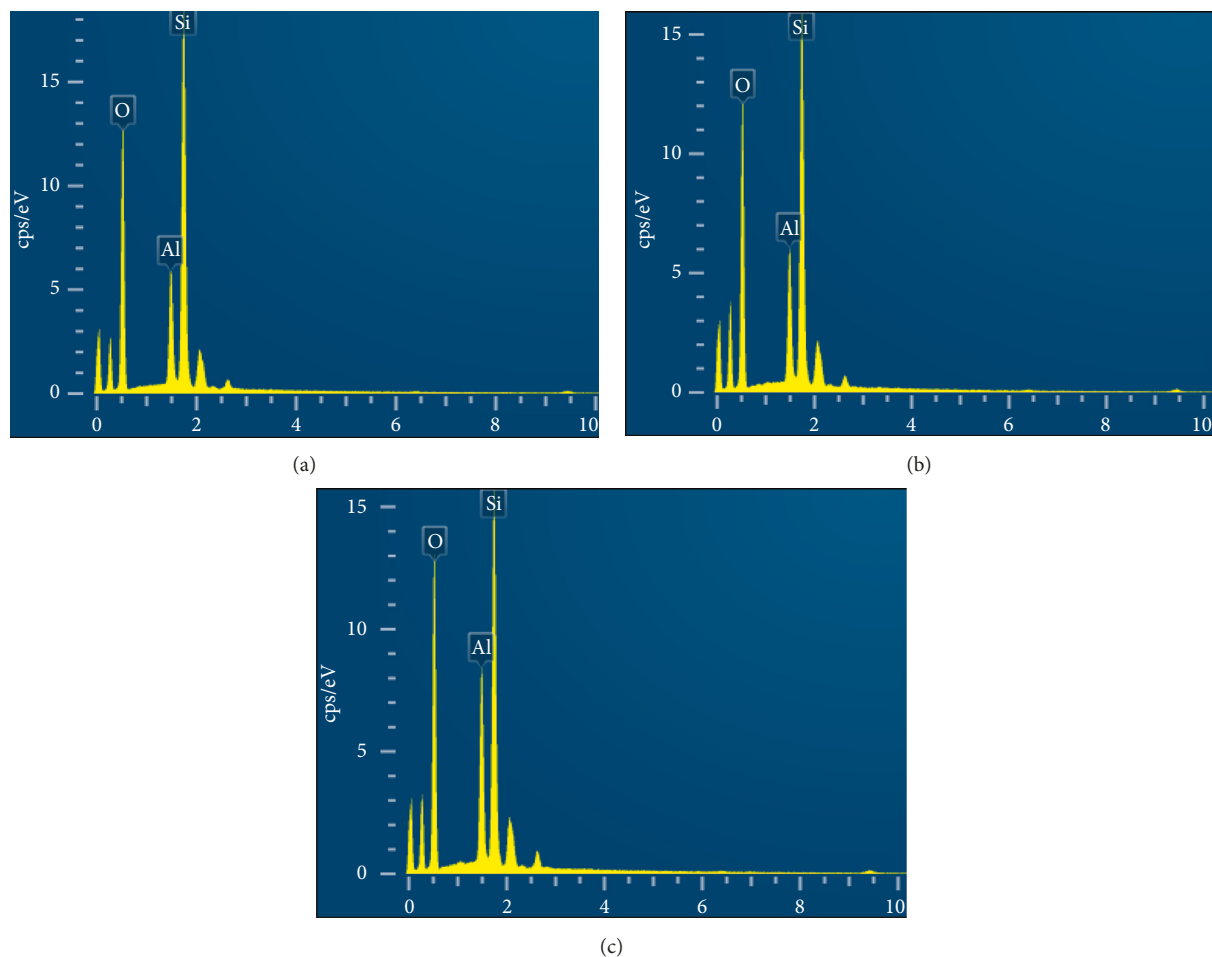


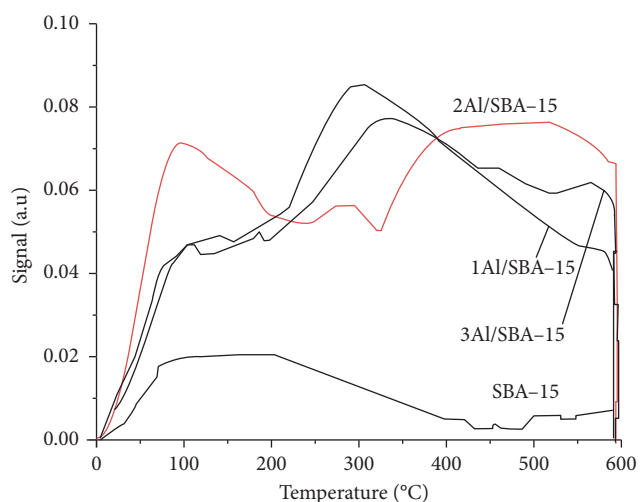
FIGURE 4: EDX of Al/SBA-15 (a), 2Al/SBA-15 (b), and 3Al/SBA (c).

TABLE 3: EDX result Si, O, and Al content in xAl/SBA-15.

Samples	Weight (%)		
	O	Si	Al
SBA-15	63.19	36.81	—
1Al/SBA-15	63.44	30.91	5.66
2Al/SBA-15	61.39	28.92	9.70
3Al/SBA-15	60.67	26.78	12.56

layers which previously deposited on SBA-15, leading to the saturation.

3.4. Temperature-Programmed Desorption (NH_3 -TPD). It is well known that cellulose hydrolysis is catalyzed by acid catalyst. The cellulose conversion is strongly dependent on the acidity of the catalysts. To determine the acidity of Al incorporated SBA-15, we used the NH_3 -TPD method [14]. Figure 5 shows NH_3 -TPD profiles of Al incorporated SBA-15. Amounts of weak ($<200^\circ\text{C}$), medium ($250\text{--}300^\circ\text{C}$), and strong ($500\text{--}550^\circ\text{C}$) acid sites are listed in Table 4. As observed in Figure 5 and Table 4, the pure SBA-15 possessed only weak acid sites (max desorption temperature $<200^\circ\text{C}$), while Al incorporated SBA-15 samples showed large amount of medium and strong acid sites (Table 4). Among them,

FIGURE 5: NH_3 -TPD pattern of SBA-15 and xAl/SBA-15 catalyst.

2Al/SBA-15 had the highest amount of medium acid sites ($T_{\text{max}} \sim 250\text{--}300^\circ\text{C}$). This may be due to the Al amount incorporated into SBA-15 is suitable, favoring to form medium and strong acid sites (isolated Al sites formation). In the case of 3Al/SBA-15, amount of acid sites is lower than that of

TABLE 4: NH₃ amount of weak, medium, and strong acid sites of SBA-15 and xAl/SBA-15.

Samples	mol NH ₃ /g cat			Total
	<200°C	250–300°C	500–550°C	
SBA-15	0.23	—	—	0.23
1Al/SBA-15	0.23	0.22	0.04	0.49
2Al/SBA-15	0.43	0.19	0.56	1.18
3Al/SBA-15	0.14	0.17	0.12	0.43

TABLE 5: Conversion and selectivity of 5-HMF over xAl/SBA-15 catalyst.

Catalysts	C _{5-HMF} (ppm)	S (%)	C (%)	Y (%)
1Al/SBA-15	4001.24	23.15	63.27	14.64
2Al/SBA-15	10740	62.14	68.51	42.57
3Al/SBA-15	7956.02	46.03	64.49	29.68
SBA-15	662.6	2.92	40.15	1.17

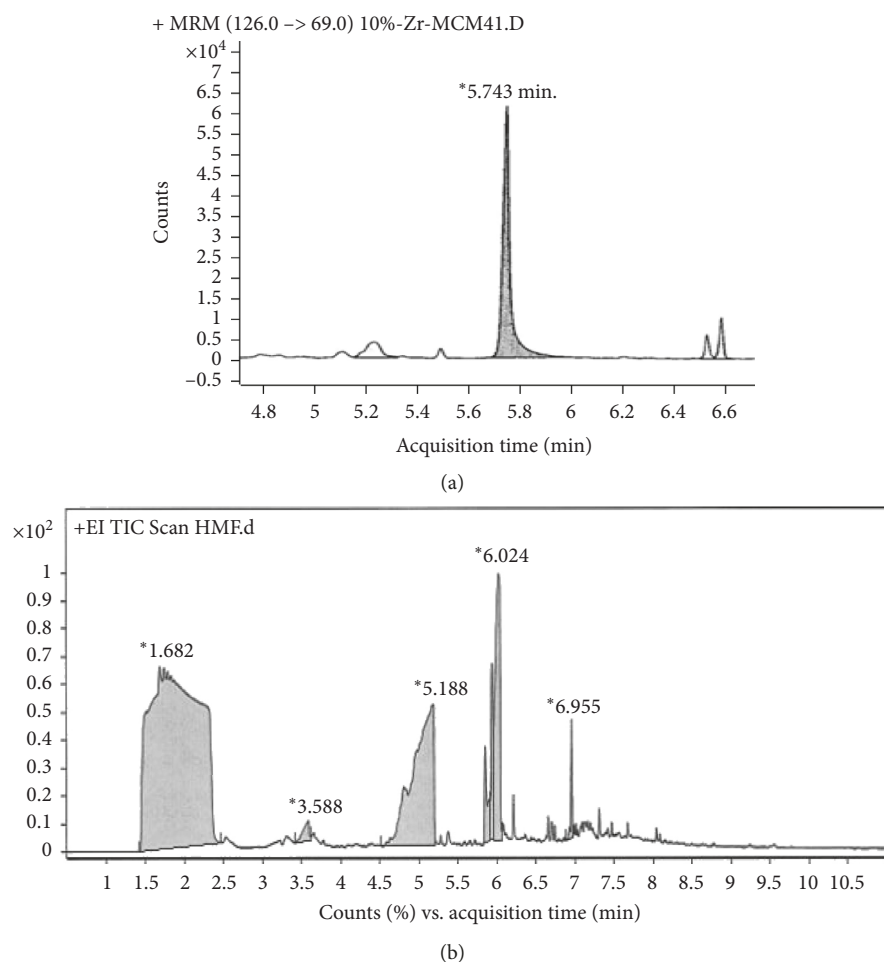


FIGURE 6: 5-HMF (a) and by-products (b) in the cellulose conversion over Al-incorporated SBA-15 samples.

2Al/SBA-15. This can be explained the formation of Al₂O₃ particles which cover the acid sites created after the second Al layer deposition (2Al/SBA-15 sample).

3.5. Catalytic Activity. Table 5 shows that the conversion, selectivity, and yield of 5 HMF over SBA-15 and xAl/SBA-15

catalysts. We have tested the SBA-15 and this showed almost no catalytic activity. Conversion of cellulose to 5-HMF is catalyzed by acid sites since only small amount of weak acid sites in SBA-15 was noted (Table 4). Among Al-incorporated SBA-15 samples, 2Al/SBA-15 catalyst exhibited the highest yield of 5-HMF (42%). This value was higher than that reported in the literature [23–26]. Some previous works

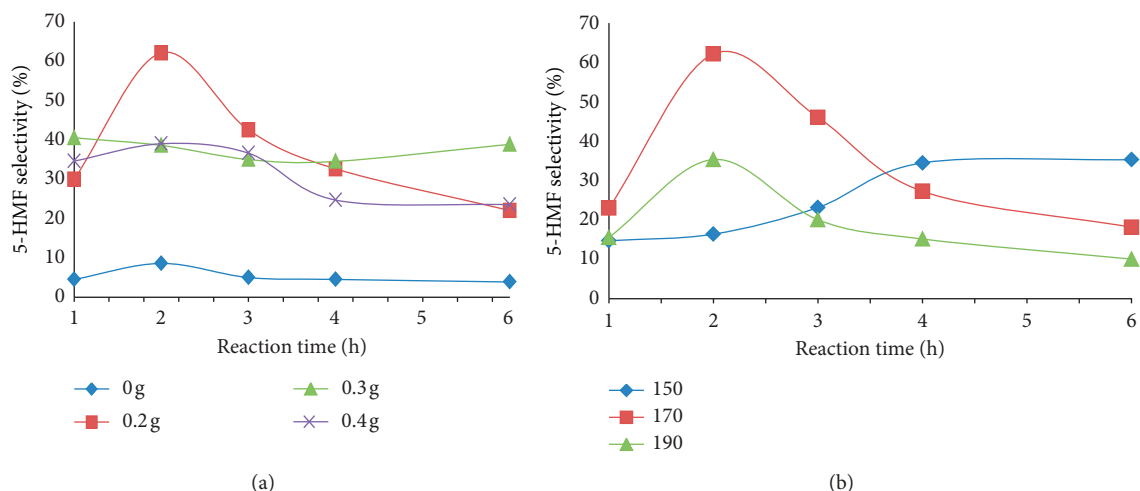


FIGURE 7: Effect of catalyst dosage (a) and reaction temperature (b) on the catalytic conversion of cellulose.

stated the low 5-HMF yield (10–20%). According to the proposed mechanism, cellulose hydrolyzed under the action of a catalyst will be converted into glucose and then isomerized to fructose and fructose followed the hydration converted into 5-HMF [27, 28]. The process of converting cellulose into glucose requires strong acidic centers, while the isomerization and dehydration process requires medium acidic centers. Therefore, in order to obtain the high 5-HMF from cellulose hydrolysis it needs both the medium and strong acid sites. However, for the sample contained high amount of very strong acid sites like ZrO_2 sulfated SBA-15, the cellulose conversion was very high but the 5-HMF selectivity was low due to the formation of intermediate products (result unpublished). This also occurred for Al-incorporated SBA-15. Thus, Figures 6(a) and 6(b) illustrate the formation of by-products such as pentanoic acid ($C_5H_8O_3$), 1,2,4-cyclopentanetriol ($C_5H_{10}O_3$); cyclo-trisiloxane, and octamethyl ($C_8H_{24}O_4Si_4$).

To investigate the effect of catalyst dosage and reaction temperature on cellulose conversion, catalyst dosage ranging from 0.2 g to 0.4 g and reaction temperature ranging from 150°C to 190°C were tested. As seen in Figure 7, catalyst dosage of 0.2 g (Figure 7(a)) and reaction temperature at 170°C (Figure 7(b)) are optimal condition for cellulose conversion. The dosage of 0.2 g is sufficient for converting cellulose to 5-HMF, introduction of high dosage of 0.3 g–0.4 g leads to the catalyst excess which cause the further conversion of 5-HMF to the by product like levulinic, formic acid. The 4-HMF yield in the cellulose conversion to 5-HMF at 150°C increased with increasing reaction time from 0 to 4 h and then maintained unchanged for prolongation time to 6 h. At higher temperature (170°C), 5-HMF yield increased because the reaction is thermodynamically favored at a high temperature. Further increase of temperature (190°C) did not lead to the increase of 5-HMF yield but it decreased. This can be explained at very high temperature, glucose formed from cellulose hydrolysis is dehydrated forward the anhydroglucose which is thermodynamically favored at very high reaction temperature [29]. Moreover, prolongation of

reaction time favored the formation of by-products including formic, acetic, levulinic, and glycollic acid [27].

4. Conclusions

Al-incorporated SBA-15 samples were successfully prepared by atomic implantation method. From XRD result, it revealed the mesoporous structure of Al-incorporated SBA-15. TEM images showed that aluminium oxide species were well dispersed and located along the SBA-15 channels. Al incorporation into SBA-15 framework created the weak, medium, and strong acid sites.

Among Al-incorporated SBA-15 samples, 2Al/SBA-15 exhibited the highest yield of 5-HMF (yield 42%). The yield obtained in this study is much higher to that reported in the literature.

Data Availability

The data used to support the findings of this study are available from the corresponding author upon request.

Conflicts of Interest

The authors declare that they have no conflicts of interest.

Acknowledgments

The authors thank the Vietnam Academy of Science and Technology (VAST) for financial support project (TĐPCCC.03/18–20).

References

- [1] F. K. Kazi, A. D. Patel, J. C. Serrano-Ruiz, J. A. Dumesic, and R. P. Anex, "Techno-economic analysis of dimethylfuran (DMF) and hydroxymethylfurfural (HMF) production from pure fructose in catalytic processes," *Chemical Engineering Journal*, vol. 169, no. 1–3, pp. 329–338, 2011.

- [2] H. Yan, Y. Yang, D. Tong, X. Xiang, and C. Hu, "Catalytic conversion of glucose to 5-hydroxymethylfurfural over $\text{SO}_4^{2-}/\text{ZrO}_2$ and $\text{SO}_4^{2-}/\text{ZrO}_2\text{-Al}_2\text{O}_3$ solid acid catalysts," *Catalysis Communications*, vol. 10, no. 11, pp. 1558–1563, 2009.
- [3] J. Zhang, J. Li, and L. Lin, "Dehydration of sugar mixture to HMF and furfural over $\text{SO}_4^{2-}/\text{ZrO}_2\text{-TiO}_2$ catalyst," *Bio-Resources*, vol. 9, no. 3, pp. 4194–4204, 2014.
- [4] S. P. Ghuge and A. K. Saroha, "Ozonation of Reactive Orange 4 dye aqueous solution using mesoporous Cu/SBA-15 catalytic material," *Journal of Water Process Engineering*, vol. 23, pp. 217–229, 2018.
- [5] S. Karthikeyan, M. P. Pachamuthu, M. A. Isaacs, S. Kumar, A. F. Lee, and G. Sekaran, "Cu and Fe oxides dispersed on SBA-15: a Fenton type bimetallic catalyst for N,N-diethyl-p-phenyl diamine degradation," *Applied Catalysis B: Environmental*, vol. 199, pp. 323–330, 2016.
- [6] J. Fan, X. Jiang, H. Min et al., "Facile preparation of Cu–Mn/CeO₂/SBA-15 catalysts using ceria as an auxiliary for advanced oxidation processes," *Journal of Materials Chemistry A*, vol. 2, no. 27, p. 10654, 2014.
- [7] T. P. Dang, H. V. T. Nguyen, H. G. Le et al., "Fe-incorporation into mesoporous SBA-15 materials by direct synthesis and post-synthesis," in *Proceedings of the SPIE 7267, Smart Materials V*, vol. 726718, Melbourne, Australia, December 2008.
- [8] C.-M. Yang, P.-H. Liu, Y.-F. Ho, C.-Y. Chiu, and K.-J. Chao, "Highly dispersed metal nanoparticles in functionalized SBA-15," *Chemistry of Materials*, vol. 15, no. 1, pp. 275–280, 2003.
- [9] E. Petala, K. Dimos, A. Douvalis et al., "Nanoscale zero-valent iron supported on mesoporous silica: characterization and reactivity for Cr(VI) removal from aqueous solution," *Journal of Hazardous Materials*, vol. 261, pp. 295–306, 2013.
- [10] F. S. D. Santos, F. R. Lago, L. Yokoyama, and F. V. Fonseca, "Synthesis and characterization of zero-valent iron nanoparticles supported on SBA-15," *Journal of Materials Research and Technology*, vol. 6, no. 2, pp. 178–183, 2017.
- [11] C. Zheng, C. Yang, X. Cheng et al., "Specifically enhancement of heterogeneous Fenton-like degradation activities for ofloxacin with synergetic effects of bimetallic Fe-Cu on ordered mesoporous silicon," *Separation and Purification Technology*, vol. 189, pp. 357–365, 2017.
- [12] M.-G. Seo, D.-W. Lee, K.-Y. Lee, and D. J. Moon, "Pt/Al-SBA-15 catalysts for hydrocracking of C₂₁–C₃₄ n-paraffin mixture into gasoline and diesel fractions," *Fuel*, vol. 143, no. 1, pp. 63–71, 2015.
- [13] G. Muthu Kumaran, S. Garg, K. Soni et al., "Synthesis and characterization of acidic properties of Al-SBA-15 materials with varying Si/Al ratios," *Microporous and Mesoporous Materials*, vol. 114, no. 1–3, pp. 103–109, 2008.
- [14] J. Socci, A. Osatiashtiani, G. Kyriakou, and T. Bridgwater, "The catalytic cracking of sterically challenging plastic feedstocks over high acid density Al-SBA-15 catalysts," *Applied Catalysis A: General*, vol. 570, pp. 218–227, 2019.
- [15] K. B. Baharudin, Y. H. Taufiq-Yap, J. Hunns, M. Isaacs, K. Wilson, and D. Derawi, "Mesoporous NiO/Al-SBA-15 catalysts for solvent-free deoxygenation of palm fatty acid distillate," *Microporous and Mesoporous Materials*, vol. 276, pp. 13–22, 2019.
- [16] Z. Yang, W. Cai, J. Chou et al., "Hydrothermal synthesis of plugged micro/mesoporous Al-SBA-15 from spent fluid catalytic cracking catalyst," *Materials Chemistry and Physics*, vol. 222, no. 15, pp. 227–229, 2019.
- [17] S. Xing, P. Lv, J. Fu et al., "Direct synthesis and characterization of pore-broadened Al-SBA-15," *Microporous and Mesoporous Materials*, vol. 239, pp. 316–327, 2017.
- [18] Y. Li, W. Zhang, L. Zhang et al., "Direct synthesis of Al-SBA-15 mesoporous materials via hydrolysis-controlled approach," *Journal of Physical Chemistry B*, vol. 108, no. 28, pp. 9739–9744, 2004.
- [19] T. T. Nguyen, G. H. Le, C. H. Le et al., "Atomic implantation synthesis of Fe-Cu/SBA-15 nanocomposite as a heterogeneous fenton-like catalyst for enhanced degradation of DDT," *Materials Research Express*, vol. 5, no. 11, article 115005, 2018.
- [20] A. Vinu, T. Mori, and K. Ariga, "New families of mesoporous materials," *Science and Technology of Advanced Materials*, vol. 7, no. 8, pp. 753–771, 2006.
- [21] S. More, R. Kadam, A. Kadam, D. Mane, and G. Bichile, "Structural properties and magnetic interactions in Al³⁺ and Cr³⁺ co-substituted CoFe₂O₄ ferrite," *Open Chemistry*, vol. 8, no. 2, pp. 419–425, 2010.
- [22] X. Song, S. Li, K. Li et al., "Preparation of Cu-Fe composite metal oxide loaded SBA-15 and its capacity for simultaneous catalytic oxidation of hydrogen sulfide and phosphine," *Microporous and Mesoporous Materials*, vol. 259, pp. 89–98, 2018.
- [23] K. Y. Nandiwale, N. D. Galande, P. Thakur, S. D. Sawant, V. P. Zambre, and V. V. Bokade, "One-pot synthesis of 5-hydroxymethylfurfural by cellulose hydrolysis over highly active bimodal micro/mesoporous H-ZSM-5 catalyst," *ACS Sustainable Chemistry & Engineering*, vol. 2, no. 7, pp. 1928–1932, 2014.
- [24] C.-W. Jiang, X. Zhong, and Z.-H. Luo, "An improved kinetic model for cellulose hydrolysis to 5-hydroxymethylfurfural using the solid $\text{SO}_4^{2-}/\text{Ti-MCM-41}$ catalyst," *RSC Advances*, vol. 4, no. 29, pp. 15216–15224, 2014.
- [25] A. Chareonlimkun, V. Champreda, A. Shotipruk, and N. Laosiripojana, "Catalytic conversion of sugarcane bagasse, rice husk and corncob in the presence of TiO₂, ZrO₂ and mixed-oxide TiO₂-ZrO₂ under hot compressed water (HCW) condition," *Bioresource Technology*, vol. 101, no. 11, pp. 4179–4186, 2010.
- [26] A. Chareonlimkun, V. Champreda, A. Shotipruk, and N. Laosiripojana, "Reactions of C₅ and C₆-sugars, cellulose, and lignocellulose under hot compressed water (HCW) in the presence of heterogeneous acid catalysts," *Fuel*, vol. 89, no. 10, pp. 2873–2880, 2010.
- [27] X. Qi, M. Watanabe, T. M. Aida, and R. L. Smith Jr., "Catalytic conversion of fructose and glucose into 5-hydroxymethylfurfural in hot compressed water by microwave heating," *Catalysis Communications*, vol. 9, no. 13, pp. 2244–2249, 2008.
- [28] S. Wang, Y. Du, W. Zhang, X. Cheng, and J. Wang, "Catalytic conversion of cellulose into 5-hydroxymethylfurfural over chromium trichloride in ionic liquid," *Korean Journal of Chemical Engineering*, vol. 31, no. 10, pp. 1786–1791, 2014.
- [29] V. Choudhary, R. I. Burnett, D. G. Vlachos, and S. I. Sandler, "Dehydration of glucose to 5-(hydroxymethyl) furfural and anhydroglucose: thermodynamic insights," *Journal of Physical Chemistry C*, vol. 116, no. 8, pp. 5116–5120, 2012.

Research Article

Synthesis of SAPO-34 Using Different Combinations of Organic Structure-Directing Agents

Tuan Doan , Khang Nguyen , Phong Dam , Thanh Huyen Vuong, Minh Thang Le ,
and Huyen Pham Thanh 

School of Chemical Engineering, Hanoi University of Science and Technology, Hanoi, Vietnam

Correspondence should be addressed to Huyen Pham Thanh; huyen.phamthanh@hust.edu.vn

Received 14 March 2019; Revised 13 May 2019; Accepted 4 July 2019; Published 22 July 2019

Guest Editor: Thanh-Dong Pham

Copyright © 2019 Tuan Doan et al. This is an open access article distributed under the Creative Commons Attribution License, which permits unrestricted use, distribution, and reproduction in any medium, provided the original work is properly cited.

The effects of different mixtures of organic structure-directing agents (OSDAs) on the formation of SAPO-34 structure have been investigated. Different OSDAs, namely, triethylamine (TEA), tetraethylammonium hydroxide (TEAOH), and morpholine (Mor) and their combinations were used to synthesize SAPO-34 by a hydrothermal method. The template concentration was optimized by eliminating the competing phases to obtain the purest form of SAPO-34 phase. The as-synthesized samples were analyzed by XRD, FE-SEM/EDS, FT-IR, surface area/pore volume measurements, NH₃-TPD, TG/DTA, and ²⁹Si NMR MAS. The selection of template notably impacts the crystal size and physicochemical characteristics of as-synthesized SAPO-34. The sample prepared with 3 Mor:3 TEA:1 TEAOH exhibited the highest total acidity, smallest crystal size below 3 μm, and high surface area up to 697 m²/g.

1. Introduction

Silicoaluminophosphate (SAPO) is a related grade of microporous material applied mostly in the scope of catalysis of processes such as hydro-isomerization of *n*-hexane, gas separations, methanol conversion to light olefins (MTO), pyrolysis reaction, or removal of NO_x by selective catalytic reduction with ammonia (NH₃-SCR). SAPO-34 is such an exciting catalyst in the SAPO generation. Since being discovered in the 1980s, large chabazite (CHA) with small channel systems, eight-membered rings (3.8 Å × 3.8 Å), and 9.4 Å in diameter cage called SAPO-34 has received significant attention, thanks to its high selectivity to light gases separation [1, 2].

Normally, SAPO-34 is prepared from a gel containing sources of an alumina source, a phosphorus source, a silica source, and leastwise one template source by using a hydrothermal method [3, 4]. The OSDA leads an essential duty in the synthesis of SAPO materials. Therefore, suitable OSDAs perform an indispensable role in the preparation of SAPO-34 involving in structure-directing, charge-compensating, and space-filling. Several organic amine compounds

are used as a/an OSDA(s) in SAPO-34 syntheses, for example, tetraethylammonium hydroxide (TEAOH), morpholine (Mor), triethyl amine (TEA), dipropyl amine (DPA), and diethyl amine (DEA) [5–10]. The combination of OSDA surveyed in the preparation of SAPO-34 aims to increase the qualities as well as the catalytic performance of SAPO-34 [11, 12]. Between these OSDAs, the nanoparticle size of SAPO-34 can be achieved by using the quaternary ammonium compound TEAOH as a template, so TEAOH is the most commonly used compound to synthesize SAPO-34. Reducing the particle size of SAPO-34 enhanced its catalytic behavior in many previous reports. Hirota et al. [13] increased the catalyst lifespan in the methanol-to-olefin reaction by using the SAPO-34 material, which synthesized nanocrystals with particle sizes of 75 nm compared to that with bigger sizes of 800 nm. Using the sonochemical method with TEAOH as OSDA, Askari et al. [14] also observed 50 nm-sized SAPO-34 nanocrystals, which were active for a long time in the same reaction. However, the high cost of TEAOH limits its industrial applications [15, 16]. Compared to TEAOH, Mor is much cheaper. However, the use of Mor as an OSDA leads to the creation of materials which have large particle sizes and

bad catalytic behavior in conversion reactions such as MTO [7, 15]. When TEOH and Mor were combined as the binary OSDAs for the synthesis of SAPO-34, the obtained catalyst had a smaller crystal size and a larger surface area, thereby improving the performance of SAPO-34 catalyst in the methanol conversion reaction [17]. A similar behavior was reported by Sedighi et al. [18] who used different combinations of TEOH and Mor to synthesize SAPO-34 and obtained the catalyst with the most extended lifetime with optimal crystal size and acidity for MTO reaction. TEA is reported to favor the formation of a SAPO-5 impurity phase, although it costs considerably lower compared to TEOH. However, until now, synthesizing SAPO-34 with a combination of templates containing TEA in the previous reports is relatively rare. Applying combined OSDAs, for instance, adding more than one directing agent into the initial solution to lead the creation of molecular sieve, has demonstrated to be an effective and cost-down method to synthesize SAPO-34 catalysts with nanoparticle size [12].

Furthermore, SAPO-34 with nanoparticle size and higher acid properties also was the most favorite parent zeolite of copper ion-exchanged SAPO-34 catalysts for NH_3 -SCR of NO_x since their Brønsted acid sites represent a coordinate role with the Cu^{2+} active sites in this reaction [19]. In SAPO-34, the substitution of aluminum and phosphorus atoms in the neutral aluminophosphate (AlPO-34) structural framework by silicon atoms will appear in Brønsted acid sites [2]. Therefore, the interactions between OSDAs and the structure of SAPO materials and the Si content in the initial mixture influence the Si contribution, resulting in the alteration of the acid properties.

The purpose of this research is the preparation at the optimal TEOH/Mor/TEA molar ratio of the SAPO-34 material with smaller particle size and high acid properties for further catalytic application in NH_3 -SCR of NO_x reaction. In this study, the combination of OSDAs between TEA, Mor, and TEOH was applied to prepare SAPO-34, and the influences of the molar ratio of TEA/Mor/TEAOH on the element composition, morphology, topology, and SAPO-34 zeolite were investigated in detail.

2. Materials and Methods

2.1. Synthesis of SAPO-34 Molecular Sieve. SAPO-34 molecular sieves were synthesized via the regular hydrothermal method. The material was prepared from a mixture gel with a molar composition of $1 \text{ Al}_2\text{O}_3 : 0.6 \text{ SiO}_2 : 1 \text{ P}_2\text{O}_5 : X \text{ OSDA(s)} : 110 \text{ H}_2\text{O}$, wherein X is shown in Table 1. Firstly, aluminum isopropoxide (98%, Merck) was mixed with distilled water, and phosphoric acid (85%, aqueous solution, Merck) was added dropwise. The mixture was stirred for one hour until completely dissolved, then tetraethyl orthosilicate TEOS (98%, Sigma) was added and stirred. After one hour, the templates including morpholine (99%w/w, ACS Reagent, Sigma), tetraethylammonium hydroxide (25%w/w, Sigma), and triethylamine (98%, Merck) were added to the solution. The resulting synthesis gel was further stirred for 6 hours until a uniform reaction mixture was formed and then aged for 12 hours. The obtained gel was crystallized at 200°C for

TABLE 1: The composition of OSDAs for SAPO-34 preparation.

Name	Organic structure-directing agents (X)		
	Mor	TEA	TEAOH
M1	—	3	—
M2	3	—	—
M3	—	—	3
M4	3	—	1
M5	—	3	1
M6	3	1	—
M7	1	3	—
M8	3	3	1

48 hours in a Teflon-lined autoclave. The as-synthesized sample was filtered, washed, and then dried at 120°C for 6 hours. The obtained sample was heated at $1^\circ\text{C}/\text{min}$ and calcinated at 550°C for 6 h to remove the organic compound from template agents.

2.2. Characterization of Samples. The power X-ray diffraction (XRD) data of catalysts were procured by a powder X-ray diffractometer Bruker D8 at room temperature using Cu anode and $K\alpha$ radiation at $\lambda = 1.54 \text{ \AA}$ in the angular scale of $5\text{--}90^\circ$ and scanning mode at 0.02° per step.

The morphology of the samples was observed by the field emission scanning electron microscope (FE-SEM) on a Hitachi S-4800 (Japan). The chemical composition of the catalysts was determined by the Hitachi system (S-4800 model) scanning electron microscope equipped with a dispersive energy X-ray (EDX) spectrometer.

Fourier transform infrared (FT-IR) experiments were carried out with a JASCO FT/IR-4600 (Japan) infrared spectroscopy. For the identification of the functional groups or organic compounds in the catalyst, the sample and the KBr powder were mixed and milled in a mortar, with the component ratio of KBr and the catalyst at 100:1.

The nitrogen adsorption-desorption isotherms measurements were performed on a Micromeritics 2020 analyzer. Firstly, the as-synthesized catalyst was degassed under vacuum at 300°C and then measured at the boiling point of nitrogen (-195°C). The total surface area was determined based on the Brunauer–Emmett–Teller (BET) theory. The external surface area, micropore surface area, and micropore volume were analyzed by using the t-plot method.

The surface acidity determination was performed on temperature-programmed desorption with ammonia (NH_3 -TPD) experiments by using the Micromeritics Auto Chem 2920 instrument. In all of the analyses, 0.1 g of the catalyst sample was placed on a quartz fixed-bed U-shaped micro-reactor and degassed in a continuous-flow nitrogen gas of $50 \text{ mL}/\text{min}$ for 1 hour at 300°C . The sample was then cooled down to 100°C and then exposed to NH_3 (helium-ammonia 10%) for 1 hour and thereafter fluxed with helium air at 100°C for 1 hour to remove any physisorbed ammonia. The progress is continued until a stable baseline is acquired. Then, the NH_3 -TPD measurements were carried out from 100°C to 550°C at a fixed heating rate of $10^\circ\text{C}/\text{min}$. Finally, the spectrum through desorption of NH_3 was recorded.

The detection of thermal amine compound decomposition of as-synthesized samples was performed by the thermal analysis method by using the thermogravimetric analysis (TGA) and differential scanning calorimeter/thermal analysis (DSC/DTA) instruments (PerkinElmer Pyris-1 TGA and DTA-7) under an airflow of 100 mL/min at a heating rate of 20°C/min from room temperature up to 800°C.

The solid state of ^{29}Si NMR (nuclear magnetic resonance) spectroscopy with MAS (magic-angle spinning) experiments were carried out on a Bruker AV-300 NMR spectrometer (Ettlingen, Germany). To be more specific, the spinning rate was 6 kHz at the magic angle while the recycling rate was 5 s. For the chemical shift, $\text{C}_6\text{H}_{15}\text{NaO}_3\text{SSi}$ sodium salt (DSS) was used as the reference material.

3. Results and Discussion

In the preparation of the SAPO-34 material, the crystallization process depends importantly on the type of organic structure-directing agents because of their interaction with inorganic species and the alkalinity, which have influence on both the nucleation and crystal growth rates.

Figure 1 shows the structure parameters and phase purity of the as-synthesized catalysts prepared by different component ratios of templates through X-ray diffraction spectroscopy. The XRD patterns of all the prepared samples match well with SAPO-34 structures, except for sample M1, which was synthesized with only TEA as a template. That means both single Mor and TEOAH and a mixture with different OSDAs can be used to synthesize SAPO-34. The template TEA was preferable to synthesize SAPO-5 molecular sieves at $2\theta = 7.5, 11.1, 14.9, 19.8, 21.1,$ and 22.5 . The template Mor, TEOAH, or mixture with TEA/Mor/TEAOH was the most appropriate template for SAPO-34 which is characterized by diffraction peaks at $2\theta = 9.6, 15.9, 19.2, 21.7,$ and 27.6 . In Figure 1, all the as-synthesized samples obtained typical diffraction peaks of the trigonal phase, respectively, for the chabazite structure of SAPO-34 as OSDAs. However, the reflection intensity and the width of peaks were different and depended on the templates. The peaks of the as-synthesized samples with a single template, especially with TEOAH, were sharp and strong, indicating its better crystallinity and phase purity compared to those of the mixed template-prepared samples. The higher intensity and broader width of peaks from the sample prepared with Mor suggest the larger crystallite size of this sample. The least intense reflection of sample M8 indicates a loss of crystallinity and the decrease of crystal size due to the incorporation of Mor with TEOAH and TEA.

Figure 2 illustrates the FE-SEM photographs of synthesized samples prepared by different components of template agents. FE-SEM images clearly show different morphologies and crystal sizes of these samples (as seen in Figure S1, supplementary data). SAPO-5 crystals were obtained when using TEA as a template (M1 sample) which had hexagonal and plate-like morphology, a variation of the particle size from 10–20 μm . Using Mor, TEOAH could observe SAPO-34 which had cube-like rhombohedra morphology with different

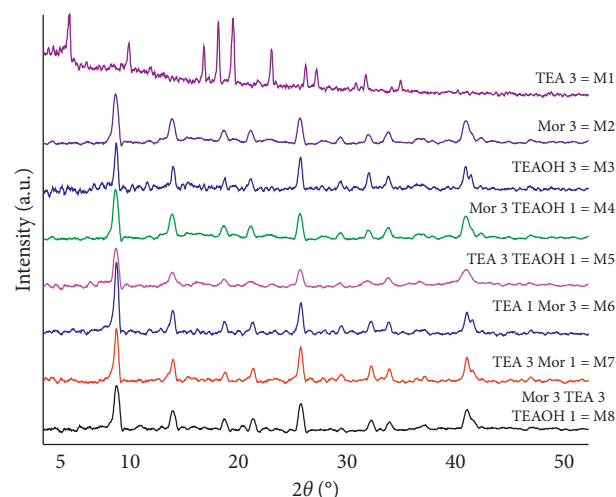


FIGURE 1: X-ray powder diffraction pattern of the as-synthesized sample.

crystal sizes. M2 and M3 samples obtained perfect crystallization and could be very similar to natural chabazite with, respectively, crystal size varying from 20–45 μm and from 3–8 μm as well. These results are in agreement with their crystallinity and phase purity from XRD.

A mixture of Mor or TEA with TEOAH has shown the cube-like morphology which is the specific characteristic of SAPO-34 with impurities. FE-SEM photographs of M4 and M5 samples exhibited that SAPO-34 crystallization by TEA/TEAOH caused the presence of more impurity and larger particles about 5 μm , whereas using Mor/TEAOH as a templating agent resulted in good material purity with mean crystallite size less than 9 μm . The use of TEA or TEOAH as a sample in the initial synthetic gel may have a favorable effect in reducing the crystal size. The presence of TEOAH compared to TEA in preparation gel caused significant particle size reduction. Besides, using Mor as a subtemplate probably supports the formation of the purity phase of SAPO-34. The results are in complete agreement with the previous publications [20, 21].

The formation of SAPO-34 morphology could be determined by using different kind of templates. M6 and M7 samples have not only same crystallinity which can be seen on XRD pattern but also similar crystal shape of cube-like agglomerating to sphere. This means that TEA and Mor can cause the agglomeration of cubic particles to form a bigger sphere-like particle. The extent of the agglomeration depends on the ratio between templates. The morphology of M6 and M7 suggests that increasing the amount of TEA in the original gel results in the aggregation of cubic crystal into spherical particles. Moreover, combinations of TEA and the other templates lead to the formation of impurity phases [22]. TEOAH template seems to be stronger than morpholine in competition with TEA and directing structure. While the particles synthesized with the mixture of TEOAH and TEA (M5 sample) only contain fewer impurities on the surface but not agglomerated, the crystals of M6 with cube-like morphology appear in competition with the cubic crystals of SAPO-34 including some impurities from the AFI

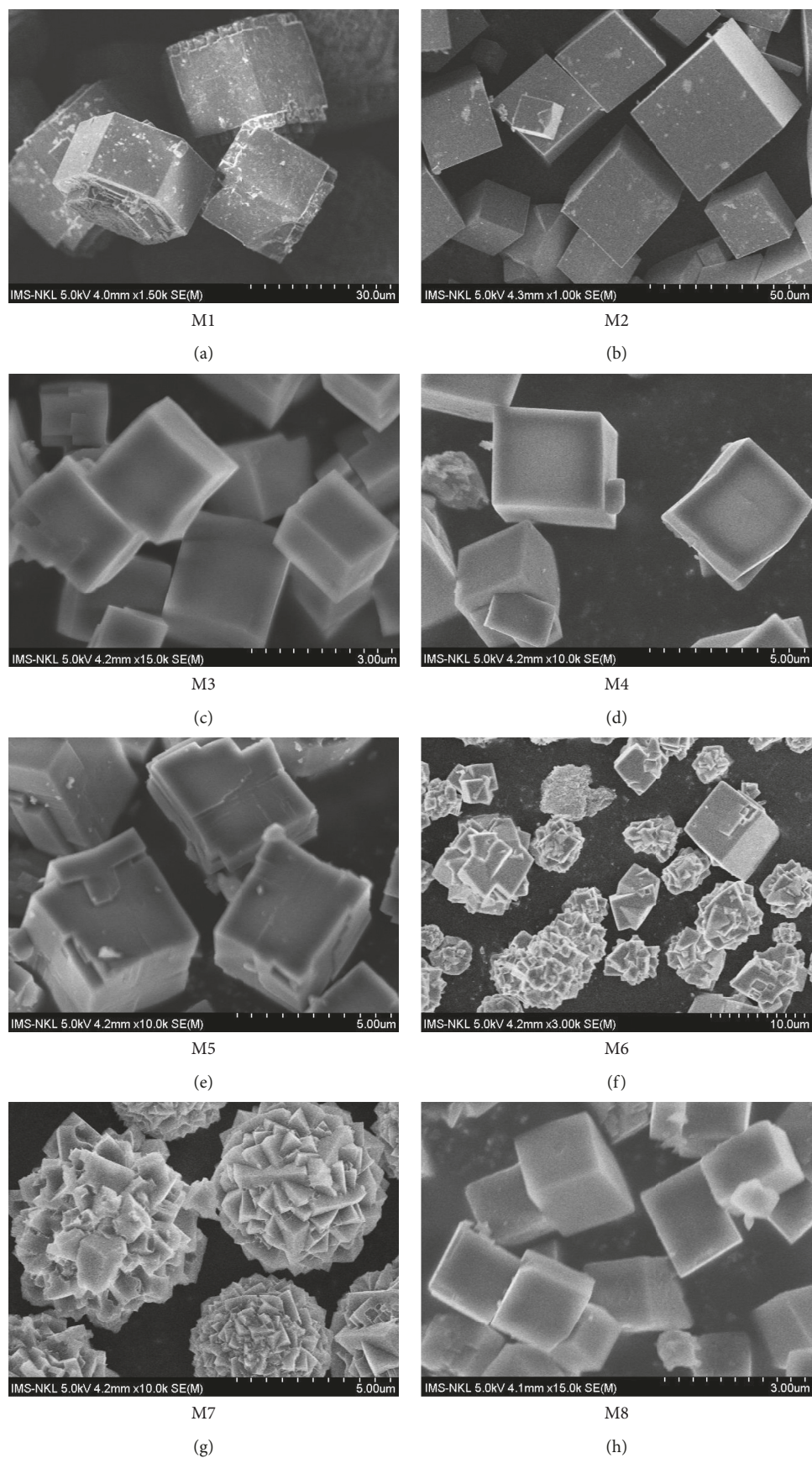


FIGURE 2: Field emission scanning electron microscope images of as-synthesized samples. (a) M1. (b) M2. (c) M3. (d) M4. (e) M5. (f) M6. (g) M7. (h) M8.

structure. Sample M7 synthesized with a higher amount of TEA than that of Mor has a dominant spherical morphology. In the formation of SAPO-34 catalysts, with the combination of TEA and morpholine, the morphology evolves from spherical agglomerates consisting of micrometer-sized cubic crystals to self-assemblies of spherical nanosheets spliced by nanosquare pieces [23].

Compared to a single and binary template(s), the mixture of tri-templating provides smaller particles of SAPO-34 below $3\ \mu\text{m}$. Three templates, including both TEOH and TEA as agents for monitoring the crystal size, result in a decrease in particle size.

Therefore, nucleation enhancement is probably liable for crystal size reduction [24]. Mixing different OSDAs leads to the reduction in particle size as well as proper arrangement in size distribution and formation of a pure SAPO-34 structure. They can be enhanced by the presence of TEOH even in little amount. This fact can be explained by the role of structure-directing substances to fill the space and impact between three different types of OSDA, including TEA, Mor, and TEOH. Furthermore, using more than one OSDA could narrow space-filling around the molecule templates, leading to a rise in the number of small crystal seeds in the nucleation process.

Table 2 shows the final elemental composition of production evaluated by the EDS analysis. The final SAPO-34 compositions concerning aluminum, silicon, and phosphorous elementals based on $(\text{Al}_x\text{P}_y\text{Si}_z)\text{O}_2$ formula were achieved by the mole percentage of each atom. Compared to all starting gel ratio $\text{Si}/(\text{Al} + \text{P} + \text{Si})$ of 0.13 (the Si content is 13%), this proportion in products was higher than 13% after crystallization. The samples synthesized by a single template showed the highest composition of Si element. The composition of Si element in samples synthesized by a single template was the highest, while that of samples prepared by mixture of OSDAs were lower. This could be attributable to alkaline environment coming from structure-directing agents and the fundamental interactions between templates and structure of SAPO materials. The influence of Si distribution by the number of framework charges are due to not only Si atoms introduced into SAPO-34 channels but also the number of OSDA molecules inserted into cages [25]. It means that if there are an additional content of silicon integrating within the structure of SAPO-34 materials, they could exist as amorphous phase in extra-framework [15, 26].

FT-IR spectroscopy is a well-known technique for identifying zeolite materials' framework structures and their acidity due to the appearance of some typical vibrations in IR spectra, which could come from the charge-balancing cations, the framework, or the relatively isolated groups [27]. Figure 3 shows the IR spectra of SAPO-34 with differing OSDA type of the samples, and the transmission bands of the as-synthesized samples are in good agreement with the published data [28–30]. In the fingerprint region ($400\text{--}1150\ \text{cm}^{-1}$), the bands collected around $500\ \text{cm}^{-1}$ and $620\ \text{cm}^{-1}$ are mainly referred to the T-O tetrahedra bending bands of SiO_4 and double-6 rings. The double-6 ring is a basic structural unit of CHA framework; hence, an appearance of this peak corresponds to the successful synthesis of SAPO-34. The vibration band at $850\ \text{cm}^{-1}$ is assigned to the symmetric stretching vibration of

TABLE 2: Elemental compositions and relative crystallinity of the products.

Sample name	Composition (mol%)		
	%Al	%P	%Si
M2	50.75	34.02	15.23
M3	49.77	34.44	15.79
M4	47.34	38.43	14.23
M5	47.16	39.23	13.61
M6	48.77	37.76	13.47
M7	49.79	37.16	13.05
M8	49.25	36.70	14.05

P-O (or Al-O), while that at $1150\ \text{cm}^{-1}$ is credited for the asymmetric stretching vibration of O-P-O. The band at $1600\ \text{cm}^{-1}$ corresponds to the vibrational bending mode of H-O-H weakly adsorbed in the SAPO-34 channels and assigned to CH_3 bending vibrational frequencies of the template molecule [31, 32]. The asymmetric stretching vibration of physically adsorbed CO_2 from the environment shows weak absorbance at $2360\ \text{cm}^{-1}$ [27, 28]. All spectra of as-synthesized samples show a broad adsorption band between $3400\ \text{cm}^{-1}$ and $3600\ \text{cm}^{-1}$, which could be allocated to the hydroxyl groups from the Si-OH-Al bond. This hydroxyl bonding evidences that the production of Brønsted acidity of SAPO-34 improves [28]. The intensity of this peak was almost similar for samples M3, M4, M5, and M8, except for M6 sample, which is lower. It could be assumed that the OH peak in FT-IR spectra of M6 sample is assigned for the formation of hydroxyl groups in the defect structure.

The nitrogen adsorption-desorption isotherms of the as-synthesized SAPO-34 samples are displayed in Figure 4, and Table 3 shows the crystal size and surface area of these samples. As seen in Figure 4, M3, M4, M5, and M8 samples displayed the curve at low relative pressures which referred to type I isotherm microporous solids. And, absorption near the saturation pressure in the isotherm lines of the as-synthesized samples can be detected due to the intercrystalline porosity, which is common in the nanostructures and microporosity of SAPO-34 [33]. As illustrated in this table, the average sizes of these samples vary from $3\ \mu\text{m}$ to $38\ \mu\text{m}$ depending on the type of templates. It is significant that the surface area of SAPO-5 material was smaller than that of the SAPO-34 molecular sieve. The surface area of pure SAPO-34 reached up to $650\ \text{m}^2/\text{g}$ in several previous reports [34–36]. Our prepared SAPO-34 samples also have a high surface area in the range from $440\ \text{m}^2/\text{g}$ to $725\ \text{m}^2/\text{g}$ depending on the type of templates. The highest surface area belonged to the sample prepared by using TEA/TEAOH as OSDAs, which is even higher than that of pure reported SAPO-34. The differences in the surface area are attributable to specific changes in channel dimensions and crystal network caused by each OSDAs.

NH_3 -TPD descriptions exhibited two desorption profiles of ammonia peaks corresponding to the weak and strong acid sites of as-synthesized SAPO-34 materials (Figure 5). The desorption of NH_3 molecules on weak acidic centers, which are mostly Lewis acid sites and/or the Brønsted acid sites produced by either P-OH hydroxyl groups not

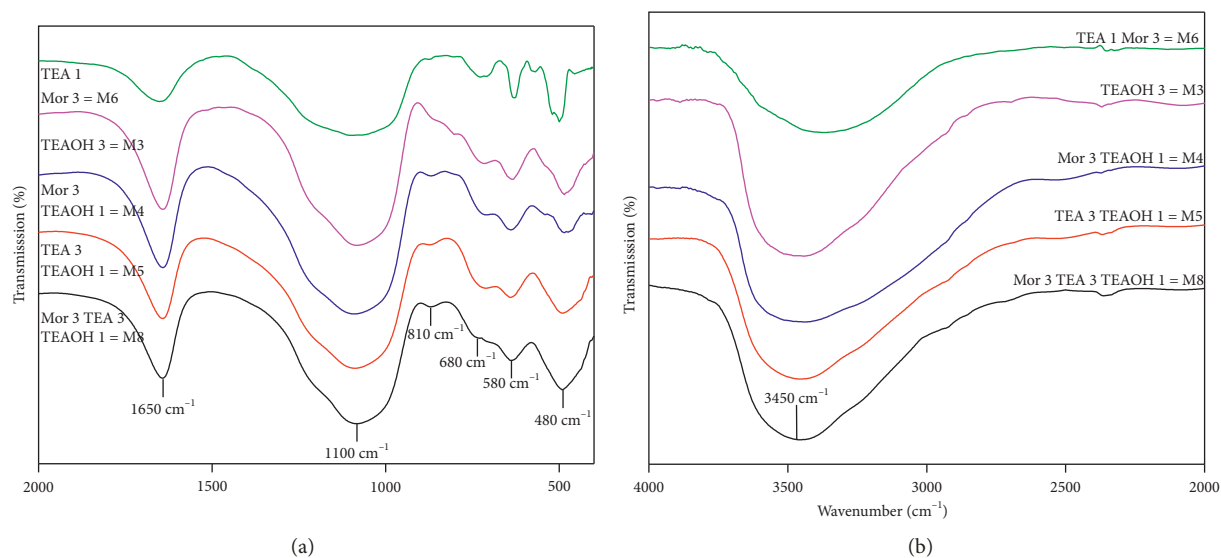


FIGURE 3: FT-IR spectra of as-synthesized samples with a range of wavelengths: (a) 2000–400 cm^{-1} ; (b) 4000–2000 cm^{-1} .

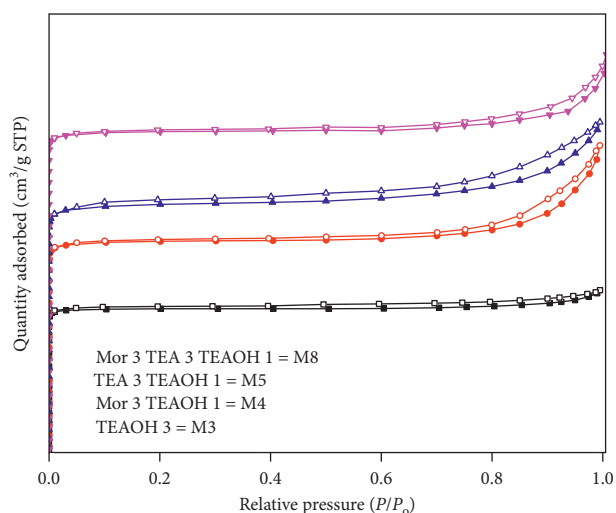


FIGURE 4: N_2 adsorption (filled symbols) and desorption isotherms (open symbols) of as-synthesized samples.

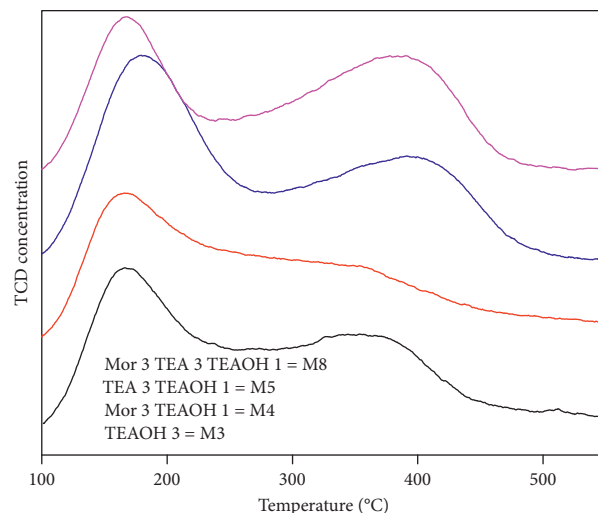


FIGURE 5: NH_3 -TPD profiles of as-synthesized samples.

TABLE 3: Physicochemical properties of synthesized samples.

Sample Name	Average Size (μm) ^a	BET Surface (m^2/g) ^b	Type of SAPO sample
M1	16	210	SAPO-5
M2	38	480	
M3	5	707	
M4	5	725	
M5	9	683	SAPO-34
M6	10	440	
M7	12	466	
M8	3	697	

^aDetermined by the FE-SEM image; ^bcalculated from N_2 adsorption data.

sufficiently linked to the $[\text{AlO}_4]$ tetrahedra or Al-OH and Si-OH groups or other zeolitic defects, causes the appearance of the first peak at a low temperature of 150–250°F [37].

The desorption peak shown at a higher temperature of 350–450°C is ascribed to the stronger acid sites, formed by the substitution of P by Si atoms in the framework of the SAPO-34. These sites are related to Si-OH-Al hydroxyl groups as strong Brønsted acid sites, which should be operated for MTO or deNO_x reaction [37, 38].

The amount of NH_3 desorption of four samples is different, which depends on the amount of Si contents. The M3 sample with the highest Si content has the highest Brønsted acid sites since these sites (Si-OH-Al) are generated by the proton produced by the template(s) for balancing the negative charges which originated from the incorporation of Si into the neutral AlPOs framework. The origin of the formation of the acid centers of SAPO-34 molecular sieves is consistent with the previous report [39], in which acid sites were produced by the incorporation of Si into the aluminophosphate channel. Although Si content of M8 was lower

than that of the M4 sample (Table 2), the M8 sample exhibited higher total acid sites due to a higher concentration of hydroxyl groups, indicating that the formation of Si islands in M4 samples might decrease its acid content. Moreover, the combination of TEA/Mor and TEOAH benefits for the Si incorporation into the SAPO-34 framework, leading to an increase in strong acid amounts of the M8 sample. There is an agreement between the ammoniac adsorption-desorption curve with the FT-IR spectrum of the samples in terms of band region of the OH vibration. The replacement of Si for other atoms (Si and P) in the AlPO framework plays an essential role in acid site production [39].

Figure 6 depicts the TG/DTA curves of the prepared samples under different templating agents burning in the air. Three weight losses (I, II, and III) in the range of 25–800°C are observed in the TG analysis. The first weight loss (I) occurring from 25 to 200°C is assigned to the desorption progress of physically adsorbed water from the as-synthesized samples. A strongly exothermic process arising between 200°C and 450°C caused the second weight loss (II) which represented combustion decomposition of the templates. The third weight loss (III) with an exothermic process at a temperature greater than 450°C is likely due to the removal of the residual templating agents in the channel molecular sieve of SAPO-34 [40]. The TGA results show that there was a competition among the decomposition of templates at temperatures higher than 500°C. Three absorption peaks were observed in all differently templating samples. Water decomposition occurred at a low temperature (70°C) with a weak signal, demonstrating the modest capacity in the molecule and the weak interactions between water molecules and the molecular sieve. The second absorption peak represents the intensity of the removal of the templates. In particular, sample M8, obtained with the tri-template TEA/Mor/TEAOH, had a sharp and strong removal peak while double-template with several structure-directing agents, namely, TEA/TEAOH and Mor/TEAOH, had different elevation peaks at this point. The results show that the interaction between the TEOAH agent and the framework of SAPO-34 was the most powerful.

The TGA results of M4, M5, and M8 samples are shown in Table 4. According to the molecular weight loss research, the reduced weight of water was quite small, and the primary reason for weight loss was caused by the removal of the templates. Besides, the weight loss of the different samples was distinct. The moles of templates located in the molecular sieves prepared with the different templates were directly calculated by using the thermogravimetric analysis results. The average number of templating agents per cage in the sample molecular sieve was 1.48, 1.25, and 1.36 with M4, M5, and M8, respectively. For sample M5, which used the dual template of Mor and TEOAH, more favorably entered the cage structure due to the presence of negative charges of morpholine in the SAPO-34 framework. Marchese et al. [41] reported that on average, 1.5 molecules of morpholine present within the chabazite channels of SAPO-34. Meanwhile, the molecular volume of cyclic morpholine is significantly lower than that of TEA, which contains three ethyl

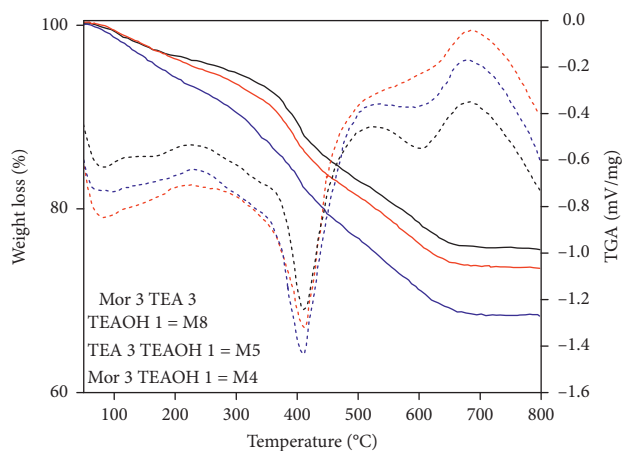


FIGURE 6: The TG (straight line) and DTA (dot line) curves for as-synthesized samples with different templates.

TABLE 4: The TGA results for as-synthesized samples.

Sample	Weight loss (%)		A mole of templates per unit cell
	200°C	200–700°C	
M4	5.62	25.815	1.48
M5	3.64	19.91	1.25
M8	4.33	22.62	1.36

branches [42]. In the case of Mor/TEA/TEAOH mixture, because the material framework and TEOAH templating agent had the most potent force and easily linked with the aluminum atoms, silicon atoms, and phosphorus atoms at the precursor process of crystallization, adding TEOAH enhances the medium number of OSDAs in the material cage.

The silicon situation in the framework of SAPO-34 was analyzed by ^{29}Si MAS NMR. In Figure 7, several peaks exhibited in the spectrum of samples M4, M5, and M8 are shown. According to [43], the strong peak at $\delta = -90.3$ ppm should be due to Si(4Al) species; the small peaks formants shown at $\delta = -93.2$ ppm and -98.9 ppm were attributed to Si(3Al) and Si(2Al) species, respectively, and the peak appeared at $\delta = -108.9$ ppm resulting from the Si(0Al) environment. The presence of different silicon situations is suitable for the silicone replacement theory [44], in which SM2 (the substitution of P atoms by Si atoms alone) and SM3 (a pair Si atoms substituted by a pair of Al + P). A silicon-island region surrounded by the SM2 method was created, and the center was substituted by SM3. Compared to the dual template of Mor/TEAOH and TEA/TEAOH, increasing the relative contents of Si(3Al), Si(2Al), Si(1Al), and Si(0Al) structures is the result of using a combination of three templates. Based on Table 5 which shows the distribution of the acid properties of as-synthesized catalysts with different template agents, it can be concluded that the creation of silicon islands enhances the acidity of the silicoaluminophosphate zeolite SAPO-34 synonymous with the acid strength of the molecular sieves SAPO-34 which gradually grew up by increasing the size of the silicon islands [45]. The strongest acid sites were located on the borders of the silicon islands.

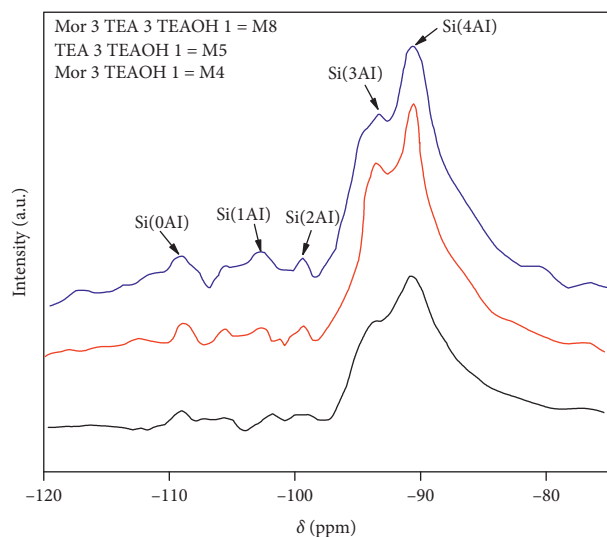


FIGURE 7: ^{29}Si MAS NMR spectrum of M4, M5, and M8 samples.

TABLE 5: Acid properties of the as-synthesized catalyst.

Samples	Peak (mmol/g)		Total (mmol/g)
	Peak 1	Peak 2	
M3	1.34	0.91	2.25
M4	1.15	0.90	2.05
M5	0.99	0.96	1.95
M8	1.25	1.19	2.34

4. Conclusions

By using the hydrothermal method, SAPO-34 molecular sieves were prepared with various combinations of Mor/TEA/TEAOH as organic structure-directing agents showed different physicochemical characteristics. The single-template TEA was preferable to synthesize SAPO-5 molecular sieves, while TEOH and Mor favored SAPO-34 formation. The morphology of all samples was the same to the uniform cube-shaped particles of the standard SAPO-34 material, except as-synthesized samples using Mor/TEA as OSDAs, which additionally includes sphere-shaped particles consisting of cubic agglomerates. Combination of tri-templates in the initial gel led to decrease in the particle size of the samples. The morphology of spherical particles can be created by a coherence of nanosized crystals, and the crystal size will be reduced to submicrometer size. The catalyst with molar ratios of Mor:TEA:TEAOH = 3:3:1 increased the surface area, decreased the crystal size of the samples to nanosize, improved the crystallinity, and enhanced the acid content. The preparation of SAPO-34 catalysts with mixture template synthesis was proven to be effective and has economic advantages.

Data Availability

The X-ray diffraction, field emission scanning electron microscope, Fourier-transform infrared method, N_2 adsorption-desorption, magic-angle spinning nuclear magnetic resonance,

thermogravimetric analysis, differential scanning calorimeter/thermal analysis, and temperature-programmed desorption of ammonia data used to support the findings of this study are included within the article. The field emission scanning electron microscope data used to support the findings of this study are included within the supplementary information file for more details with images of increased resolution.

Conflicts of Interest

The authors declare that they have no conflicts of interest.

Acknowledgments

This work was supported by the RoHan Project funded by the German Academic Exchange Service (DAAD, no. 57315854) and the Federal Ministry for Economic Cooperation and Development (BMZ) inside the framework SDG Bilateral Graduate School Programme. And, this research was also funded by the Vietnam National Foundation for Science and Technology Development (NAFOSTED) under grant no. 104.05-2018.306.

Supplementary Materials

Supplementary Figure S1. field emission scanning electron microscope images of as-synthesized SAPO-34 from different organic structure-directing agents. FE-SEM images clearly show different morphologies and crystal sizes of these samples on a larger scale. (*Supplementary Materials*)

References

- [1] B. M. Lok, C. A. Messina, R. L. Patton, R. T. Gajek, T. R. Cannan, and E. M. Flanigen, "Silicoaluminophosphate molecular sieves: another new class of microporous crystalline inorganic solids," *Journal of the American Chemical Society*, vol. 106, no. 20, pp. 6092-6093, 1984.
- [2] M. Zokaie, U. Olsbye, K. P. Lillerud, and O. Swang, "A computational study on heteroatom distribution in zeotype materials," *Microporous and Mesoporous Materials*, vol. 158, pp. 175-179, 2012.
- [3] Z. Yan, B. Chen, and Y. Huang, "A solid-state NMR study of the formation of molecular sieve SAPO-34," *Solid State Nuclear Magnetic Resonance*, vol. 35, no. 2, pp. 49-60, 2009.
- [4] A. T. Aguayo, A. G. Gayubo, R. Vivanco, M. Olazar, and J. Bilbao, "Role of acidity and microporous structure in alternative catalysts for the transformation of methanol into olefins," *Applied Catalysis A: General*, vol. 283, no. 1-2, pp. 197-207, 2005.
- [5] G. Sastre, D. W. Lewis, and C. R. A. Catlow, "Modeling of silicon substitution in SAPO-5 and SAPO-34 molecular sieves," *Journal of Physical Chemistry B*, vol. 101, no. 27, pp. 5249-5262, 1997.
- [6] G. Liu, P. Tian, J. Li, D. Zhang, F. Zhou, and Z. Liu, "Synthesis, characterization and catalytic properties of SAPO-34 synthesized using diethylamine as a template," *Microporous and Mesoporous Materials*, vol. 111, no. 1-3, pp. 143-149, 2008.
- [7] Ø. B. Vistad, D. E. Akporiaye, and K. P. Lillerud, "Identification of a key precursor phase for synthesis of SAPO-34 and kinetics of formation investigated by in situ X-ray diffraction,"

- Journal of Physical Chemistry B*, vol. 105, no. 50, pp. 12437–12447, 2001.
- [8] Y. Chen, H. Zhou, J. Zhu et al., “Direct synthesis of a fluidizable SAPO-34 catalyst for a fluidized dimethyl ether-to-olefins process,” *Catalysis Letters*, vol. 124, no. 3-4, pp. 297–303, 2008.
- [9] M. Hunger, M. Seiler, and A. Buchholz, “*In situ* MAS NMR spectroscopic investigation of the conversion of methanol to olefins on silicoaluminophosphates SAPO-34 and SAPO-18 under continuous flow conditions,” *Catalysis Letters*, vol. 74, pp. 61–68, 2001.
- [10] I. M. Dahl, H. Mostad, D. Akporiaye, and R. Wendelbo, “Structural and chemical influences on the MTO reaction: a comparison of chabazite and SAPO-34 as MTO catalysts,” *Microporous and Mesoporous Materials*, vol. 29, no. 1-2, pp. 185–190, 1999.
- [11] Y.-J. Lee, S.-C. Baek, and K.-W. Jun, “Methanol conversion on SAPO-34 catalysts prepared by mixed template method,” *Applied Catalysis A: General*, vol. 329, pp. 130–136, 2007.
- [12] H.-J. Chae, I.-J. Park, Y.-H. Song et al., “Physicochemical characteristics of SAPO-34 molecular sieves synthesized with mixed templates as MTO catalysts,” *Journal of Nanoscience and Nanotechnology*, vol. 10, no. 1, pp. 195–202, 2010.
- [13] Y. Hirota, K. Murata, M. Miyamoto, Y. Egashira, and N. Nishiyama, “Light olefins synthesis from methanol and dimethylether over SAPO-34 nanocrystals,” *Catalysis Letters*, vol. 140, no. 1-2, pp. 22–26, 2010.
- [14] S. Askari, R. Halladj, and M. Sohrabi, “Methanol conversion to light olefins over sonochemically prepared SAPO-34 nanocatalyst,” *Microporous and Mesoporous Materials*, vol. 163, pp. 334–342, 2012.
- [15] A. M. Prakash and S. Unnikrishnan, “Synthesis of SAPO-34: high silicon incorporation in the presence of morpholine as template,” *Journal of the Chemical Society, Faraday Transactions*, vol. 90, no. 15, pp. 2291–2296, 1994.
- [16] L. Ye, F. Cao, W. Ying, D. Fang, and Q. Sun, “Methanol conversion on SAPO-34 catalysts synthesized by tri-templates,” *MRS Proceedings*, vol. 1279, pp. 22–30, 2010.
- [17] R. B. Rostami, M. Ghavipour, R. M. Behbahani, and A. Aghajafari, “Improvement of SAPO-34 performance in MTO reaction by utilizing mixed-template catalyst synthesis method,” *Journal of Natural Gas Science and Engineering*, vol. 20, pp. 312–318, 2014.
- [18] M. Sedighi, H. Bahrami, and J. Towfighi Darian, “Thorough investigation of varying template combinations on SAPO-34 synthesis, catalytic activity and stability in the methanol conversion to light olefin,” *RSC Advances*, vol. 4, no. 91, pp. 49762–49769, 2014.
- [19] J. Ma, Z. Si, X. Wu, D. Weng, and Y. Ma, “Optimizing the crystallinity and acidity of H-SAPO-34 by fluoride for synthesizing Cu/SAPO-34 NH₃-SCR catalyst,” *Journal of Environmental Sciences*, vol. 41, pp. 244–251, 2016.
- [20] N. Nishiyama, M. Kawaguchi, Y. Hirota, D. Van Vu, Y. Egashira, and K. Ueyama, “Size control of SAPO-34 crystals and their catalyst lifetime in the methanol-to-olefin reaction,” *Applied Catalysis A: General*, vol. 362, no. 1-2, pp. 193–199, 2009.
- [21] G. Liu, P. Tian, and Z. Liu, “Synthesis of SAPO-34 molecular sieves templated with diethylamine and comparison with other templates,” *Chinese Journal of Catalysis*, vol. 33, pp. 174–182, 2012.
- [22] B. Valizadeh, S. Askari, R. Halladj, and A. Haghmoradi, “Effect of synthesis conditions on selective formation of SAPO-5 and SAPO-34,” *Synthesis and Reactivity in Inorganic, Metal-Organic, and Nano-Metal Chemistry*, vol. 44, no. 1, pp. 79–83, 2014.
- [23] J. Zhong, J. Han, Y. Wei et al., “Recent advances of the nano-hierarchical SAPO-34 in the methanol-to-olefin (MTO) reaction and other applications,” *Catalysis Science & Technology*, vol. 7, no. 21, pp. 4905–4923, 2017.
- [24] B. Topuz, E. E. Oral, and H. Kalıpçılar, “Low temperature synthesis of SAPO-34 in a recirculating-flow system,” *Journal of Porous Materials*, vol. 20, no. 6, pp. 1491–1500, 2013.
- [25] L. Ye, F. Cao, W. Ying, D. Fang, and Q. Sun, “Effect of different TEAOH/DEA combinations on SAPO-34’s synthesis and catalytic performance,” *Journal of Porous Materials*, vol. 18, no. 2, pp. 225–232, 2011.
- [26] M. Salmasi, S. Fatemi, and A. Taheri Najafabadi, “Improvement of light olefins selectivity and catalyst lifetime in MTO reaction; using Ni and Mg-modified SAPO-34 synthesized by combination of two templates,” *Journal of Industrial and Engineering Chemistry*, vol. 17, no. 4, pp. 755–761, 2011.
- [27] S. M. Auerbach, K. A. Carrado, and P. K. Dutta, *Handbook of Zeolites Science and Technology*, Marcel Dekker, Inc., New York, NY, USA, 2003.
- [28] E. Aghaei and M. Haghghi, “High temperature synthesis of nanostructured Ce-SAPO-34 catalyst used in conversion of methanol to light olefins: effect of temperature on physicochemical properties and catalytic performance,” *Journal of Porous Materials*, vol. 22, no. 1, pp. 187–200, 2015.
- [29] S. Tian, S. Ji, D. Lü, B. Bai, and Q. Sun, “Preparation of modified Ce-SAPO-34 catalysts and their catalytic performances of methanol to olefins,” *Journal of Energy Chemistry*, vol. 22, no. 4, pp. 605–609, 2013.
- [30] N. Rajić, V. Kaučič, and D. Stojaković, “Synthesis and characterization of the CoSAPO-14 and CoSAPO-34,” *Zeolites*, vol. 10, no. 3, pp. 169–173, 1990.
- [31] P. R. H. P. Rao and M. Matsukata, “Dry-gel conversion technique for synthesis of zeolite BEA,” *Chemical Communications*, no. 12, pp. 1441–1442, 1996.
- [32] Z. Li, J. Martínez-Triguero, P. Concepción, J. Yu, and A. Corma, “Methanol to olefins: activity and stability of nanosized SAPO-34 molecular sieves and control of selectivity by silicon distribution,” *Physical Chemistry Chemical Physics*, vol. 15, no. 35, pp. 14670–14680, 2013.
- [33] Q. Sun, Y. Ma, N. Wang et al., “High performance nanosheet-like silicoaluminophosphate molecular sieves: synthesis, 3D EDT structural analysis and MTO catalytic studies,” *Journal of Materials Chemistry A*, vol. 2, no. 42, pp. 17828–17839, 2014.
- [34] J. W. Yoon, S. H. Jhung, Y. H. Kim, S. E. Park, and J. S. Changa, “Selective crystallization of SAPO-5 and SAPO-34 molecular sieves in alkaline condition: effect of heating method,” *Bulletin of the Korean Chemical Society*, vol. 26, no. 4, pp. 558–562, 2005.
- [35] S. Masoumi, J. Towfighi, A. Mohamadizadeh, Z. Kooshki, and K. Rahimi, “Tri-templates synthesis of SAPO-34 and its performance in MTO reaction by statistical design of experiments,” *Applied Catalysis A: General*, vol. 493, pp. 103–111, 2015.
- [36] C. Kong, J. Zhu, S. Liu, and Y. Wang, “SAPO-34 with a low acidity outer layer by epitaxial growth and its improved MTO performance,” *RSC Advances*, vol. 7, no. 63, pp. 39889–39898, 2017.
- [37] B. Parlitz, E. Schreier, H. L. Zubowa et al., “Isomerization of *n*-heptane over Pd-loaded silico-alumino-phosphate molecular sieves,” *Journal of Catalysis*, vol. 155, no. 1, pp. 1–11, 1995.
- [38] E. Dumitriu, A. Azzouz, V. Hulea, D. Lutic, and H. Kessler, “Synthesis, characterization and catalytic activity of SAPO-34

- obtained with piperidine as templating agent," *Microporous Materials*, vol. 10, no. 1–3, pp. 1–12, 1997.
- [39] S. Svelle, S. Aravinthan, M. Bjorgen et al., "The methyl halide to hydrocarbon reaction over H-SAPO-34," *Journal of Catalysis*, vol. 241, no. 2, pp. 243–254, 2006.
- [40] M. Luo, H. Zang, B. Hu, B. Wang, and G. Mao, "Evolution of confined species and their effects on catalyst deactivation and olefin selectivity in SAPO-34 catalyzed MTO process," *RSC Advances*, vol. 6, no. 21, pp. 17651–17658, 2016.
- [41] L. Marchese, A. Frache, E. Gianotti, G. Martra, M. Causà, and S. Coluccia, "ALPO-34 and SAPO-34 synthesized by using morpholine as templating agent. FTIR and FT-Raman studies of the host-guest and guest-guest interactions within the zeolitic framework," *Microporous and Mesoporous Materials*, vol. 30, no. 1, pp. 145–153, 1999.
- [42] Y. Zhang, Z. Ren, Y. Wang, Y. Deng, and J. Li, "Synthesis of small-sized SAPO-34 crystals with varying template combinations for the conversion of methanol to olefins," *Catalysts*, vol. 8, no. 12, p. 570, 2018.
- [43] J. Tan, Z. Liu, X. Bao et al., "Crystallization and Si incorporation mechanisms of SAPO-34," *Microporous and Mesoporous Materials*, vol. 53, no. 1–3, pp. 97–108, 2002.
- [44] R. Vomscheid, M. Briend, M. J. Peltre, P. P. Man, and D. Barthomeuf, "The role of the template in directing the Si distribution in SAPO zeolites," *Journal of Physical Chemistry*, vol. 98, no. 38, pp. 9614–9618, 1994.
- [45] G. Sastre, D. W. Lewis, and C. R. A. Catlow, "Modeling of silicon substitution in SAPO-5 and SAPO-34 molecular sieves," *Journal of Physical Chemistry B*, vol. 101, no. 27, pp. 5249–5262, 1997.

Research Article

Sonochemical Synthesis and Properties of $\text{YVO}_4:\text{Eu}^{3+}$ Nanocrystals for Luminescent Security Ink Applications

Chinh Dung Trinh ^{1,2}, Phuong Thi Pham Hau,¹ Thi My Dung Dang,¹
and Chien Mau Dang ¹

¹Institute for Nanotechnology, Vietnam National University, Ho Chi Minh City, Vietnam

²The University of Science, Vietnam National University, Ho Chi Minh City, Vietnam

Correspondence should be addressed to Chien Mau Dang; dmchien@vnuhcm.edu.vn

Received 30 January 2019; Revised 1 April 2019; Accepted 18 April 2019; Published 10 July 2019

Guest Editor: Van Duong Dao

Copyright © 2019 Chinh Dung Trinh et al. This is an open access article distributed under the Creative Commons Attribution License, which permits unrestricted use, distribution, and reproduction in any medium, provided the original work is properly cited.

Solutions and redispersible powders of nanocrystalline, europium-doped YVO_4 , are prepared via a wet chemical method using the ultrasonic processor (sonochemical) and microwave and thermal stirring. From X-ray diffraction (XRD) results, $\text{YVO}_4:\text{Eu}^{3+}$ nanoparticles synthesized using sonochemical method have better crystallinity than those prepared using thermal stirring and microwave methods exhibiting the tetragonal structure known for bulk material. From field-emission scanning electron microscopy (FE-SEM) and transmission electron microscopy (TEM) results, it is found that the size of nanoparticles is around 25 nm and increasing after annealing at 900°C. From UV-Vis result, there is a peak at 270 nm corresponding to the absorption of VO_4^{3-} groups. The photoluminescence (PL) results clearly show the strongest red emission peak at the wavelength around 618 nm. The highest luminescent intensity is obtained for the sample prepared by the sonochemical method at pH = 12 and annealing temperature at 900°C for 4 h. The average lifetimes of the Eu^{3+} ions in the samples annealed at 300, 600, and 900°C for 1 h at 618 nm emission under 275 nm excitation are 0.36, 0.62, and 0.64 ms, whereas sample annealed at 900°C for 4 h has lifetime of 0.70 ms. The security ink, containing synthesized $\text{YVO}_4:\text{Eu}^{3+}$ nanoparticles, is dispersed in glycerol and other necessary solvents. The experimental security labels are printed by inkjet using the electrohydrodynamic printing technique. The resulting lines represented to the security labels are analyzed by the 3D microscope equipment and UV 20 W mercury lamp with a wavelength of ~254 nm. The seamless line of the printed security label has the value of the width at ~230 μm , thickness at ~0.68 μm , and distance between two adjacent lines at 800 μm . This result is compatible for producing security labels in small size (millimeter) in order to increase security property.

1. Introduction

The study of rare earth doped luminescence materials has been largely motivated by the prospect of original specific applications such as electroluminescent techniques, biological labels, and integrated optics [1–6].

Moreover, rare earth nanoparticles are interesting due to their marked improvement in lumen output, color rendering index, energy efficiency, and greater radiation stability [6–11].

$\text{YVO}_4:\text{Eu}^{3+}$ has large application in color television cathode ray tube displays [12] and high-pressure mercury

lamps [13] as a red phosphor. The photoluminescence quantum yield of the europium emission is as high as 70% in YVO_4 with the excitation by UV light [14]. It is also applied in biology [15–17] and specially in producing security ink. The vanadate group ($\text{V}^{5+}-\text{O}^{2-}$ charge transfer band) in $\text{YVO}_4:\text{Eu}^{3+}$ phosphor is excited by ultraviolet radiation, and this provides efficient energy transfer to Eu^{3+} [18].

$\text{YVO}_4:\text{Eu}^{3+}$ phosphor can be prepared by different methods, for example, high-temperature solid state method [19], combination method [20], microwave rapid heating method [21–23], sol-gel method [24], and hydrothermal reaction method [25]. Recent studies have shown that there

is a tremendous potential in nanoscale rare earth doped luminescence materials in abovementioned fields.

In recent years, the inkjet technique has been in research to make spare parts such as electric circuits and biosensor [26–35]. The advantage of this technique is having fewer steps in preparation and ability to print in many different bases such as conductive base, uncondutive base, solid base, and flexible base. This inkjet technique requires research in the printing process and inkjet ink. In 2012, Meruga et al. investigated security ink from the rare earth nanoparticles β - NaYF_4 -doped $\text{Yb}^{3+}/\text{Er}^{3+}$ and $\text{Yb}^{3+}/\text{Tm}^{3+}$ to print security QR code on paper and PET by Optomec direct-write aerosol jetting [36]. According to the work of Gupta et al. in 2010, they evaluated the security ink made of rare earth nanoparticle Y_2O_3 doped Eu^{3+} ($\text{Y}_2\text{O}_3:\text{Eu}^{3+}$), and the samples in this research were printed by screen printing techniques [37]. The purpose of our security inkjet technique is making products with high security. With inkjet technology and this security ink, we study printing the labels with the demand of high security on money, visa, certificate, and military products. The high security characteristic of the product is determined by two factors—the first is small size and delicacy of the printed label (related to the printing technique) and second is the strong emissivity of printed label under UV (related to optical emission of $\text{YVO}_4:\text{Eu}^{3+}$ nanoparticles in the ink). The emissivity of $\text{YVO}_4:\text{Eu}^{3+}$ nanoparticles is affected by many factors such as particle size and crystallinity, doping level of Eu^{3+} ions into YVO_4 , etc. All these parameters are affected by the production method applied for nanoparticles [38–42].

In this study, we use the wet chemical method to synthesize $\text{YVO}_4:\text{Eu}^{3+}$. Our purpose is to apply $\text{YVO}_4:\text{Eu}^{3+}$ as phosphor in security ink. Hence, performing research in producing the $\text{YVO}_4:\text{Eu}^{3+}$ nanoparticles with strong luminescent intensity is crucial along with the research in inkjet process. Regarding the references on synthesis of $\text{YVO}_4:\text{Eu}^{3+}$ nanoparticles by wet-chemical method [12–21, 38–42], we use three different routes to synthesize $\text{YVO}_4:\text{Eu}^{3+}$ nanoparticles, which are thermal stirring, microwave methods, and ultrasonic methods, in order to compare the luminescent level of the nanoparticles. According to the published results, the best doping level of Eu^{3+} in YVO_4 for luminescence properties is 5 mol% [38, 43–55]. We use $\text{YVO}_4:\text{Eu}^{3+}$ nanoparticles to produce ink for PS JET 300 V inkjet printer. This printer is operated by the electrohydrodynamic (EHD) inkjet technique. The advantage of EHD inkjet technique is the ability to print labels in small size (in micrometers) on various material substrates.

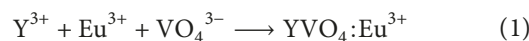
2. Materials and Methods

2.1. Materials. $\text{Y}(\text{NO}_3)_3 \cdot 6\text{H}_2\text{O}$ (99.8%, Aldrich), $\text{Eu}(\text{NO}_3)_3 \cdot 5\text{H}_2\text{O}$ (99.9%, Aldrich), and Na_3VO_4 (99.98%, Aldrich) are used as starting materials. NaOH (99%, Merck) is used to control pH.

$\text{C}_3\text{H}_8\text{O}_3$ (99.5%, Merck), $\text{C}_2\text{H}_6\text{O}$ (99.5%), $\text{C}_4\text{H}_8\text{O}_2$ (99.8%, Merck), and $\text{C}_2\text{H}_6\text{O}_2$ (99.5%, Merck) are solvents and binding agents used in the synthesis of security ink.

2.2. Synthesis of $\text{YVO}_4:\text{Eu}^{3+}$ Nanoparticles and Security Ink. $\text{YVO}_4:\text{Eu}^{3+}$ nanoparticles are synthesized by the wet chemical method. Dissolving 0.88 g of $\text{Y}(\text{NO}_3)_3 \cdot 6\text{H}_2\text{O}$ (2.3 mmol) and 0.05 g of $\text{Eu}(\text{NO}_3)_3 \cdot 5\text{H}_2\text{O}$ (0.12 mmol) into 15 ml DI water (Eu^{3+} doping molar concentration is 5%) in 15 min leads to the formation of solution A, whereas 0.44 g of Na_3VO_4 (2.4 mmol) in 15 ml DI water is solution B. Mixing solution A with solution B dropwise leads to white precipitation in the mixture. The pH value of mixture is adjusted to 12 by using 5 M of NaOH .

This mixture is heat-treated by three different ways for comparison, which are thermal stirring at $\sim 150^\circ\text{C}$ in 1 h, microwave in 15 min by Mars 6 (CEM Corporation) [21–23], and sonochemical by ultrasonic liquid processors VCX 750 (Sonics and Materials) with electrical frequency 20 kHz in 15 min. Synthesized $\text{YVO}_4:\text{Eu}^{3+}$ nanoparticles are dried at 60°C and annealed at 300, 600, and 900°C in an oven (Carbolite Gero, Max. temp. up to 1100°C) for 1 h. The formation of $\text{YVO}_4:\text{Eu}^{3+}$ nanoparticles follows equation (1):



The security ink using $\text{YVO}_4:\text{Eu}^{3+}$ nanoparticles is synthesized by mixing $\text{YVO}_4:\text{Eu}^{3+}$ nanoparticles in such solvents as glycerin, ethanol, ethyl acetate, and ethylene glycol at appropriate ratios.

2.3. Security Printing. The test patterns are printed onto glass substrate by a commercial printer (PS JET 300 V). This printer is operated by the electrohydrodynamic (EHD) inkjet technique.

2.4. Characterization. The prepared $\text{YVO}_4:\text{Eu}^{3+}$ nanoparticle samples are studied by UV-Vis absorption spectroscopy by using a double-beam spectrophotometer in the wavelength range from 200 to 900 nm. Particle size is determined by transmission electron microscopy (TEM) and field emission scanning electron microscopy (FE-SEM). Samples for TEM measurements are suspended in ethanol and ultrasonically dispersed. The suspension drops are placed on a copper grid coated with carbon. The crystallite structure of $\text{YVO}_4:\text{Eu}^{3+}$ is analyzed by X-ray diffraction spectroscopy. The emission spectra are recorded at room temperature using a Hitachi F-4500 spectrophotometer. The decay of luminescence is measured by a Horiba Deltaflex™ with 275 nm SpectraLED excitation source.

The security ink viscosity is analyzed by an m-VROC™ VISCOMETER. The samples after printed by inkjet printer are synthesized by a 3D microscope (Sensofar Metrology) and UV 20 W mercury lamps (Germicidal lamp, Sankyo Denki Co.) having a wavelength of around 254 nm.

3. Results and Discussion

3.1. Effect of Different Synthesis Methods on the Formation of $\text{YVO}_4:\text{Eu}^{3+}$ Nanoparticles. The wet chemical method is applied in all experiments; however, there is difference in the

heating method during synthesis process as mentioned above. Three synthesized samples correspond to three different methods with the same chemical components and ratios. The doping concentration of Eu^{3+} is 5 mol% in YVO_4 host ($\text{Y}_{0.95}\text{Eu}_{0.05}\text{VO}_4$), which had been optimized previously by Georgescu et al. [43], Kumar et al. [44], and He et al. [45]. Each heating method has different effect to YVO_4 particles crystallinity and doped ability of ion Eu^{3+} to host matrix. The crystallization and doped ability have crucial effect to luminescent intensity of $\text{YVO}_4:\text{Eu}^{3+}$ nanoparticles. The XRD patterns recorded for the $\text{YVO}_4:\text{Eu}^{3+}$ samples are shown in Figure 1. All diffraction peaks were successfully attributed to known tetragonal phase of YVO_4 (JCPDS, No. 17-0341) [41, 42, 46].

Among three preparation methods, the highest peak intensity is observed for the sample fabricated by the sonochemical treatment, that reveals the best crystallinity level of $\text{YVO}_4:\text{Eu}^{3+}$ nanoparticles in this sample. According to theory and references of sound waves, the constitution of ultrasound region happens with sound wave frequency above 20 kHz. The ultrasound region can be divided into two parts: one where the cavitation phenomenon takes place (20–100 kHz), called power ultrasound, and the other where no cavitation occurs (5–10 MHz), used for diagnostics. Sonochemical effects depend on the cavitation phenomenon. According to the “hot spot” theory, each cavitation bubble behaves like a microreactor, which, in aqueous systems, at an ultrasonic frequency of 20 kHz each cavitation bubble collapse acts as a localized “hotspot” generating temperatures of about 4000 K and pressures in excess of 1000 atmospheres [47–51].

A series of radicals, such as H^* and OH^* , are formed, by the irradiation process of ultrasound to water, at the gas-phase interface of the cavitation bubbles, and the responsibility for the enhanced reactivity to a lesser extent, in the bulk solution [51].

These factors have positive effect to the crystalline nanoparticle formation and incorporation of Eu^{3+} ions into YVO_4 lattice. These factors have effect to the luminescent intensity of $\text{YVO}_4:\text{Eu}^{3+}$ nanoparticles.

The TEM micrographs and size distribution diagrams of $\text{YVO}_4:\text{Eu}^{3+}$ nanoparticles prepared by sonochemical and thermal stirring methods are shown in Figure 2. The monodispersion state of $\text{YVO}_4:\text{Eu}^{3+}$ nanoparticles is evident. In Figure 2(a), more even size distribution is observed with maximum at ~ 25 nm. The wider and nonhomogeneous size distribution is seen in Figure 2(b). The TEM results agreed with the XRD results shown in Figure 1.

There are three major steps in the excitation-emission process of $\text{YVO}_4:\text{Eu}^{3+}$ under UV radiation. Firstly, UV radiation is absorbed by VO_4^{3-} groups. However, UV radiation can be directly absorbed by Eu^{3+} ions, and this is dependent on the wavelength. Secondly, the migration of activation energy through vanadate sublattice leads to the transferring of the excited energy to Eu^{3+} ions, and the last step is the production of strong red emission by the de-excitation process of excited Eu^{3+} ions [15, 41, 52, 56]. A proposed energy transfer mechanism demonstrating the above process is shown in Figure 3.

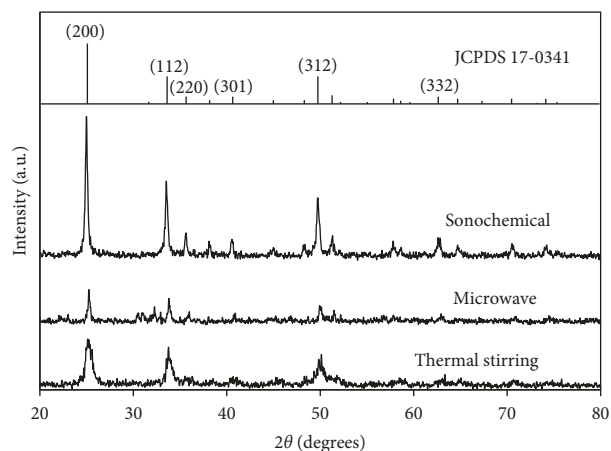


FIGURE 1: The XRD pattern of $\text{YVO}_4:\text{Eu}^{3+}$ nanoparticles synthesized with a different method.

In Figure 4 (left inset), the UV-V is spectra of $\text{YVO}_4:\text{Eu}^{3+}$ nanoparticles prepared by sonochemical and wavelength and thermal stirring methods are shown. The redispersed dry powder of $\text{YVO}_4:\text{Eu}^{3+}$ in the same amount of deionized water was stirred 2-3 min, resulting in the transparent colloid representing the absorption spectrum. There is a peak at around 270 nm in these three samples that proved the existence of absorption in the VO_4^{3-} groups [39, 41, 52, 56]. According to references, it is explained as the attribution to the charge transfer from oxygen ligands to the central vanadium atom in VO_4^{3-} group [15, 40, 41]. The UV-Vis spectra in Figure 4 (left inset) are crucial regarding to the luminescence mechanism of $\text{YVO}_4:\text{Eu}^{3+}$ nanoparticles, and it proves that there is an energy absorption and transfer from VO_4^{3-} to Eu^{3+} . The sample of the sonochemical method exhibits the strongest absorption while the one of the thermal stirring methods exhibits the weakest absorption.

In Figure 4, the photoluminescence emission spectra of $\text{YVO}_4:\text{Eu}^{3+}$ nanoparticles prepared by three synthesis methods are shown. The samples were excited at ~ 275 nm. The sharp lines in the range from 550 to 750 nm correspond to the transitions from the excited $^5\text{D}_0 \rightarrow ^7\text{F}_j$ of Eu^{3+} ions (Figure 3) [15, 41, 57–59]. There is no obvious vanadate group emission band indicating the transfer of absorption energy of the vanadate groups to Eu^{3+} ions. There is assignment of strongest red emission peak at 618 nm to the $^5\text{D}_0 \rightarrow ^7\text{F}_2$ transition, emission peak at 590 nm to $^5\text{D}_0 \rightarrow ^7\text{F}_1$ of Eu^{3+} ions, and strong emission peak at 692 nm to the $^5\text{D}_0 \rightarrow ^7\text{F}_4$ transition [15, 40, 41]. Eu^{3+} ions occupy asymmetry inversion center instead of Y^{3+} in the strongest emission from $^5\text{D}_0 \rightarrow ^7\text{F}_2$ transition [15, 41]. The sample produced by the sonochemical method has the strongest intensity at 618 nm, as compared to that of other samples. Regarding this result, the characteristics of the ultrasonic processor, high local temperature and pressure, are attributed to the forming of $\text{YVO}_4:\text{Eu}^{3+}$ nanoparticles with high crystalline structure and better doping of Eu^{3+} ions to YVO_4 lattice. We also assumed that sound waves with characteristic of mechanical waves affect the doping of Eu^{3+}

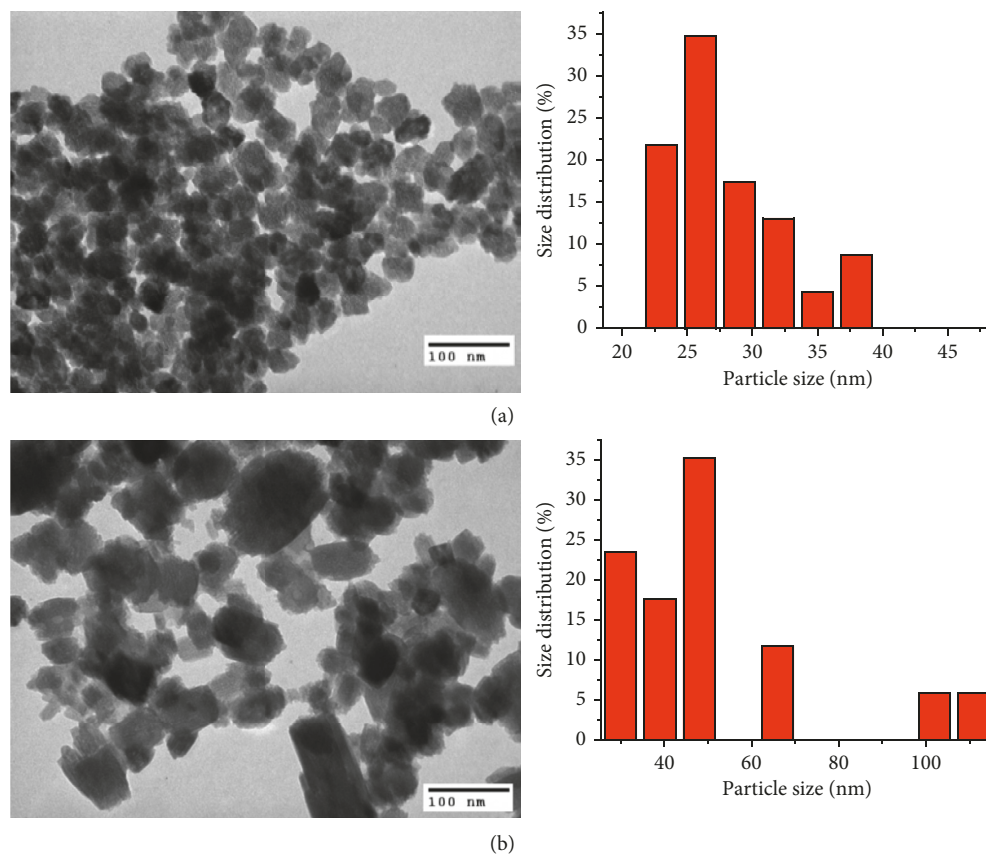


FIGURE 2: TEM micrographs and the size distribution diagram of $\text{YVO}_4:\text{Eu}^{3+}$ nanoparticles synthesized by sonochemical (a) and thermal stirring (b).

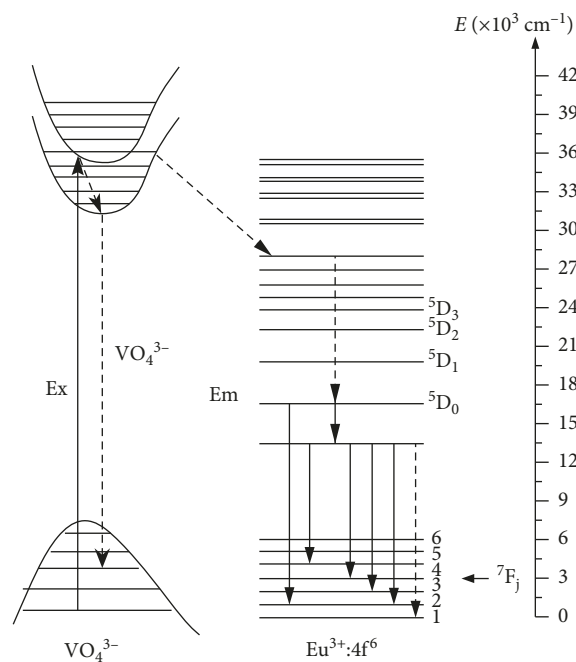


FIGURE 3: Energy levels and transitions scheme of Eu^{3+} . Vertical arrows: absorption and emission transitions.

ions to the YVO_4 lattice. And, it leads to the highest intensity of emission peak [51]. Figure 4 (right inset) is the image of $\text{YVO}_4:\text{Eu}^{3+}$ nanoparticles powder, synthesized by

sonochemical method, under excitation at 254 nm by the UV lamp. The powder turns red under the UV lamp corresponding to dominant emission at 618 nm.

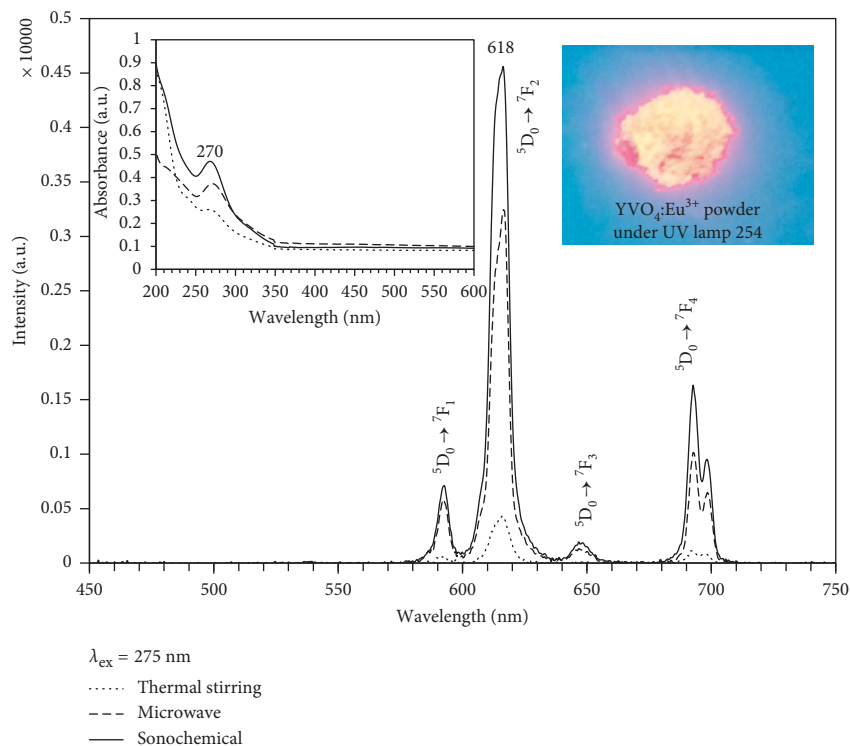


FIGURE 4: Photoluminescence spectra of $\text{YVO}_4:\text{Eu}^{3+}$ nanoparticles synthesized with a different method. Right inset shows UV-VIS spectra of $\text{YVO}_4:\text{Eu}^{3+}$ nanoparticles synthesized with a different method. Left inset is image of $\text{YVO}_4:\text{Eu}^{3+}$ powder synthesized with sonochemical method under UV lamp 254 nm.

The purpose is synthesizing $\text{YVO}_4:\text{Eu}^{3+}$ nanoparticles with strong luminescence. There are many factors which affect the light emitting of $\text{YVO}_4:\text{Eu}^{3+}$ nanoparticles (related to the light emitting mechanism) such as the doping level of Eu^{3+} ions, particle crystalline, and nanoparticle size. Among these factors, the nanoparticle crystallinity and the incorporation of Eu^{3+} ion into the Y^{3+} positions in the lattice of $\text{YVO}_4:\text{Eu}^{3+}$ nanoparticles play important roles in the increasing of luminescence. As to the above result, the $\text{YVO}_4:\text{Eu}^{3+}$ nanoparticles with highest luminescent intensity are synthesized by the sonochemical method, and so, this method will be used for the future research.

$\text{YVO}_4:\text{Eu}^{3+}$ nanoparticles are synthesized by the wet chemical method with De-ion water as solvent, in which the pH parameter affects the forming of particles as well as the crystalline growth of nanoparticles. Hence, the pH of aqueous vanadate solution is an important parameter in the synthesis [22, 23, 43, 60]. The samples are synthesized with the pH value variation (adjusted by 5 M·NaOH) in the solution as follows: 8, 10, 12, and 14 (with sonochemical method and the ratio of chemical as mentioned above). The change in the luminescence intensity of $\text{YVO}_4:\text{Eu}^{3+}$ nanoparticles is shown in Figure 5.

Figure 5 shows the main emission is at 618 nm due to ${}^5\text{D}_0 \rightarrow {}^7\text{F}_2$ transition with the strongest emissivity. The samples are excited at ~ 275 nm. At 618 nm, the luminescence intensity of sample with pH=12 is strongest, the second is pH=14, and the weakest is pH=8. This can be explained that the reaction does not occur when pH > 12 and

only the precipitation of very small particles of $\text{Y}(\text{OH})_3$ takes place instead of YVO_4 . When the pH is smaller than 12, the color of the solution changes slowly from light to dark yellow. This may be the attribution to the forming of polyanvanadate species [23, 43]. Hence, pH=12 is optimal for emissivity of $\text{YVO}_4:\text{Eu}^{3+}$ nanoparticles.

3.2. Effect of Annealing Temperature on the Characteristics of $\text{YVO}_4:\text{Eu}^{3+}$ Nanoparticles Synthesized by Sonochemical Method. The annealing process is carried out after nanoparticles formation, and it plays an important role in increasing the crystallinity and decreasing structure distortion of rare earth nanocrystals [38, 40, 45]. $\text{YVO}_4:\text{Eu}^{3+}$ nanoparticles are synthesized by the sonochemical method and then centrifuged at 9000 rpm. The final powder is dried at 60°C in 6 h and then annealed at 300, 600, and 900°C in 1 h.

Figure 6 shows the XRD patterns, as recorded for the $\text{YVO}_4:\text{Eu}^{3+}$ nanoparticles prepared at 300, 600, and 900°C . Only the tetragonal phase of YVO_4 (JCPDS, No. 17-0341) is observed in all samples. The sample annealed at 900°C for 1 h has better crystallinity in comparison to that of the samples annealed at 300 and 600°C for 1 h. This result shows that annealing at 900°C is preferable for the sample synthesis.

Figure 7 shows the FE-SEM patterns of the samples annealed at 300, 600, and 900°C for 1 h and the energy dispersive X-ray (EDX) spectra of $\text{YVO}_4:\text{Eu}^{3+}$ nanoparticles annealed at 900°C for 1 h. Using ImageJ software for calculation, the correlative average particle sizes are found to be

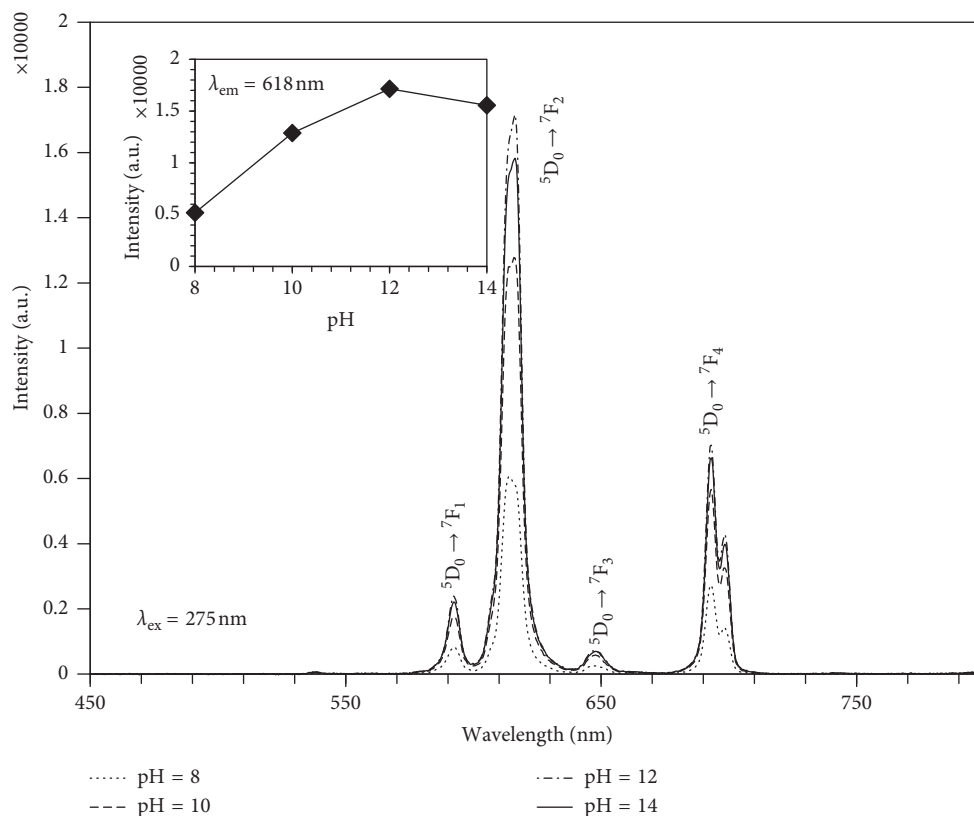


FIGURE 5: Photoluminescence spectra of samples with different pH values. Inset shows pH value dependence on ${}^5D_0 \rightarrow {}^7F_2$ intensity.

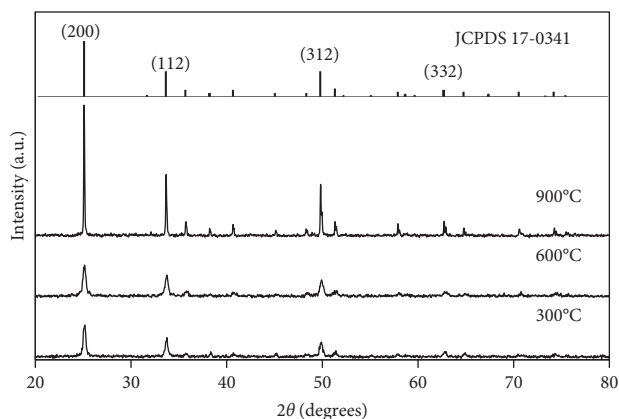


FIGURE 6: XRD samples of $YVO_4:Eu^{3+}$ nanoparticles synthesized at different annealing temperatures.

47 nm, 78 nm, and 170 nm. Thus, when the annealing temperature increases, the particle size also increases. The increasing of $YVO_4:Eu^{3+}$ nanoparticles size along with increasing annealing temperature has been observed by Georgescu et al. [38] and Li et al. [61]. This phenomenon can be explained by the nephelauxetic effect which is related to the metal-ligand bond covalency. Therefore, the covalency of $Eu^{3+}-O^{2-}$ bonds in $YVO_4:Eu^{3+}$ increases as the temperature increases in thermal treatment. There is a relation between the increase of covalency with nanoparticle size and the expansion of the cell parameters of $YVO_4:Eu^{3+}$ nanoparticles in rapport with the bulk material.

The EDX spectrum in samples of $YVO_4:Eu^{3+}$ nanoparticles affirms the existence of yttrium (Y), oxygen (O), vanadium (V), and europium (Eu) factors, indicating that Eu^{3+} ions are doped into the YVO_4 nanocrystals.

The photoluminescence spectra which appeared under excitation at 275 nm of samples fabricated at different annealing temperatures are shown in Figure 8. Right inset is the UV-Vis spectra of $YVO_4:Eu^{3+}$ nanoparticles with different annealing temperatures—left inset is the diagram presenting the dependence of ${}^5D_0 \rightarrow {}^7F_2$ intensity on annealing temperature. The optical emission mechanism is the absorption of ultraviolet light by VO_4^{3-} groups and transfer of energy to Eu^{3+} , the energy which is released in the form of fluorescence [61–63]. Hence, the absorption of VO_4^{3-} is displayed in Figure 8 (right inset). There is an absorption in the VO_4^{3-} groups related to the peaks at 270 nm of three samples. In accordance with references, we can explain that the oxygen ligands attributed to the charge transfer to central vanadium atom in VO_4^{3-} group. The result of UV-Vis spectra is important because of the luminescent characteristic of $YVO_4:Eu^{3+}$ nanoparticles resulting in the energy absorption and transfer from VO_4^{3-} to Eu^{3+} [22, 41]. All three samples have the strongest peak at 618 nm resulting from ${}^5D_0 \rightarrow {}^7F_2$ transition. This leads to the indication of the occupying of Eu^{3+} ions to the asymmetry inversion center instead of Y^{3+} . Figure 8 (left inset) shows the dependence of luminescence intensity on annealing temperature. With the annealing at 900°C for 1 h, $YVO_4:Eu^{3+}$ nanoparticles have the strongest luminescence intensity, which can be explained that the increase of temperature will

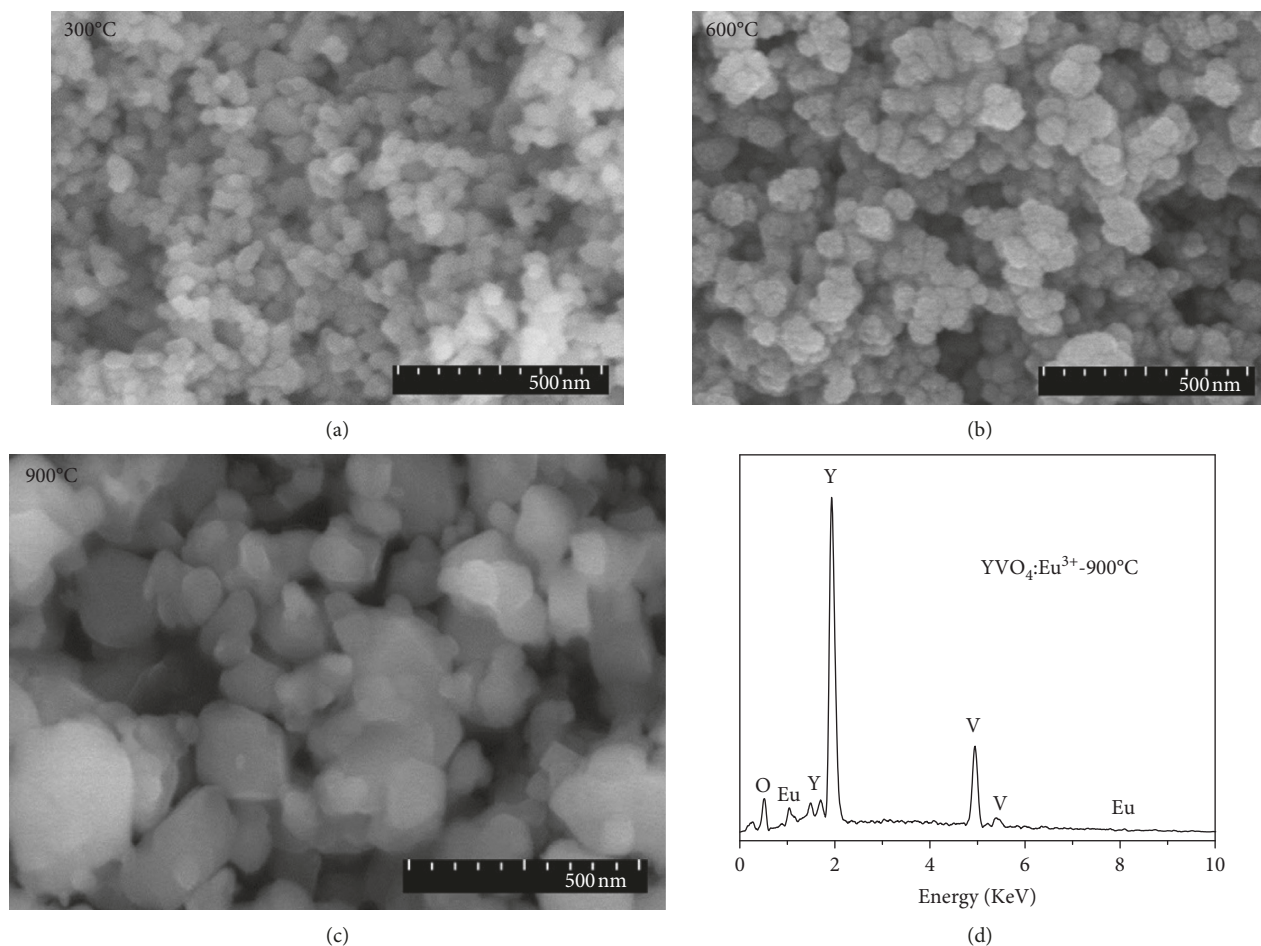


FIGURE 7: FE-SEM micrographs of $\text{YVO}_4:\text{Eu}^{3+}$ nanoparticles at different annealing temperatures and corresponding EDX spectrum of samples annealed at 900°C (in 1 h).

decrease the number of top surface defects. However, the annealing temperature in this research remains not over 900°C in order to control the size of nanoparticles. Due to the nanoparticle size increasing, the disadvantage appeared in the preparation of security ink.

Figure 9 shows the photoluminescence spectra of samples annealed at 900°C for 2, 4, and 5 h with excitation at ~275 nm. The more increasing of Eu^{3+} local symmetry environment causes the increase of the strongest emission from $^5\text{D}_0 \rightarrow ^7\text{F}_2$ transition over annealing time from 2 h to 4 h. However, the annealing time of 5 h leads to the lower intensity than that at 4 h. The relative intensity ratio of $^5\text{D}_0 \rightarrow ^7\text{F}_2$ to $^5\text{D}_0 \rightarrow ^7\text{F}_1$ peaks can show the symmetry rate of local environment of Eu^{3+} ions [23, 61, 64]. To reveal the influence of heat treating temperature and time on the luminescence properties, the relative intensity ratios of $^5\text{D}_0 \rightarrow ^7\text{F}_2$ and $^5\text{D}_0 \rightarrow ^7\text{F}_1$ transitions in the samples are calculated, and the results are shown in Table 1.

In three samples annealed at 300, 600, and 900°C for 1 h, a tendency to decrease the intensity ratio with increasing heat treating temperature indicates the increase of symmetry of local environment of Eu^{3+} ions heat treatment temperature. The highest relative intensity ratio was obtained in the sample annealed at 300°C and the lowest in the sample at

900°C, which shows that highest Eu^{3+} local symmetry environment is in the sample treated at 900°C. These results can be explained that the low annealing temperature (at 300°C) leads to the slower crystal growth rate, the sample obtains enough energy due to increase in the annealing temperature (at 900°C) and has better crystallinity.

In four samples annealed at 900°C for 2, 3, 4, and 5 h, the relative intensity ratio decreases gradually from 2 h to 4 h sample, but this ratio in 5 h sample is higher than 4 h sample. It shows that the local symmetry of Eu^{3+} environment is the highest in the 4 h sample in comparison with other samples. The reason is that the particles have enough time and energy to have better crystallite growth [38, 40, 65]. However, increasing of the heat-treating time to 5 h leads to structure distortion and decrease of Eu^{3+} local symmetry environment.

In Figure 10, the room-temperature luminescence decay curves of $^5\text{D}_0 \rightarrow ^7\text{F}_2$ transition of Eu^{3+} are shown for the samples annealed at 300, 600, and 900°C for 1 h (Figures 10(a)–10(c)) and at 900°C for 4 h (Figure 10(d)). The excitation wavelength is fixed at 275 nm. The common factors affecting the decay kinetics behavior are the number of different luminescent centers, defects, energy transfer, and impurities in the host [62]. The raw data recorded for the

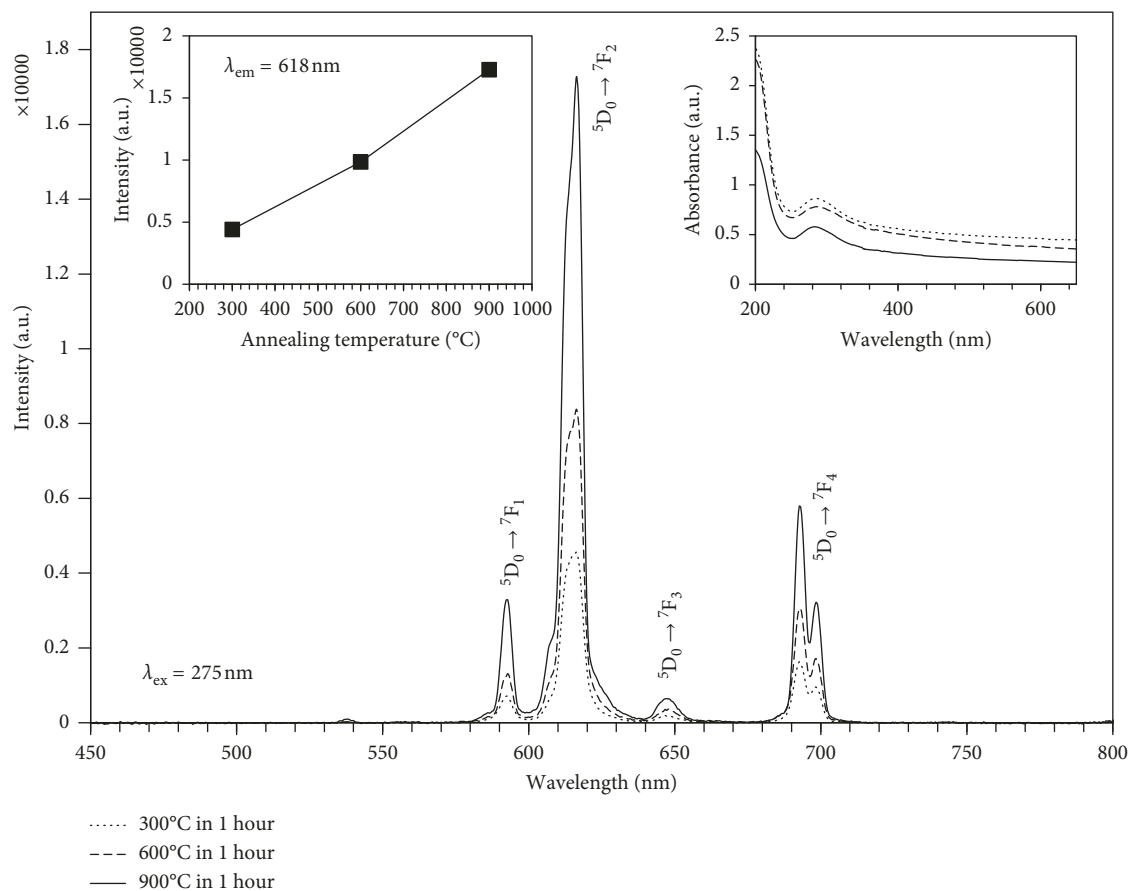


FIGURE 8: Photoluminescence spectra of samples at different annealed temperatures. Inset (right) shows the UV-V spectra of $\text{YVO}_4:\text{Eu}^{3+}$ nanoparticles with different annealed temperatures; left inset is the diagram of dependence of $^5\text{D}_0 \rightarrow ^7\text{F}_2$ intensity on annealing temperature.

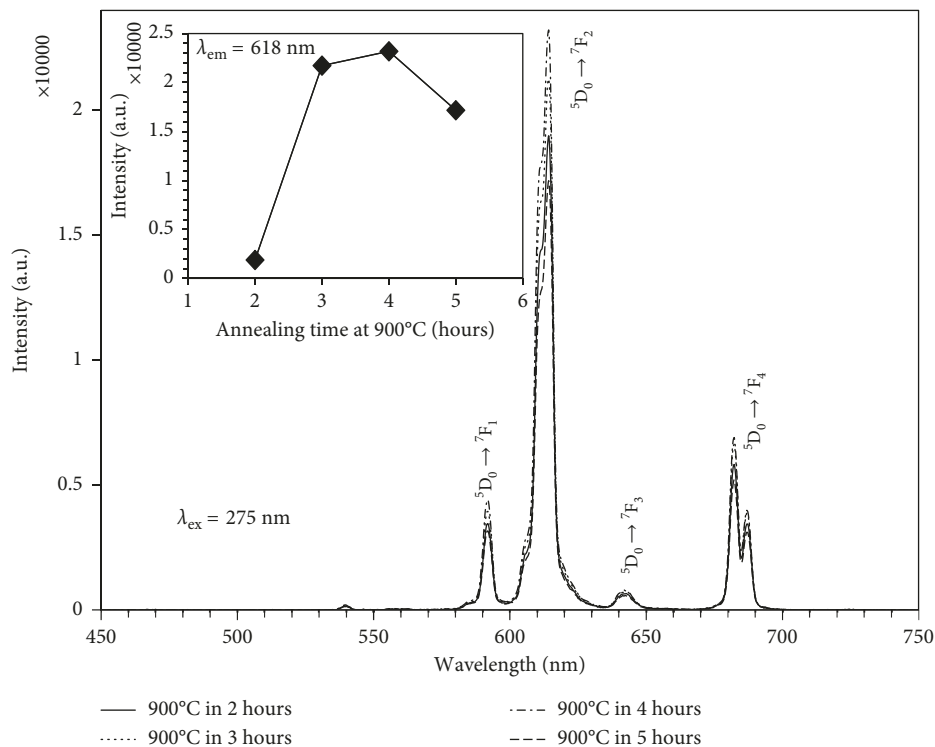
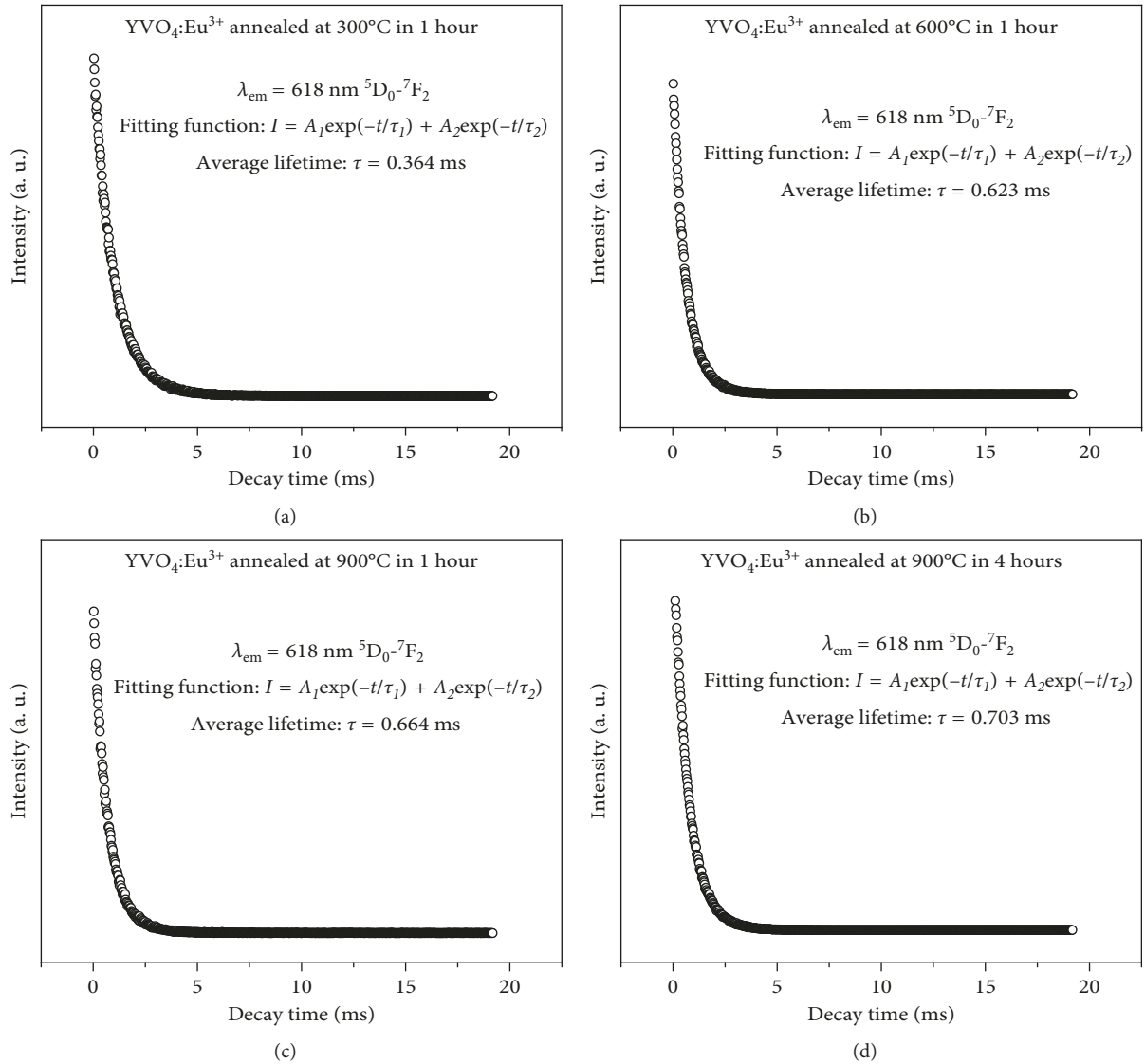


FIGURE 9: Photoluminescence spectra of samples annealed at 900°C in different durations. Inset shows diagram of dependence of $^5\text{D}_0 \rightarrow ^7\text{F}_2$ intensity on the annealing time at 900°C.

TABLE 1: ${}^5D_0 \rightarrow {}^7F_2/{}^5D_0 \rightarrow {}^7F_1$ relative emission intensity ratio.

Sample	${}^5D_0 \rightarrow {}^7F_2/{}^5D_0 \rightarrow {}^7F_1$
300°C-1 h	8.80
600°C-1 h	5.58
900°C-1 h	5.26
900°C-2 h	6.38
900°C-3 h	5.97
900°C-4 h	5.71
900°C-5 h	5.87

FIGURE 10: The luminescence decay curves for the 5D_0 excited state of Eu^{3+} under 275 nm excitation for $\text{YVO}_4:\text{Eu}^{3+}$ samples synthesized with different annealing temperatures and durations.

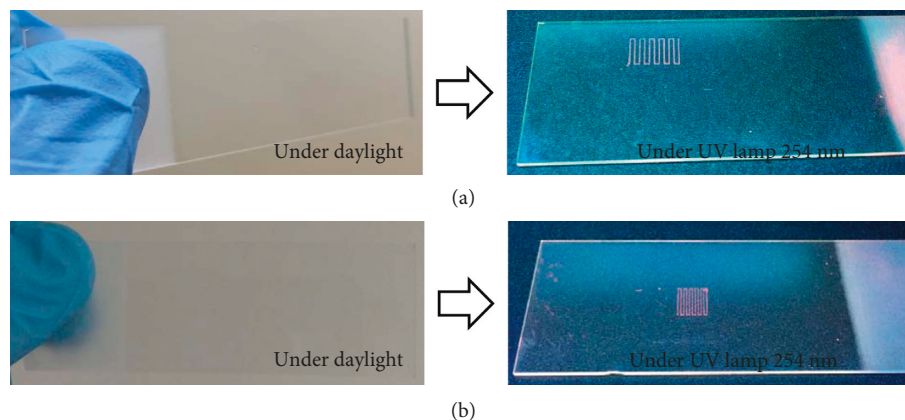
decay curves of all samples are well-fitted by a double-exponential function (equation (2)).

$$I = A_1 \exp\left(\frac{-t}{\tau_1}\right) + A_2 \exp\left(\frac{-t}{\tau_2}\right), \quad (2)$$

where I is the luminescence intensity at time t , A is the fitting parameter, and τ is the decay lifetime, respectively. The average lifetimes of the Eu^{3+} ions in samples annealed at 300, 600, and 900°C in 1 h at 618 nm emission under 275 nm excitation are calculated to be 0.364, 0.623, and 0.644 ms. The

TABLE 2: Formulation of $\text{YVO}_4:\text{Eu}^{3+}$ nanoparticles ink.

Ingredient	$\text{YVO}_4:\text{Eu}^{3+}$	Glycerin	Ethanol	Ethyl acetate	Ethylene glycol
Percentage (% wt.)	8	62	16	4	10

FIGURE 11: The image of lines under daylight and UV lamp, labels with distance between two lines at $300\ \mu\text{m}$ (a) and $800\ \mu\text{m}$ (b).

average lifetime increases with the increase of annealing temperature from 300°C to 900°C . The decay lifetime difference may appear due to the nonradiative transition caused by the surface defects and/or crystallinity rate [42]. The higher the annealing temperature, the lower the surface effect. As shown in Figures 10(c) and 10(d) the average decay lifetime of Eu^{3+} ions in sample annealed at 900°C for 4 h is $0.703\ \text{ms}$, which is longer than that in the sample annealed at 900°C for 1 h. The measured decay time comprises both radiative and nonradiative transmission. The radiative decay component is dependent upon the number of light emitting activator ions in the nanoparticles [44]. We assume that Eu^{3+} ions doped in host lattice are light emitting activators, meaning that the occupancy of Eu^{3+} ions to Y^{3+} sites in the samples annealed at 900°C for 4 h is better than that in the sample treated for 1 h.

3.3. Test Security Printing. There are very few reports on the use of rare earth ions as luminescent colloids. The typical report of Gupta et al. is the usage of spherical $\text{Y}_2\text{O}_3:\text{Eu}^{3+}$ nanoparticles as security ink for screen printing technique, and Meruga et al. studied the security ink from the rare earth nanoparticles $\beta\text{-NaYF}_4$ -doped $\text{Yb}^{3+}/\text{Er}^{3+}$ and $\text{Yb}^{3+}/\text{Tm}^{3+}$ to print security QR code by Optomec direct-write aerosol jetting. Our purpose is printing label at small size, from micrometer to millimeter, with high sharpness in order to increase the security ability for product. Therefore, we use $\text{YVO}_4:\text{Eu}^{3+}$ to produce ink for the PS JET 300 V inkjet printer. This printer is operated by the electrohydrodynamic (EHD) inkjet technique. The advantage of the EHD inkjet technique is the ability to print labels at small size (in micrometer) on various material substrates.

For the preparation of security ink, the $\text{YVO}_4:\text{Eu}^{3+}$ nanoparticles are synthesized by the sonochemical method and then redissolved into organic solvents. On the basis of the above results, $\text{YVO}_4:\text{Eu}^{3+}$ nanoparticles, synthesized by the sonochemical method and annealed at 900°C for 4 h, are most appropriate to be used as security ink in inkjet printing due to

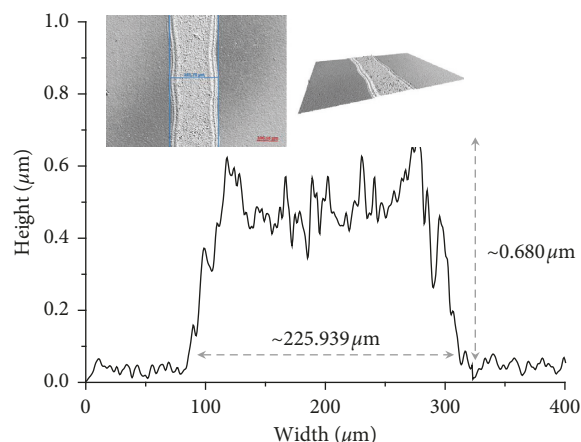


FIGURE 12: The height-width diagram of section of line after printed. Inset shows the micrograph of the respective line taken by Sensofar Metrology 3D microscope technique.

high luminescent intensity at $618\ \text{nm}$ and proper size for not clogging the printhead. Formulation of $\text{YVO}_4:\text{Eu}^{3+}$ nanoparticles ink is shown in Table 2 with the viscosity at $\sim 350\ \text{cP}$. The printhead is made of metal with diameter at $\sim 198\ \mu\text{m}$, DC voltage at $1500\ \text{V}$, frequency at $500\ \text{Hz}$, distance between print head and substrate at around $150\ \mu\text{m}$, and printing speed at $20\ \text{mm/s}$. We perform printing experiment with representative line security labels at small size length of $5\ \text{mm}$ and distance between two lines set at 300 and $800\ \mu\text{m}$.

The printed line image on glass substrate under daylight and UV lamp $254\ \text{nm}$ is shown in Figure 11. The lines printed in Figure 11(a) are with distance set at $800\ \mu\text{m}$ apart and length at $5\ \text{mm}$ and Figure 11(b) with length at $5\ \text{mm}$ and distance set at $300\ \mu\text{m}$ apart. In this experiment, the printed lines are nearly transparent under daylight and have red color luminescence under UV lamp working at $254\ \text{nm}$. The lines are clear, sharp, seamless, and not overlapped over each other even at small distance, $300\ \mu\text{m}$.

The sample with distance of 800 μm between two lines set is analyzed by Sensofar Metrology 3D microscope technique. Figure 12 and inset present the height-width diagram of section of line after being printed and the micrograph of the respective line. The line is seamless with the width at $\sim 230 \mu\text{m}$ and thickness at $\sim 0.68 \mu\text{m}$. According to this result, there is a possibility of printing small security labels with micrometer to millimeter size on glass substrate in order to enhance security property.

4. Conclusion

The $\text{YVO}_4:\text{Eu}^{3+}$ nanoparticles are synthesized by thermal stirring and microwave and sonochemical methods. According to the analyzed result, the crystallization of $\text{YVO}_4:\text{Eu}^{3+}$ nanoparticles appears in the tetragonal structure and the phosphor has the strongest luminescence at wavelength of 618 nm due to ${}^5\text{D}_0 \rightarrow {}^7\text{F}_2$ transition. The creation of the high local temperature and pressure by the sonochemical method has positive effect on the formation of crystalline $\text{YVO}_4:\text{Eu}^{3+}$ nanoparticles and doping of Eu^{3+} ions into Y^{3+} position. As shown by TEM observation, the average size of $\text{YVO}_4:\text{Eu}^{3+}$ nanoparticles synthesized by the sonochemical method is $\sim 23 \text{ nm}$.

The value of pH in the synthesized solution has influence on the emission intensity of $\text{YVO}_4:\text{Eu}^{3+}$ nanoparticles, as pH at 12 is the most appropriate value. Concerning annealing at different temperatures, $\text{YVO}_4:\text{Eu}^{3+}$ nanoparticles show the strongest luminescence intensity when being annealed at 900°C. The optimal luminescence intensity appears in the sample annealed at 900°C for 4 h. The size of $\text{YVO}_4:\text{Eu}^{3+}$ nanoparticles is proportional to the annealing temperature, and the average size of $\text{YVO}_4:\text{Eu}^{3+}$ nanoparticles is $\sim 170 \text{ nm}$ at 900°C applied for 1 h. The average lifetimes of the Eu^{3+} ions emission at 618 nm under 275 nm excitation of the samples annealed at 300, 600, and 900°C for 1 h are 0.364, 0.623, and 0.644 ms, whereas the value in the sample annealed at 900°C for 4 h is 0.703 ms.

Analysis of the results shows that the lines printed by inkjet technique is solid and even with the width at $\sim 230 \mu\text{m}$, the thickness at $\sim 0.68 \mu\text{m}$, and the smallest distance of two adjacent lines at 300 μm . The test lines are nearly invisible under daylight, and they are red under UV mercury lamps with wavelength of $\sim 254 \text{ nm}$.

Data Availability

No data were used to support this study.

Conflicts of Interest

The authors declare that they have no conflicts of interest.

Acknowledgments

The authors would like to give the appreciation to the Vietnam National University, Ho Chi Minh City (VNU-HCM), no. C2017-32-01/HĐ-KHCN.

References

- [1] T. Jüstel, H. Nikol, and C. Ronda, "New developments in the field of luminescent materials for lighting and displays," *Angewandte Chemie International Edition*, vol. 37, no. 22, pp. 3084–3103, 1998.
- [2] V. L. Colvin, M. C. Schlamp, and A. P. Alivisatos, "Light-emitting diodes made from cadmium selenide nanocrystals and a semiconducting polymer," *Nature*, vol. 370, no. 6488, pp. 354–357, 1994.
- [3] B. O. Dabbousi, M. G. Bawendi, O. Onitsuka, and M. F. Rubner, "Electroluminescence from CdSe quantum-dot/polymer composites," *Applied Physics Letters*, vol. 66, no. 11, pp. 1316–1318, 1995.
- [4] V. I. Klimov, A. A. Mikhailovsky, S. Xu et al., "Optical gain and stimulated emission in nanocrystal quantum dots," *Science*, vol. 290, no. 5490, pp. 314–317, 2000.
- [5] M. P. Bruchez, M. Moronne, P. Gin, S. Weiss, and A. P. Alivisatos, "Semiconductor nanocrystals as fluorescent biological labels," *Science*, vol. 281, no. 5385, pp. 2013–2016, 1998.
- [6] Z. Xia, Y. Zhang, M. S. Molokeev, and V. V. Atuchin, "Structural and luminescence properties of yellow-emitting $\text{NaScSi}_2\text{O}_6:\text{Eu}^{2+}$ phosphors: Eu^{2+} site preference analysis and generation of red emission by codoping Mn^{2+} for white-light-emitting diode applications," *Journal of Physical Chemistry C*, vol. 117, no. 40, pp. 20847–20854, 2013.
- [7] C. Shen and Y. Yang, "Synthesis and luminous characteristics of $\text{Ba}_2\text{MgSiO}_5:\text{Eu}^{2+}$ Phosphor," *Materials and Manufacturing Processes*, vol. 26, no. 10, pp. 1335–1337, 2011.
- [8] J. Chandradass and K. H. Kim, "Reverse micelle-directed synthesis of GdAlO_3 Nanopowders," *Materials and Manufacturing Processes*, vol. 25, no. 12, pp. 1428–1431, 2010.
- [9] S. K. Sahoo, M. Mohapatra, A. K. Singh, and S. Anand, "Hydrothermal synthesis of single crystalline nano CeO_2 and its structural, optical, and electronic characterization," *Materials and Manufacturing Processes*, vol. 25, no. 9, pp. 982–989, 2010.
- [10] B. Dong, D. P. Liu, X. J. Wang, T. Yang, S. M. Miao, and C. R. Li, "Optical thermometry through infrared excited green upconversion emissions in $\text{Er}^{3+}\text{-Yb}^{3+}$ codoped Al_2O_3 ," *Applied Physics Letters*, vol. 90, no. 18, article 181117, 2007.
- [11] R.-S. Liu, Y.-H. Liu, N. C. Bagkar, and S.-F. Hu, "Enhanced luminescence of $\text{SrSi}_2\text{O}_7:\text{Eu}^{2+}$ phosphors by codoping with Ce^{3+} , Mn^{2+} , and Dy^{3+} ions," *Applied Physics Letters*, vol. 91, no. 6, article 061119, 2007.
- [12] C.-J. Jia, L.-D. Sun, F. Luo, X.-C. Jiang, L.-H. Wei, and C.-H. Yan, "Structural transformation induced improved luminescent properties for $\text{LaVO}_4:\text{Eu}$ nanocrystals," *Applied Physics Letters*, vol. 84, no. 26, pp. 5305–5307, 2004.
- [13] F. C. Palilla and A. K. Levine, " $\text{YVO}_4:\text{Eu}$: a highly efficient, red-emitting phosphor for high pressure mercury lamps," *Applied Optics*, vol. 5, no. 9, pp. 1467–1468, 1966.
- [14] L. W. Wanmaker, A. Bril, W. J. Vrugt, and J. Broos, "Luminescent properties of Eu-activated phosphors of the type $\text{A}^{\text{III}}\text{B}^{\text{V}}\text{O}_4$," *Philips Research Reports*, vol. 21, pp. 270–273, 1966.
- [15] K. Riwozki and M. Haase, "Wet-chemical synthesis of doped colloidal nanoparticles: $\text{YVO}_4:\text{Ln}$ ($\text{Ln} = \text{Eu}, \text{Sm}, \text{Dy}$)," *Journal of Physical Chemistry B*, vol. 102, no. 50, pp. 10129–10135, 1998.
- [16] M. Darbandi, W. Hoheisel, and T. Nann, "Silica coated, water dispersible and photoluminescent $\text{Y}(\text{V,P})\text{O}_4:\text{Eu}^{3+}, \text{Bi}^{3+}$

- nanophosphors," *Nanotechnology*, vol. 17, no. 16, pp. 4168–4173, 2006.
- [17] J. Kang, X.-Y. Zhang, L.-D. Sun, and X.-X. Zhang, "Bio-conjugation of functionalized fluorescent YVO₄:Eu nanocrystals with BSA for immunoassay," *Talanta*, vol. 71, no. 3, pp. 1186–1191, 2007.
- [18] G. Blasse and C. B. Grabmaier, *Luminescent Materials*, Springer-Verlag, Berlin, Germany, 1994.
- [19] W. Park, M. Jung, and D. Yoon, "Influence of Eu³⁺, Bi³⁺ co-doping content on photoluminescence of YVO₄ red phosphors induced by ultraviolet excitation," *Sensors and Actuators B: Chemical*, vol. 126, no. 1, pp. 324–327, 2007.
- [20] F. M. Nirwan, T. K. Gundu Rao, P. K. Gupta, and R. B. Pode, "Studies of defects in YVO₄:Pb²⁺, Eu³⁺ red phosphor material," *Physica Status Solidi (a)*, vol. 198, no. 2, pp. 447–456, 2003.
- [21] W. J. Park, M. K. Jung, T. Masaki, S. J. Im, and D. H. Yoon, "Characterization of YVO₄:Eu³⁺, Sm³⁺ red phosphor quick synthesized by microwave rapid heating method," *Materials Science and Engineering: B*, vol. 146, no. 1–3, pp. 95–98, 2008.
- [22] Y. Liu, H. Xiong, N. Zhang, Z. Leng, R. Li, and S. Gan, "Microwave synthesis and luminescent properties of YVO₄:Ln³⁺ (Ln = Eu, Dy and Sm) phosphors with different morphologies," *Journal of Alloys and Compounds*, vol. 653, no. 25, pp. 126–134, 2015.
- [23] D. Natacha, A. Chrystel, P. Franck et al., "New synthesis strategies for luminescent YVO₄:Eu and EuVO₄ nanoparticles with H₂O₂ selective sensing properties," *Chemistry of Materials*, vol. 27, no. 15, pp. 5198–5205, 2015.
- [24] X. Wu, Y. Tao, C. Song, C. Mao, L. Dong, and J. Zhu, "Morphological control and luminescent properties of YVO₄:Eu nanocrystals," *Journal of Physical Chemistry B*, vol. 110, no. 32, pp. 15791–15796, 2006.
- [25] Y.-S. Cho and Y.-D. Huh, "Photoluminescence properties of YVO₄:Eu nanophosphors prepared by the hydrothermal reaction," *Bulletin of the Korean Chemical Society*, vol. 31, no. 8, pp. 2368–2370, 2010.
- [26] J. F. Dijkstra, P. C. Duineveld, M. J. J. Hack et al., "Precision ink jet printing of polymer light emitting displays," *Journal of Materials Chemistry*, vol. 17, no. 6, pp. 511–522, 2007.
- [27] B.-J. de Gans, S. Hoepfener, and U. S. Schubert, "Polymer-relief microstructures by inkjet etching," *Advanced Materials*, vol. 18, no. 7, pp. 910–914, 2006.
- [28] S. M. Bidoki, D. M. Lewis, M. Clark, A. Vakorov, P. A. Millner, and D. McGorman, "Ink-jet fabrication of electronic components," *Journal of Micromechanics and Microengineering*, vol. 17, no. 5, pp. 967–974, 2007.
- [29] S. B. Fuller, E. J. Wilhelm, and J. M. Jacobson, "Ink-jet printed nanoparticle microelectromechanical systems," *Journal of Microelectromechanical Systems*, vol. 11, no. 1, pp. 54–60, 2002.
- [30] K. J. Lee, B. H. Jun, T. H. Kim, and J. Joung, "Direct synthesis and inkjetting of silver nanocrystals toward printed electronics," *Nanotechnology*, vol. 17, no. 9, pp. 2424–2428, 2002.
- [31] B. K. Park, D. Kim, S. Jeong, J. Moon, and J. S. Kim, "Direct writing of copper conductive patterns by ink-jet printing," *Thin Solid Films*, vol. 515, no. 19, pp. 7706–7711, 2007.
- [32] B. T. Nguyen, J. E. Gautrot, M. T. Nguyen, and X. X. Zhu, "Nitrocellulose-stabilized silver nanoparticles as low conversion temperature precursors useful for inkjet printed electronics," *Journal of Materials Chemistry*, vol. 17, no. 17, pp. 1725–1730, 2007.
- [33] A. Apilux, Y. Ukita, M. Chikae, O. Chailapakul, and Y. Takamura, "Development of automated paper-based devices for sequential multistep sandwich enzyme-linked immunosorbent assays using inkjet printing," *Lab Chip*, vol. 13, no. 1, pp. 126–135, 2013.
- [34] C. M. Dang, C. D. Trinh, D. M. T. Dang, and E. F. Blanc, "Characteristics of colloidal copper particles prepared by using polyvinyl pyrrolidone and polyethylene glycol in chemical reduction method," *International Journal of Nanotechnology*, vol. 10, no. 3–4, pp. 296–303, 2013.
- [35] M. C. Dang, T. M. Dung Dang, and E. Fribourg-Blanc, "Inkjet printing technology and conductive inks synthesis for microfabrication techniques," *Advances in Natural Sciences: Nanoscience and Nanotechnology*, vol. 4, no. 1, pp. 015009–015016, 2013.
- [36] J. M. Meruga, W. M. Cross, P. S. May, Q. Luu, G. A. Crawford, and J. J. Kellar, "Security printing of covert quick response codes using upconverting nanoparticle inks," *Nanotechnology*, vol. 23, no. 39, pp. 395201–395210, 2012.
- [37] B. K. Gupta, D. Haranath, S. Saini, V. N. Singh, and V. Shanker, "Synthesis and characterization of ultra-fine Y₂O₃:Eu³⁺ nanophosphors for luminescent security ink applications," *Nanotechnology*, vol. 21, no. 5, pp. 055607–055615, 2010.
- [38] S. Georgescu, E. Cotoi, A. M. Voiculescu, and O. Toma, "Effects of particle size on the luminescence of YVO₄:Eu nanocrystals," *Romanian Reports in Physics*, vol. 60, no. 4, pp. 947–955, 2008.
- [39] V. Buissette, D. Giaume, T. Gacoin, and J.-P. Boilot, "Aqueous routes to lanthanide-doped oxide nanophosphors," *Journal of Materials Chemistry*, vol. 16, no. 6, pp. 529–539, 2006.
- [40] H. Yu, Y. Li, Y. Song et al., "Ultralong well-aligned TiO₂:Ln³⁺ (Ln = Eu, Sm, or Er) fibres prepared by modified electrospinning and their temperature-dependent luminescence," *Scientific Reports*, vol. 7, no. 1, pp. 44099–44106, 2017.
- [41] H. Wang, O. Odawara, and H. Wada, "Facile and chemically pure preparation of YVO₄:Eu³⁺ colloid with novel nanostructure via laser ablation in water," *Scientific Reports*, vol. 6, no. 1, pp. 20507–20515, 2016.
- [42] B. Shao, Q. Zhao, N. Guo et al., "Monodisperse YVO₄:Eu³⁺ submicrocrystals: controlled synthesis and luminescence properties," *CrystEngComm*, vol. 15, no. 29, pp. 5776–5783, 2013.
- [43] S. Georgescu, E. Cotoi, A. M. Voiculescu, O. Toma, and C. Matei, "Reflectance spectra of YVO₄:Eu³⁺ phosphors synthesized by direct precipitation," *Romanian Journal of Physics*, vol. 55, no. 7, pp. 750–757, 2010.
- [44] V. Kumar, A. F. Khan, and S. Chawla, "Intense red-emitting multi-rare-earth doped nanoparticles of YVO₄ for spectrum conversion towards improved energy harvesting by solar cells," *Journal of Physics D: Applied Physics*, vol. 46, no. 36, pp. 365101–365108, 2013.
- [45] F. He, P. Yang, N. Niu et al., "Hydrothermal synthesis and luminescent properties of YVO₄:Ln³⁺ (Ln = Eu, Dy, and Sm) microspheres," *Journal of Colloid and Interface Science*, vol. 343, no. 1, pp. 71–78, 2010.
- [46] Y.-S. Cho and Y.-D. Huh, "Preparation of transparent red-emitting YVO₄:Eu nanophosphor suspensions," *Bulletin of the Korean Chemical Society*, vol. 32, no. 1, pp. 335–337, 2011.
- [47] E. A. Neppiras, "Acoustic cavitation series: part one," *Ultrasonics*, vol. 22, no. 1, pp. 25–28, 1984.
- [48] A. Henglein, "Sonochemistry: historical developments and modern aspects," *Ultrasonics*, vol. 25, no. 1, pp. 6–16, 1987.
- [49] E. B. Flint and K. S. Suslick, "The temperature of cavitation," *Science*, vol. 253, no. 5026, pp. 1397–1399, 1991.

- [50] K. S. Suslick, S.-B. Choe, A. A. Cichowlas, and M. W. Grinstaff, "Sonochemical synthesis of amorphous iron," *Nature*, vol. 353, no. 6343, pp. 414–416, 1991.
- [51] C. Bendicho, I. Lavilla, F. Pena, and M. Costas, "RSC green chemistry, chapter 4," in *Challenges in Green Analytical Chemistry*, vol. 13, RSC Publishing, Cambridge, UK, 2011.
- [52] A. Bao, H. Lai, Y. Yang, Z. Liu, C. Tao, and H. Yang, "Luminescent properties of $\text{YVO}_4\text{:Eu/SiO}_2$ core-shell composite particles," *Journal of Nanoparticle Research*, vol. 12, no. 2, pp. 635–643, 2010.
- [53] L. G. Van Uitert, "Characterization of energy transfer interactions between rare earth ions," *Journal of the Electrochemical Society*, vol. 114, no. 10, pp. 1048–1053, 1967.
- [54] C. W. Struck and W. H. Fonger, "Quantum-mechanical treatment of $\text{Eu}^{3+} 4f \rightarrow 4f$ and $4f \rightarrow 4f$ charge-transfer-state transitions in Y_2O_3 and La_2O_3 ," *Journal of Chemical Physics*, vol. 64, no. 4, pp. 1784–1790, 1976.
- [55] J. V. Nicholas, "Origin of the luminescence in natural Zircon," *Nature*, vol. 215, no. 5109, p. 1476, 1967.
- [56] Z. Hou, P. Yang, C. Li et al., "Preparation and luminescence properties of $\text{YVO}_4\text{:Ln}$ and $\text{Y(V, P)O}_4\text{:Ln}$ ($\text{Ln} = \text{Eu}^{3+}$, Sm^{3+} , Dy^{3+}) nanofibers and microbelts by sol-gel/electrospinning process," *Chemistry of Materials*, vol. 20, no. 21, pp. 6686–6696, 2008.
- [57] V. V. Atuchi, A. S. Aleksandrovsk, O. D. Chimitova et al., "Synthesis and spectroscopic properties of monoclinic $\alpha\text{-Eu}_2(\text{MoO}_4)_3$," *Journal of Physical Chemistry C*, vol. 118, no. 28, pp. 15404–15411, 2014.
- [58] P. Shi, Z. Xia, M. S. Molokeev, and V. V. Atuchin, "Crystal chemistry and luminescence properties of red-emitting $\text{CsGd}_{1-x}\text{Eu}_x(\text{MoO}_4)_2$ solid-solution phosphors," *Dalton Transactions*, vol. 43, no. 25, pp. 9669–9676, 2014.
- [59] V. V. Atuchin, A. S. Aleksandrovsky, B. G. Bazarov et al., "Exploration of structural, vibrational and spectroscopic properties of self-activated orthorhombic double molybdate $\text{RbEu}(\text{MoO}_4)_2$ with isolated MoO_4 units," *Journal of Alloys and Compounds*, vol. 785, no. 15, pp. 692–697, 2019.
- [60] A. Huignard, V. Buissette, G. Laurent, T. Gacoïn, and J.-P. Boilot, "Synthesis and characterizations of $\text{YVO}_4\text{:Eu}$ colloids," *Chemistry of Materials*, vol. 14, no. 5, pp. 2264–2269, 2002.
- [61] Y. H. Li, G. F. Zang, and J. Ma, "Synthesis and luminescence properties of $\text{YVO}_4\text{:Eu}^{3+}$ nanocrystals by a sol-gel method," *Advanced Materials Research*, vol. 634–638, pp. 2268–2271, 2013.
- [62] Y. Pu, K. Tang, D.-C. Zhu, T. Han, C. Zhao, and L.-L. Peng, "Synthesis and luminescence properties of (Y, Gd) (P, V)O₄:Eu³⁺, Bi³⁺ red nano-phosphors with enhanced photoluminescence by Bi³⁺, Gd³⁺ doping," *Nano-Micro Letters*, vol. 5, no. 2, pp. 117–123, 2013.
- [63] Z. Xu, X. Kang, C. Li et al., " Ln^{3+} ($\text{Ln} = \text{Eu}, \text{Dy}, \text{Sm}, \text{and Er}$) ion-doped YVO_4 nano/microcrystals with multiform morphologies: hydrothermal synthesis, growing mechanism, and luminescent properties," *Inorganic Chemistry*, vol. 49, no. 14, pp. 6706–6715, 2010.
- [64] C. Li, Z. Hou, C. Zhang et al., "Controlled synthesis of Ln^{3+} ($\text{Ln} = \text{Tb}, \text{Eu}, \text{Dy}$) and V^{5+} ion-doped YPO_4 nano-/microstructures with tunable luminescent colors," *Chemistry of Materials*, vol. 21, no. 19, pp. 4598–4607, 2009.
- [65] R. L. Penn and J. F. Banfield, "Imperfect oriented attachment: dislocation generation in defect-free nanocrystals," *Science*, vol. 281, no. 5379, pp. 969–971, 1998.

Research Article

Fast and Effective Route for Removing Methylene Blue from Aqueous Solution by Using Red Mud-Activated Graphite Composites

Ha Xuan Linh,¹ Ngo Thi Thu,² Tran Quoc Toan,² Do Tra Huong,² Bui Thanh Giang,² Huynh Ky Phuong Ha ,³ Hong-Tham T. Nguyen,⁴ N. T. K. Chung,⁵ Tri Khoa Nguyen ,⁴ and Nguyen Thanh Hai ^{6,7}

¹International School-Thai Nguyen University, Thai Nguyen, Vietnam

²Department of Chemistry, Thai Nguyen University of Education, Thai Nguyen, Vietnam

³Faculty of Chemical Engineering, Ho Chi Minh City University of Technology, Ho Chi Minh City, Vietnam

⁴NTT Hi-Tech Institute, Nguyen Tat Thanh University, 300A Nguyen Tat Thanh, District 4, Ho Chi Minh City 755414, Vietnam

⁵Department of Physics, Thu Dau Mot University, 6 Tran Van on Street, Thu Dau Mot, 820000 Binh Duong Province, Vietnam

⁶Research and Development Center for Advanced Technology, Hanoi, Vietnam

⁷Nanotechnology Program, VNU Vietnam-Japan University, Hanoi, Vietnam

Correspondence should be addressed to Tri Khoa Nguyen; nguyentrikhoa702@gmail.com and Nguyen Thanh Hai; haidhsp95@gmail.com

Received 14 March 2019; Accepted 29 May 2019; Published 1 July 2019

Guest Editor: Van Duong Dao

Copyright © 2019 Ha Xuan Linh et al. This is an open access article distributed under the Creative Commons Attribution License, which permits unrestricted use, distribution, and reproduction in any medium, provided the original work is properly cited.

In this work, the mixture of red mud slurry and inorganic salt ((NH₄)₂SO₄) has been used as an electrolyte for electrochemical activation of graphite. The red mud-activated graphite composite was then used as an adsorbent for removing methylene blue from aqueous solution by the batch method. The effect of pH, contact time, adsorbent dosage, and the initial concentration of methylene blue was investigated. The optimal condition was found at pH 6, contact time 120 min, and amount of adsorbent 1 mg/L. The maximum adsorption capacity was found to be 89.28 mg/g based on the Langmuir isotherm equation, suggesting that the red mud-activated graphite composite is a very potential adsorbent for removing methylene blue and is also used in other coloured wastewater treatments.

1. Introduction

Dyes and pigments (e.g., methylene blue (MB)) are widely used in textile, dyeing, printing, and coating industries. Their wastewater contains a high concentration of non-biodegradable organic compounds which can cause long-term health effects on human beings and animals and significantly qualitative changes in the environment [1]. Therefore, it is essential to remove the contaminants such as dyes and heavy metal ions in the wastewater before discharging into the water source. Several methods such as biodegradation, chemical treatment, the use of UV and ozone, and adsorption have been applied to get rid of MB

from wastewater [2–6]. Among them, the utilization of agricultural or industrial by-products as adsorbents for wastewater treatment has received lots of attention [7]. Recently, chemically or thermally activated seawater neutralized treated red mud (RM) has been effectively used as a promising candidate for removing heavy metal ions and dyes from aqueous solution as a result of the reaction between the hydroxyl groups and active site on red mud or through adsorption onto external surfaces [8, 9]. Besides, the application of graphene oxide (GO) or graphene nanosheets (GSs) adsorbent has been shown to be a simple and effective method for the removal of dye contaminants from wastewater [1, 10]. Moreover, the modification of graphene under

basic conditions or the combination of graphene with other metal oxides showed a great potential for removal of heavy metals ions in water [11–13]. In order to generate porosity for adsorptive purposes, the activation of graphite using alkaline hydroxides such as KOH or NaOH usually requires concentrated alkali solution, long reaction time, and high temperature [14, 15]. Therefore, finding a simple, effective, and energy-saving process for producing activated graphite materials is highly demanded.

As previously discussed, red mud with a high basic property must be activated simultaneously with other materials [16], using acidic conditions [17] or high temperature [18] before utilization. Also, $(\text{NH}_4)_2\text{SO}_4$ solution has been demonstrated to be an effective electrolyte for one-step fast electrochemical exfoliation of graphite [19]. These works show a great possibility of using the mixture of RM slurry and $(\text{NH}_4)_2\text{SO}_4$ as an electrolyte for activating graphite. Therefore, in this study, we combine red mud slurry with $(\text{NH}_4)_2\text{SO}_4$ as an electrolyte for simultaneous activation and exfoliation of graphite and employ the as-product for removing MB from aqueous solution.

2. Materials and Methods

2.1. Synthesis and Characterization of Materials. 300 mL of red mud slurry (Tan Rai factory, Lam Dong Province, Vietnam) was added with 100 mL of 5% w/w $(\text{NH}_4)_2\text{SO}_4$ solution under a magnetic stirrer to form a homogeneous electrolyte at pH 14. Graphite rod was then activated by electrochemical exfoliation using this electrolyte with the voltage of 15 V and temperature from 50–70°C for 120 min (Scheme 1). The beaker was cooled to room temperature in 1 h, and the material was filtrated and washed with DI water until natural pH is reached. The obtained material was finally put in drying oven at 150°C for 24 h and placed in a desiccator at 25°C (denoted as RMGC). The activated graphite without red mud (named as electrochemically exfoliated graphite (EEG)) was also prepared for the comparison purpose using conventional electrolytic solution at pH 14 (200 mL of 7.5% KOH and 50 mL of 5% $(\text{NH}_4)_2\text{SO}_4$, pH 14).

XRD patterns were characterized by using a diffractometer (D2 PHASER using Cu $K\alpha$ radiation). RMGC and EEG structures were examined using high-resolution confocal Raman microscopy (HORIBA, Lab RAM HR 800 equipped with a 514.5 nm Ar laser source). Morphology of materials was determined by using a high-resolution transmission electron microscope (HRTEM, JEOL 2100F apparatus operated at 200 kV). Field emission scanning electron microscopy (SEM) images were collected using the JEOL JSM-6500F scanning electron microscope operated at 15 kV.

2.2. Adsorption Studies. The adsorption experiments for RMGC were carried out by the batch method at room temperature. Several factors including contact time (0 to 270 minutes), initial MB concentration (10, 25, 50, 75, and 100 mg/L), amount of adsorbent (0.01–0.1 g), and solution pH (2.0–12.0) were investigated. The solution of 10% HCl

and 0.1 M NaOH was used to adjust pH solution before addition of the adsorbent. After the test periods, the samples were separated by centrifugation for 15 min at 4000 rpm and the collected supernatant determined the concentration of MB by absorbance measurement using a UV-Vis spectrophotometer (Hitachi UH5300) at a wavelength of 665 nm.

pH_{pzc} (the point of zero charge) of the RMGC was determined in a similar method as Faria et al. [10] At first, 25 mL of 0.01 M NaCl solution was prepared and added into conical flasks, and the pH solution was adjusted by adding NaOH and HCl solutions from 2 to 12. After that, each conical flask was added 0.1 g of the obtained material and shaken for 48 h at room temperature. After the tests, the pH solution was redetermined and denoted as the final pH. Concomitantly, the difference between the initial pH and final pH (initial pH—final pH) was plotted against the initial pH. The point at which the resulting curve intersected with abscissa was pH_{pzc} of the RMGC.

The adsorption capacity and removal efficiency of MB on RMGC was calculated by the following equation:

$$q = \frac{(C_0 - C_e)V}{M}, \quad (1)$$

$$R\% = \frac{(C_0 - C_e)}{C_0} \times 100\%,$$

where V (L) is the solvent volume and M (g) is the mass of adsorbent. C_0 and C_e (mg/L) are initial and equilibrium concentrations, respectively. q (mg/g) is the adsorption capacity at equilibrium time, and R (%) is the removal efficiency of MB.

Adsorption isotherms were conducted at pH 6, contact time 120 min, and room temperature. The different initial concentrations of MB (10, 25, 50, 75, and 100 mg/L) were experimented to analyse the data. The isotherm models of Freundlich and Langmuir are expressed by the following equations:

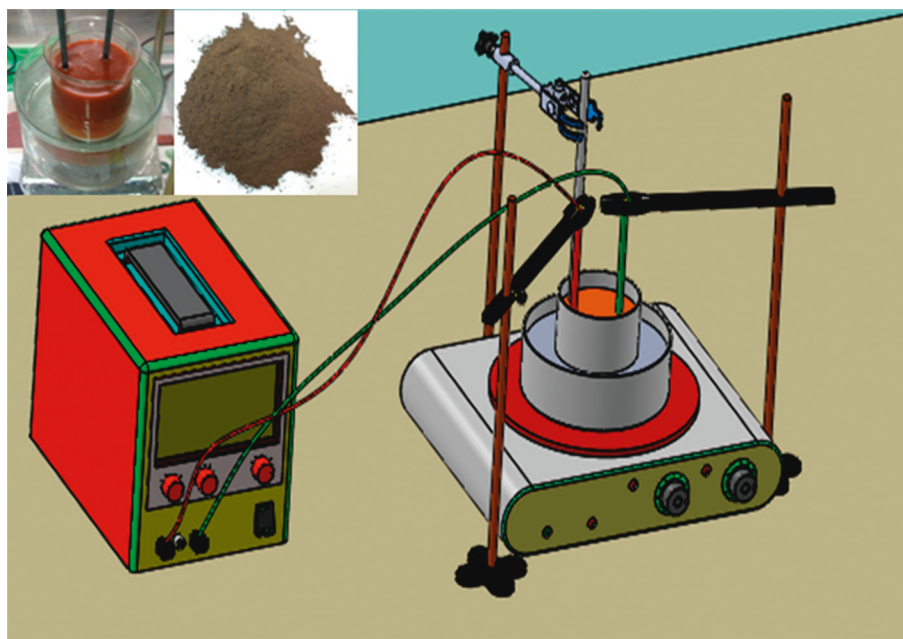
$$\text{Freundlich: } q_e = K_f C_e^{1/n}, \quad (2)$$

$$\text{Langmuir: } q_e = \frac{q_0 b C_e}{1 + b C_e},$$

where K_f and n are Freundlich constants related to sorption capacity and sorption intensity of adsorbent. q_e and C_e are the adsorption capacity and concentration at equilibrium of MB in solution, respectively. q_0 and b are the monolayer adsorption capacity and the Langmuir constant.

3. Results and Discussion

3.1. Structural Analysis. To investigate the morphology of the materials, SEM micrographs are depicted in Figure 1. EEG image displayed flattened morphology and turned into a particle-on-sheet structure in RMGC after exfoliating, which can be further observed by the TEM image in Figure 2. Clearly, exfoliated graphite flakes were overlapped with nanoparticles, which were fairly uniformly distributed on its surface layer (Figure 1(c)). In situ EDS also revealed that the



SCHEME 1: Schematic of RMGC formation (the inset is the working system and as-product).

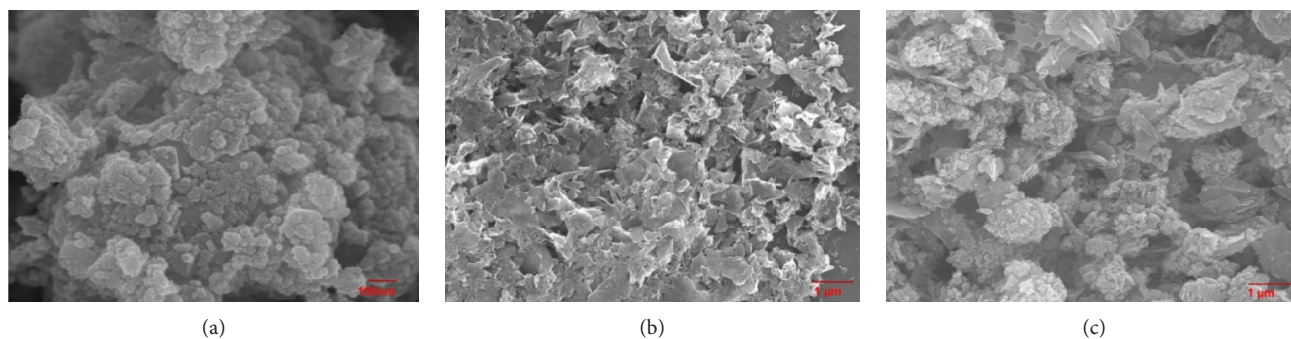


FIGURE 1: SEM images of (a) RM, (b) EEG, and (c) RMGC.

RMGC mainly consisted of C, O, Fe, Si, and Al elements (Figure 2).

The XRD patterns of all collected materials are displayed in Figure 3. The EEG pattern shows a sharp and high-intensity peak at a value of 2θ of 26.6° , indexing to the 002 reflection. In addition, there are three small peaks at values of 2θ of 42.8 , 21.6 , and 34.6° , indexing to the 100, 101, and 004 reflections, respectively. After exfoliating, these peaks still remained, while new small peaks appeared at 2θ values of 18.1 , 21.3 , 29.6 , 33.1 , 35.6 , 37.1 , 54.2 , 62.2 , and 64.3° . These new peaks can be assigned to the phases of quartz (Qz = SiO_2), gibbsite (Gb = $\gamma\text{-Al}(\text{OH})_3$), goethite (Gt = $\alpha\text{-FeOOH}$), and hematite (Hm = Fe_2O_3) [13]. Raman spectroscopy was used to further verify the structure of RMGC. As shown in Figure 4, the characteristic peaks of exfoliated graphite flakes were D- and G-band at 1573 cm^{-1} and 1583 cm^{-1} , respectively, also presented in RMGC [20]. Previously, the OH^- ions will initially oxidize graphite at the edge and/or grain boundaries and were proposed to expand the distance between graphite layers as well as for the following anion intercalation. Concretely, the sulfate ions

SO_4^{2-} intercalate and facilitate in separating weakly bonded graphite layers [19]. In addition, RM is a heterogeneous mixture of fine-grained solids, mainly consisting of hematite, gibbsite, quartz, titanium oxide, carbonates, and desalination products (e.g., cancrinite and sodalite) with high alkalinity, resulted in the exits of hydrated OH^- together with SO_4^{2-} ions. We considered that applying bias voltage, oxygen evolution of SO_4^{2-} and OH^- ions could attach the edge sites and grain boundaries of graphitic layers, which eventually lead to exfoliation including activation with fine RM particles.

3.2. Adsorption Studies. The effect of pH on the RMGC's adsorption of MB is shown in Figure 5. In pH range of 2 to 6, it is obvious that the removal efficiency increased rapidly and was then stable when pH increased from 6 to 12. In the pH drift test (Figure 5(b)), the pH_{pzc} value of the RMGC was observed at 8.3 ± 0.1 . At lower pH, a large number of H^+ ions compete with cationic dye for adsorption sites on RMGC. Moreover, the presence of H^+ ions could protonate the

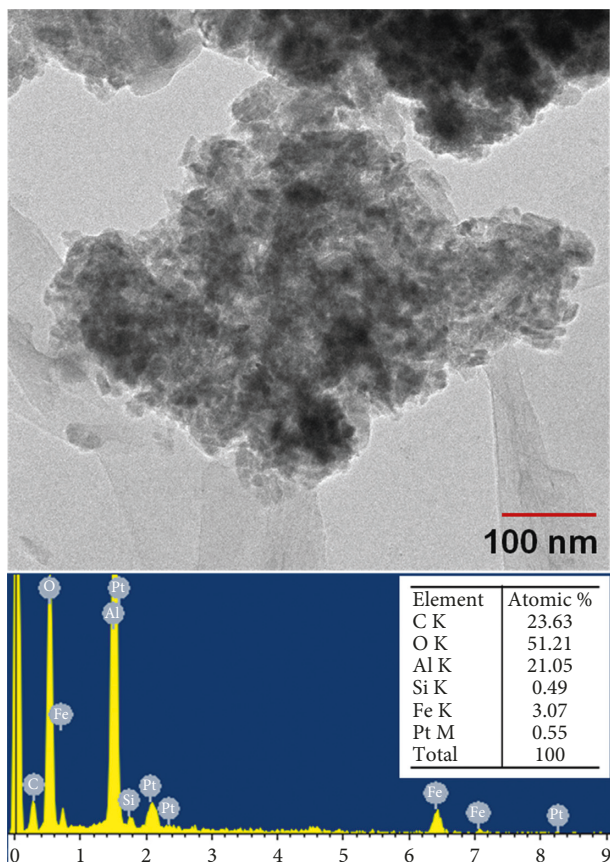
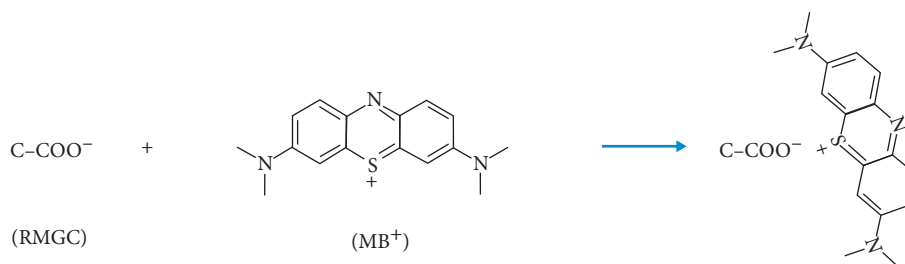


FIGURE 2: TEM image of RMGC, EDS spectrum of RMGC.

functional groups of the graphene and further decreases the adsorption amount of MB. On the contrary, the deprotonation of surface groups at a higher pH would increase the negative charges on the surface, which could result in a greater adsorption amount of MB. Therefore, the electrostatic attraction is responsible for adsorption of MB on RMGC, and the mechanism is proposed as follows:



The highest removal efficiency of MB on RMGC was at pH = 6. In the actual environment, the wastewater generally occurs at the neutral pH value. Thus, the pH value for further experiments was from 5 to 6.

To determine the equilibrium time of removal of MB on RMGC, time intervals up to 270 min of experiment were

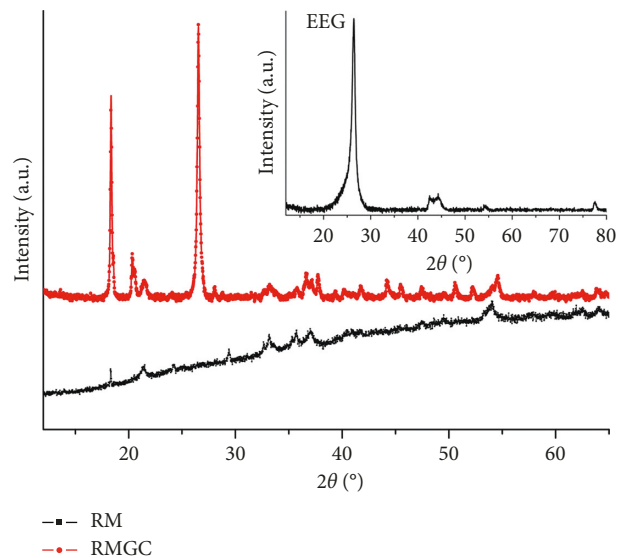


FIGURE 3: XRD patterns of RM and RMGC (inset is that of EEG).

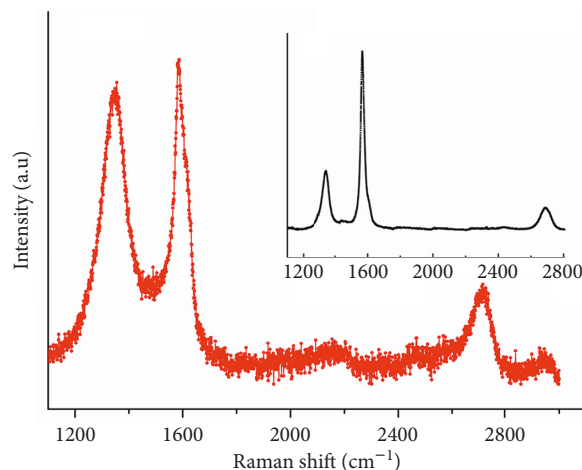


FIGURE 4: Raman spectrum of RMGC (inset is that of EEG).

conducted. As can be seen from Figure 6, MB was rapidly absorbed after 120 min at a removal efficiency of 96.02% but slowed down gradually when reached equilibrium. The reason could be explained by the availability of active sites during the adsorption process, generally in the first stage and after a certain time period of adsorption. Specifically, the active sites

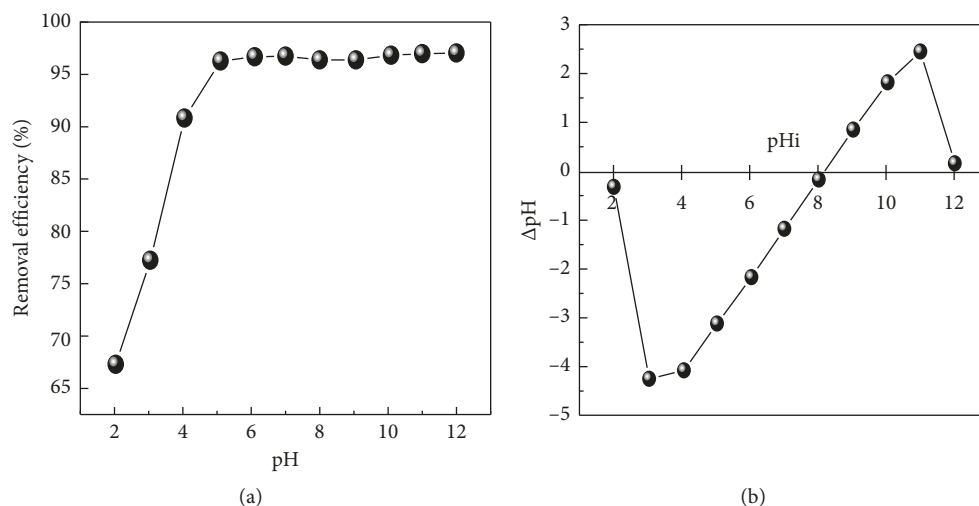


FIGURE 5: (a) Effect of pH value on MB adsorption and (b) pH_{pzc} (MB concentration: 50 mg/L; adsorbent dose: 0.05 g).

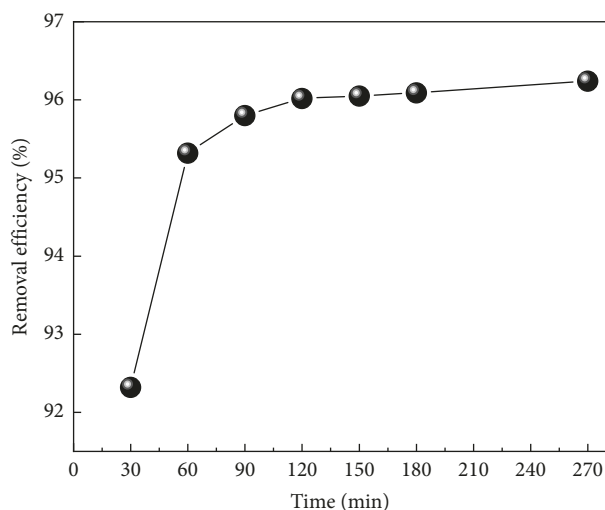


FIGURE 6: Effect of contact time on MB adsorption (MB concentration: 50 mg/L; adsorbent dose: 0.05 g).

will be settled by MB molecules when contact time is increased. At a certain time, the active sites will be fully occupied and could cause to create a repulsive force between the adsorbate on the adsorbent surface and in the bulk phase. After equilibrium conditions are attained, the removal efficiency kept was almost invariable. The contact time at 120 min was preferred as the equilibrium time for further experiments.

Figure 7 illustrates the effect of adsorbent dosage on MB removal efficiency using RMGC. It can be clear that the removal efficiency of MB gradually risen with an increase in an adsorbent dosage up to 0.05 g and thereafter remained unchanged. The more the adsorbent dosage could be added, the more the active sites are available. As a result, the more vacant surface sites were utilized at a fixed MB concentration. The amount of adsorbent was chosen to be 0.05 g for further experiments.

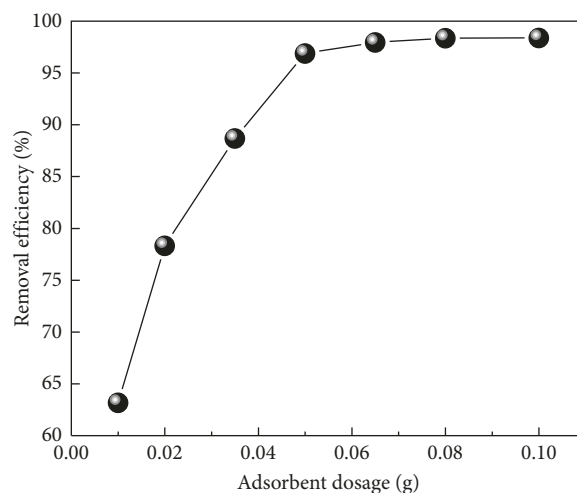


FIGURE 7: Effect of adsorbent dosage on MB adsorption (MB concentration: 50 mg/L; time: 120 min).

Figure 8 presents the effect of initial concentration on the adsorption of MB on RMGC, revealing that removal efficiency decreased from 98.75 to 84.16% as the MB concentration increased from 50 to 250 mg/L, as a result of the progressive increase in the electrostatic interaction between MB and RMGC active sites. Under these circumstances, the active sites were covered since MB concentration increases. Additionally, the higher initial concentrations lead to an increase in the affinity of the cationic dyes towards the active sites.

The relative isotherm parameters and correlation coefficient (R^2) values are listed in Table 1. The analyzed data suggested that MB adsorption could be described in the Langmuir model than the Freundlich model since its R^2 value was higher. This demonstrated that the adsorption of MB on RMGC was monolayer adsorption and controlled by a homogeneous process. Additionally, the maximum capacity (q_{max}) of MB adsorbed on RMGC was predicted as 89.28 mg/g, which was similar to some other adsorbents [21, 22]. The

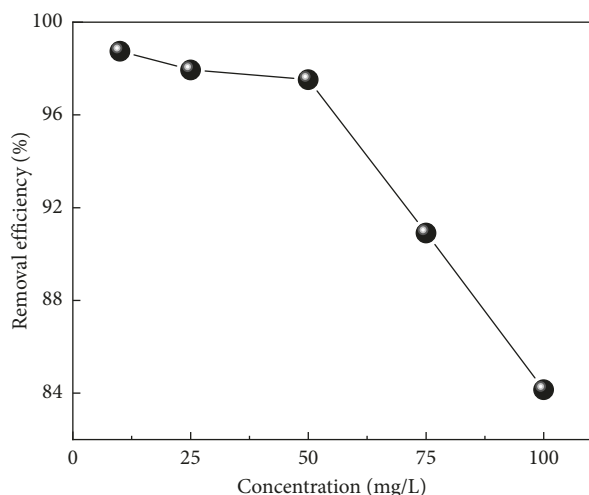


FIGURE 8: Effect of initial concentration on MB adsorption (adsorbent dose: 0.05 g; time: 120 min).

TABLE 1: Adsorption isotherm constants for the adsorption of MB by RMGC.

Model	Parameters	Value
Langmuir	q_{\max} (mg/g)	89.28
	b (L/mg)	0.77
	R^2	0.9995
Freundlich	n	2.315
	K_f (mg/g)/(mg/L) ⁿ	30.489
	R^2	0.894

TABLE 2: Comparison of RMGC with other adsorbents.

Adsorbents	pH	Time	q_{\max} (mg/g)	References
Charcoal	—	~6 h	67.2	[21]
Fibrous clay minerals	4	24 h	85.5	[22]
Graphene/Fe ₃ O ₄ composites	2–11	20 min	43.82	[23]
Graphene/carbon nanotube	6–7	180 min	81.97	[24]
RMGC	6	120 min	89.28	This work

—, no information.

comparison of q_{\max} and experimental conditions of various adsorbents is given in Table 2.

4. Conclusions

The adsorbent of red mud-activated graphite composites (RMGC) was successfully prepared via electrochemical exfoliation of graphite in the mixture of RM slurry and (NH₄)₂SO₄ as an electrolyte and applied for the adsorption of methylene blue in aqueous solution. The optimal conditions for removal of MB were at pH 6 and 120 min. According to the Langmuir model, the maximum adsorption capacity was found to be 89.28 mg/g. The RMGC has proven to be an effective low-cost adsorbent for the removal

of MB, which could be studied extensively in order to apply it for wastewater treatment in the future.

Data Availability

No data were used to support this study.

Conflicts of Interest

The authors declare that there are no conflicts of interest regarding the publication of this paper.

References

- [1] M. Yusuf, F. M. Elfghi, S. A. Zaidi, E. C. Abdullah, and M. A. Khan, "Applications of graphene and its derivatives as an adsorbent for heavy metal and dye removal: a systematic and comprehensive overview," *RSC Advances*, vol. 5, no. 62, pp. 50392–50420, 2015.
- [2] M. Dezfoulian, F. Rashchi, and R. K. Nekouei, "Synthesis of copper and zinc oxides nanostructures by brass anodization in alkaline media," *Surface and Coatings Technology*, vol. 275, pp. 245–251, 2015.
- [3] B. Hameed, A. Din, and A. Ahmad, "Adsorption of methylene blue onto bamboo-based activated carbon: kinetics and equilibrium studies," *Journal of Hazardous Materials*, vol. 141, no. 3, pp. 819–825, 2007.
- [4] P. T. P. Hoa, S. Managaki, N. Nakada et al., "Antibiotic contamination and occurrence of antibiotic-resistant bacteria in aquatic environments of northern Vietnam," *Science of the Total Environment*, vol. 409, no. 15, pp. 2894–2901, 2011.
- [5] D. K. Padhi, K. M. Parida, and S. K. Singh, "Mechanistic aspects of enhanced Congo red adsorption over graphene oxide in presence of methylene blue," *Journal of Environmental Chemical Engineering*, vol. 4, no. 3, pp. 3498–3511, 2016.
- [6] O. Legrini, E. Oliveros, and A. M. Braun, "Photochemical processes for water treatment," *Chemical Reviews*, vol. 93, no. 2, pp. 671–698, 1993.
- [7] N. Nasuha and B. H. Hameed, "Adsorption of methylene blue from aqueous solution onto NaOH-modified rejected tea," *Chemical Engineering Journal*, vol. 166, no. 2, pp. 783–786, 2011.
- [8] M. Starowicz and B. Stypuła, "Electrochemical synthesis of ZnO nanoparticles," *European Journal of Inorganic Chemistry*, vol. 2008, no. 6, pp. 869–872, 2008.
- [9] S. Wang, Y. Boyjoo, A. Choueib, and Z. H. Zhu, "Removal of dyes from aqueous solution using fly ash and red mud," *Water Research*, vol. 39, no. 1, pp. 129–138, 2005.
- [10] P. C. C. Faria, J. J. M. Órfão, and M. F. R. Pereira, "Adsorption of anionic and cationic dyes on activated carbons with different surface chemistries," *Water Research*, vol. 38, no. 8, pp. 2043–2052, 2004.
- [11] Y. Li, M. van Zijll, S. Chiang, and N. Pan, "KOH modified graphene nanosheets for supercapacitor electrodes," *Journal of Power Sources*, vol. 196, no. 14, pp. 6003–6006, 2011.
- [12] J. G. S. Moo, B. Khezri, R. D. Webster, and M. Pumera, "Graphene oxides prepared by hummers', hofmann's, and staudenmaier's methods: dramatic influences on heavy-metal-ion adsorption," *ChemPhysChem*, vol. 15, no. 14, pp. 2922–2929, 2014.
- [13] D. N. H. Tran, S. Kabiri, L. Wang, and D. Losic, "Engineered graphene-nanoparticle aerogel composites for efficient removal of phosphate from water," *Journal of Materials Chemistry A*, vol. 3, no. 13, pp. 6844–6852, 2015.

- [14] T.-T.-N. Nguyen and J. L. He, "Preparation of titanium monoxide nanopowder by low-energy wet ball-milling," *Advanced Powder Technology*, vol. 27, no. 4, pp. 1868–1873, 2016.
- [15] T. Kim, G. Jung, S. Yoo, K. S. Suh, and R. S. Ruoff, "Activated graphene-based carbons as supercapacitor electrodes with macro- and mesopores," *ACS Nano*, vol. 7, no. 8, pp. 6899–6905, 2013.
- [16] H. S. Altundoğan, S. Altundoğan, F. Tümen, and M. Bildik, "Arsenic adsorption from aqueous solutions by activated red mud," *Waste management*, vol. 22, no. 3, pp. 357–363, 2002.
- [17] M. P. Elizalde-González, J. Mattusch, W.-D. Einicke, and R. Wennrich, "Sorption on natural solids for arsenic removal," *Chemical Engineering Journal*, vol. 81, no. 1–3, pp. 187–195, 2001.
- [18] S. J. Palmer, M. Nothling, K. H. Bakon, and R. L. Frost, "Thermally activated seawater neutralised red mud used for the removal of arsenate, vanadate and molybdate from aqueous solutions," *Journal of Colloid and Interface Science*, vol. 342, no. 1, pp. 147–154, 2010.
- [19] K. Parvez, Z.-S. Wu, R. Li et al., "Exfoliation of graphite into graphene in aqueous solutions of inorganic salts," *Journal of the American Chemical Society*, vol. 136, no. 16, pp. 6083–6091, 2014.
- [20] A. C. Ferrari, J. C. Meyer, V. Scardaci et al., "Raman spectrum of graphene and graphene layers," *Physical Review Letters*, vol. 97, no. 18, article 187401, 2006.
- [21] F. Banat, S. Al-Asheh, R. Al-Ahmad, and F. Bni-Khalid, "Bench-scale and packed bed sorption of methylene blue using treated olive pomace and charcoal," *Bioresource Technology*, vol. 98, no. 16, pp. 3017–3025, 2007.
- [22] M. Hajjaji, A. Alami, and A. E. Bouadili, "Removal of methylene blue from aqueous solution by fibrous clay minerals," *Journal of Hazardous Materials*, vol. 135, no. 1–3, pp. 188–192, 2006.
- [23] L. Ai, C. Zhang, and Z. Chen, "Removal of methylene blue from aqueous solution by a solvothermal-synthesized graphene/magnetite composite," *Journal of Hazardous Materials*, vol. 192, no. 3, pp. 1515–1524, 2011.
- [24] L. Ai and J. Jiang, "Removal of methylene blue from aqueous solution with self-assembled cylindrical graphene-carbon nanotube hybrid," *Chemical Engineering Journal*, vol. 192, pp. 156–163, 2012.

Research Article

Enhancing Activity of Pd-Based/rGO Catalysts by Al-Si-Na Addition in Ethanol Electrooxidation in Alkaline Medium

Minh Dang Nguyen , Lien Thi Tran, Quang Minh Nguyen, Thao Thi Nguyen, and Thu Ha Thi Vu 

Key Laboratory for Petrochemical and Refinery Technologies, No. 2, Pham Ngu Lao Street, Hoan Kiem District, Hanoi 100000, Vietnam

Correspondence should be addressed to Minh Dang Nguyen; nmd.hd.bk.13@gmail.com and Thu Ha Thi Vu; ptntd2004@yahoo.fr

Received 21 February 2019; Revised 30 May 2019; Accepted 12 June 2019; Published 23 June 2019

Guest Editor: Thanh-Dong Pham

Copyright © 2019 Minh Dang Nguyen et al. This is an open access article distributed under the Creative Commons Attribution License, which permits unrestricted use, distribution, and reproduction in any medium, provided the original work is properly cited.

The article presents modified Pd-based catalysts supported on reduced graphene oxide (rGO), used in the electrooxidation reaction of ethanol in alkaline medium. When NaBH_4 reducing agent was used, the random presence of Na was found out. According to this result, Na was used as a promoter of Pd-based catalyst. Consequently, the Al-Si-Na addition not only assisted active phase Pd nanoparticles to disperse homogeneously on graphene support, but also contributed to increase catalytic activity in the reaction. This value, $16138 \text{ mA}\cdot\text{mg}^{-1}_{\text{Pd}}$, is about 1.5 times higher than that of the catalyst modified by Al-Si. Moreover, the stability of the catalyst is enhanced more. The electrochemical stability of PASGN.N catalyst was relatively good: after 500 scanning cycles, the current density diminished 32% compared with the highest peak current density of the 15th cycle, which was chosen as a reference. These significant improvement results in electrooxidation of ethanol have opened up the high potential application of these catalysts in direct-ethanol fuel cell.

1. Introduction

Nowadays, the direct ethanol fuel cell (DEFC) is one of the potential options for use in portable electronic devices, storage, and small electrical appliances. DEFC has high energy efficiency, remarkable efficiency in energy conversion, low temperature in operation, and considerable poison gas emissions. Moreover, producing ethanol from agricultural products and biomass fermentation process on a large scale is widely carried out [1, 2]. However, in DEFC, noble metal-based catalysts, despite their good activity, are highly costly and easily poisoned by the adsorption process of the intermediate compounds formed during electrooxidation of ethanol. In addition, the electrode kinetics are sluggish [3, 4].

In the noble metal group, Pd and Pt had similar structure and electrochemical properties. However, for the electrooxidation of ethanol, Pd showed more advantages in comparison with Pt by the better resistance in alkaline

medium, faster anionic film exchange capacity, and higher possibility of combination with other metals or transition metal oxides.

Some Pd-based catalysts such as Pd-Co [5], Pd-Ni [6–8], Pd-Ni-Sn [9], Pd-Ru-Ni [10], Pd-Cu [11], Pd-Au [12], Pd-Ag [13], or Pt-Pb [14] have been studied to minimize Pd content and poisoning effect in high electrochemical activity of remaining Pd. According to various researches, the presence of transition metals such as Co and Ni, provided $\text{M-ROH}_{\text{ads}}$ or formed M-(ROH)_x species (where M is the metal atom, ROH are methanol or ethanol), which changed the ethanol adsorption ability and enhanced the adsorption process of intermediate CHO_{ads} , CO_{ads} , limiting the poisoning process and thus improving the catalytic activity [5–7, 9, 10].

On the other hand, choosing the support for Pd-based catalyst is an important factor that affects the electrochemical activity of catalyst. Carbon nanotubes (CNTs) and carbon black (Vulcan XC-72) are commonly used as support [15–18]. Recently, graphene materials have been attracting a

high attention because of their advantages of physical and chemical properties such as electrical conductivity and a very high surface area ($\sim 2630 \text{ cm}^2\text{-g}^{-1}$) [19]. And, more especially, graphene enhances the dispersion of active metal particles.

In a recent research of Tan and colleagues [20], it was observed that the combination of Pd and Ni on graphene remarkably augmented catalytic activity of electrooxidation of ethanol in alkaline medium in comparison with PdNi/C and Pd-Ni catalysts. Liu et al. [21] obtained similar results at the same conditions of the catalytic test for catalyst of MnO_2 -promoted Pd supported on graphene oxide (GO) and multiwalled carbon nanotubes. This was explained by the few-layer structure, a high conductivity, and the large accessible area of GO which enhanced the interaction and dispersion of the Pd-active phase on graphene surface. In addition, GO also contains oxygen-functional groups which are the combination site of metal ions, thereby increasing catalytic stability in the electrolyte medium.

In our paper [22], Si-Al was a very good bimetallic promoter phase in modified catalyst based on Pt/rGO in methanol electrooxidation. The results in this paper showed that modified Pt-rGO with 7% Si-Al was the best catalyst which had the highest activity in methanol electrooxidation with more than $1700 \text{ mA}\cdot\text{mg}^{-1}\text{Pt}$ current density. The Al and Si compounds obtained in the catalyst exist as pseudo-boehmite (AlOOH) and silica (SiO_2), and they improve dispersion of the active phase on GO surface.

In this article, the preparation of Pd/rGO-based catalysts modified by promoters such as Al, Si, Al-Si, and Al-Si-Na and reduced by NaBH_4 and ethylene glycol (EG) was reported. These catalysts are intended to be used as an anode catalyst for DEFC. These catalysts modified by promoters exhibited high activity in electrooxidation of ethanol in alkaline medium, and a highly improved resistance against poisoning of intermediary compounds in comparison with non-modified Pd/rGO catalysts.

2. Materials and Methods

2.1. Chemicals. Exfoliated graphite was provided by SGL Carbon GmbH (GFG). Tetraethyl orthosilicate (TEOS) 99%, aluminum tri-isopropoxide 99.9%, CH_3COONa 99%, NaOH 98.8%, H_2SO_4 96%, and ethanol 99.9% were purchased from Merck. And, Nafion® solution (whose mass fraction is 5%), ethylene glycol (EG), sodium borohydrite (NaBH_4), isopropanol (IPA) 99.5%, and PdCl_2 99% were purchased from Sigma Aldrich. The nitrogen gas of high purity (99.95% (Air Liquide)) and deionized water were used in all experiments.

2.2. Catalyst Preparation and Characterization. GO slurry synthesized by the modified Hummers' method [23] was diluted to the content of $5 \text{ mg}\cdot\text{mL}^{-1}$. Several catalysts based on graphene-supported palladium modified by metallic promoters were prepared in this study.

Sample of 28.57% Pd by active metal loadings (theoretically calculated, denoted as PG.E) and sample of 26.40% Pd-7.60% Na (PNG.E) made from GO, EG, CH_3COONa ,

and PdCl_2 were synthesized in the similar way of preparation of 40% Pt/rGO following a procedure described in [22].

In this catalyst, theoretical total mass fraction of Al and Si was 4.76% and mass fraction of Pd was 27.21%. The PdAlSiNa/rGO catalyst was reduced by EG as PASG.E catalyst with the addition of CH_3COONa precursor (whose mass fraction of Na is 7.26%) during the synthesis (denoted as PASNG.E).

The PdAl/rGO and PdSi/rGO catalysts reduced by EG (PAG.E and PSG.E) were synthesized in the similar way of preparation of PASG.EG catalysts but in absence of Si or Al precursors during synthesis, respectively. The theoretical elemental composition is 4.76 wt% of Al and 27.21 wt% of Pd in PAG.E catalyst, and 4.76 wt% of Si and 27.21 wt% of Pd in PSG.E catalyst.

All catalysts reduced by NaBH_4 are Pd/rGO, PdNa/rGO, PdAlSi/rGO, and PdAlSiNa/rGO, respectively, were denoted as PG.N, PNG.N, PASG.N, and PASGN.N. The PASGN.N catalyst synthesis process was performed as follows: a precursor mixture of 18.8 mL of PdCl_2 0.01 M and 10 mL of the solution GO $5 \text{ mg}\cdot\text{mL}^{-1}$ was mixed and ultrasonicated for 2 min before adding 8.2 mg Al-isopropoxide, 2 mL IPA, 20 μL TEOS, and 34 mg CH_3COONa . The obtained mixture was sonicated by probe ultrasonic for 2 min. Then, 20 mL of NaBH_4 0.15 M was slowly added into the mixture for 15 min. The reaction mixture was continuously stirred for 15 h before being washed with distilled water. The final product was dried by using a vacuum oven at 80°C for 2 h. The PG.N, PNG.N, and PASG.N catalysts were synthesized by the same method as above with the addition of corresponding precursors.

Transmission electron microscope (TEM) JEOL JEM 2010 and scanning electron microscope (SEM) in a S-4800 microscope (Hitachi, Japan) were used to investigate the morphology and microstructure of catalysts. A LabRam HR (Horiba Jobin Yvon) spectrometer was operated to record Raman spectra. A KRATOS Axis Ultra DLD spectrometer was applied to perform the XPS analyser. The ICP-OES analyses were performed after pretreatment of the samples, in an ICP-OES ACTIVA (Horiba Jobin Yvon). The infrared spectrum of the samples, in the wavelength range of $400\text{--}4000 \text{ cm}^{-1}$, was measured on a Tensor 27-Bruker FTIR spectrometer. XRD patterns of the catalysts were measured on a D8 Advance (Bruker) apparatus. The process of these measurement preparations was clearly presented in [22].

2.3. Electrochemical Measurement. Electrochemical measurements were performed on a PGS-ioc-HH12 Potentiostat/Galvanostat electrochemical workstation (Institute of Chemistry—Vietnam Academy of Science and Technology). All experiments were conducted in a three-electrode system at room temperature: a glassy carbon working electrode (whose diameter is 5 mm), a platinum counterelectrode, and an Ag/AgCl reference electrode. The procedure of preparing catalyst ink was similar to the one described in [22]. The catalyst ink was prepared by dispersing 2 mg of the catalyst powder in a mixture containing 0.9 mL ethanol and 0.1 mL Nafion solution 5 wt % under sonication for 30 min.

Electrochemical active surface area (EASA) measurements were carried out in 0.5 M NaOH aqueous solutions at a scan rate of $50 \text{ mV}\cdot\text{s}^{-1}$, in the potential range of -0.8 V to 0.5 V .

Cyclic voltammetry was carried out in (NaOH 0.5 M + $\text{C}_2\text{H}_5\text{OH}$ 1 M) aqueous solutions at a scan rate of $50 \text{ mV}\cdot\text{s}^{-1}$, in the potential range of -0.8 V to 0.5 V . The chronoamperometric curves for the catalysts were recorded in a (NaOH 0.5 M + $\text{C}_2\text{H}_5\text{OH}$ 1 M) solution at a constant potential value of -0.25 V (vs. Ag/AgCl) for 4000 s.

3. Results and Discussion

Cyclic voltammograms and chronoamperometry curves in a (NaOH 0.5 M + $\text{C}_2\text{H}_5\text{OH}$ 1 M) solution at a room temperature for ethanol electrooxidation on Pd/rGO-based catalysts modified by different metals in ethylene glycol environment were introduced in Figure 1 and Table 1.

From the catalytic activity evaluation results for catalysts reduced by EG during synthesis, Pd-based catalyst that is nonmodified (PG.E) clearly showed a lower electrooxidation activity of ethanol than Pd-based catalyst modified by metal (see Figure 1(a)). Specifically, in alkaline medium, the activity of the catalysts is in ascending order as follows: PG.E ($5369 \text{ mA}\cdot\text{mg}^{-1}_{\text{Pd}}$) < PAG.E ($5374 \text{ mA}\cdot\text{mg}^{-1}_{\text{Pd}}$) \approx PSG.E ($5574 \text{ mA}\cdot\text{mg}^{-1}_{\text{Pd}}$) < PASG.E ($7822 \text{ mA}\cdot\text{mg}^{-1}_{\text{Pd}}$) (see Table 1).

On the other side, the forward scanning peak current density (or called anodic current density)— I_F —means current density of ethanol electrooxidation on the electrode surface. And, the reverse scanning peak current density (or called cathodic current density) means current density in reduction of the oxygen group on the electrode surface. If I_F/I_R ratio and I_F are higher, ethanol electrooxidation on electrode surface will happen more completely [24–27]. Therefore, in alkaline medium, the Pd-based catalysts modified by monometallic such as Al and Si showed only a slight improvement of catalytic activity in comparison with PG.E (see Table 1). Meanwhile, the one modified by bimetallic Al-Si (PASG.E) showed a significant increase in activity, which indicates a positive synergistic effect with Pd of two metals.

Some intermediate species such as CHO_{ads} and CO_{ads} formed during the ethanol electrooxidation poisoned the catalysts, which explained why all catalysts display an initial fast current decay in the chronoamperometry test (see Figure 1(b)). It is noted that the PASG.E catalyst exhibited better activity and resistance against poisoning by intermediate compounds in comparison with other catalysts reduced by EG during synthesis. After 4000 s of working, the current density of the PASG.E catalyst was $104.4 \text{ mA}\cdot\text{mg}^{-1}_{\text{Pd}}$, significantly higher than that of PG.E catalysts ($21.6 \text{ mA}\cdot\text{mg}^{-1}_{\text{Pd}}$), PAG.E ($48.1 \text{ mA}\cdot\text{mg}^{-1}_{\text{Pd}}$), and PSG.E ($34.35 \text{ mA}\cdot\text{mg}^{-1}_{\text{Pd}}$). These remarkable results may be explained by the presence of pseudoboehmite (AlOOH) and silica (SiO_2) that preferentially prevented the adsorption of toxic intermediate and/or formed products on the surface of catalyst, leading to the increase in the number of available catalytic site for reactants.

Thus, the addition of the metal as promoter phase in general, and the bimetallic phase Al-Si in particular, increased the electrochemical activity and also significantly improved resistance against poisoning of intermediate compounds of Pd/rGO catalysts reduced by EG agent.

The content of noble metals and other elements in the catalysts was determined by the ICP-OES characterization and shown in Table 2. It is interesting to note that the mass fraction of Pd found in most catalysts is approximately 10%, compared to the theoretical value of Pd ranging from 25% to 28%. The mass fraction of other metals was measured from 0.2% to 2.7%. The Pd loading of the catalysts reduced by NaBH_4 is higher than that reduced by EG. Especially, the ICP-OES measurement showed the presence of Na in all catalysts reduced by NaBH_4 .

The valence state and surface composition of PASG.N catalyst were determined by X-ray photoelectron spectroscopy (XPS) measurements (see Figure 2). Figure 2(a) presents the XPS spectrum included the characteristic peaks of C 1s, O 1s, Al 2s, Al 2p, Si 2s, and Si 2p. Accordingly, Al and Si existing at the Al and Si compounds obtained in the catalysts exist as pseudoboehmite (AlOOH) and amorphous silica (SiO_2) [22]. In addition, a characteristic peak of Pd 3d is also observed on the spectrum. Especially, the random appearance of Na 1s and Na KLL that corresponds with the ICP results may be an important factor to augment activity of PASG.N catalyst.

Moreover, an intense peak of the C 1s core level was observed in the XPS spectrum of rGO (see Figure 2(c)). After the deconvolution, two major peaks were identified and assigned as $\text{sp}^2 \text{ C}=\text{C}$ at 284.4 eV (due to the graphitic carbon), $\text{sp}^3 \text{ C}-\text{O}$ at 285.8 eV and 289.4 eV (due to the hydroxyl and epoxy groups with graphene framework) [28].

Figure 2(b) shows the Pd 3d core level XPS spectrum of PASG.N catalyst which is resolved into $3d_{5/2}$ and $3d_{3/2}$ doublets caused by spin-orbital coupling [28]. The Pd 3d signals for catalysts can be deconvoluted into two pairs of doublets, which can be attributed to metallic Pd (0) and Pd (II). The deconvolution energies for Pd (0) and Pd (II) were at 335.7 and 340.9 eV, and 336.7 eV and 342.6 eV, respectively. Metallic Pd phase was proved to be the major contribution as the intensities of Pd (II) were quite lower than those of Pd (0). It means that reducing from Pd (II) to Pd (0) reaction has happened successfully.

Besides, the relative signal intensities of Pd (0) and Pd (II) of PASG.N catalyst were different, 53.56% and 37.81%, respectively. In addition, the Pd weight density on the catalyst surface was 8.23%, while that of Al, Si, and Na was 2.38%, 3.44%, and 2.19%, respectively, which are similar to ICP results. It means that Pd nanoparticles were dispersed evenly both inside and outside of the catalyst. Moreover, the ratio between Pd (0) and Pd (II) PASG.N in XPS result of PASG.N, approximately 1.41, is higher than that of PASG.E, approximately 1.01. This may be a cause of the different electrochemical activity of these catalysts.

In fact, when the agent NaBH_4 was used instead of EG, the catalyst presented more catalytic activity and resistance against poisoning of intermediate compounds. Specifically, with the bimetallic Al-Si promoter phase, catalyst reduced by

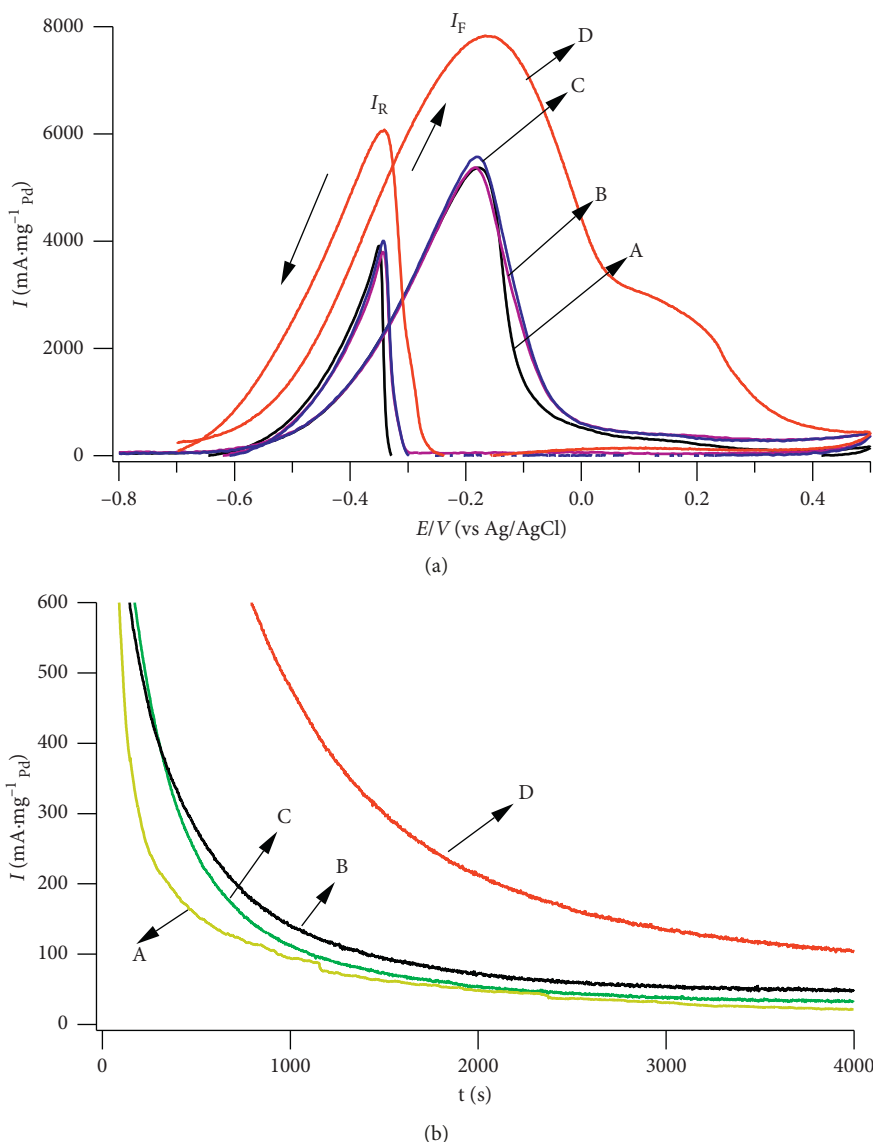


FIGURE 1: CV (a) and CA curves (b) of (A) PGE, (B) PAGE, (C) PSGE, and (D) PASGE catalysts in a (NaOH 0.5 M + C₂H₅OH 1 M) solution at a scan rate of 50 mV·s⁻¹.

TABLE 1: CV results of Pd/rGO-based catalysts after 15 scanning cycles in a (NaOH 0.5 M + C₂H₅OH 1 M) solution at a scan rate of 50 mV·s⁻¹.

Catalyst	I_F (mA·mg ⁻¹ _{Pd})	I_R (mA·mg ⁻¹ _{Pd})	I_F/I_R
PGE	5369	3915	1.37
PAGE	5374	3799	1.41
PSGE	5574	4010	1.39
PNGE	6988	5273	1.33
PASGE	7822	6111	1.28
PASNGE	8800	4367	2.02
PG.N	7457	3967	1.88
PNG.N	8357	4687	1.78
PASG.N	10705	5531	1.94
PASGN.N	16138	7949	2.03

NaBH₄ (PASG.N) showed 1.4 times higher activity than by EG (PASGE) (see Table 1). In addition, after 4000 s of working, the current density of the PASG.N catalyst was 6.5

times higher than that of PASGE. Furthermore, both electrochemical activity and the ratio of the forward scanning peak current density to the reverse scanning peak current density, (I_F/I_R) of the PASG.N catalyst (1.93), were also higher than those of the PASGE catalyst (1.28). Consequently, NaBH₄ could be a better agent for Pd-based catalyst reduction than EG.

Na presence may cause increasing adsorption of oxygen and fuel on surface of the catalyst [29], which brings out increase of catalytic activity. To evaluate the role of Na, the electrochemical activity of catalysts with and without addition of Na during synthesis for both EG and NaBH₄ reducing agents was investigated (see Figure 3(a) and Table 1). It is obvious that whatever reducing agents were used during synthesis (EG or NaBH₄), all Na-doped catalysts showed significantly higher electrocatalytic activity compared with the non-Na-doped catalysts. Therefore, the role of promoter of Na was completely independent of the effect of the

TABLE 2: ICP-OES results of Pd/rGO-based catalysts reduced by EG and NaBH₄.

Catalysts	Elemental mass fraction by ICP-OES measurement		Theoretical elemental mass fraction	
	Pd (%)	Other metal (%)	Pd (%)	Other metals (%)
PG.E	8.53	—	28.57	—
PNG.E	7.51	2.52 (Na)	26.40	7.61 (Na)
PAG.E	8.03	2.33 (Al)	26.40	7.61 (Al)
PSG.E	7.86	2.54 (Si)	26.40	7.61 (Si)
PASG.E	8.34	0.34 (Al); 2.15 (Si)	27.20	1.36 (Al); 3.42 (Si)
PASGN.E	7.57	2.40 (Na); 0.27 (Al); 2.30 (Si)	25.23	7.25 (Na); 1.26 (Al); 3.15 (Si)
PG.N	9.71	0.15 (Na)	28.57	—
PNG.N	9.21	2.72 (Na)	26.40	7.61 (Na)
PASG.N	8.78	0.34 (Al); 2.41 (Si); 0.12 (Na)	27.20	1.36 (Al); 3.42 (Si)
PASGN.N	8.54	2.62 (Na); 0.29 (Al); 1.83 (Si)	25.23	7.25 (Na); 1.26 (Al); 3.15 (Si)

reducing agent on the electrooxidation of ethanol. Moreover, the results obtained are also consistent with previous conclusions: catalysts modified by the Al-Si system owned a superior activity in comparison with Pd/rGO catalysts and catalysts reduced by NaBH₄, whose activities are much higher than those reduced by EG.

Besides, the poisoning resistance capacity of these catalysts in the electrochemical ethanol oxidation in alkaline mediums estimated by chronoamperometry (CA) (see Figure 3(b)) provided the same results. After 4000 s of working, the PASGN.N catalytic current density reached 680 mA·mg⁻¹_{Pd} ($I_F^{4000} \sim 32.27\%$ compared with the value of CA- I_F^0 at the beginning), 2.36 times higher than non-Na-doped PASG.N catalyst ($I_F^{4000} \sim 17.85\% \cdot I_F^0$), and 6.1 times higher than Na-doped PASNG.E reduced by EG ($I_F^{4000} \sim 15.64\% \cdot I_F^0$). Consequently, Na presence may assist the Pd-base catalysts in enhancing the resistance against poisoning of intermediate compounds in ethanol electrooxidation in alkaline media.

Figure 4 presents Raman spectra of GO and PASG.N catalyst. The peak intensities of the G band (I_G) at ~ 1600 cm⁻¹ corresponding to the sp²-hybrid carbon state in the hexagonal lattice of graphite and the D band (I_D) at 1350 cm⁻¹ being characteristic for the vibration of sp³-hybrid C in the disorder structure of graphene sheets are clearly presented in [22]. The Raman spectra of catalysts were also similar to those of GO, but the intensity of I_D/I_G ratio of catalyst increased in the following order: GO (0.92) < PASG.N (1.02) < PASGN.N (1.10) < PASG.E (1.98). In addition, $I_D > I_G$ due to the presence of defects as well as the presence of Pd cluster, of metal or metal oxides on the graphene support [20, 30, 31]. This confirmed that the catalyst synthesis using chemical reduction process removes effectively the functional groups containing oxygen on the GO surface to form rGO.

FT-IR spectra of catalysts are shown in Figure 5. In the infrared spectra of graphene oxide, there are some

characteristic vibration bands containing oxygen groups such as O-H near 3500 cm⁻¹ and around 1400 cm⁻¹, C=O at 1760 cm⁻¹, and C-O around 1100 cm⁻¹, respectively. However, in that of PASGN.N catalyst, intensity of these peaks was reduced clearly. Moreover, the presence of C=C bond near 1600 cm⁻¹ was found out in the catalyst. Consequently, the reduction from GO to rGO was successful.

TEM images of the catalysts are introduced in Figure 6. The average particles size d_n was calculated from particle size distribution using the following equation [32]:

$$d_n = \frac{\sum n_k d_k}{\sum n_k}, \quad (1)$$

where n_k is the frequency of occurrence of particles with size d_k from the TEM images.

The result showed that a less uniform and sparse dispersion of metallic nanoparticles are described for the catalysts. In addition, the PASG catalysts reduced by both EG and NaBH₄ have a quite homogenous dispersion of active phase (dark spherical particles on rGO surface), but their sizes are different. For example, the PASG.N and PASGN.N catalysts (reduced by NaBH₄) have their activity particle size from 7 nm to 14 nm, while that of PASG.E catalyst (reduced by ethylene glycol) was three times larger, about 20 nm to 36 nm. It means that reducing agent NaBH₄ is improving the size of the catalytic active phase particle. Furthermore, TEM images of the PASGN.N (Na-doped) (see Figure 6(c)) and PASG.N (non-Na-doped) (see Figure 6(b)) catalyst introduced that Na-doped significantly enhanced the dispersion of metallic nanoparticles on graphene support surface. The metal nanoparticles of PASGN.N catalysts expanded with higher density than those of PASG.N catalyst, which explained the increase in the number of active sites on the surface of graphene support, considerably enhancing the catalytic activity of electrooxidation of ethanol. Moreover, the metal

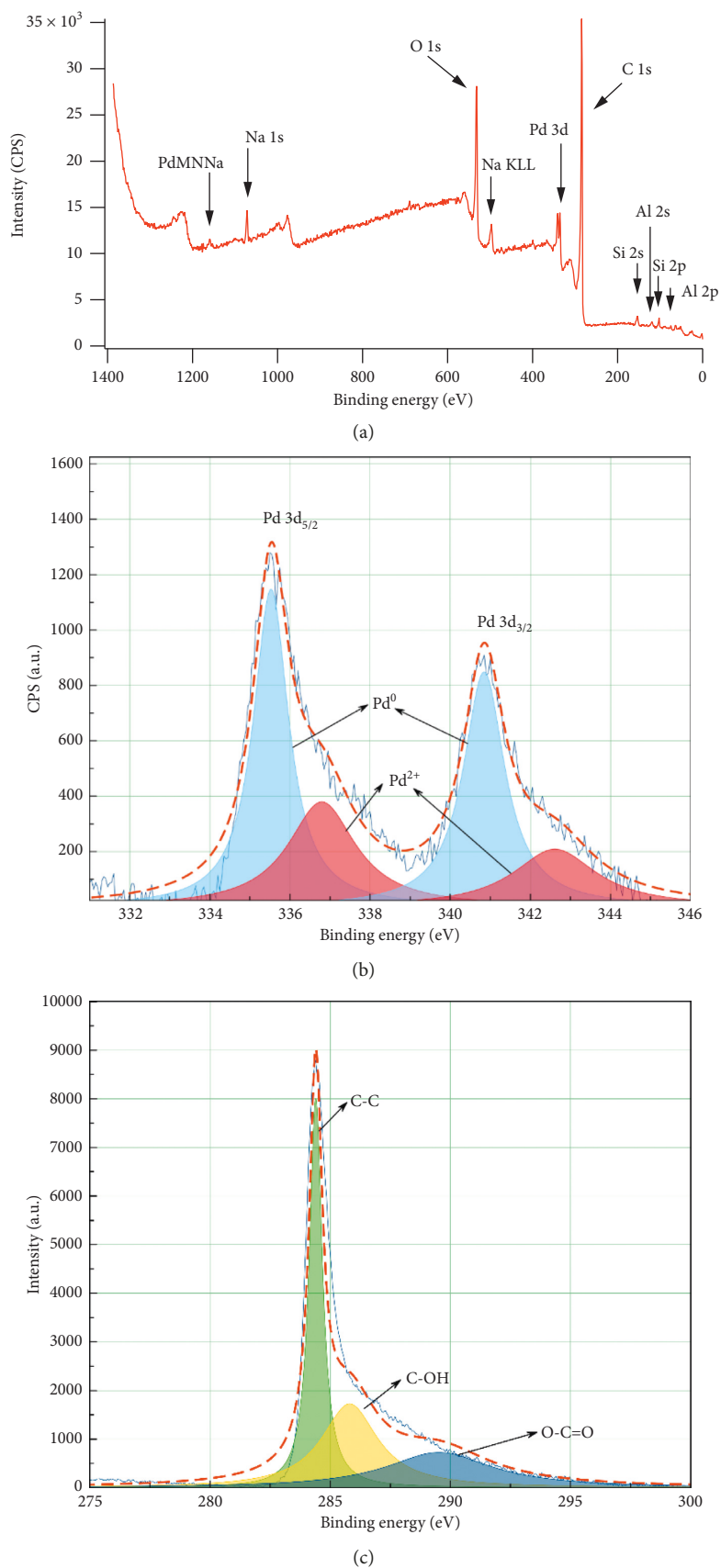


FIGURE 2: XPS spectrum (a), Pd 3d spectrum (b), and C 1s spectrum of the PASG.N catalyst (c).

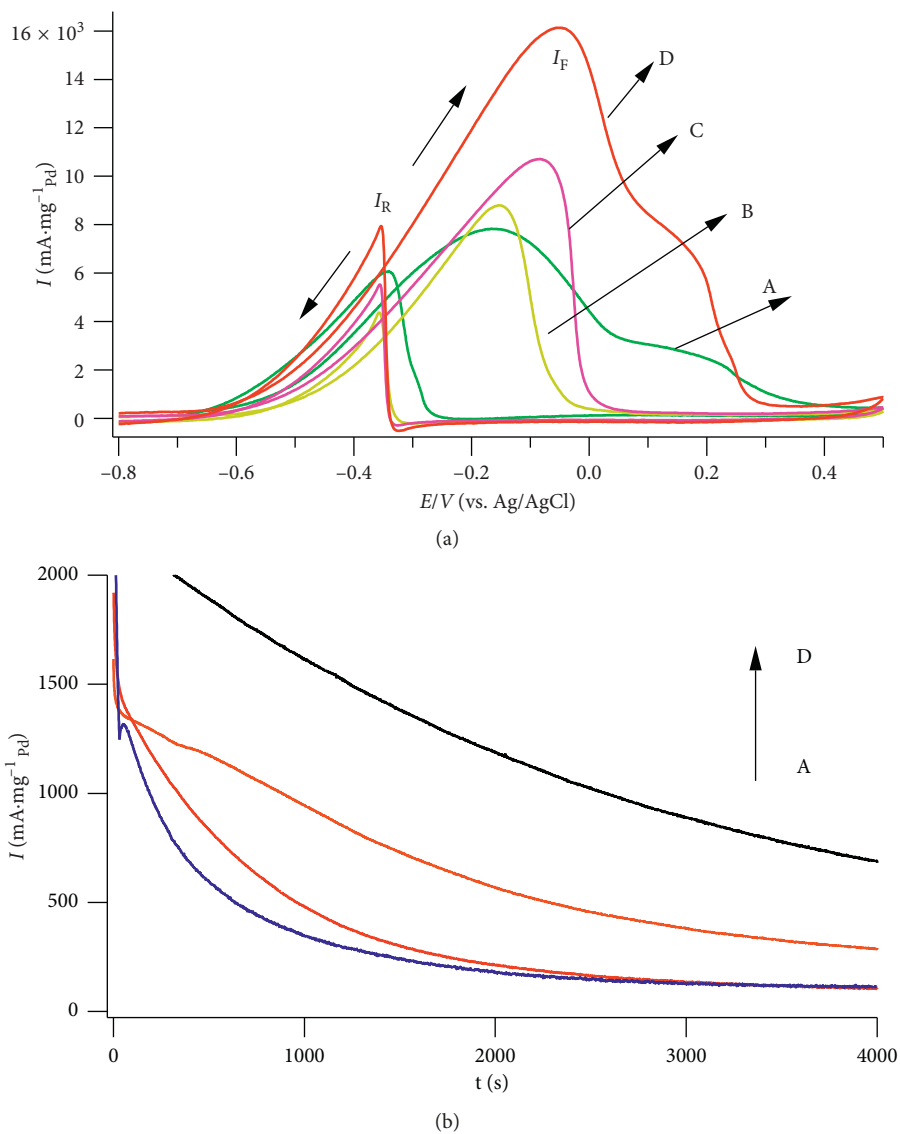


FIGURE 3: CV (a) and CA (b) curves of (A) PASG.E, (B) PASG.N.E, (C) PASG.N, and (D) PASG.N.N catalysts in a (NaOH 0.5 M + C₂H₅OH 1 M) solution at a scan rate of 50 mV·s⁻¹.

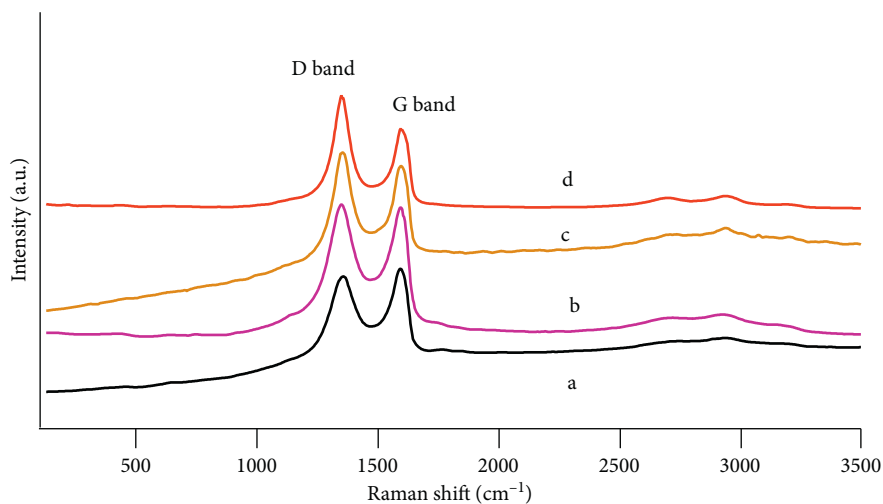


FIGURE 4: Raman spectra of (a) GO, (b) PASG.N, (c) PASG.N.N, and (d) PASG.E.

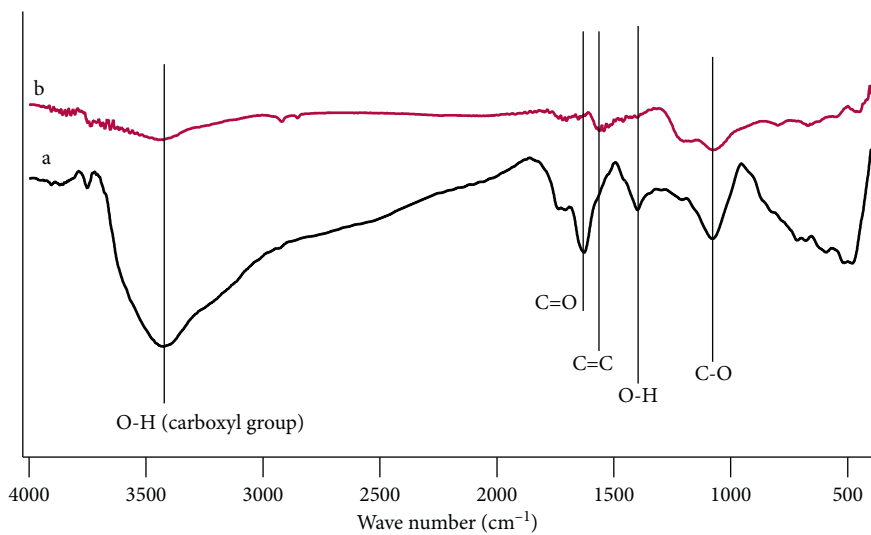


FIGURE 5: FTIR spectra of (a) GO and (b) PASGN.N.

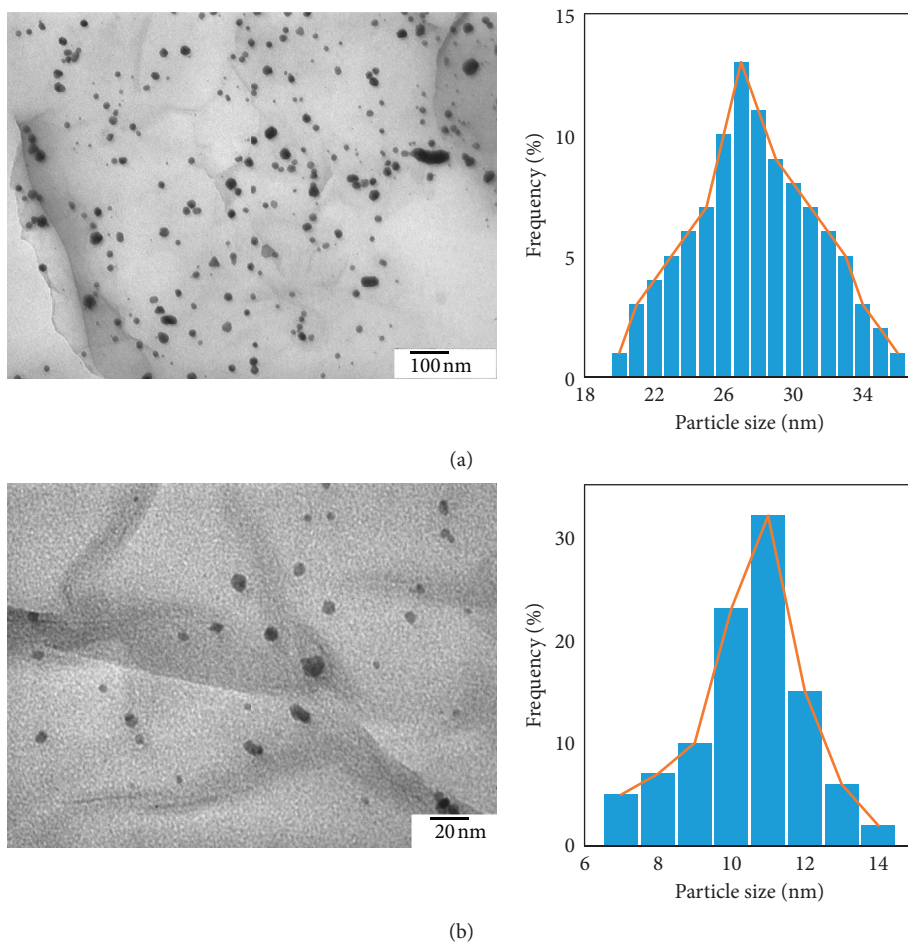


FIGURE 6: Continued.

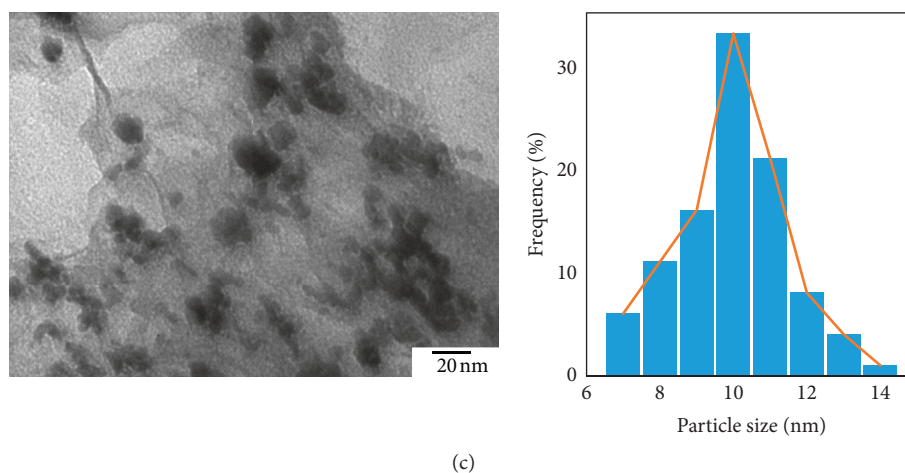


FIGURE 6: TEM images and particle size distributions of PASG.E (a), PASG.N (b), and PASGN.N (c) catalysts with different magnifications.

nanoparticles in the PASGN.N catalyst tend to aggregate from 2 to 3 particles to form larger ones at the edges of graphene sheets.

The EASA (electrochemical active surface area) of the Pd-based electrodes is determined by estimating the charge used in the reduction of palladium (II) oxide into palladium metal and using relation: $EASA = Q/S$, where Q is the Coulombic charge (in mC) and S is the proportionality constant which is taken $0.405 \text{ mC}\cdot\text{cm}^{-2}$ in the case of reduction of a monolayer of PdO [4]. Average particles size d_n and EASA are present in Table 3.

In fact, EASA of catalysts were in descending order as follows: PASG.E ($150.2 \text{ m}^2\cdot\text{g}^{-1}_{\text{Pd}}$) < PASG.N ($193.7 \text{ m}^2\cdot\text{g}^{-1}_{\text{Pd}}$) < PASGN.N ($207.6 \text{ m}^2\cdot\text{g}^{-1}_{\text{Pd}}$). This affection is similar to the TEM image described in Figure 6. The particles size is higher, the activity surface is lower [33].

On the other hand, the Na addition also improved stability of Pb-based catalyst in ethanol electrooxidation. In order to study the catalytic lifetime of PASGN.N and PASG.N catalyst in alkaline medium, 500 cycles of a successive sweep from -0.8 V to 0.5 V were carried out. The corresponding electrochemical activity results were noted in Table 4. The CV curve of the scanning cycles of PASGN.N catalyst was exhibited by the forward scanning peak current density in Figure 7. After the first 15 cycles to activate the catalysts, electrochemical activity of PASGN.N catalyst became stable. Therefore, the highest peak current density of the 15th cycle ($I_F 15^{\text{th}}$) was chosen as a reference. After 200 cycles, the electrochemical activity of the catalysts decreased quite slowly where $I_F 200^{\text{th}}$ was equal to 84% of the reference. The slow reactivity holds up to 500 cycles, where the forward current density value $I_F 500^{\text{th}}$ was equal to 68% of the reference. Similarly, the electrochemical activity of PASG.N also decreased as the number of sweep rounds increased. However, the rate of decreasing catalytic activity of PASG.N is faster than that of PASGN.N (see Table 4), where its 500th current density remained 27%.

Besides, the combination between active phase (Pd nanoparticles) and support, graphene can become more

TABLE 3: EASA result of catalyst.

Catalyst	Average particles size (nm)	EASA ($\text{m}^2\cdot\text{g}^{-1}_{\text{Pd}}$)
PASG.E	28.07	150.2
PASG.N	10.49	193.7
PASGN.N	9.97	207.6

sustainable under the presence of Al-Si-Na addition, which is observed on TEM images of the catalysts after 500 scanning cycles (see Figure 8). For instance, in case of PASGN.N, the metal particles tend to aggregate into clusters of very large size, from 60 nm to 130 nm, which dispersed in separate zones. The density of metallic nanoparticles on the graphene surface is also considerably reduced while that at the edges of graphene sheets tends to increase. However, in case of PASG.N catalyst, almost no metallic particles are presented on the surface of the graphene after 500 scanning cycles. This result is in accordance with the catalytic deactivation after 500 scanning cycles as described previously.

The morphology characteristic of PASGN.N catalyst before and after 500 scanning cycles were observed more clearly on the SEM image (see Figure 9). The result showed that the catalyst looked as a homogeneous “block;” however, it was broken to pieces after the reaction. Moreover, Figure 9(b) also shows the number of particles with columnar shape. It seems that the active phase Pd may be separated from support and may agglomerate after hundreds of cycles. As a result, catalytic activity was reduced.

Figure 10 presented XRD patterns of PASGN.N catalyst before and after 500 cycles of the reaction. The peak at 2θ value of 40.1° corresponding to the planes Pd (111) [34, 35] was shown in the pattern of catalyst before the reaction (see Figure 10(a)) while two peaks of planes PdO (110) and PdO (103) [35] were introduced in the catalyst after the reaction. Consequently, PdO crystal is forming during the reaction. This may be a cause of reduction of the catalytic activity.

TABLE 4: Forward current density of PASGN.N and PASG.N catalysts after 500 scanning cycles in a (NaOH 0.5 M + C₂H₅OH 1 M) solution at a scan rate of 50 mV·s⁻¹.

Catalyst	Forward current density I_F (mA·mg ⁻¹ _{Pd})							
	I_F 15 th	I_F 100 th	I_F 100 th / I_F 15 th	I_F 200 th	I_F 300 th	I_F 400 th	I_F 500 th	I_F 500 th / I_F 15 th
PASGN.N	16138	14175	0.88	13816	12751	12342	10864	0.68
PASG.N	10705	9100	0.85	8565	6884	4956	2884	0.27

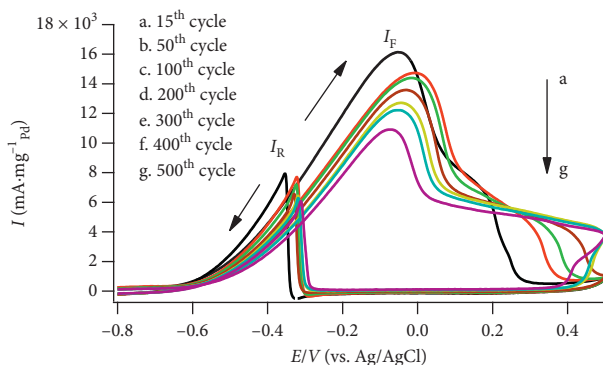


FIGURE 7: CV curves of catalytic PASGN.N after 500 scanning cycles in a (NaOH 0.5 M + C₂H₅OH 1 M) solution at a scan rate of 50 mV·s⁻¹.

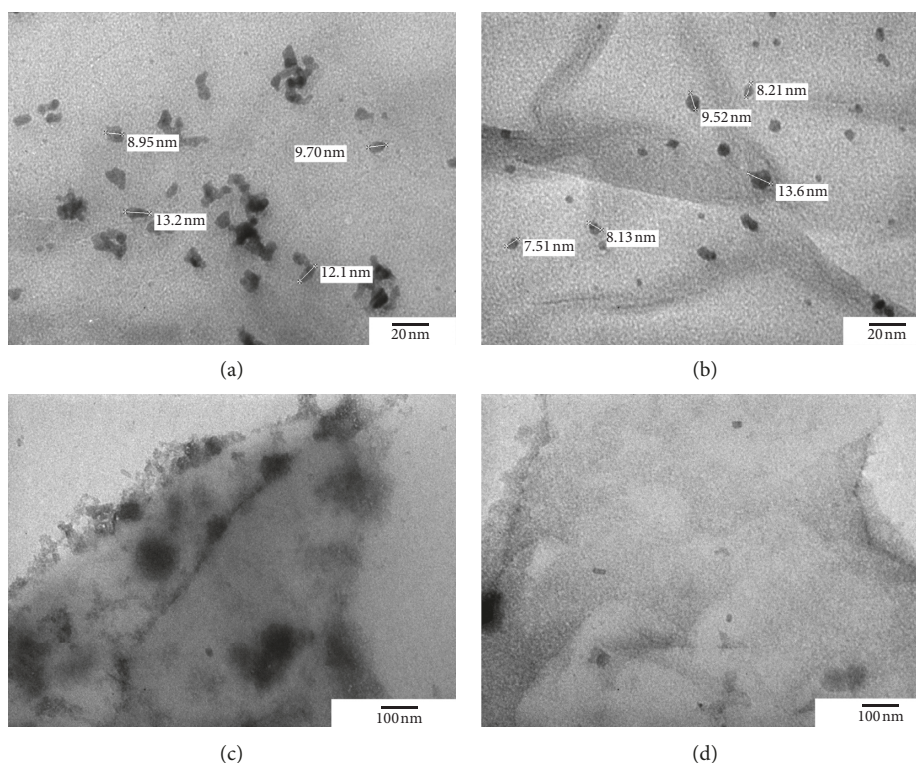


FIGURE 8: TEM images of PASGN.N and PASG.N catalysts before (a, b) and after 500 scanning cycles (c, d) in a (NaOH 0.5 M + C₂H₅OH 1 M) solution at a scan rate of 50 mV·s⁻¹.

4. Conclusion

In conclusion, electrooxidation of ethanol was carried out on several Pd-based bimetallic or multimetallic catalysts

supported on graphene. For all catalysts investigated, the role of promoting agents was confirmed when catalytic activity was enhanced in the presence of Al, Si, Al-Si, and Al-Si-Na. In addition, in comparison with the reducing

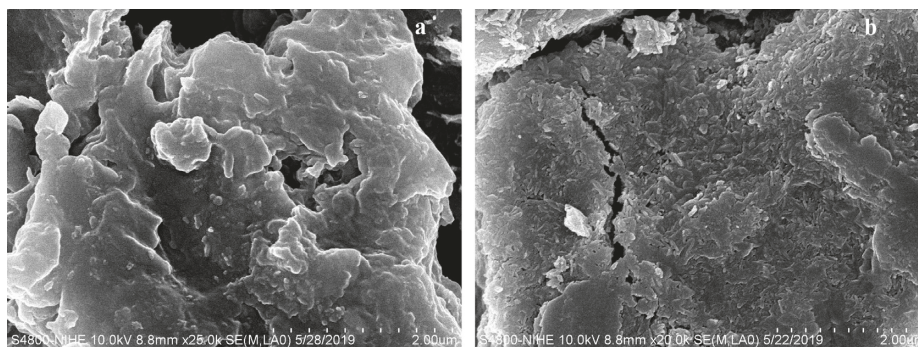


FIGURE 9: SEM images of PASGN.N catalysts before (a) and after (b) 500 scanning cycles in a (NaOH 0.5 M + C₂H₅OH 1 M) solution at a scan rate of 50 mV·s⁻¹.

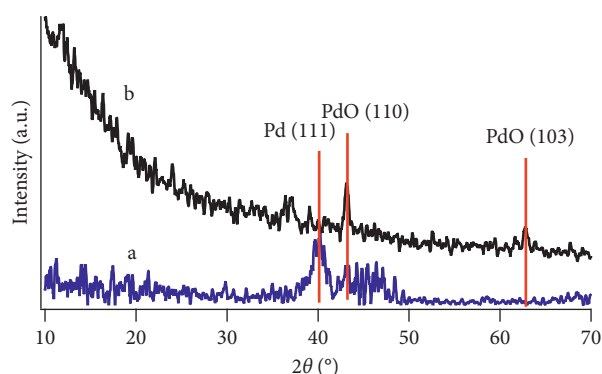


FIGURE 10: XRD patterns of PASGN.N catalysts before (a) and after (b) 500 scanning cycles in a (NaOH 0.5 M + C₂H₅OH 1 M) solution at a scan rate of 50 mV·s⁻¹.

agent EG during synthesis, NaBH₄ significantly not only improved the dispersion of metal nanoparticles on the support surface but also reduced crystalline size. As a result, catalytic electrochemical activity was increased. Specifically, PASGN.N catalysts presented the superior activity in electrooxidation of ethanol in the alkaline medium when the current density was more than 16000 mA·mg⁻¹_{Pd}, which is the best results reported in this study. This value is higher than activity of Pd-based catalyst with different promoter [20, 36] or activity of Pt-base catalyst [37] with the same promoter. Another result in this particle is that the electrochemical stability of PASGN.N catalyst was relatively good: after 500 scanning cycles, the current density diminished 32% compared with the highest peak current density of the 15th cycle. In conclusion, the obtained results have opened a new studying direction about synergistic effects of Al-Si-Na addition which both enhances activity and improves stability of Pd-based catalysts in ethanol electrooxidation in alkaline medium. In the same way, the content of noble metal is also reduced.

Symbols

d_k :	Particle size
d_n :	Average particle size

EASA:	Electrochemical active surface area
FT-IR:	Fourier transform infrared
ICP-OES:	Inductively coupled plasma-optical emission spectrometry
I_D :	Peak intensity of the D band in Raman spectra/cm ⁻¹
I_F :	Forward scanning peak current density in cyclic voltammetry curves/mA·mg ⁻¹ _{Pd}
I_F 15 th :	Highest peak current density of the 15 th cycle in cyclic voltammetry curves/mA·mg ⁻¹ _{Pd}
I_F 200 th :	Peak current density of the 200 th cycle in cyclic voltammetry curves/mA·mg ⁻¹ _{Pd}
I_F 500 th :	Peak current density of the 500 th cycle in cyclic voltammetry curves/mA·mg ⁻¹ _{Pd}
I_F^0 :	Catalytic current density at the beginning in chronoamperometry curves/mA·mg ⁻¹ _{Pd}
I_F^{4000s} :	Catalytic current density in chronoamperometry curves/mA·mg ⁻¹ _{Pd}
I_G :	Peak intensity of the G band in Raman spectra/cm ⁻¹
I_R :	Reverse scanning peak current density in cyclic voltammetry curves/mA·mg ⁻¹ _{Pd}
n_k :	Frequency of occurrence of particles
Q:	Coulombic charge used in the reduction of palladium (II) oxide into palladium metal/mC
S:	Proportionality constant in the case of reduction of a monolayer of PdO/mC·cm ⁻²
SEM:	Scanning electron microscope
TEM:	Transmission electron microscope
XPS:	X-ray photoelectron spectroscopy
XRD:	X-ray diffraction.

Data Availability

The data used in the study are available from the corresponding authors upon request.

Additional Points

Highlights. Nanocatalysts based on Pd/rGO were synthesized for the electro-oxidation of ethanol in alkaline medium. The random presence of Na was found out when reduced agent NaBH₄ was used instead of EG. Al-Si-Na addition enhances the

activity of Pd-base catalyst and improves its electrochemical stability after 500 scanning cycles. Al-Si-Na addition improves dispersion and combination of the active phase Pd on reduced graphene oxide surface. NaBH₄-reducing PdAlSiNa/rGO has the highest electrocatalytic activity, 16138 mA·mg_{Pd}⁻¹.

Conflicts of Interest

The authors declare that there are no conflicts of interest regarding the publication of this paper.

Acknowledgments

The research and publication of our article was funded by the Project Management Unit of Fostering Innovation through Research, Science, and Technology (FIRST) for the subproject through grant agreement no. 06/FIRST/2a/KEYLABPRT and Ministry of Industry and Trade (MOIT) for the project no. ĐTKHCN.224/17. The authors gratefully acknowledge the financial supports from the Project Management Unit of Fostering Innovation through Research, Science, and Technology (FIRST) and Ministry of Industry and Trade (MOIT).

References

- [1] Y. Li, W. Gao, L. Ci, C. Wang, and P. M. Ajayan, "Catalytic performance of Pt nanoparticles on reduced graphene oxide for methanol electro-oxidation," *Carbon*, vol. 48, no. 4, pp. 1124–1130, 2010.
- [2] Q.-L. Zhang, J.-N. Zheng, T.-Q. Xu et al., "Simple one-pot preparation of Pd-on-Cu nanocrystals supported on reduced graphene oxide for enhanced ethanol electrooxidation," *Electrochimica Acta*, vol. 132, pp. 551–560, 2014.
- [3] L. Dong, R. R. S. Gari, Z. Li, M. M. Craig, and S. Hou, "Graphene-supported platinum and platinum–ruthenium nanoparticles with high electrocatalytic activity for methanol and ethanol oxidation," *Carbon*, vol. 48, no. 3, pp. 781–787, 2010.
- [4] R. Awasthi and R. N. Singh, "Graphene-supported Pd–Ru nanoparticles with superior methanol electrooxidation activity," *Carbon*, vol. 51, pp. 282–289, 2010.
- [5] Y. Wang, Y. Zhao, J. Yin, M. Liu, Q. Dong, and Y. Su, "Synthesis and electrocatalytic alcohol oxidation performance of Pd–Co bimetallic nanoparticles supported on graphene," *International Journal of Hydrogen Energy*, vol. 39, no. 3, pp. 1325–1335, 2014.
- [6] R. S. Amin, R. M. A. Hameed, and K. M. El-Khatib, "Microwave heated synthesis of carbon supported Pd, Ni and Pd–Ni nanoparticles for methanol oxidation in KOH solution," *Applied Catalysis B: Environmental*, vol. 148–149, pp. 557–567, 2014.
- [7] R. S. Amin, R. M. Abdel Hameed, K. M. El-Khatib, and M. Elsayed Youssef, "Electrocatalytic activity of nanostructured Ni and Pd–Ni on Vulcan XC-72R carbon black for methanol oxidation in alkaline medium," *International Journal of Hydrogen Energy*, vol. 39, no. 5, pp. 2026–2041, 2014.
- [8] C. A. L. Ricoa, J. G. Rosa, E. O. Ortega et al., "High performance of ethanol co-laminar flow fuel cells based on acrylic, paper and Pd–NiO as anodic catalyst," *Electrochimica Acta*, vol. 207, pp. 164–176, 2016.
- [9] S. Jongsomjit, P. Prapainainar, and K. Sombatmankhong, "Synthesis and characterisation of Pd–Ni–Sn electrocatalyst for use in direct ethanol fuel cells," *Solid State Ionics*, vol. 288, pp. 147–153, 2016.
- [10] K. Charoen, C. Warakulwit, C. Prapainainar, A. Seubsai, M. Chareonpanich, and P. Prapainainar, "Optimization of metal atomic ratio of Pd x Ru y Ni z on carbon support for ethanol oxidation," *Applied Surface Science*, vol. 421, pp. 2–17, 2017.
- [11] Q. Dong, Y. Zhao, X. Han, Y. Wang, M. Liu, and Y. Li, "Pd/Cu bimetallic nanoparticles supported on graphene nanosheets: facile synthesis and application as novel electrocatalyst for ethanol oxidation in alkaline media," *International Journal of Hydrogen Energy*, vol. 39, no. 27, pp. 14669–14679, 2014.
- [12] Z.-Z. Yang, L. Liu, A.-J. Wang et al., "Simple wet-chemical strategy for large-scaled synthesis of snowflake-like PdAu alloy nanostructures as effective electrocatalysts of ethanol and ethylene glycol oxidation," *International Journal of Hydrogen Energy*, vol. 42, no. 4, pp. 2034–2044, 2016.
- [13] Y.-G. Jo, S.-M. Kim, J.-W. Kim, and S.-Y. Lee, "Composition-tuned porous Pd–Ag bimetallic dendrites for the enhancement of ethanol oxidation reactions," *Journal of Alloys and Compounds*, vol. 688, pp. 447–453, 2016.
- [14] R. Jana, U. Subbarao, and S. C. Peter, "Ultrafast synthesis of flower-like ordered Pd₃Pb nanocrystals with superior electrocatalytic activities towards oxidation of formic acid and ethanol," *Journal of Power Sources*, vol. 301, pp. 160–169, 2016.
- [15] F. Zhang, D. Zhou, and M. Zhou, "Ethanol electrooxidation on Pd/C nanoparticles in alkaline media," *Journal of Energy Chemistry*, vol. 25, no. 1, pp. 71–76, 2016.
- [16] C. Hu and X. Wang, "Highly dispersed palladium nanoparticles on commercial carbon black with significantly high electro-catalytic activity for methanol and ethanol oxidation," *International Journal of Hydrogen Energy*, vol. 40, no. 36, pp. 12382–12391, 2015.
- [17] G. Yang, Y. Zhou, H.-B. Pan et al., "Ultrasonic-assisted synthesis of Pd–Pt/carbon nanotubes nanocomposites for enhanced electro-oxidation of ethanol and methanol in alkaline medium," *Ultrasonics Sonochemistry*, vol. 28, pp. 192–198, 2016.
- [18] W. Chen, Y. Zhang, and X. Wei, "Catalytic performances of PdNi/MWCNT for electrooxidations of methanol and ethanol in alkaline media," *International Journal of Hydrogen Energy*, vol. 40, no. 2, pp. 1154–1162, 2015.
- [19] M. D. Stoller, S. Park, Y. Zhu, J. An, and R. S. Ruoff, "Graphene-based ultracapacitors," *Nano Letters*, vol. 8, no. 10, pp. 3498–3502, 2008.
- [20] J. L. Tan, A. M. De Jesus, S. L. Chua et al., "Preparation and characterization of palladium-nickel on graphene oxide support as anode catalyst for alkaline direct ethanol fuel cell," *Applied Catalysis A: General*, vol. 531, pp. 29–35, 2017.
- [21] Q. Liu, K. Jiang, J. Fan et al., "Manganese dioxide coated graphene nanoribbons supported palladium nanoparticles as an efficient catalyst for ethanol electrooxidation in alkaline media," *Electrochimica Acta*, vol. 203, pp. 91–98, 2016.
- [22] T. H. T. Vu, T. T. T. Tran, H. N. T. Le et al., "Pt–AlOOH–SiO₂/graphene hybrid nanomaterial with very high electrocatalytic performance for methanol oxidation," *Journal of Power Sources*, vol. 276, pp. 340–346, 2015.
- [23] W. S. Hummers and R. E. Offeman, "Preparation of graphitic oxide," *Journal of the American Chemical Society*, vol. 80, no. 6, 1339 pages, 1958.
- [24] H. Mao, T. Huang, and A. Yu, "Surface noble metal modified PdM/C (M = Ru, Pt, Au) as anode catalysts for direct ethanol fuel cells," *Journal of Alloys and Compounds*, vol. 676, pp. 390–396, 2016.
- [25] A. M. Hofstead-Duffy, D.-J. Chen, S.-G. Sun, and Y. J. Tong, "Origin of the current peak of negative scan in the cyclic

- voltammetry of methanol electro-oxidation on Pt-based electrocatalysts: a revisit to the current ratio criterion,” *Journal of Materials Chemistry*, vol. 22, no. 11, pp. 5205–5208, 2012.
- [26] D. Y. Chung, K.-J. Lee, and Y.-E. Sung, “Methanol electro-oxidation on the Pt surface: revisiting the cyclic voltammetry interpretation,” *Journal of Physical Chemistry C*, vol. 120, no. 17, pp. 9028–9035, 2016.
- [27] Y. Zhao, X. Li, J. M. Schechter, and Y. Yang, “Revisiting the oxidation peak in the cathodic scan of the cyclic voltammogram of alcohol oxidation on noble metal electrodes,” *RSC Advances*, vol. 6, no. 7, pp. 5384–5390, 2016.
- [28] R. Krishna, D. M. Fernandes, A. Marinho, J. Ventura, C. Freire, and E. Titus, “Facile synthesis of well dispersed Pd nanoparticles on reduced graphene oxide for electrocatalytic oxidation of formic acid,” *International Journal of Hydrogen Energy*, vol. 42, no. 37, pp. 23639–23646, 2017.
- [29] N. Seriani, “Sodium promoter inducing a phase change in a palladium catalyst,” *Journal of Physical Chemistry C*, vol. 116, no. 43, pp. 22974–22979, 2012.
- [30] S. Yang, J. Dong, Z. Yao et al., “One-Pot synthesis of graphene-supported monodisperse Pd nanoparticles as catalyst for formic acid electro-oxidation,” *Scientific Reports*, vol. 4, no. 1, article 4501, 2014.
- [31] A. H. Al-Marri, M. Khan, M. R. Shaik et al., “Green synthesis of Pd@graphene nanocomposite: catalyst for the selective oxidation of alcohols,” *Arabian Journal of Chemistry*, vol. 9, no. 6, pp. 835–845, 2016.
- [32] Y. Fan, Y. Zhao, D. Chen, X. Wang, X. Peng, and J. Tian, “Synthesis of Pd nanoparticles supported on PDDA functionalized graphene for ethanol electro-oxidation,” *International Journal of Hydrogen Energy*, vol. 40, no. 1, pp. 322–329, 2015.
- [33] J. Perez, V. A. Paganin, and E. Antolini, “Particle size effect for ethanol electro-oxidation on Pt/C catalysts in half-cell and in a single direct ethanol fuel cell,” *Journal of Electroanalytical Chemistry*, vol. 654, no. 1-2, pp. 108–115, 2011.
- [34] L. Wang, J.-J. Zhai, K. Jiang, J.-Q. Wang, and W.-B. Cai, “Pd–Cu/C electrocatalysts synthesized by one-pot polyol reduction toward formic acid oxidation: structural characterization and electrocatalytic performance,” *International Journal of Hydrogen Energy*, vol. 40, no. 4, pp. 1726–1734, 2015.
- [35] J. Lin, T. Mei, M. Lv, C. Zhang, Z. Zhao, and X. Wang, “Size-controlled PdO/graphene oxides and their reduction products with high catalytic activity,” *RSC Advances*, vol. 4, no. 56, pp. 29563–29570, 2014.
- [36] J. Ma, J. Wang, G. Zhang et al., “Deoxyribonucleic acid-directed growth of well dispersed nickel-palladium-platinum nanoclusters on graphene as an efficient catalyst for ethanol electrooxidation,” *Journal of Power Sources*, vol. 278, pp. 43–49, 2015.
- [37] L. T. Tran, Q. M. Nguyen, M. D. Nguyen, H. N. T. Le, T. T. Nguyen, and T. H. T. Vu, “Preparation and electrocatalytic characteristics of the Pt-based anode catalysts for ethanol oxidation in acid and alkaline media,” *International Journal of Hydrogen Energy*, vol. 43, no. 45, pp. 20563–20572, 2018.

Research Article

Enhanced Photocatalytic Degradation of Rhodamine B Using C/Fe Co-Doped Titanium Dioxide Coated on Activated Carbon

Thuy Le Thi Thanh ¹, Lan Nguyen Thi,¹ Trinh Tran Dinh ^{2,3} and Noi Nguyen Van^{2,3}

¹Department of Chemistry, Faculty of Science, Qui Nhon University, No. 170 An Duong Vuong Street, Qui Nhon, Vietnam

²Faculty of Chemistry, VNU-University of Science, No. 19 Le Thanh Tong Street, Hanoi, Vietnam

³VNU Key Laboratory of Advanced Materials for Green Growth, No. 334 Nguyen Trai Street, Hanoi, Vietnam

Correspondence should be addressed to Thuy Le Thi Thanh; lethithanhthuy@qnu.edu.vn and Trinh Tran Dinh; trinhtd@vnu.edu.vn

Received 15 March 2019; Accepted 21 May 2019; Published 23 June 2019

Academic Editor: Mallikarjuna N. Nadagouda

Copyright © 2019 Thuy Le Thi Thanh et al. This is an open access article distributed under the Creative Commons Attribution License, which permits unrestricted use, distribution, and reproduction in any medium, provided the original work is properly cited.

Carbon and iron co-doped titanium dioxide catalyst coated on activated carbon (Fe-C-TiO₂/AC) was successfully synthesized using the sol-gel method, followed by hydrothermal treatment. Commercial activated carbon was treated by HNO₃ prior to being coated by the as-synthesized catalyst. The composite was characterized by XPS, XRD, UV-Vis spectrophotometry, IR, TEM, HR-TEM, and BET. The performance of the supported catalysts was evaluated in the degradation of rhodamine B (RhB) in the solution under visible-light irradiation. The results showed that, with the appropriate amount of activated carbon, prepared Fe-C-TiO₂/AC catalysts exhibited higher catalytic activities and Fe-C-TiO₂/AC system showed the best performance. The photocatalytic degradation efficiency of Fe-C-TiO₂/AC was enhanced due to the synergistic effect between AC (adsorption effect) and Fe-C-TiO₂ (photocatalysis effect). This facilitated the photocatalytic degradation of RhB by Fe-C-TiO₂.

1. Introduction

TiO₂ photocatalyst has been widely used in the wastewater treatment and other environmental remediation because of its high efficiency, nontoxicity, propitious recycle ability, and low cost. Besides, the final products of the photocatalysis in the advanced oxidation process are CO₂, H₂O, inorganic ions, and minerals that usually have insignificant impacts on environments [1, 2]. However, the application of TiO₂ is limited because the TiO₂ with band gap ~3.2 eV is only activated under UV radiation and it is difficult to recycle. Therefore, modification of catalyst is crucial to enhance its photocatalytic activity. To present, catalytic efficiency of TiO₂ was significantly improved by being doped with metals such as V, Cr, W, and Fe or with metal oxides like ZnO, CuO, and so on for expanding the absorption edge to the visible region [3–6]. Among these metals, TiO₂ doped with Fe is in progress because Fe can replace the positions of Ti⁴⁺ in the crystalline, reducing the band gap energy, which is conducive to the activation in the visible light [3, 4, 7].

Moreover, Fe ions act as traps to incarcerate electrons and hinder the recombination of electron/hole pairs, resulting in the increase in catalysts' performance. In addition, the addition of some nonmetal elements such as N, C, S, P, and halogens into TiO₂ structure can also narrow the band gap of TiO₂, reinforcing the photocatalytic activity of the catalyst [2, 8]. Some research reported that transition metals/(N, C, S) co-doped into TiO₂ would greatly facilitate the photocatalytic performance of the corresponding catalysts under visible irradiation conditions, which was attributed to the synergistic effects between the doped C and N atoms and lower band gap energy [1, 3]. TiO₂-based photocatalysts are usually employed either as slurry or on support. In slurry condition, a big challenge lies in the separation and recovery of the small-sized particles after treatment of pollutants, which limits the application of the photocatalyst in real conditions. The utilization of support immobilization such as glass fibers, glass beads, or steel has also been employed. However, they have issue due to adhesion force between the photocatalyst surface and the support [9]. Recently, there are increasing interests in

a synergetic approach. Different materials are usually designed to provide a high surface area to support the catalyst [8, 10]. These materials share some common characteristics: binding to the catalyst, nondestroying catalyst, high surface area, and high affinity to the adsorption of pollutant molecules [10]. Activated carbon is one of the cost-effective synergist with not only clutching the photo-agents and free radicals (HO^\bullet) but also adsorbing pollutant molecules on the photochemical centers of the catalyst apart from its mechanical stability [10]. There are surprisingly quite a few papers using this method, and there is no published work on C/Fe co-doped titanium dioxide coated on activated carbon that is reported in this manuscript. Hence, in the present work, TiO_2 co-doped iron and carbon coated on activated carbon that was treated by HNO_3 was prepared by sol-gel followed by solvothermal method. The characterization of the catalyst was conducted by X-ray photoelectron spectroscopy (XPS), X-ray diffraction (XRD), infrared spectroscopy (IR), transmission electron microscopy (TEM), high-resolution transmission electron microscopy (HR-TEM), ultraviolet-visible (UV-Vis) spectroscopy, and Brunauer–Emmett–Teller (BET) surface area measurement. The catalytic activity of the catalyst was examined by the degradation of RhB dye.

2. Experimental

2.1. Catalyst Preparation

2.1.1. Chemicals. TIOT (tetraisopropyl orthotitanate 98%), nitric acid (HNO_3 68%), ethyl alcohol ($\text{C}_2\text{H}_5\text{OH}$ 99.7%), iron (III) nitrate ($\text{Fe}(\text{NO}_3)_3 \cdot 9\text{H}_2\text{O}$ pure), and rhodamine B ($\text{C}_{28}\text{H}_{31}\text{ClN}_2\text{O}_3$) were purchased from Sigma-Aldrich. Activated carbon Tra Bac (AC—particle sizes from 0.075 mm to 4.75 mm, surface area BET 928 m^2/g) was obtained with the aid of a TriStar 3000 V6.07 A.

2.1.2. Preparation of Fe-C-TiO₂ Coated on Activated Carbon Pretreated by HNO₃ (Fe-C-TiO₂/AC)

- (i) Treatment of carbon with HNO_3 : The coal is ground to a fine powder 0.16 mm before being washed with water and boiled for 2 hours to eliminate gases such as O_2 , CO_2 , and SO_2 . Next, extracted carbon was immersed into HNO_3 12M and stirred for 3 hours at room temperature and then soaked for 24 hours. Finally, activated carbon (AC) was washed several times with distilled water and then dried for 3 hours at 100°C .
- (ii) Preparation of Fe-C-TiO₂/AC: 6 mL of TIOT was added into 34 mL of ethyl alcohol to make solution A. Solution B was prepared from 17 mL of ethanol, 0.4 mL of nitric acid (68%), 1.6 mL distilled water, 48.2 mg of $\text{Fe}(\text{NO}_3)_3 \cdot 9\text{H}_2\text{O}$, and 0.2 g of AC. The solution A was dropped into solution B under slow stir for 14 hours at room temperature and left for gelation for 2 days before being autoclaved in a Teflon vessel for 10 hours at 180°C . The resulted powder was washed and dried at 100°C for 24 hours to obtain the Fe-C-TiO₂/AC catalyst.

2.2. Characterization of As-Synthesized Photocatalyst. The crystal structure of catalyst was determined by XRD (D8-Advance 5005). Transmission electron microscope (TEM, JEOL JEM-1010 electron Microscope) and high-resolution transmission electron microscopy (HR-TEM, Hitachi H-9000 NAR, Japan Advanced Institute of Science and Technology) were used to investigate the particle size and morphology of the samples. XPS spectra of the prepared samples were measured by an X-ray photoelectron spectroscopy (XPS) (Kratos Axis Ultra—Frederick Seitz Materials Research laboratory-University of Illinois, Urbana-Champaign, USA). The absorbance was conducted by UV-Vis spectroscopy (Tasco-V670 photospectrometer). Functional groups were identified by IR spectroscopy (IR prestige 21). Nitrogen isothermal adsorption (Brunauer–Emmett–Teller (BET)) was determined by TriStar 3000 V6.07 A. Rhodamine B (RhB) concentrations were determined by a UV-Vis spectroscopy at the wavelength of 553 nm (the absorption maximum wavelength of RhB).

2.3. Photocatalytic Performance of As-Synthesized Photocatalysts. The catalytic activity of prepared materials was examined by the degradation of RhB solution (20 mg/L) under visible-light irradiation. The compact light (36W) was used instead of solar light with a range of wavelengths from 400 to 700 nm. An appropriate amount of catalyst (1–3 g/L) was added into 100 mL of RhB solution in a 250 mL beaker. The mixture was mixed at a constant rate in the dark for 30 minutes to ensure the desorption/adsorption equilibrium before being irradiated. After certain periods of time, the mixtures were sampled to determine the RhB concentrations by the UV-Vis spectroscopy.

3. Results and Discussion

3.1. Characterization of Synthesized Photocatalysts. Overall XPS spectra of principal elements Ti 2p, O 1s, C 1s, N 1s, and Fe 2p in synthesized photocatalysts are presented in Figure 1(a). The high-resolution scan over Ti 2p, O 1s, C 1s, N 1s, and Fe 2p spectral regions is shown in Figures 1(b)–1(f), respectively. The Ti 2p spectrum consists of peaks located at 459.1 eV and 464.8 eV, indicating the existence of Ti (IV) in TiO_2 component [1]. This suggests that the doping of iron and carbon then attached to the AC carrier does not alter the chemical state of TiO_2 . This result is consistent with the XRD results (Figure 2). O 1s spectrum consists of the main peak at 529.9 eV and shoulder peak at 531.9 eV. These peaks correspond to Ti-O bond and O-H groups in TiO_2 [8]. This hydrogen hydroxyl group is useful for adsorption of organic substances or it can capture photogenic holes to form HO^\bullet free radicals that increase photocatalytic activity of photocatalysts.

The presence of peaks at 711.1 eV and 723.1 eV is attributed to $\text{Fe}^{\text{III}} 2p_{3/2}$ and $\text{Fe}^{\text{III}} 2p_{1/2}$; it is possible to predict the presence of iron in Fe^{3+} oxidation state. In addition, there is also the binding energy value at 709.2 eV corresponding to $\text{Fe}^{\text{II}} 2p_{3/2}$, which characterizes the existence of Fe^{2+} ions, possibly in FeO [5]. Coexistence of Fe^{3+} and Fe^{2+}

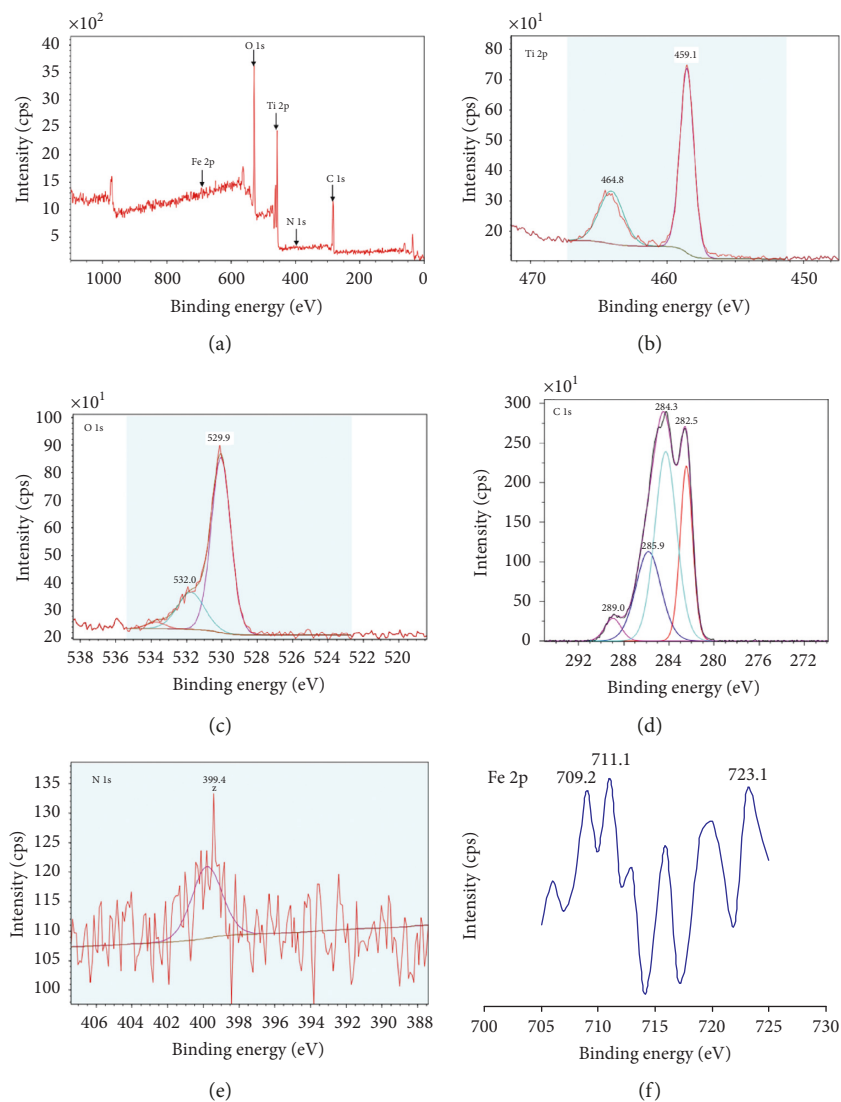


FIGURE 1: XPS spectra of Fe-C-TiO₂/AC (a), Ti 2p (b), O 1s (c), C 1s (d), N 1s (e), and Fe 2p (f).

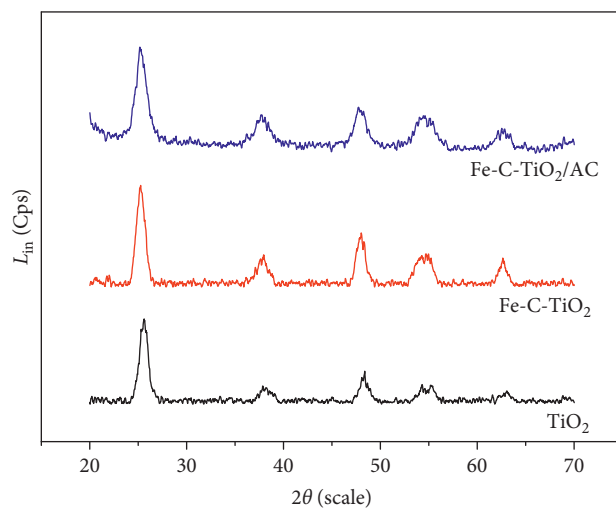
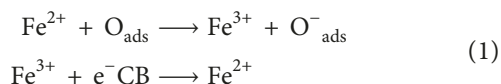


FIGURE 2: XRD patterns of Fe-C-TiO₂/AC, Fe-C-TiO₂, and TiO₂.

can enhance the photocatalytic efficiency based on the following reactions:



in which Fe^{3+} acts as a conductive photonic electron trap to prevent recombination of electrons and holes, while Fe^{2+} provides electrons to adsorb oxygen on the catalytic surface and helps the charge transfer on the surface faster [1, 5].

Typical peaks of C are shown in Figure 1(d). The main peak with energy value at 284.3 eV is assigned to carbon graphite. The presence of 285.9 eV and 288.4 eV peaks is associated with C-O and C=O bonds of catalytic surface carbonates [11]. The existence of this carbonate radical increases the sensitivity for catalysis, because of the involvement of carbon-containing functional groups in activated carbon [1]. A peak at 282.5 eV corresponds to the Ti-C bond in the nanocrystalline catalyst attached to AC, and this link proves that part of the carbon is involved in replacing the oxygen in the network TiO_2 anatase crystals. The XPS analysis confirmed that iron and carbon had successfully entered the TiO_2 network and also showed the successful binding of catalyst to activated carbon activated by HNO_3 .

The XRD patterns (Figure 2) show that Fe-C- TiO_2 after being coated on activated carbon exhibits the typical peaks referring to the anatase form [6]. The phase composition of nanoscale particles is preserved compared with the original materials (Figure 3).

The TEM images of the Fe-C- TiO_2/AC sample (Figure 3(a)) show that the catalyst system contains very fine particles, with typical size of 5 nm, evenly distributed on the surface of activated carbon. The result of HR-TEM (Figure 3(b)) confirms the Fe-C- TiO_2 catalyst binding on AC is based on black spots covered by catalytic spheres [10].

Proposed mechanism of TiO_2 coating process on AC is shown in Figure 4. After AC was pretreated with HNO_3 , carbon supplied more hydroxyl and acid groups on the surface, which bond to OH^- and H^+ ions of catalyst to enhance the adhesiveness.

Table 1 shows that the surface areas of pristine AC and AC carrying catalysts measured by BET are different. The reason is that during the treatment of AC, HNO_3 is a strong oxidant, leading to changes in porous structure, which might reduce the number of small capillaries and increase the number of large ones, therefore reducing the surface area.

IR spectra of pristine TiO_2 , Fe-C- TiO_2 , and Fe-C- TiO_2/AC are presented in Figure 5. Peak at 1436 cm^{-1} refers to the -COO-Ti vibration. The peaks at 551 cm^{-1} and $502\text{--}505\text{ cm}^{-1}$ are assigned to the bonds of Ti-O and Ti-O-C, respectively.

The UV-Vis spectra of the samples are displayed in Figure 6. The results show that by coating Fe-C- TiO_2 on AC, the absorption band of Fe-C- TiO_2/AC was significantly expanded to the visible region in comparison with the absorption band of pristine TiO_2 and Fe-C- TiO_2 . Indeed, as expected, the main absorption edge of TiO_2 was estimated to be about 398 nm (2.96 eV) due to its intrinsic band gap absorption. The onset of the absorption spectrum of Fe-C-

TiO_2 was shifted to the visible region because of the Fe and C dopants while Fe-C- TiO_2/AC presented main absorption spectrum at the region above 480 nm. This result suggests that the Fe-C- TiO_2/AC catalyst is more active under visible light.

From the UV-Vis spectra of pristine TiO_2 , Fe-C- TiO_2 , and Fe-C- TiO_2/AC (Figure 7), the band gap energies estimated from the intercept of the tangents to the plots by using Kubelka-Munk method were 2.96, 2.17, and 1.63 eV for pristine TiO_2 , Fe-C- TiO_2 , and Fe-C- TiO_2/AC , respectively.

3.2. Catalytic Activity of Fe-C- TiO_2/AC in the Degradation of RhB under Visible Light. The comparison of photocatalytic performance of Fe-C- TiO_2/AC , Fe-C- TiO_2 , and TiO_2 with that of pure AC in the degradation of RhB under visible-light irradiation with the same catalyst load (1.6 g/L) is presented in Figure 8. AC adsorbs RhB and reaches the equilibrium after 60 min of reaction, which can be proved by unchanged RhB concentration over time. The results also indicate that Fe-C- TiO_2/AC is the best photocatalyst in degradation of RhB in solutions with more than 99% of RhB removal after 90 min while pristine TiO_2 exhibits the lowest performance (only some 40% of RhB is removed after the same reaction time). Pure AC and Fe-C- TiO_2 present photocatalytic efficiency in between pristine TiO_2 and Fe-C- TiO_2/AC . This illustrates the synergy between adsorption capacity of AC and the improvement of Fe-C- TiO_2 compared with pristine TiO_2 .

Figure 9 shows that the optimal catalyst load was 1.6 mg/L in the degradation of RhB in solutions while more dilute or concentrated catalyst concentrations will result in lower levels of RhB degradation. In fact, more than 99% of RhB was decomposed after 90 min of visible-light irradiation with a catalyst load of 1.6 mg/L while these figures for the catalyst loads at 1, 1.2, 1.4, 1.8, and 2.5 were, respectively, 40%, 50%, 53%, 78%, and 62%. This can be explained by the fact that the higher quantity of catalyst load may cause the light absorption hindrance, decreasing the efficiency of RhB degradation, whereas the lower catalyst load would lead to lower active sites ready for the degradation of the pollutant.

The photocatalytic degradation of RhB by the Fe-C- TiO_2/AC system can be explained by the following mechanism proposal (Figure 10): (1) when $h\nu \geq (E_C - E_V)$, then electrons would be excited in the valence band of TiO_2 by the process: $\text{TiO}_2 + h\nu (\text{UV}) \longrightarrow \text{TiO}_2 (e_{\text{CB}^-} + h\nu_{\text{VB}^+})$; (2) when $(E_C - E_V) \leq h\nu < (E_C - E_V)$, electrons can be excited from the Fe-C- TiO_2/AC energy level by the following process: $\text{Fe-C-TiO}_2/\text{C} + h\nu (\text{visible}) \longrightarrow \text{Fe-C-TiO}_2/\text{AC} (e_{\text{CB}^-} + h\nu_{\text{VB}^+})$; and (3) when $(E_V^* - E_V) \leq h\nu < (E_C - E_V)$, electrons would be excited and moved from the valence band of TiO_2 to the Fe-C- TiO_2/AC energy level by the process: $\text{TiO}_2 + \text{Fe-C-TiO}_2/\text{C} + h\nu (\text{visible}) \longrightarrow \text{Fe-C-TiO}_2/\text{AC} (e_{\text{CB}^-}) + \text{TiO}_2 (h\nu_{\text{VB}^+})$. The departed electrons and holes subsequently migrate to the surface of the catalysts and react with adsorbed H_2O and O_2 molecules, forming HO^\cdot and O_2^\cdot , respectively. HO^\cdot and O_2^\cdot radicals are mainly responsible for the degradation of RhB in solution [12].

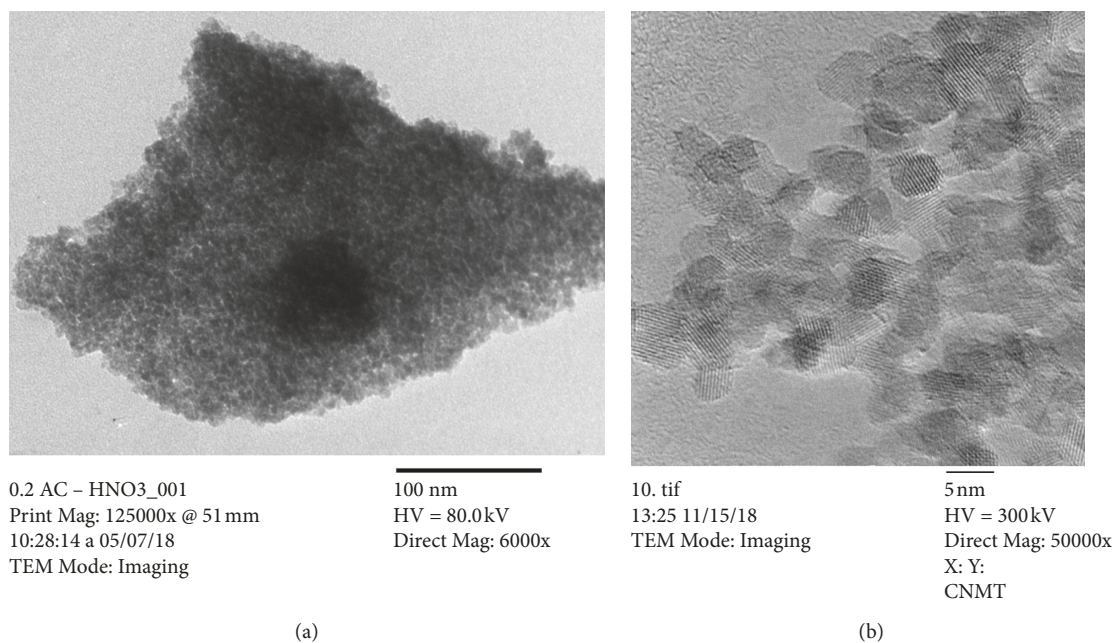


FIGURE 3: TEM images of Fe-C-TiO₂/AC (a) and HR-TEM of Fe-C-TiO₂/AC (b).

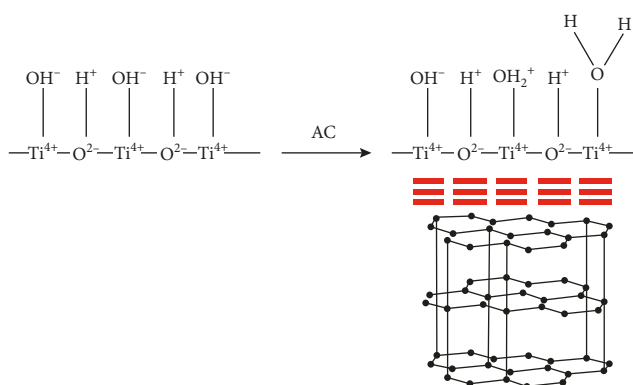


FIGURE 4: Proposed mechanism of TiO₂ coating process on AC.

TABLE 1: Physical properties of AC, Fe-C-TiO₂, and Fe-C-TiO₂/AC.

Materials	Mean size (nm) from the XRD results	BET surface area (m ² ·g ⁻¹)	V _p (cm ³ ·g ⁻¹)
Fe-C-TiO ₂ /AC	5.13	264.8	0.30
Fe-C-TiO ₂	4.23	237.2	0.23
AC	—	928.2	—

The catalytic stability in RhB decomposition under visible-light irradiation was studied. After each decomposition cycle (90 min), the catalyst was centrifuged and washed with distilled water and then used for further treatment of RhB in solution. The results show that the catalyst exhibited good photocatalytic activity after 5 cycles, as shown in Figure 11. The ability to decompose RhB over 5 cycles remained high (>87%). This research has proved that Fe-C-TiO₂/AC is a highly durable, economically suitable, and practical catalyst.

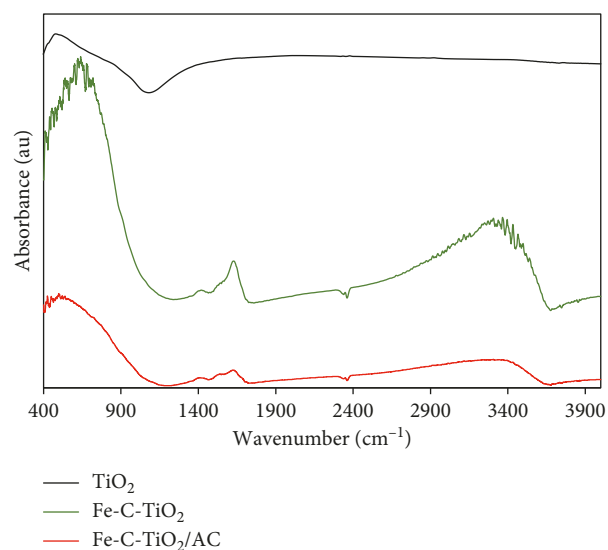


FIGURE 5: IR spectra of Fe-C-TiO₂/AC, Fe-C-TiO₂, and TiO₂.

4. Conclusions

The Fe-C-TiO₂ catalyst was successfully carried on the AC treated by HNO₃. The nature of the catalyst remained to be unchanged regarding phase composition, particle sizes, and structure. Furthermore, the large surface area of AC adsorbs more organic molecules, leading to enhance the RhB degradation in solutions. The catalyst after being deposited on AC carriers activated with HNO₃ has better photocatalytic activity than activated carbon without catalysts. The Fe-C-TiO₂/AC catalyst also presented better photocatalytic performance in RhB degradation compared with pristine TiO₂ and with Fe-C-TiO₂. The optimal catalyst load for RhB

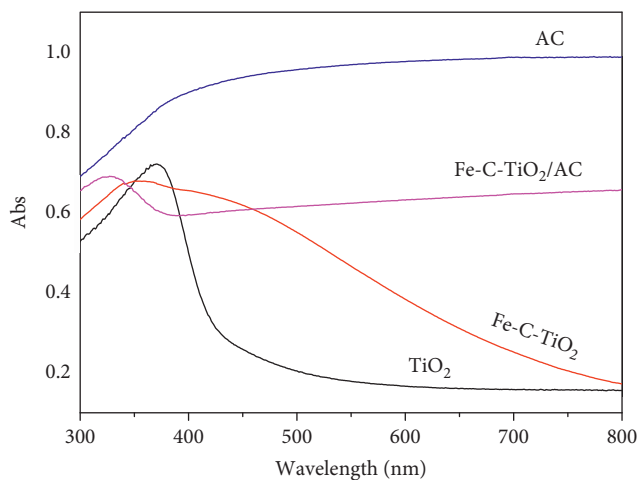


FIGURE 6: UV-Vis spectra of pure AC, Fe-C-TiO₂/AC, Fe-C-TiO₂, and TiO₂.

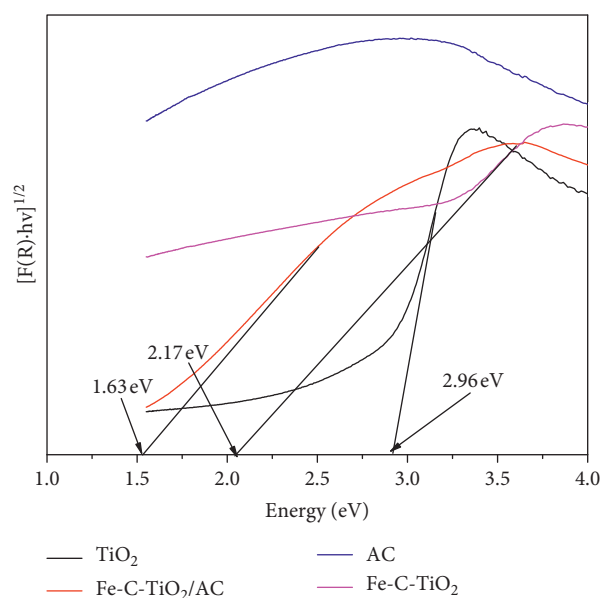


FIGURE 7: Plot of $[F(R) \cdot hv]^{1/2}$ vs energy (eV) for pure AC, Fe-C-TiO₂/AC, Fe-C-TiO₂, and TiO₂.

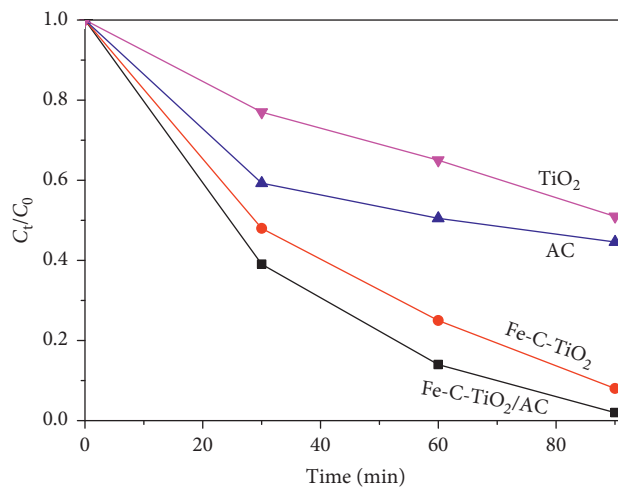


FIGURE 8: Comparison of photocatalytic activity of Fe-C-TiO₂/AC, Fe-C-TiO₂, and TiO₂ with that of pure AC.

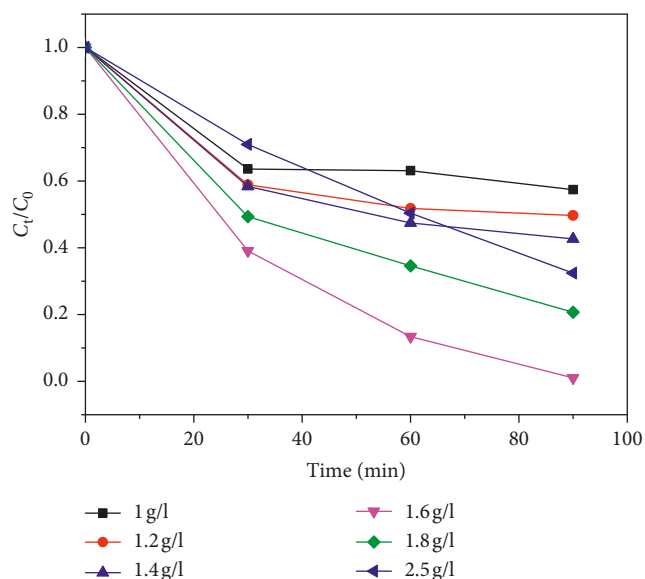


FIGURE 9: Optimization of catalyst load in the degradation of RhB by Fe-C-TiO₂/AC.

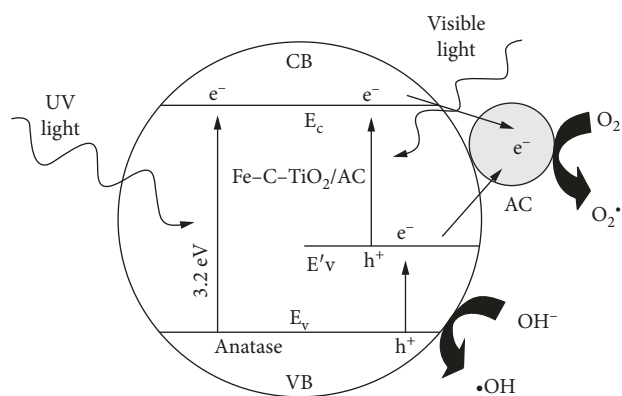


FIGURE 10: Schematic mechanism of photocatalytic degradation of RhB by Fe-C-TiO₂/AC (adopted from [12]).

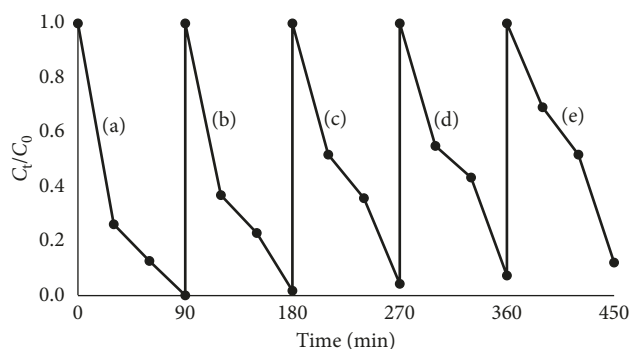


FIGURE 11: Photocatalytic recycling of Fe-C-TiO₂/AC in RhB decomposition: first cycle (a); second cycle (b); third cycle (c); fourth cycle (d); fifth cycle (e).

decomposition (initial concentration of 20 mg/L) was found to be of 1.6 g/L. The catalysts with larger size favor the catalyst separation from solution and recycling. The Fe-C-

TiO₂ carried on AC sample is a potential catalyst in degradation of toxic organic compounds under visible-light irradiation.

Data Availability

The data used to support the findings of this study are included within the article.

Conflicts of Interest

The authors declare that there are no conflicts of interest regarding the publication of this paper.

Acknowledgments

This work was partly supported by the team project of VLIR-UOS with code number ZEIN2016PR431. The authors would like to thank the RoHan project for the utilization of instruments.

References

- [1] X. Wang, Y. Tang, M.-Y. Leiw, and T.-T. Lim, "Solvochemical synthesis of Fe-C codoped TiO₂ nanoparticles for visible-light photocatalytic removal of emerging organic contaminants in water," *Applied Catalysis A: General*, vol. 409-410, pp. 257-266, 2011.
- [2] S. Jafari, B. Tryba, E. Kusiak-Nejman, J. Kapica-Kozar, A. W. Morawski, and M. Sillanpää, "The role of adsorption in the photocatalytic decomposition of Orange II on carbon-modified TiO₂," *Journal of Molecular Liquids*, vol. 220, pp. 504-512, 2016.
- [3] Y. Wu, J. Zhang, L. Xiao, and F. Chen, "Properties of carbon and iron modified TiO₂ photocatalyst synthesized at low temperature and photodegradation of acid orange 7 under visible light," *Applied Surface Science*, vol. 256, pp. 260-268, 2010.
- [4] Z. Hu, T. Xu, and B. Fang, "Photocatalytic degradation of vehicle exhaust using Fe-doped TiO₂ loaded on activated carbon," *Applied Surface Science*, vol. 420, pp. 34-42, 2017.
- [5] Y. Li, J. Chen, J. M. Liu, M. Ma, W. Chen, and L. Li, "Activated carbon supported TiO₂-photocatalysis doped with Fe ions for continuous treatment of dye wastewater in a dynamic reactor," *Journal of Environmental Sciences*, vol. 22, no. 8, pp. 1290-1296, 2010.
- [6] A. Eshaghi and H. Moradi, "Optical and photocatalytic properties of the Fe-doped TiO₂ nanoparticles loaded on the activated carbon," *Advanced Powder Technology*, vol. 29, no. 8, pp. 1879-1885, 2018.
- [7] N. C. Birben, C. S. Uyguner-Demirel, S. S. Kavurmaci et al., "Application of Fe-doped TiO₂ specimens for the solar photocatalytic degradation of humic acid," *Catalysis Today*, vol. 281, no. 1, pp. 78-84, 2017.
- [8] P.-S. Yap and T.-T. Lim, "Effect of aqueous matrix species on synergistic removal of bisphenol-A under solar irradiation using nitrogen-doped TiO₂/AC composite," *Applied Catalysis B: Environmental*, vol. 101, no. 3-4, pp. 709-717, 2011.
- [9] Z. F. Shi, S. M. Zhang, and S. Guo, "Characteristics and photocatalytic activity of TiO₂," *Applied Mechanics and Materials*, vol. 295-298, pp. 413-417, 2013.

- [10] D. Huang, Y. Miyamoto, J. Ding et al., "A new method to prepare high-surface-area N-TiO₂/activated carbon," *Materials Letters*, vol. 65, pp. 326–328, 2011.
- [11] X. Cheng, X. Yu, and Z. Xing, "Synthesis and characterization of C-N-S-tridoped TiO₂ nano-crystalline photocatalyst and its photocatalytic activity for degradation of rhodamine B," *Journal of Physics and Chemistry of Solids*, vol. 74, pp. 684–690, 2013.
- [12] L. Youji, Z. Xiaoming, C. Wei et al., "Photodecolorization of Rhodamine B on tungsten-doped TiO₂/activated carbon under visible-light irradiation," *Journal of Hazardous Materials*, vol. 227, no. 228, pp. 25–33, 2012.

Research Article

Modeling and Optimization of the BSCF-Based Single-Chamber Solid Oxide Fuel Cell by Artificial Neural Network and Genetic Algorithm

Minh-Vien Le,¹ Tuan-Anh Nguyen ¹ and T.-Anh-Nga Nguyen ²

¹Faculty of Chemical Engineering, Ho Chi Minh City University of Technology, VNU-HCM, 268 Ly Thuong Kiet, Ho Chi Minh City, Vietnam

²Faculty of Applied Sciences, Ton Duc Thang University, 19 Nguyen Huu Tho Str., Tan Phong Ward, District 7, Ho Chi Minh City, Vietnam

Correspondence should be addressed to Tuan-Anh Nguyen; anh.nguyen@hcmut.edu.vn and T.-Anh-Nga Nguyen; nguyenthianhnga@tdtu.edu.vn

Received 21 February 2019; Revised 2 May 2019; Accepted 21 May 2019; Published 20 June 2019

Guest Editor: Thanh-Dong Pham

Copyright © 2019 Minh-Vien Le et al. This is an open access article distributed under the Creative Commons Attribution License, which permits unrestricted use, distribution, and reproduction in any medium, provided the original work is properly cited.

Fuel cells could be a highly effective and eco-friendly technology to transform chemical energy stored in fuel to useful electricity and thus are presently appraised as a standout among the most encouraging advancements for future energy demand. Solid oxide fuel cells (SOFCs) have several advantages over other types of fuel cells, such as the flexibility of fuel used, high energy conversion, and relatively inexpensive catalysts due to high-temperature operation. The single chambers, wherein the anode and cathode are exposed to the same mixture of fuel, are promising for the portable power application due to the simplified, compact, sealing-free cell structure. The empirical regression models, such as artificial neural networks (ANNs), can be used as a black-box tool to simulate systems without solving the complicated physical equations merely by utilizing available experimental data. In this study, the performance of the newly proposed BSCF/GDC-based cathode SOFC was modeled using ANNs. The cell voltage was estimated with cathode preparation temperature, cell operating temperature, and cell current as input parameters by the one-layer feed-forward neural network. In order to acquire the appropriate model, several network structures were tested, and the network was trained by backpropagation algorithms. The data used during the training, validation, and test are the actual experimental results from our previous study. The optimum conditions to achieve maximum power of the cell were then determined by the genetic algorithm and the developed ANN.

1. Introduction

Fuel cells could be a highly effective and eco-friendly technology to transform chemical energy stored in fuel to useful electricity and thus are presently appraised as a standout among the most encouraging advancements for future energy demand [1]. Among different classes of fuel cells, the solid oxide fuel cell (SOFC) has displayed an extraordinary integration of benefits, including high energy efficiency, broad fuel versatility, significant contamination allowance, and low waste discharge [2, 3]. Currently, yttria-stabilized zirconia (YSZ), a zirconia-based electrolyte, is the

most widely utilized electrolyte as it has sufficient oxide-ion conductivity and, furthermore, demonstrates suitable phase durability in both oxidizing and reducing environments [4]. However, in order to lessen the ohmic polarization loss, the zirconia-based electrolyte needs a very high operation temperature $\sim 1000^{\circ}\text{C}$, which provides adequate oxygen conductivity. Therefore, high temperature places rigorous constraints on its accompanying materials. Reducing the operation temperature to $500\text{--}800^{\circ}\text{C}$, classified as the intermediate temperature range, is supposed to elongate the lifespan of SOFC, minimize its degradation rate, and diversify the range of material selections [5].

On the contrary, reducing operation temperature requires a new pair of electrolyte-cathode, which is more ion conductive than the conventional pair of Y-stabilized ZrO_2 and $(\text{La}_{1-x}\text{Sr}_x)\text{MnO}_3$. Therefore, the nickel cermet has been the unanimous selection for the anode composition. LAMOX is an oxide conductor family based initially on the parent $\text{La}_2\text{Mo}_2\text{O}_9$ crystal. The lanthanide-doped LAMOX has the fundamental characteristics of an electrolyte at intermediate temperatures such as high ion conductivity [6, 7] and good phase stability [8]. However, the LAMOX composition is only occasionally investigated as the SOFC electrolyte.

On the cathode side, $\text{Ba}_{0.5}\text{Sr}_{0.5}\text{Co}_{1-x}\text{Fe}_x\text{O}_{3-\delta}$ (BSCF) is usually suggested as a candidate in the intermediate temperature range, in perspective of its exceptional catalytic activity toward oxygen reduction combined with high ion conductivity [9], low electrochemical surface-exchange resistance [10], and reasonable fabrication cost [10]. However, the perovskite of BSCF does have its own drawback. The composition has the phase instability problem, similar to many other perovskites with cobalt on the B site [11]. It should be noted that the cathodic loss contributes the significant part of SOFC's polarization loss. The large cathode polarization loss normally occurs from the fact that the mixed conductor of the cathode perovskite frequently shows the ionic conductivity significantly lower than its electronic conductivity [12, 13]. Hence, a composite cathode of ionic conductor and mixed conductor is adopted to minimize the cathodic loss.

The BSCF, gadolinium-doped ceria (GDC), and $\text{La}_{1.8}\text{Dy}_{0.2}\text{Mo}_2\text{O}_9$ (LDM) powders, therefore, were synthesized and characterized for fuel cell evaluation. The effect of different preparation conditions on the fuel cell behavior was found in this study. On the contrary, modeling and simulation of SOFCs are useful approaches to investigate effects of various design parameters and operating conditions on SOFC performances and also to help in SOFC improvements. The obtained results can be used in optimization, control, improvement, and design of the fuel cell system [14–16]. Currently, there are plenty of models that have been published to contribute more knowledge of the fuel cell phenomena. The approaches for fuel cell modeling can be classified into two categories: theoretical and empirical [15, 17, 18]. In the theoretical mathematical approach, the spatial dimensions of the models vary from simplified zero (0-D) [19, 20] and one (1-D) [18, 21–23] to more complex two (2-D) [24–27] and three (3-D) [28–30], with different characteristics and targets to different research purposes. The mathematical models, which are generally founded based on momentum, mass, and energy conservation laws, necessitate the information about many parameters and properties of the fuel cell system, the complicated equations, and the time-consuming numerical techniques. Therefore, using theoretical models makes the problem too complicated and impractical for some engineering applications.

Another approach, namely, empirical or data-driven modeling, might be more practical for the fuel cell user from the viewpoint the SOFC behavior can be inferred without deeply understanding the internal components [15, 17].

The empirical approaches can be applied to simulate the object's behavior without an algorithmic solution, merely by utilizing available experimental data. These approaches include least-squares support vector machine (LS-SVM) [31] and the Hammerstein model [32, 33]. Among them, artificial neural network (ANN) presents some advantages such as high nonlinearity, matches experimental data with a low degree of error, and does not require any specific analytical equations and system descriptions. ANN is a black-box model, whereas numerical models allow for the examination of parameter distributions inside the cell. Numerical models may also be more accurate than ANN models if, for example, the operating conditions change significantly during dynamic operation. However, utilization of ANNs for modeling SOFCs appears a very promising way due to its rapid computation. Genetic algorithms (GAs) are a class of metaheuristic searching optimization techniques inspired by the mechanics of natural evolution and genetics [34]. Compared to conventional optimization methods, GAs are remarkably simple, robust, and able to handle the nondifferentiable, discontinuous, or multimodal problems. GAs have been successfully applied in a wide range of applications in various engineering, manufacturing, and management areas [35].

In this study, the performance of the BSCF/GDC-based cathode SOFC was modeled using ANNs. The cell voltage was estimated with cathode preparation temperature, cell operating temperature, and cell current as input parameters by the one-layer feed-forward neural network. In order to acquire the appropriate model, several network structures were tested, and the network was trained by back-propagation algorithms. The data used during the training, validation, and test have been obtained from the actual experimental results from our previous study [36]. The optimum condition to achieve maximum power was then determined by genetic algorithms and the developed ANN.

2. Experiments and Methodology

2.1. Experiments. The description of experimental configuration could be found in our study [36, 37]. The brief explanation of the cell is summarized as follows. The porous structure of the anode-supported cell was fabricated through the following steps. Commercial NiO (>99.5%), 1000°C calcined GDC, and 1000°C calcined LDM powders were mixed in a weight ratio of 4.8:3.2:0.8. Then, the mixture was mixed with 15 wt.% of graphite flash, uniaxial pressed, and then sintered for 2 h at 1175°C to form an anode with a size of ~0.4 mm in thickness and ~13.2 mm in diameter.

$\text{La}_{1.8}\text{Dy}_{0.2}\text{Mo}_2\text{O}_9$ (LDM) electrolyte was applied to the polished porous anode pellet by the spin-coating method with a desired thickness of ~60 μm . As mentioned above, BFSC cannot be applied directly onto LDM due to chemical reaction. Therefore, it needs an additional barrier layer to prevent undesirable reaction.

A barrier layer of 0.5 wt.% Fe_2O_3 -doped $\text{Gd}_{0.1}\text{Ce}_{0.9}\text{O}_{1.95}$ (i-GDC) was applied on the LDM layer for one time to form NiO + GDC/LDM/i-GDC button. The button was then co-sintered at 1225°C for 5 hours with a heating and cooling rate of 2°C min^{-1} .

To complete the final cell of NiO + GDC/LDM/i-GDC/BSCF + GDC, the surface of the i-GDC layer was screen-printed on by the blend of composite cathode and then sintered in air at 1000°C (cell a), 1015°C (cell b), 1025°C (cell c), or 1050°C (cell d) for 2 h. In this study, three single-cell sets were fabricated, all of which use a cathode gradient. The composite layer of 50 wt.% BSCF and 50 wt.% GDC was applied onto the i-GDC; meanwhile, the composite layer of 90 wt.% BSCF and 10 wt.% GDC layer was exposed to the air atmosphere.

The configuration of the fuel cell system of NiO + GDC/LDM/i-GDC/GDC-BSCF is shown in Figure 1(a). Two Au wires were connected to the single cell for current collecting, using the Keithley 238 source-measure unit. There is a coil arranged before the cell, which extends the heating time for the inflow. Both the coil and the cell were placed inside a quartz tube, together with a thermocouple which monitors the cell temperature. To activate the anode on-site, an extra Ni + GDC disk was attached above the anode. A sketch of the button cell was represented in Figure 1(b). The dimensions of the system are summarized in Figure 1(c).

The cell was operated in a mixture of methane/air with the flow rate of 650 sccm and the molar ratio of 1.5 : 1. The data were collected on the current density and the cell voltage of the fuel cell button for each combination of the sintering temperature of the cathode (1000, 1015, 1025, and 1050°C) and the cell operating temperatures (625, 650, 675, and 700°C).

2.2. Artificial Neural Network Models. Artificial neural network (ANN) is an information processing method inspired by the biological nervous systems. An ANN consists of a number of highly interconnected nodes, called neurons, which are able to receive and transmit the data [38, 39]. Feed-forward multilayer architectures, the simplest form of ANNs, are composed of an input layer, one or more hidden layers, and an output layer. The number of neurons in the input and output layers is equal to the number of inputs and outputs in the system to be modeled. Each neuron is linked to all neurons in the following layer by methods of weighted connections. The input of a neuron is the weighted aggregate of the data from its linked neurons. The response or output of a neuron is the transformation of its input using an appropriate activation function. The neurons will equally transmit their responses to all the neurons in the next layer. Input neurons do not activate their inputs; they just receive and send them to all the neurons in the first hidden layer. The number of neurons in the hidden layers is an important parameter which impacts the precision of the estimation. If too few neurons are used, the ANN might not have enough flexibility to satisfactorily approximate the data. However, if larger than the necessary number of neurons is included, the network then becomes overfitting, and it can memorize the data exactly but fail to generalize to a new situation [40]. In general, there is no rule for the number of neurons in the hidden layer, and it is usually determined by experiments. Figure 2 shows a feed-forward artificial neural

network (3-5-1) structure with the input of operating temperature, sintering temperature, and current.

The activation function is used to calculate the output response of a neuron and can take any form, linear or nonlinear. The popular activation function, which is also employed in this study, is the logistic sigmoid [41]. The general form of the function is given as $f(x) = 1/(1 + e^{-x})$.

In order to enhance the performance of the network, the supplied input-output data should be normalized. In this study, the input data (x_i) are scaled to the normalized value (x_{norm}) as follows:

$$x_{\text{norm}} = 0.8 \frac{(x - x_{\text{min}})}{x_{\text{max}} - x_{\text{min}}} + 0.1, \quad (1)$$

where x_{max} and x_{min} are the maximum and minimum of the experimental data, respectively.

The values of mean squared error (MSE) and coefficient of determination (R^2) are frequently employed to evaluate the performance of the ANN. They were, respectively, calculated as follows [42]:

$$\text{MSE} = \frac{1}{n} \sum_{i=1}^n (t_i - a_i)^2, \quad (2)$$

$$R^2 = \frac{(\sum_{i=1}^n (t_i - \bar{t})(a_i - \bar{a}))^2}{\sum_{i=1}^n (t_i - \bar{t})^2 \sum_{i=1}^n (a_i - \bar{a})^2},$$

where n is the total data points, t_i is the predicted value from the networks, a_i is the experimental response, and \bar{t} and \bar{a} are the average of predicted value and actual value, respectively.

There are several important factors affecting fuel cell performance, including cathode and anode structure, electrolyte material and thickness, cell temperature, and inlet and outlet gas compositions. In this study, two significant factors, namely, cathode sintering temperature and cell operating temperature, were examined. The range for sintering temperature is from 1000°C to 1050°C, and the range for the operating temperature is from 625°C to 700°C. As depicted in our earlier report, the sintering temperature affects the structure of the obtained cathode. The range for the investigated parameters is explained as follows. At the cathode sintering temperature below 1000°C, the low degree crystallization of BSCF minimizes the redox reaction, thus reducing the fuel cell performance. On the contrary, the phase compatibility between BSCF and GDC is ensured only up to 1050°C. Similarly, at the lower operating temperature of 600°C, there are not enough kinetic rate of ionic conducting, leading to poor performance of the fuel cell. However, at operating temperature over 700°C, the BSCF crystal becomes instable under the methane/air atmosphere, which limits the performance of the fuel cell.

Therefore, the network architecture is designed with three inputs, one hidden layer, and one output. The inputs are current density, sintering temperature of the cathode, and cell operating temperature. The network was trained using the backpropagation algorithm [43]. The maximum number of epochs and the minimum performance gradient are assigned to 400 and 10^{-5} , respectively. Training

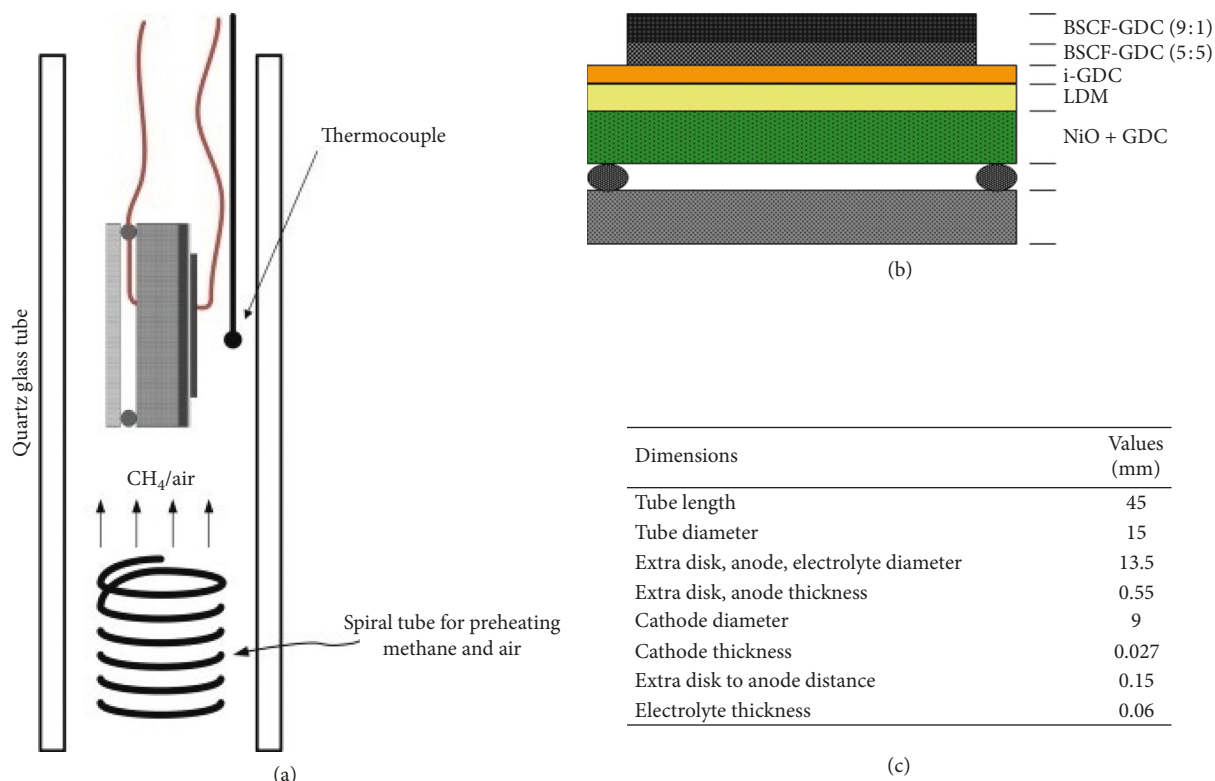


FIGURE 1: (a) Configurations of single-chamber solid oxide fuel cells (SOFCs) and the detail of anode-supported cell [37]. (b) A sketch of the button cell. (c) Geometry dimensions of the experimental setup.

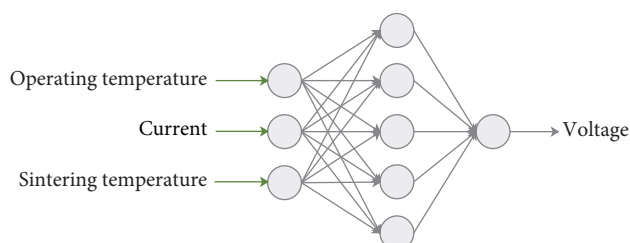


FIGURE 2: Artificial neural network (3-5-1) structure.

stops when the maximum number of epochs is reached or when either the MSE or performance gradient is less than the predetermined goal. Through various trial experiments, the appropriate network structure for the current simulation is decided. The data sets were randomly divided into three subsets, namely, training, validation, and test, each of which contains 70%, 20%, and 10% number of samples, respectively. The validation and test sets are essential for the evaluation of the validation and modeling power of the networks.

The parameters of the model from the neural network were stored and used to optimize the power density using genetic algorithms in the next section.

2.3. Optimization by Genetic Algorithms. Genetic algorithms (GAs) are heuristic search algorithms inspired by

the evolutionary ideas of natural selection and genetics. Genetic algorithms start with randomly generated chromosomes from the feasible region to produce a population. The fitness of each chromosome was defined by the objective function after converting the chromosomes to natural values. The algorithms iteratively modify a population of individual solutions analogous to processes happening in the nature—selection, reproduction, and mutation. The best fitness of the population comes toward an optimal solution by the principle of “survival of the fittest” [44]. The basic steps of genetic algorithms can be summarized as follows:

- (1) Randomly generating a primary population of N individuals
- (2) Producing the next generation by crossing over and mutation among individuals
- (3) Selecting the new population of N individuals from the parents and generation of (2)
- (4) Creating the next population by iterating steps (2) and (3) until the maximum number of generations is reached

The algorithm flow of the GA approach is shown in Figure 3.

The objective function in this study is the power density of the fuel cell, which is defined as

$$P = I \times V, \quad (3)$$

where P is the power density ($\text{mW}\cdot\text{cm}^{-2}$), I is the current density ($\text{mA}\cdot\text{cm}^{-2}$) and is the input to the ANN model, and V is the cell voltage (V) which is estimated from the ANN model.

The design variables in the optimization problem are the inputs of the artificial neural network model. Their corresponding intervals were discussed in the previous section and are summarized as follows:

- (i) Sintering temperature of the cathode, [1000–1050] ($^{\circ}\text{C}$)
- (ii) Operating temperature of the cell, [625–700] ($^{\circ}\text{C}$)
- (iii) Electric current of the cell, [0–1500] ($\text{mA}\cdot\text{cm}^{-2}$)

The binary GA was used as the optimization method. A MATLAB™ program which was adapted from the literature [45] is used for the GA computations. The parameters of the GA such as population size and mutation probability values were set to be 100 and 0.10, respectively. The survival of the chromosomes was determined as the roulette wheel selection with elitism; it means that the best solution is always survive to the next population. The number of generations was assigned to be 500.

3. Results and Discussion

3.1. Microstructure of the Button Cell. In order to better understand the structure of the fabricated single cell, the single cell after I - V measurement was observed using the SEM method. The microstructure of the single cell in a cross-sectional image is shown in Figure 4. The SEM image shows an electrolyte thickness of $\sim 60\ \mu\text{m}$, total cathode thickness (including 2 layers) of $\sim 27\ \mu\text{m}$, and barrier layer i-GDC thickness of $6\text{--}8\ \mu\text{m}$. Moreover, the cross section shows well adherence between the cathode, i-GDC, electrolyte, and anode layers. Note that a crack of electrolyte at the left-hand side was formed by breaking out for the SEM measurement. Finally, the good adherence between layers and appropriate microstructures reveal that it is a good technique to fabricate the single cell for experimental and simulation study.

3.2. Artificial Neural Network Model Validation. An artificial neural network was used for modeling the cell voltage of the fuel cell. Experimental data obtained under different operating conditions were used to train and validate the neural network model. In ANN modeling, the number of hidden neurons is critical because excessive neurons will cause overfitting; however, too small number of neurons may not adequately capture the complexity of the system [46]. After performing some trials, the sufficient number of neurons in the hidden layer was 7. Consequently, a 3-7-1 feed-forward ANN architecture was employed in this study.

The results of the ANN modeling were described using current versus cell voltage graphs (or I - V plots) and were compared with data from experiments. The correlation coefficients (R^2) for three subsets (training, validation, and testing) were 99.92%, 99.88%, and 99.87%, respectively. The

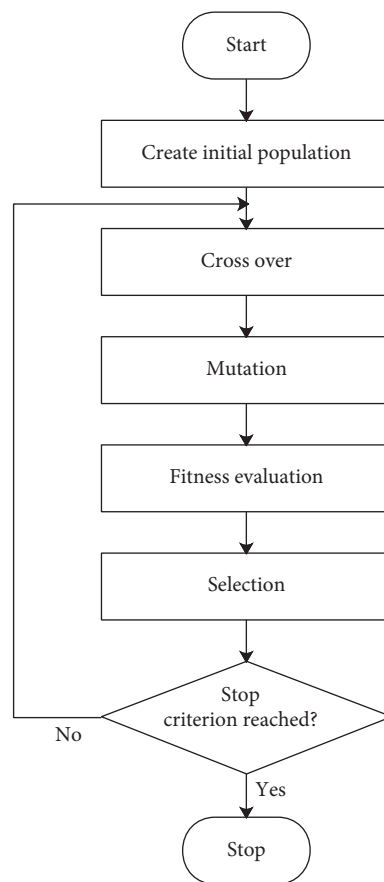


FIGURE 3: Block diagram of the genetic algorithm process.

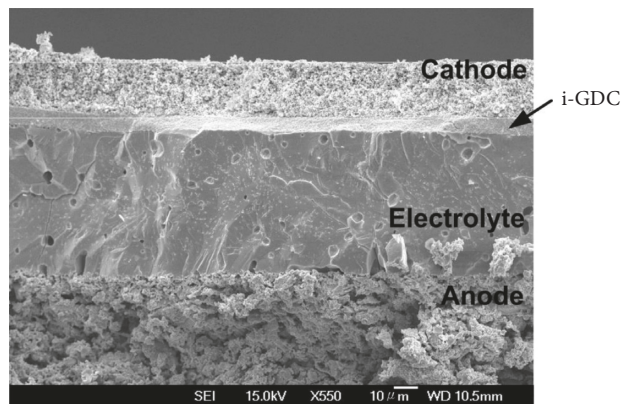


FIGURE 4: The cross-sectional image shows the interface structure of the cell.

MSE values for three subsets (training, validation, and testing) were 4.19×10^{-5} , 7.14×10^{-5} , and 7.04×10^{-5} , respectively. The correlation coefficient and MSE of all data were 99.91% and 5.06×10^{-5} , respectively.

Figure 5 shows the cell performances from the ANN modeling and the experimental data at the cathode sintering temperature of 1000°C as the operating temperature changes from 625°C to 700°C . The correlation and MSE for this subset are 99.95% and 2.86×10^{-5} , respectively.

Figure 6 presents the cell voltage versus current density curves of the ANN predictions and the experimental data at

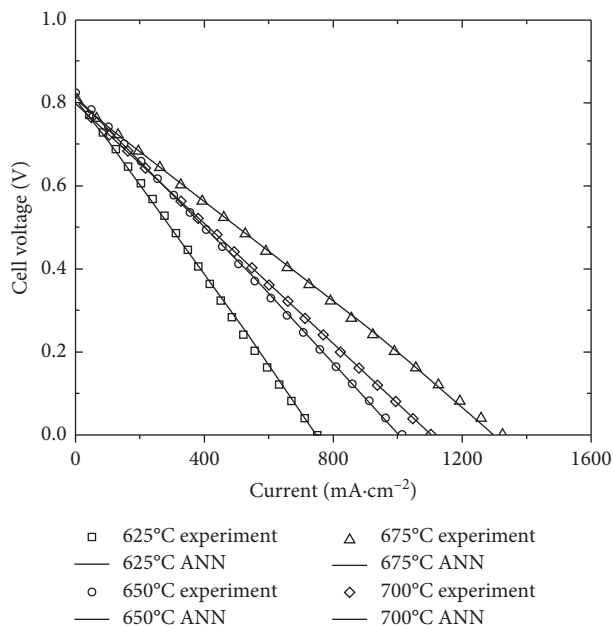


FIGURE 5: Comparison of I - V curves for the cathode sintered at 1000°C and operated at different temperatures by the ANN model and experimental data.

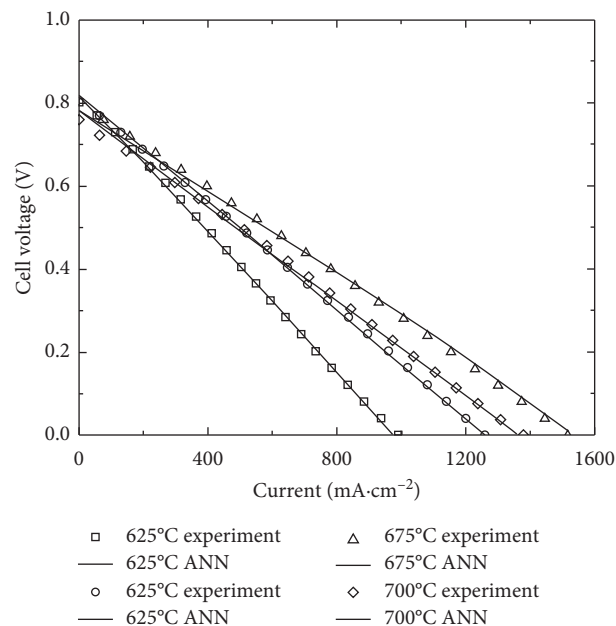


FIGURE 7: Comparison of I - V curves for the cathode sintered at 1025°C and operated at different temperatures by the ANN model and experimental data.

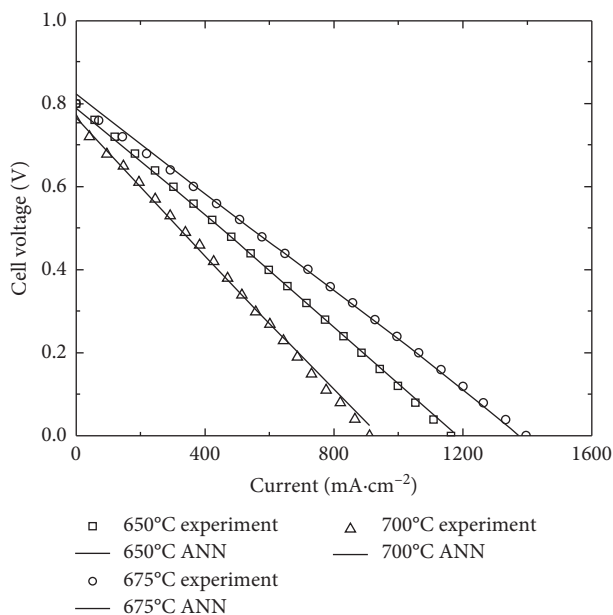


FIGURE 6: Comparison of I - V curves for the cathode sintered at 1015°C and operated at different temperatures by the ANN model and experimental data.

1015°C of cathode sintering temperature as the operating temperature is varied from 650°C to 700°C . The correlation coefficient and MSE of the model for this subset are 99.83% and 9.74×10^{-5} , respectively.

In Figure 7, it can be seen that the cell voltage versus current density curves with various operating temperatures modeled by the ANN agrees well with the experimental data at the sintering temperature of 1025°C . The operating

temperature ranges from 625°C to 700°C . The results show that the ANN model is in good agreement with the experimental data with a correlation coefficient of 99.89% and a MSE of 6.58×10^{-5} .

Figure 8 shows I - V curves of the cells with the sintering temperature of 1050°C from the ANN and experimental data as the operating temperature changes from 650°C to 700°C . The correlation coefficient is 99.98%, and the MSE is 1.28×10^{-5} for this subset. The results show a good agreement between the model estimated and the experimental data.

From the results, it can be obtained that the ANN model succeeded in predicting the SOFC performance at an acceptable level of precision. It also confirms the capability of the ANN in investigating the effect of various parameters on its behavior.

3.3. Sensitivity Analysis. In order to identify the critical parameters and their degree of importance on the response outputs, a sensitivity analysis should be investigated. The analysis shows that the network output varies corresponding to the change of inputs and identifies the more sensitive parameters, which should be controlled precisely. The results of this analysis would also contribute deeper understanding about the model parameters for the design process.

In this study, the sensitivity analysis based on the weight matrix was chosen because of its simplicity. From the weight magnitude, several expressions have been proposed which have common properties: calculation of the product of the weights w_{ij} that connects the input neuron i and the hidden neuron j and v_{jk} that connects the hidden neuron j and the output neuron k for each of the

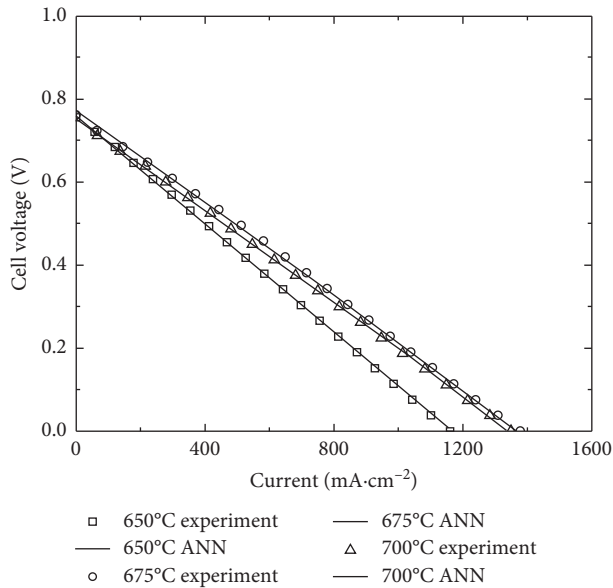


FIGURE 8: Comparison of I - V curves for the cathode sintered at 1050°C and operated at different temperatures by the ANN model and experimental data.

hidden neurons of the network, which gives the sum of the calculated products. The following equation, reported by Garson [47], is widely used:

$$Q_{ik} = \frac{\sum_{j=1}^L \left(\left(w_{ij} / \sum_{r=1}^N w_{rj} \right) v_{jk} \right)}{\sum_{i=1}^N \left(\sum_{j=1}^L \left(\left(w_{ij} / \sum_{r=1}^N w_{rj} \right) v_{jk} \right) \right)}, \quad (4)$$

in which $\sum_{r=1}^N w_{rj}$ is the sum of the connection weights between the N input neurons and the hidden neuron j . Q_{ik} denotes the effect of the input i on the output k , in relation to the other input variables.

The relative significance of each input variable on the output is presented in Figure 9. From the results, it can be obtained that the most important factor affecting the cell voltage is the sintering temperature of the BSCF cathode.

The importance of sintering temperature of the BSCF cathode was also reported in our previous study [36] or it can be seen in Figure 10. From the figure, even though the sintering temperature differs slightly, the cell power performance is significantly affected. Therefore, the sintering temperature should be precisely controlled and carefully decided in order to obtain the cell's best performance.

3.4. Optimization Results. From the artificial neural network modeling results, genetic algorithm was utilized to search the optimum condition for the power density. The decision parameters were the sintering temperature of the cathode, operating temperature of the furnace, and current density. The boundary constraints for the design parameters were indicated earlier in Section 2.3. The fitness function is the power density.

Figure 11 depicts the fitness values (maximum and mean) of the population versus generation. As indicated

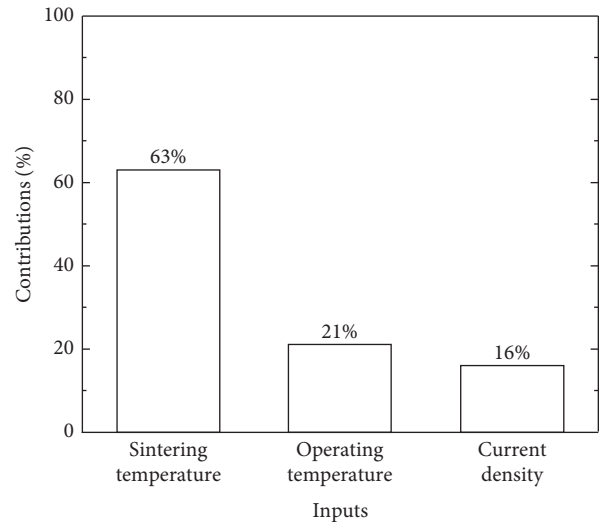


FIGURE 9: Relative contribution of input variables on cell voltage.

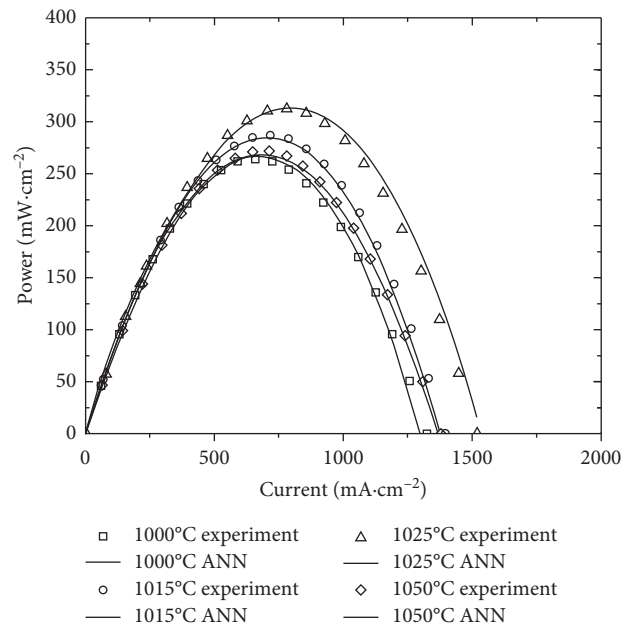


FIGURE 10: The power performance of the cell at different sintering temperatures.

in the figure, after about 20 generations, the value of fitness function attained a maximum value and then remained unchanged. After 100 generations, the maximum fuel cell power density of $451.64 \text{ mW}/\text{cm}^2$ could be achieved at the sintering temperature of 1005°C , operating temperature of 668°C , and current density of $777 \text{ mA}/\text{cm}^2$.

4. Conclusions

In this study, an artificial neural network was successfully applied to model the behavior of a BSCF-based single-chamber solid oxide fuel cell. The ANN model can adequately predict the SOFC performance without knowledge of numerous physical, chemical, and electrochemical factors

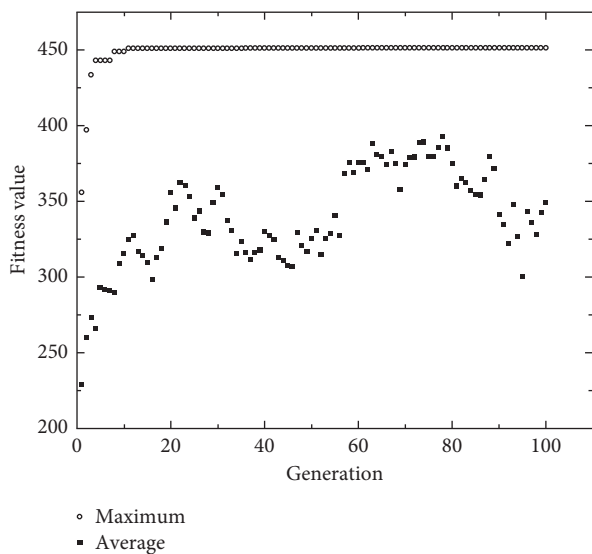


FIGURE 11: The fitness values versus generation.

and is validated with actual experimental data. The proposed network has a simple structure with one hidden layer and a small number of neurons. The prediction from the ANN model matched the experimental data with a low degree of error. From the trained ANN, the power density was estimated as fitness function, and the genetic optimization algorithm was employed to predict the optimal cell parameters such as sintering temperature of the cathode, operating temperature of the furnace, and current density of the cell. The maximum power density is 451.64 mW/cm^2 , which could be achieved at the sintering temperature of 1005°C , operating temperature of 668°C , and current density of 777 mA/cm^2 . The results suggested that the BSCF should be fabricated at 1005°C , and the button cell should be operated at 668°C .

Data Availability

The data used to support the findings of this study are available from the corresponding author upon request.

Disclosure

Part of this study (with different cathode materials-LSCF) was presented at the Third International Conference on Computational Science and Engineering in Ho Chi Minh City, Vietnam, November 2016.

Conflicts of Interest

The authors declare that they have no conflicts of interest.

Acknowledgments

The authors would like to thank the Vietnam National Foundation for Science and Technology Development (NAFOSTED) for the financial support under grant number 104.03-2013.20. The authors would also like to thank Prof. Dah-Shyang Tsai (National Taiwan University

of Science and Technology) for the kind support during the project.

References

- [1] E. D. Wachsman, C. A. Marlowe, and K. T. Lee, "Role of solid oxide fuel cells in a balanced energy strategy," *Energy and Environmental Science*, vol. 5, no. 2, pp. 5498–5509, 2012.
- [2] N. Minh, J. Mizusaki, and S. C. Singhal, "Advances in solid oxide fuel cells: review of progress through three decades of the international symposia on solid oxide fuel cells," *ECS Transactions*, vol. 78, no. 1, pp. 63–73, 2017.
- [3] H. Ghezal-Ayagh and B. P. Borglum, "(Invited) Review of progress in solid oxide fuel cell at FuelCell energy," *ECS Transactions*, vol. 80, no. 9, pp. 47–56, 2017.
- [4] N. Mahato, A. Banerjee, A. Gupta, S. Omar, and K. Balani, "Progress in material selection for solid oxide fuel cell technology: a review," *Progress in Materials Science*, vol. 72, pp. 141–337, 2015.
- [5] L. Fan, B. Zhu, P.-C. Su, and C. He, "Nanomaterials and technologies for low temperature solid oxide fuel cells: recent advances, challenges and opportunities," *Nano Energy*, vol. 45, pp. 148–176, 2018.
- [6] M.-V. Le, D.-S. Tsai, C.-C. Yao, J.-C. Lo, and T. P. G. Vo, "Properties of 10% Dy-doped $\text{La}_2\text{Mo}_2\text{O}_9$ and its electrolyte performance in single chamber solid oxide fuel cell," *Journal of Alloys and Compounds*, vol. 582, pp. 780–785, 2014.
- [7] D.-S. Tsai, M.-J. Hsieh, J.-C. Tseng, and H.-Y. Lee, "Ionic conductivities and phase transitions of lanthanide rare-earth substituted $\text{La}_2\text{Mo}_2\text{O}_9$," *Journal of the European Ceramic Society*, vol. 25, no. 4, pp. 481–487, 2005.
- [8] T. Jin, M. Madhavarao, C. Cheng, D. Tsai, and M. Hung, "Structural stability and ion conductivity of the Dy and W substituted $\text{La}_2\text{Mo}_2\text{O}_9$," *Solid State Ionics*, vol. 178, no. 5-6, pp. 367–374, 2007.
- [9] Z. Shao and S. M. Haile, "A high-performance cathode for the next generation of solid-oxide fuel cells," *Nature*, vol. 431, no. 7005, pp. 170–173, 2004.
- [10] W.-X. Kao, M.-C. Lee, T.-N. Lin, C.-H. Wang, and Y.-C. Chang, "Fabrication and characterization of a $\text{Ba}_{0.5}\text{Sr}_{0.5}\text{Co}_{0.8}\text{Fe}_{0.2}\text{O}_{3-\delta}$ -Gadolinia-doped ceria cathode for an anode-supported solid-oxide fuel cell," *Journal of Power Sources*, vol. 195, no. 8, pp. 2220–2223, 2010.
- [11] B.-K. Kang, H.-C. Lee, Y.-W. Heo, J.-J. Kim, J. Y. Kim, and J.-H. Lee, "Thermal expansion behavior of La-doped ($\text{Ba}_{0.5}\text{Sr}_{0.5}\text{Co}_{0.5}\text{Fe}_{0.2}$) $\text{O}_{3-\delta}$ cathode material," *Ceramics International*, vol. 39, no. 7, pp. 8267–8271, 2013.
- [12] C. Ftikos, S. Carter, and B. C. H. Steele, "Mixed electronic/ionic conductivity of the solid solution $\text{La}_{(1-x)}\text{Sr}_x\text{Co}_{(1-y)}\text{Ni}_y\text{O}_{3-\delta}$ (x : 0.4, 0.5, 0.6 and y : 0.2, 0.4, 0.6)," *Journal of the European Ceramic Society*, vol. 12, no. 1, pp. 79–86, 1993.
- [13] F. S. da Silva and T. M. de Souza, "Novel materials for solid oxide fuel cell technologies: a literature review," *International Journal of Hydrogen Energy*, vol. 42, no. 41, pp. 26020–26036, 2017.
- [14] S. Kakac, A. Pramanjaroenkij, and X. Zhou, "A review of numerical modeling of solid oxide fuel cells," *International Journal of Hydrogen Energy*, vol. 32, no. 7, pp. 761–786, 2007.
- [15] S. A. Hajimolana, M. A. Hussain, W. M. A. W. Daud, M. Soroush, and A. Shamiri, "Mathematical modeling of solid oxide fuel cells: a review," *Renewable and Sustainable Energy Reviews*, vol. 15, no. 4, pp. 1893–1917, 2011.

- [16] L. Ma, D. B. Ingham, M. Pourkashanian, and E. Carcadea, "Review of the computational fluid dynamics modeling of fuel cells," *Journal of Fuel Cell Science and Technology*, vol. 2, no. 4, pp. 246–257, 2005.
- [17] K. Wang, D. Hissel, M. C. Péra et al., "A Review on solid oxide fuel cell models," *International Journal of Hydrogen Energy*, vol. 36, no. 12, pp. 7212–7228, 2011.
- [18] M. Karcz, "From 0D to 1D modeling of tubular solid oxide fuel cell," *Energy Conversion and Management*, vol. 50, no. 9, pp. 2307–2315, 2009.
- [19] P. Costamagna, L. Magistri, and A. F. Massardo, "Design and part-load performance of a hybrid system based on a solid oxide fuel cell reactor and a micro gas turbine," *Journal of Power Sources*, vol. 96, no. 2, pp. 352–368, 2001.
- [20] F. Zabihian and A. S. Fung, "Macro-level modeling of solid oxide fuel cells, approaches, and assumptions revisited," *Journal of Renewable and Sustainable Energy*, vol. 9, no. 5, article 054301, 2017.
- [21] T. Ota, M. Koyama, C.-j. Wen, K. Yamada, and H. Takahashi, "Object-based modeling of SOFC system: dynamic behavior of micro-tube SOFC," *Journal of Power Sources*, vol. 118, no. 1-2, pp. 430–439, 2003.
- [22] P.-W. Li and K. Suzuki, "Numerical modeling and performance study of a tubular SOFC," *Journal of The Electrochemical Society*, vol. 151, no. 4, pp. A548–A557, 2004.
- [23] R. Bove, P. Lunghi, and N. Msammes, "SOFC mathematic model for systems simulations? Part 2: definition of an analytical model," *International Journal of Hydrogen Energy*, vol. 30, no. 2, pp. 189–200, 2005.
- [24] R. Ma, F. Gao, E. Breaz, Y. Huangfu, and B. Pascal, "Multi-dimensional reversible solid oxide fuel cell modeling for embedded applications," *IEEE Transactions on Energy Conversion*, vol. 33, no. 2, pp. 692–701, 2018.
- [25] M. Ni, "2D thermal-fluid modeling and parametric analysis of a planar solid oxide fuel cell," *Energy Conversion and Management*, vol. 51, no. 4, pp. 714–721, 2010.
- [26] H. Geisler, S. Dierickx, A. Weber, and E. Ivers-Tiffée, "A 2D stationary FEM model for hydrocarbon fuelled SOFC stack layers," *ECS Transactions*, vol. 68, no. 1, pp. 2151–2158, 2015.
- [27] X. J. Luo and K. F. Fong, "Development of 2D dynamic model for hydrogen-fed and methane-fed solid oxide fuel cells," *Journal of Power Sources*, vol. 328, pp. 91–104, 2016.
- [28] K. Nikooyeh, A. A. Jeje, and J. M. Hill, "3D modeling of anode-supported planar SOFC with internal reforming of methane," *Journal of Power Sources*, vol. 171, no. 2, pp. 601–609, 2007.
- [29] M. Andersson, H. Paradis, J. Yuan, and B. Sundén, "Three dimensional modeling of an solid oxide fuel cell coupling charge transfer phenomena with transport processes and heat generation," *Electrochimica Acta*, vol. 109, pp. 881–893, 2013.
- [30] C. Yang, G. Yang, D. Yue, J. Yuan, and B. Sundén, "Computational fluid dynamics model development on transport phenomena coupling with reactions in intermediate temperature solid oxide fuel cells," *Journal of Renewable and Sustainable Energy*, vol. 5, no. 2, article 021420, 2013.
- [31] H.-B. Huo, X.-J. Zhu, and G.-Y. Cao, "Nonlinear modeling of a SOFC stack based on a least squares support vector machine," *Journal of Power Sources*, vol. 162, no. 2, pp. 1220–1225, 2006.
- [32] H.-B. Huo, Z.-D. Zhong, X.-J. Zhu, and H.-Y. Tu, "Nonlinear dynamic modeling for a SOFC stack by using a Hammerstein model," *Journal of Power Sources*, vol. 175, no. 1, pp. 441–446, 2008.
- [33] F. Jurado, "A method for the identification of solid oxide fuel cells using a Hammerstein model," *Journal of Power Sources*, vol. 154, no. 1, pp. 145–152, 2006.
- [34] D. E. Goldberg, *Genetic Algorithms in Search, Optimization and Machine Learning*, Addison-Wesley Longman Publishing Co., Inc., Boston, MA, USA, 1989.
- [35] M. Gen and R. Cheng, *Genetic Algorithms and Engineering Optimization*, Wiley, Hoboken, NJ, USA, 2000.
- [36] M.-V. Le, D.-S. Tsai, and T.-A. Nguyen, "BSCF/GDC as a refined cathode to the single-chamber solid oxide fuel cell based on a LAMOX electrolyte," *Ceramics International*, vol. 44, no. 2, pp. 1726–1730, 2018.
- [37] J.-C. Lo, D.-S. Tsai, Y.-C. Chen, M.-V. Le, W.-H. Chung, and F.-J. Liu, "La₂Mo₂O₉-Based electrolyte: ion conductivity and anode-supported cell under single chamber conditions," *Journal of the American Ceramic Society*, vol. 94, no. 3, pp. 806–811, 2011.
- [38] J. Milewski and K. Świrski, "Modelling the SOFC behaviours by artificial neural network," *International Journal of Hydrogen Energy*, vol. 34, no. 13, pp. 5546–5553, 2009.
- [39] D. R. Baughman and Y. A. Liu, *Neural Networks in Bioprocessing and Chemical Engineering*, Academic Press, Cambridge, MA, USA, 1995.
- [40] K. G. Sheela and S. N. Deepa, "Review on methods to fix number of hidden neurons in neural networks," *Mathematical Problems in Engineering*, vol. 2013, Article ID 425740, 11 pages, 2013.
- [41] M. Y. Rafiq, G. Bugmann, and D. J. Easterbrook, "Neural network design for engineering applications," *Computers and Structures*, vol. 79, no. 17, pp. 1541–1552, 2001.
- [42] D. M. Himmelblau, "Accounts of experiences in the application of artificial neural networks in chemical engineering," *Industrial and Engineering Chemistry Research*, vol. 47, no. 16, pp. 5782–5796, 2008.
- [43] B. J. Wythoff, "Backpropagation neural networks," *Chemo-metrics and Intelligent Laboratory Systems*, vol. 18, no. 2, pp. 115–155, 1993.
- [44] R. L. Haupt and S. E. Haupt, *Practical Genetic Algorithms*, Wiley, Hoboken, NJ, USA, 2004.
- [45] C. Guo and X. Yang, "A programming of genetic algorithm in Matlab7.0," *Modern Applied Science*, vol. 5, no. 1, p. 230, 2011.
- [46] D. R. Baughman and Y. A. Liu, *Neural Networks in Bioprocessing and Chemical Engineering*, Elsevier Science, Amsterdam, Netherlands, 2014.
- [47] G. D. Garson, "Interpreting neural-network connection weights," *AI Expert*, vol. 6, no. 4, pp. 46–51, 1991.

Research Article

Influence of Organoclay on the Flame Retardancy and Thermal Insulation Property of Expandable Graphite/Polyurethane Foam

Nhung Hac Thi ^{1,2}, Duy Linh Pham,¹ Nguyen Thi Hanh ^{1,2}, Ho Thi Oanh ^{1,2},
Thi Hai Yen Duong,¹ Thanh Nhan Nguyen ¹, Nguyen Duc Tuyen ¹, Dinh Long Phan,^{1,2}
Ha Thu Trinh,¹ Ha Tran Nguyen,³ Tung Ngo Trinh,¹ and Mai Ha Hoang ^{1,2}

¹Institute of Chemistry, Vietnam Academy of Science and Technology, 18 Hoang Quoc Viet, Cau Giay, Hanoi, Vietnam

²Graduate University of Science and Technology, Vietnam Academy of Science and Technology, 18 Hoang Quoc Viet, Cau Giay, Hanoi, Vietnam

³Faculty of Materials Technology, Ho Chi Minh City University of Technology, Vietnam National University, 268 Ly Thuong Kiet, District 10, Ho Chi Minh City, Vietnam

Correspondence should be addressed to Mai Ha Hoang; hoangmaiha@ich.vast.vn

Received 15 March 2019; Accepted 28 May 2019; Published 17 June 2019

Guest Editor: Nguayen Van Noi

Copyright © 2019 Nhung Hac Thi et al. This is an open access article distributed under the Creative Commons Attribution License, which permits unrestricted use, distribution, and reproduction in any medium, provided the original work is properly cited.

The rigid polyurethane foams (RPUFs) filled with organoclay cloisite 20A and expandable graphite (EG) were prepared by the one-step expanding foam method. Flame behavior, mechanical properties, and thermal conductivity of the composites were investigated. The vertical burning test (UL-94V) and limiting oxygen index (LOI) showed that the flame retardancy was increased proportionally with the content of EG in PU composite. However, the presence of EG filler impaired the thermal insulation and the compressive strength of the composite. In this report, we proved that organoclay could improve the compressive strength, thermal insulation, and flame retardancy of EG/polyurethane composites. This work can contribute to the development of environment-friendly flame-retardant products for green growth.

1. Introduction

Rigid polyurethane foams (RPUFs) are commonly used in the construction industry as an insulating and soundproof barrier because of their low thermal conductivity, low density, high compression strength, and excellent adhesion [1, 2]. Additionally, RPUF can be frequently found as an insulation layer in pipes, tanks, refrigerators, boats, and aircraft [3, 4]. However, RPUFs are flammable materials and release polluted gases if burned, limiting its application [5].

The most effective and simplest method to improve the flame-retardant properties of RPUF is the addition of flame-retardant additives into the polymer matrix. The common additives include halogen, phosphorus, and nitrogen compounds [6–12]. Unfortunately, these flame-retardant

compounds generate toxic gases in the burning process which are harmful to people and the environment [13, 14].

Expandable graphite (EG) is an intumescent fire retardant material and has been widely utilized in the polyurethane matrix. When EG is exposed to a heat source, it will be expanded to a carbonaceous layer on the surface of the PU composite. This char layer prevents oxygen diffusion and mass and heat transfer between the flame and PU matrix, thus discontinuing the self-sustained combustion of the composite [15–20]. Modesti et al. [13, 16] investigated the fire behavior of low-density EG/PUF and proved that good flame-retardant composites could be acquired by increasing EG loading. However, the presence of EG reduced the compressive strength of EG/PUF composites [13, 15, 19–21]. Moreover, it was also found that the thermal

conductivity of the EG/PUF composites increased in comparison with pure PUF [13, 15, 20–24]. The higher thermal conductivity could hamper the application of PUFs as a thermal insulation material. So, it is necessary to develop novel EG/RPUF composites that meet the requirement of high flame retardancy while retaining mechanical strength and thermal insulation. Nonetheless, there have been few reports devoted to solving the problem.

Organoclay is known as a common reinforcement for polymers because of its unique properties such as nanoscale lamellar structures, high aspect ratio, and high tensile strength [25, 26]. Besides, it was also found that the flame-retardant properties of PU foam were enhanced upon the incorporation of nanoclay [27, 28]. In this work, we demonstrated that incorporation of organoclay into EG/PU composite is an effective, simple, and scalable method to improve the mechanical, thermal insulation, and flame-retardant properties of the polyurethane foams.

2. Materials and Methods

2.1. Materials. The polyol used for RPUF preparation was a polypropylene glycol with the viscosity at $20^{\circ}\text{C} = 1500 \pm 300$ cps (MCNS Inc.) containing *n*-pentane (technical grade) as a blowing agent. The isocyanate used was 4,4'-diphenylmethane diisocyanate (MDI) with NCO % = 31% and average functionality = 2.8 (Tosoh Corporation, Japan). Additional components used for RPUF composites were expandable graphite flakes (EG): +50 mesh ($>300\ \mu\text{m}$, $\geq 75\%$ minimum), pH = $5 \div 10$ (Sigma-Aldrich), and cloisite 20A: d-spacing (001) = $31.5\ \text{\AA}$ (Southern Clay Products Inc., Texas, USA).

2.2. Preparation of the Rigid Foam. Rigid polyurethane foam was prepared by the one-step expanding foam method using cast molding. EG and cloisite 20A were dispersed into the polyol before adding isocyanate. Polyol, blowing agent, and additives were mixed and stirred together until a uniform mixture was obtained. Afterward, a certain amount of isocyanate MDI (MDI/polyol = 1.4 w/w) was added into the mixture with vigorous stirring for 10 s. The mixture was then quickly poured into a mold to produce PU foam. For the completion of the polymerization between MDI and polyol, the molds containing PU were kept in an oven at 70°C for 24 h. Finally, the PU foams were separated from the mold and the hard surface of the foams was removed. The components of the flame-retardant foam are given in Table 1.

2.3. Characterizations. The horizontal and vertical burning tests were carried out with the GT-MC35F-2 horizontal and vertical flame chamber, according to the standard horizontal burning test (ASTMD 635-98) and the standard vertical burning test (ASTMD 3801-96). The size of the specimen was $130 \times 13 \times 3\ \text{mm}^3$ (length \times width \times thickness). Limiting oxygen index (LOI) was determined by a Yasuda 214 instrument on the sample whose size was $130 \times 10 \times 10\ \text{mm}^3$ according to ASTMD 2863-97. Thermal gravimetric analysis

(TGA) was performed on a LABSYS Evo STA under air with the heating rate of $10^{\circ}\text{C}\cdot\text{min}^{-1}$ from 30°C to 800°C . The thermal conductivity of the foams was measured with a THB-500-Transient hot bridge (Linseis) instrument according to standard DIN EN 993-15. The size of the samples was $60 \times 40 \times 5\ \text{mm}^3$. The sensor was sandwiched between two sheets of the sample. The compression test of the composites was taken on an Instron 3383 system, and the size of samples was $50 \times 50 \times 50\ \text{mm}^3$ according to the standard ISO 4898. The rate of compression was $5\ \text{mm}\cdot\text{min}^{-1}$. The surface morphology of RPUF composites before and after burning was observed by using a Hitachi S-4800 scanning electron microscope instrument with an accelerating voltage of 5 kV at the room temperature. Transmission electron micrographs (TEM) were taken by a JEM 1400 (JEOL, Japan) of 70 nm thick layers of the composites. The TEM specimen was prepared by an epoxy embedding method at ambient temperature. The crystal structures of PU composites were determined by AD8 Advance diffractometer with scan detectors and Cu K α radiation ($\lambda = 1.5406\ \text{\AA}$), a tube voltage of 40 kV, and a current of 40 mA.

3. Results and Discussion

3.1. Flame-Retardant Properties of the Foams. Flame-resistant properties of RPUF composites with different contents of EG and Cloisite 20A were investigated by the horizontal-vertical burning test (UL-94) and the LOI test. The results of the burning test are presented in Figure 1 and Table 2. The surface of burned composites was covered by worm-like structures of the expanded graphite char layer which could protect the PU matrix. The horizontal test (Figure 1(a) and Table 2) exhibited that the pure RPUF burned very fast and completely. By contrast, the flame of EG-filled composites was stopped in front of the first mark and the flame retardancy of the EG-containing composite reached UL94HB rating. In the case of the vertical burning test, the neat RPUF and the RPUF filled with 5 wt% EG burnt up to the holding clamp, so the samples failed according to the classification of UL94V test. When the loading of EG was 10 wt% or higher, the burning of samples stopped immediately after taking out from the flame source, implying that the sample passed V0-rating (Figure 1(b)).

The flame retardancy of PU composites was further investigated by LOI experiments (Figure 2). According to the ASTMD 2863-97 standard, a material is classified as flame retardant if the LOI value is above 23%. As indicated in Figure 2, the inclusion of EG significantly enhanced the flame retardancy of the foam, changing pure RPUF from a highly flammable material (LOI value: 20.2%) to a flame-resistant composite. The LOI value was increased proportionally with the content of EG. In particular, RPUF with 20 wt% EG showed the LOI value up to 30.5% (Table 2).

To clearly understand the flame-retardant behavior, the structure of EG/RPUF composites before and after burning test was observed by SEM images (Figure 3). Initially, EG stiff flakes with the size of $300\text{--}500\ \mu\text{m}$ was distributed at some locations in the PU matrix as shown in Figures 3(a) and 3(b).

TABLE 1: Compositions of RPUF samples.

No.	Samples	Polyol (wt %)	MDI (wt %)	Flame-retardant additives	
				EG (wt %)	Cloisite 20A (wt %)
1	Pure RPUF	41.67	58.33	—	—
2	EG5-RPUF	39.58	55.42	5	—
3	EG10-RPUF	37.50	52.50	10	—
4	EG15-RPUF	35.42	49.58	15	—
5	EG15-20A2.5-RPUF	34.38	48.12	15	2.5
6	EG15-20A5-RPUF	33.33	46.67	15	5
7	EG17.5-RPUF	34.38	48.12	17.5	—
8	EG17.5-20A2.5-RPUF	33.33	46.67	17.5	2.5
9	EG20-RPUF	33.33	46.67	20	—



FIGURE 1: Images of the samples after the horizontal (a) and vertical burning tests (b): (1) pure RPUF; (2) EG5-RPUF; (3) EG10-RPUF; (4) EG15-RPUF; (5) EG15-20A2.5-RPUF; (6) EG15-20A5-RPUF; (7) EG17.5-RPUF; (8) EG17.5-20A2.5-RPUF; (9) EG20-RPUF.

TABLE 2: Flame-retardant and physical properties of RPUF composites.

No.	Sample	HB-rating	V-rating	LOI (vol%)	Stress at 10% strain (Mpa)	Thermal conductivity ($W \cdot m^{-1} \cdot K^{-1}$)
1	Pure RPUF	300 mm/min. -fail	Fail	20.2	0.2464	0.028
2	EG5-RPUF	HB	Fail	23.7	0.2421	0.036
3	EG10-RPUF	HB	V-0	25.9	0.2367	0.047
4	EG15-RPUF	HB	V-0	28.1	0.2313	0.053
5	EG15-20A2.5-RPUF	HB	V-0	28.5	0.2485	0.048
6	EG15-20A5-RPUF	HB	V-0	28.7	0.2536	0.041
7	EG17.5-RPUF	HB	V-0	29.2	0.2284	0.055
8	EG17.5-20A2.5-RPUF	HB	V-0	29.4	0.2426	0.05
9	EG20-RPUF	HB	V-0	30.5	0.2217	0.058

After burning, the surface of the composite was covered entirely by spongy expanded graphite (Figures 3(c) and 3(d)). This phenomenon was also reported in the previous literature which found that EG was expanded more than 100 times its original size under higher temperatures by fast volatilization of the intercalation [29, 30]. The expanded graphite thus acted as a physical barricade which inhibited the oxygen diffusion and mass and heat transfer between the flame and PU matrix.

However, the presence of EG in PU foams increased the thermal conductivity and diminished the mechanical behavior of the composites. In order to solve this problem, we

incorporated organoclay into EG/PU composites. The LOI test indicated that, with the same EG content, the clay-additive could lead to an increase of LOI value of EG/PU foam. In particular, in comparison with EG15-RPUF (LOI value of 28.1%), EG15-20A2.5-RPUF, and EG15-20A5-RPUF, samples displayed higher LOI values of 28.5% and 28.7%, respectively. The similar behavior was observed when adding 2.5 wt% clay to EG17.5-RPUF. There may be two factors attributed to the enhancement in the LOI value of the EG/clay/RPUF composite. Firstly, clay increased the viscosity of polyol so the dispersion of the EG filler in the

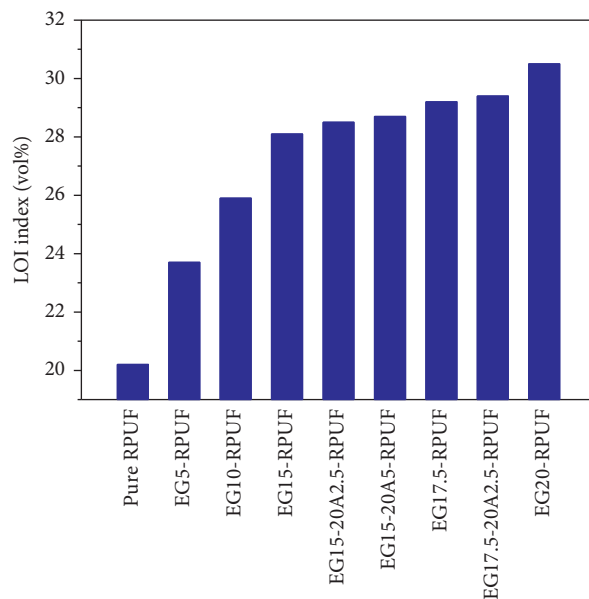


FIGURE 2: LOI values of the PU foams using different flame-retardant additives.

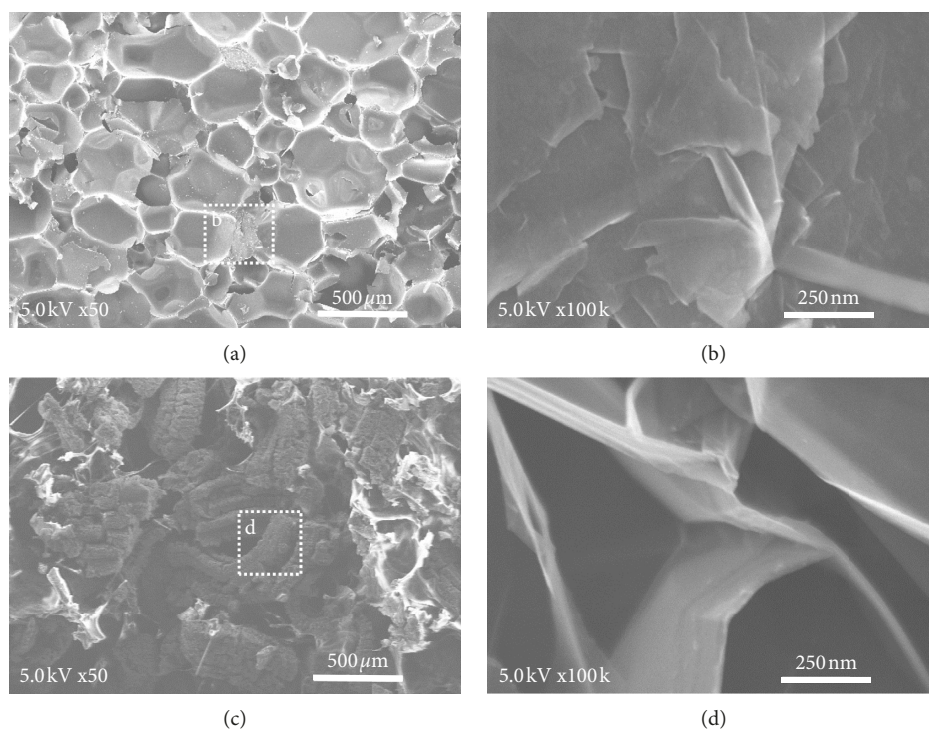


FIGURE 3: SEM micrographs of EG/RPUF composite before (a) and after (c) burning and their high magnification images (b) and (d), respectively.

polymer matrix was improved. Besides, as the burning occurs, organoclay forms a char layer on the surface of the materials, which prevents the heat transfer and the permeability of oxygen into the material as well as the evaporation of inflammable degradation products [31]. Thus, clay and EG exhibited a synergetic effect in the improvement of flame retardancy of PU composites.

3.2. Thermal Stability of the Composites. To better understand the role of EG and clay to the flame-retardant behavior of PU composite, the thermal stability of these composites was studied by TGA (Figure 4). The degradation of all samples consisted of two steps. The first maximum weight loss temperature, T_{1max} , of pure PU was about 330°C due to the depolycondensation of PU [32]. In the case of

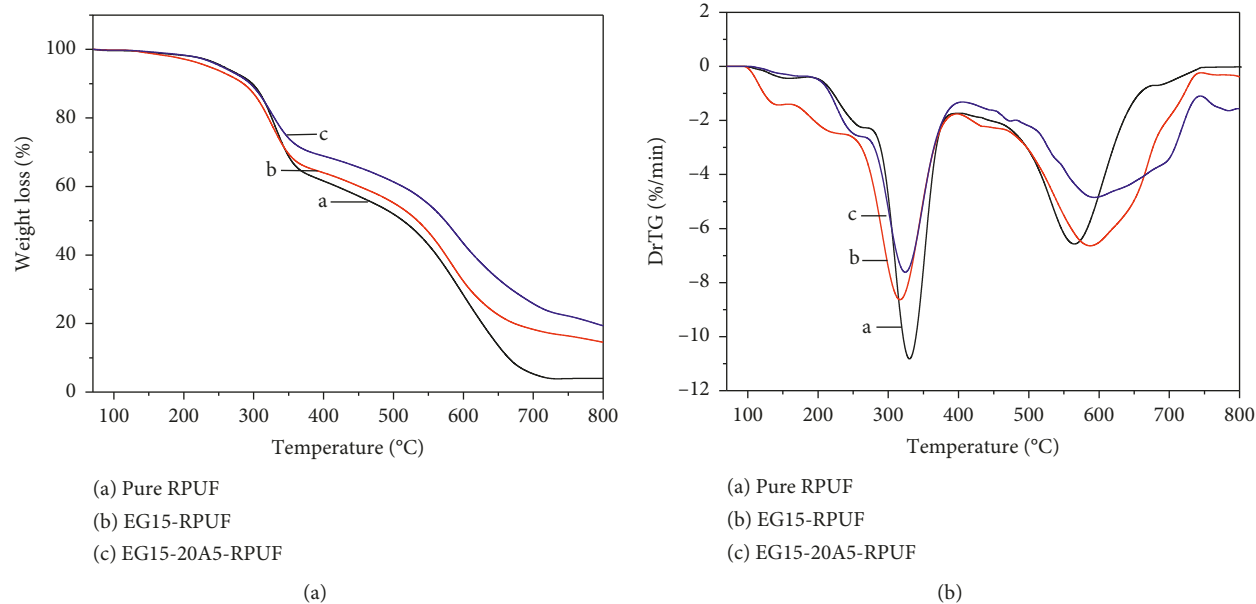


FIGURE 4: (a) TGA and (b) DTG curves of pure PU foam and the PU composites.

EG15-RPUF composite, T_{1max} decreased to 318°C that was assigned for the volatilization of the intercalated substances of EG, which started at about 300°C. For EG15-20A5-RPUF composite, the first maximum weight loss took place at 315°C, due to the decomposition of the ammonium modifier in the clay. The second maximum weight loss temperature T_{2max} of pure PU, EG15-RPUF, and EG15-20A5-RPUF was about 568, 574, and 585°C, respectively. The thermal stability of EG15-RPUF sample was slightly improved compared to the pure counterpart resulting from char formation of EG at a high temperature which slowed down the decomposition of the polymer. In the case of EG15-20A5-RPUF composite, organoclay constituted nanostructured barriers that delayed the diffusion of volatiles. As a result, the EG/clay/RPUF composite had better thermal stability than the EG/RPUF composite.

3.3. Mechanical Properties. To evaluate the mechanical properties of the pure RPUF and the RPUF composites, the compressive strength of the foams was measured, and the result is shown in Figure 5 and Table 2. These data showed that the presence of 15 wt% EG significantly reduced the compressive strength of RPUF from 0.2464 MPa to 0.2313 MPa at 10% strain. This may have been owing to the fact that microsized EG flakes caused the low compatibility between EG and the polyurethane polymer matrix. Furthermore, the big size of EG particles induced an inhomogeneous cell structure of the foam which affects the mechanical stability of the cellular structure. The result was consistent with previous reports [22–24].

By contrast, the compressive strength of the EG-PU foam increased upon adding clay. In particular, by adding 2.5 wt% clay to EG15-RPUF, the compressive strength of the EG15-20A2.5 composite increased notably from 0.2313 MPa

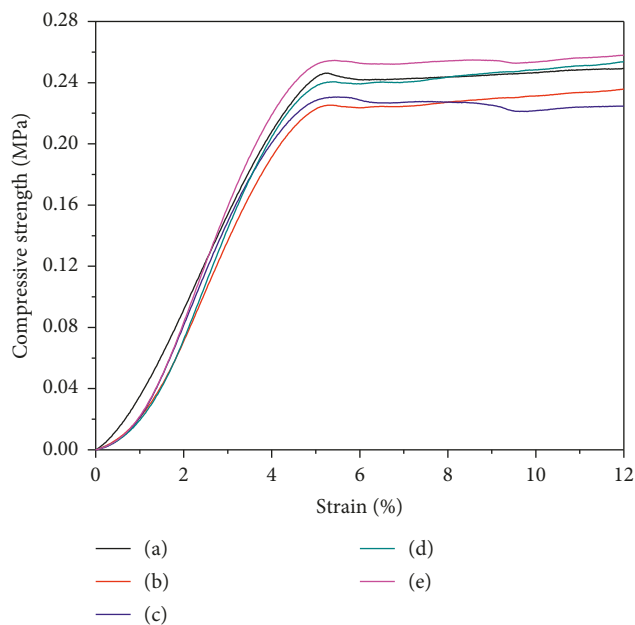


FIGURE 5: The compressive strength of the PU foams: (a) pure RPUF; (b) EG15-RPUF; (c) EG20-RPUF; (d) EG15-20A2.5-RPUF; (e) EG15-20A5-RPUF.

to 0.2485 MPa, which is comparable to neat PU foam. A further addition to 5 wt% clay, the compressive strength of EG15-20A5RPUF displayed a slight increase to 0.2536 MPa. As shown in Figure 6(a), the 2θ peak of pure clay is 2.8°. According to Bragg's Law, the calculated d -spacing (d_{001}) of clay is 31.5 Å, which is consistent with the datasheet of Cloisite 20A provided by the supplier Southern Clay Products Inc. However, there were no distinct features in the small angle XRD pattern of the clay/EG/PU composite. The result revealed silicate layers in nanometer size were mostly

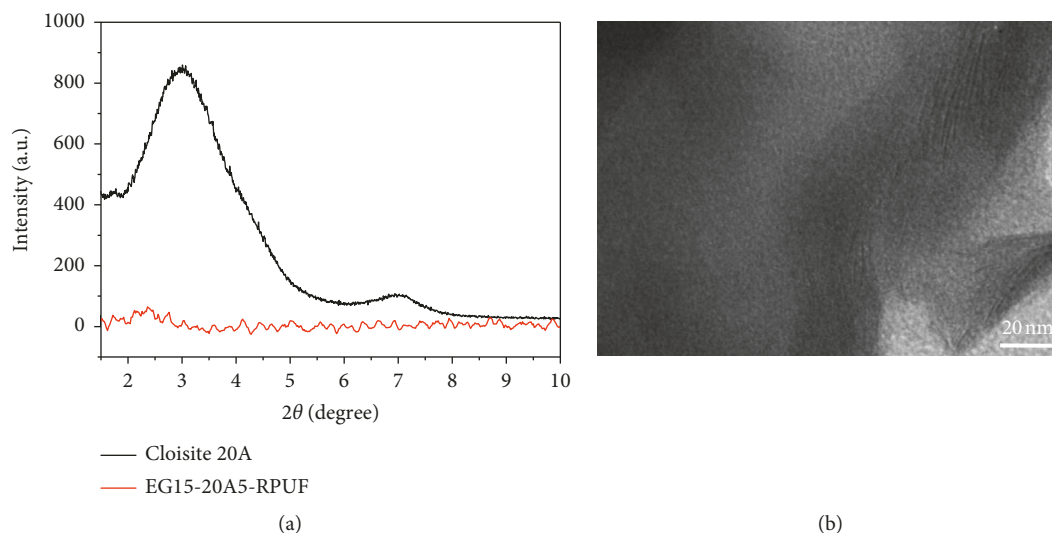


FIGURE 6: XRD patterns of clay and the RPUF composite (a) and TEM micrograph of EG15-20A5-RPUF composite (b).

exfoliated with a certain amount of intercalation in the PU matrix, which was further confirmed by TEM image (Figure 6(b)). The dispersion of exfoliated organoclay increased the interfacial interaction between clay and PU matrix that may enhance the compressive strength of the composite. In addition, the clay made polyol more viscous, which decreased the accumulation of EG, hence improving the dispersion of EG in the polymer. Thus, the presence of clay could enhance the compressive strength of the EG/PU composites.

3.4. Thermal Conductivity. The thermal conductivity of RPUF composites is represented in Figure 7 and Table 2. It was clear that adding EG filler to PU foam caused a significant increase in the thermal conductivity of PU composites. Adding 15 wt% EG increased the thermal conductivity of the EG15-RPUF composite by ~90%. If the content of EG was 20%, the thermal conductivity increased to $0.058 \text{ W}\cdot\text{m}^{-1}\cdot\text{K}^{-1}$, which was twice as much as pure RPUF. EG is a high thermal-conductive material, increasing the rate of heat transfer. As a result, EG impeded the insulation property of a PU foam.

The addition of clay reduced the thermal conductivity of the EG/RPUF composites. EG15-20A2.5-RPUF has a thermal conductivity of $0.048 \text{ W}\cdot\text{m}^{-1}\cdot\text{K}^{-1}$, lower than that of EG15-RPUF ($0.053 \text{ W}\cdot\text{m}^{-1}\cdot\text{K}^{-1}$). The thermal conductivity of EG15-20A5-RPUF was further decreased by 23% compared to EG15-RPUF. It may have been due to the fact that silicate nanolayers created defects and formed effective barriers against the phonon transfer in the EG/PU matrix, therefore disrupting the thermal conducting network. The addition of organoclay seems to be a suitable method to improve the thermal insulation of the EG/RPUF composite.

4. Conclusions

In this work, flame retardancy, mechanical property, and thermal conductivity of the EG/RPUF and EG/organoclay/

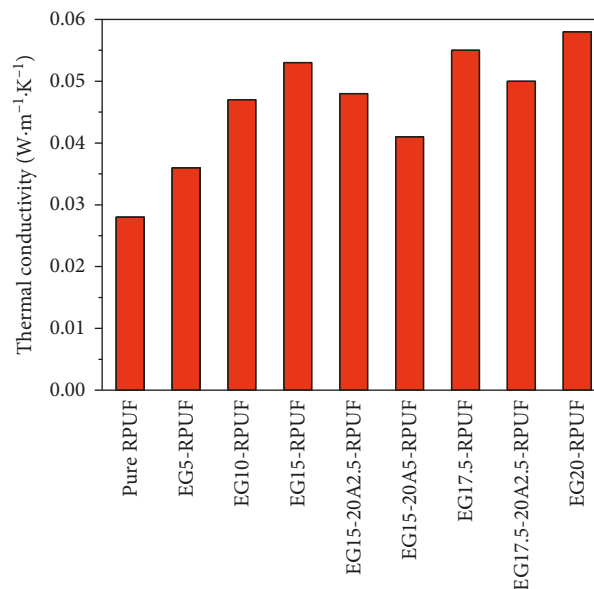


FIGURE 7: Thermal conductivity of pure RPUF and RPUF composites.

RPUF composites were investigated. Although the introduction of EG into the PU polymer matrix significantly enhanced the flame retardancy of the foam, the thermal insulation and compressive strength were reduced. Organoclay was incorporated into EG/PU composites to minimize this drawback. The LOI test indicated that, with the same EG content, the addition of organoclay could increase the LOI value of EG/PU foam. Furthermore, the compressive strength and thermal insulation of the composite were also improved in the presence of organoclay. The organoclay content of 2-3 wt% was suitable to incorporate into EG/PU composite. The combination of EG and organoclay is a potential method for the fabrication of flame-retardant PU foams. This report could make a contribution to developing eco-friendly flame-retardant PU products in the future.

Data Availability

The data used to support the findings of this study are available from the corresponding author upon request.

Conflicts of Interest

The authors declare that there are no conflicts of interest regarding the publication of this paper.

Acknowledgments

This research was funded by the Vietnam Academy of Science and Technology under grant number “TĐPCCC.02/18-20.”

References

- [1] M. Thirumal, D. Khastgir, N. K. Singha, B. S. Manjunath, and Y. P. Naik, “Effect of foam density on the properties of water blown rigid polyurethane foam,” *Journal of Applied Polymer Science*, vol. 108, no. 3, pp. 1810–1817, 2008.
- [2] A. R. Kakroodi, M. Khazabi, K. Maynard, M. Sain, and O.-S. Kwon, “Soy-based polyurethane spray foam insulations for light weight wall panels and their performances under monotonic and static cyclic shear forces,” *Industrial Crops and Products*, vol. 74, pp. 1–8, 2015.
- [3] W. J. Seo, H. C. Jung, J. C. Hyun et al., “Mechanical, morphological, and thermal properties of rigid polyurethane foams blown by distilled water,” *Journal of Applied Polymer Science*, vol. 90, no. 1, pp. 12–21, 2003.
- [4] W. J. Seo, J. H. Park, Y. T. Sung, D. H. Hwang, W. N. Kim, and H. S. Lee, “Properties of water-blown rigid polyurethane foams with reactivity of raw materials,” *Journal of Applied Polymer Science*, vol. 93, no. 5, pp. 2334–2342, 2004.
- [5] K. Pielichowski, K. Kulesza, and E. M. Pearce, “Flammability of rigid polyurethane foams blown with pentane: limiting oxygen index data and thermovision characteristic,” *Journal of Polymer Engineering*, vol. 22, no. 3, pp. 195–207, 2002.
- [6] S. Duquesne, M. L. Bras, S. Bourbigot et al., “Expandable graphite: a fire retardant additive for polyurethane coatings,” *Fire and Materials*, vol. 27, no. 3, pp. 103–117, 2003.
- [7] C. Y. H. Chao and J. H. Wang, “Comparison of the thermal decomposition behavior of a non-fire retarded and a fire retarded flexible polyurethane foam with phosphorus and brominated additives,” *Journal of Fire Sciences*, vol. 19, no. 2, pp. 137–156, 2001.
- [8] M. Ravey and E. M. Pearce, “Flexible polyurethane foam. III. Phosphoric acid as a flame retardant,” *Journal of Applied Polymer Science*, vol. 74, no. 5, pp. 1317–1319, 1999.
- [9] M. Ravey, I. Keidar, E. D. Weil, and E. M. Pearce, “Flexible polyurethane foam. II. Fire retardation by tris(1,3-dichloro-2-propyl) phosphate part A. Examination of the vapor phase (the flame),” *Journal of Applied Polymer Science*, vol. 68, no. 2, pp. 217–229, 1998.
- [10] S. Hörold, “Phosphorus-based and intumescent flame retardants,” *Polymer Green Flame Retardants*, vol. 22, pp. 221–254, 2014.
- [11] X. Shi, S. Jiang, J. Zhu, G. Li, and X. Peng, “Establishment of a highly efficient flame-retardant system for rigid polyurethane foams based on bi-phase flame-retardant actions,” *RSC Advances*, vol. 8, no. 18, pp. 9985–9995, 2018.
- [12] D. Price, Y. Liu, G. J. Milnes, R. Hull, B. K. Kandola, and A. R. Horrocks, “An investigation into the mechanism of flame retardancy and smoke suppression by melamine in flexible polyurethane foam,” *Fire and Materials*, vol. 26, no. 4–5, pp. 201–206, 2002.
- [13] M. Modesti, A. Lorenzetti, F. Simioni, and G. Camino, “Expandable graphite as an intumescent flame retardant in polyisocyanurate-polyurethane foams,” *Polymer Degradation and Stability*, vol. 77, no. 2, pp. 195–202, 2002.
- [14] V. Babrauskas, R. Fuoco, and A. Blum, “Flame retardant additives in polymers,” *Polymer Green Flame Retardants*, vol. 22, pp. 87–118, 2014.
- [15] M. Thirumal, D. Khastgir, N. K. Singha, B. S. Manjunath, and Y. P. Naik, “Effect of expandable graphite on the properties of intumescent flame-retardant polyurethane foam,” *Journal of Applied Polymer Science*, vol. 110, no. 5, pp. 2586–2594, 2008.
- [16] L. Shi, Z.-M. Li, B.-H. Xie, J.-H. Wang, C.-R. Tian, and M.-B. Yang, “Flame retardancy of different-sized expandable graphite particles for high-density rigid polyurethane foams,” *Polymer International*, vol. 55, no. 8, pp. 862–871, 2006.
- [17] L. Shi, Z.-M. Li, W. Yang, M.-B. Yang, Q.-M. Zhou, and R. Huang, “Properties and microstructure of expandable graphite particles pulverized with an ultra-high-speed mixer,” *Powder Technology*, vol. 170, no. 3, pp. 178–184, 2006.
- [18] X.-C. Bian, J.-H. Tang, Z.-M. Li, Z.-Y. Lu, and A. Lu, “Dependence of flame-retardant properties on density of expandable graphite filled rigid polyurethane foam,” *Journal of Applied Polymer Science*, vol. 104, no. 5, pp. 3347–3355, 2007.
- [19] H. Yang, H. Liu, Y. Jiang, M. Chen, and C. Wan, “Density effect on flame retardancy, thermal degradation, and combustibility of rigid polyurethane foam modified by expandable graphite or ammonium polyphosphate,” *Polymers*, vol. 11, no. 4, p. 668, 2019.
- [20] P. Acuña, Z. Li, M. Santiago-Calvo, F. Villafañe, M. Ángel Rodríguez-Perez, and De-Y. Wang, “Influence of the characteristics of expandable graphite on the morphology, thermal properties, fire behaviour and compression performance of a rigid polyurethane foam,” *Polymers*, vol. 11, p. 168, 2019.
- [21] M. Modesti and A. Lorenzetti, “Improvement on fire behaviour of water blown PIR-PUR foams: use of an halogen-free flame retardant,” *European Polymer Journal*, vol. 39, no. 2, pp. 263–268, 2003.
- [22] L. Shi, Z.-M. Li, M.-B. Yang et al., “Expandable graphite for halogen-free flame-retardant of high-density rigid polyurethane foams,” *Polymer-Plastics Technology and Engineering*, vol. 44, no. 7, pp. 1323–1337, 2005.
- [23] X.-C. Bian, J.-H. Tang, and Z.-M. Li, “Flame retardancy of hollow glass microsphere/rigid polyurethane foams in the presence of expandable graphite,” *Journal of Applied Polymer Science*, vol. 109, no. 3, pp. 1935–1943, 2008.
- [24] X.-Y. Meng, L. Ye, X.-G. Zhang et al., “Effects of expandable graphite and ammonium polyphosphate on the flame-retardant and mechanical properties of rigid polyurethane foams,” *Journal of Applied Polymer Science*, vol. 114, no. 2, pp. 853–863, 2009.
- [25] P. S. Khobragablr, D. P. Hansora, J. B. Naik, and A. Chatterjee, “Flame retarding performance of elastomeric nanocomposites: a review,” *Polymer Degradation and Stability*, vol. 130, pp. 194–244, 2016.
- [26] A. Kausar, “Polyurethane composite foams in high-performance applications: a review,” *Polymer-Plastics Technology and Engineering*, vol. 57, no. 4, pp. 346–369, 2018.
- [27] M. Modesti, A. Lorenzetti, S. Besco et al., “Synergism between flame retardant and modified layered silicate on thermal

- stability and fire behaviour of polyurethane nanocomposite foams,” *Polymer Degradation and Stability*, vol. 93, no. 12, pp. 2166–2171, 2008.
- [28] H. Kadam, S. Bandyopadhyay-Ghosh, N. Malik, and S. B. Ghosh, “Bio-based engineered nanocomposite foam with enhanced mechanical and thermal barrier properties,” *Journal of Applied Polymer Science*, vol. 136, no. 7, pp. 47063–47069, 2018.
- [29] Z. Sun, Y. Ma, Y. Xu et al., “Effect of the particle size of expandable graphite on the thermal stability, flammability, and mechanical properties of high-density polyethylene/ethylene vinyl-acetate/expandable graphite composites,” *Polymer Engineering & Science*, vol. 54, no. 5, pp. 1162–1169, 2014.
- [30] Y. F. Zhao, M. Xiao, S. J. Wang, X. C. Ge, and Y. Z. Meng, “Preparation and properties of electrically conductive PPS/expanded graphite nanocomposites,” *Composites Science and Technology*, vol. 67, no. 11-12, pp. 2528–2534, 2007.
- [31] T. Widya and C. W. Macosko, “Nanoclay-modified rigid polyurethane foam,” *Journal of Macromolecular Science, Part B*, vol. 44, no. 6, pp. 897–908, 2005.
- [32] S. Ganguli, A. K. Roy, and D. P. Anderson, “Improved thermal conductivity for chemically functionalized exfoliated graphite/epoxy composites,” *Carbon*, vol. 46, no. 5, pp. 806–817, 2008.

Research Article

Kinetics, Isotherm, Thermodynamics, and Recyclability of Exfoliated Graphene-Decorated MnFe_2O_4 Nanocomposite Towards Congo Red Dye

Van Thinh Pham,^{1,2,3} Hong-Tham T. Nguyen,^{1,2} Thuan Van Tran ^{1,2},
Duyen Thi Cam Nguyen ^{1,2,4}, Hanh T. N. Le,⁵ Thuong Thi Nguyen,^{1,2} Dai-Viet N. Vo,^{1,2}
Thi Hong Nhan Le ⁶, and Duy Chinh Nguyen ⁷

¹NTT Hi-Tech Institute, Nguyen Tat Thanh University, Ho Chi Minh City, Vietnam

²Center of Excellence for Green Energy and Environmental Nanomaterials, Nguyen Tat Thanh University, Ho Chi Minh City, Vietnam

³Graduate University of Science and Technology, Vietnam Academy of Science and Technology, Ha Noi City, Vietnam

⁴Department of Pharmacy, Nguyen Tat Thanh University, Ho Chi Minh City, Vietnam

⁵Institute of Hygiene and Public Health, Ho Chi Minh City, Vietnam

⁶Ho Chi Minh City University of Technology, Vietnam National University-Ho Chi Minh City, Ho Chi Minh City 703500, Vietnam

⁷Center of Excellence for Functional Polymers and NanoEngineering, Nguyen Tat Thanh University, Ho Chi Minh City, Vietnam

Correspondence should be addressed to Thuan Van Tran; tranuv@gmail.com and Thi Hong Nhan Le; lthnhan@hcmut.edu.vn

Received 8 March 2019; Revised 10 May 2019; Accepted 27 May 2019; Published 17 June 2019

Guest Editor: Nguuyen Van Noi

Copyright © 2019 Van Thinh Pham et al. This is an open access article distributed under the Creative Commons Attribution License, which permits unrestricted use, distribution, and reproduction in any medium, provided the original work is properly cited.

Herein, we described the use of exfoliated graphene- (EG-) decorated magnetic MnFe_2O_4 nanocomposite ($\text{EG@MnFe}_2\text{O}_4$) for the removal and adsorption of Congo red (CR) dye from wastewater. Firstly, the precursors (EG, MnFe_2O_4) and $\text{EG@MnFe}_2\text{O}_4$ were fabricated, characterized using several physical analytical techniques such as X-ray powder diffraction (XRD), scanning electron microscope (SEM), transmission electron microscopy (TEM), and N_2 adsorption/desorption isotherm measurement. For the adsorption experiments, the effect of contact time (0–240 min), concentration (10–60 mg/L), solution pH (2–10), adsorbent dosage (0.03–0.07 g), and temperature (283–313 K) was rigorously studied. To elucidate the adsorption mechanism and behaviour of CR over $\text{EG@MnFe}_2\text{O}_4$ and MnFe_2O_4 adsorbents, the kinetic models (pseudo-first-order, pseudo-second-order, Elovich, and Bangham) and isotherm models (Langmuir, Freundlich, Temkin, and Dubinin–Radushkevich) have been adopted. The kinetic results indicated that models adhered to the pseudo-second-order equation, exhibiting the chemisorption mechanism in heterogeneous phase. Meanwhile, the isotherm results revealed the adsorption of CR over $\text{EG@MnFe}_2\text{O}_4$ obeyed the monolayer behaviour (Langmuir model) rather than multilayer behaviour (Freundlich equation) over MnFe_2O_4 . The thermodynamic study also suggested that such adsorption was an endothermic and spontaneous process. With high maximum adsorption capacity (71.79 mg/g) and good recyclability (at least 4 times), $\text{EG@MnFe}_2\text{O}_4$ can be a potential alternative for the adsorptive removal of CR dye from water.

1. Introduction

Research interest in nanomaterials (metalorganic frameworks, nanoparticles, porous nanomaterials, etc.) has become an integral part in the development of future technologies [1–4]. Among these, multiferroic nanomaterials (e.g., MFe_2O_4 , M

stands for transition metals) have afforded an abundance of widely practical applications, hence, giving rise in research interests, especially in environmental remediation [5, 6]. With their outstanding properties in inherent structure, such as excellent magnetism for easy separation, high chemical stability, and tunable production in both laboratory scale and

industrial scale, many studies focused on ferrites and their modified compounds on the removal and degradation of contaminants [7–9]. Among these emergent pollutants [10–12], however, synthetic dyes (e.g., Congo red, CR) have been considered as potential carcinogenic chemicals because they can contain several toxic functional groups and nondegradable skeletons including amine, imine, and benzene rings (Scheme 1), and hence, this topic have been paid much attention over the past decades [9, 13–16].

In terms of eliminating dye compounds, some works reported the outstanding removal efficiency using ferrite nanoparticles [17–19]. For example, Wojciech et al. investigated the adsorption of acid dye Acid Red 88 using magnetic ZnFe_2O_4 spinel ferrite nanoparticles. With relatively high surface area ($139\text{ m}^2/\text{g}$), this ferriic material has given a desirable maximum adsorption capacity, at 111.1 mg/g [20]. Interestingly, Mahmoodi et al. also reported the use of sodium dodecyl sulfate (SDS) as a strongly modified agent for nickel ferrite nanoparticle (NFN) to remove a wide range of dyes including basic blue 41 (BB41), basic green 4 (BG4), and basic red 18 (BR18) with a considerable improvement in maximum adsorption capacity compared with nonmodified counterparts (control samples) [21]. These reports inspired many breakthroughs to chemically modify the ferrite structures to enhance the absorbability towards dye molecules.

Generally, the ferrites can be easily modified by coatings containing diverse functional groups, which facilitate the capture of dyes. Exfoliated graphene (EG), a typically modified material synthesizing from natural graphene, can be a brilliant candidate [22]. Although EG presents as a primary adsorbent, one of the biggest drawbacks of EG material is the difficulty to separate it from the mixture after the adsorption process due to its low density towards water [23]. Moreover, EG itself can be hardly regenerated by common methods, thus, restraining its practical applications [24]. Therefore, combination between EG and ferrites may be an optimum solution aiming at taking advantage of both attractive properties.

Herein, EG-decorated MnFe_2O_4 (namely, $\text{EG@MnFe}_2\text{O}_4$) as a promising adsorbent for the adsorption of CR as an emerging and typical dye was addressed. This material was firstly characterized using several analytical techniques such as X-ray powder diffraction (XRD), scanning electron microscope (SEM), Fourier-transform infrared spectroscopy (FT-IR), transmission electron microscopy (TEM), and N_2 adsorption/desorption isotherm measurement and used for kinetic and isotherms studies. Moreover, a series of parameters including contact time, dosage, solution pH, and temperature were employed to compare the adsorption between MnFe_2O_4 with and without EG decoration. To confirm the recyclability, $\text{EG@MnFe}_2\text{O}_4$ could be recycled for many times. To our best knowledge, its characterization and application for CR remediation was not previously addressed; hence, more investigations need to be conducted.

2. Materials and Methods

2.1. Chemicals and Instruments. Natural graphite flake (GF) was obtained from Yen Bai province, Vietnam. The material

was selected to have the particle size of 60 mesh. Chemicals including Congo red, H_2SO_4 (98%), and H_2O_2 (30%) were purchased from Merck. The XRD profile was obtained using the D8 Advance Bruker powder diffractometer with $\text{Cu-K}\alpha$ beams used as excitation sources. The SEM images with the magnification of 7000x were captured with the S4800 instrument (Japan) with an accelerating voltage source (15 kV). The infrared FT-IR spectra obtained by the Nicolet 6700 spectrophotometer were used to explore the characteristics of chemical bonds and functional groups. CR concentration was determined with UV-vis spectrophotometer at wavelength of 500 nm.

2.2. Synthesis of EG. The EG porous material was produced from the natural flaky graphite source by the microwave-irradiated method [22]. Initially, flaky graphite was carefully immersed in a mixture of H_2SO_4 (98%) and H_2O_2 (30%) (100:7 by volume) at room temperature during 2 hours. Next, the chemically treated solid was repeatedly washed with H_2O and neutralized by diluted NaOH solution. The exfoliation of bulky powder was performed by the microwave-irradiated oven (750 W, 10 sec). The as-received EG sample can be collected and stored for the characterization and experiments.

2.3. Synthesis of MnFe_2O_4 . Manganese-based magnetic nanoparticle MnFe_2O_4 was produced using the conventional polymerized-complex method according to our recent work [25]. Citric acid (93 g) was mixed with 140 mL of ethylene glycol and distilled water (2:5 by volume) and heated up 80°C under air atmosphere. Then, an amount of 0.303 g- $\text{MnCl}_2\cdot 6\text{H}_2\text{O}$ solid was poured into the above mixture and heated up at 130°C . After 2 hours, the polymeric resin precursor was transferred into heat-resistant furnace and heated up at 1000°C for 2 h and allowed to cool down at room temperature. The black as-received sample can be collected and stored for the characterization and experiments.

2.4. Synthesis of $\text{EG@MnFe}_2\text{O}_4$. The synthesis procedure was followed as reported previously [26]. A mixture of 0.7 g $\text{Fe}(\text{NO}_3)_3\cdot 9\text{H}_2\text{O}$ and 0.25 g- $\text{Mn}(\text{NO}_3)_2\cdot 6\text{H}_2\text{O}$ was dissolved in 50 mL H_2O , and heated up at 90°C under stirring continuously. After that, 50 mL citric acid solution (0.02 M) was added dropwise slowly and stirred for 60 min. 0.8 g-EG was carefully poured into such solution, and then NH_3 solution was added to reach the weakly basic solution (pH 8-9). After 30 min, a slow addition of NH_3 solution for the second time into the beaker (pH 10) was employed. The mixture was dried at 80°C and calcined at 700°C during 120 min to obtain as-received sample.

2.5. Experimental Batch. To determine the absorbability of EG towards CR, batch experiments could be conducted by an addition of adsorbent (0.5 g/L) into 100 mL of dye solutions (20–60 mg/L). The samples were employed to agitate on the shaker table. Preliminary runs indicated that the adsorption process reached an equilibrium state during



SCHEME 1: Schematic process for the formation of EG@MnFe₂O₄ for the removal of Congo red.

210 min. After the adsorption completion, the adsorbent was extracted from the aqueous solution using a filter syringe, while remaining concentration of dye was measured by the UV-vis spectrophotometer at 500 nm. The removal efficiency ($H\%$) and adsorption capacity (Q) was calculated on the basis of the concentrations by the following equations:

$$H(\%) = \frac{C_0 - C_e}{C_0} \cdot 100,$$

$$Q_t = \frac{C_0 - C_t}{m} \cdot V, \quad (1)$$

$$Q_e = \frac{C_0 C_e}{m} \cdot V,$$

where C_0 and C_e are, respectively, the initial and equilibrium dye concentrations, V is the volume of solution, and m represents the weight of adsorbent.

3. Results and Discussion

3.1. Structural Characterization

3.1.1. PXRD Spectra of EG, MnFe₂O₄, and EG@MnFe₂O₄ Materials. To compare the crystallinity of EG@MnFe₂O₄ with their precursors including EG and MnFe₂O₄, the PXRD was used as a means of analysis. According to the observation from Figure 1, the profile of EG material witnessed a sharp peak at 26.6°, which was highly commensurate with previous publications, proving that EG has been successfully synthesized [27]. At a glance, the figure for MnFe₂O₄ had an apparent difference with that for EG mentioned. Indeed, there was an abundance of main peaks emerging at 24.4°, 34.0°, 36.7°, 50.0°, 54.5°, 62.5°, and 64.8°. Many works reported the same PXRD profiles of MnFe₂O₄ by various synthesis pathways (microwave-assisted ball-milling, wet-milling, solvothermal, etc.) [28–33]. The third diffraction spectrum belongs to EG@MnFe₂O₄, which had the mutual patterns of EG and MnFe₂O₄. Accordingly, a sharp peak at 26.6° again repeated at the constant position in the spectrum of EG@MnFe₂O₄ confirmed that the EG was successfully decorated in MnFe₂O₄. More interestingly, several peak traces of MnFe₂O₄ can be observed in the spectrum of EG@MnFe₂O₄. However, their signal intention seems very low, mainly because the EG may coat the peripheral shell of the MnFe₂O₄ nanoparticles. These results were totally in line with recent studies on the same structure [34–36].

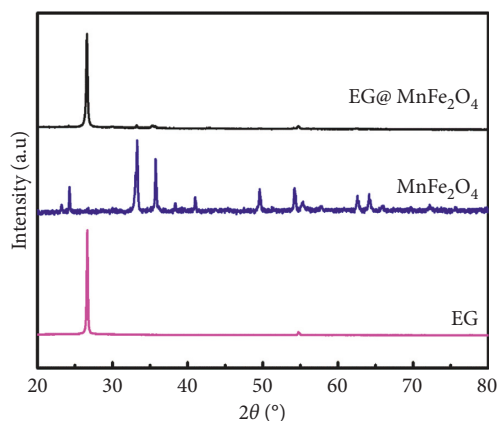


FIGURE 1: XRD spectra of EG, MnFe₂O₄, and EG@MnFe₂O₄.

3.1.2. SEM Images of EG@MnFe₂O₄ Materials. To gain more understanding about the morphological properties of EG@MnFe₂O₄ material, the SEM technique can be used. Based on the SEM images in Figure 2, which showed at two various magnification levels (50 and 100 μm), it is evident that the EG@MnFe₂O₄ structure exposed a heterogeneous, highly defective, amorphous morphology. This phenomenon may be due to the effect of a full decoration by EG nanosheets, which MnFe₂O₄ is dispersed on the flexible graphene sheet, resulting in the typical kind of rough surface of EG@MnFe₂O₄. Kalimuthu also reported the same morphology of MnFe₂O₄/graphene produced by eco-friendly hydrothermal and in situ polymerization method, offering a deep degree of wrinkled and unsmooth surface [37].

3.1.3. TEM Images of EG and EG@MnFe₂O₄ Materials. TEM technique is necessary to gain insight into inherent structure of exfoliated graphite and exfoliated graphite decorated MnFe₂O₄ materials. Figure 3 illustrates the SEM images of above materials at various scales 1 μm and 200 nm. Figures 3(a) and 3(b) show the highly opaque towards electron beams, and hence, implying that the EG obtained a thick structure [38]. In contrast, the structure of EG@MnFe₂O₄ in Figures 3(c) and 3(d) indicates a considerable difference from the EG structure. As illustrated, the existence of black spots in the opaque EG region can be due to the presence of MnFe₂O₄ particles, demonstrating the fact that MnFe₂O₄ particles were decorated by the EG sheets [39].

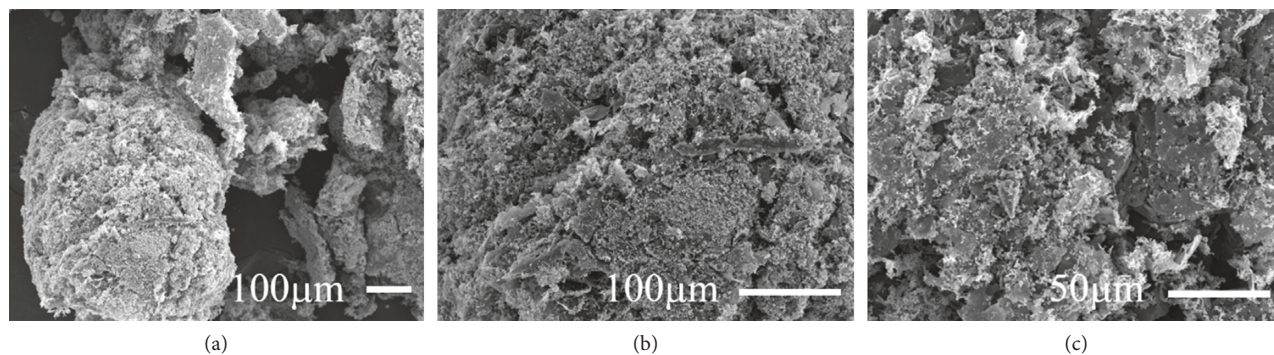


FIGURE 2: SEM images of EG@MnFe₂O₄.

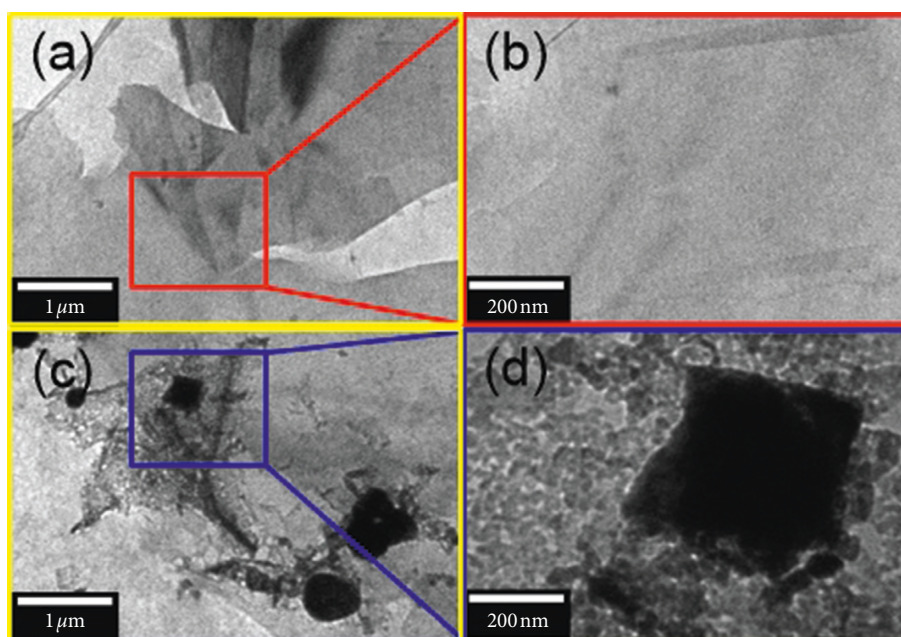


FIGURE 3: TEM images of EG (a, b) and EG@MnFe₂O₄ (c, d) materials.

3.1.4. N₂ Adsorption/Desorption Isotherm Measurement of EG and EG@MnFe₂O₄. To characterize more properties of the inherent structure, the nitrogen adsorption/desorption isotherm of EG and EG@MnFe₂O₄ can be measured at 77 K and is illustrated in Figure 4(a). Generally, these isotherms mostly exhibit no hysteresis loops, representing a type II isotherm, means that both they were likely to offer a low degree of porosity. Indeed, the surface area values calculated by BET theory and pore volume of EG and EG@MnFe₂O₄ were relatively low, but those of EG were slightly higher than those of EG@MnFe₂O₄ composite, at 33.0 m²/g, 0.1299 cm³/g compared with 40.95 m²/g, and 0.1559 cm³/g, respectively. These results can be due to the effect of aggregation under magnetism of MnFe₂O₄, resulting in the depletion in porosity in EG@MnFe₂O₄ [40, 41]. Meanwhile, pore size distribution plots of both materials in Figure 4(b) also show the existence of both micropore (<2 nm) and mesopore (2–50 nm) in their structures.

3.1.5. EDS Mapping Spectrum of EG@MnFe₂O₄. EDS mapping technique plays an important role in identifying how the components of EG@MnFe₂O₄ are included. Herein, Figure 5 shows the composition of elements existed in EG@MnFe₂O₄, which mainly consisted of carbon, iron, oxygen, and manganese. Especially, the mean content of iron in EG@MnFe₂O₄ can be measured, at 6.4%. In addition, the saturation magnetization value of EG@MnFe₂O₄ was found to be 1.5 emu/g, suggesting that EG@MnFe₂O₄ is possibly eligible to separate from an aqueous solution using a simple magnet [42, 43]. Consequently, the EG@MnFe₂O₄ structure obtained a combination of EG and MnFe₂O₄ components [34–36].

3.2. Adsorption Studies

3.2.1. Effect of pH. Theoretically, the pH is one of the most influential parameters in any adsorption process, because

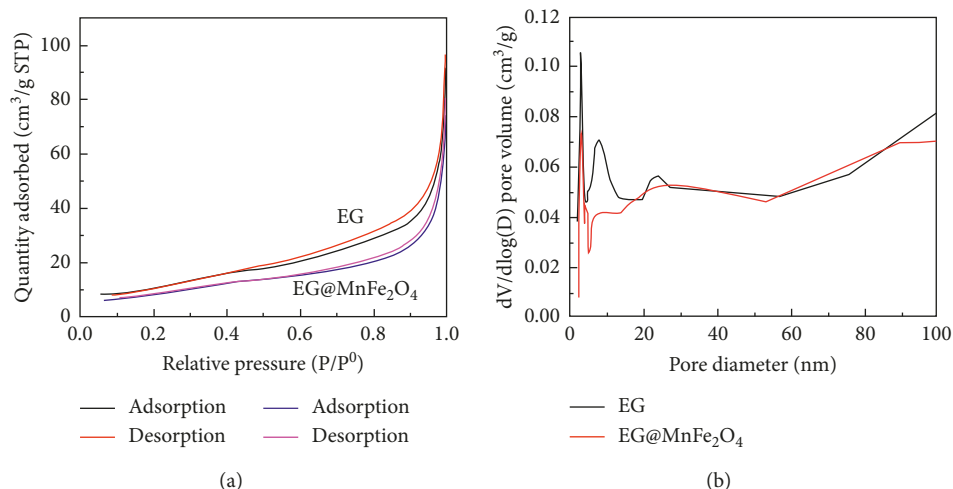


FIGURE 4: N₂ adsorption-desorption isotherm measurement (a) and pore size distribution (b) plots of EG and EG@MnFe₂O₄ materials.

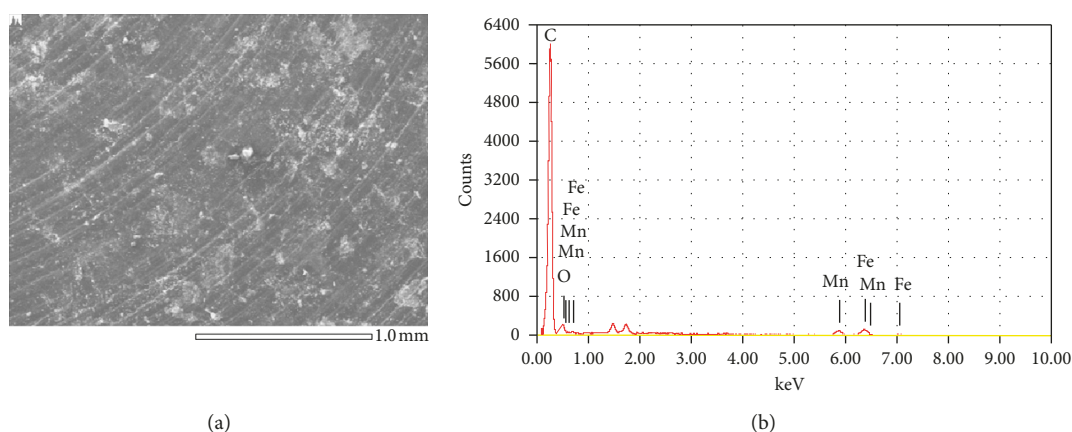


FIGURE 5: EDS mapping spectrum of EG@MnFe₂O₄.

the acidic, neutral, or basic solutions affect the charge natures (e.g., anionic, cationic, and zwitterionic) of adsorbate molecules and surface of adsorbent [44–48]. To compare the difference between MnFe₂O₄ and EG@MnFe₂O₄ materials in terms of CR adsorption efficiency, a range of pH from 2 to 12, which can be tuned by alkaline and acidic solutions, was investigated (Figure 6).

At a glance, it is evident that the adsorption uptake by EG@MnFe₂O₄ was remarkably higher than that by MnFe₂O₄ at any pH values. In detail, the highest adsorption capacity towards CR onto EG@MnFe₂O₄ could attain at nearly 66 mg/g under the pH condition of 6.0, while the optimal pH figure for MnFe₂O₄ was determined at 4.0, giving a capacity of only 35.5 mg/g. Enhancing the CR amount absorbed on EG@MnFe₂O₄ may be contributed by the component of EG coating, which contains functional groups essential for the adsorption. In our previous reports, we demonstrated the role of surface functional groups in improving the adsorption capacity of adsorbate [49, 50]. On the other hand, the CR adsorption of EG@MnFe₂O₄ by pH parameter seems to slightly drop, about 50 mg/g at the relatively weak acidic or basic media. By contrast, the adsorption of CR by

MnFe₂O₄ at neutral or strongly basic solution was highly likely to be uncondusive. These results suggested that the decoration of EG may be a considerable advantage because EG@MnFe₂O₄ material can obtain higher uptake at a harsher adsorption condition (e.g., at very strong basic/acidic solutions) in comparison to its precursor MnFe₂O₄. Based on the above results and analysis, we decided to conduct the next experiments under the pH condition at 4 and 6 for EG@MnFe₂O₄ and MnFe₂O₄ as adsorbents, respectively.

3.2.2. Effect of Dosage. Optimizing the dosage of materials is of significance to boost the cost-effectiveness in any treatment process [51]. Herein, we investigated a series of dosage by adding the amount (0.03–0.07 g) of EG@MnFe₂O₄ (a) and MnFe₂O₄ into 100 mL CR solution at the initial concentration of 60 mg/L under room temperature. After that, the concentration residuals were determined by the spectroscopy method. The effect of dosage on CR adsorption capacity was plotted and is shown in Figure 7. It is evident that the adsorption uptake by EG@MnFe₂O₄ was

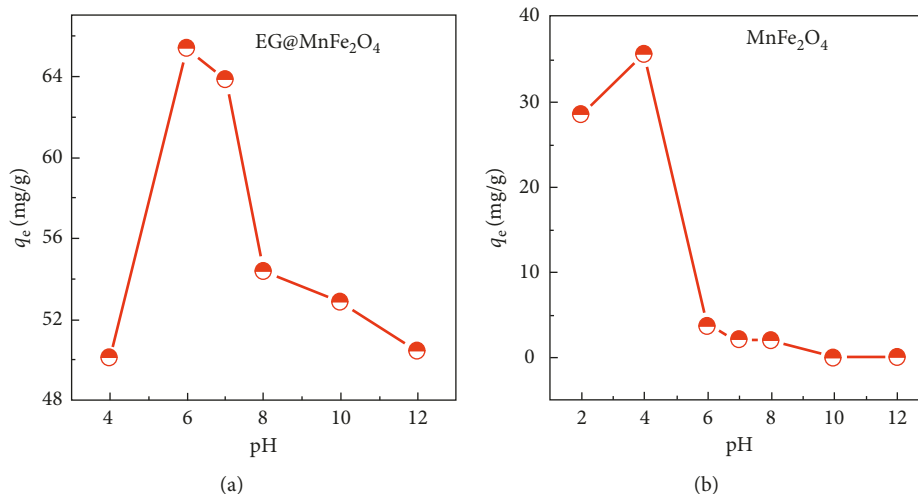


FIGURE 6: Effect of pH on the adsorption efficiency of CR over the EG@MnFe₂O₄ (a) and MnFe₂O₄ (b) materials. Experimental conditions included adsorbent dose of 0.5 g/L, solution volume of 100 mL, and dye concentration of 60 mg/L at various pH (2–12). Experiments were run at room temperature (25°C) during 210 min.

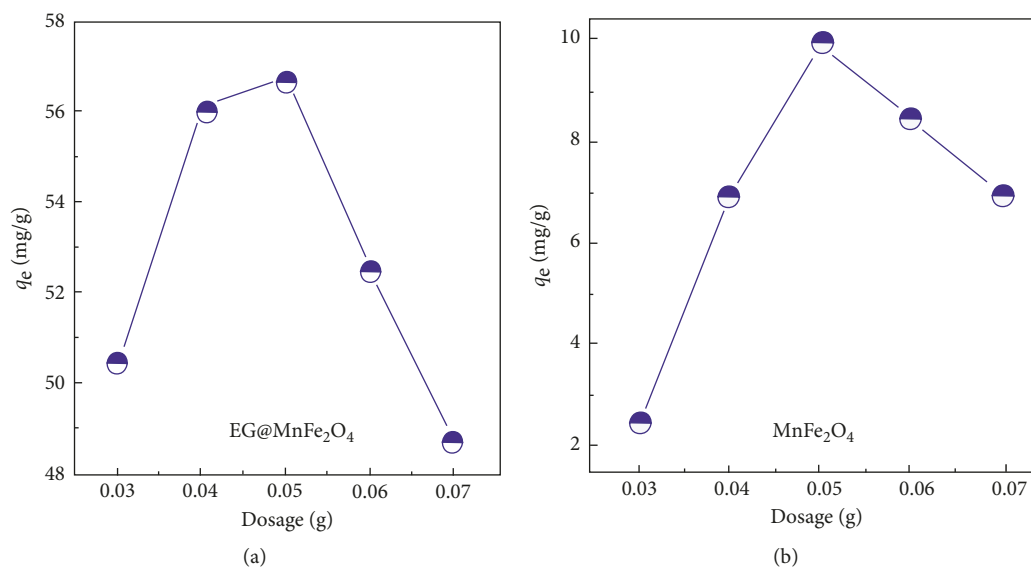


FIGURE 7: Effect of dosage the adsorption efficiency of CR over the EG@MnFe₂O₄ (a) and MnFe₂O₄ (b) materials. Experimental conditions included solution volume of 100 mL and dye concentration of 60 mg/L at pH 4 for MnFe₂O₄ and pH 6 for EG@MnFe₂O₄. Experiments were run at room temperature (25°C) during 210 min.

remarkably higher than that by MnFe₂O₄ at any dosage values. Moreover, larger amount of adsorbents (0.03–0.05 g for both EG@MnFe₂O₄ and MnFe₂O₄) led to an enhancement in CR adsorption capacity, reached the peaks of capacity at 57 and 10 mg/g, respectively. However, the adsorption efficiency rapidly dropped down until pouring higher dosage of 0.05 g. This phenomenon may be mainly due to larger amount of adsorbents resulting in hampering the mass transfer of CR molecules into the pores of materials and changing the physical properties of solution (e.g., viscosity) [52, 53]. Consequently, the optimal dosage, which compromises all factors affecting the adsorption uptake, was found at 0.05 g.

3.2.3. Effect of Contact Time and Adsorption Kinetics. According to the optimized conditions obtained from Figures 6 and 7, we carried out the kinetic experiments to investigate the influence of contact time on adsorbability towards CR of EG@MnFe₂O₄ and MnFe₂O₄ at various concentrations (20–60 mg/L). Figure 8(a) shows the plots of the adsorption capacity (Q_t , mg/g) against contact time (t , min). It is obvious that CR dye over EG@MnFe₂O₄ was rapidly absorbed during the first 60 minutes and steadily proceeded until the process became equilibrium. At the opposite trend, the plot in Figure 8(b) for MnFe₂O₄ showed a relatively gradual increase in adsorption capacity, in which adsorption at 50 mg/L gave the better adsorption results than others.

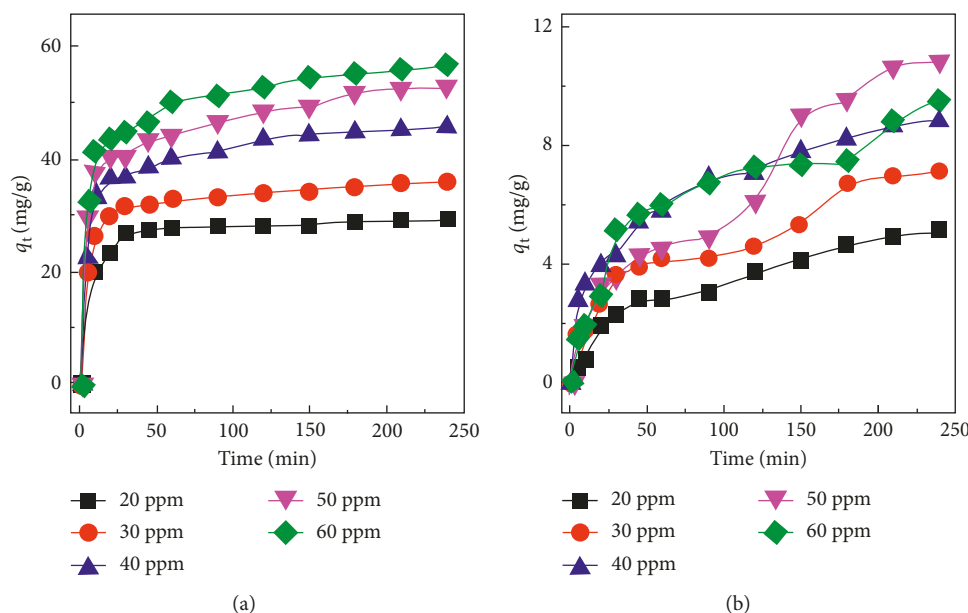


FIGURE 8: Effect of material dosage on CR adsorption capacity onto EG@MnFe₂O₄ (a) and MnFe₂O₄ (b). Experimental conditions: solution volume of 100 mL, and dye concentrations of 20–60 mg/L at pH 4 for MnFe₂O₄ and pH 6 for EG@MnFe₂O₄. Experiments were run at room temperature (25°C) during the period of 0–240 min.

To gain more insight into the profound effect of contact time, an array of commonplace kinetic equations (e.g., pseudo-first-order, pseudo-second-order, Elovich, and Bangham) were adopted and are shown in Figures 9 and 10 [52, 53]. After evaluating these models based on the coefficients of determination (R^2), adsorption mechanism in CR/EG@MnFe₂O₄ and CR/MnFe₂O₄ systems can be elucidated. Experimental data were transformed onto a mathematically linear form, which can be fitted by using the Origin Lab® version 9.0 software. Among the most prevalent kinetic models, the pseudo-first-order and pseudo-second-order models were applied herein. While equation (2) tends to explain the rate of adsorption relating to the number of unabsorbed sites from EG@MnFe₂O₄ and MnFe₂O₄, equation (3) describes the adsorption of CR over these magnetic nanocomposites through a chemisorption mechanism controlled by functional groups available on the surface of adsorbents [54].

$$\log(q_e - q_t) = \log q_e - \frac{k_1 \cdot t}{2.303}, \quad (2)$$

where k_1 (1/min) is defined as the pseudo-first-order adsorption rate constant, q_t (mg/g) is defined as the adsorption capacity at the period time t (min), and q_e (mg/g) is defined as equilibrium adsorption capacity at the equilibrium period (min).

$$\frac{t}{q_t} = \frac{1}{k_2 \cdot q_e^2} + \frac{t}{q_e}, \quad (3)$$

$$H = k_2 \cdot q_e^2, \quad (4)$$

where k_2 (g/mg min) is defined as the pseudo-second-order adsorption constant rate and H (mg/g min) is defined as initial adsorption rate (equation (4)).

Tables 1 and 2 show the parameters of these models and their respective values at five CR concentrations (20, 30, 40, 50, and 60 mg/L) by over EG@MnFe₂O₄ and MnFe₂O₄, respectively. According to Table 1, which listed kinetic parameters of the CR adsorption models over EG@MnFe₂O₄, the coefficients of determination R^2 for pseudo-second-order model (0.9987–0.9997) at all CR concentrations were far higher than those for pseudo-first-order model (0.8396–0.9749), indicating that the predicted data were well fitted with experimental data. This was also supported by Figures 9(a) and 9(b), which experimental data were depicted by the models. It is evident that the data points distributed well on the linear lines of pseudo-second-order model rather than the pseudo-first-order model. At the same trend for the CR adsorption models over MnFe₂O₄, Table 2 and Figures 10(a) and 10(b) show excellent fitness with R^2 (0.8234–0.9706) better than the others (0.6957–0.9672). Therefore, the adsorption of CR over both adsorbents obeyed the pseudo-second-order model with the dominance of chemisorption process via electrostatic attraction between adsorbent and adsorbate, while the other tends to be ineligible to explain the adsorption mechanisms. Ali et al. also reported the lower fitness of pseudo-first-order model in describing the adsorption mechanism [55]. Liu et al. proved the role of the surface functional groups in enhancing the adsorbability on modified activated carbon [56]. More interestingly, based on the values of Q_2 , the adsorption of CR over EG@MnFe₂O₄ (29.61–57.54 mg/g) was observed to be so far higher than that over MnFe₂O₄ (6.34–18.19 mg/g).

Otherwise, other two equations including (Elovich and Bangham) can be used to assess the adsorption kinetic of CR over EG@MnFe₂O₄ and MnFe₂O₄. In detail, the Elovich equation (equation (5)) assumes that the heterogeneous

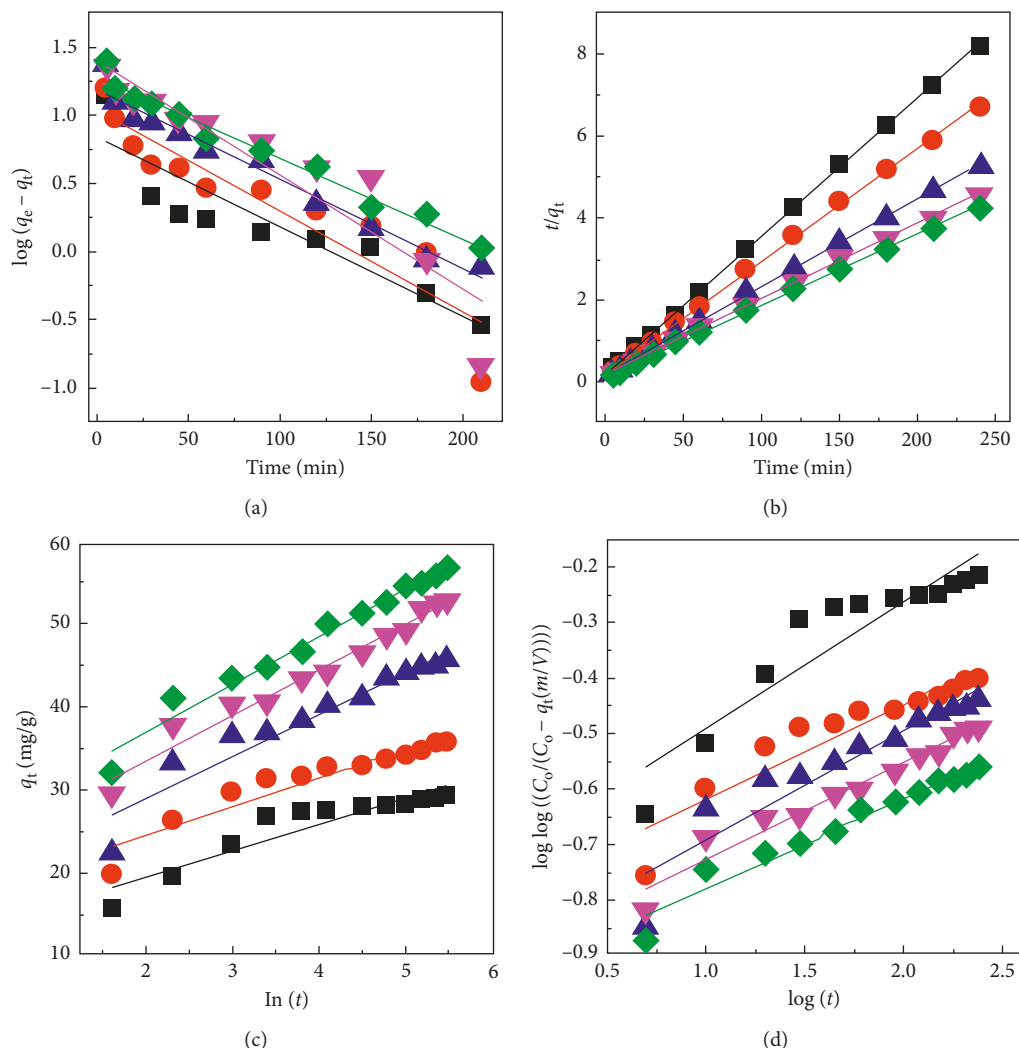


FIGURE 9: Linear plots of kinetic models: (a) pseudo-first-order, (b) pseudo-second-order, (c) Elovich, and (d) Bangham for the adsorption of CR over EG@MnFe₂O₄.

diffusion towards gases on heterogeneous surfaces or liquid/gas phase is related to the reaction rate and diffusion factor. Meanwhile, the Bangham equation (equation (6)) is typical for intraparticle diffusion mechanism of CR molecules over EG@MnFe₂O₄ and MnFe₂O₄ materials at room temperature. These equations can be described as follows:

$$Q_t = \frac{1}{\beta} \cdot \ln(\alpha \cdot \beta) + \frac{1}{\beta} \cdot \ln(t), \quad (5)$$

where α (mg/g) and β (g/mg) are defined as adsorption and desorption rates of CR molecules over EG@MnFe₂O₄ and MnFe₂O₄.

$$\log \log \left(\frac{VC_o}{VC_o - Q_t \cdot m} \right) = \log \left(\frac{k_B}{2.303 V} \right) + \alpha_B \cdot \log(t), \quad (6)$$

where k_B is defined as the Bangham equation constant and m (g) and V (mL) are defined as dosage and volume of adsorbent and solution, respectively.

According to the results from Table 1, all kinetic data by Elovich model fitted well with the experimental data due to their better goodness ($R^2 = 0.8427-0.9705$) rather than those by Bangham model ($R^2 = 0.8453-0.9512$), revealing the heterogeneous diffusion of CR over EG@MnFe₂O₄. Figures 9(c) and 9(d) were also eligible to support these results since the data points were distributed well on the linear lines of Elovich model. For analysing the adsorption data of CR onto MnFe₂O₄ via the Elovich and Bangham models, however, Figures 10(c) and 10(d) indicate the former model (0.9272–0.9901) was only better fitted with the adsorption of CR at concentrations 30–50 mg/L than the latter (0.8007–0.9616). For observation with more detail in Table 2, the CR adsorption rates (α , mg/g min) were extremely higher than CR desorption rates (β , g/mg) onto EG@MnFe₂O₄, while the figures for MnFe₂O₄ present the lower difference. This therefore follows that the adsorption of CR over EG@MnFe₂O₄ was more inclining to be favourable than over MnFe₂O₄.

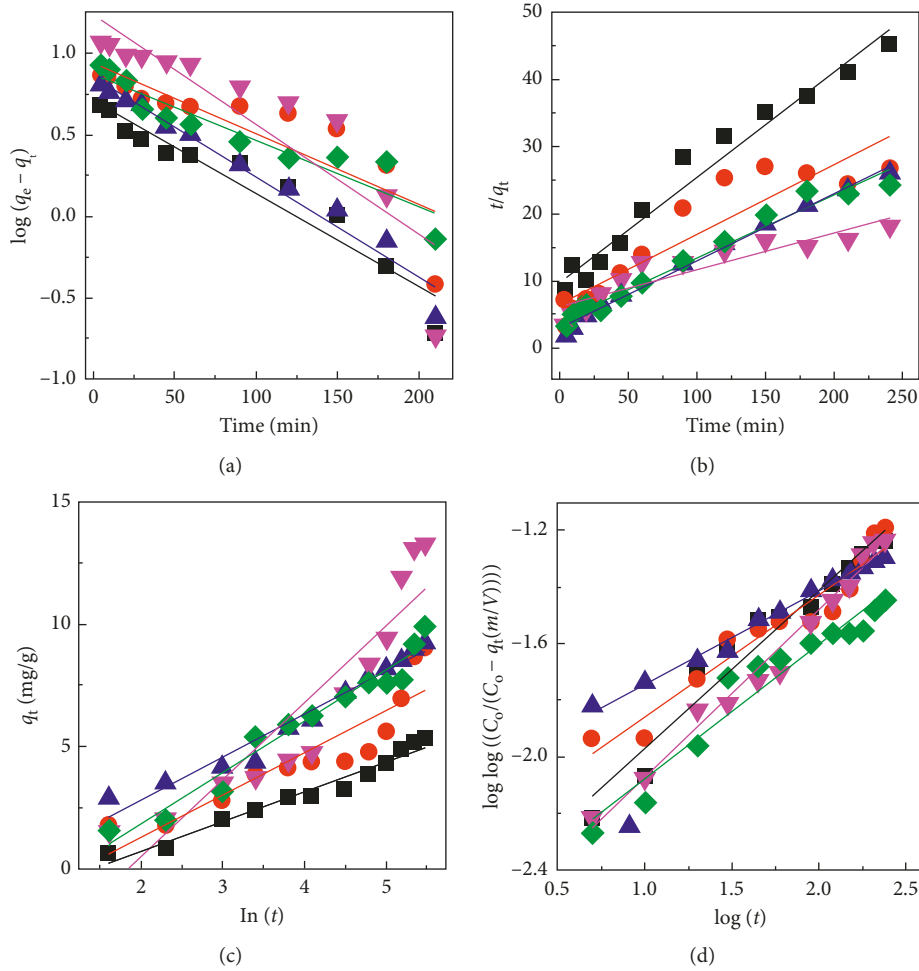


FIGURE 10: Kinetic plots of kinetic models: (a) pseudo-first-order, (b) pseudo-second-order, (c) Elovich, and (d) Bangham for the adsorption of CR over MnFe_2O_4 .

TABLE 1: Kinetic parameters of the CR adsorption models over $\text{EG@MnFe}_2\text{O}_4$.

Kinetic models	Parameters	Concentration (mg/L)				
		20	30	40	50	60
Pseudo-first-order	k_1 ($\text{min}^{-1}/(\text{mg/L})^{1/n}$)	0.0152	0.01695	0.01519	0.01920	0.01365
	Q_1 (mg/g)	6.92	10.82	15.43	24.71	18.98
	R^2	0.8396	0.8380	0.9635	0.8622	0.9749
Pseudo-second-order	$k_2 10^4$ ($\text{g}/(\text{mg}\cdot\text{min})$)	1.838	1.181	0.738	0.581	0.404
	Q_2 (mg/g)	29.61	36.10	46.51	53.82	57.54
	$H = k_2 Q_2^2$	6.2065	6.4960	6.2657	5.914	7.471
	R^2	0.9997	0.9992	0.9991	0.9974	0.9987
Elovich	β (g/mg)	0.32	0.29	0.20	0.18	0.17
	α ($\text{mg}/(\text{g}\cdot\text{min})$)	214.27	597.31	210.61	346.76	477.96
	R^2	0.8489	0.8870	0.9128	0.9683	0.9705
Bangham	k_B ($\text{mL}/(\text{g}\cdot\text{L})$)	0.0440	0.0373	0.0297	0.0289	0.0263
	α_B	0.2280	0.1717	0.1974	0.1742	0.1631
	R^2	0.8453	0.8578	0.8707	0.9571	0.9512

3.2.4. *Effect of Concentration and Adsorption Isotherms.* The isotherm models play a crucial role in better understanding the correlation between equilibrium concentration and adsorption capacity in liquid/solid phase at a constant temperature [57]. Several common isotherm

equations including Langmuir, Freundlich, Temkin, and Dubinin–Radushkevich (D–R) can be used to investigate such relationship [58–61]. To conduct adsorption isotherm investigation, the initial concentration of CR was in the range from 20 to 60 mg/L. The plots of equilibrium

TABLE 2: Kinetic parameters of the CR adsorption models over MnFe₂O₄.

Kinetic models	Parameters	Concentration (mg/L)				
		20	30	40	50	60
Pseudo-first-order	k_1 (min ⁻¹ /(mg/L) ^{1/n})	0.013	0.010	0.014	0.016	0.009
	Q_1 (mg/g)	5.12	8.67	7.13	17.31	7.42
	R^2	0.9187	0.6957	0.9672	0.7726	0.8762
Pseudo-second-order	k_2 (g/(mg·min))	0.238	0.07	0.03	0.019	0.035
	Q_2 (mg/g)	6.34	9.63	10.00	18.19	10.57
	$H = k_2 Q_2^2$	9.57	6.52	2.94	6.14	3.92
	R^2	0.9663	0.8234	0.9882	0.8312	0.9706
Elovich	β (g/mg)	0.82	0.58	0.57	0.32	0.48
	α (mg/(g·min))	2.9	4.9	1.2	0.50	0.67
	R^2	0.9592	0.8007	0.9616	0.8472	0.9558
Bangham	$k_B 10^4$ (mL/(g·L))	6.82	1.17	1.96	5.01	6.39
	α_B	0.559	0.434	0.327	0.590	0.475
	R^2	0.9439	0.9272	0.9901	0.9803	0.9333

adsorption capacity against equilibrium concentration are afforded to describe the mentioned models. In detail, the definition of four isotherms can be described as follows. Firstly, the Langmuir equation (equation (7)) assumes that the adsorption of CR molecules onto EG@MnFe₂O₄ and MnFe₂O₄ surface tends to reach the monolayer adsorption behaviour. This process may be caused by dynamically balancing the relative rates of adsorption/desorption without lateral interaction of CR molecules [62].

$$\frac{1}{Q_e} = \left(\frac{1}{Q_m K_L} \right) \frac{1}{C_e} + \frac{1}{Q_m}, \quad (7)$$

$$R_L = \frac{1}{1 + K_L C_e}, \quad (8)$$

where Q_e (mg/g), Q_m (mg/g), and C_e (mg/L) are defined as equilibrium adsorption capacity, maximum adsorption capacity, and equilibrium CR concentration, respectively. K_L (L/mg) is defined as Langmuir's constant [63]. R_L is a separate parameter and can be defined by equation (8). Based on the magnitude of R_L parameter, there are four kinds of adsorption processes: " R_L is larger than 1.0" referring to unfavourable process, " R_L is as equal as 1.0" referring to linear process, " R_L is in range from 0 to 1.0" referring to favourable process, and " R_L is as equal as 0" referring to irreversible process [64]. In addition, describing the multilayer adsorption behaviour is based on the Freundlich isotherm (equation (9)). This model proposes that the adsorption process occurs on heterogenous phase surfaces without any uniform distribution of heat of energies.

$$\ln Q_e = \ln K_F + \frac{1}{n} \ln C_e, \quad (9)$$

where K_F (mg/g) (L/mg) and $1/n$ are Freundlich's constant and exponent of nonlinearity, respectively, which can be determined from the intercept and slope of the Freundlich equation. Moreover, $1/n$ value shows the linearity of adsorption or the degree of curvature of the isotherms, and hence, its magnitude in the range from 0.1 to 0.5 indicates

the good favourability of the adsorption of CR over EG@MnFe₂O₄ and MnFe₂O₄. One of the most useful isotherm models is the Temkin equation (equation (10)), which serves to describe the influence of indirect interactions between CR molecules and "adsorption sites" of EG@MnFe₂O₄ and MnFe₂O₄ adsorbents [65].

$$Q_e = B_T \ln K_T + B_T \ln C_e, \quad (10)$$

$$B_T = \frac{RT}{b}, \quad (11)$$

where B_T , K_T (L/g), and b (J/mol) are determined from slope and intercept from equations (10) and (11). R is the ideal gas constant (8.314 J/mol·K). Finally, the Dubinin-Radushkevich (D-R) isotherm (equations (12)) is used to explain the state of chemical/physical adsorption with D-R activity coefficient B (mol²/kJ²) and adsorption capacity Q_m (mg/g), Polanyi potential ϵ (kJ/mol), and energy of adsorption E (kJ/mol), which can be calculated from equations (13) and (14):

$$\ln q_e = \ln Q_m - B\epsilon^2, \quad (12)$$

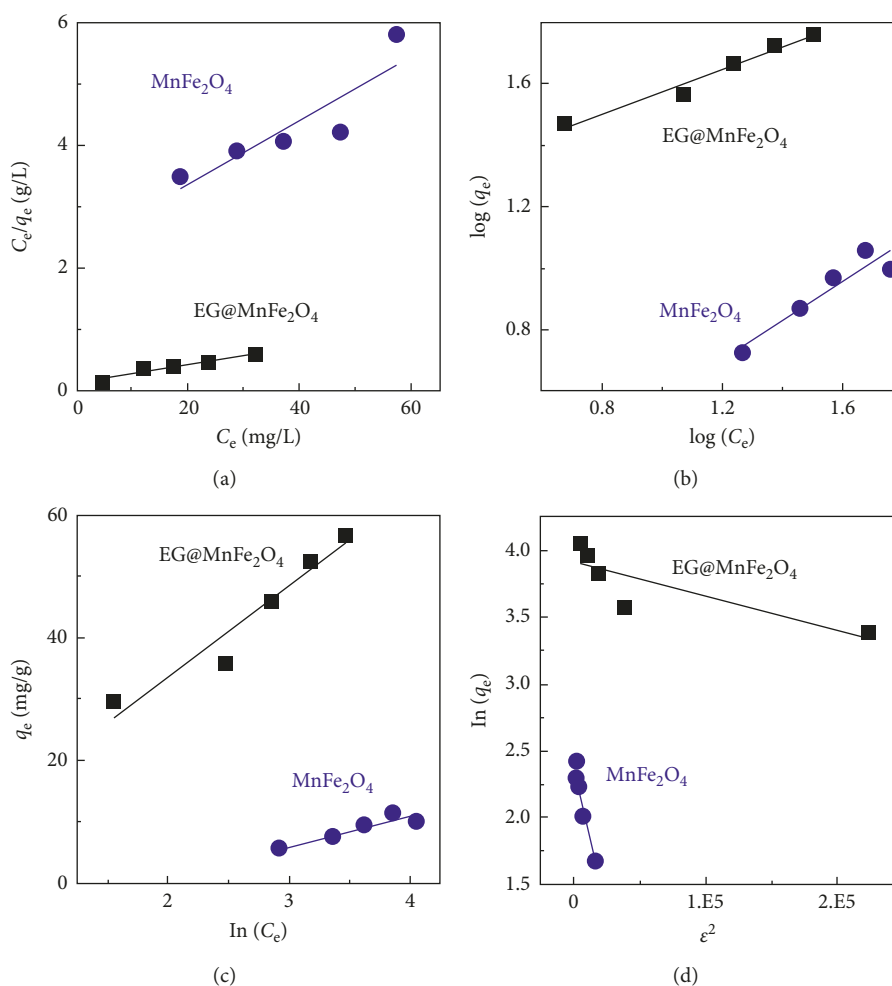
$$\epsilon = RT \ln \left(1 + \frac{1}{C_e} \right), \quad (13)$$

$$E = \frac{1}{\sqrt{-2B}}, \quad (14)$$

Table 3 lists the parameters, values, and R^2 of isotherm models for the adsorption of CR, and Figure 11 shows linear plots of isotherm models including Langmuir, Freundlich, Temkin, and D-R. It is clear that the adsorption of CR over EG@MnFe₂O₄ obeyed the Langmuir equation because of the highest R^2 (0.9572) and experimental data well fitted on the linear, assuming that the monolayer adsorption behaviour is likely to be a dominant process [66]. Meanwhile, adsorption of CR over MnFe₂O₄ adhered to the Freundlich models ($R^2 = 0.8519$), which is more inclining to occur upon multilayer adsorption behaviour. In addition, R_L (0.4–0.9) and $1/n$ (0.39–0.63) constant values confirmed that the sorption of

TABLE 3: Isotherm parameters over EG@MnFe₂O₄ and MnFe₂O₄.

Model	Parameters	Value	
		EG@MnFe ₂ O ₄	MnFe ₂ O ₄
Langmuir	k_L (L/mg)	0.0018	0.0210
	Q_m (mg/g)	71.79	19.57
	$R_L = 1/(1 + K_L C_0)$	0.90	0.44
	R^2	0.9572	0.7310
Freundlich	k_F (mg/g)/(mg/L) ^{1/n}	14.956	0.885
	1/n	0.39	0.63
	R^2	0.9274	0.8519
Temkin	k_T (L/mg)	1.00	6.01
	B_T	16.58	4.87
	R^2	0.8687	0.8205
D-R	B (kJ ² /mol ²)	2.64	0.46
	Q_m (mg/g)	50.69	11.302
	E (J/mol)	435.19	103.75
	R^2	0.5811	0.8483

FIGURE 11: Linear plots of isotherm models: (a) Langmuir, (b) Freundlich, (c) Temkin, and (d) D-R for the adsorption of CR over EG@MnFe₂O₄ and MnFe₂O₄.

CR over EG@MnFe₂O₄ and MnFe₂O₄ was the favourable process. Based on the results from Table 3, the maximum adsorption capacity (Q_m) calculated from Langmuir

equation can be found at 71.79 and 19.57 mg/g for EG@MnFe₂O₄ and MnFe₂O₄, respectively. These results are compared with those of previous studies (Table 4), showing

TABLE 4: Compared BET surface area and maximum adsorption capacity of various materials.

No.	Adsorbents	BET surface area (m ² /g)	Maximum adsorption capacity (mg/g)	Ref.
1	EG@MnFe ₂ O ₄	33.0	71.79	This study
2	MnFe ₂ O ₄	45.7	19.57	This study
3	Anilinepropylsilica xerogel	150	22.62	[67]
4	NaBentonite	25.7	35.84	[68]
5	Kaolin	20.28	5.44	[68]
6	Zeolite	8.31	3.77	[68]
7	Bentonite	32	40.4	[69]
8	Kaolin	168.8	11.88	[70]
9	Activated red mud	20.7	7.08	[71]
10	Activated coir pitch	—	6.72	[72]

the higher Q_m values than porous adsorbent mentioned. Therefore, EG@MnFe₂O₄ can be a promising candidate for the adsorption of CR in wastewater.

3.3. Thermodynamic Study. In general, the thermodynamic equation, which is represented in equation (15), can be used to diagnose the adsorption occur spontaneously or not and to elucidate the influence of temperature on the adsorption of CR over EG@MnFe₂O₄ and MnFe₂O₄. Because the determination of K_C is based on equation (16), the thermodynamic equation can be rewritten by a linear form (van't Hoff isotherm equation) as shown in equation (17).

$$\Delta G = -RT \ln K_C, \quad (15)$$

$$\ln K_C = \frac{C_A}{C_e}, \quad (16)$$

$$\ln K_C = \left(\frac{-\Delta H}{R} \right) \cdot \frac{1}{T} + \frac{\Delta S}{R}, \quad (17)$$

where K_C and T (K) are defined as the adsorption equilibrium constant and temperature, respectively; C_A (mg/g) and C_e (mg/L) are the equilibrium CR concentrations in solid phase and solution phase, respectively; ΔH (kJ/mol), ΔS (kJ/mol K), and ΔG (kJ/mol) are defined as standard enthalpy and entropy and Gibb's free energy.

Figure 12(a) plots the impact of temperature (283–313 K) on CR adsorption onto EG@MnFe₂O₄. Obviously, boosting the temperature led to a slight enhancement in the adsorption capacity. The correlation between temperature and equilibrium constant is described in Figure 11(b), which shows the plot of $\log(K_C)$ against $(1/T)$. As can be seen from Figure 12(b), experimental data were fitted well with the thermodynamic model. Moreover, high R^2 in Table 5 confirms that the van't Hoff equation obtained the excellent fitness; thus, it can be used to identify the standard thermodynamic constants (e.g., ΔH , ΔS , and ΔG). A positive ΔH reveals that the adsorption process of CR onto EG@MnFe₂O₄ tends to be endothermic. These results were highly in line with many previous works studying the adsorption of CR over various porous materials [73–77]. Meanwhile, positive value of ΔS shows an increase in disorder levels occurring in heterogeneous phase because of migration between aqueous solution and CR molecules during sorption [78]. Finally, the Gibbs free energy with minus values is

eligible to assert that the adsorption of CR on EG@MnFe₂O₄ was a spontaneous process.

3.4. Recyclability Study. On the other hand, to assess the cost-effectiveness and practical applicability of any solid adsorbent, recyclability study needs to be investigated. Herein, we selected the best materials for recyclability performance. Therefore, EG@MnFe₂O₄ can be regenerated according to the following procedure. To begin with, CR-loaded EG@MnFe₂O₄ separated from the first run was washed with 10 mL ethanol for 3 times and then with 10 mL distilled water for another 3 times. The nanomaterial was reactivated at 105°C and then used for the next use. The number of recyclability experiments was repeated to be 5 runs. The first reuse was found to be 58.41%, which was the same percentage as the standard run (60%). However, the second and third runs witnessed the slight decrease in removal efficiency, at approximately 46 and 40%. This result was commensurate with a previous work reporting about the adsorption of Congo red from aqueous solution by zeolitic imidazolate framework-8 [79]. The percentage of CR removal for another runs was rapidly dropped down. As a result, the EG@MnFe₂O₄ can be totally recycled at least four times, revealing good stability and regeneration performance of EG@MnFe₂O₄ material in eliminating the CR dye.

3.5. Proposed Mechanism. It is known that the dissociation constant (pKa) of Congo red is 4.0 [80]. In addition, we measured the point of zero charge (pHpzc) of MnFe₂O₄ and EG@MnFe₂O₄ at 5.0, and 6.8, respectively. In adsorption factors, pH 6 is best condition to make the maximum removal efficiency. This can be explained based on the theory of electrostatic interaction.

In fact, at $\text{pH} < \text{pKa}$ (CR) = 4.0, the solute tends to contain more protons, and the surface of EG@MnFe₂O₄ also becomes more positively charged. This phenomenon appears an electrostatic repulsion between the surface of EG@MnFe₂O₄ and CR cations, thus resulting in a decrease in adsorption. In contrast, when the pH value is higher than pKa of CR but lower than pH_{pzc} of EG@MnFe₂O₄, or $4.0 < \text{pH} < \text{pH}_{\text{pzc}} = 6.8$, CR molecules are deprotonated to transfer a form of anion while EG@MnFe₂O₄ surface is still positively charged due to $\text{pH} < \text{pH}_{\text{pzc}}$. This results in an electrostatic attraction, leading to a considerable increase in

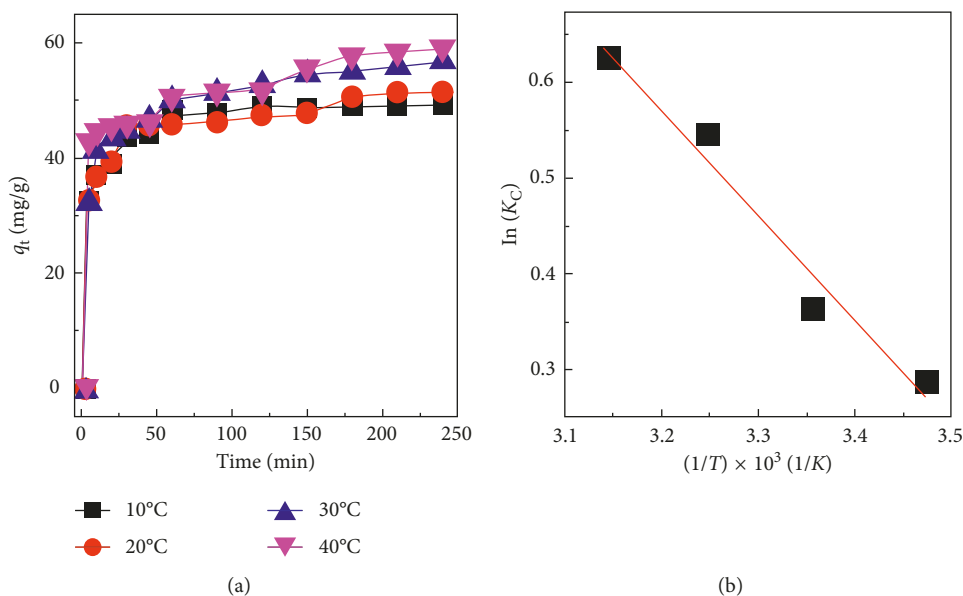


FIGURE 12: Effect of temperature on adsorption of CR over EG@MnFe₂O₄ (a) and thermodynamic study (b). Experimental conditions included solution volume of 100 mL at pH 4 for MnFe₂O₄ and pH 6 for EG@MnFe₂O₄. Experiments were run at various temperatures (10–40°C).

TABLE 5: Thermodynamic parameters for the adsorption of CR over EG@MnFe₂O₄.

van't Hoff equation	ΔH° (kJ/mol)	ΔS° (J/mol K)	ΔG_{283} (kJ/mol)	ΔG_{293} (kJ/mol)	ΔG_{303} (kJ/mol)	ΔG_{313} (kJ/mol)
$\ln K_C = -1.097(1/T) + 4.081$ $R^2 = 0.9688$	9.12	33.93	-0.652	-0.991	-1.331	-1.670

adsorption. In this study, you can see the optimum pH at 6, which is appropriate to the above analysis. However, overcoming the pH_{pzc} value tends to intercept the adsorption because both surfaces of EG@MnFe₂O₄ and CR molecules are negatively charged, causing a decline in the decontamination of CR dye. Consequently, the adsorption process is more likely to be favourable at pH varying from pK_a to pH_{pzc} .

In addition, we measured the functional groups on the surface of EG@MnFe₂O₄ with the total acidic groups (carboxylic, lactonic, and phenolic groups) at 0.096 mmol/g and total basic groups at 0.156 mmol/g, while there was no detection of any groups on MnFe₂O₄ without EG decoration. In fact, the CR adsorption capacity of EG@MnFe₂O₄ (71.79 mg/g) was found to be higher than that of MnFe₂O₄ (19.57 mg/g); therefore, these groups can have an important role in improving the adsorption. In general, the surface functional groups can create a wide range of interactions such as the H-bond, π - π interaction, n - π interaction, and electrostatic force between CR molecules and adsorbate surface [81–83]. Meanwhile, the adsorption of MnFe₂O₄ was attributable to the weak forces such as “oxygen-metal” bridge and van der Waals [54].

4. Conclusions

The present study successfully fabricated the EG, MnFe₂O₄, and EG@MnFe₂O₄ materials. The characterization results showed the EG@MnFe₂O₄ obtained a heterogeneous, highly

defective, amorphous morphology with surface area of 33 m²/g. The adsorption results showed the equilibrium time at 240 min, optimal dosage of 0.05 g and solution pH 6 for EG@MnFe₂O₄ and pH 4 for MnFe₂O₄. Moreover, kinetic and isotherm models pointed out that the adsorption of CR over EG@MnFe₂O₄ at various concentrations adhered to chemisorption mechanism (pseudo-second-order) and monolayer adsorption behaviour (Langmuir equation). In addition, the thermodynamic study confirmed that the nature of adsorption is an endothermic and spontaneous process. The maximum adsorption capacity obtained from the Langmuir model for EG@MnFe₂O₄ was calculated to be 71.79 mg/g, which was so far higher than that of MnFe₂O₄ and several previous studies, indicating that EG@MnFe₂O₄ can be a potential adsorbent for the adsorption of CR dye in water.

Data Availability

The data used to support the findings of this study are available from the corresponding author upon request.

Conflicts of Interest

The authors declare no conflicts of interest.

Acknowledgments

The Foundation for Science and Technology Development, Nguyen Tat Thanh University, Ho Chi Minh city, Vietnam, is acknowledged.

References

- [1] H. Q. Pham, T. T. Huynh, A. Van Nguyen, T. Van Thuan, L. G. Bach, and V. T. Thanh Ho, "Advanced Ti_{0.7}W_{0.3}O₂ nanoparticles prepared via solvothermal process using titanium tetrachloride and tungsten hexachloride as precursors," *Journal of Nanoscience and Nanotechnology*, vol. 18, no. 10, pp. 7177–7182, 2018.
- [2] T. V. Tran, H. T. N. Le, H. Q. Ha et al., "A five coordination Cu(II) cluster-based MOF and its application in the synthesis of pharmaceuticals via sp³ C-H/N-H oxidative coupling," *Catalysis Science & Technology*, vol. 7, no. 16, pp. 3453–3458, 2017.
- [3] H. T. N. Le, T. V. Tran, N. T. S. Phan, and T. Truong, "Efficient and recyclable Cu₂(BDC)₂(BPY)-catalyzed oxidative amidation of terminal alkynes: role of bipyridine ligand," *Catalysis Science & Technology*, vol. 5, no. 2, pp. 851–859, 2015.
- [4] C. Tan, X. Cao, X.-J. Wu et al., "Recent advances in ultrathin two-dimensional nanomaterials," *Chemical Reviews*, vol. 117, no. 9, pp. 6225–6331, 2017.
- [5] N. Ortega, A. Kumar, J. F. Scott, and R. S. Katiyar, "Multi-functional magnetoelectric materials for device applications," *Journal of Physics: Condensed Matter*, vol. 27, no. 50, article 504002, 2015.
- [6] M. J. Polking, A. P. Alivisatos, and R. Ramesh, "Synthesis, physics, and applications of ferroelectric nanomaterials," *MRS Communications*, vol. 5, no. 1, pp. 27–44, 2015.
- [7] A. Kanwal, H. N. Bhatti, M. Iqbal, and S. Noreen, "Basic dye adsorption onto clay/MnFe₂O₄ composite: a mechanistic study," *Water Environment Research*, vol. 89, no. 4, pp. 301–311, 2017.
- [8] X. Hou, J. Feng, Y. Ren, Z. Fan, and M. Zhang, "Synthesis and adsorption properties of sponge like porous MnFe₂O₄," *Colloids and Surfaces A: Physicochemical and Engineering Aspects*, vol. 363, no. 1–3, pp. 1–7, 2010.
- [9] W. Wang, Z. Ding, M. Cai et al., "Synthesis and high-efficiency methylene blue adsorption of magnetic PAA/MnFe₂O₄ nanocomposites," *Applied Surface Science*, vol. 346, pp. 348–353, 2015.
- [10] M. Iqbal, "Bioassays based on higher plants as excellent dosimeters for ecotoxicity monitoring: a review," *Chemistry International*, vol. 5, pp. 1–80, 2019.
- [11] M. Iqbal, "Vicia faba bioassay for environmental toxicity monitoring: a review," *Chemosphere*, vol. 144, pp. 785–802, 2016.
- [12] M. Abbas, M. Adil, S. Ehtisham-ul-Haque et al., "Vibrio fischeri bioluminescence inhibition assay for ecotoxicity assessment: a review," *Science of the Total Environment*, vol. 626, pp. 1295–1309, 2018.
- [13] S. Chatterjee, S. Chatterjee, B. P. Chatterjee, and A. K. Guha, "Adsorptive removal of Congo red, a carcinogenic textile dye by chitosan hydrobeads: binding mechanism, equilibrium and kinetics," *Colloids and Surfaces A: Physicochemical and Engineering Aspects*, vol. 299, no. 1–3, pp. 146–152, 2007.
- [14] Z. Hu, H. Chen, F. Ji, and S. Yuan, "Removal of Congo red from aqueous solution by cattail root," *Journal of Hazardous Materials*, vol. 173, no. 1–3, pp. 292–297, 2010.
- [15] N. Tahir, H. N. Bhatti, M. Iqbal, and S. Noreen, "Biopolymers composites with peanut hull waste biomass and application for crystal violet adsorption," *International Journal of Biological Macromolecules*, vol. 94, pp. 210–220, 2017.
- [16] A. Kausar, M. Iqbal, A. Javed et al., "Dyes adsorption using clay and modified clay: a review," *Journal of Molecular Liquids*, vol. 256, pp. 395–407, 2018.
- [17] X. Zhao, W. Wang, Y. Zhang, S. Wu, F. Li, and J. P. Liu, "Synthesis and characterization of gadolinium doped cobalt ferrite nanoparticles with enhanced adsorption capability for Congo red," *Chemical Engineering Journal*, vol. 250, pp. 164–174, 2014.
- [18] L. Yang, Y. Zhang, X. Liu et al., "The investigation of synergistic and competitive interaction between Congo red and methyl blue on magnetic MnFe₂O₄," *Chemical Engineering Journal*, vol. 246, pp. 88–96, 2014.
- [19] L. Wang, J. Li, Y. Wang, L. Zhao, and Q. Jiang, "Adsorption capability for Congo red on nanocrystalline MFe₂O₄ (M = Mn, Fe, Co, Ni) spinel ferrites," *Chemical Engineering Journal*, vol. 181–182, pp. 72–79, 2012.
- [20] W. Konicki, D. Sibera, E. Mijowska, Z. Lendzion-Bieluń, and U. Narkiewicz, "Equilibrium and kinetic studies on acid dye acid red 88 adsorption by magnetic ZnFe₂O₄ spinel ferrite nanoparticles," *Journal of Colloid and Interface Science*, vol. 398, pp. 152–160, 2013.
- [21] N. M. Mahmoodi, "Nickel ferrite nanoparticle: synthesis, modification by surfactant and dye removal ability," *Water, Air, & Soil Pollution*, vol. 224, no. 2, p. 1419, 2013.
- [22] T. V. Pham, T. T. Nguyen, D. T. Nguyen et al., "The preparation and characterization of expanded graphite via microwave irradiation and conventional heating for the purification of oil contaminated water," *Journal of Nanoscience and Nanotechnology*, vol. 19, no. 2, pp. 1122–1125, 2019.
- [23] Y. Si and E. T. Samulski, "Exfoliated graphene separated by platinum nanoparticles," *Chemistry of Materials*, vol. 20, no. 21, pp. 6792–6797, 2008.
- [24] M. Yi and Z. Shen, "A review on mechanical exfoliation for the scalable production of graphene," *Journal of Materials Chemistry A*, vol. 3, no. 22, pp. 11700–11715, 2015.
- [25] L. G. Bach, T. Van Tran, T. D. Nguyen, T. Van Pham, and S. T. Do, "Enhanced adsorption of methylene blue onto graphene oxide-doped XFe₂O₄ (X = Co, Mn, Ni) nanocomposites: kinetic, isothermal, thermodynamic and recyclability studies," *Research on Chemical Intermediates*, vol. 44, no. 3, pp. 1661–1687, 2018.
- [26] V. T. Pham, H.-T. T. Nguyen, D. T. C. Nguyen et al., "Process optimization by response surface methodology for adsorption of Congo red dye onto exfoliated graphite-decorated MnFe₂O₄ nanocomposite: pivotal role of surface chemistry," *Processes*, vol. 7, no. 5, p. 305, 2019.
- [27] S. Stankovich, D. A. Dikin, R. D. Piner et al., "Synthesis of graphene-based nanosheets via chemical reduction of exfoliated graphite oxide," *Carbon*, vol. 45, no. 7, pp. 1558–1565, 2007.
- [28] L. Shao, Z. Ren, G. Zhang, and L. Chen, "Facile synthesis, characterization of a MnFe₂O₄/activated carbon magnetic composite and its effectiveness in tetracycline removal," *Materials Chemistry and Physics*, vol. 135, no. 1, pp. 16–24, 2012.
- [29] Z. Zhang, Y. Wang, Q. Tan, Z. Zhong, and F. Su, "Facile solvothermal synthesis of mesoporous manganese ferrite (MnFe₂O₄) microspheres as anode materials for lithium-ion batteries," *Journal of Colloid and Interface Science*, vol. 398, pp. 185–192, 2013.
- [30] A. Han, J. Liao, M. Ye, Y. Li, and X. Peng, "Preparation of nano-MnFe₂O₄ and its catalytic performance of thermal decomposition of ammonium perchlorate," *Chinese Journal of Chemical Engineering*, vol. 19, no. 6, pp. 1047–1051, 2011.
- [31] T. Şimşek, S. Akansel, Ş. Özcan, and A. Ceylan, "Synthesis of MnFe₂O₄ nanocrystals by wet-milling under atmospheric

- conditions," *Ceramics International*, vol. 40, no. 6, pp. 7953–7956, 2014.
- [32] B. Aslibeiki, P. Kameli, M. H. Ehsani et al., "Solvochemical synthesis of MnFe_2O_4 nanoparticles: the role of polymer coating on morphology and magnetic properties," *Journal of Magnetism and Magnetic Materials*, vol. 399, pp. 236–244, 2016.
- [33] D. Chen, Y. Zhang, and Z. Kang, "A low temperature synthesis of MnFe_2O_4 nanocrystals by microwave-assisted ball-milling," *Chemical Engineering Journal*, vol. 215–216, pp. 235–239, 2013.
- [34] Y. Yao, Y. Cai, F. Lu, F. Wei, X. Wang, and S. Wang, "Magnetic recoverable MnFe_2O_4 and MnFe_2O_4 -graphene hybrid as heterogeneous catalysts of peroxymonosulfate activation for efficient degradation of aqueous organic pollutants," *Journal of Hazardous Materials*, vol. 270, pp. 61–70, 2014.
- [35] N. Ueda Yamaguchi, R. Bergamasco, and S. Hamoudi, "Magnetic MnFe_2O_4 -graphene hybrid composite for efficient removal of glyphosate from water," *Chemical Engineering Journal*, vol. 295, pp. 391–402, 2016.
- [36] S. Li, B. Wang, B. Li, J. Liu, M. Yu, and X. Wu, "Self-assembly of 2D sandwich-structured MnFe_2O_4 /graphene composites for high-performance lithium storage," *Materials Research Bulletin*, vol. 61, pp. 369–374, 2015.
- [37] K. V. Sankar and R. K. Selvan, "The ternary MnFe_2O_4 /graphene/polyaniline hybrid composite as negative electrode for supercapacitors," *Journal of Power Sources*, vol. 275, pp. 399–407, 2015.
- [38] A. Hadi, J. Zahirifar, J. Karimi-Sabet, and A. Dastbaz, "Graphene nanosheets preparation using magnetic nanoparticle assisted liquid phase exfoliation of graphite: the coupled effect of ultrasound and wedging nanoparticles," *Ultrasonics Sonochemistry*, vol. 44, pp. 204–214, 2018.
- [39] T. V. Tran, U. T. T. Nguyen, T. T. Nguyen et al., "Synthesis and magnetic properties of graphene oxide-decorated cobalt, manganese and nickel ferrite nanoparticles prepared by polymerized route," *IOP Conference Series: Materials Science and Engineering*, vol. 479, p. 12114, 2019.
- [40] Y. Xiao, X. Li, J. Zai et al., "CoFe₂O₄-graphene nanocomposites synthesized through an ultrasonic method with enhanced performances as anode materials for Li-ion batteries," *Nano-Micro Letters*, vol. 6, no. 4, pp. 307–315, 2014.
- [41] T. Van Tran, D. T. C. Nguyen, H. T. N. Le et al., "Combined minimum-run resolution IV and central composite design for optimized removal of tetracycline drug over metal-organic framework-templated porous carbon," *Molecules*, vol. 24, no. 10, p. 1887, 2019.
- [42] H. A. Hamad, M. M. Abd El-latif, A. B. Kashyout, W. A. Sadik, and M. Y. Feteha, "Study on synthesis of superparamagnetic spinel cobalt ferrite nanoparticles as layered double hydroxides by co-precipitation method," *Russian Journal of General Chemistry*, vol. 84, no. 10, pp. 2031–2036, 2014.
- [43] M. A. E. A. Ali and H. A. Hamad, "Synthesis and characterization of highly stable superparamagnetic CoFe_2O_4 nanoparticles as a catalyst for novel synthesis of thiazolo [4, 5-b] quinolin-9-one derivatives in aqueous medium," *Journal of Molecular Catalysis A: Chemical*, vol. 404–405, pp. 148–155, 2015.
- [44] T. V. Tran, D. T. C. Nguyen, H. T. N. Le et al., "Tunable synthesis of mesoporous carbons from $\text{Fe}_3\text{O}(\text{BDC})_3$ for chloramphenicol antibiotic remediation," *Nanomaterials*, vol. 9, no. 2, p. 237, 2019.
- [45] M. Elkady, H. Shokry, and H. Hamad, "Microwave-assisted synthesis of magnetic hydroxyapatite for removal of heavy metals from groundwater," *Chemical Engineering & Technology*, vol. 41, no. 3, pp. 553–562, 2018.
- [46] N. A. El Essawy, S. M. Ali, H. A. Farag, A. H. Konsowa, M. Elnouby, and H. A. Hamad, "Green synthesis of graphene from recycled PET bottle wastes for use in the adsorption of dyes in aqueous solution," *Ecotoxicology and Environmental Safety*, vol. 145, pp. 57–68, 2017.
- [47] S. E. A. Elhafez, H. A. Hamad, A. A. Zaatout, and G. F. Malash, "Management of agricultural waste for removal of heavy metals from aqueous solution: adsorption behaviors, adsorption mechanisms, environmental protection, and techno-economic analysis," *Environmental Science and Pollution Research*, vol. 24, no. 2, pp. 1397–1415, 2017.
- [48] M. El kady, H. Shokry, and H. Hamad, "Effect of superparamagnetic nanoparticles on the physicochemical properties of nano hydroxyapatite for groundwater treatment: adsorption mechanism of Fe(ii) and Mn(ii)," *RSC Advances*, vol. 6, no. 85, pp. 82244–82259, 2016.
- [49] T. Van Tran, D. T. Cam Nguyen, H. T. N. Le et al., "A hollow mesoporous carbon from metal-organic framework for robust adsorbability of ibuprofen drug in water," *Royal Society Open Science*, vol. 6, no. 5, article 190058, 2019.
- [50] T. Van Tran, D. T. C. Nguyen, H. T. N. Le et al., "Facile synthesis of manganese oxide-embedded mesoporous carbons and their adsorbability towards methylene blue," *Chemosphere*, vol. 227, pp. 455–461, 2019.
- [51] T. V. Tran, D. T. C. Nguyen, H. T. N. Le et al., "MIL-53 (Fe)-directed synthesis of hierarchically mesoporous carbon and its utilization for ciprofloxacin antibiotic remediation," *Journal of Environmental Chemical Engineering*, vol. 7, no. 1, article 102881, 2019.
- [52] M. R. Esfahani, E. M. Languri, and M. R. Nunna, "Effect of particle size and viscosity on thermal conductivity enhancement of graphene oxide nanofluid," *International Communications in Heat and Mass Transfer*, vol. 76, pp. 308–315, 2016.
- [53] K. Wang, L. Zhang, W. Zhang, and G. Luo, "Mass-transfer-controlled dynamic interfacial tension in microfluidic emulsification processes," *Langmuir*, vol. 32, no. 13, pp. 3174–3185, 2016.
- [54] T. V. Tran, V. D. Cao, V. H. Nguyen et al., "MIL-53 (Fe) derived magnetic porous carbon as a robust adsorbent for the removal of phenolic compounds under the optimized conditions," *Journal of Environmental Chemical Engineering*, article 102902, 2019.
- [55] R. M. Ali, H. A. Hamad, M. M. Hussein, and G. F. Malash, "Potential of using green adsorbent of heavy metal removal from aqueous solutions: adsorption kinetics, isotherm, thermodynamic, mechanism and economic analysis," *Ecological Engineering*, vol. 91, pp. 317–332, 2016.
- [56] Y. Liu, X. Liu, W. Dong, L. Zhang, Q. Kong, and W. Wang, "Efficient adsorption of sulfamethazine onto modified activated carbon: a plausible adsorption mechanism," *Scientific Reports*, vol. 7, no. 1, article 12437, 2017.
- [57] T. Van Tran, Q. T. P. Bui, T. D. Nguyen, V. T. T. Ho, and L. G. Bach, "Application of response surface methodology to optimize the fabrication of ZnCl_2 -activated carbon from sugarcane bagasse for the removal of Cu^{2+} ," *Water Science and Technology*, vol. 75, no. 9, pp. 2047–2055, 2017.
- [58] D. Balarak, F. Mostafapour, H. Azarpira, and A. Joghataei, "Mechanisms and equilibrium studies of sorption of

- metronidazole using graphene oxide," *Journal of Pharmaceutical Research International*, vol. 19, no. 4, pp. 1–9, 2017.
- [59] D.A.O, A. P. Olalekan, A. M. Olatunya, and O. Dada, "Langmuir, Freundlich, Temkin and dubinin-radushkevich isotherms studies of equilibrium sorption of Zn^{2+} unto phosphoric acid modified rice husk," *IOSR Journal of Applied Chemistry*, vol. 3, no. 1, pp. 38–45, 2012.
- [60] C. Nguyen and D. D. Do, "The Dubinin-Radushkevich equation and the underlying microscopic adsorption description," *Carbon*, vol. 39, no. 9, pp. 1327–1336, 2001.
- [61] S. Azizian, M. Haerifar, and J. Basiri-Parsa, "Extended geometric method: a simple approach to derive adsorption rate constants of Langmuir-Freundlich kinetics," *Chemosphere*, vol. 68, no. 11, pp. 2040–2046, 2007.
- [62] V. T. Tran, D. T. Nguyen, V. T. T. Ho, P. Q. H. Hoang, P. Q. Bui, and L. G. Bach, "Efficient removal of Ni^{2+} ions from aqueous solution using activated carbons fabricated from rice straw and tea waste," *Journal of Material and Environmental Sciences*, vol. 8, pp. 426–437, 2017.
- [63] P. S. Ghosal and A. K. Gupta, "Determination of thermodynamic parameters from Langmuir isotherm constant-revisited," *Journal of Molecular Liquids*, vol. 225, pp. 137–146, 2017.
- [64] T. Van Tran, Q. T. P. Bui, T. D. Nguyen, N. T. H. Le, and L. G. Bach, "A comparative study on the removal efficiency of metal ions (Cu^{2+} , Ni^{2+} , and Pb^{2+}) using sugarcane bagasse-derived $ZnCl_2$ -activated carbon by the response surface methodology," *Adsorption Science & Technology*, vol. 35, no. 1-2, pp. 72–85, 2017.
- [65] D. T. C. Nguyen, "Metal-organic framework MIL-53(Fe) as an adsorbent for ibuprofen drug removal from aqueous solutions: response surface modeling and optimization," *Journal of Chemistry*, vol. 2019, Article ID 5602957, 11 pages, 2019.
- [66] T. Van Thuan, B. T. P. Quynh, T. D. Nguyen, V. T. T. Ho, and L. G. Bach, "Response surface methodology approach for optimization of Cu^{2+} , Ni^{2+} and Pb^{2+} adsorption using KOH-activated carbon from banana peel," *Surfaces and Interfaces*, vol. 6, pp. 209–217, 2017.
- [67] F. A. Pavan, S. L. P. Dias, E. C. Lima, and E. V. Benvenutti, "Removal of congo red from aqueous solution by aniline-propylsilica xerogel," *Dyes and Pigments*, vol. 76, no. 1, pp. 64–69, 2008.
- [68] V. Vimonses, S. Lei, B. Jin, C. W. K. Chow, and C. Saint, "Kinetic study and equilibrium isotherm analysis of congo red adsorption by clay materials," *Chemical Engineering Journal*, vol. 148, no. 2-3, pp. 354–364, 2009.
- [69] M. A. Akl, A. M. Youssef, and M. M. Al-Awadhi, "Adsorption of acid dyes onto bentonite and surfactant-modified bentonite," *Journal of Analytical & Bioanalytical Techniques*, vol. 4, no. 4, pp. 3–7, 2013.
- [70] I. D. Mall, V. C. Srivastava, N. K. Agarwal, and I. M. Mishra, "Removal of congo red from aqueous solution by bagasse fly ash and activated carbon: kinetic study and equilibrium isotherm analyses," *Chemosphere*, vol. 61, no. 4, pp. 492–501, 2005.
- [71] A. Tor and Y. Cengeloglu, "Removal of congo red from aqueous solution by adsorption onto acid activated red mud," *Journal of Hazardous Materials*, vol. 138, no. 2, pp. 409–415, 2006.
- [72] C. Namasivayam and D. Kavitha, "Removal of congo red from water by adsorption onto activated carbon prepared from coir pith, an agricultural solid waste," *Dyes and Pigments*, vol. 54, no. 1, pp. 47–58, 2002.
- [73] T. Şişmanoğlu and G. S. Pozan, "Adsorption of congo red from aqueous solution using various TiO_2 nanoparticles," *Desalination and Water Treatment*, vol. 57, no. 28, pp. 13318–13333, 2016.
- [74] M. Foroughi-Dahr, H. Abolghasemi, M. Esmaili, A. Shojaoradi, and H. Fatoorehchi, "Adsorption characteristics of Congo red from aqueous solution onto tea waste," *Chemical Engineering Communications*, vol. 202, no. 2, pp. 181–193, 2015.
- [75] K. S. P.-M. Adolphe, T. G. Merlain, L. N. R. Blaise et al., "Kinetics and equilibrium studies of the adsorption of nickel (II) ions from aqueous solution onto modified natural and synthetic iron oxide," *International Journal of Basic and Applied Sciences*, vol. 4, no. 3, p. 277, 2015.
- [76] T. M. Rao and V. V. B. Rao, "Biosorption of congo red from aqueous solution by crab shell residue: a comprehensive study," *Springerplus*, vol. 5, no. 1, p. 537, 2016.
- [77] Y. Zhou, L. Ge, N. Fan, and M. Xia, "Adsorption of congo red from aqueous solution onto shrimp shell powder," *Adsorption Science & Technology*, vol. 36, no. 5-6, pp. 1310–1330, 2018.
- [78] H. Guedidi, L. Reinert, J.-M. Lévêque, Y. Soneda, N. Bellakhal, and L. Duclaux, "The effects of the surface oxidation of activated carbon, the solution pH and the temperature on adsorption of ibuprofen," *Carbon*, vol. 54, pp. 432–443, 2013.
- [79] C. Jiang, B. Fu, H. Cai, and T. Cai, "Efficient adsorptive removal of congo red from aqueous solution by synthesized zeolitic imidazolate framework-8," *Chemical Speciation & Bioavailability*, vol. 28, no. 1–4, pp. 199–208, 2016.
- [80] C. Wu, J. Scott, and J.-E. Shea, "Binding of congo red to amyloid protofibrils of the alzheimer β 9-40 peptide probed by molecular dynamics simulations," *Biophysical Journal*, vol. 103, no. 3, pp. 550–557, 2012.
- [81] H. N. Tran, Y.-F. Wang, S.-J. You, and H.-P. Chao, "Insights into the mechanism of cationic dye adsorption on activated charcoal: the importance of π - π interactions," *Process Safety and Environmental Protection*, vol. 107, pp. 168–180, 2017.
- [82] H. N. Tran, H.-P. Chao, and S.-J. You, "Activated carbons from golden shower upon different chemical activation methods: synthesis and characterizations," *Adsorption Science & Technology*, vol. 36, no. 1-2, pp. 95–113, 2017.
- [83] H. N. Tran, S.-J. You, and H.-P. Chao, "Insight into adsorption mechanism of cationic dye onto agricultural residues-derived hydrochars: negligible role of π - π interaction," *Korean Journal of Chemical Engineering*, vol. 34, no. 6, pp. 1708–1720, 2017.

Research Article

Study on Fire Resistance Ability and Mechanical Properties of Composites Based on Epikote 240 Epoxy Resin and Thermoelectric Fly Ash: An Ecofriendly Additive

Tuan Anh Nguyen , Quang Tung Nguyen, Xuan Canh Nguyen , and Van Hoan Nguyen

Faculty of Chemical Technology, Hanoi University of Industry (HaUI), No. 298 Cau Dien, North Tu Liem District, Hanoi, Vietnam

Correspondence should be addressed to Tuan Anh Nguyen; anhnt@hau.edu.vn

Received 16 March 2019; Accepted 2 May 2019; Published 16 June 2019

Guest Editor: Van Duong Dao

Copyright © 2019 Tuan Anh Nguyen et al. This is an open access article distributed under the Creative Commons Attribution License, which permits unrestricted use, distribution, and reproduction in any medium, provided the original work is properly cited.

In this study, fly ash was tested as a filler in epoxy with concentrations of 5, 10, and 20 wt.%. Fly ash particles were modified by chemical treatments (using NaOH and HCl) to enhance the compatibility and adhesion, making mechanical properties and flame retardancy of materials better. Flexural strength, tensile strength, and impact resistance decrease as fly ash content increases. The compressive strength is further increased by the addition of fly ash (compressive strength of the materials including 5, 10, 20 wt.% of fly ash modified with NaOH is 176.01, 189.90, and 197.07 MPa, respectively). The interface between fly ash and epoxy matrix plays an important role in determining the mechanical strength and flame retardancy of synthetic materials. The results of UL-94HB and LOI test method for composite materials including 20 wt.% fly ash (modified by NaOH) reached 13.45 mm/min and 22.4%, respectively. These results showed that fly ash is an efficient additive as a flame retardant which decreases the amounts of additives in products and improves their efficiency. Fly ash was also dispersed into epoxy resin to enhance its resistance to oxidation.

1. Introduction

Flame retardants (FRs) used as additives in a wide range of production play a very important role in suppressing fire generation and delaying fire spread [1, 2]. A composite material based on epoxy resin and fly ash (a by-product from thermal power plant) with a good fire resistance ability was developed. Fly ash used as a flame retardant instead of current ones (for example, organic halogen compounds) reduces environmental problems when compared to using flame retardant epoxy resin [3]. Some popular commercial flame retardants are not only dangerous to human and environment but they also have negative effects on mechanical properties of materials [4]. For this reason, it is necessary to find an ecofriendly material which is harmless to human. Additives such as clay and fly ash are being paid great attention. Many authors studied the use of ecofriendly additives such as fly ash, multiwalled carbon nanotube, and

nanoclay in enhancing fire resistance of epoxy resin [5–7]. In this study, ultrafine fly ash has been used. Fly ash has been surface-treated with NaOH and HCl acid to improve dispersion in Epikote 240 epoxy matrix. The purpose of this study was to improve fire retardancy and improve some mechanical durability, thereby expanding the application area of fly ash for thermal power plants in Vietnam and reducing the impact on the environment. Methods such as UL 94 and limiting oxygen index (LOI) are used to study the combustibility of composites.

2. Materials and Methods

2.1. Materials

- (i) Epikote 240 (EP) epoxy resin from Shell Chemicals (USA) with epoxy group content of 24.6%, Mw 5100–5400 mmol/kg, density 1.12 g/cm³, and

viscosity at 25°C 007–1.1 Pa·s. Diethylenetriamine (DETA) from Dow Chemicals (USA), with density 0.953 g/cm³ at 20°C, boiling point 207°C, and Mw 103.2 g/mol⁻¹. HCl and NaOH from Dow Chemicals (USA).

- (ii) The fly ash primarily consisted of inorganic materials such as silica, alumina, and calcium oxide. Fly ash taken from the ash waste of Pha Lai Thermal Power Station was collected from Song Da Joint Stock Company 12-Cao Cuong, Vietnam.

2.2. Methods

2.2.1. Sample Preparation. First, the fly ash was kept in a drier at 100°C for 24 hours to remove the moisture present in it. After 24 hrs, the fly ash was taken out of the drier. Then, the amount of fly ash, epoxy resin (Epikote 240), and hardener (DETA) was calculated for five different composites (0, 5, 10, and 20 w.% fly ash). Curing was performed at room temperature for approx. 24 hrs. After curing, the mould was opened, and the slab was taken out of the mould and cleaned and cured under room temperature for 1 and 7 days.

2.2.2. Characterizations

- (i) The morphology of the samples was carried out by scanning electron microscopy (SEM, Evaseq error codes, S-4800, Japan). An ultramicrotome (Leica microsystem) was used to cut ultrathin sections (80 nm) of samples before recovered on a copper grid.
- (ii) The flame retardant properties was tested by the limiting oxygen index (LOI) (Yasuda Seiki Seisakusho Ltd, Japan) according to JIS K720-1976, with sheet dimensions of 120 × 6.5 × 3.2 mm.
- (iii) The UL-94 rating was tested according to the UL-94 (ASTMD635-12) with sheet dimensions of 125 ± 5 mm length by 13.0 ± 0.5 mm width and with the minimum thickness of 3.0 (−0.0 + 0.2) mm.
- (iv) The combustion rate was measured by COMBUSTION RESISTANCE COD 6145000 according to ASTM D757-77 standard. The specimen's dimensions were 3.17 × 12.7 × 121 mm³. Mechanical properties were measured on an INSTRON-5582 100 KN (USA) according to ISO 527-1993 at an extension speed of 5 mm/min.
- (v) All data were the average of five independent measurements; the relative errors committed on each data were reported as well. IR spectrum was measured at the Department of Chemistry, University of Natural Sciences (Hanoi National University).

3. Results and Discussion

3.1. Investigation of Characteristics of Fly Ash. Fly ash from the ash waste of Pha Lai Thermal Power Station was collected in Song Da Joint Stock Company 12-Cao Cuong, Vietnam.

Before the investigation, fly ash was washed by acetone to remove impurities. Scanning electronic microscopy (SEM) was used to determine fly ash particles' morphological structure. The results are shown in Figure 1. As seen in Figure 1, fly ash particles have spherical smooth structure. They are abundant and different in size.

In Figure 2, the IR spectroscopy of fly ash with vibration bands 400–4000 cm⁻¹ shows that there is a peak at 3649 cm⁻¹ and 1065 cm⁻¹ corresponding to -OH (free) and Si-O, respectively, proving the presence of -OH in fly ash's surface, thus making it easier for the modification process to attach silane groups to fly ash's surface to enhance compatibility between inorganic material and polymer substrate. Besides, there are also peaks at 792 cm⁻¹, 562 cm⁻¹ and 480 cm⁻¹, and 452 cm⁻¹ corresponding to the presence of quartz, O-Fe, and O-Al, respectively.

3.2. Treatment of Fly Ash's Surface

3.2.1. Treatment of Fly Ash's Surface with NaOH

(1) IR Spectroscopy of Fly Ash Modified with NaOH. NaOH is a strong base containing active hydroxide groups. NaOH with concentration of 3 M was used to modify fly ash. In the modification process, fly ash particles were stirred in 3 M solution of NaOH at 80°C for 5 hours. Efficiency of the process is qualitatively evaluated through IR spectroscopy of modified fly ash (Figure 3).

Figure 3 shows that there are new peaks at 3451 cm⁻¹ and 1653 cm⁻¹ in IR spectra of modified fly ash in comparison with spectra of initial fly ash. In IR spectra, there is the appearance of a peak at 3451 cm⁻¹ and 1653 cm⁻¹ corresponding to the stretching vibrations of -OH groups of NaOH and H₂O, respectively. On other hand, there is no change in the fingerprint region, indicating that metallic oxides exist on modified fly ash. Therefore, it can be said that the structure of fly ash is quite stable.

(2) Effects of Alkaline Treatment on Fly Ash's Size and Surface Area. The surface of initial fly ash is smooth, making it difficult for adhesion between fly ash and polymer substrate. So, it is necessary to treat fly ash surface to increase roughness and surface area or form active groups on the surface.

Fly ash modified with NaOH was filtered, washed, and dried. The contribution of fly ash particles is observed by the SEM method in low resolution.

In Figure 4, the SEM image of fly ash modified with NaOH shows that when the contribution of NaOH is higher, the size of modified fly ash particles is more even in comparison with initial ones. In other words, NaOH makes the size of fly ash particles smaller.

The morphological structure of treated fly ash showed in Figure 4 (fly-NaOH) is rough in comparison with initial ones. There are many cracks and small particles which are aluminum silicate or aluminum sulfate formed from abrasion process on the surface. It was caused by reactions between NaOH and oxides of fly ash. Although the size of fly ash particles of experiments is not similar, there is no

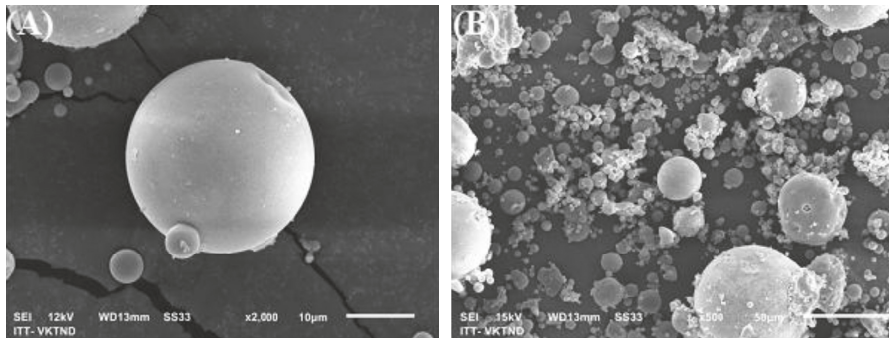


FIGURE 1: SEM image of fly ash/Epikote 240 composites.

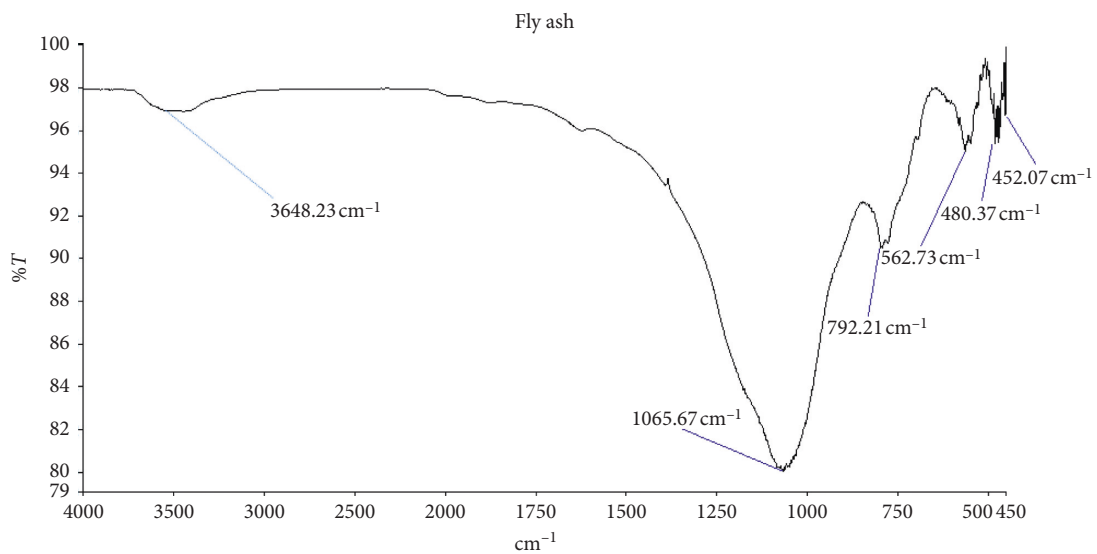


FIGURE 2: IR spectroscopy of the original fly ash sample.

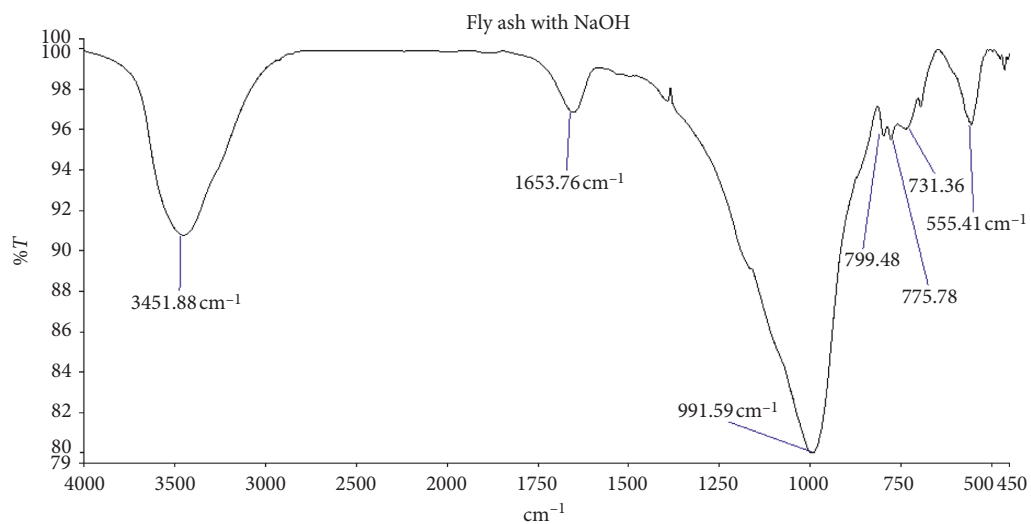


FIGURE 3: IR spectroscopy of the original fly ash-NaOH sample.

difficulty in enhancing properties of fly ash by this method. The surface becomes rough, and the increase of surface area may make the interaction between fly ash and epoxy resin better.

3.2.2. Treatment of Fly Ash Surface with HCl Acid

(1) IR Spectroscopy of Fly Ash Modified by HCl Acid. HCl is a strong acid used to corrode metallic oxides included in fly

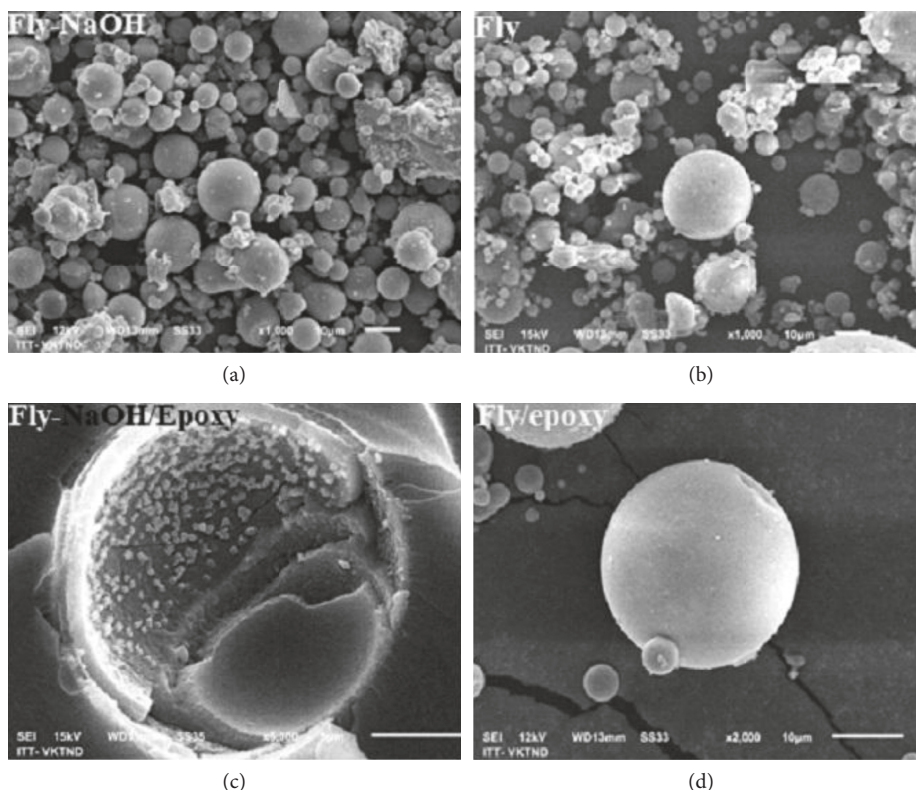


FIGURE 4: SEM image of fly ash modified with NaOH. (a) Fly-NaOH: modified fly ash; (b) fly: not yet counted; (c) fly-NaOH/epoxy: composite epoxy resin surface has modified fly ash; and (d) fly/epoxy: composite epoxy resin substrate has unmodified fly ash surface.

ash. The modification process used 2 M HCl solution. Fly ash particles were stirred in HCl 2 M, at 95°C, for 6 hours to modify. By observing peaks appearing on IR spectroscopy of modified fly ash in Figure 5, efficiency of this method was qualitatively evaluated. There is little difference in IR spectroscopy of modified fly ash in comparison with the initial one. This proves a bad compatibility between acid HCl and fly ash. So, using acid HCl to change the structure of fly ash is ineffective.

(2) *Effects of Acidic Treatment on Fly Ash's Size and Surface Area.* The SEM image in Figure 6 is observed to more clearly understand the change of fly ash particles after modified with HCl. Images in other resolutions of modified fly ash particles show that there are crystals attached to fly ash particles, making fly ash surface area rough, thus increasing contact area between fly ash particles and polymer substrate (see Figure 6).

Besides, the size of modified fly ash particles is more even than that of initial ones, making the dispersion of fly ash particles in resin better (see Figure 6). However, there are only crystals but no cracks on fly ash surface. Therefore, it can be concluded that acid HCl has no strong impact on fly ash and this method is not an optimal one.

3.3. Study on Preparation of Fly Ash/Epoxy Composites

3.3.1. Effects of the Amount of Fly Ash Modified by Inorganic Compounds on Mechanical Properties, Flame Retardant Ability, and Structure of the Materials

(1) *Effects on Mechanical Properties.* Effects of the amount of fly ash modified by inorganic compounds (NaOH and HCl) on tensile strength of the materials are shown in Figure 7. As a result, materials' tensile strength follows the order: materials including fly ash modified by NaOH > materials including fly ash modified by HCl > materials including fly ash without modification. Besides, increasing the amount of fly ash makes tensile strength decrease, but it is insignificant. This shows that the compatibility with resin of modified fly ash is better than of initial fly ash, leading to the increase of tensile strength. Concretely, tensile strength of the materials including 5, 10, and 20 wt.% of fly ash modified with NaOH is 82.43, 79.20, and 75.75 MPa, respectively. Tensile strength of the materials including 5, 10, and 20 wt.% of fly ash modified with HCl is 79.98, 78.39, and 75.37 MPa, respectively.

Effects of the amount of fly ash modified by inorganic compounds (NaOH and HCl) on tensile modulus of the materials are shown in Figure 8. As a result, materials' tensile modulus follows the order: materials including fly ash modified with NaOH > materials including fly ash without modification > materials including fly ash modified with HCl. Besides, increasing the amount of fly ash makes tensile modulus decrease, but it is insignificant. This shows that the compatibility with resin of modified fly ash is better than of initial fly ash, leading to the stability of tensile modulus. Concretely, tensile modulus of the materials including 5, 10, and 20 wt.% of fly ash modified with NaOH is 52.27, 49.98, and 47.75 MPa, respectively. Tensile modulus of the

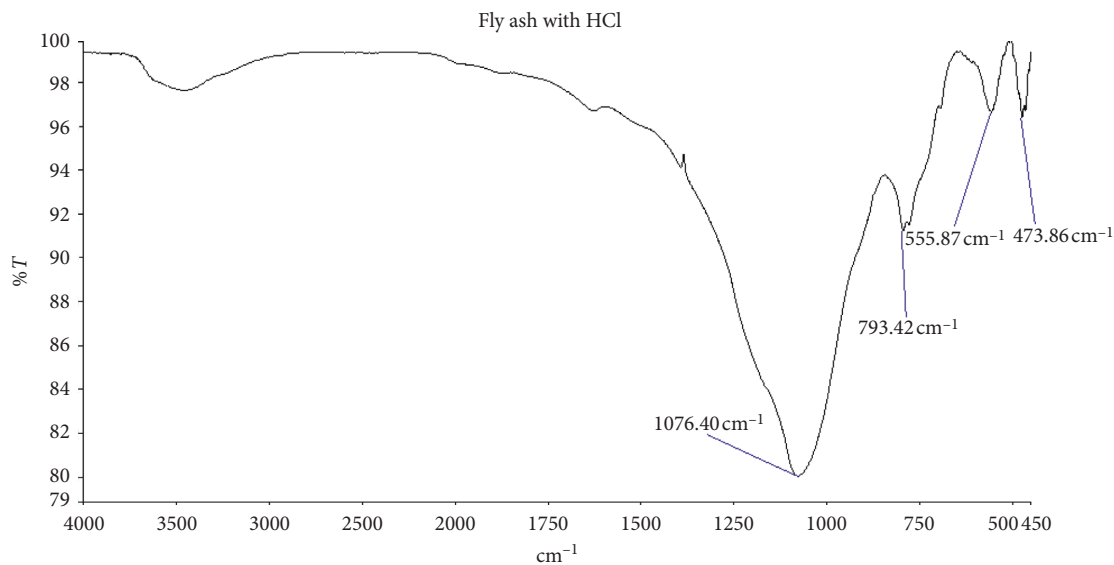


FIGURE 5: IR spectroscopy of the original fly-HCl ash sample.

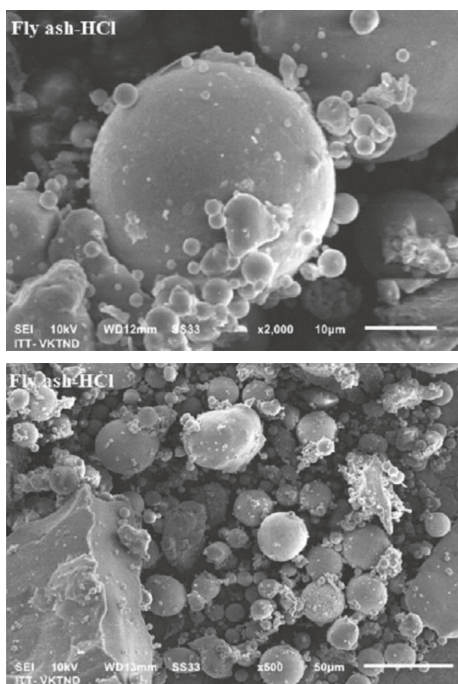


FIGURE 6: SEM image of fly ash modified with HCl.

materials including 5, 10, and 20 wt.% of fly ash modified with HCl is 45.09, 43.79, and 41.08 MPa, respectively.

Figure 9 shows effects of the amount of fly ash modified with inorganic compounds (NaOH and HCl) on compressive strength of the materials. As a result, materials' compressive strength follows the order: materials including fly ash modified by NaOH > materials including fly ash modified by HCl > materials including fly ash without modification. Moreover, impressive strength of the materials significantly increases with the increase of the amount of fly ash. This is caused by the increase in compatibility, adhesion, and filling ability of modified fly ash with resin, thus leading to the improvement of compressive strength. Concretely,

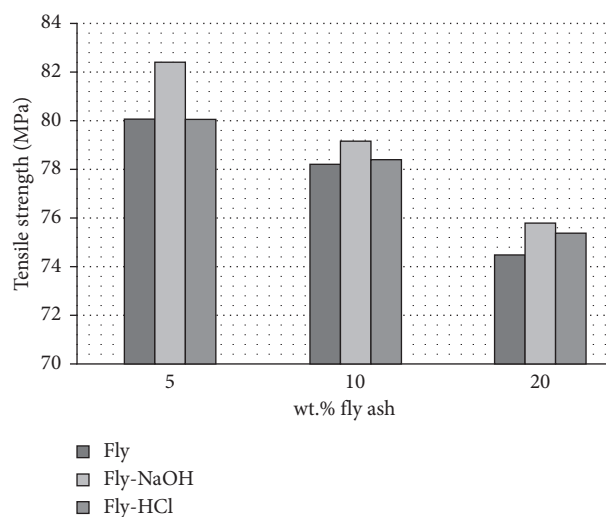


FIGURE 7: Comparison of flexural strength.

compressive strength of the materials including 5, 10, and 20 wt.% of fly ash modified with NaOH is 176.01, 189.90, and 197.07 MPa, respectively. Compressive strength of the materials including 5, 10, and 20 wt.% of fly ash modified with HCl is 145.33, 180.07, and 196.78 MPa, respectively.

When epoxy resin is cured with diethylenetriamine (DETA), cross-linking forms a three-dimensional space circuit. Fly ash acts as an inorganic filler that loses the space between polymer chains, reducing the flexibility of the polymer molecule to increase hardness. Besides, fly ash particles were filled into spaces between polymers in the epoxy matrix, creating pressure on polymers in the vicinity. As a result, the tension was reduced and the hardness was enhanced. In addition, the adhesion of the particle/matrix has a significant influence on the durability of granular polymer composites. A strong interfering link between particles and polymer matrix is important for effective stress transfer resulting in high intensity of synthesis [5].

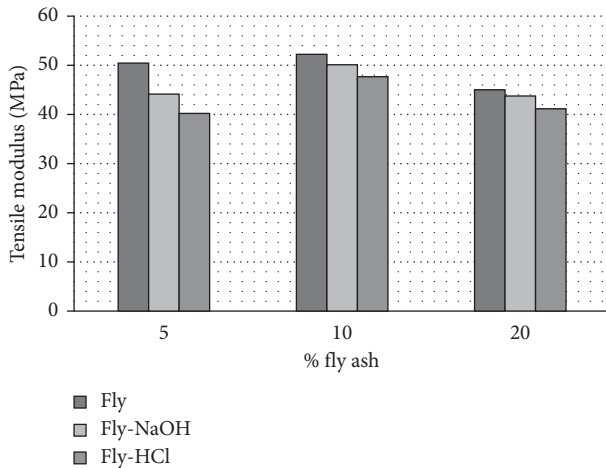


FIGURE 8: Comparison of tensile strength.

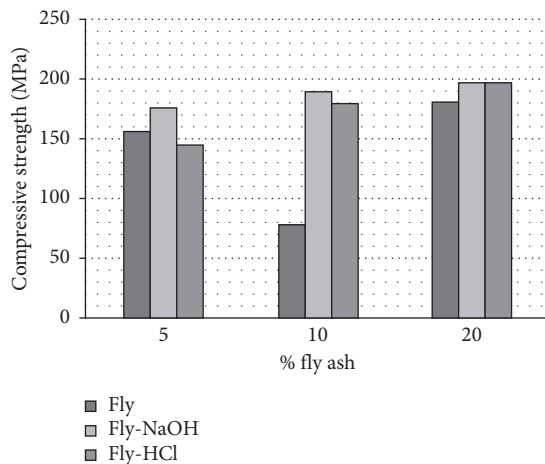


FIGURE 9: Comparison of compressive strength.

Figure 10 shows effects of the amount of fly ash modified with inorganic compounds (NaOH and HCl) on compact strength of the materials. As a result, materials' compact strength follows the order: materials including fly ash modified by HCl > materials including fly ash modified by NaOH > materials including fly ash without modification. Moreover, compact strength of the materials insignificantly decreases with the increase of the amount of fly ash. After modification, compatibility of fly ash with resin is better, leading to the improvement of compact strength. Concretely, compact strength of the materials including 5, 10, and 20 wt.% of fly ash modified with NaOH is 6.89, 6.01, and 5.70 MPa, respectively. Compact strength of the materials including 5, 10, and 20 wt.% of fly ash modified with HCl is 6.54, 6.55, and 5.98 (kJ/m²), respectively.

The results show that the amount of fly ash affects mechanical properties of the materials. Like fly ash without modification, there are effects on the materials in the case of modified fly ash such as increasing compressive strength and decreasing tensile modulus, compact strength, and tensile strength. However, effects made by modified fly ash are more significant than by initial fly ash because of good contribution and adhesion of modified fly ash particles with resin.

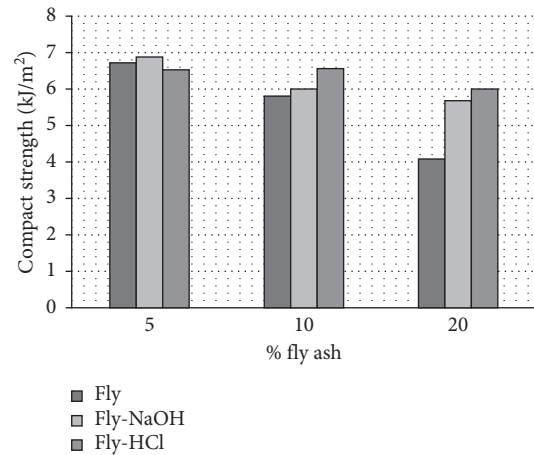


FIGURE 10: Comparison of compact strength.

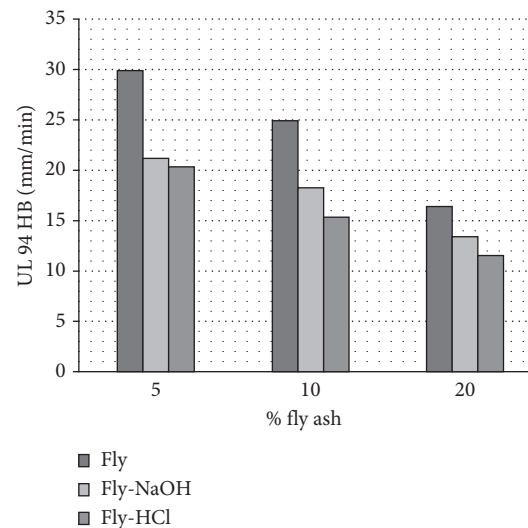


FIGURE 11: Flame retardancy according to the UL 94HB research method.

Thus, fly ash modified with NaOH is better than fly ash modified with HCl.

(2) *Investigation of Effects of the Amount of Fly Ash on Flame Retardancy of the Materials by UL 94 HB Standard.* Figure 11 shows effects of the amount of fly ash modified with inorganic compounds (NaOH and HCl) on the burning rate of the materials following UL 94 HB standard. As a result, the burning rate of the materials follows the order: the materials including fly ash modified with HCl < the materials including fly ash modified with NaOH < the materials including fly ash without modifications. Besides, the higher the amount of fly ash is, the lower the burning rate is or the better the flame retardancy of the materials is. This proves that after modification, fly ash's compatibility with resin is better, making flame retardancy of the materials better. Concretely, the burning rate following UL 94 HB standard of the materials including 5, 10, and 20 wt.% of NaOH is 21.15, 18.22, and 13.45 mm/min, respectively. The burning rate following UL 94 HB standard of the materials

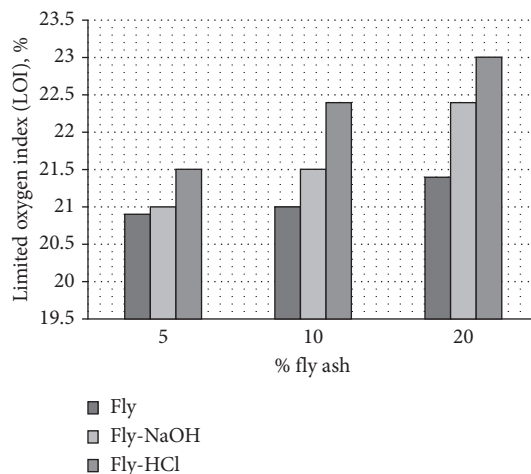


FIGURE 12: Effects of the amount of fly ash on limited oxygen index (LOI).

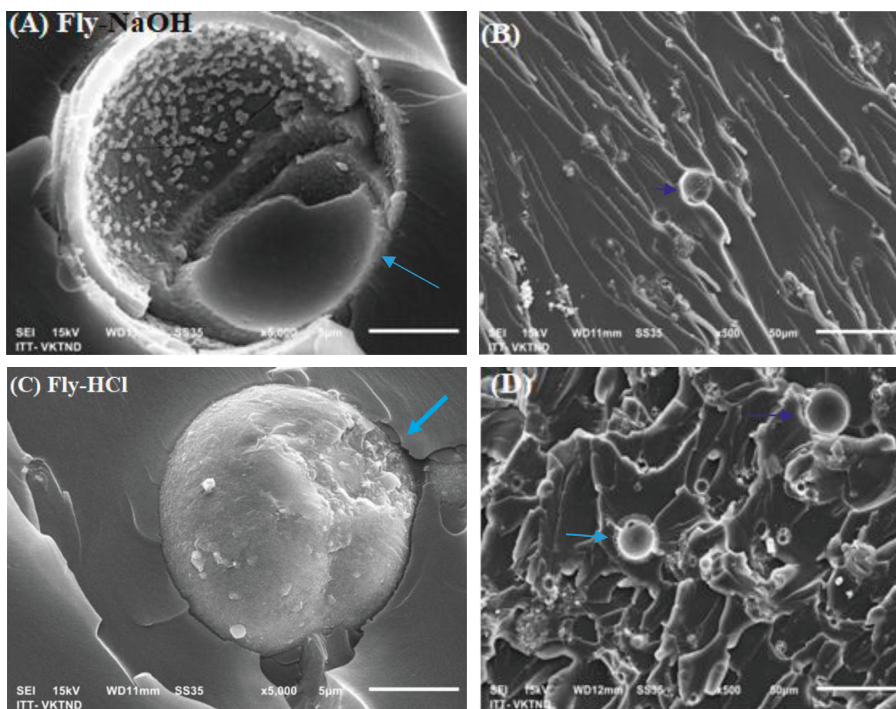


FIGURE 13: SEM image of fly ash modified with HCl (C, D) and fly ash modified with NaOH (A, B).

including 5, 10, and 20 wt.% of HCl is 20.27, 15.37, and 11.51 mm/min, respectively.

Figure 12 shows effects of the amount of fly ash modified with inorganic compounds (NaOH and HCl) on LOI of the materials. As a result, LOI of the materials follows the order: the materials including fly ash modified with HCl > the materials including fly ash modified with NaOH > the materials including fly ash without modifications. Besides, the higher the amount of fly ash is, the higher the LOI is or the better the flame retardancy of the materials is. This proves that after modification, fly ash's compatibility with resin is better, making flame retardancy of the materials better. Concretely, LOI of the materials including 5, 10, and 20 wt.%

of NaOH is 21, 21.5, and 22.4%, respectively. LOI of the materials including 5, 10, and 20 wt.% of HCl is 21.5, 22.4, and 23%, respectively.

Figures 11 and 12 show that modified fly ash makes flame retardancy of the materials better than initial fly ash. This is caused by the good contact and dispersion of modified fly ash. Among them, fly ash modified with HCl is better than with NaOH. However, the difference is insignificant. From the aforementioned results, it can be said that the sample including 20 wt.% of fly ash is the best with stable mechanical properties and good flame retardancy. Therefore, it will be selected for further experiments.

3.3.2. *Effects of the Amount of Fly Ash Modified with Inorganic Compounds on Structure of the Materials.* SEM images in Figure 13 show the dispersion and adhesion of modified fly ash in resin. Figure 13 shows fracture surface of the material including 20 wt.% of fly ash modified with NaOH and HCl.

For fly ash modified with NaOH, it can be seen that fly ash particles have a broken shell to release smaller inside particles which adhere and contact with resin (Figure 13(a)). Therefore, adhesion ability and contact surface area of fly ash modified with NaOH are better than of initial one. Besides, there are high density and good contribution of spherical fly ash particles in resin (Figure 13(b)). For fly ash modified with HCl, it can be seen that there are rough surfaces of fly ash particles (Figure 13(c)) leading to the higher contact surface area of modified fly ash than initial ones. Besides, there are also high density and good contribution of spherical fly ash particles in resin (Figure 13(d)).

4. Conclusions

In this study, fly ash collected from Vietnamese thermal power plants was modified by NaOH and HCl to improve its efficiency and reduce its negative impacts on the environment. The aim is to improve the flame retardant properties and improve some mechanical properties. According to research results, the following conclusions are given:

- (i) High compatibility between fly ash (denatured by NaOH and HCl) and epoxy resin substrate. As a result, the fire resistance of the material has been enhanced.
- (ii) The interface between fly ash and epoxy resin substrate plays a very important role in improving mechanical properties and flame retardancy of materials. SEM images show that fly ash particles are evenly dispersed into epoxy resin substrate.
- (iii) There is an increase in the compressive strength of the material when increasing the fly ash content. Besides, there is decrease in flexural strength, tensile strength, and compact strength but without significant effects on the material.

Data Availability

For any questions relating to the data or the original data requirements of the article, contact the corresponding author at anhnt@hau.edu.vn.

Conflicts of Interest

The authors declare that there are no conflicts of interest regarding the publication of this paper.

Acknowledgments

The authors wish to thank the Faculty of Chemical Technology, Hanoi University of Industry, for funding this work.

References

- [1] H. A. Rahman, S. H. Amirnordin, and N. Khan, "Eco-friendly flame-retardant additives for polyurethane foams: a short review," *Key Engineering Materials*, vol. 791, pp. 19–28, 2018.
- [2] M. Soyama, K. Inoue, and M. Iji, "Flame retardancy of polycarbonate enhanced by adding fly ash," *Polymer for Advanced Technologies*, vol. 18, no. 5, pp. 386–391, 2007.
- [3] M. Singla and V. Chawla, "Mechanical properties of epoxy resin-fly ash composite," *Journal of Minerals and Materials Characterization and Engineering*, vol. 9, no. 3, pp. 199–210, 2010.
- [4] B. T. Phuc, T. V. Dieu, and N. T. Anh, "Improved flame retardant properties of polymers epoxy based on antimonytrioxide/chlorinated paraffin," *Materials Science and Engineering: A-Journal*, vol. 4, p. 146, 2014.
- [5] K. Aschberger, I. Campia, L. Q. Pesudo, A. Radovnikovic, and V. Reina, "Chemical alternatives assessment of different flame retardants—a case study including multi-walled carbon nanotubes as synergist," *Environment International*, vol. 101, pp. 27–45, 2017.
- [6] T. Uygunoglu, I. Gunes, and W. Brostow, "Physical and mechanical properties of polymer composites with high content of wastes including boron," *Materials Research*, vol. 18, no. 6, pp. 1188–1196, 2015.
- [7] N. T. Anh, N. Q. Tung, B. T. Phuc, and N. X. Canh, "The use of multi-walled carbon nanotubes and nanoclay for simultaneously improving the flame retardancy and mechanical properties of epoxy nanocomposites," *International Journal of Engineering and Technology*, vol. 7, no. 4.36, pp. 1149–1160, 2018.

Research Article

Mechanical Properties and Flame Retardancy of Epoxy Resin/Nanoclay/Multiwalled Carbon Nanotube Nanocomposites

Tuan Anh Nguyen ¹, Quang Tung Nguyen,¹ and Trong Phuc Bach²

¹Faculty of Chemical Technology, Hanoi University of Industry (HaUI), No. 298 Cau Dien, North District Tu Liem, Hanoi, Vietnam

²Hanoi University of Science and Technology, No. 1 Dai Co Viet Road, Hanoi, Vietnam

Correspondence should be addressed to Tuan Anh Nguyen; anhnt@hau.edu.vn

Received 19 February 2019; Revised 6 May 2019; Accepted 23 May 2019; Published 16 June 2019

Guest Editor: Thanh-Dong Pham

Copyright © 2019 Tuan Anh Nguyen et al. This is an open access article distributed under the Creative Commons Attribution License, which permits unrestricted use, distribution, and reproduction in any medium, provided the original work is properly cited.

This paper reports the improvement of the mechanical properties and flame retardant properties of epoxy Epikote 240/nanoclay I.30E/multiwalled carbon nanotube nanocomposite prepared by mechanical stirring method combined with ultrasonic vibration, nanoclay I.30E content (1; 2; 3 wt.%) and content of MWNT (0.01; 0.02; 0.03 wt.%). When burned, MWCNT reduces degradation speed of epoxy Epikote 240 resin and increases the char yield, and nanoclay acts as an energy storage medium to hinder the heat transfer in epoxy resin. The limiting oxygen index value and UL94 test indicated improvement of flame retardancy of the nanocomposites. The results exhibit the potentiality of these based epoxy Epikote 240 resin/nanoclay I.30E/MWCNTs nanocomposites for multifaceted advanced applications. These fillers can produce environmental friendly products with high thermal and mechanical properties.

1. Introduction

Currently, multicarbon carbon nanotubes and nanoclay are the stuffing widely used because they improve both the fire-retardant properties and mechanical properties of epoxy plastic; they do not create toxic fumes or smoke corrosion during burning process, unlike common fire-retardant materials based on halogen compounds [1, 2]. Some studies have investigated the fire resistance of epoxy-based nanocomposite materials in MWCNTs and stated that, for MWCNTs, at the content of 2 and 4%, 5% by weight, the fire resistance of the material increases. It is explained that the formation of coal coating on the surface of the sample separated from oxygen in the environment leads to the prevention of the development of flame [3, 4]. Therefore, the improvement of fire resistance of materials is clearly shown. For nanoclay additives, Cevdet et al. conducted research on mechanical properties, flammability, and structural morphology of epoxy/clay nanocomposite; nanoclay has been prepared with the content of 0.5, 1, 2, and 3% by weight [5].

This work focuses on the study of flammability and mechanical properties of epoxy Epikote 240 substrate nanocomposites materials by adding MWCNT (0.02 wt.%) and nanoclay I.30E (2 wt.%), a small amount compared to the other works announced.

2. Materials and Methods

2.1. Materials. The epoxy Epikote 240 (EP240) was provided by Shell Chemicals (USA). EP240 is a low viscosity, based on a blend of bisphenol A resin and bisphenol B resin, contented epoxy group of 24.6%, molecular weight (Mw) of 5100–5400 mmol/kg, density of 1.12 g/ml, and viscosity at 25°C to be 0.7–1.1 Pa·s. Diethylenetriamine (DETA) received from Dow Chemical (USA) has a density of 0.95 g/ml boiling point of 207°C and Mw of 103 mmol/kg and is used directly without any further purification. Multiwalled carbon nanotubes (MWCNTs) of Showa Denko (Japan). Synthesized by catalyst deposition method, MWCNTs have an average diameter of 40–45 nm, an average length of 3 μm,

and a density of 0.08 g/cm^3 . Nanomer® I.30E nanoclay (Nanocor USA) is a surface-changing montmorillonite (MMT) mineral that will disperse into nanoparticles in epoxy resin systems. Dispersion creates a mixture close to the molecule often called nanocomposite. This new composite model shows enhanced strength, heat and barrier properties. I.30E is provided in the form of white powder dispersed into thin particles that are almost transparent in the plastic matrix. Type E raw glass cloth 600 g/m^2 (China).

2.2. Methods

2.2.1. Sample Preparation and Characterization. The nanoclay-MWCNT hybrids were prepared according to Table 1. MMT (1, 2, and 3 wt.%) and MWCNT (0.01, 0.02, and 0.03 wt.%) were dispersed in epoxy Epikote 240 resin, stirred at 3500 rpm for 8 h (HS-100T, WiseStir, Korea). In order to break up the MWCNT bundles and disperse the additives, sonication was performed using an ultrasonic bath (Elmasonic S300 H, 37 kHz, Germany) for 6 h, 65°C . After the mixtures were homogeneously mixed, the curing agent DETA (amount of curing agent was calculated by epoxy content of epoxy resin, stirred for 15 min at 200 rpm/min) was added, and the mixtures were moulded for curing. The mould was coated with a uniform thin film of silicone—a releasing agent for easy removal of cured specimen. The samples were cured at room temperature for about 24 h and further cured at 80°C in the laboratory oven for 3 h. Then, the samples were removed from the mould, and after 7 days, mixture was analyzed and mechanical properties measured.

Produce glass/epoxy nanomaterials. The glass/epoxy nanomaterials are fabricated using a combination of manual hot and hot compressing techniques. The layers of glass-woven fabrics are stacked into 9 layers, and the orientation of the yarn in the fabric is kept constant.

2.2.2. Characterizations

- (i) Limiting Oxygen Index (LOI) according to ASTM D2863-12 and JIS K720 standard (Japan): the sample bars used for the test were $150 \times 6.5 \times 3 \text{ mm}^3$.
- (ii) The Horizontal Burning tests (UL-94HB): Standard bar specimens are $125 \pm 5 \text{ mm}$ in length with $13.0 \pm 0.5 \text{ mm}$ width and provided with the minimum thickness of $3.0 (-0.0 + 0.2) \text{ mm}$ (ASTM D635-12).
- (iii) Combustion Resistance: The apparatus is specifically designed for combustion and incandescence resistance of thermoplastics, thermosetting, rigids, and laminates. The apparatus was designed and built to meet the following standards: ASTM D 757; specimen's dimensions $3.17 \times 12.7 \times 121 \text{ mm}$; maximum temperature of 950°C .
- (iv) The combustion rate was measured by COMBUSTION RESISTANCE COD 6145000 according to the ASTM D757-77 standard. Specimen's dimensions are $3.17 \times 12.7 \times 121 \text{ mm}^3$.

TABLE 1: Taguchi orthogonal array of designed experiments based on the coded levels.

Trial	Sample code	MWCNT content (wt.%)	Nanoclay content (wt.%)
1	EP1	0.01	1
2	EP2	0.02	1
3	EP3	0.03	1
4	EP4	0.01	2
5	EP5	0.02	2
6	EP6	0.03	2
7	EP7	0.01	3
8	EP8	0.02	3
9	EP9	0.03	3

Mechanical tests were conducted on at least five specimens by a 100 kN universal testing machine (INSTRON-5582, USA).

- (i) Flexural properties were determined by using three-point bending test specimens with dimensions of $100 \times 15 \times 4 \text{ mm}$ according to ISO 178.
- (ii) Compressive properties were determined by using three-point bending test specimens with dimensions of $15 \times 10 \times 10 \text{ mm}$ according to ISO 178-1993.
- (iii) Izod Impact Strength was determined according to the ASTM D265 standard in Tinius Olsen (USA). The standard specimen for ASTM is $64 \times 12.7 \times 3.2 \text{ mm}$ ($2(1/2) \times 1/2 \times 1/8 \text{ inch}$), Izod Sample Geometry: 2 mm.
- (iv) Tensile properties were determined by using three-point bending test specimens according to ISO 178. Specimen size according to ISO is $10 \text{ mm} \times 4 \text{ mm} \times 80 \text{ mm}$.
- (v) The morphology of the samples was carried out by scanning electron microscope (SEM, Evacseq error codes, S-4800, Japan). Structural characterizations were studied by X-ray diffraction (XRD, D8-Advance, Brucker, Germany).

3. Results and Discussion

3.1. Distribution of MMT/MWCNT Additives in the Epoxy Complex. Morphology of the nanocomposites is as follows: Figure 1 presents cross sections of the EP1, EP2, and EP3 samples to investigate the dispersion.

The fracture surface is so rough, proving high strength of the material lead to it is difficult to destroy. MWCNTs and nanoclay play so important a role in limiting the development of the fracture (Figures 1(a)–1(c); Figures 2(a)–2(c); and Figures 3(a)–3(c)). Therefore, in order to break the material, the force must be higher. Figures 1–3 show that there were rough surfaces in the regions including nanoparticles in comparison to other regions with higher and flatter cracks (Figure 1(c)). For the distribution of nanoparticles, EP5 sample (Figure 2(b)) had the uniform distribution of nanoparticles in epoxy resin E 240 and a so rough fracture surface. FE-SEM images in Figures 1–3

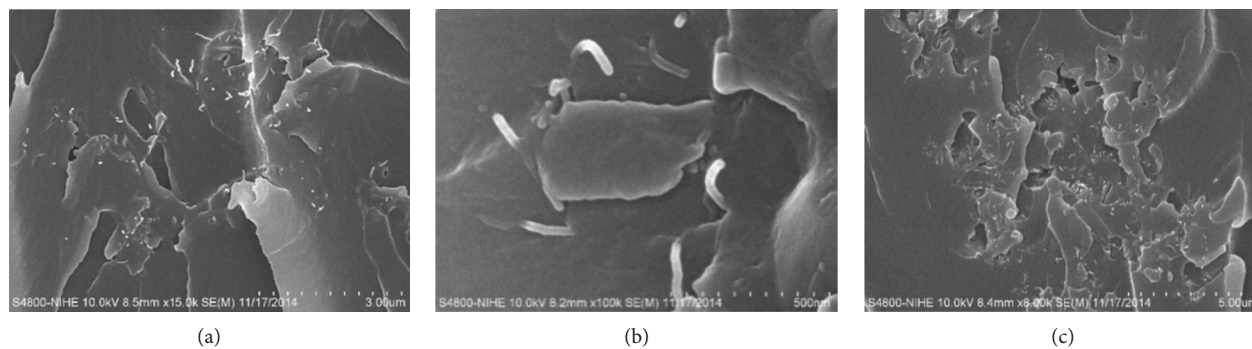


FIGURE 1: Cross-section images of (a) EP1, (b) EP2, and (c) EP3.

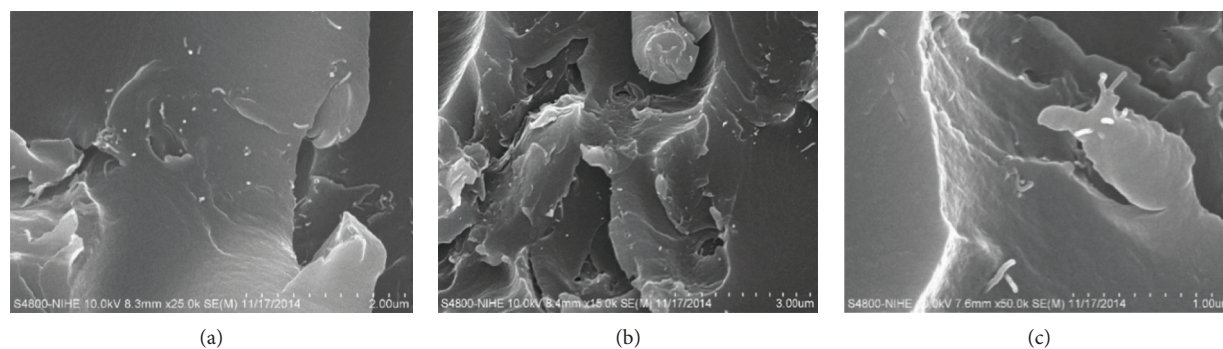


FIGURE 2: Cross-section images of (a) EP4, (b) EP5, and (c) EP6.

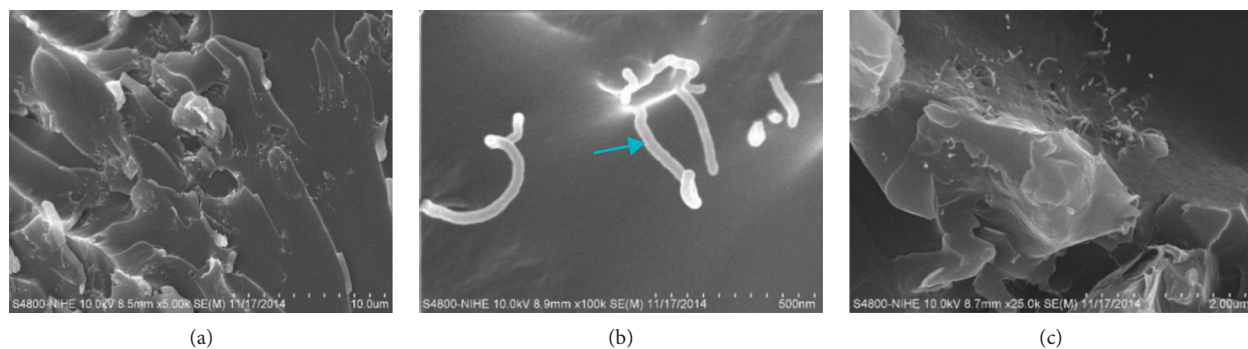


FIGURE 3: Cross-section images of (a) EP1, (b) EP2, and (c) EP3.

indicate that nanoparticles were well stuck on epoxy resin E 240. Because, after breaking the sample, nanoparticles were still maintained on the surfaces and covered by the resin. Moreover, FE-SEM images of the fracture surfaces of tensile samples show that cracks often begun at nanoparticles' agglomeration.

In the magnitude of 100.000 times, the uniform distribution of MWCNTs in epoxy resin E 240 is so clearly observed, and there was no nanoparticles' agglomeration (Figures 4(a) and 4(b)). Figure 4(c) also shows the uniform distribution of nanoclay in epoxy resin. So, MWCNTs and nanoclay were quite well distributed in epoxy resin E 240 by stirring combined with the ultrasonic vibration. The distribution pattern of the nanoclay in the polymer matrix can be identified by the X-ray diffraction patterns of the

nanocomposites (Figure 5). In Figure 4, the captured surfaces not only observe the dispersion of MWCNTs but also nanoclay, though not in any strict order but the thermal conductivity of nanomaterials as well as coal layers. The formation after fire can fully explain to us the flame flammability and heat transfer of composite materials with additives MWCNTs/nanoclay I.30E. The difference in the addition of MWCNTs and nanoclay helped the nanoparticles/epoxy mixtures not easily get melted as for pure epoxy resin samples, even at high temperatures. If a layer of ash can be formed during combustion of the polymer, it can act as an insulating sheet, limiting heat transfer from the source to the polymer. Therefore, the number and texture of the ash layers is important to limit the combustion of the polymer. In Figure 4(b), it can be seen that the MWCNTs are evenly

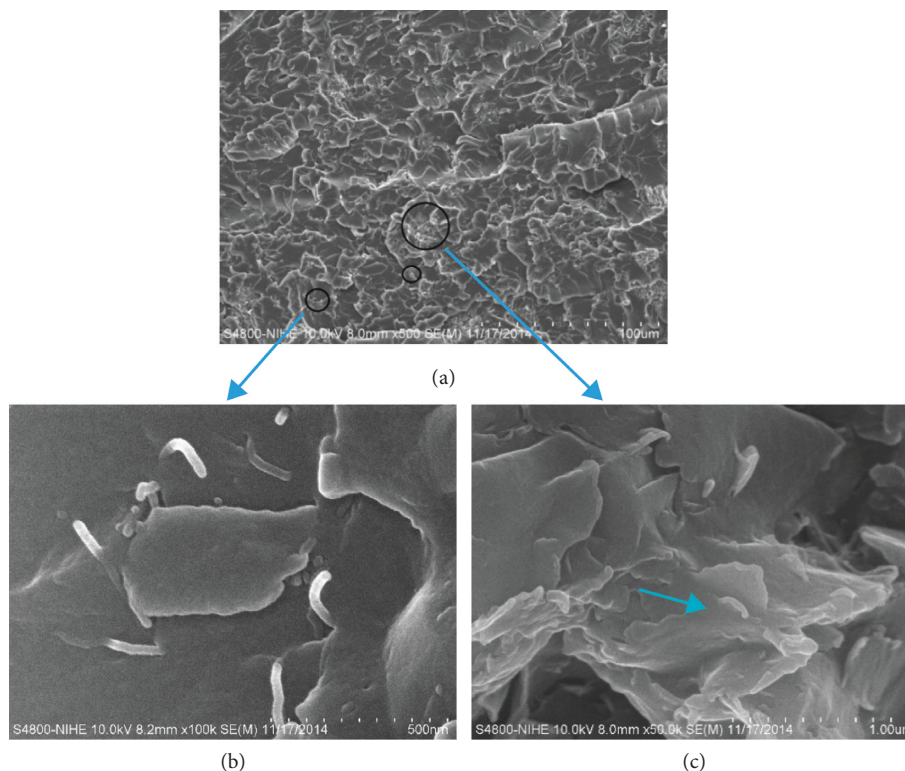


FIGURE 4: FE-SEM image of broken surface material MWCNTs/nanoclay I.30E/epoxy E 240. (a) 500 times, (b) 100,000 times, and (c) 50,000 times.

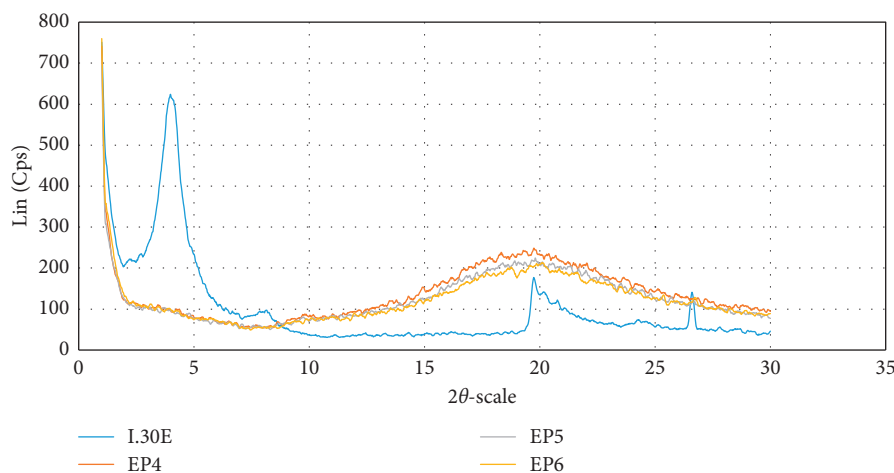


FIGURE 5: XRD patterns for I.30E: nanoclay (MMT), EP4: nanocomposite of epoxy resin with 2 wt.% MMT/0.01 wt.%, EP5: nanocomposite of epoxy resin with 2 wt.% MMT/0.02 wt.%, EP6: nanocomposite of epoxy resin with 2 wt.% MMT/0.03 wt.%; nanoclay (MMT) shows a basal reflection at 4.1° (d-spacing = 6.4 nm) corresponding to [0 0 1] plane. It also shows another peak at 20.1° . The nanocomposites with 1, 2.5, and 5 wt.% clay exhibit no Bragg's scattering, indicating that silicate layers of organoclay may be exfoliated as they do not have any regular repeating distance.

dispersed in epoxy; besides, nanoclay layers (Figure 4(c)) are also dispersed evenly [6–8].

3.2. Mechanical Properties. Presence of multiwalled carbon nanotubes in epoxy base materials reduces partial free volume and fills in the gaps and defects formed from the

epoxy resin curing process [9]. Thus increasing thermal stability, fire retardation as well as mechanical durability. Because if there are gaps in the epoxy material (defects), it is the higher flare of combustion.

Uniform dispersion and perfect adhesion of MWCNTs in epoxy plastic is the main reason to increase the mechanical properties of epoxy resin. In this work, multiwalled

carbon nanotubes were relatively uniformly dispersed, with no cumulative contraction observed in FE-SEM images. Cracks start from interface, and then, the MWCNTs are affected by the outside [10]. Improved mechanical properties are shown in this work. MWCNTs increase the ability to withstand external forces. MWCNTs in the epoxy material matrix have prevented the development of microscopic cracks, altering the movement trajectory of the crack [11]. The spread of cracks is prevented, clearly displayed in Figure 6 (results of our research related to this work).

Mechanical strength of samples was increased with the contents of nanoclay and MWCNTs of 2% and 0.02% by weight, respectively. For other contents, mechanical strength was less increased, due to limiting of the contribution (Table 2). If there are layers of ash formed from burning polymers, they can play as heat-isolation layers, restricting the heat transfer from heat resources to polymers. Thus, the number and structure of ash layers play an important role to restrict the combustion of polymers.

The degree of dispersion of MWCNTs and nanoclay in epoxy E 240 is a decisive factor for fire resistance and mechanical properties of nanocomposites. At other ratios, mechanical properties tend to decrease because of the limited dispersion capacity, so the mechanical strength is slightly reduced. Particularly, for the level of distribution of nanoparticles, sample MWCNTs/nanoclay = 0.02/2 (EP5) has nanoparticles distributed evenly in epoxy E 240 resin. This can be explained by the blending level of MWCNTs/nanoclay = 0.02/2 (EP5), the material achieves high compatibility, and the structure is more compact than the rest. Therefore, the mechanical properties and the fire retardancy increase. As for other mixing ratios, it may be due to the residual mass of MWCNTs or nanoclay remaining after fabrication. This leads to the creation of a lower compatibility structure so that when there is a high-temperature impact, the material is easily destroyed at the points, the structure area is unstable, the combustion rate is high, and the mechanical strength is reduced.

3.3. Flame Retardancy. The LOI, representing the lowest oxygen volume content for sustaining the flame in an environment, was used for quantifying the flame retardancy of epoxy resin. The oxygen volume content in ambient atmosphere is about 21%. Therefore, a material exhibiting its LOI above 21 might show flame-retardant property. Generally, materials with LOI values higher than 26 might show self-extinguishing behavior and were considered to be highly flame-retardant. The results of LOI and UL-94 for epoxy resin and its composites are listed in Table 3. Table 3 shows that the best results were achieved with 0.02% and 2% by weight of MWCNTs and nanoclay, respectively. The result was LOI of 25%, the burning rate of 20.5 mm/min, and UL 94HB of 18.6 mm/min. The quality of flame-protecting layers of materials and characteristics of burned material's surfaces was evaluated by FE-SEM method (Figures 1(a) and 2–4).

With epoxy resin, oxidizing agents are easy to attack, and therefore, this plastic sample will easily ignite. MWCNTs have formed a thin film covering the outside of the material.

Although thin, it is interwovenly complicated by MWCNTs with the ability to conduct heat along the pipe as well as the heat resistance in the middle of the tubes very well. This leads to the fact that the oxidizing agents are difficult to penetrate and help the material's fire resistance, especially when the protective coal layer is formed [4].

When MWCNTs are well dispersed in the substrate, the coal layer produced will be more evenly spread over the surface. Also, this barrier will minimize the ability to catch fire as well as exposure to air oxygen. At the same time, the tendency to reignite is reduced, making the fire impossible to spread and fade [4]. The compact structure also increases the fire resistance of the material.

A barrier-like barrier is created by nanoclay elements that are heat-resistant and heat-retaining, which slows down the diffusion of oxygen and prevents flammable substances from burning in the material. The process of heat transfer to the material has therefore reduced the time to sustain the combustion. The formation of a silicate ash layer evenly spread on the surface of nanocomposite has prevented the penetration of the flame to help the combustion process be extinguished.

In the case of MWCNTs/nanoclay/epoxy resin materials, there was no crack in flat surfaces (Figure 7(b)), in which when the epoxy material is burned, the surface of the burning gas has many cracks (Figure 7(a): neat epoxy). The ash layers formed from burning MWCNTs and nanoclay in surfaces play an important role like heat shields to prevent the heat transfer. If there are layers of ash formed from burning polymers, they can play as heat-isolation layers, restricting the heat transfer from heat resources to polymers. Thus, the number and structure of ash layers play an important role to restrict the combustion of polymers. It can delay the heat transfer from heat resources, leading to more slow increase temperature. A phenomenon observed in experiments with the presence of MWCNTs was the dripping of samples when burned, proving the important role of MWCNTs in improving the fire-retardant properties of materials. It can delay the heat transfer from heat resources, leading to more slowly increase temperature. A phenomenon observed in experiments with the presence of MWCNTs was the dripping of samples when burned, proving the important role of MWCNTs in improving the fire-retardant properties of materials.

If the nanocontent increases, the viscosity increases and affects dispersion. If the nanocontent exceeds the threshold leading to a decrease in the compatibility with epoxy base resin and the accumulation of nanoparticles (Figures 8 and 9), the amount of residual nanomaterial creates holes (Figure 10) inside. Whether these factors are responsible for the reduction of mechanical strength and fire resistance. In the case of small nanoadditives, the mechanical strength and fire resistance are not met.

On the other hand, if the dispersion technique is not suitable, there will be nanoparticles aggregation in some places right above the interface of nano-epoxy E 240. There are residual nanoparticles, forming a separate phase of breaking down, where cracks are formed and grown,

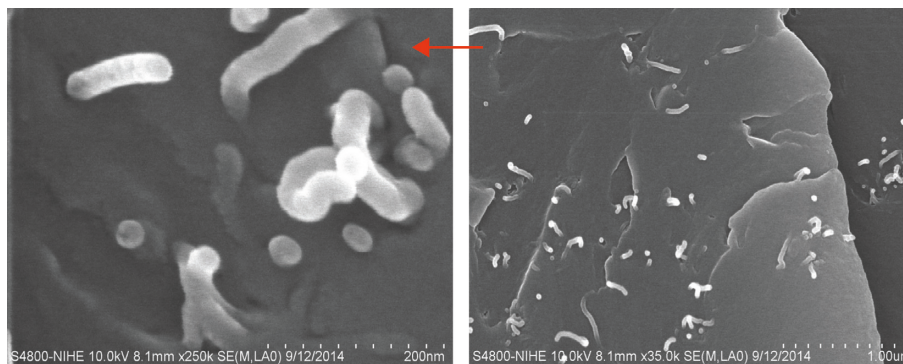


FIGURE 6: FE-SEM micrographs of MWCNTs 0.02 wt.%/nanoclay 2 wt.%/epoxy Epikotre 240 nanocomposites.

TABLE 2: Optimum mechanical properties of epoxy/nanoclay/MWNT nanocomposites from fine tuning experiments.

Trial	Sample code	MWCNT content (wt.%)	Nanoclay content (wt.%)	Tensile strength (MPa)	Flexural strength (MPa)	Compressive strength (MPa)	Impact strength (kJ/m^2)
1	Neat epoxy resin	0.00	0	55.90 ± 0.6	86.75 ± 0.5	156.08 ± 0.3	7.11 ± 0.45
2	EP1	0.01	1	87.56 ± 0.5	93.70 ± 0.5	205.99 ± 0.4	10.60 ± 0.50
3	EP2	0.02	1	88.34 ± 0.6	93.60 ± 0.4	195.23 ± 0.3	12.70 ± 0.45
4	EP3	0.03	1	90.42 ± 0.4	94.26 ± 0.5	216.08 ± 0.2	19.70 ± 0.60
5	EP4	0.01	2	93.43 ± 0.6	98.56 ± 0.3	203.76 ± 0.5	21.54 ± 0.70
6	EP5	0.02	2	95.50 ± 0.5	115.45 ± 0.5	219.10 ± 0.3	22.30 ± 0.45
7	EP6	0.03	2	92.12 ± 0.8	108.60 ± 0.3	203.51 ± 0.6	19.70 ± 0.60
8	EP7	0.01	3	93.45 ± 0.6	108.90 ± 0.6	212.08 ± 0.4	20.27 ± 0.50
9	EP8	0.02	3	90.67 ± 0.4	103.60 ± 0.4	202.13 ± 0.2	18.13 ± 0.40
10	EP9	0.03	3	90.67 ± 0.5	102.78 ± 0.2	200.10 ± 0.3	16.04 ± 0.70

TABLE 3: Results of flammability tests (reaction to small flame): oxygen index (OI) and UL 94 for nanocomposites.

Trial	Material	MWCNT content (wt.%)	Nanoclay content (wt.%)	LOI (vol.% $\text{O}_2 \pm 2\sigma$)	Combustion rate (mm/min)	UL94 HB (mm/min)
1	Neat epoxy resin	0.00	0	20.6 ± 0.3	28.41	Not rated (NR)
2	EP1	0.01	1	22.8 ± 0.3	24.25	25.78 (HB)
3	EP2	0.02	1	24.2 ± 0.5	23.01	22.35 (HB)
4	EP3	0.03	1	24.6 ± 0.4	22.45	22.03 (HB)
5	EP4	0.01	2	24.2 ± 0.3	22.34	20.01 (HB)
6	EP5	0.02	2	25.0 ± 0.3	20.05	18.60 (HB)
7	EP6	0.03	2	24.6 ± 0.5	19.03	18.85 (HB)
8	EP7	0.01	3	24.2 ± 0.4	20.45	19.65 (HB)
9	EP8	0.02	3	24.6 ± 0.6	21.43	18.68 (HB)
10	EP9	0.03	3	24.6 ± 0.3	20.80	18.76 (HB)

reducing mechanical properties and fire resistance of the materials (Figures 10 and 11).

3.4. E-Glass/Epoxy Nanocomposites. Figures 12(a)–12(d) show the magnified SEM micrographs of fractured fibers. Evident from these micrographs, the fiber in e-glass/epoxy composites sample contains considerable amount of epoxy resin residue and rougher fracture surface in comparison to control samples. Similarly, in 2 wt.% nanoclay/e-glass/epoxy composites samples, distributed resin residue and rougher fracture surface were observed but not as profound as in

0.02 wt.% MWCNTs/e-glass/epoxy composites counterpart. In 2 wt.% nanoclay/0.02 wt.% MWCNTs/e-glass/epoxy composite samples, there are mixed regions of dispersed and agglomerated MWCNTs. The interfacial bonding in a well-dispersed region may have improved the interfacial bonding, whereas the agglomerated region contributed to the initiation of fracture. As a result, a distributed residue of resin, rougher fracture surface (Figure 12(d)), and several cracks (Figure 12(d)) were observed in 2 wt.% nanoclay/0.02MWCNTs/e-glass/epoxy composites sample.

The purpose of the research team is to manufacture epoxy E 240 substrates based on MWCNTs and nanoclay

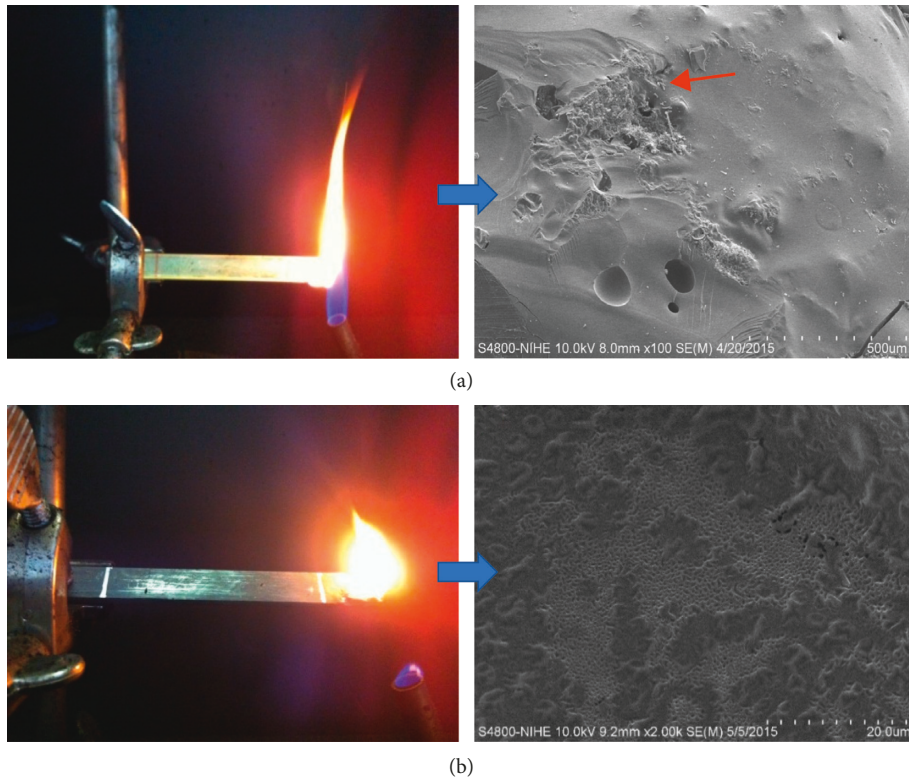


FIGURE 7: SEM images of the residual of (a) neat epoxy and (b) composites MWCNTs 0.02 wt.%/nanoclay 2 wt.%/epoxy resin (UL-94HB).

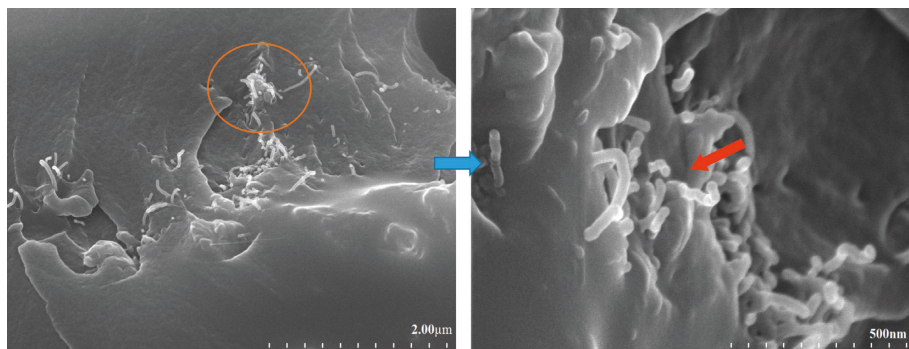


FIGURE 8: FE-SEM image of nanocomposite material MWCNTs/nanoclay mixing ratio: 0.03/2 (percentage mass).

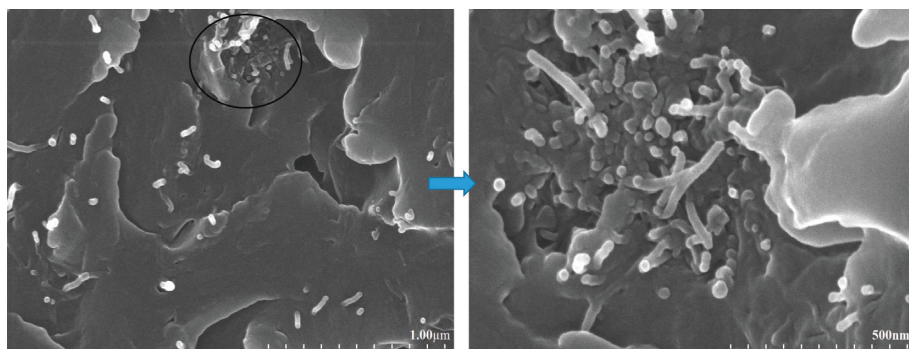


FIGURE 9: FE-SEM image of nanocomposite material MWCNTs/nanoclay mixing ratio: 0.03/3 (percentage mass).

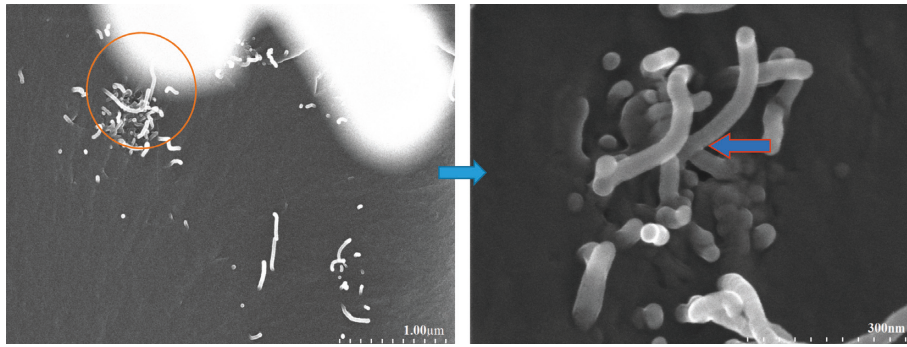


FIGURE 10: FE-SEM of MWCNTs/epoxy Epikote 240 nanocomposites.

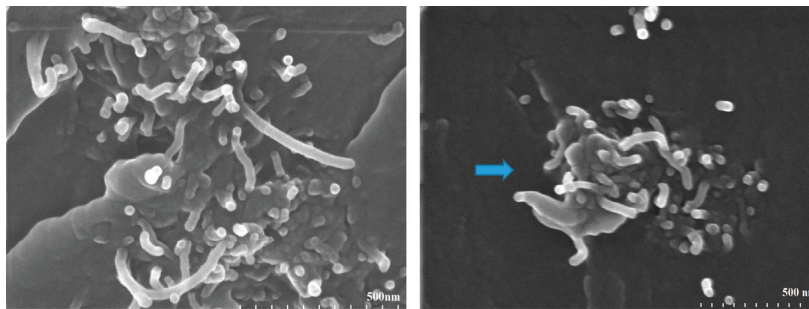


FIGURE 11: FE-SEM of MWCNTs/epoxy Epikote 240 nanocomposites.

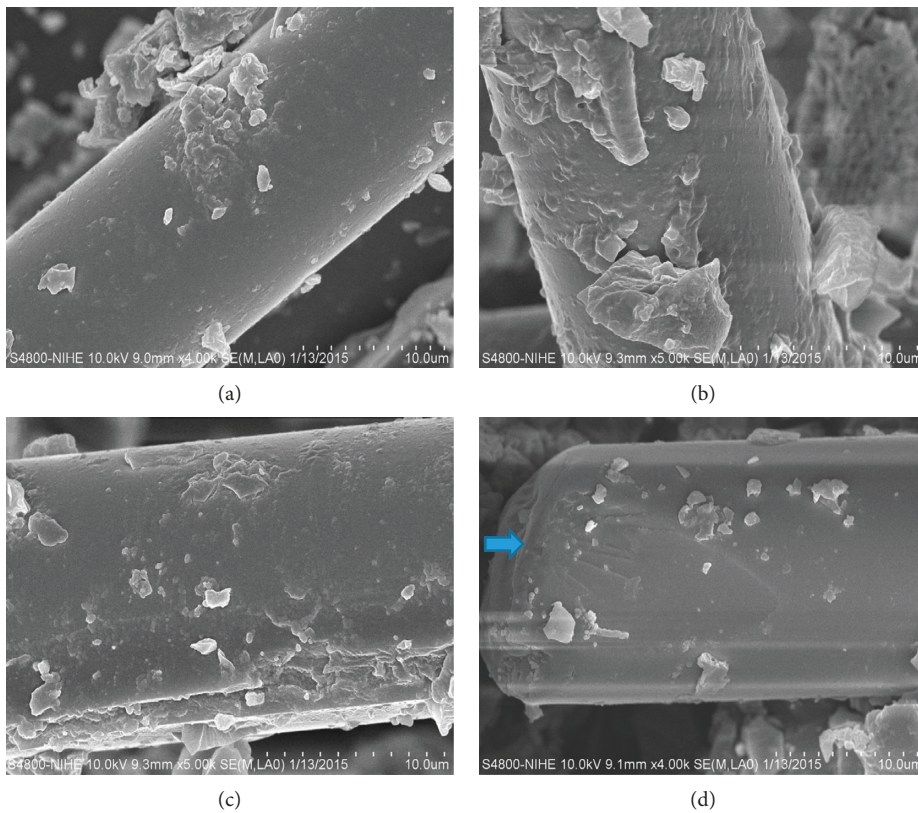


FIGURE 12: FE-SEM micrographs of fractured fiber of (a-e) glass/epoxy composites; (b) 2 wt.% nanoclay/e-glass/epoxy composites; (c) 0.02 wt.% MWCNTs/e-glass/epoxy composites; and (d) 2 wt.% nanoclay/0.02MWCNTs/e-glass/epoxy composites.

I.30E reinforced with glass cloth. Evaluate adhesion between epoxy base material (dispersed MWCNTs and nanoclay) and glass fiber-reinforced substance. The adhesion between substrate and reinforcement (MWCNTs, nanoclay, and glass fiber) plays an important role for the mechanical strength and fire resistance of nanocomposite-reinforced fiberglass materials. It may be directly related to the roughness of the fracture surface where crack development occurs [10].

4. Conclusions

Results show that epoxy resin with an improved flame-retardant property was prepared by addition of nanoclay I.30E and MWCNT. In conclusion, mechanical properties and flame retardancy of epoxy resin were significantly improved by nanoclay I.30E/MWCNT additives. MWCNT and nanoclay I.30E uniformly distributed in epoxy resin form ash layers covering in material surface and preventing the contact between oxygen and the materials, limiting the development of flame. It can be said that the distribution ability of retardants in binders is more uniform, mechanical and retardant properties of materials are more improved. Thus, better dispersion and enhanced interfacial bonding between epoxy, MWCNT, nanoclay I.30E, and e-glass fibers leads to the improvement in thermomechanical and flexural properties of epoxy and consequently of glass/epoxy composites.

Data Availability

For any questions relating to the data or the original data requirements of the article, contact the corresponding author at anhnt.haui@gmail.com (anhnt@haui.edu.vn).

Conflicts of Interest

The authors declare that they have no conflicts of interest.

Acknowledgments

The authors wish to thank the Faculty of Chemical Technology, Hanoi University of Industry, for funding this work.

References

- [1] H. Azman, M. K. Siti, M. Zurina, S. Zalilah, M. Munirah, and A. Faiz, "Exploring the effects of nanofillers of epoxy nanocomposite coating for sustainable corrosion protection," *Chemical Engineering Transaction*, vol. 72, pp. 121–126, 2019.
- [2] L. Jie, Y. Haiou, W. Xin et al., "Charring polymer wrapped carbon nanotubes for simultaneously improving the flame retardancy and mechanical properties of epoxy resin," *Polymer*, vol. 52, no. 21, pp. 4891–4898, 2011.
- [3] D. Bettina, W. Karen-Alessa, H. Daniel, M. Rolf, and S. Bernhard, "Flame retardancy through carbon nanomaterials: carbon black, multiwall nanotubes, expanded graphite, multi-layer graphene and graphene in polypropylene," *Polymer Degradation and Stability*, vol. 98, pp. 1495–1505, 2013.
- [4] F. Laoutid, L. Bonnaud, M. Alexandre, J.-M. Lopez-Cuesta, and P. Dubois, "New prospects in flame retardant polymer materials: from fundamentals to nanocomposites," *Materials Science and Engineering: R: Reports*, vol. 63, no. 3, pp. 100–125, 2009.
- [5] K. Cevdet, G. Ipek Nakas, and A. I. Nihat, "Mechanical properties, flammability and char morphology of epoxy resin/montmorillonite nanocomposites," *Applied Clay Science*, vol. 46, pp. 319–324, 2009.
- [6] M.D. Tomić, B. Dunjić, V. Likić, J. Bajat, J. Rogan, and J. Djonlagić, "The use of nanoclay in preparation of epoxy anticorrosive coatings," *Progress in Organic Coatings*, vol. 77, no. 2, pp. 518–527, 2014.
- [7] M. M. Shokrieh, A. R. Kefayati, and M. Chitsazzadeh, "Fabrication and mechanical properties of clay/epoxy nanocomposite and its polymer concrete," *Materials and Design*, vol. 40, pp. 443–452, 2012.
- [8] S. K. Lee, B. C. Bai, J. S. Im, S. J. In, and Y.-S. Lee, "Flame retardant epoxy complex produced by addition of montmorillonite and carbon nanotube," *Journal of Industrial and Engineering Chemistry*, vol. 16, no. 6, pp. 891–895, 2010.
- [9] A. Montazeri, K. Pourshamsian, and M. Riazian, "Viscoelastic properties and determination of free volume fraction of multi-walled carbon nanotube/epoxy composite using dynamic mechanical thermal analysis," *Materials and Design*, vol. 36, pp. 408–414, 2012.
- [10] V. K. Srivastava, "Modeling and mechanical performance of carbon nanotube/epoxy resin composites," *Materials and Design*, vol. 39, pp. 432–436, 2012.
- [11] S. Zainuddin, A. Fahim, T. Arifin et al., "Optimization of mechanical and thermo-mechanical properties of epoxy and E-glass/epoxy composites using NH₂-MWCNTs, acetone solvent and combined dispersion methods," *Composite Structures*, vol. 110, pp. 39–50, 2014.

Research Article

Preparation and Characterization of a Hydrophilic Polysulfone Membrane Using Graphene Oxide

Hoan Thi Vuong Nguyen ¹, Thu Hong Anh Ngo ², Khai Dinh Do,² Minh Ngoc Nguyen,¹ Nu Thi To Dang,¹ Tham Thi Hong Nguyen,³ Vo Vien ¹ and Tuan Anh Vu ⁴

¹Faculty of Chemistry, Quy Nhon University, Quy Nhon, Vietnam

²Faculty of Chemistry, VNU University of Science, Hanoi, Vietnam

³NTT Hi-Tech Institute, Nguyen Tat Thanh University, Ho Chi Minh City, Vietnam

⁴Institute of Chemistry, Vietnam Academy of Science and Technology, Ha Noi, Vietnam

Correspondence should be addressed to Hoan Thi Vuong Nguyen; nguyenthivuonghoan@qnu.edu.vn and Thu Hong Anh Ngo; anhthu@hus.edu.vn

Received 1 March 2019; Revised 13 May 2019; Accepted 21 May 2019; Published 13 June 2019

Guest Editor: Van Duong Dao

Copyright © 2019 Hoan Thi Vuong Nguyen et al. This is an open access article distributed under the Creative Commons Attribution License, which permits unrestricted use, distribution, and reproduction in any medium, provided the original work is properly cited.

In general, the polysulfone (PSf) membranes are popular choices for water treatment because they have high thermal stability and good chemical resistance. On the other hand, the filtration capacity of the polysulfone membrane is limited because of its low water flux and poor antifouling ability, which are caused by the low surface hydrophilicity of the membranes. In this research, blending of graphene oxide (GO) or graphene oxide-titanium dioxide (GO-TiO₂) mixture into the polysulfone matrix had been carried out through the phase inversion method to enhance the hydrophilic and antifouling properties. Methods such as energy-dispersive X-ray spectroscopy, scanning electron microscopy, Fourier transform infrared spectroscopy, and water contact angle measurement were used to examine the surface properties of the prepared membranes. Experimental results have led to a conclusion that graphene oxide can be stabilized into prepared membranes, and then, by reducing the water contact angle values, the surface of these membranes becomes hydrophilic, which increases the permeability and the water flux of methylene blue from the aqueous feed solution, improving the membrane's antifouling resistance.

1. Introduction

Today, membranes and membrane processes have been applied in cleaning technology and the environmental field [1, 2]. Efficiency and utility from membrane applications have led to the need for new membrane materials with properties suitable for their applications. Therefore, the type of material selected and the method of membrane preparation are the determining factors for the properties of the membrane.

Polysulfone (PSf) is the preferred choice in membrane fabrication, and its prominence is derived from chemical resistance, wide operating temperature and pH, and high mechanical strength [2–5]. However, at present, the operating costs of PSf membrane processes are still quite high

because of fouling, limitations on filtering capacity, and longevity, which are due to their high hydrophobic properties [2–4, 6, 7]. Recently, the increase in hydrophilicity and the minimization of fouling of PSf membranes have been tested through a variety of solutions including modifying the surface [8, 9], coating onto the membrane surface [10–14], and blending the hydrophilic materials into the membrane casting solution before fabricating the membrane [2, 5, 15–20]. Among the aforementioned methods, the method of blending PSf with some hydrophilic polymers or inorganic nanoparticles to increase the surface hydrophilic and antifouling properties has proven remarkably effective [2, 5, 20–23].

Zodrow et al. [21] blended nanosilver particles into the matrix of the PSf membrane to increase the membrane

hydrophilicity and reduce the biofouling and virus penetration. By using the phase inversion method, Kang et al. [2] prepared more hydrophilic PSf/SGO (sulfonated graphene oxide) membranes. After conducting the tests, the researchers found that mixing 1.5 w/w% SGO into the PSf matrix made this membrane reach a water flux higher than 125% compared to that of the PSf membrane. Prabhu et al. [5] blended the chitosan derivative 1H-pyrazole-4-carbaldehyde into the PSf matrix by the wet coagulation method. These observations indicate that hydrophilic groups (such as hydroxyl, amine, and imine) improved the hydrophilicity of the blended membrane as they cause a decrease in the contact angle (from $70 \pm 1^\circ$ of the PSf membrane down to $62 \pm 1^\circ$ of blended membranes) and the improvement in water flux (from 24 of the PSf membrane to $351 \text{ L}\cdot\text{m}^{-2}\cdot\text{h}^{-1}$ of the blended membrane at 0.8 MPa). Ravishankar et al. [20] blended graphene oxide (GO) nanoparticles into the PSf matrix to prepare PSf/GO membranes. The results showed that the PSf/GO membrane has a better hydrophobicity than the PSf membrane (the contact angle of water is 34.2° and the permeability is $52.1 \text{ L}\cdot\text{m}^{-2}\cdot\text{h}^{-1}\cdot\text{bar}^{-1}$).

Recently, graphene oxide (GO) has been one of the most common hydrophilic inorganic particles that are used for preparing blended membranes [3, 20]. It has been proven that the appearance of oxygen-containing groups including hydroxyl, epoxy, and carboxyl when fabricating a graphene oxide-blended membrane has shown that the membrane possess high effective flux and better antifouling capacity [20]. The strong hydrogen network with the water molecules is made up of oxygen functionalities, so it creates a strong hydrophilicity [22, 24]. The combination (blend) of GO into the membrane is prominent in increasing the permeability [25, 26] and antifouling [7] and antibacterial [23, 25–30] properties for membrane applications as have been recorded in many previous studies. All results show that GO-blended polymer membranes are more hydrophilic and antifouling than unblended membranes, and it means that GO membranes are hydrophilic [26–28].

To enhance the membrane-blending properties, titanium dioxide (TiO_2) or other hydrophilic nanoparticle materials are integrated into the polymer membrane by modifying these nanoparticles with GO by the surface hydrothermal method [29, 31]. Safarpour et al. [32] prepared the reverse osmosis membrane by incorporating the reduced graphene oxide (rGO)/ TiO_2 material onto its surface. The researchers found that the separation efficiency and the antifouling capacity of the membranes increased compared to unblended membranes (water flux improved from 34.3 to $51.3 \text{ L}\cdot\text{m}^{-2}\cdot\text{h}^{-1}$, and antifouling resistance increased from 49% to 75% after 180 minutes filtering bovine serum albumin solution). In another article, Faria et al. [33] showed that the growth of bacteria and biofilm on membranes has been prevented by adding silver and graphene oxide to TFC-PA membranes. The reason for the decline in the flux is due to biofilm development, which has decreased by 30% after incorporating GOAg nanocomposites onto the TFC membrane.

Most polysulfone membranes are prepared by the phase inversion method as other polymer membranes. To begin the membrane forming process, the researchers dissolve the

polymer in the solvent or in an organic solvent mixture. Then, the coating solution is spread in the form of a thin layer onto the plate or on a rotating disc, and the next membrane is coagulated in a solvent-free medium to form a porous membrane [33, 34]. A spin coating method is a technique for making a highly homogeneous membrane [34].

In general, the coating of hydrophilic layers such as GO and TiO_2 onto the membrane matrix is an effective method for improving the membrane separation performance.

However, very little information on the preparation of the polysulfone membranes with GO and TiO_2 has been known.

In this study, graphene oxide nanoparticles and graphene oxide/titanium dioxide were blended into the polysulfone matrix to prepare polysulfone/GO (PSf/GO) and polysulfone/GO- TiO_2 (PSf/GO- TiO_2) membranes using the phase inversion method. Effects of GO and TiO_2 on the hydrophilic and antifouling properties of the blended membranes were also compared by determining permeability, retention, flux, and fouling resistance of methylene blue in aqueous solution.

2. Experimental Methods

2.1. Materials. Graphene oxide (GO) prepared from graphite powder (Merck) by Hummers' method [35] and TiO_2 prepared from tetrachloride TiCl_4 (Merck) titanium by the sol-gel method were used as additives in the coating solution. Polysulfone (molecular weight: $22,000 \text{ g}\cdot\text{mol}^{-1}$) was used as the original polymer supplied by Sigma-Aldrich in the casting solution. *N,N*-Dimethyl formamide (DMF) purchased from China Science Co., Ltd. was used as a solvent. Methylene blue (MB) (China) has been used to prepare feed solutions for membrane filtration experiments.

2.2. Preparation of PSf, PSf/GO, and PSf/GO- TiO_2 Membranes. The PSf, PSf/GO, and PSf/GO- TiO_2 membranes were prepared through phase inversion with DMF used as a solvent, GO and GO-modified TiO_2 as additives to prepare PSf/GO and PSf/GO- TiO_2 membranes, and deionized water as the nonsolvent in the coagulation bath.

Polysulfone and a different amount of GO (0.0, 1.0, and 2.0% by weight of PSf) were added to DMF and dissolved for 24 hours at 60°C by sonication to obtain a homogeneous mixture, and then to allow the mixture to release all the bubbles, it was left overnight.

To prepare PSf/GO- TiO_2 membranes, a different amount of TiO_2 (10, 15, and 20% by weight of GO) and GO were added to DMF and dissolved for 24 hours at 60°C by sonication to obtain a homogeneous mixture and then left overnight.

Using the spin coating method, the solutions are then dripped on clean glass supports (coating speed in the range of 1400 to 2400 rpm). Then, the solvent is evaporated in 30 seconds, and this solution is soaked in a freezer. After that, the membrane that was formed was peeled off and deionized water was used to wash it in order to remove any

remaining solvents. Before testing, the blended membranes must be kept carefully in deionized water.

2.3. Characteristics of Materials and Membranes. A D8 Advanced Bruker anode X-ray diffractometer with CuK α ($\lambda = 0.154$ nm) radiation using the scanning step of $0.02^\circ \cdot \text{s}^{-1}$ in the range of 2° to 80° was used to analyze X-ray diffraction (XRD). An electron microscope (SEM-EDX, Nova Nano SEM 450) and a transmission electron microscope (TEM, JEOL 2100F) were used to determine the morphology, size, and elemental mapping of the samples to be summed; the case is characterized by energy-dispersive X-ray spectroscopy. The results of the Fourier transform infrared (FTIR-ATR) spectroscopy method used for samples were recorded on a PerkinElmer spectrophotometer. Water contact angle measurement was used to calculate the moisture content of the unblended and blended membranes via CAM 101/KSV Instruments (Finland), which was used to capture ionized water drops located on the dry surface of the membrane at 25°C .

2.4. Assessment of Membrane Filtration Properties. Membrane separation tests are performed in a terminal filtration system, including 200 cm^3 stainless steel cylindrical cells and a paddle impeller; working pressure in all experiments is 0.87 bar. The filtrate was collected every 5 minutes, and the average throughput was calculated after 90 minutes of filtration. In all experiments, we carefully washed membrane cells with pure water (both before and after use).

Membrane filtration properties are determined through permeability J_w ($\text{L} \cdot \text{m}^{-2} \cdot \text{h}^{-1} \cdot \text{bar}^{-1}$) = $[V_w/(AtP)]$, where V_w is the volume of water through the membrane area of A during the pressure determination of P . Ratio of permeability normalization (J_w/J_{w0}), where J_w and J_{w0} are the permeabilities of the blended and unblended membranes, was used to examine the improved permeability of the membrane. The flux (J , $\text{L} \cdot \text{m}^{-2} \cdot \text{h}^{-1}$) is evaluated by $J = [V/(At)]$, where V is the volume of the filtrate. The normalized flux ratio (J/J_0) has been used to determine the enhancement of flux of blended membranes, in which J and J_0 are the flux of the blended and unblended membranes, respectively. The retention (R) of methylene blue is calculated by $R = [(C_0 - C)/C_0] * 100$ (%), where C_0 and C are methylene blue concentrations in feed and filtrate, respectively.

2.5. Assessment of Membrane Antifouling Property. The antifouling property was determined via the maintained flux ratios (FM, %) during filtration. The maintained flux ratio was evaluated by $\text{FM} = (J_t/J_{t0}) * 100$ (%), where J_t and J_{t0} are the fluxes of membranes at t time and initial time ($\text{L} \cdot \text{m}^{-2} \cdot \text{h}^{-1}$).

3. Results and Discussion

3.1. Characteristics of GO and GO-TiO₂ Nanoparticles. The successful synthesis of GO, TiO₂, and GO-TiO₂ materials has been confirmed through X-ray diffraction (XRD) spectroscopy, scanning electron microscopy (SEM), energy-

dispersive X-ray spectroscopy-mapping (EDX-mapping), transmission electron microscopic (TEM) image, and Fourier transform infrared (FTIR) spectral analysis.

3.1.1. X-Ray Diffraction (XRD) Spectrum. Figure 1 shows the XRD spectrum of GO, TiO₂, and GO-TiO₂. The diffraction peak at a lower angle of about 11.4° GO implies the introduction of oxygen-containing functional groups of GO [36, 37]. However, two broad peaks at about 26° and 44° assigned to graphite can clearly see the complete non-oxidation of graphite. Also, Figures 1(a) and 1(b) shows the appearance of a titanium element in the TiO₂ and GO-TiO₂ nanoparticles, respectively. We can see that the TiO₂ materials appeared in the anatase phase (based on the standard library JCPDS 21-1272), with the occurrence of sharp peaks (101), (004), (105), (211), and (204) at 2θ 25.5° , 37.0° , 54.0° , 56.5° , and 62.5° . Besides, rutile phase also appeared (according to the standard library JCPDS 65-0190) along (110) and (111) at 2θ 27.5° and 41.2° . In Figure 1(b), the characteristic peaks of GO and TiO₂ appeared. Therefore, GO and GO-TiO₂ were synthesized successfully.

3.1.2. SEM, EDX Mapping, and TEM Images. Figures 2 and 3 display the SEM, EDX-mapping, and TEM images of GO and GO-TiO₂ nanoparticles. The results showed that GO had a wrinkled surface with some small pieces. This indicated the successful exfoliation of the GO sheet from graphite during graphite oxidation. As can be seen more clearly via the TEM image, there were many layers of GO onto the graphite surface. Thus, the GO material was synthesized successfully from graphite.

SEM images (Figure 3(a1) and 3(a2)) of synthesized GO-TiO₂ materials showed that the aggregated TiO₂ nanoparticles appeared with GO particles. TEM image of GO-TiO₂ materials showed that the average particle size of TiO₂ particles dispersed onto the GO sheet was 10 nm (Figure 3). Thus, the GO-TiO₂ material was synthesized successfully. EDX-mapping images were used to check the components in the synthesized material. Figures 3(b)–3(d) show that there is a homogeneous distribution of the C, O, and Ti elements in the materials.

3.1.3. FTIR Spectra. The FTIR-ATR spectra of GO, TiO₂, and GO-TiO₂ are shown in Figure 4. The peaks of GO (Figure 4(a)) were observed via the appearance of C-O stretching, C=O stretching, and O-H stretching, which include the bands at 1050 cm^{-1} , 1720 cm^{-1} , and 3350 cm^{-1} after oxidizing graphite into GO. These groups are hydrophilic. Thus, GO is also hydrophilic. Moreover, the spectrum of TiO₂ (Figure 4(b)) and GO-TiO₂ (Figure 4(c)) showed peaks at approximately $580\text{--}1000\text{ cm}^{-1}$ attributed to Ti-O-Ti stretching [38], showing the successful synthesis of TiO₂ particles into the GO-TiO₂ material.

3.2. Membrane Characteristics. After preparation of unblended and blended membranes with GO and GO-TiO₂, the hydrophilic ability of membranes was evaluated through

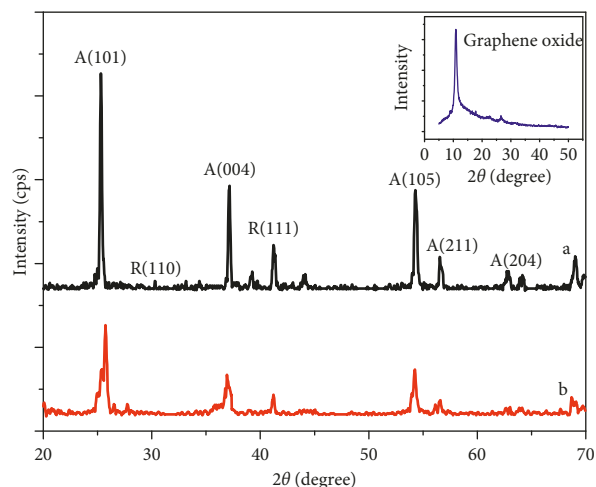


FIGURE 1: XRD spectrum of GO (inset), TiO₂ (a), and GO/TiO₂ (b).

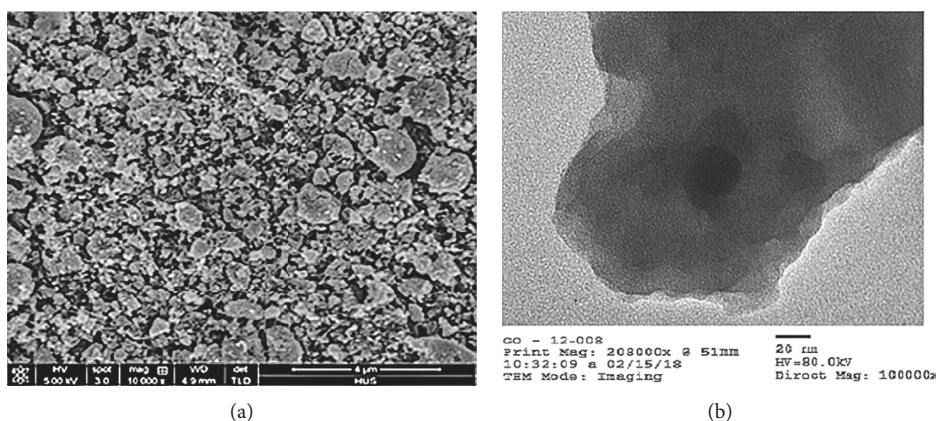


FIGURE 2: SEM and TEM images of GO.

scanning electron microscopy (SEM), energy-dispersive X-ray (EDX) spectroscopy analysis, Fourier transform infrared (FTIR) spectroscopy analysis, and water contact angle (WCA) measurement.

3.2.1. SEM Images. SEM images of PSf, PSf/GO, and PSf/GO-TiO₂ membranes with various amounts of TiO₂ (10, 15, and 20 wt.% based on the weight of GO) are displayed in Figure 5.

Following the cross-sectional images, the PSf membrane has a porous structure with the dense skin layer and the membrane thickness was 64 μm. Adding GO to the membrane leads to a dramatic change in the PSf membrane structure. Figure 5 shows that GO is deposited onto the membrane surface, and the dispersed grain structure appeared smooth. GO particles make the membrane thickness higher (79 μm). With the increased addition of TiO₂ to the polymer matrix, surface roughness and membrane thickness increase continuously (from 87.0 to 96.7 μm). It is clear that GO and TiO₂ nanoparticles are uniformly dispersed in the PSf matrix. In the higher content of TiO₂, the holes have disappeared; the surface of the

blended membrane becomes thicker than that of the unblended membrane.

The formations of materials containing both hydrophilic GO and TiO₂ can lead to changes in chemical functionality and separation performance of the membrane.

3.2.2. FTIR-ATR Spectrum. Characteristics of the membrane surface were investigated by FTIR spectroscopy, and FTIR-ATR technique was used to demonstrate the successful incorporation of GO and TiO₂ into the polymer matrix of membranes.

Absorptions of the polysulfone layer are characterized by O=S=O (1000–1300 cm⁻¹) and C=C (1400–1600 cm⁻¹) for the polysulfone membrane (Figure 6(a)). The appearance of oxygen-containing groups of GO such as C-O stretching (1674 cm⁻¹) and C=O stretching (1101 cm⁻¹) was observed using spectroscopy (Figure 6(b)) for the blended PSf/GO membrane. With the existence of oxygen-containing groups of GO, the spectroscopy (Figure 6(c)) exhibits a new peak at 600–1000 cm⁻¹ for the blended PSf/GO-TiO₂ membrane, which attributes to the Ti-O-Ti stretching [39, 40]; it shows the successful

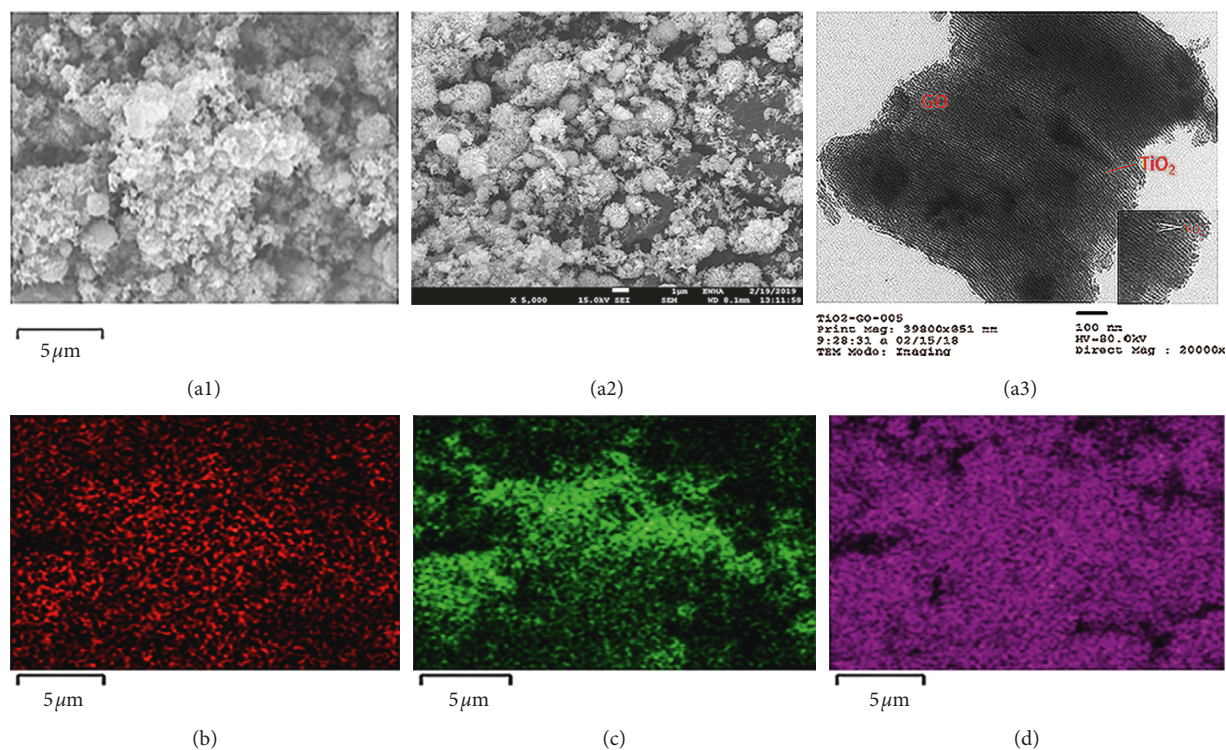


FIGURE 3: SEM (a1, a2), TEM (a3), and EDX-mapping images of C K series (b), O K series (c), and Ti K series (d) elements of GO-TiO₂ materials.

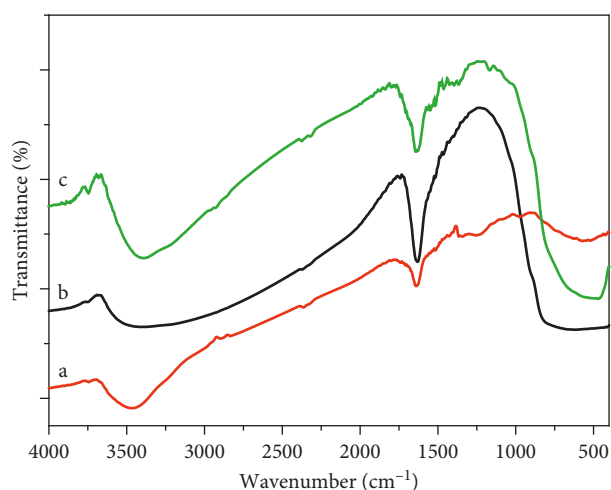


FIGURE 4: FTIR spectra of GO (a), TiO₂ (b), and GO-TiO₂ (c) materials.

blending of TiO₂ and GO particles into the PSf membrane. Thus, the reason why the membrane becomes hydrophilic is the presence of GO and TiO₂.

3.2.3. EDX Analysis. To study the amount of elements of membranes, EDX had been conducted. Figure 7 shows the EDX spectra of unblended and blended membranes and the changes in the proportion of each element.

As can you see, compared to the PSf membrane (Figure 7(a)), the PSf/GO membrane (Figure 7(b)) increased

oxygen (from 9.76% to 19.26%) atomic ratio, but carbon and sulfur ratios were decreased (with a sharp decrease of C atoms from 87.85% to 79.34% and a sharp decrease of S atoms from 2.39% to 1.40%). For the PSf/GO-TiO₂ membrane (Figure 7(c)), the oxygen atomic ratio increased to 33.99% and carbon atomic ratio decreased to 64.79%; meanwhile, the Ti atomic ratio was 0.08%. These results proved that GO and TiO₂ nanoparticles exist on the PSf membrane.

3.2.4. Water Contact Angle Measurement. Changes in the water flux of membranes as a result of blending of hydrophilic materials (GO and TiO₂) were investigated via the water contact angle (WCA) measurements. Figure 8 shows the WCAs of the unblended and blended membranes. The results indicated that, by adding GO and TiO₂ into the PSf matrix, the blended membranes became more hydrophilic with a significant decrease of the WCA (Table 1), reducing from 83.4° for the unblended membrane to around 60.2° for the blended ones, which is because of the formation of the hydrophilic material on the blended membrane. Thus, the increase of the hydrophilic groups on the membrane reduced the water contact angle values. The obtained results imply that the presence of the GO and TiO₂ improves the hydrophilicity of the membrane.

3.3. Membrane Filtration Property. Indeed, with the appearance of the oxygen-containing groups of GO and TiO₂,

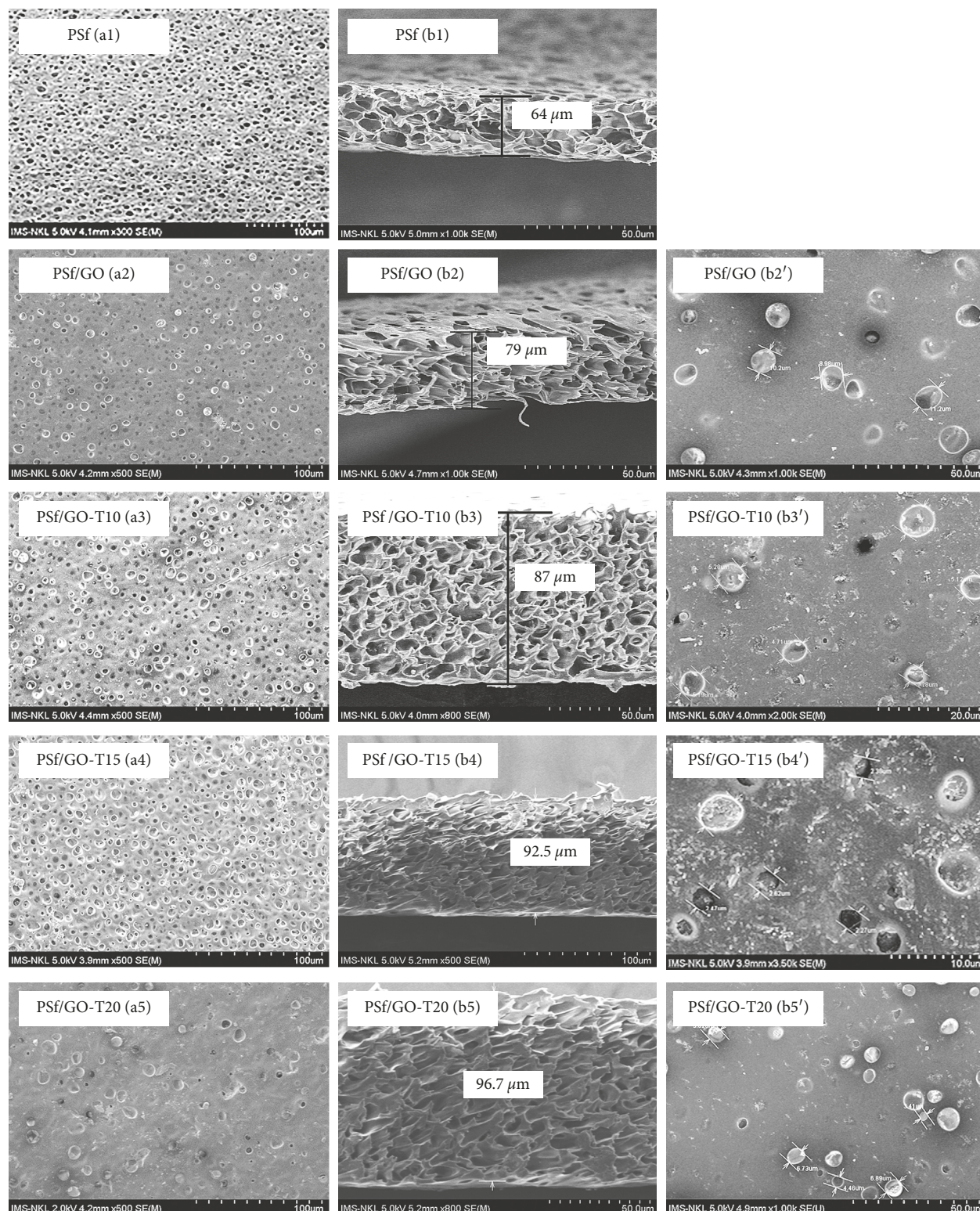


FIGURE 5: SEM images of the surface (a1, a2, a3, a4, a5; b2', b3', b4', b5') and the cross-sectional images (b1, b2, b3, b4, b5) of PSf, PSf/GO, and PSf/GO-TiO₂ membranes.

the blended membranes became more hydrophilic, and the obtained experimental results related to membrane separation performance are shown below.

3.3.1. *Permeability.* The permeability can be selected to characterize the changes in the hydrophilic property of the membrane surface. The permeability of the membrane will

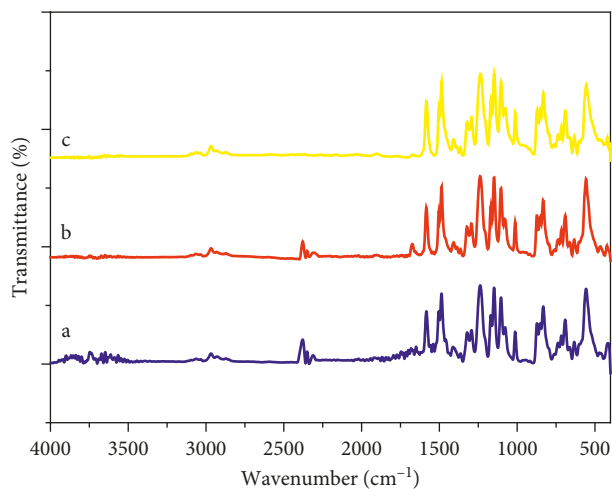


FIGURE 6: FTIR-ATR spectra of PSf (a), PSf/GO (b), and PSf/GO-Ti15 (c) membranes.

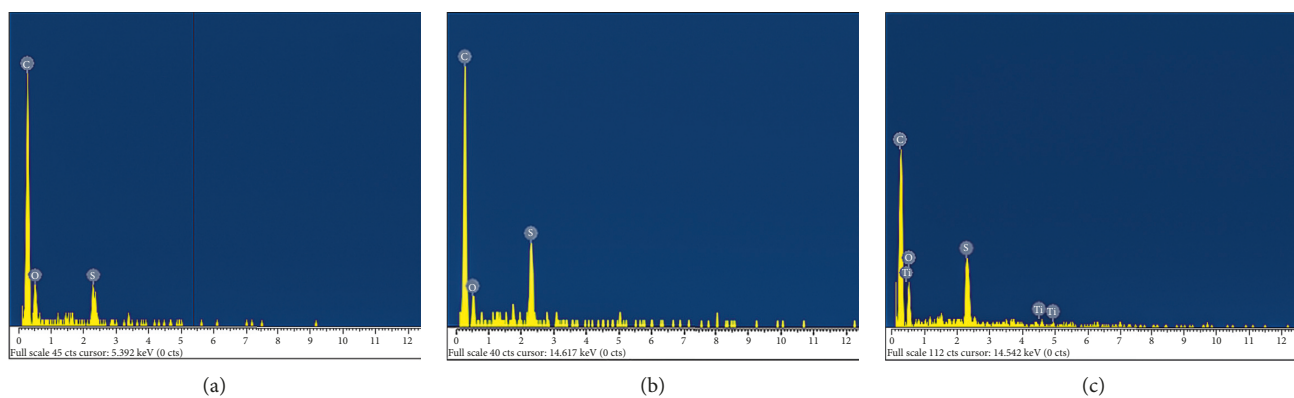


FIGURE 7: EDX spectra of PSf (a), PSf/GO (b), and PSf/GO-Ti15 (c) membranes.

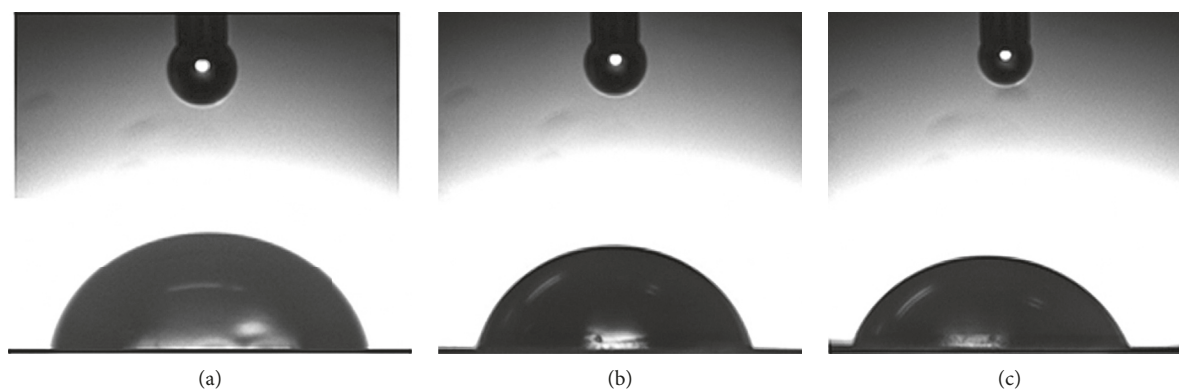


FIGURE 8: Water contact angle images of (a) PSf, (b) PSf/GO, and (c) PSf/GO-Ti15 membranes.

TABLE 1: Water contact angle values of PSf, PSf/GO, and PSf/GO-Ti15 membranes.

Membranes	PSf	PSf/GO	PSf/GO-Ti15
WCA (°)	83.4	76.2	60.2

be increased if the membrane becomes hydrophilic, which can be achieved by blending GO and TiO_2 into the membrane [22]. The normalized permeability between the unblended membrane and the blended membrane at different conditions of TiO_2 is shown in Figure 9. There is an increase

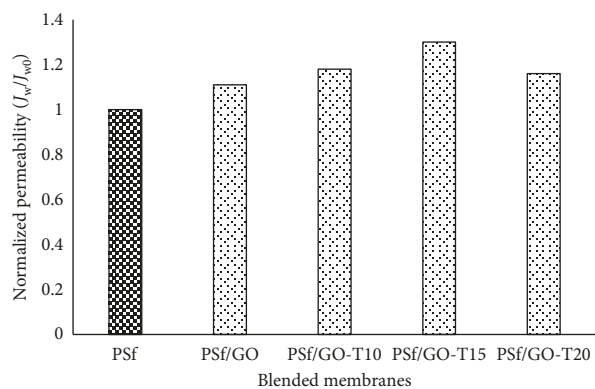


FIGURE 9: Normalized permeability of unblended and blended membranes.

(about 11 to 30%) in the permeability in membranes blended with GO and TiO_2 compared to unblended membranes. Thus, the presence of GO and TiO_2 functional groups that contain oxygen caused changes in water permeability. This also corresponds to the results of the WCA.

3.3.2. Separation Performance. Figure 10 shows the experimental results about the separation property of unblended and blended membranes at different conditions of TiO_2 .

These results show that the flux in the filtrate of the blended membranes could increase dramatically (from 20 to 40%) compared to that of the unblended ones. These results are similar to the result of Badrinezhad et al. [1]. By increasing the amount of titanium dioxide, the separation performance of blended membranes is also higher, approximately 20% higher than unblended ones. This improvement is due to a thin layer of hydration formed on the surface of the membrane caused by hydrogen bonding between water molecules under the influence of oxygen-containing groups. This layer makes the water flux higher. In addition, the retention improves from 38% to 59% for the blended membranes. The increase in the retention is due to a hydrophilic thin layer formed, making the membrane surfaces compact.

3.3.3. Antifouling Property. The hydrophilicity also helps mitigate adhesion of foulants and increase the membrane antifouling ability. Figure 11 shows the comparison of the maintained flux ratios of unblended and blended membranes. The results indicate that the flux degradation of the blended membrane is greatly reduced compared to that of the unblended membrane. However, the time required to keep the flow stable is shortened. After 90 min of filtration of the methylene blue feed solution, the flux maintaining ratio of the unblended membrane was about 41%; meanwhile, it was higher than 45% that of the blended one.

4. Conclusions

In this research, the PSf, PSf/GO, and PSf/GO- TiO_2 composite membranes with different ratios of TiO_2 are fabricated

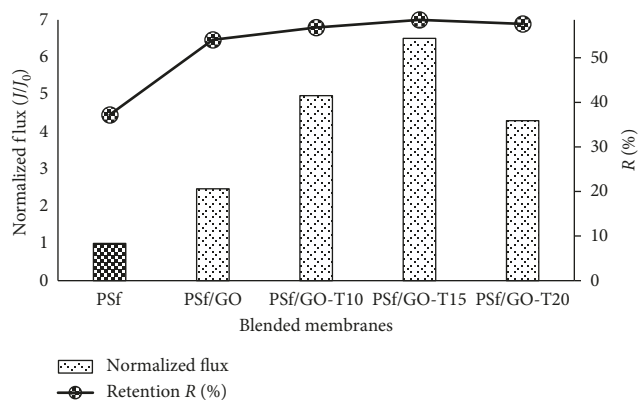


FIGURE 10: Normalized flux and retention of unblended and blended membranes.

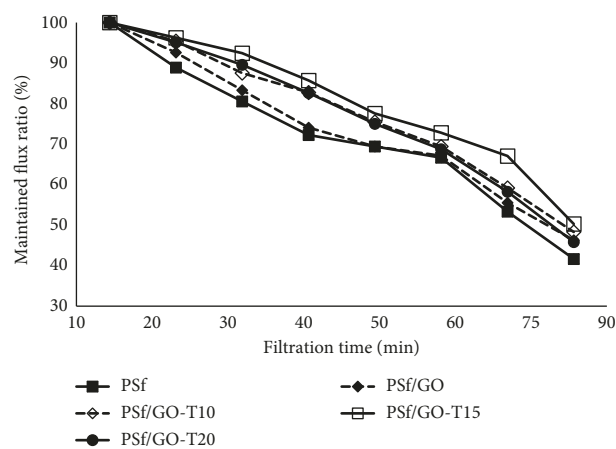


FIGURE 11: Maintained flux ratio of unblended and blended membranes.

and characterized. The presence of graphene oxide and titanium dioxide in the polysulfone polymer matrix is confirmed by SEM images, EDX spectra, FTIR-ATR spectroscopy, and WCA. The obtained results confirm the appearance of oxygen-containing groups of GO and TiO_2 . This makes the blended membrane more hydrophilic with the increase of permeability, retention, flux, and antifouling capacity.

Data Availability

The data used to support the findings of this study are available from the corresponding author upon request.

Conflicts of Interest

The authors declare that they have no conflicts of interest.

Acknowledgments

The authors sincerely thank the National Foundation for Science and Technology Development (NAFOSTED) for financial support under grant no. 104.06-2017.56.

References

- [1] L. Badrinezhad, S. Ghasemi, Y. Azizian-Kalandaragh, and A. Nematollahzadeh, "Preparation and characterization of polysulfone/graphene oxide nanocomposite membranes for the separation of methylene blue from water," *Polymer Bulletin*, vol. 75, no. 2, pp. 469–484, 2017.
- [2] Y. Kang, M. Obaid, J. Jang, M.-H. Ham, and I. S. Kim, "Novel sulfonated graphene oxide incorporated polysulfone nanocomposite membranes for enhanced-performance in ultrafiltration process," *Chemosphere*, vol. 207, pp. 581–589, 2018.
- [3] M. Ionita, E. Vasile, L. E. Crica et al., "Synthesis, characterization and in vitro studies of polysulfone/graphene oxide composite membranes," *Composites Part B: Engineering*, vol. 72, pp. 108–115, 2015.
- [4] B. M. Ganesh, A. M. Isloor, and A. F. Ismail, "Enhanced hydrophilicity and salt rejection study of graphene oxide-polysulfone mixed matrix membrane," *Desalination*, vol. 313, pp. 199–207, 2013.
- [5] K. B. Prabhu, M. B. Saidutta, A. M. Isloor, and R. Hebbar, "Improvement in performance of polysulfone membranes through the incorporation of chitosan-(3-phenyl-1h-pyrazole-4-carbaldehyde)," *Codent Engineering*, vol. 4, no. 1, article 1403005, 2017.
- [6] H. C. Bidsorkhi, H. Riazi, D. Emadzadeh et al., "Preparation and characterization of a novel highly hydrophilic and antifouling polysulfone/nanoporous TiO₂ nanocomposite membrane," *Nanotechnology*, vol. 27, no. 41, article 415706, 2016.
- [7] C. Zhao, X. Xu, J. Chen, and F. Yang, "Effect of graphene oxide concentration on the morphologies and antifouling properties of PVDF ultrafiltration membranes," *Journal of Environmental Chemical Engineering*, vol. 1, no. 3, pp. 349–354, 2013.
- [8] J. Qiu, Y. Zhang, Y. Shen, Y. Zhang, H. Zhang, and J. Liu, "Hydrophilic modification of microporous polysulfone membrane via surface-initiated atom transfer radical polymerization of acrylamide," *Applied Surface Science*, vol. 256, no. 10, pp. 3274–3280, 2010.
- [9] H.-B. Dong, Y.-Y. Xu, Z. Yi, and J.-L. Shi, "Modification of polysulfone membranes via surface-initiated atom transfer radical polymerization," *Applied Surface Science*, vol. 255, no. 21, pp. 8860–8866, 2009.
- [10] M.-L. Luo, J.-Q. Zhao, W. Tang, and C.-S. Pu, "Hydrophilic modification of poly(ether sulfone) ultrafiltration membrane surface by self-assembly of TiO₂ nanoparticles," *Applied Surface Science*, vol. 249, no. 1–4, pp. 76–84, 2005.
- [11] A. Rahimpour, S. S. Madaeni, A. H. Taheri, and Y. Mansourpanah, "Coupling TiO₂ nanoparticles with UV irradiation for modification of polyethersulfone ultrafiltration membranes," *Journal of Membrane Science*, vol. 313, no. 1–2, pp. 158–169, 2008.
- [12] J.-H. Li, Y.-Y. Xu, L.-P. Zhu, J.-H. Wang, and C.-H. Du, "Fabrication and characterization of a novel TiO₂ nanoparticle self-assembly membrane with improved fouling resistance," *Journal of Membrane Science*, vol. 326, no. 2, pp. 659–666, 2009.
- [13] T.-H. Bae and T.-M. Tak, "Effect of TiO₂ nanoparticles on fouling mitigation of ultrafiltration membranes for activated sludge filtration," *Journal of Membrane science*, vol. 249, no. 1–2, pp. 1–8, 2005.
- [14] K. C. Chong, S. O. Lai, W. J. Lau, H. S. Thiam, A. F. Ismail, and A. K. Zulhairun, "Fabrication and characterization of polysulfone membranes coated with polydimethylsiloxane for oxygen enrichment," *Aerosol and Air Quality Research*, vol. 17, no. 11, pp. 2735–2742, 2017.
- [15] D. J. Miller, D. R. Dreyer, C. W. Bielawski, D. R. Paul, and B. D. Freeman, "Surface modification of water purification membranes: a review," *A Journal of the Gesellschaft Deutscher Chemiker, Angewandte Chemie International Edition*, vol. 56, no. 17, pp. 4662–4711, 2016.
- [16] A. Rahimpour and S. S. Madaeni, "Improvement of performance and surface properties of nano-porous polyethersulfone (PES) membrane using hydrophilic monomers as additives in the casting solution," *Journal of Membrane science*, vol. 360, no. 1–2, pp. 371–379, 2010.
- [17] M. Padaki, A. M. Isloor, G. Belavadi, and K. N. Prabhu, "Preparation, characterization and performance study of poly(isobutylene-alt-maleic anhydride) [PIAM] and polysulfone [PSf] composite membranes before and after alkali treatment," *Industrial & Engineering Chemistry Research*, vol. 50, no. 11, pp. 6528–6534, 2011.
- [18] B. M. Ganesh, A. M. Isloor, and M. Padaki, "Preparation and characterization of polysulfone and modified poly isobutylene-alt-maleic anhydride blend NF membrane," *Desalination*, vol. 287, pp. 103–108, 2012.
- [19] R. Raslan and A. W. Mohammad, "Polysulfone/pluronic F127 blend ultrafiltration membranes: preparation and characterizations," *Journal of Applied Sciences*, vol. 10, no. 21, pp. 2628–2632, 2010.
- [20] H. Ravishankar, J. Christy, and V. Jegatheesan, "Graphene oxide (GO)-Blended polysulfone (PSf) ultrafiltration membranes for lead ion rejection," *Membranes*, vol. 8, no. 3, p. 77, 2018.
- [21] K. Zodrow, L. Brunet, S. Mahendra et al., "Polysulfone ultrafiltration membranes impregnated with silver nanoparticles show improved biofouling resistance and virus removal," *Water Research*, vol. 43, pp. 715–723, 2009.
- [22] G. S. Lai, W. J. Lau, P. S. Goh, A. F. Ismail, N. Yusof, and Y. H. Tan, "Graphene oxide incorporated thin film nanocomposite nanofiltration membrane for enhanced salt removal performance," *Desalination*, vol. 387, pp. 14–24, 2016.
- [23] L. Yu, Y. Zhang, B. Zhang, J. Liu, H. Zhang, and C. Song, "Preparation and characterization of HPEI-GO/PES ultrafiltration membrane with antifouling and antibacterial properties," *Journal of Membrane science*, vol. 447, pp. 452–462, 2013.
- [24] J. Zhu, M. Tian, J. Hou et al., "Surface zwitterionic functionalized graphene oxide for a novel loose nanofiltration membrane," *Journal of Materials Chemistry A*, vol. 4, no. 5, pp. 1980–1990, 2016.
- [25] H. M. Hegab and L. Zou, "Graphene oxide-assisted membranes: fabrication and potential applications in desalination and water purification," *Journal of Membrane Science*, vol. 484, pp. 95–106, 2015.
- [26] Z. Wang, H. Yu, J. Xia et al., "Novel GO-blended PVDF ultrafiltration membranes," *Desalination*, vol. 299, pp. 50–54, 2012.
- [27] J. Lee, H.-R. Chae, Y. J. Won et al., "Graphene oxide nanoplatelets composite membrane with hydrophilic and antifouling properties for wastewater treatment," *Journal of Membrane Science*, vol. 448, pp. 223–230, 2013.
- [28] J. Zhang, Z. Xu, M. Shan et al., "Synergetic effects of oxidized carbon nanotubes and graphene oxide on fouling control and anti-fouling mechanism of polyvinylidene fluoride ultrafiltration membranes," *Journal of Membrane Science*, vol. 448, pp. 81–92, 2013.

- [29] J. Wang, Y. Wang, J. Zhu, Y. Zhang, J. Liu, and B. Van der Bruggen, "Construction of TiO_2 @graphene oxide incorporated antifouling nanofiltration membrane with elevated filtration performance," *Journal of Membrane Science*, vol. 533, pp. 279–288, 2017.
- [30] L. Duan, Y. Wang, Y. Zhang, and J. Liu, "Graphene immobilized enzyme/polyethersulfone mixed matrix membrane: enhanced antibacterial, permeable and mechanical properties," *Applied Surface Science*, vol. 355, pp. 436–445, 2015.
- [31] F. Perreault, M. E. Tousley, and M. Elimelech, "Thin-film composite polyamide membranes functionalized with biocidal graphene oxide nanosheets," *Environmental Science & Technology Letters*, vol. 1, no. 1, pp. 71–76, 2013.
- [32] M. Safarpour, A. Khataee, and V. Vatanpour, "Thin film nanocomposite reverse osmosis membrane modified by reduced graphene oxide/ TiO_2 with improved desalination performance," *Journal of Membrane science*, vol. 489, pp. 43–54, 2015.
- [33] A. F. Faria, C. Liu, M. Xie et al., "Thin-film composite forward osmosis membranes functionalized with graphene oxide-silver nanocomposites for biofouling control," *Journal of Membrane science*, vol. 525, pp. 146–156, 2017.
- [34] T. T. Dung, *Surface Modification of RO Membrane by Glow Discharge Plasma*, Ph.D. thesis, Tokyo Institute of Technology, Tokyo, Japan, 2001.
- [35] K. Norrman, A. Ghanbari-Siahkali, and N. B. Larsen, "6 studies of spin-coated polymer films," *Annual Reports Section C*, vol. 101, pp. 174–201, 2005.
- [36] W. S. Hummers and R. E. Offeman, "Preparation of graphitic oxide," *Journal of the American Chemical Society*, vol. 80, no. 6, p. 1339, 1958.
- [37] L. Guo, P. Ye, J. Wang, F. Fu, and Z. Wu, "Three-dimensional Fe_3O_4 -graphene macroscopic composites for arsenic and arsenate removal," *Journal of Hazardous Materials*, vol. 298, pp. 28–35, 2015.
- [38] P. S. Teo, H. N. Lim, N. M. Huang, C. H. Chia, and I. Harrison, "Room temperature in situ chemical synthesis of Fe_3O_4 /graphene," *Ceramics International*, vol. 38, no. 8, pp. 6411–6416, 2012.
- [39] Y. H. Teow, B. S. Ooi, A. L. Ahmad, and J. K. Lim, "Mixed-matrix membrane for humic acid removal: influence of different types of TiO_2 on membrane morphology and performance," *International Journal of Chemical Engineering and Applications*, vol. 3, no. 6, pp. 374–379, 2012.
- [40] K. E. Tettey, M. Q. Yee, and D. Lee, "Photocatalytic and conductive MWCNT/ TiO_2 nanocomposite thin films," *ACS Applied Materials & Interfaces*, vol. 2, no. 9, pp. 2646–2652, 2010.

Research Article

Platinum Nanoflower-Modified Electrode as a Sensitive Sensor for Simultaneous Detection of Lead and Cadmium at Trace Levels

Thi Lieu Nguyen ^{1,2}, Van Hoang Cao,² Thi Hai Yen Pham,³ and Truong Giang Le ^{1,3}

¹Graduate University of Science and Technology, Vietnam Academy of Science and Technology, 18-Hoang Quoc Viet, Hanoi, Vietnam

²Department of Chemistry, Quy Nhon University, 170-An Duong Vuong, Quy Nhon, Binh Dinh, Vietnam

³Institute of Chemistry, Vietnam Academy of Science and Technology, 18-Hoang Quoc Viet, Hanoi, Vietnam

Correspondence should be addressed to Thi Lieu Nguyen; nguyenthilieu@qnu.edu.vn and Truong Giang Le; hoasinhmoitruong.vast@gmail.com

Received 1 March 2019; Revised 7 May 2019; Accepted 29 May 2019; Published 12 June 2019

Guest Editor: Ajit Kumar Sharma

Copyright © 2019 Thi Lieu Nguyen et al. This is an open access article distributed under the Creative Commons Attribution License, which permits unrestricted use, distribution, and reproduction in any medium, provided the original work is properly cited.

We introduce the fabrication and electrochemical application of platinum nanoflower-modified glassy carbon electrode (PtNFs/GCE) for the trace level determination of lead and cadmium using differential pulse anodic stripping voltammetry (DPASV). The modified electrodes have been characterized by EDX, XRD, SEM, and AFM techniques to confirm chemical and physical properties. The effect of potential electrodeposition on the properties of the electrode was investigated. At -0.2 V of potential, platinum developed with a nanoflower shape and dispersed densely all over the glassy carbon surface. In this condition, the highest of lead and cadmium electrochemical signals was clearly observed. The sensor showed wide linearity in the concentration range of $1-100 \mu\text{g}\cdot\text{L}^{-1}$ with detection limits of $0.408 \mu\text{g}\cdot\text{L}^{-1}$ and $0.453 \mu\text{g}\cdot\text{L}^{-1}$ for lead and cadmium ions, respectively. The produced electrodes have good reproducibility with relative standard deviations of 4.65% for lead and 4.36% for cadmium ions. The results demonstrate that this simple, stable, and sensitive sensor is suitable for the simultaneous electrochemical determination of Pb^{2+} and Cd^{2+} at trace levels.

1. Introduction

One of the crucial factors leading to worldwide environmental pollution is the presence of heavy metal ions. Among heavy metals, cadmium is one of the most toxic heavy metals found in some surface and subsurface waters. A number of acute and chronic illnesses such as emphysema, hypertension, and skeletal malformation in the fetus have been attributed to the harmful properties of cadmium [1]. Another frequently encountered toxic contaminant in the environment is lead due to its application for car batteries, paints, and gasoline [2]. In detail, lead can disturb the metabolism of calcium and other critical nutrients by competing for binding sites [3]. Lead poisoning causes a variety of symptoms such as digestive, neurological, cardiac, and abdominal pain [4]. Several critical health problems have been

attributed to lead and most of the effects are observed in children, infants, and unborn individuals [5]. The significant environmental and biological damages caused by cadmium and lead call for rapid, sensitive, and simple analytical methods for their detection and monitoring.

Among analytical methods, electrochemical methods are the most efficient techniques for the determination of heavy metal ions because of their simple operation, low cost, high sensitivity, and capability to analyze elemental speciation. The efficiency of electrochemical analysis is strongly affected by the properties of the working electrode. Platinum has been commonly used as the electrode material. The major advantages of platinum in electrochemistry are chemical inertness, stability, easy fabrication, high conductivity, high reactivity, low background current [6], and high catalytic activity for a wide variety of reactions. The catalytic activity

of platinum depends on the size and orientation of platinum particles [7–9]; platinum nanoparticles (PtNPs) are over 100 times more active than microsized platinum powder and 1000 times more active than macrosized platinum [10]. Besides the high catalytic activity, nanoplatinum shows the fast electron exchange and the high ratio of surface area to volume [11]. Thus, the nanostructured electrode could help significantly increase the sensitivity in the analysis at trace levels.

So far, platinum nanostructured electrodes have been used for substrate modification and applied in detection of various organic compounds such as glucose [12], cholesterol [13], ascorbic acid [14], dopamine, uric acid [15], and granisetron [16]. In these research studies, the electrochemical signals of targets observed on the modified electrodes increased dramatically compared with those observed on the substrate that demonstrates the faster electron transfer and a larger electroactive surface of the nanostructured electrodes. However, there are a few authors studying Pt nanostructured electrodes for heavy-metal determination. In [17], Yoon et al. blended Pt nanoparticles with carbon powder and organic binder for electrode manufacturing to investigate the catalytic activity of platinum nanoparticles in the copper analysis. This modified electrode improved the copper peak current which is three times higher than that measured on the nonmodified electrode. Besides, almost fabricated Pt nanoelectrode for determination of organic compounds and heavy metals were at the construction of the sphere [17] or cube [14]. The platinum nanothorn with sharp tips and edges was electrochemically prepared; however, this material was used as a platform in surface-enhanced Raman scattering (SERS) measurement with high activity [18]. Besides, Pt nanoflowers, that is, nanostructures of Pt with flower-like shape, were prepared by using different methods such as chemical method [19, 20] and electrochemical method with cyclic voltammetric technique [12]. These electrodes exhibited a high electrochemically active surface area, thus leading to a high electrocatalytic activity.

In the present work, we developed a nanoflower-shaped platinum on a glassy carbon electrode by a one-step electrochemical deposition method and used it as a sensing probe in the simultaneous measurement of Pb^{2+} and Cd^{2+} ions at trace levels. The modified electrode was characterized by cyclic voltammetry (CV), field-emission scanning electron microscope (FE-SEM), energy dispersive X-ray (EDX), atomic force microscopy (AFM), and X-ray diffraction (XRD). The electrochemical behavior of lead and cadmium has been investigated with a sensitive, fast, and simple different pulse anodic stripping voltammetry (DPASV) method. In addition, the enhancement of the sensibility in Pb and Cd analysis has been evaluated when using the fabricated platinum nanoflowers electrodes.

2. Experimental

2.1. Reagents. All reagents necessary for the construction of Pt nanoflowers and subsequent measurements, hexachloroplatinic (IV) acid hexahydrate, potassium hexacyanoferrate (III),

sodium dihydrogen phosphate, disodium hydrogen phosphate, potassium chloride, sodium acetate, sulfuric acid, hydrochloric acid, acetic acid, lead stock solution (1000 ppm), and cadmium stock solution (1000 ppm), were purchased from Merck (KGaA, 64271 Darmstadt, Germany).

2.2. Apparatus. All electrochemical measurements were performed at room temperature. A three-electrode system with platinum nanoflower-modified glassy carbon electrode (PtNFs/GCE) as a working electrode, an Ag/AgCl reference electrode, and a platinum wire counter electrode were used to perform electrochemical measurements. The three-electrode system was connected to a custom-made multifunction potentiostat/galvanostat manufactured at the Vietnam Academy of Science and Technology (Hanoi, Vietnam). It was equipped with 12-bit analog-digital, digital-analog converters (ADC-DAC) with two operational amplifiers, which can provide ultrasensitive measurements with current resolution down to 0.008 nA. A field-emission scanning electron microscope (FE-SEM, S-4800, Hitachi Company, Japan) was employed to evaluate the morphologies of the PtNFs/GCE. The crystal phase was determined by D8 ADVANCE, Bruker, using $\text{CuK}\alpha$ ($\lambda = 1.54060$ nm) and scanning degree $2\theta = 20\text{--}70^\circ$. Energy dispersive X-ray spectroscopy (EDX) was performed with a JSM-6510LV, JEOL Ltd. Company, Japan. Atomic force microscopy (AFM) was performed with a Solver PRO SPM, NT-MDT Company, Russian.

2.3. Preparation of Modified Electrode. The glassy carbon electrode ($d = 3.0$ mm) was washed with water and ethanol, then polished with a water slurry of $0.05\ \mu\text{m}$ size of alumina powder to get a smooth and shiny surface, then electrodes were rinsed with double-distilled water and placed in an ultrasonic bath for a few minutes to remove any residual polishing material on the electrode surface, and then the electrode was dried at room temperature. The electrodeposition of platinum nanoparticles on the bare glassy carbon electrode was carried out in $0.1\ \text{M}\cdot\text{H}_2\text{SO}_4$ solution containing $1.0\ \text{mM}\cdot\text{H}_2\text{PtCl}_6$. The effect of deposition potential (E_{Pt}) on properties of the fabricated Pt layer was investigated. The effect of deposition time (t_{Pt}) was evaluated in our previous study and herein we used the optimal value of t_{Pt} , that is, 150 s for further experiences. Following that, the Pt/GCE was gently cleaned with distilled water before use.

2.4. Electrochemical Measurements. The electrochemical measurements of the proposed sensor were carried out at room temperature ($25 \pm 1^\circ\text{C}$) by the cyclic voltammetry (CV) and different pulse anodic stripping voltammetry (DPASV) methods. The electrochemical properties of the PtNFs/GCE were investigated by the cyclic voltammetric (CV) method in $0.5\ \text{M}\cdot\text{H}_2\text{SO}_4$ solution from -0.1 V to 1.4 V and solution of $0.2\ \text{M}\cdot\text{PBS}$ pH 7 containing $5\ \text{mM}\ [\text{Fe}(\text{CN})_6]^{3-}$ from -0.3 V to 0.8 V at a scan rate of $0.1\ \text{V}\cdot\text{s}^{-1}$. The DPASV studies were carried out with preconcentration time 120 s, pulse amplitude

0.060 V, pulse time 0.050 s, step potential 0.007 V, step time 0.03 s, and sweep rate $0.25 \text{ V}\cdot\text{s}^{-1}$. The Pb^{2+} and Cd^{2+} ions were stripped of the electrode surface in the scan range -1.2 to 0.2 V , and the peak currents were measured.

3. Results and Discussion

3.1. Formation and Properties of PtNFs/GCE. Platinum nanoflowers (PtNFs) were electrochemically deposited on GC by chronoamperometry in $1.0 \text{ mM}\cdot\text{H}_2\text{PtCl}_6/0.1 \text{ M}\cdot\text{H}_2\text{SO}_4$ solution. An overview of the electrochemical behavior of this system is provided in Figure 1(a), which is a current-potential curve obtained from a cyclic voltammetric experiment at a polished GC electrode in $0.1 \text{ M}\cdot\text{H}_2\text{SO}_4$ and in $0.1 \text{ M}\cdot\text{H}_2\text{SO}_4$ solution containing $10.0 \text{ mM}\cdot\text{H}_2\text{PtCl}_6$. This wave exhibits three potential regions: the hydrogen region (from -0.2 to $+0.15 \text{ V}$) corresponds the adsorption/desorption of hydrogen with different energies, a broad oxidation peak for the Pt-oxide formation (commences at 0.7 V and extends up to 1.2 V), and a single reduction peak at 0.5 V corresponding to the reduction of Pt(IV) to Pt(0) on the electrode surface. The result is in agreement with previous studies [21–23]. Therefore, in order to deposit Pt onto the GCE by chronoamperometry, the applied potential must be lower than 0.3 V .

Typical CV measured in $0.5 \text{ M}\cdot\text{H}_2\text{SO}_4$ solution on the prepared Pt electrode is presented (Figure 1(b)). After the oxidation of Pt in the scanning at the anodic direction from -0.1 to 1.5 V , in the reverse direction, the clear cathodic peak is observed at 0.5 V presented for the reduction of Pt (IV) on GC. These observations are in agreement with the data of other authors [23, 24]. This means that Pt had been deposited on glassy carbon platforms at the studied potential.

3.2. Characterization of Platinum Nanoparticles. In order to study the surface morphology, chemical characterization, and structure of the platinum particles, the field-emission scanning electron microscopy, X-ray diffraction, energy dispersive X-ray spectroscopy, and atomic force microscopy techniques were used in the next experiment.

3.2.1. EDX Study. The presence of Pt nanoparticles on the glassy carbon electrode surface is verified by the EDX analysis (Figure 2). The spectrum contained two peaks which were assigned to C, Pt.

The major peaks are around $0.28, 2.10 \text{ keV}$, which correspond to the binding energy of C, Pt. This also confirms that no other impurities have been identified. The weight ratios of prepared Pt on the electrodes increase as E_{Pt} changes from 0.2 V to -0.3 V then decrease at -0.5 V . This can be concluded that the amount of platinum deposited on the GCE strongly depends on the electrodeposition potential. These data show that platinum was successfully deposited on the surface of the glassy carbon with the highest amount at the applied potential of -0.3 V .

3.2.2. XRD Study. Figure 3 shows the X-ray diffraction patterns of platinum nanoparticles deposited on the glassy

carbon electrode. There were three well-defined characteristic diffraction peaks at $39.9^\circ, 46.2^\circ,$ and 67.5° respectively, indexed to reflections from (111), (200), and (220) planes of the face-centered cubic (fcc) crystal structure of metallic platinum. This result evidently exhibits that Pt exists on the GCE surface. The result is in agreement with previous studies [25–27].

3.2.3. SEM Study. The surface morphology of the Pt/GCE was investigated by microscopic imaging analysis. Figure 4 shows the typical SEM images of the GCE (Figure 4(a)) and Pt layer electrodeposited on the GCE under different electrodeposition potentials. The size of individual PtNF piece rises up to exceed the nanoscale. According to the SEM images, Pt was formed separately in nanoparticles shape at the deposition potential of 0.2 V and 0.0 V (Figures 4(b) and 4(c)) and in nanoflowers shape at the deposition potential of -0.2 V and -0.3 V (Figures 4(d) and 4(e)), and at the deposition potential of -0.5 V , Pt developed into a film on the GCE (Figure 4(f)). This can be explained that at a negative potential, both hydrogen bubble release and Pt formation occur simultaneously, which resulted in the flower shape of Pt, while a positive potential represented the potential range at which only Pt formation occurred. At the deposition potential of -0.3 V , the flower-shaped form is still maintained; however, large Pt clusters are observed due to the formation of Pt particles between flowers. It is observed in Figure 4(e) that there are some defects at which no Pt occupied resulting from the attachment of large H_2 bubble at those sites. At the deposition potential of -0.5 V , the Pt flower pieces developed slapping whereby they aggregated into a film, they had not been single, free flower-shaped structures at nanoscale any longer. In addition, the stronger hydrogen bubble release at that potential should significantly prevent the formation of Pt on the electrode surface; thus, many sites of glassy carbon surface (black spots) that have no Pt occupying can be seen in Figure 4(f). This structure would lead to a decrease of electrochemically active surface area of an electrode. This result will be reaffirmed in the next section.

3.2.4. AFM Study. The surface morphology of the GCE, platinum nanoparticle-modified GCE with deposition potential of 0.2 V (Pt0.2/GCE), and -0.2 V (Pt-0.2/GCE) was examined by atomic force microscopy (AFM). The main goal was to determine and characterize a possible difference between the surface morphologies of the electrodes. A set of typical AFM images obtained for electrode surfaces tested in our study is shown in Figure 5. The images clearly reveal that the electrodes are used in different surface morphology.

The surface of the glassy carbon electrode appears to be smooth, atomically flat terraces (Figure 5(a)). To describe the electrode surface more quantitatively and to provide a quantitative comparison of the surface quality among the tested electrodes, we employed the root-mean-square (RMS) roughness [28]. RMS has been established as a rigorous quantitative measure of the surface roughness, and the

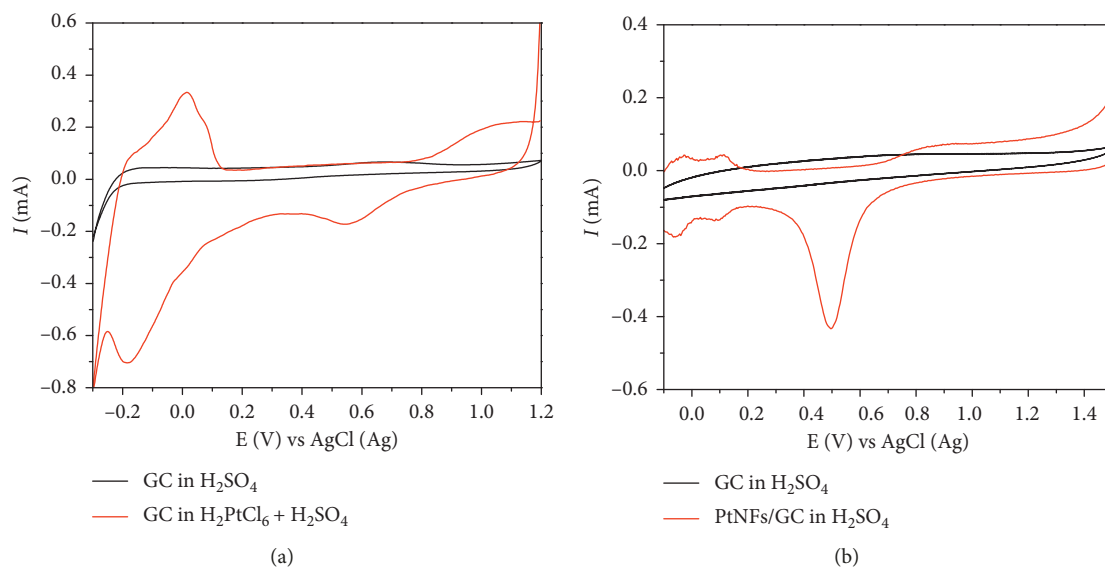


FIGURE 1: The cyclic voltammograms of a glassy carbon electrode in 0.1 M- H_2SO_4 solution and in 0.1 M- H_2SO_4 solution containing 10.0 mM- H_2PtCl_6 solution (a); a glassy carbon electrode and Pt/GCE in 0.1 M- H_2SO_4 solution (b), scanning rate of 0.1 V/s.

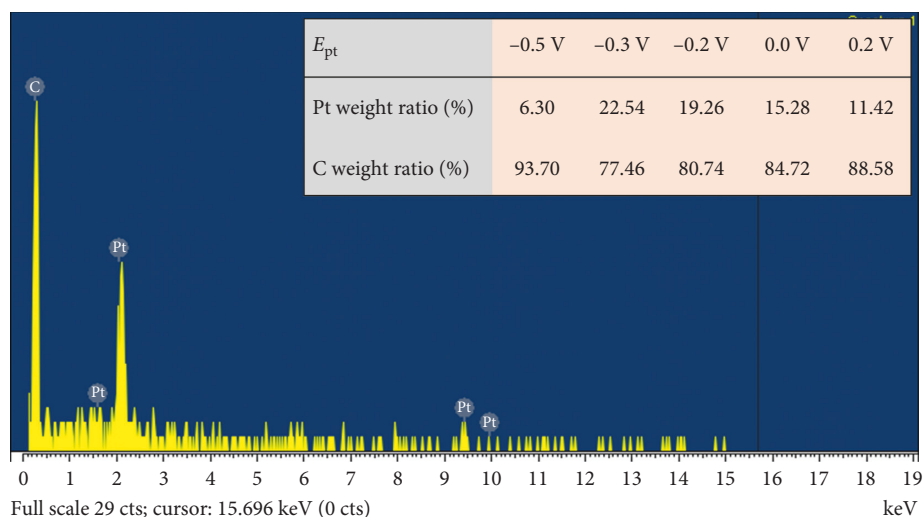


FIGURE 2: EDX spectra for the Pt/GCE prepared at the deposition potential of -0.3 V and the weight ratio of Pt element on the GCE at the different deposition potential (E_{pt}) (inset).

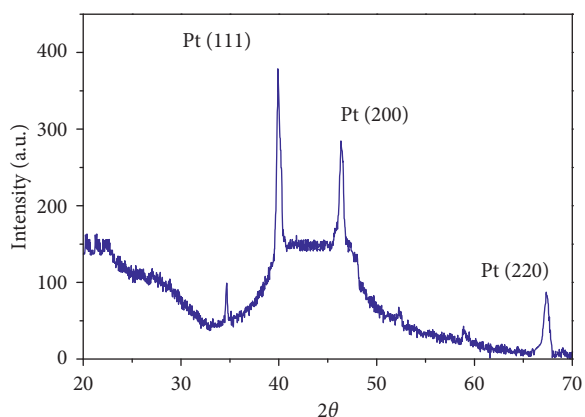


FIGURE 3: The X-ray diffraction pattern of platinum nanoparticles showing the face-centered cubic (fcc) crystal structure.

surface quality has often been used for such purpose. Apparently, it is one of the simplest morphology parameters that can be used for the surface quality description. For the GC electrode, we found that the average RMS is 672.82 nm. Contrary to the smooth and homogeneous surface of the GC electrode, the AFM image in Figure 5(b) reveals numerous features distributed all over the Pt-0.2/GC electrode surface. Typical morphology of Pt-0.2/GC electrode surface is shown in Figure 5(c). The AFM images of the electrode surface reveal mainly nodular features. However, they appear to be of a different shape and a lower height than those observed at the Pt-0.2/GC electrode surface. As expected, the Pt-0.2/GC electrode surface possessed a lower RMS value (730.53 nm) than that of the Pt-0.2/GC electrode surface (777.09 nm). In comparison with other electrodes, it is obvious that the Pt-0.2/GC electrode surface has the most

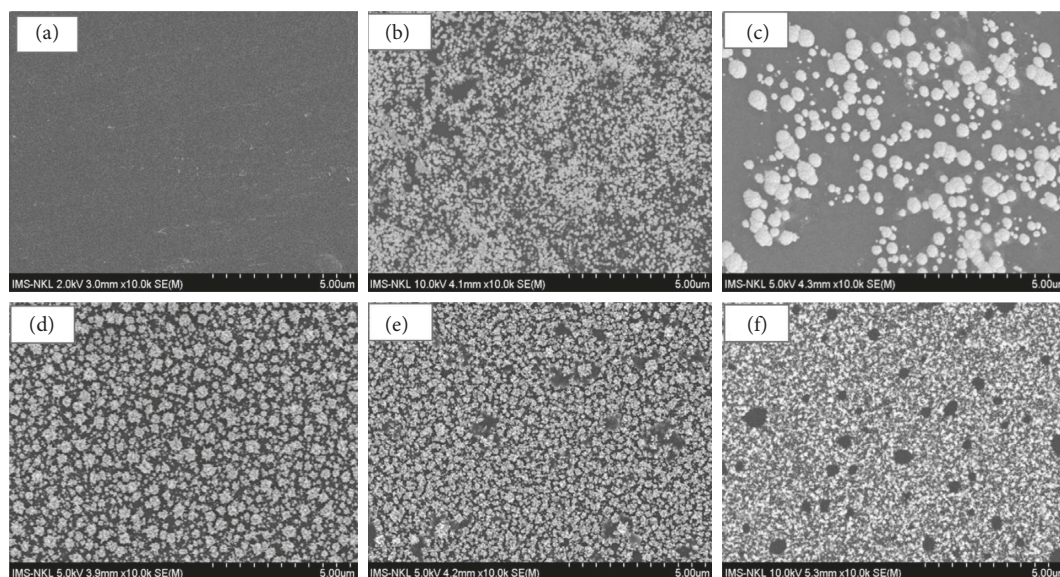


FIGURE 4: SEM images of GCE (a); PtNFs/GCE deposited at potential of 0.2 V (b), 0.0 V (c), -0.2 V (d), -0.3 V (e), and -0.5 V (f). Solution of 0.1 M·H₂SO₄ containing 1.0 mM·H₂PtCl₆; stirring at 50 rpm.

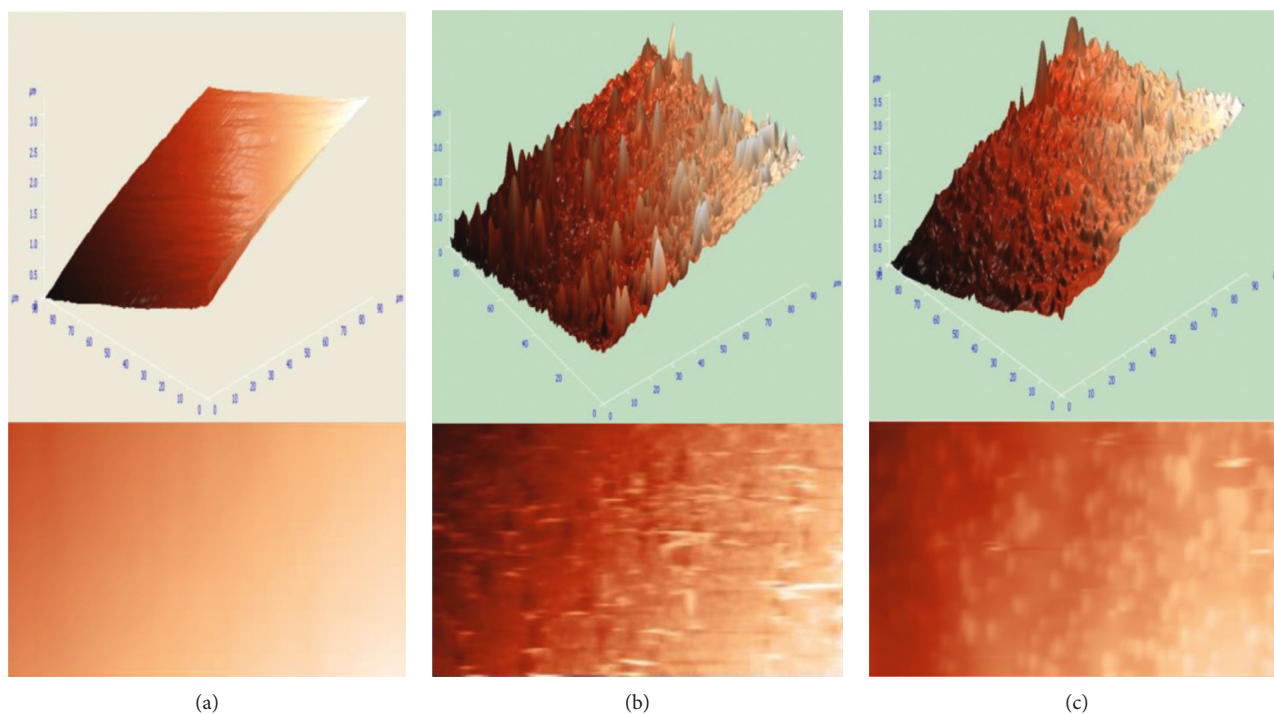


FIGURE 5: AFM images show the characteristic surface morphology form GCE (a); PtNFs/GCE deposited at the potential of -0.2 V (b); 0.2 V (c).

roughness and which consequently leads to an increase of electrochemically active surface area of the electrode. This result will be reaffirmed in the next section.

3.3. Electrochemical Characterization of PtNFs/GCE. Electrochemical characterization of Pt/GC electrodes prepared at different electrodeposition potentials of -0.5 V, -0.3 V, -0.2 V, 0.0 V, and 0.2 V was carried out by cyclic

voltammetry in two solutions which are 0.5 M·H₂SO₄ and 5 mM K₃[Fe(CN)]₆. The electrochemically active surface areas of electrodes are calculated from the charge of hydrogen desorption peaks in 0.5 M·H₂SO₄ solution and [Fe(CN)₆]³⁻ reduction peaks in K₃Fe(CN)₆ solution through Randles-Sevcik equation [29–31]. As can be seen from the obtained results (Figure 6), the variation of surface areas of Pt electrodes estimated from both methods vs. deposition potential has the same trend in general. However, the data

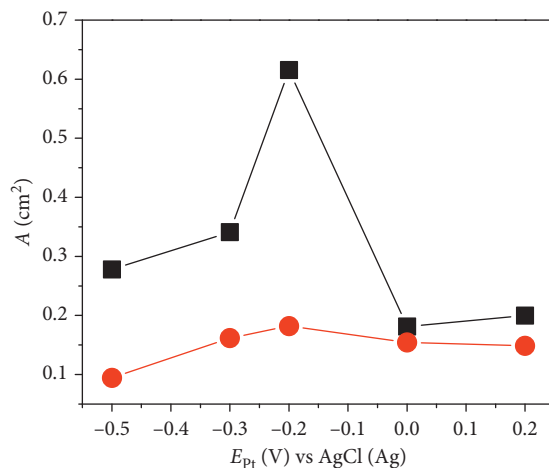


FIGURE 6: Effect of Pt electrodeposition potential on active surface area obtained from hydrogen desorption peaks (■) and ferricyanide reduction peaks (●).

calculated from hydrogen desorption peaks are higher than that obtained from ferricyanide reduction peaks. This could be explained by the fact that the size of the hydrogen atom is much smaller than that of the ferricyanide complex. As a result, the number of hydrogen is higher than the number of ferricyanide on the same electrode surface, especially on the Pt electrodes having a complex structure (flower-shaped nanostructure) that were prepared at -0.2 V, -0.3 V, and -0.5 V. Obviously, surface areas calculated from charge of hydrogen desorption as well as from the ferricyanide peak current are directly proportional to the number of active species on the surface. Therefore, the surface areas of Pt electrodes calculated from the former method are higher than those obtained from the latter one. The data reveal that the largest area is reached at -0.2 V of electrodeposition potential for both methods.

3.4. Effect of Pt Electrodeposition Potential on Cadmium and Lead Signals. As mentioned above, Pt deposition potential had a significant influence on the surface structure as well as the active surface area of the electrodes. Therefore, it certainly affects the electrochemical signal of cadmium and lead on these modified electrodes. Figure 7 shows DPASVs using GCE and the modified electrodes prepared at different electrodeposition potentials (E_{Pt}) in acetate buffer solution pH 4.5 containing $10 \mu\text{g}\cdot\text{L}^{-1}\cdot\text{Pb}^{2+}$ and Cd^{2+} . The higher peak signal on the PtNFs/GCE compared with the one on the GCE confirms the ability to detect cadmium and lead of the modified electrodes with higher sensitivity. It is observed that the peak height raises as E_{Pt} decreases and reaches a peak at E_{Pt} of -0.2 V, suggesting the amount of Pb^{2+} and Cd^{2+} preconcentrated onto the Pt/GCE depends on the surface morphology of this modified electrode. At more negative electrodeposition potential, the surface area of the electrode significantly decreases. This can be explained by the fact that the stronger generation of hydrogen at lower potential can damage the aggregation of metal crystals [32]. In addition, the formation of larger hydrogen bubble prevented the deposition of Pt on the electrode surface,

resulting in the exposure of large areas of GC substrate which can be clearly observed on the SEM image.

3.5. Repeatability, Reproducibility, and Selectivity of PtNFs/GCE. In this section, the repeatability, reproducibility, and selectivity of the PtNFs/GCE were studied. The repeatability of the modified electrode was evaluated by measuring the Pb^{2+} and Cd^{2+} ($10 \mu\text{g}\cdot\text{L}^{-1}$), respectively, in acetate buffer (pH 4.5) at the same electrode (Figure 8(a)). The relative standard deviation (RSD) values were calculated to investigate the repeatability of the PtNFs/GCE as 1.59% for Cd^{2+} and 1.45% for Pb^{2+} , showing the good stability of cadmium and lead signal at the electrode. The reproducibility of the PtNFs/GCE was calculated through the Pb^{2+} and Cd^{2+} ($10 \mu\text{g}\cdot\text{L}^{-1}$) signals from measurements of five different electrodes (Figure 8(b)). The RSD value of reproducibility was calculated to be 4.36% for Cd^{2+} and 4.65% for Pb^{2+} indicating that the fabrication procedure was reliable.

In order to evaluate the selectivity of the modified electrode, some common interferences were tested under optimized conditions. The effects of Cu^{2+} , Zn^{2+} , and Fe^{3+} were studied by recording the stripping peak current of $20 \mu\text{g}\cdot\text{L}^{-1}\cdot\text{Pb}^{2+}$ and Cd^{2+} in the presence of interferences. The obtained results indicate that the presence of a 100-fold excess of Zn^{2+} and Fe^{3+} does not influence the Pb^{2+} and Cd^{2+} signals. The interference of Cu^{2+} on the stripping peaks of Pb and Cd on the PtNFs/GCE was obtained even at Cu(II)-to-Pb(II) or Cu(II)-to-Cd(II) concentration ratios 10:1 and was more severe as the Cu(II)-to-metal concentration ratio increased. In terms of the effects of organic compounds, especially surfactants could be absorbed on the electrode surface and so that they could influence the electrochemical responses of the Pb^{2+} and Cd^{2+} stripping peak current.

3.6. Calibration and Detection Limit. The linear range and detection limit were evaluated by using the optimal PtNFs/GCE in acetate buffer solution (pH 4.5). The DPASVs of increased amounts of metal ion species in the

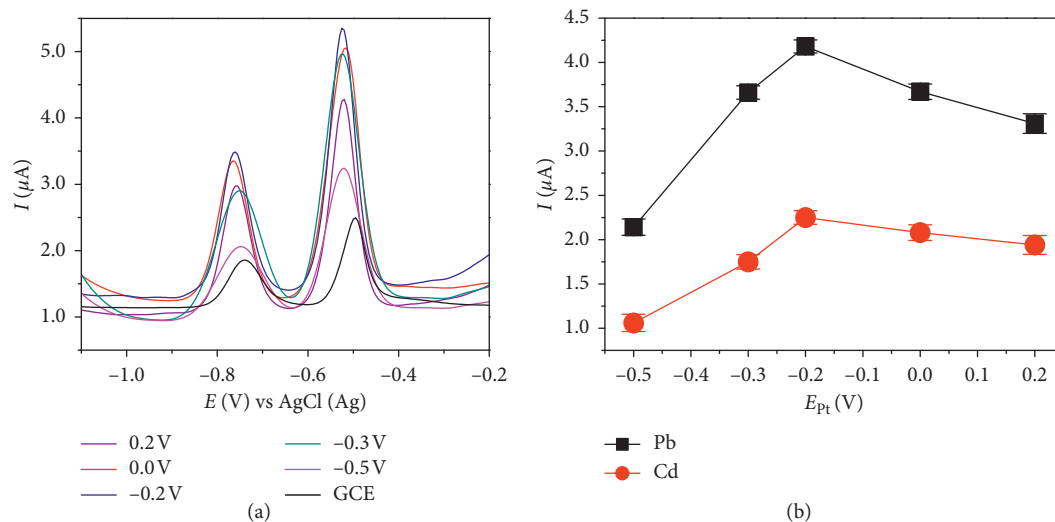


FIGURE 7: DPASVs at GCE and PtNFs/GCE prepared at different electrodeposition potentials (E_{Pt}) in acetate buffer solution pH 4.5 containing $10 \mu\text{g}\cdot\text{L}^{-1}\cdot\text{Pb}^{2+}$ and Cd^{2+} (a); the influence of E_{Pt} of electrode fabrication on peak current of Pb^{2+} and Cd^{2+} (b).

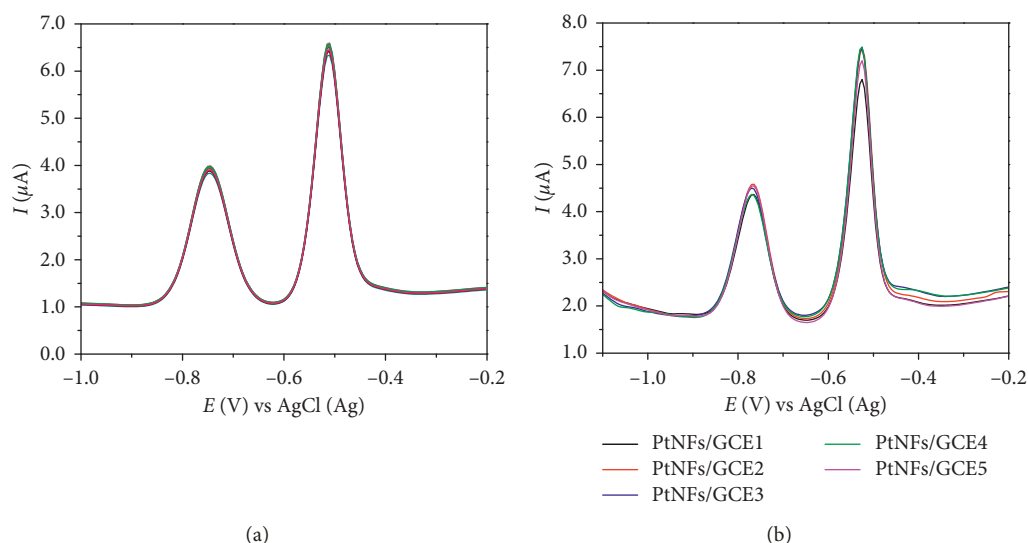


FIGURE 8: The DPASVs of $10 \mu\text{g}\cdot\text{L}^{-1}\cdot\text{Pb}^{2+}$ and Cd^{2+} in acetate buffer (pH 4.5) at one PtNFs/GCE with ten successive measurements (a) and at five different electrodes (b).

concentration range of $1\text{--}100 \mu\text{g}\cdot\text{L}^{-1}$ are illustrated in Figure 9(a). The corresponding calibration curves are shown in Figures 9(b) and 9(c) for lead and cadmium ions, respectively. Each point on these curves is an averaged value of three repeated measurements. The correlation equations were $I = (1.754 \pm 0.479) + (0.366 \pm 0.0095) C$ with a correlation coefficient of 0.998 for Pb^{2+} and $I = (0.463 \pm 0.302) + (0.203 \pm 0.006) C$ with a correlation coefficient of 0.997 for Cd^{2+} , where C is the concentration of metal ions ($\mu\text{g}\cdot\text{L}^{-1}$) and I is the peak current (μA). The detection limits of 0.408 and $0.453 \mu\text{g}\cdot\text{L}^{-1}$ of Pb^{2+} and Cd^{2+} were estimated from 10 replicate determination of blank solution under optimum conditions, respectively. The comparison results of the proposed sensor with previously reported voltammetric procedures for lead and cadmium

ions determination are presented in Table 1. This compares the sensing characteristics such as the linear range and the detection limit of some developed platforms based on different modified electrode materials. The limit of detection (LOD) of this our electrode is much lower than that of some sensors reported in Table 1. The results confirm that the proposed sensor had an acceptable utility for the simultaneous detection of Pb^{2+} and Cd^{2+} with high sensitivity and accuracy, low cost, and fast and simple operation.

4. Conclusions

Electrodeposition of platinum nanoflowers on GC electrodes was achieved by controlling the electrochemical

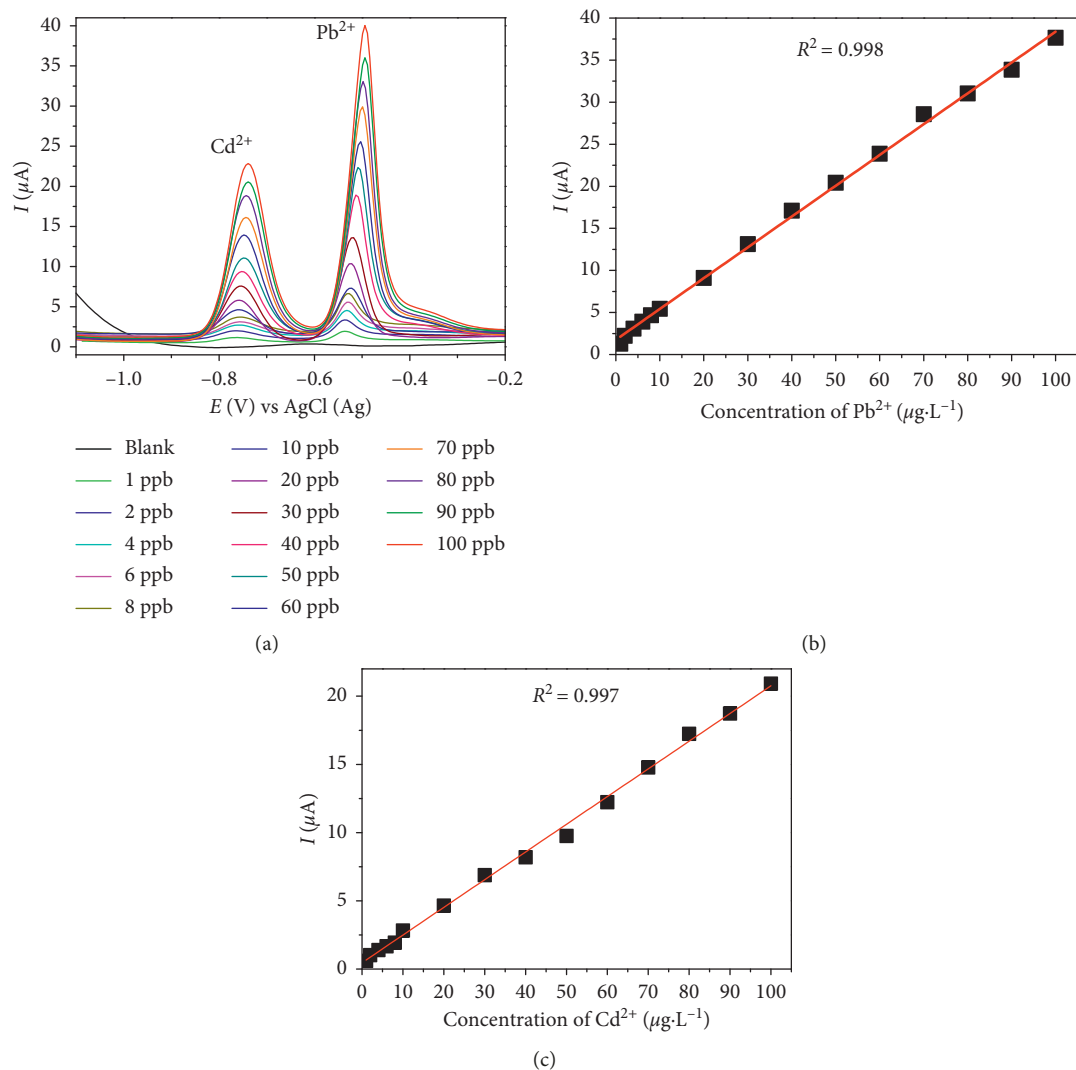


FIGURE 9: DPASVs at different concentrations of Pb^{2+} and Cd^{2+} ions at the PtNFs/GCE (a) and relationship between Pb^{2+} and Cd^{2+} concentrations with corresponding peak currents (b, c).

TABLE 1: Comparison of the proposed sensor with other reported methods.

Electrodes	Linear range ($\mu g \cdot L^{-1}$)		Detection limit ($\mu g \cdot L^{-1}$)		Reference
	Pb^{2+}	Cd^{2+}	Pb^{2+}	Cd^{2+}	
ZnFe ₂ O ₄ /GCE	10–130	10–130	0.6	1.3	[33]
Polyaniline/GCE	0–414	0–224	20.7	14.6	[34]
CB-15-crown-5/GCE	10.9–186.5	15.7–191.1	3.3	4.7	[35]
GSH@Fe ₃ O ₄	0.5–100	0.5–100	0.2	0.2	[1]
Sb-BDDE	50–500	100–500	25.4	38.1	[36]
PtNFs/GCE	1–100	1–100	0.4	0.5	This work

GCE: glassy carbon electrode; CB-15-crown-5: 4-carboxybenzo-15-crown-5; GSH@Fe₃O₄: glutathione functionalized magnetic nanocomposite; Sb-BDDE: antimony nanoparticle-modified boron-doped diamond electrode.

deposition time and potential. Our results show that the total active surface area of Pt, as well as density and surface construction, can be controlled by adjusting deposition conditions. The composition and the microstructure of the modified PtNFs/GCE were characterized by XRD, EDX, SEM, and AFM techniques. Application of PtNFs/GCEs for

the simultaneous electrochemical determination of Pb^{2+} and Cd^{2+} is reported for the first time. The proposed sensor showed good analytical signal response and exhibited very low detection limits of 0.408 and 0.453 $\mu g \cdot L^{-1}$ for Pb^{2+} and Cd^{2+} , respectively. The RSD of reproducibility of the PtNFs/GCE of 4.36% for Cd^{2+} and 4.65% for Pb^{2+} demonstrated

that the PtNFs/GCE is stable in sensing Cd^{2+} and Pb^{2+} and the procedure of preparation of PtNFs/GCE is reliable.

Data Availability

The data used to support the findings of this study are available from the corresponding author upon request.

Conflicts of Interest

The authors declare that there are no conflicts of interest regarding the publication of this paper.

Acknowledgments

This work was financially supported by Quy Nhon University, Vietnam, under grant no. T2018.557.06.

Supplementary Materials

Platinum nanoflowers modified glassy carbon electrodes (PtNFs/GCE) was prepared by electrodeposition. The modified electrodes have been characterized by EDX, SEM and AFM techniques to confirm chemical and physical properties. The electrochemical properties of PtNFs/GCE were investigated by cyclic voltammetry method (CV). Application of PtNFs/GCE for the simultaneous electrochemical determination of Pb and Cd were performed by anodic stripping voltammetry method (ASV). (*Supplementary Materials*)

References

- [1] M. Baghayeri, A. Amiri, B. Maleki, Z. Alizadeh, and O. Reiser, "A simple approach for simultaneous detection of cadmium(II) and lead(II) based on glutathione coated magnetic nanoparticles as a highly selective electrochemical probe," *Sensors and Actuators B: Chemical*, vol. 273, pp. 1442–1450, 2018.
- [2] A. Kawde, A. Ismail, A. R. Al-betar, and O. Muraza, "Microporous and mesoporous materials novel ce-incorporated zeolite modified-carbon paste electrode for simultaneous trace electroanalysis of lead and cadmium," *Microporous and Mesoporous Materials*, vol. 243, pp. 1–8, 2017.
- [3] J. E. L. Villa, R. R. A. Peixoto, and S. Cadore, "Cadmium and lead in chocolates commercialized in Brazil," *Journal of Agricultural and Food Chemistry*, vol. 62, no. 34, pp. 8759–8763, 2014.
- [4] H. Needleman, "Lead poisoning," *Annual Review of Medicine*, vol. 55, no. 1, pp. 209–222, 2004.
- [5] K. N. Dietrich, O. G. Berger, P. A. Succop, P. B. Hammond, and R. L. Bornschein, "The developmental consequences of low to moderate prenatal and postnatal lead exposure: intellectual attainment in the cincinnati lead study cohort following school entry," *Neurotoxicology and Teratology*, vol. 15, no. 1, pp. 37–44, 1993.
- [6] D.-D. La, C. K. Kim, T. S. Jun et al., "Pt nanoparticle-supported multiwall carbon nanotube electrodes for amperometric hydrogen detection," *Sensors and Actuators B: Chemical*, vol. 155, no. 1, pp. 191–198, 2011.
- [7] B. C. Han, C. R. Miranda, and G. Ceder, "Effect of particle size and surface structure on adsorption of O and OH on platinum nanoparticles: a first-principles study," *Physical Review B*, vol. 77, article 075410, pp. 1–9, 2008.
- [8] V. Komanicky, H. Iddir, K.-C. Chang et al., "Fabrication and characterization of platinum nanoparticle arrays of controlled size, shape and orientation," *Electrochimica Acta*, vol. 55, no. 27, pp. 7934–7938, 2010.
- [9] T. Bru, "Catalytic activity of platinum nanoparticles on highly boron-doped and 100-oriented epitaxial diamond towards HER and HOR," *Physical Chemistry Chemical Physics*, vol. 13, no. 28, pp. 12883–12891, 2011.
- [10] E. Society and K. Kinoshita, "Particle size effects for oxygen reduction on highly dispersed platinum in acid electrolytes," *Journal of Electrochemical Society*, vol. 137, no. 3, pp. 845–848, 1990.
- [11] J. Clausmeyer and W. Schuhmann, "Nanoelectrodes: applications in electrocatalysis, single-cell analysis and high-resolution electrochemical imaging," *TrAC Trends in Analytical Chemistry*, vol. 79, pp. 46–59, 2016.
- [12] L. Su, W. Jia, L. Zhang, C. Beacham, H. Zhang, and Y. Lei, "Facile synthesis of a platinum nanoflower monolayer on a single-walled carbon nanotube membrane and its application in glucose detection," *Journal of Physical Chemistry C*, vol. 114, no. 42, pp. 18121–18125, 2010.
- [13] Y.-J. Lee and J.-Y. Park, "Nonenzymatic free-cholesterol detection via a modified highly sensitive macroporous gold electrode with platinum nanoparticles," *Biosensors and Bioelectronics*, vol. 26, no. 4, pp. 1353–1358, 2010.
- [14] X. Wang, L. Li, Z. Li, J. Wang, H. Fu, and Z. Chen, "Determination of ascorbic acid in individual liver cancer cells by capillary electrophoresis with a platinum nanoparticles modified electrode," *Journal of Electroanalytical Chemistry*, vol. 712, pp. 139–145, 2014.
- [15] Z. Dursun and B. Gelmez, "Simultaneous determination of ascorbic acid, dopamine and uric acid at Pt nanoparticles decorated multiwall carbon nanotubes modified GCE," *Electroanalysis*, vol. 22, no. 10, pp. 1106–1114, 2010.
- [16] M. Douliche, N. K. Bakirhan, B. Uslu, B. Saidat, M. Trari, and S. A. Ozkan, "Simple and sensitive adsorptive stripping voltammetric assay of granisetron from its dosage form by platinum nanoparticles modified electrodes," *Sensors and Actuators B: Chemical*, vol. 251, pp. 572–582, 2017.
- [17] J.-H. Yoon, G. Muthuraman, J. Yang, Y.-B. Shim, and M.-S. Won, "Pt-nanoparticle incorporated carbon paste electrode for the determination of Cu(II) ion by anodic stripping voltammetry," *Electroanalysis*, vol. 19, no. 11, pp. 1160–1166, 2007.
- [18] N. Tian, Z. Zhou, S. Sun, L. Cui, B. Ren, and Z. Tian, "Electrochemical preparation of platinum nano thorn assemblies Raman scattering activity with high surface enhanced," *Chemical Communications*, vol. 39, no. 39, pp. 4090–4092, 2006.
- [19] X. Chen, B. Su, G. Wu et al., "Platinum nanoflowers supported on graphene oxide nanosheets: their green synthesis, growth mechanism, and advanced electrocatalytic properties for methanol oxidation," *Journal of Materials Chemistry*, vol. 22, no. 22, pp. 11284–11289, 2012.
- [20] Y. Zhang, Z. Shao, Q. Shen, M. Li, L. Xu, and Z. Luo, "Aqueous preparation of platinum nanoflowers on three-dimensional graphene for efficient methanol oxidation," *Catalysts*, vol. 8, no. 11, p. 519, 2018.
- [21] R.-X. Wang, J.-J. Fan, Y.-J. Fan et al., "Platinum nanoparticles on porphyrin functionalized graphene nanosheets as a superior catalyst for methanol electrooxidation," *Nanoscale*, vol. 6, no. 24, pp. 14999–15007, 2014.

- [22] G. A. El-Nagar, A. M. Mohammad, and M. S. El-deab, "Acrylonitrile-contamination induced enhancement of formic acid electro-oxidation at platinum nanoparticles modified glassy carbon electrodes," *Journal of Power Sources*, vol. 265, pp. 57–61, 2014.
- [23] A. Tabet-Aoul and M. Mohamedi, "Interrelated functionalities of hierarchically CNT/CeO₂/Pt nanostructured layers: synthesis, characterization, and electroactivity," *Physical Chemistry Chemical Physics*, vol. 14, no. 13, p. 4463, 2012.
- [24] S. V. Doronin, R. A. Manzhos, A. G. Krivenko, and A. P. Manzhos, "Electron transfer kinetics of the ferrous/ferric redox system on the platinum deposits on gold," *Journal of Electroanalytical Chemistry*, vol. 784, pp. 140–144, 2017.
- [25] P. K. Kalambate and A. K. Srivastava, "Simultaneous voltammetric determination of paracetamol, cetirizine and phenylephrine using a multiwalled carbon nanotube-platinum nanoparticles nanocomposite modified carbon paste electrode," *Sensors and Actuators B: Chemical*, vol. 233, pp. 237–248, 2016.
- [26] S. Kim, Y. Jung, and S.-J. Park, "Catalytic activity of electrically deposited platinum nanoparticle catalysts on graphite nanofibers," *Colloids and Surfaces A: Physicochemical and Engineering Aspects*, vol. 313–314, pp. 220–223, 2008.
- [27] E. Proniewicz, B. Gralec, T. K. Olszewski, and B. Boduszek, "Aqueous platinum nanoparticles solution for the detection of pyridine derivatives of aminophosphinic acid. Influence of positional isomerism," *Applied Surface Science*, vol. 425, pp. 941–947, 2017.
- [28] A. Kumaravel and M. Chandrasekaran, "Nanosilver/surfactant modified glassy carbon electrode for the sensing of thiamethoxam," *Sensors and Actuators B: Chemical*, vol. 174, pp. 380–388, 2012.
- [29] J. Wang, *Analytical Electrochemistry*, John Wiley & Sons, New York, NY, USA, 43rd edition, 2006.
- [30] A. Gamero-quijano, F. Huerta, D. Salinas-torres, E. Morallón, and F. Montilla, "Electrocatalytic performance of SiO₂-SWCNT nanocomposites prepared by electroassisted deposition," *Electrocatalysis*, vol. 4, no. 4, pp. 259–266, 2013.
- [31] T. N. Huan, T. Ganesh, K. S. Kim, S. Kim, S.-H. Han, and H. Chung, "A three-dimensional gold nanodendrite network porous structure and its application for an electrochemical sensing," *Biosensors and Bioelectronics*, vol. 27, no. 1, pp. 183–186, 2011.
- [32] I. Švancara, C. Prior, S. B. Hočevár, and J. Wang, "A decade with bismuth-based electrodes in electroanalysis," *Electroanalysis*, vol. 22, no. 13, pp. 1405–1420, 2010.
- [33] N. S. Arun Kumar, S. Ashoka, and P. Malingappa, "Nano zinc ferrite modified electrode as a novel electrochemical sensing platform in simultaneous measurement of trace level lead and cadmium," *Journal of Environmental Chemical Engineering*, vol. 6, no. 6, 2018.
- [34] Z. Wang, E. Liu, and X. Zhao, "Glassy carbon electrode modified by conductive polyaniline coating for determination of trace lead and cadmium ions in acetate buffer solution," *Thin Solid Films*, vol. 519, no. 15, pp. 5285–5289, 2011.
- [35] N. Serrano, A. González-Calabuig, and M. del Valle, "Crown ether-modified electrodes for the simultaneous stripping voltammetric determination of Cd(II), Pb(II) and Cu(II)," *Talanta*, vol. 138, pp. 130–137, 2015.
- [36] K. E. Toghill, L. Xiao, G. G. Wildgoose, and R. G. Compton, "Electroanalytical determination of cadmium(II) and lead(II) using an antimony nanoparticle modified boron-doped diamond electrode," *Electroanalysis*, vol. 21, no. 10, pp. 1113–1118, 2009.

Research Article

An Initial Evaluation on the Adsorption of SO₂ and NO₂ over Porous Fe₃O₄ Nanoparticles Synthesized by Facile Scalable Method

Xuan-Manh Pham ¹, Duy Linh Pham ¹, Nguyen Thi Hanh ^{1,2}, Tuyet Anh Dang Thi ^{1,2},
Le Nhat Thuy Giang ^{1,2}, Hoang Thi Phuong ¹, Nguyen Tuan Anh ¹, Hac Thi Nhung ^{1,2},
Giang Trung Le,¹ Mai Ha Hoang ^{1,2} and Tuyen Van Nguyen ^{1,2}

¹Institute of Chemistry, Vietnam Academy of Science and Technology, 18 Hoang Quoc Viet, Cau Giay, Hanoi, Vietnam

²Graduate University of Science and Technology, Vietnam Academy of Science and Technology, 18 Hoang Quoc Viet, Cau Giay, Hanoi, Vietnam

Correspondence should be addressed to Mai Ha Hoang; hoangmaiha@ich.vast.vn and Tuyen Van Nguyen; ngvtuyen@hotmail.com

Received 13 March 2019; Revised 24 April 2019; Accepted 9 May 2019; Published 12 June 2019

Guest Editor: Van Duong Dao

Copyright © 2019 Xuan-Manh Pham et al. This is an open access article distributed under the Creative Commons Attribution License, which permits unrestricted use, distribution, and reproduction in any medium, provided the original work is properly cited.

In this study, Fe₃O₄ nanoparticles used as an adsorbent for the removal of toxic gases were successfully synthesized via the facile coprecipitation method. The Fe₃O₄ nanoparticles displayed a well-defined morphology with the size of ~10 nm and a porous structure with a specific area of 115.90 m²/g and a wide range of pore sizes. These nanoparticles exhibited effective adsorption abilities upon the exposure to toxic gases. In particular, the amount of 40.5 mg SO₂ and 108.5 mg NO₂ was adsorbed in 1 g of Fe₃O₄ nanoparticles after 60 minutes of exposure, making the Fe₃O₄ nanoparticles become a promising adsorbent for the removal of toxic gases.

1. Introduction

Toxic gases that are present during the fires are one of the main causes of fire deaths [1]. Depending on the materials that are burning, some kind of different toxic gases might be produced. These gases may include carbon monoxide (CO), nitrogen dioxide (NO₂), sulfur dioxide (SO₂), and hydrogen cyanide (HCN) [2]. They prevent cellular respiration, leading these cells to death or causing irritation, and are toxic for the body, at a higher level causing death quickly [3]. In addition to carbon monoxide, the main agent of deaths in the fire, nitrogen dioxide and sulfur dioxide are also known as dangerous agents for the humans' life. Hence, the removal of these gases from the fire is necessary to protect humans. Nanoparticle powders with a large specific surface area have been proposed for adsorption and cleaning up of fumes and toxic gases generated in fires [4]. The hydroxide, carbonate,

bicarbonate, and oxides of metal have attracted wide attention for that because they can be decomposed to CO₂ and H₂O to extinguish the fire or can be resistant to the fire flame improving the isolating ability of flammable materials with fire and oxygen [5–8]. Among them, the Fe₃O₄ nanostructured material is a potential candidate due to its stability, high surface area, and easy synthesis [9]. Some researchers have pointed out that Fe₃O₄ can be an efficient adsorbent for the removal of heavy metal ions [9–11] and inorganic anions [12] from aqueous solutions. However, there have been very few reports using Fe₃O₄ as an adsorbent for the removal of nitrogen dioxide and sulfur dioxide.

The removal of SO₂ and NO₂ has been also investigated in the field of environment because the amount of these gases released in atmosphere can induce acid rain which is harmful to humans [13, 14]. Active carbon has been known as an effective adsorbent in processes of removing stack

gases [15]. Nevertheless, it is difficult to apply active carbon for the removal of SO₂ and NO₂ in fires due to its flammable nature.

In this work, Fe₃O₄ nanoparticles were prepared by a facile scalable method and applied as an adsorbent for the adsorption of NO₂ and SO₂. The material was characterized by a number of analytical techniques. The Fe₃O₄ nanoparticles exhibited good adsorption abilities in the removal of SO₂ and NO₂.

2. Experimental Section

2.1. Synthesis of Fe₃O₄ Nanoparticles. All chemicals were of analytical grade. Iron(III) chloride hexahydrate (FeCl₃·6H₂O), iron(II) chloride tetrahydrate (FeCl₂·4H₂O), ammonia solution 25% (NH₃·H₂O), sulfur dioxide (99.9%), nitrogen dioxide (99.5%), and nitrogen (99.999%) were purchased from Sigma-Aldrich and used without any further purification. The magnetite (Fe₃O₄) nanoparticles were prepared by the following coprecipitation method [16–18].

In brief, FeCl₃·6H₂O (0.05 mol, 13.52 g) and FeCl₂·4H₂O (0.03 mol, 5.96 g) were dissolved in 100 mL DI water with a Fe²⁺/Fe³⁺ molar ratio of 0.6. Then, the ammonium solution was added dropwise into the solution until pH = 11.0 over a period of 2 h, under vigorous stirring to achieve Fe₃O₄ nanoparticles with high purity. The obtained precipitate was filtered, washed with DI water, and dried in vacuum at 60°C for 24 h.

2.2. Material Characterization. The specific surface area was determined from N₂ adsorption/desorption at 77 K by the Brunauer–Emmett–Teller (BET) method using a Micromeritics surface area analyzer (TriStar II Plus, Micromeritics Instrument Corp, USA). The morphology and particle size were determined by field emission scanning electron microscope (FE-SEM, S-4800, Hitachi, Japan) and particle-size distribution measurement (Litesizer™ 500, Anton Paar Instrument Co. Ltd., Austria). The structure of adsorbents was characterized by high-resolution XRD (D/max Ultima III, Rigaku, Japan). The thermogravimetric analysis (TGA) was determined on TGA-50, Shimadzu, Japan, in an air atmosphere with a heating rate of 5°C·min⁻¹ from room temperature to 700°C. Temperature-programmed reduction (TPR) was carried out under 5% CO in Ar flow (100 cc/min) at a heating rate of 10°C/min, from room temperature to about 900°C using AutoChem™ II 2920 (Micromeritics Instrument Corp, USA).

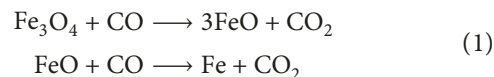
2.3. Adsorption Experiments. For the adsorption study, 1 g of Fe₃O₄ nanoparticles were exposed to dried SO₂ and NO₂ at a particular time in the fixed bed reactor under ambient temperature. These gases were mixed with nitrogen as a carrier gas (5% SO₂ or NO₂ in the N₂ atmosphere). The Fe₃O₄ nanoparticles were pretreated under an Ar flow at 400°C during 2 h and then cooled to the room temperature. After that, the gas stream was supplied with a flow rate of 200 cc/min. The uptake quantities were recorded as a function of time based on a mass change of samples. The

presence of the gas phase in contact with the materials was monitored by the FTIR measurement (Thermo Fisher, USA) at 8 cm⁻¹ resolution. In addition, energy-dispersive X-ray spectroscopy (SEM-EDX) (HORIBA-EMAX80; Hitachi High-Technology) was used to evaluate the presence as well as the adsorbed quantity of SO₂ and NO₂.

3. Results and Discussion

3.1. Characterization of Fe₃O₄ Nanoparticles. The porous, interconnected Fe₃O₄ nanoparticles were synthesized using a facile scalable method. The mixture solution of FeCl₃ and FeCl₂ was prepared with a Fe²⁺/Fe³⁺ molar ratio of 0.6. The used Fe²⁺/Fe³⁺ molar ratio is higher than the Fe²⁺/Fe³⁺ molar ratio in Fe₃O₄ because a part of Fe²⁺ oxidized to Fe³⁺ will lead to the lower Fe²⁺/Fe³⁺ molar ratio. The increase of Fe²⁺ concentration can attain the ideal Fe²⁺/Fe³⁺ molar ratio of ~0.5. Then, the ammonium solution was added dropwise into the solution until pH = 11.0 to achieve Fe₃O₄ nanoparticles with high purity. Figure 1 shows the X-ray diffraction (XRD) patterns of the synthesized Fe₃O₄. All peaks were indexed to cubic Fe₃O₄ (JCPDS: 01-088-0315) without any impurity phase. However, γ-Fe₂O₃ has the same crystal structure and a lattice spacing as Fe₃O₄. To distinguish Fe₃O₄ from γ-Fe₂O₃, the *d* value of lattice spacing of (311) was calculated by Bragg's equation. The *d*-spacing value (311) of Fe₃O₄ was calculated to be 2.5249 Å, similar to the value of 2.52516 Å (standard cubic Fe₃O₄: 01-088-0315). As reported by Iida et al. [18], the standard *d*-spacing value (311) of γ-Fe₂O₃ is 2.5177 Å (γ-Fe₂O₃, JCPDS: 00-039-1346). It can infer that the phase of the obtained material is completely matched with the phase of the standard cubic Fe₃O₄.

Moreover, TPR_{CO} profiles of synthesized Fe₃O₄ further proved that the obtained material was pure Fe₃O₄. As shown in Figure 2, TPR_{CO} profiles illustrated two distinct peaks of the reduction process, corresponding to two-step reduction of Fe₃O₄ → FeO and FeO → Fe. There was no peak of the Fe₂O₃ → Fe₃O₄ reduction process, referring that there was no presence of Fe₂O₃ in the synthesized material. The reduction temperature of the two-step reduction was approximately 285°C (Fe₃O₄ → FeO) and 595°C (FeO → Fe). These reduction reactions can be described as follows [19–21]:



According to these reports [19–21], the reduction of Fe₃O₄ by carbon monoxide starts in the temperature range of ~509–807°C, which was higher than the reduction temperature of Fe₃O₄ in our study. The lower reaction temperature can be explained due to nanometer-sized Fe₃O₄, reacting with carbon monoxide more easily than crystalline Fe₃O₄.

The morphology of Fe₃O₄ was observed using FE-SEM. As shown in Figure 3(a), Fe₃O₄ exhibited a uniform granular shape with nanoparticles interconnected to each other. The Fe₃O₄ nanoparticles have a diameter of ~10 nm. Besides, the

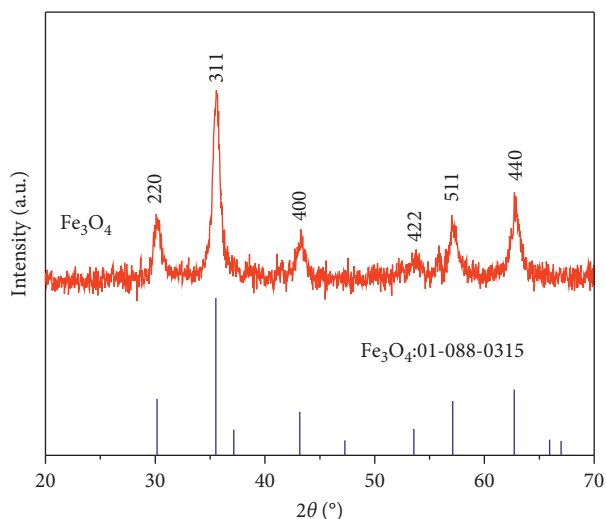


FIGURE 1: XRD patterns of synthesized Fe_3O_4 nanoparticles.

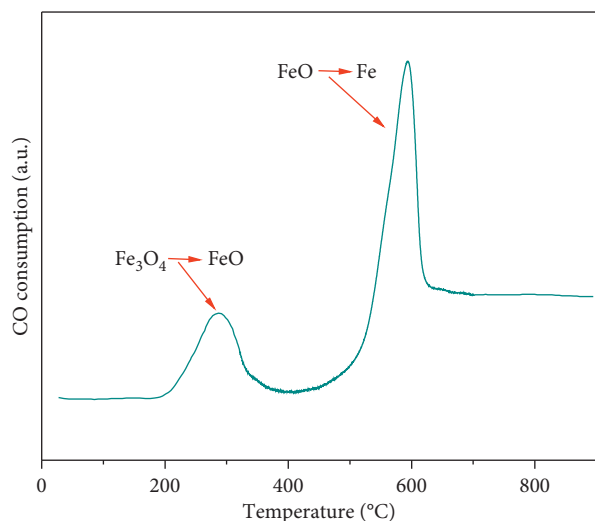
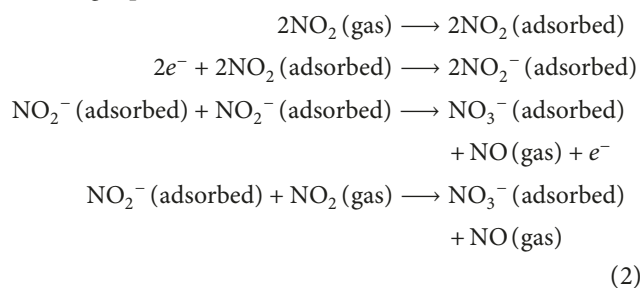


FIGURE 2: TPR_{CO} profile for Fe_3O_4 nanoparticles, a heating rate of $5^\circ\text{C}/\text{min}$.

interconnected Fe_3O_4 nanoparticles formed void spaces which intercalated among Fe_3O_4 nanoparticles as a porous structure. This unique structure plays an important role: it enables better the access of toxic gases to the inside of material, which can improve the adsorption capacity of materials [22]. Furthermore, using Scherrer's equation, the size of Fe_3O_4 particles was calculated to be ~ 9.8 nm based on the XRD results (Figure 1), suggesting the similar results between XRD and FE-SEM measurement. Figure 3(b) further affirmed the uniform of Fe_3O_4 nanoparticles with the narrow particle-size distribution and the nanosize of Fe_3O_4 [23]. The particle-size distribution of Fe_3O_4 changes from 7 to 13 nm, revealing the good uniform of Fe_3O_4 nanoparticles. The nanometer-sized Fe_3O_4 was expecting to achieve a high specific area. The porous structure of Fe_3O_4 was characterized using N_2 adsorption-desorption isotherms. As shown in Figure 3(c), isotherm adsorption of Fe_3O_4 depicted typical type-IV (multilayer adsorption) that

has a broad range of pore sizes and the Barrett-Joyner-Halenda (BJH) pore size distribution (inset) of the Fe_3O_4 . Via BET and BJH analysis, the specific area, average pore diameter, and pore volume of Fe_3O_4 were determined to be approximately $115.90 \text{ m}^2/\text{g}$, 10.63 nm , and $0.30 \text{ cm}^3/\text{g}$, respectively. The relatively high pore size of the Fe_3O_4 particles allow the access of toxic gases inside materials easily. Moreover, the large surface area can facilitate the adsorption of stack gases at the material surface/gases interface [24]. The TGA has proceeded in an air atmosphere with a heating rate of $5^\circ\text{C}/\text{min}$ from room temperature to 700°C to evaluate the purity of Fe_3O_4 materials again, as shown in Figure 3(d). The weight gain near 100°C was attributed to the oxidation of Fe_3O_4 to $\gamma\text{-Fe}_2\text{O}_3$. Interestingly, the oxidation temperature in our study is lower than the previous study [25]. This behaviour might be due to the high surface area of the nanometer-sized Fe_3O_4 , making them react with oxygen more easily than crystalline Fe_3O_4 . Nevertheless, the temperature near 100°C was also the evaporation temperature of moisture from the sample. Because the loss weight owing to the removal of moisture was lower than the weight gain due to the oxidation, the mass change in TG data just shows the mass gain. The content of moisture and Fe_3O_4 in the obtained sample was estimated to be 2.21 and 97.79%, respectively (Figure 3(d)).

3.2. Adsorption Ability of Fe_3O_4 Nanoparticles. Figure 4 shows the adsorption abilities of Fe_3O_4 after exposing to NO_2 in conditions of the study. As shown in Figure 4(a), the intensities of the IR features after 15 minutes exposure to NO_2 start to change, suggesting that the amount of NO_2 was adsorbed on the surface of Fe_3O_4 . The adsorption of NO_2 at room temperature leads to an intensity increase of the 1386 cm^{-1} band, corresponding to the band of nitrate (NO_3^-) [26]. The adsorption mechanism of NO_2 on the Fe_3O_4 surface was reported by Eltouny et al. [27] via the following equations:



The intensity of this peak increases as the time exposing to NO_2 gas increases, suggesting that the larger amount of NO_2 was adsorbed. The uptake of NO_2 by the Fe_3O_4 nanoparticles was shown in Figure 4(b). The amount of NO_2 adsorbed by the Fe_3O_4 reached the saturation level after 60 minutes of exposure. The mass of NO_2 adsorbed by the Fe_3O_4 after 60 minutes of exposure was recorded at $108.5 \text{ mg}/\text{g}$ of Fe_3O_4 . The high adsorption values of the Fe_3O_4 sample were owing to its larger pore volume and high surface area. Furthermore, the presence and mass of NO_2 in the Fe_3O_4 sample were also measured by SEM-EDX

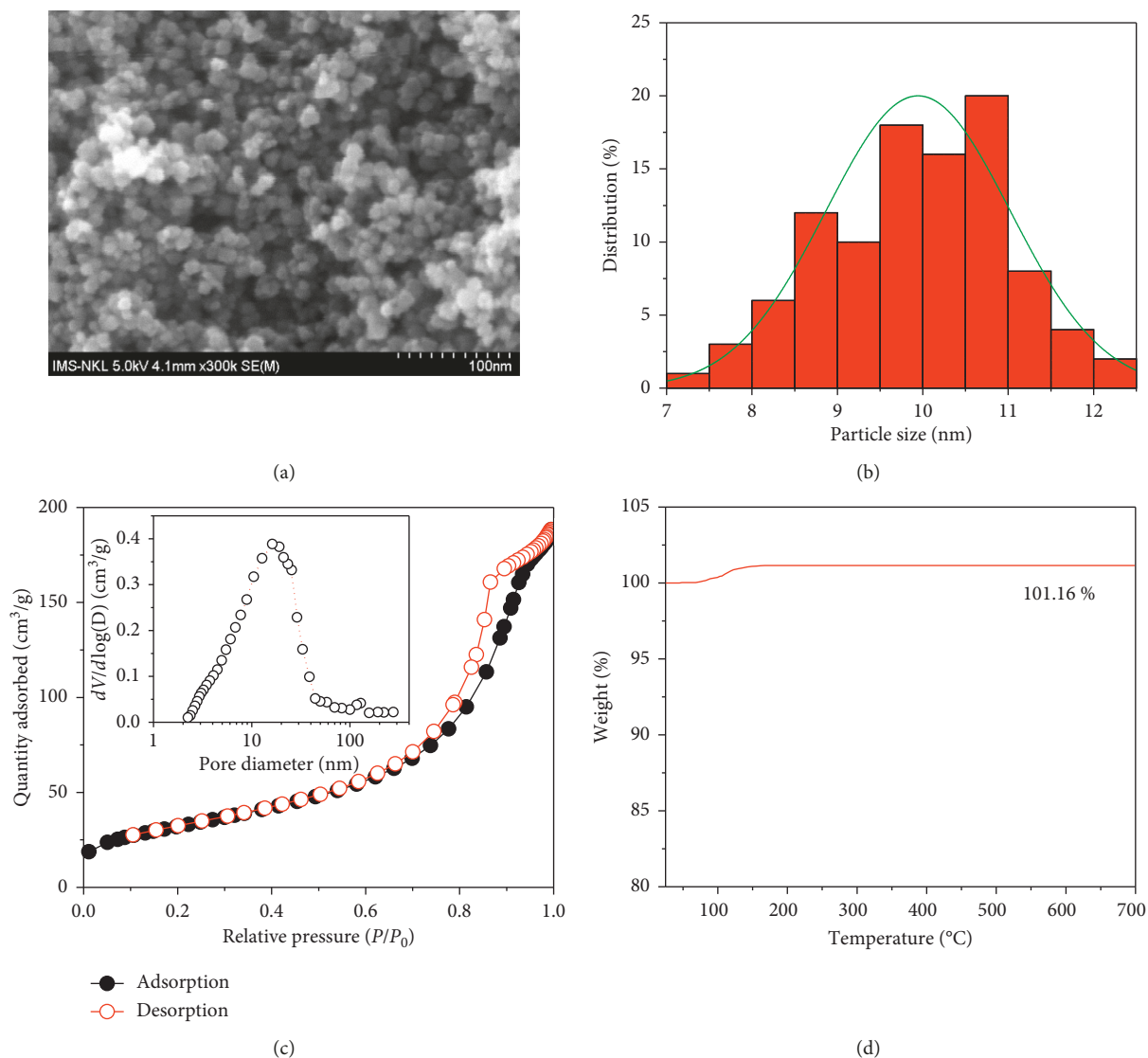
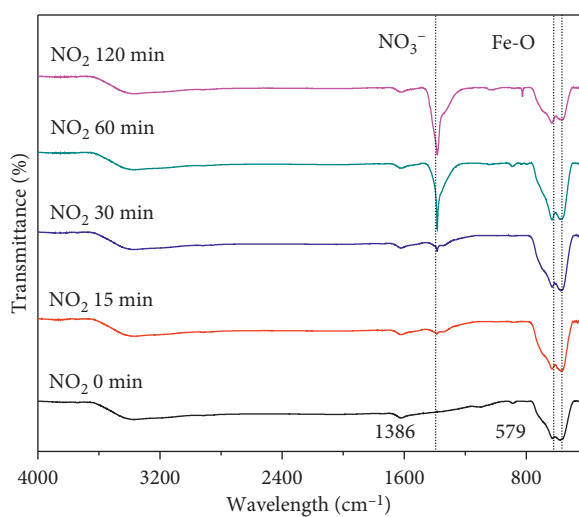


FIGURE 3: (a) FE-SEM image; (b) particle-size distribution; (c) N_2 adsorption/desorption isotherms; (d) thermogravimetric analysis (TGA) of synthesized Fe_3O_4 . Inset in Figure 3(c) shows the pore size distribution calculated from the Barrett-Joyner-Halenda (BJH) formula of synthesized Fe_3O_4 .

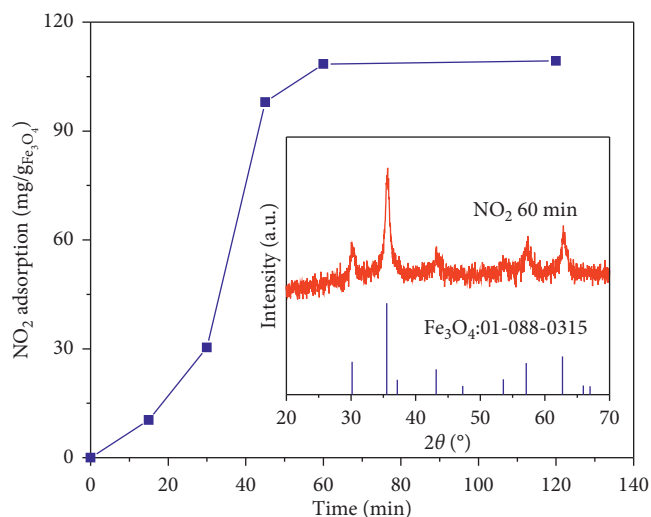
analysis. As shown in Figure 4(c), the signal of N, Fe, and O elements was detected in the Fe_3O_4 sample exposing to NO_2 after 60 minutes. Based on the intensity of the N element in the sample, %wt. NO_2 in the sample can be, respectively, calculated to be ~ 9.79 %wt., corresponding to the NO_2 adsorption of ~ 108.6 mg/g of Fe_3O_4 . This result was similar to the adsorption mass of NO_2 by the Fe_3O_4 in Figure 4(b). The morphology of the Fe_3O_4 sample after 60 minutes of exposure to NO_2 was analyzed using the FE-SEM measurement. There was no change in the morphology of Fe_3O_4 nanoparticles before (Figure 3(a)) and after (Figure 4(d)) exposing to the NO_2 gas environment, referring to the stable structure of the Fe_3O_4 sample. Furthermore, the XRD pattern of Fe_3O_4 after exposing with NO_2 (Figure 4(b) inset) did not show any change, compared with the XRD pattern of Fe_3O_4 (Figure 1). The good stable structure can retain the adsorption ability after the

regeneration and repeating the NO_2/Fe_3O_4 adsorption many times.

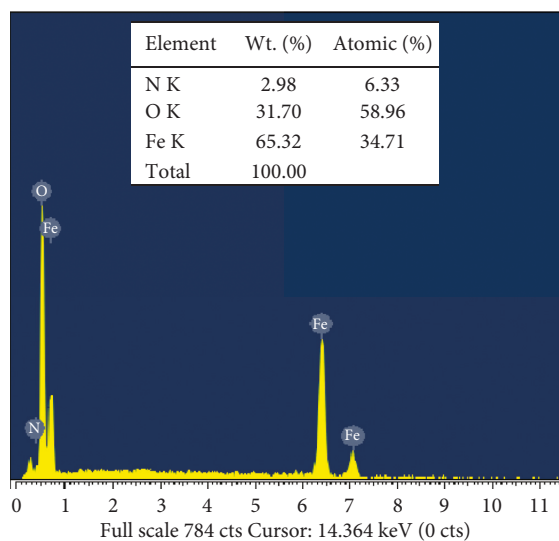
The adsorption abilities of Fe_3O_4 were further examined with the SO_2 gas. Figure 5 shows the adsorption ability of Fe_3O_4 with SO_2 . Figure 5(a) shows the FTIR spectra obtained after exposing the Fe_3O_4 sample to SO_2 at different times. The signal at the band of ~ 1400 and ~ 1120 cm^{-1} , corresponding to the species of physical adsorption of SO_2 , was detected [15]. However, the intensities of SO_2 species were low, suggesting that the small amount of SO_2 was adsorbed on the surface of the Fe_3O_4 sample. The adsorbed amount of SO_2 was displayed in Figure 5(b). The mass of SO_2 adsorbed by the Fe_3O_4 at the saturation level after 60 minutes of exposure. Moreover, the presence and the adsorption mass of SO_2 in the Fe_3O_4 sample was evaluated by SEM-EDX analysis (Figure 5(c)). The signal of the S element was found to be



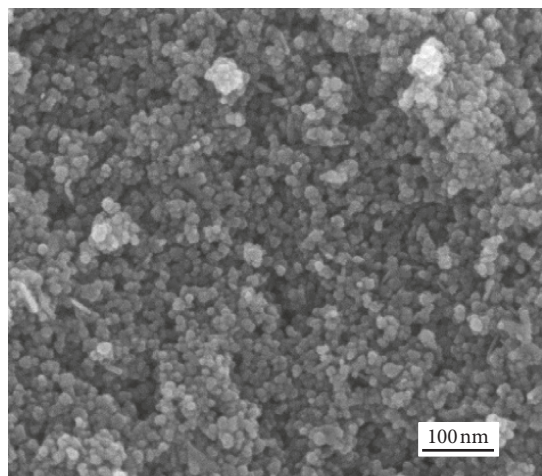
(a)



(b)

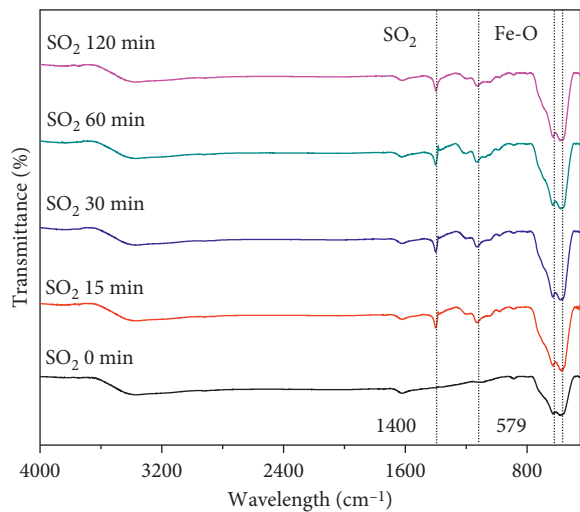


(c)

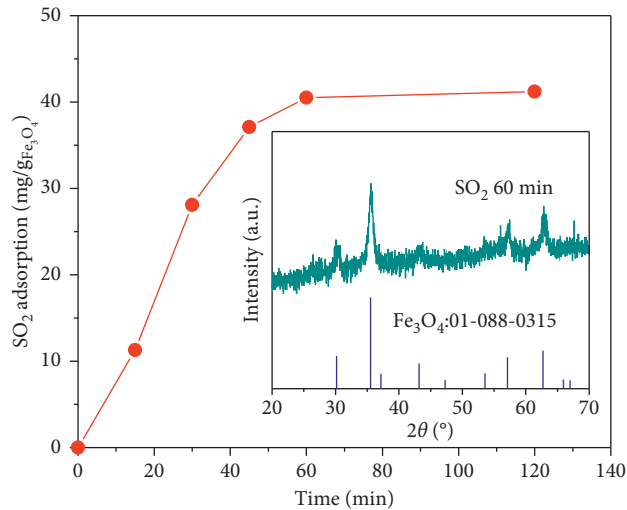


(d)

FIGURE 4: (a) FTIR of Fe_3O_4 samples after exposing to NO_2 gas at the particular time; (b) NO_2 adsorption on Fe_3O_4 samples; (c) SEM-EDX spectra; (d) FE-SEM image of Fe_3O_4 after 60 min of exposure to NO_2 . Inset in Figure 4(b) shows the XRD pattern of Fe_3O_4 after 60 min of exposure to NO_2 .



(a)



(b)

FIGURE 5: Continued.

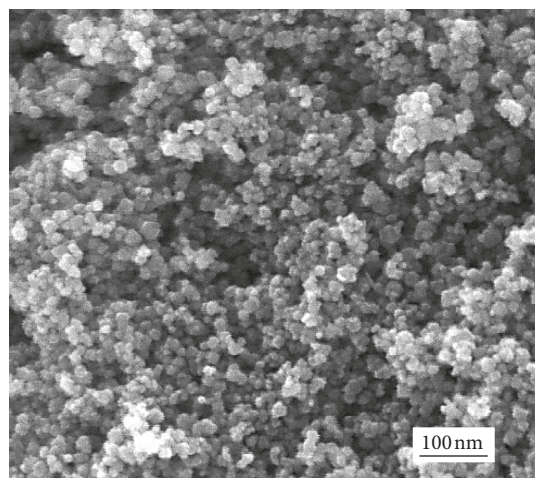
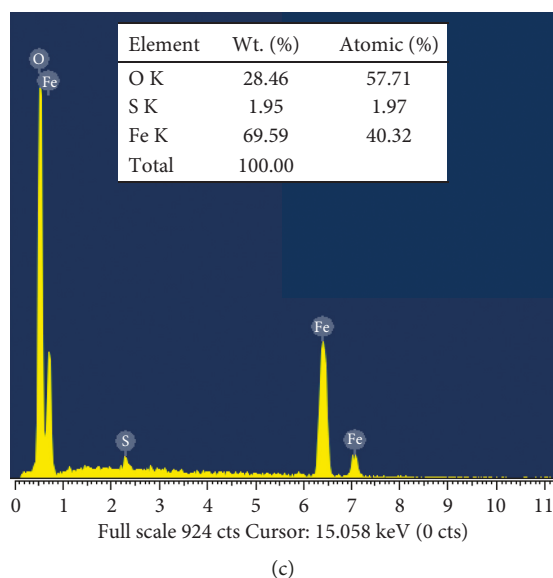


FIGURE 5: (a) FTIR of Fe_3O_4 samples after exposing to SO_2 gas at the particular time; (b) SO_2 adsorption on Fe_3O_4 samples; (c) SEM-EDX spectra; (d) FE-SEM image of Fe_3O_4 after 60 min of exposure to SO_2 . Inset in Figure 5(b) shows the XRD pattern of Fe_3O_4 after 60 min of exposure to SO_2 .

1.95 %wt. of SO_2 in the sample, corresponding to 3.90 SO_2 %wt. in the sample after 60 minutes of exposure. This quantity was calculated to ~ 40.6 mg/g of Fe_3O_4 , similar to the obtained adsorption of Fe_3O_4 in Figure 5(b). The surface of the Fe_3O_4 sample after 60 minutes of exposure with SO_2 was analyzed using FE-SEM measurement. As shown in Figure 5(d), the highly porous structure of Fe_3O_4 was sustained, and no significant change was realized (compared with Figure 3(a)). Moreover, the phase state of Fe_3O_4 (Figure 5(b) inset) after the adsorption also remains, demonstrating the stable-phase state and porous structure. This structure was promising to be recycled and continuously adsorbs gases many times.

4. Conclusions

Fe_3O_4 nanoparticles have successfully been synthesized via the facile scalable method, in which Fe_3O_4 nanoparticles well achieved a porous structure with the high specific area and purity. The Fe_3O_4 nanoparticles exhibited good adsorption with toxic gases. The surface of the Fe_3O_4 nanoparticles adsorbed high amounts of SO_2 and NO_2 of 40.5 mg/g of Fe_3O_4 and 108.5 mg/g of Fe_3O_4 , respectively, at a saturation state after 60 minutes of exposure. The high adsorption performance was attributed to the high porosity and specific areas, which enabled the better diffusion and adsorption of toxic gases to the surface of the porous material. The resultant structure of Fe_3O_4 after exposing to the toxic gases would be the good adsorbent, which can be regenerated and adsorb gases many times.

Data Availability

The data used to support the findings of this study are available from the corresponding author upon request.

Conflicts of Interest

The authors declare that there are no conflicts of interest.

Authors' Contributions

Xuan-Manh Pham and Duy Linh Pham contributed equally to this work.

Acknowledgments

This research was funded by Vietnam Academy of Science and Technology under grant number "TĐPCCC.01/18-20."

References

- [1] S. Doroudiani, B. Doroudiani, and Z. Doroudiani, "9-Materials that release toxic fumes during fire," in *Toxicity of Building Materials*, F. Pacheco-Torgal, S. Jalali, and A. Fucic, Eds., pp. 241–282, Woodhead Publishing, Cambridge, UK, 2012.
- [2] J. Terrill, R. Montgomery, and C. Reinhardt, "Toxic gases from fires," *Science*, vol. 200, no. 4348, pp. 1343–1347, 1978.
- [3] W. D. Woolley and M. M. Raftery, "Smoke and toxicity hazards of plastics in fires," *Journal of Hazardous Materials*, vol. 1, no. 3, pp. 215–222, 1975.
- [4] B. Truchot, F. Fouillen, and S. Collet, "An experimental evaluation of toxic gas emissions from vehicle fires," *Fire Safety Journal*, vol. 97, pp. 111–118, 2018.
- [5] T. Hatakeyama, E. Aida, T. Yokomori, R. Ohmura, and T. Ueda, "Fire extinction using carbon dioxide hydrate," *Industrial & Engineering Chemistry Research*, vol. 48, no. 8, pp. 4083–4087, 2009.
- [6] K.-Y. Li, S.-Y. Tsai, C.-P. Lin, Y.-T. Tsai, and C.-M. Shu, "Smart Technology for evaluating fire extinguishing effect of tert-butyl hydroperoxide," *Industrial and Engineering Chemistry Research*, vol. 52, no. 32, pp. 10969–10976, 2013.

- [7] S. E. Hunter, L. Li, D. Dierdorf, and T. Armendinger, "Improving water spray efficacy for fire suppression via CO₂ addition at high pressures and low temperatures: evidence for CO₂ clathrate hydrate formation," *Industrial and Engineering Chemistry Research*, vol. 45, no. 21, pp. 7275–7286, 2006.
- [8] J.-M. Hsu, M.-S. Su, C.-Y. Huang, and Y.-S. Duh, "Calorimetric studies and lessons on fires and explosions of a chemical plant producing CHP and DCPO," *Journal of Hazardous Materials*, vol. 217–218, pp. 19–28, 2012.
- [9] Y. Lu, J. Yu, and S. Cheng, "Magnetic composite of Fe₃O₄ and activated carbon as a adsorbent for separation of trace Sr(II) from radioactive wastewater," *Journal of Radioanalytical and Nuclear Chemistry*, vol. 303, no. 3, pp. 2371–2377, 2015.
- [10] A. A. Mohammed and I. a. S. Samaka, "Bentonite coated with magnetite Fe₃O₄ nanoparticles as a novel adsorbent for copper (II) ions removal from water/wastewater," *Environmental Technology and Innovation*, vol. 10, pp. 162–174, 2018.
- [11] S. L. Iconaru, R. Guégan, C. L. Popa, M. Motelica-Heino, C. S. Ciobanu, and D. Predoi, "Magnetite (Fe₃O₄) nanoparticles as adsorbents for as and Cu removal," *Applied Clay Science*, vol. 134, pp. 128–135, 2016.
- [12] L. Chai, Y. Wang, N. Zhao, W. Yang, and X. You, "Sulfate-doped Fe₃O₄/Al₂O₃ nanoparticles as a novel adsorbent for fluoride removal from drinking water," *Water Research*, vol. 47, no. 12, pp. 4040–4049, 2013.
- [13] J. N. Armor, "Catalytic solutions to reduce pollutants," *Catalysis Today*, vol. 38, no. 2, pp. 163–167, 1997.
- [14] E. Raymundo-Piñero, D. Cazorla-Amorós, and A. Linares-Solano, "Temperature programmed desorption study on the mechanism of SO₂ oxidation by activated carbon and activated carbon fibres," *Carbon*, vol. 39, no. 2, pp. 231–242, 2001.
- [15] J. Zawadzki and M. Wiśniewski, "An infrared study of the behavior of SO₂ and NO_x over carbon and carbon-supported catalysts," *Catalysis Today*, vol. 119, no. 1–4, pp. 213–218, 2007.
- [16] M. R. Ghazanfari, M. Kashefi, S. F. Shams, and M. R. Jaafari, "Perspective of Fe₃O₄ nanoparticles role in biomedical applications," *Biochemistry Research International*, vol. 2016, Article ID 7840161, 32 pages, 2016.
- [17] S. Wu, A. Sun, F. Zhai et al., "Fe₃O₄ magnetic nanoparticles synthesis from tailings by ultrasonic chemical co-precipitation," *Materials Letters*, vol. 65, no. 12, pp. 1882–1884, 2011.
- [18] H. Iida, K. Takayanagi, T. Nakanishi, and T. Osaka, "Synthesis of Fe₃O₄ nanoparticles with various sizes and magnetic properties by controlled hydrolysis," *Journal of Colloid and Interface Science*, vol. 314, no. 1, pp. 274–280, 2007.
- [19] W. K. Jozwiak, E. Kaczmarek, T. P. Maniecki, W. Ignaczak, and W. Maniukiewicz, "Reduction behavior of iron oxides in hydrogen and carbon monoxide atmospheres," *Applied Catalysis A: General*, vol. 326, no. 1, pp. 17–27, 2007.
- [20] B. Hou, H. Zhang, H. Li, and Q. Zhu, "Determination of the intrinsic kinetics of iron oxide reduced by carbon monoxide in an isothermal differential micro-packed bed," *Chinese Journal of Chemical Engineering*, vol. 23, no. 6, pp. 974–980, 2015.
- [21] T. S. T. Saharuddin, F. Salleh, A. Samsuri, R. Othaman, and M. A. Yarmo, "Influence of noble metal (Ru, Os and Ag) on the reduction behaviour of iron oxide using carbon monoxide: TPR and kinetic studies," *International Journal of Chemical Engineering and Applications*, vol. 6, no. 6, pp. 405–409, 2015.
- [22] T. Jiao, L. Balan, X. Chen, and Q. Zhang, "Functionalized nanocomposites for environmental applications 2015," *Journal of Chemistry*, vol. 2015, Article ID 793265, 1 pages, 2015.
- [23] H. Meng, Z. Zhang, F. Zhao, T. Qiu, and J. Yang, "Orthogonal optimization design for preparation of Fe₃O₄ nanoparticles via chemical coprecipitation," *Applied Surface Science*, vol. 280, pp. 679–685, 2013.
- [24] T. Jiao, X. Yan, L. Balan, A. L. Stepanov, X. Chen, and M. Z. Hu, "Chemical functionalization, self-assembly, and applications of nanomaterials and nanocomposites," *Journal of Nanomaterials*, vol. 2014, Article ID 291013, 2 pages, 2014.
- [25] I. Kazeminezhad and S. Mosivand, "Phase transition of electrooxidized Fe₃O₄ to gamma and alpha-Fe₂O₃ nanoparticles using sintering treatment," *Acta Physica Polonica Series A*, vol. 125, no. 5, pp. 1210–1214, 2014.
- [26] C. Sedlmair, B. Gil, K. Seshan, A. Jentys, and J. A. Lercher, "An in situ IR study of the NO_x adsorption/reduction mechanism on modified Y zeolites," *Physical Chemistry Chemical Physics*, vol. 5, no. 9, pp. 1897–1905, 2003.
- [27] N. Eltouny and P. A. Ariya, "Competing reactions of selected atmospheric gases on Fe₃O₄ nanoparticles surfaces," *Physical Chemistry Chemical Physics*, vol. 16, no. 42, pp. 23056–23066, 2014.

Research Article

Synthesis of Acidic Heterogeneous Catalysts with High Stability Based on Graphene Oxide/Activated Carbon Composites for the Esterification of Lactic Acid

Thu Ha Thi Vu ¹, Manh Ha Nguyen ^{1,2} and Minh Dang Nguyen ¹

¹National Key Laboratory for Petrochemical and Refinery Technologies, Hanoi, Vietnam

²Faculty of Chemical Technology, Hanoi University of Industry, Hanoi, Vietnam

Correspondence should be addressed to Thu Ha Thi Vu; ptntd2004@yahoo.fr

Received 21 February 2019; Revised 3 May 2019; Accepted 21 May 2019; Published 4 June 2019

Guest Editor: Nguayen Van Noi

Copyright © 2019 Thu Ha Thi Vu et al. This is an open access article distributed under the Creative Commons Attribution License, which permits unrestricted use, distribution, and reproduction in any medium, provided the original work is properly cited.

In this article, acidic heterogeneous catalysts based on graphene oxide and sulfonated biochar were prepared, characterized, and used for lactic acid esterification to form ethyl lactate. Graphene oxide was supported on activated carbon (GO/AC) to more easily filter the catalyst from the reactants. The catalysts were characterized by such methods as XRD, FT-IR, SEM, BET, and the acid-base titration. Catalytic activity was evaluated through the esterification of lactic acid. As a result, the activity of the catalysts decreased in the following order: graphene oxide > sulfonated biochar ≈ GO/AC >> activated carbon. In addition, the GO/AC catalyst showed good stability with an unchanged yield from the 3rd to the 6th recycling test. These results suggest potential applications for new acidic heterogeneous catalysts based on graphene oxide and sulfonated biochar that could replace homogeneous acids in the future.

1. Introduction

Ethyl lactate is an ecofriendly solvent with valuable properties such as low volatility, high biodegradability, and low toxicity. Ethyl lactate is used as a “green” solvent in different fields such as organic synthesis, pharmaceuticals, coatings, printing, food, and perfume additives [1]. Ethyl lactate has many positive characteristics and can replace traditional solvents originating from petroleum.

Ethyl lactate is a product of lactic acid esterification in the presence of an acidic catalyst. Acidic homogeneous catalysts, such as H₂SO₄ and HCl, have been used for esterification. However, acidic homogeneous catalysts cannot be recycled and have to be neutralized, thereby complicating the process. To overcome their disadvantages, heterogeneous catalysts have been used in esterifications despite them having lower activity than homogeneous catalysts.

Over the years, many solid acid catalysts for lactic acid esterification such as Preysler [2], K₃PW₁₂O₄₀ [3], and Amberlyst ionic resins [4–7] have been investigated. Among

these catalysts, solid acid catalysts based on sulfonated carbon have attracted the attention of many scientists. These catalysts are synthesized by the sulfonation of carbonated products such as starch, cellulose, and glucose [8]. With the abundance of such acidic functional groups as -SO₃H and -COOH on their surface, these catalysts have been applied in esterification [9–11] and transesterification [12, 13] reactions. However, during the reaction, -SO₃H groups leach into the reactive medium, reducing catalytic activity [14].

Recently, graphene and graphene oxide (GO) have earned more attention from researchers due to their high stabilities in the liquid phase and their high resistance in the acidic medium. Moreover, many of their applications have been implemented, such as energy storage, electronic devices, optoelectronics, sensors, and catalysis [15–17]. Graphene oxide was synthesized by the oxidation of graphite forming acidic functional groups such as -SO₃H and carboxylic acid on the surface of the material. Due to these functional groups, graphene oxide has been used as an acidic catalyst in organic synthesis, such as in the cellulose

hydrolysis reaction [18]; the dehydration and etherification of fructose, xylose, and inulin [19, 20]; the etherification of HMF [21]; the esterification of levulinic acid with alcohol [22]; the esterification of glycerol and acetic acid [23]; and biodiesel synthesis [24]. The results showed that the catalytic activity of graphene oxide was good for these reactions. For example, using graphene oxide as catalyst, Wei et al. reported that the yield of forming ethyl acetate was 93.5% for esterification between acetic acid and ethanol, higher than the yield when using the homogeneous catalyst H_2SO_4 [25]. Samir Kundu and Basudeb Basu used and reused GO as a catalyst for 2-aminopyridine, acetophenone, and thiophenol synthesis. The conversion was quite stable with a value of 84% and 80% for the 1st and 4th cycles, respectively [26].

Graphene oxide is a potentially acidic heterogeneous catalyst with good solubility in aqueous solutions (or polar solvents) because it includes many oxygen-rich functional groups (-OH, -COOH, -CHO, etc.), which are very highly hydrophilic [17]. However, this property makes it difficult to separate the graphene oxide catalyst from the reaction mixture. Therefore, the separation of graphene oxide from the reaction mixture usually requires a high-speed centrifugation process instead of normal filtrations or vacuum extractions [17, 21, 23, 24].

To solve this problem, graphene oxide should be supported on a solid with a high surface area, not only limiting its "high solubility" but also avoiding the "leaching" of graphene oxide into the reaction medium. In this article, the synthesis of solid catalysts based on sulfonated biochar and graphene oxide was studied. Graphene oxide was supported on activated carbon to more easily filter the catalysts from the reactants. Their catalytic activities were tested by demonstrating lactic acid esterification from ethyl lactate.

2. Materials and Methods

2.1. Materials. Pine sawdust, taken from Ninh Binh province, Vietnam, was crushed, sieved, and collected. All sawdust particles are in the range of 0.5 to 0.85 mm in diameter. Then, the collected sawdust was dried at 105°C for 2 h. Commercially activated carbon, made from coconut shells in Vietnam, was washed with distilled water, dried at 105°C, and finally crushed. Expanded graphite powder (<45 μm , 99.9995%), NaNO_3 ($\geq 99\%$), KMnO_4 ($\geq 99\%$), H_2O_2 (30%), HCl (37%), H_2SO_4 (95–98%), lactic acid 85%, and ethanol (99.95%) were all purchased from Sigma-Aldrich (Singapore). All experiments were conducted using deionized water.

2.2. Synthesis of Graphene Oxide Supported on Activated Carbon (GO/AC). Graphene oxide synthesis was conducted using the modified method of Hummers [27]. GO after synthesis is dispersed in water with a concentration of 5.0 $\text{mg}\cdot\text{mL}^{-1}$. GO is dispersed on AC support by the dry impregnation method: 100 mL of the suspension was stirred into 5.000 g of 85°C-dried AC in a 250 mL glass beaker at room temperature for 5 h. Then, the mixture was dried at 85°C for 48 h. Then, it was cooled off in a desiccator. Finally,

we obtained 5.495 g of GO/AC catalyst with a weight ratio of GO to AC of 1 : 10. The efficiency on the supporting process was at 99.91%.

2.3. Synthesis of Sulfonated Biochar. The synthesis followed two processes:

- (i) Carbonation: 40 g of pine sawdust was carbonated in a furnace under an N_2 environment, at 400°C for 5 h (heating rate of 10°C/min). The product obtained was denoted as biochar.
- (ii) Sulfonation: 15 g of obtained biochar was stirred at 150°C in 300 ml of 98% H_2SO_4 solution in a three-neck glass flask of 500 ml for 15 h. The reaction system was cooled and slowly diluted with 1 L of distilled water. Then, hot distilled water (80°C) was used to wash the filtered mixture until the sulfate ion disappeared (checked by 10% BaCl_2 solution). The solid was dried at 105°C for 8 h to obtain the final product—sulfonated biochar catalyst.

2.4. Catalyst Characterization. Sample morphology was observed by scanning electron microscopy (SEM) using an S-4800 microscope (Hitachi, Japan). The specific surface area of the catalysts was measured by BET Micromeritics 201-A. The infrared spectrum of the samples, in the wavelength range of 400–4000 cm^{-1} , was measured on a Tensor 27-Bruker FTIR Spectrometer. XRD patterns of the catalysts were measured on a D8 Advance (Bruker) apparatus. A shaker and pH meter were used for titration. The acidic content (- SO_3H) of all catalysts was determined by an acid-base titration method [28]. For example, a suspension which contains 1 g of catalyst and 50 mL of 1 M NaCl solution in a 250 mL Erlenmeyer flask was shaken at a speed of 130 rpm for 4 hours. Next, the mixture was filtered. Then, the liquid was titrated by 0.1 M NaOH solution.

The - SO_3H content per 1 g of catalyst is calculated by the following formula:

$$N_{-\text{SO}_3\text{H}} = \frac{(0.1 \times V)}{1} \times \frac{50}{20} (\text{mmol}\cdot\text{g}^{-1}), \quad (1)$$

where V is the volume of used NaOH solution (mL) and $N_{-\text{SO}_3\text{H}}$ is the - SO_3H content per 1 g of catalyst.

2.5. Catalytic Tests. The activity of the catalysts was evaluated through the esterification reaction between lactic acid 50% (obtained from 85% lactic acid solution by the dilution) and ethanol (mole ratio 1 : 4) at 82°C [29]. The weight ratios of the sulfonated biochar and GO catalysts to lactic acid are 5% and 1%, respectively. Because of the difficulty in filtering, the weight ratio of GO catalyst cannot be not higher than 1%. To make it easier to compare the catalytic activity between GO and GO/AC, the contents of GO included in the GO/AC catalyst are equal to that of the GO catalyst.

Ethyl lactate product was determined by the internal standardization method on an Agilent 7890A gas

chromatograph equipped with an FID. The yield of ethyl lactate was calculated by the following formula:

$$\text{ethyl lactate yield (\%)} = \frac{n_{\text{ethyl lactate}}}{n_{\text{ethyl lactate}}^0} \times 100, \quad (2)$$

where $n_{\text{ethyl lactate}}$ is the real mole of ethyl lactate that is determined by the gas chromatography test and $n_{\text{ethyl lactate}}^0$ is the theory mole of ethyl lactate that is a value with 100% conversion of lactic acid.

2.6. Recycling Catalyst Tests. After completion of the reaction, the GO/AC and sulfonated biochar catalysts were filtered and washed three times by using hot distilled water ($\geq 80^\circ\text{C}$). Then, the catalysts were dried at 105°C for 8 h. The recycled catalysts were reused for lactic acid esterification.

3. Results and Discussion

3.1. Catalyst Characterization. The structural properties of sulfonated biochar, activated carbon, graphene oxide, and GO/AC determined by the XRD method are shown in Figure 1. There is a broad peak at 20° to 30° of 2-theta-scale; these data mean that the sulfonated biochar catalyst has an amorphous structure [10]. There is a specific peak observed at 11° of 2-theta-scale (corresponding to the crystal of graphene oxide) for both graphene oxide and the GO/AC catalysts [22]. However, in the case of GO/AC catalyst, the peak is much lower in intensity. This result confirmed the successful synthesis of graphene oxide from expanded graphite and indicated that there was interaction between the graphene oxide and activated carbon in the GO/AC catalyst.

Figure 2 shows the SEM images of the sulfonated biochar, activated carbon, graphene oxide, and GO/AC catalysts. The results indicate a porous structure with large capillaries, a solid structure, and a transparently layered structure for the sulfonated biochar (Figure 2(a)), activated carbon (Figure 2(b)), and graphene oxide (Figure 2(c)), respectively. Figure 2(d) shows that the GO/AC catalyst shows a “sandwich” structure in which the activated carbon is surrounded by graphene oxide layers, proving that the GO/AC catalyst was successfully prepared.

The FT-IR spectra of the catalysts are shown in Figure 3. In the infrared spectra of sulfonated biochar, graphene oxide, and GO/AC catalysts, there are characteristic vibration bands of -OH bonding and the C=O group, including the -COOH functional group at 3416 , 3387 , 3444 cm^{-1} and 1709 , 1698 , 1694 cm^{-1} , respectively. There are also valence vibrations of S=O bonding included in the -SO₃H group at 1040 , 1059 , and 1108 cm^{-1} [10, 23]. Meanwhile, valence vibrations of S=O are not observed in the case of the activated carbon catalyst, indicating that there is no presence of -SO₃H groups in the activated carbon structure.

Specific surface areas of the catalysts are presented in Table 1. The results showed that the areas of the catalysts are quite high (over 400 m^2 g^{-1}). Because of the filling of GO particles in the micropores of the activated carbon, there is a decrease in the specific surface area of the GO/AC in

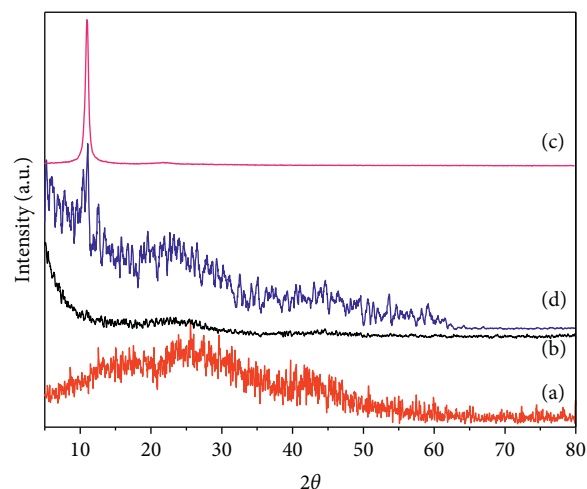


FIGURE 1: XRD patterns of sulfonated biochar (a), activated carbon (b), graphene oxide (c), and GO/AC (d).

comparison with the original activated carbon (150.7 m^2 g^{-1} lower). However, after 6 cycles, there was a slight increase of S_{BET} of GO/AC (49 m^2 g^{-1} higher) in comparison with initial GO/AC. This can be explained by some reasons. Firstly, during the esterification, small amounts of GO may be removed from the surface of AC to the reaction medium. Moreover, the specific surface area of AC is higher than that of GO.

Table 1 also presents the sulfonic acid group (-SO₃H) contents of the catalysts. The results showed that the sulfonic acid group contents were 1.14 $\text{mmol}\cdot\text{g}^{-1}$, 0.35 $\text{mmol}\cdot\text{g}^{-1}$, and 0.92 $\text{mmol}\cdot\text{g}^{-1}$ for sulfonated biochar, GO/AC, and GO catalysts, respectively. There was not much difference in sulfonic acid content between GO and sulfonated biochar catalysts.

3.2. Catalytic Tests. Figure 4 presents the ethyl lactate yield related to the reaction time for all the catalysts. All the tests were carried out under the same conditions.

According to the results presented in Figure 4, it can be seen that the catalytic activity decreases in the following order: graphene oxide (51.0%) > sulfonated biochar (37.0%) \approx GO/AC (35.4%) \gg activated carbon (20.0%) after 420 min of reaction time. This order seems to be related to the sulfonic acid content and dispersion properties of each catalyst. Although the sulfonic acid content of sulfonated biochar and graphene oxide is similar (1.14 $\text{mmol}\cdot\text{g}^{-1}$ and 0.92 $\text{mmol}\cdot\text{g}^{-1}$, respectively), graphene oxide catalysts showed much higher activity than the sulfonated biochar catalysts, which may be due to the higher dispersion of graphene oxide in aqueous medium compared to sulfonated biochar. As previously mentioned, the dispersion of graphene oxide was high as a “pseudo-homogeneous” catalyst because there is the presence of numerous hydrophilic functional groups (-COOH, -OH, and -CHO) in its structure. Consequently, it is easy for the “accessible sulfonic groups” of graphene oxide catalyst to be active in the reaction that leads to an increase in ethyl lactate yield. However, its

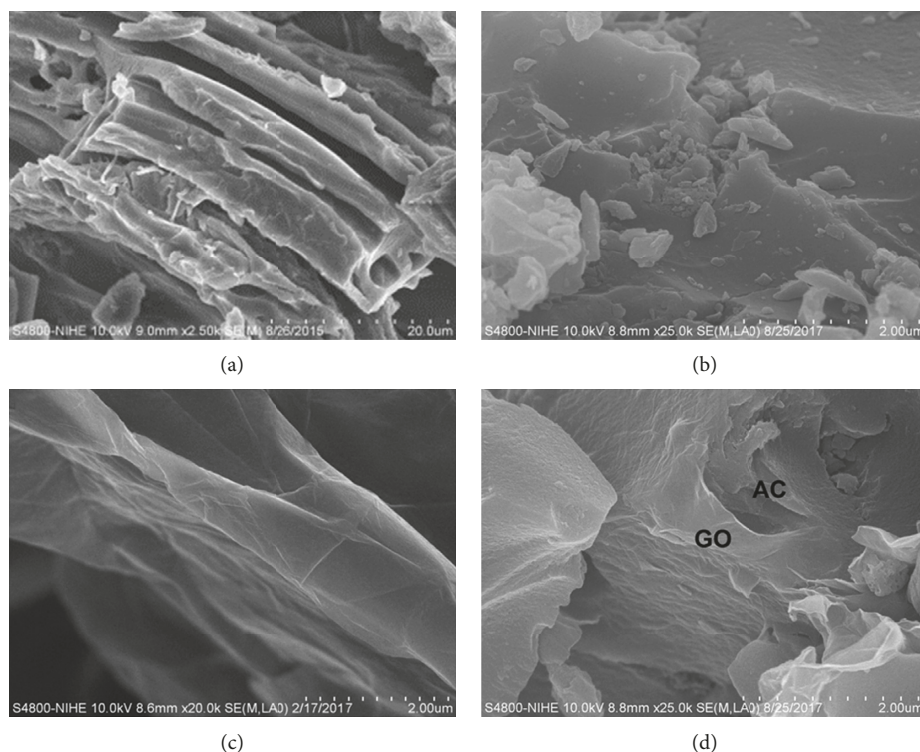


FIGURE 2: SEM images of sulfonated biochar (a), activated carbon (b), graphene oxide (c), and GO/AC (d).

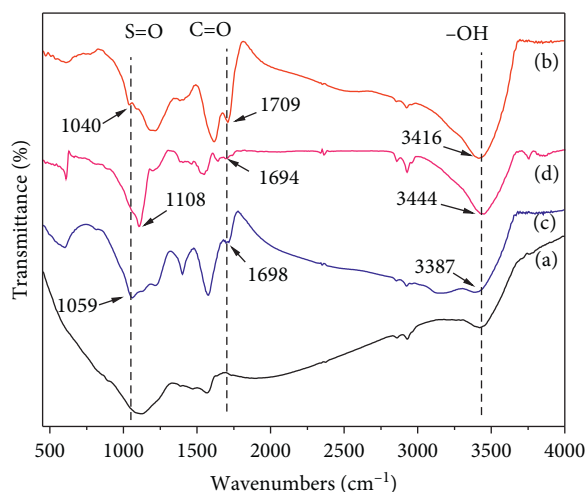


FIGURE 3: FT-IR spectra of activated carbon (a), sulfonated biochar (b), graphene oxide (c), and GO/AC (d).

drawback is a difficulty with filtering or taking the catalyst away from the reactants. Hence, we only used 1% by weight of graphene oxide in order to be able to analyze ethyl lactate by gas chromatography.

In the case of the sulfonated biochar and GO/AC catalysts, their catalytic activities are similar, although the $-\text{SO}_3\text{H}$ content of the GO/AC catalyst is only $0.35 \text{ mmol}\cdot\text{g}^{-1}$, which is three times lower than that of the sulfonated biochar catalyst. This result confirms that a good combination of graphene oxide and activated carbon can serve as a catalyst for the esterification of lactic acid. As shown in

TABLE 1: Specific surface areas and sulfonic acid group ($-\text{SO}_3\text{H}$) content of the catalysts.

Catalysts	S_{BET} ($\text{m}^2\cdot\text{g}^{-1}$)	$-\text{SO}_3\text{H}$ content ($\text{mmol}\cdot\text{g}^{-1}$)
Sulfonated biochar	423.4	1.14
Sulfonated biochar after 4 cycles of reaction	—	0.64
Activated carbon	721.1	0
Graphene oxide	215.9	0.92
GO/AC	570.3	0.35
GO/AC after 6 cycles of reaction	618.9	0.29

Table 1, there is no $-\text{SO}_3\text{H}$ group included in the structure of activated carbon, explaining why this catalyst showed the lowest catalytic activity.

3.3. Recycling Tests of Catalysts. The GO/AC and sulfonated biochar catalysts were recycled six and four times, respectively. Ethyl lactate yields of each recycling test are presented in Figure 5. Figure 5(a) noted that the activity of GO/AC catalyst decreased slowly from the 1st to the 3rd cycle, respectively, from 35.4% to 30.3% after a reaction time of 420 min, that means 14.4% of reduction, and it seem to be unchanged from 3rd to 6th cycles, the percentage of decrease is only 3.3%. In the same way, with sulfonated biochar catalyst (see Figure 5(b)), the activity was decreased from 37.0% in the 1st cycle to 26.1% in the 4th cycle, that is equal to 29.5% of reduction. Hence, stability of GO/AC is much higher than sulfonated biochar catalyst.

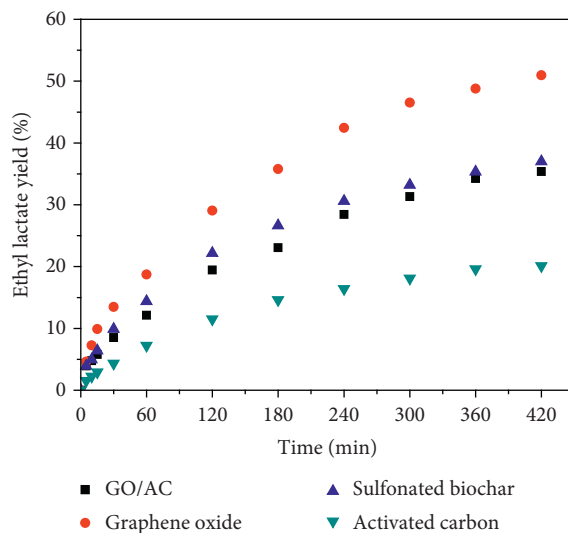


FIGURE 4: Ethyl lactate yield versus reaction time.

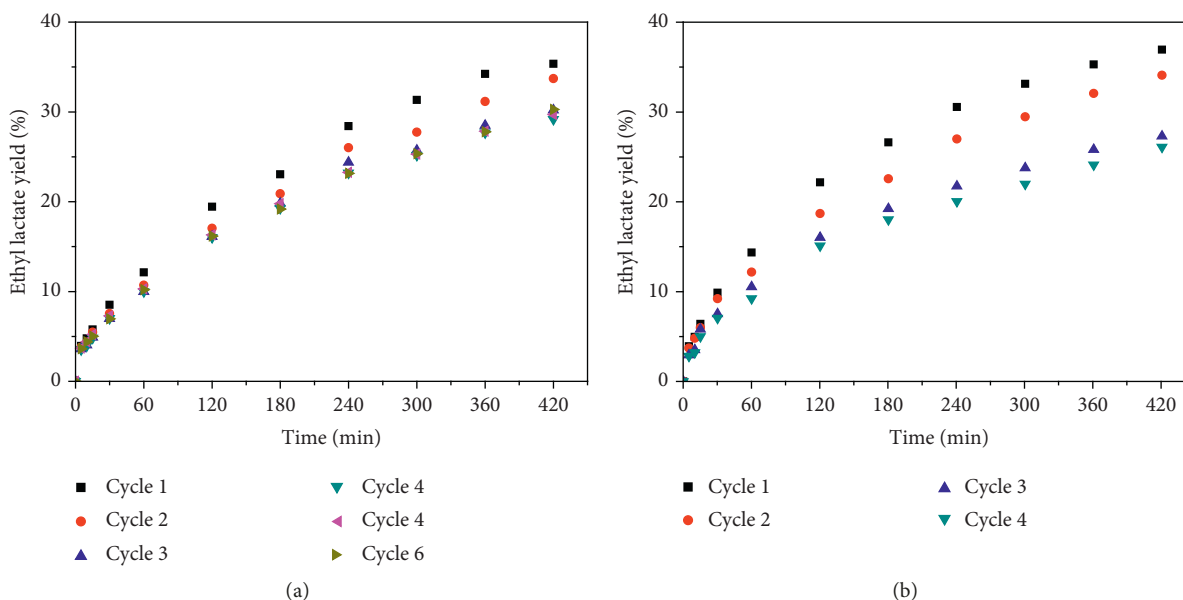


FIGURE 5: Test of recycled GO/AC (a) and sulfonated biochar (b) catalysts.

The $-\text{SO}_3\text{H}$ contents presented in Table 1 confirm that the durability of GO/AC is higher than sulfonated biochar catalyst. In details, the functional group in GO/AC reduced from $0.35 \text{ mmol}\cdot\text{g}^{-1}$ to $0.29 \text{ mmol}\cdot\text{g}^{-1}$ that means 17.1% of decrease after 6 cycles. However, the value of sulfonated biochar is near 2.6 times higher, 43.9%, after 4 cycles. The result also confirms that in the active phase, GO was well dispersed and attached onto the support, activated carbon.

In addition to the strong attachment of graphene oxide onto activated carbon, it seems that the sulfonic group $-\text{SO}_3\text{H}$ of the GO/AC catalyst was more stable than that of the sulfonated bio-char. To explain this phenomenon, FT-IR spectra of 6-times recycled graphene oxide catalyst are presented in Figure 6. The FT-IR spectra of the GO/AC after

6 cycles of reaction also showed vibrations at 3423 cm^{-1} , 1705 cm^{-1} , and 1080 cm^{-1} corresponding to the presence of the $-\text{OH}$, $-\text{COOH}$, and $-\text{SO}_3\text{H}$ groups, respectively.

In our knowledge, there are some qualitative causes of the bond between GO and AC support. Firstly, the connection as esterification of the similar functional groups like carboxyl ($-\text{COOH}$) and hydroxyl ($-\text{OH}$) (see Figure 7), which present in both GO and AC surface [30], can contribute to the combination to become stronger. Moreover, Ai and Jiang [31] reported another explanation that both GO and AC include aromatic rings in their structure. It means that π - π interactions may present when GO is coated on AC surface. As a result, the combination becomes better.

Because of some above results, GO/AC catalyst shows not only better catalytic activity but also higher stability than

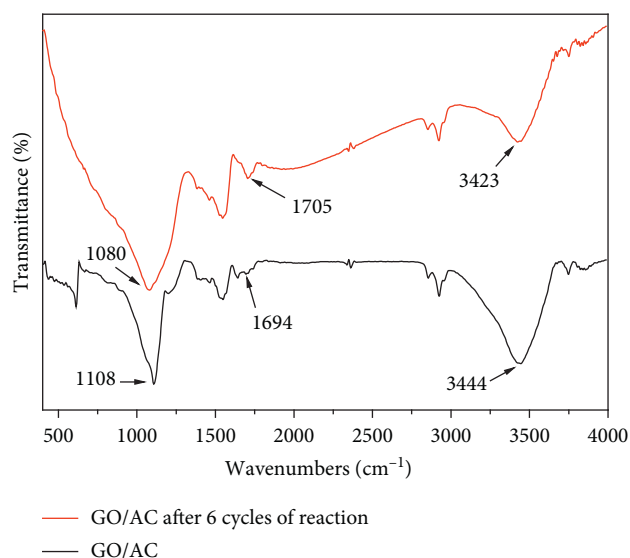


FIGURE 6: FT-IR spectra of GO/AC and GO/AC after 6 reaction cycles.

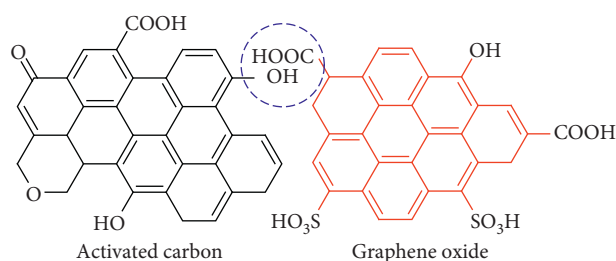


FIGURE 7: Self-esterification of activated carbon and graphene oxide.

sulfonated biochar in lactic acid esterification to form ethyl lactate. This catalyst demonstrates a combination of “solubility” of the active-phase graphene oxide and a high surface area as well as ease of separation of the activated carbon.

4. Conclusions

Graphene oxide, graphene oxide supported on activated carbon (GO/AC), and sulfonated biochar catalysts were synthesized and investigated as acidic heterogeneous catalysts for lactic acid esterification to form ethyl lactate. The catalytic activity of the catalysts is in the following order: graphene oxide > sulfonated bio-char \approx GO/AC > activated carbon. It seems that catalytic activities are related to the $-\text{SO}_3\text{H}$ content, especially the accessible $-\text{SO}_3\text{H}$ content. Among the catalysts, the GO/AC and sulfonated biochar catalysts showed similar activity with an approximate yield of 35% ethyl lactate after 420 min of reaction time. This catalytic activity of GO/AC is remarkable because of the presence of only 1% by weight GO as the active phase. In addition, the results of the recycled catalyst tests showed that the GO/AC catalytic activity was stable after the 3rd cycle and reached a yield of 30.3% ethyl lactate after 420 min of reaction time. Under the same reaction conditions, the

catalytic activities of sulfonated biochar decreased sharply with a decrease in ethyl lactate yield from 37.0% to 26.1% after four recycling times. The remarkable catalytic activity and stability of the GO/AC catalyst are explained by good dispersion, stability of partial esterification, and the π - π interactions between active-phase graphene oxide and activated carbon. From the point of view of application, it is concluded that the GO/AC catalyst shows high potential as a catalyst for the esterification of lactic acid.

Data Availability

The data used to support the findings of this study are available from the corresponding author upon request.

Conflicts of Interest

The authors declare that they have no conflicts of interest.

Acknowledgments

The authors gratefully acknowledge the financial supports from the Project Management Unit of FIRST for this subproject through grant agreement no. 06/FIRST/2A/KEYLABPRT.

References

- [1] P. G. Jessop, “Searching for green solvents,” *Green Chemistry*, vol. 13, no. 6, pp. 1391–1398, 2011.
- [2] F. F. Bamoharram, M. M. Heravi, P. Ardalán, and T. Ardalán, “A kinetic study of the esterification of lactic acid by ethanol in the presence of Preyssler acid an eco-friendly solid acid catalyst,” *Reaction Kinetics, Mechanisms and Catalysis*, vol. 100, no. 1, pp. 71–78, 2010.
- [3] T. H. T. Vu, H. T. Au, T. H. T. Nguyen et al., “Esterification of lactic acid by catalytic extractive reaction: an efficient way to produce a biosolvent composition,” *Catalysis Letters*, vol. 143, no. 9, pp. 950–956, 2013.
- [4] Y. Zhang, L. Ma, and J. Yang, “Kinetics of esterification of lactic acid with ethanol catalyzed by cation-exchange resins,” *Reactive and Functional Polymers*, vol. 61, no. 1, pp. 101–114, 2004.
- [5] P. Delgado, M. T. Sanz, and S. Beltrán, “Kinetic study for esterification of lactic acid with ethanol and hydrolysis of ethyl lactate using an ion-exchange resin catalyst,” *Chemical Engineering Journal*, vol. 126, no. 2-3, pp. 111–118, 2007.
- [6] C. S. M. Pereira, S. P. Pinho, V. M. T. M. Silva, and A. E. Rodrigues, “Thermodynamic equilibrium and reaction kinetics for the esterification of lactic acid with ethanol catalyzed by acid ion-exchange resin,” *Industrial & Engineering Chemistry Research*, vol. 47, no. 5, pp. 1453–1463, 2008.
- [7] O. Edidiong, S. Habiba, and E. Gobina, “Batch process esterification of lactic acid catalysed by cation-exchange resins for the production of environmental-friendly solvent,” in *Proceedings of the World Congress on Engineering and Computer Science. Lecture Notes in Engineering and Computer Science 2015*, vol. II, pp. 623–628, WCECS, San Francisco, CA, USA, October 2015.
- [8] S. Kang, J. Ye, and J. Chang, “Recent advances in carbon-based sulfonated catalyst: preparation and application,” *International Review of Chemical Engineering*, vol. 5, no. 2, pp. 133–145, 2013.

- [9] T. Liu, Z. Li, W. Li, C. Shi, and Y. Wang, "Preparation and characterization of biomass carbon-based solid acid catalyst for the esterification of oleic acid with methanol," *Bioresource Technology*, vol. 133, pp. 618–621, 2013.
- [10] W.-Y. Lou, Q. Guo, W.-J. Chen, M.-H. Zong, H. Wu, and T. J. Smith, "A highly active bagasse-derived solid acid catalyst with properties suitable for production of biodiesel," *ChemSusChem*, vol. 5, no. 8, pp. 1533–1541, 2012.
- [11] M.-L. Tao, H.-Y. Guan, X.-H. Wang, Y.-C. Liu, and R.-F. Louh, "Fabrication of sulfonated carbon catalyst from biomass waste and its use for glycerol esterification," *Fuel Processing Technology*, vol. 138, pp. 355–360, 2015.
- [12] M. Zhang, A. Sun, Y. Meng, L. Wang, H. Jiang, and G. Li, "Catalytic performance of biomass carbon-based solid acid catalyst for esterification of free fatty acids in waste cooking oil," *Catalysis Surveys from Asia*, vol. 19, no. 2, pp. 61–67, 2014.
- [13] J. R. Kastner, J. Miller, D. P. Geller, J. Locklin, L. H. Keith, and T. Johnson, "Catalytic esterification of fatty acids using solid acid catalysts generated from biochar and activated carbon," *Catalysis Today*, vol. 190, no. 1, pp. 122–132, 2012.
- [14] X.-Y. Liu, M. Huang, H.-L. Ma et al., "Preparation of a carbon-based solid acid catalyst by sulfonating activated carbon in a chemical reduction process," *Molecules*, vol. 15, no. 10, pp. 7188–7196, 2010.
- [15] N. M. Julkapli and S. Bagheri, "Graphene supported heterogeneous catalysts: an overview," *International Journal of Hydrogen Energy*, vol. 40, no. 2, pp. 948–979, 2015.
- [16] B. F. Machado and P. Serp, "Graphene-based materials for catalysis," *Catalysis Science & Technology*, vol. 2, no. 1, pp. 54–75, 2012.
- [17] S. Bykkam, K. V. Rao, C. S. Chakra, and T. Thunugunta, "Synthesis and characterization of graphene oxide and its antibacterial activity against *Klebsiella* and *Staphylococcus*," *International Journal of Advanced Biotechnology and Research*, vol. 4, no. 1, pp. 1005–1009, 2013.
- [18] X. Zhao, J. Wang, C. Chen, Y. Huang, A. Wang, and T. Zhang, "Graphene oxide for cellulose hydrolysis: how it works as a highly active catalyst?," *Chemical Communications*, vol. 50, no. 26, pp. 3439–3442, 2014.
- [19] E. Lam, J. H. Chong, E. Majid et al., "Carbocatalytic dehydration of xylose to furfural in water," *Carbon*, vol. 50, no. 3, pp. 1033–1043, 2012.
- [20] D. Mondal, J. P. Chaudhary, M. Sharma, and K. Prasad, "Simultaneous dehydration of biomass-derived sugars to 5-hydroxymethyl furfural (HMF) and reduction of graphene oxide in ethyl lactate: one pot dual chemistry," *RSC Advances*, vol. 4, no. 56, pp. 29834–29839, 2014.
- [21] H. Wang, Y. Wang, T. Deng, C. Chen, Y. Zhu, and X. Hou, "Carbocatalyst in biorefinery: selective etherification of 5-hydroxymethylfurfural to 5,5'-(oxy-bis(methylene))bis-2-furfural over graphene oxide," *Catalysis Communications*, vol. 59, pp. 127–130, 2015.
- [22] S. Zhu, C. Chen, Y. Xue, J. Wu, J. Wang, and W. Fan, "Graphene oxide: an efficient acid catalyst for alcoholysis and esterification reactions," *Chemcatchem*, vol. 6, no. 11, pp. 3080–3083, 2014.
- [23] X. Gao, S. Zhu, and Y. Li, "Graphene oxide as a facile solid acid catalyst for the production of bioadditives from glycerol esterification," *Catalysis Communications*, vol. 62, pp. 48–51, 2015.
- [24] J. Cheng, Y. Qiu, R. Huang, W. Yang, J. Zhou, and K. Cen, "Biodiesel production from wet microalgae by using graphene oxide as solid acid catalyst," *Bioresource Technology*, vol. 221, pp. 344–349, 2016.
- [25] Z. Wei, Y. Yang, Y. Hou, Y. Liu, X. He, and S. Deng, "A new approach towards acid catalysts with high reactivity based on graphene nanosheets," *ChemCatChem*, vol. 6, no. 8, pp. 2354–2363, 2014.
- [26] S. Kundu and B. Basu, "Graphene oxide (GO)-catalyzed multi-component reactions: green synthesis of library of pharmacophore 3-sulfonylimidazo[1,2-a]pyridines," *RSC Advances*, vol. 5, no. 62, pp. 50178–50185, 2015.
- [27] W. S. Hummers and R. E. Offeman, "Preparation of graphitic oxide," *Journal of the American Chemical Society*, vol. 80, no. 6, p. 1339, 1958.
- [28] D. Lee, "Preparation of a sulfonated carbonaceous material from lignosulfonate and its usefulness as an esterification catalyst," *Molecules*, vol. 18, no. 7, pp. 8168–8180, 2013.
- [29] V. C. Nguyen, N. Q. Bui, P. Mascunan, T. T. H. Vu, F. Pascal, and N. Essayem, "Esterification of aqueous lactic acid solutions with ethanol using carbon solid acid catalysts: amberlyst 15, sulfonated pyrolyzed wood and graphene oxide," *Applied Catalysis A: General*, vol. 552, pp. 184–191, 2018.
- [30] M. S. Shafeeyan, W. M. A. W. Daud, A. Houshmand, and A. Shamiri, "A review on surface modification of activated carbon for carbon dioxide adsorption," *Journal of Analytical and Applied Pyrolysis*, vol. 89, no. 2, pp. 143–151, 2010.
- [31] L. Ai and J. Jiang, "Removal of methylene blue from aqueous solution with self-assembled cylindrical graphene-carbon nanotube hybrid," *Chemical Engineering Journal*, vol. 192, pp. 156–163, 2012.

Research Article

Effect of Silver Nanoparticles on Tropical Freshwater and Marine Microalgae

Thanh-Luu Pham 

Sustainable Management of Natural Resources and Environment Research Group, Faculty of Environment and Labour Safety, Ton Duc Thang University, Ho Chi Minh City, Vietnam

Correspondence should be addressed to Thanh-Luu Pham; phamthanhluu@tdtu.edu.vn

Received 4 March 2019; Accepted 14 May 2019; Published 30 May 2019

Guest Editor: Thanh-Dong Pham

Copyright © 2019 Thanh-Luu Pham. This is an open access article distributed under the Creative Commons Attribution License, which permits unrestricted use, distribution, and reproduction in any medium, provided the original work is properly cited.

The increase in synthesis and application of silver nanoparticles (AgNPs) in the last decade has resulted in contamination of AgNPs in the aquatic environment. The presence of AgNPs in aquatic environments has posed toxic effects to aquatic organisms and ecological damage. In this study, two tropical microalgae species including the freshwater *Scenedesmus* sp. and the marine diatom *Thalassiosira* sp. were employed to examine the toxic effects of AgNPs. The toxic effects were determined by analyzing different end points, such as half maximal effective concentration (EC₅₀), algae growth inhibition, algae cell size, chlorophyll-*a* content, and total lipid accumulation. The results suggested that AgNPs presented different toxicity mechanisms for microalgae and showed to be more toxic in freshwater than in marine environment. The EC₅₀ values of AgNPs after 72 h for the growth inhibition of *Scenedesmus* sp. and *Thalassiosira* sp. were 89.92 ± 9.68 and 107.21 ± 7.43 $\mu\text{g/L}$, respectively. AgNPs at a certain concentration have resulted in change in cell diameter, reduction in chlorophyll-*a* content, and enhancement of the total lipid production in the tested microalgae. Thus, local species should be involved in the toxic assessment. This research contributes on understanding the toxicity of AgNPs on freshwater and marine environments.

1. Introduction

The rapid development and application of nanomaterials in different industrial sectors have resulted in contamination of nanomaterials in the aquatic environment [1, 2]. In particular, nanomaterials containing silver have been widely used in various industries and applications [3], because of its antibacterial activity. More than 1300 products associated with NP technology are now available [4], in which 438 products (account for 24%) contain AgNPs [5]. In the USA, over 50% of the registered biocidal silver products by the Environmental Protection Agency (EPA) likely contain AgNPs. And, about 230 tons production with AgNPs is produced each year from European countries [6]. Although the concentration from nondetectable to over 0.1 mg/L of AgNPs has been detected from surface waters, the quantitative monitoring program for AgNPs in water environment is not currently available [7]. Therefore, the contamination of these nanomaterials has recently become environmental concerns due to the potential hazards in aquatic ecosystem [8, 9].

In ecological ecosystems, the microalgae are primary producers and play a vital role in the food chains. Thus, the bad effects of pollutants on microalgae species may break the balance of whole ecosystems [10]. The toxic effect and behavior of nanomaterial in the ecosystems on microalgae have been recently reviewed [3, 11]. Previous studies have indicated that AgNPs caused inhibition of growth in freshwater green microalgae [12], decrease photosynthesis activity in the unicellular green algae *Chlamydomonas reinhardtii* [13], and stimulate the antioxidant activities in the marine flagellate *Chattonella marina* [14]. AgNPs caused depletion in chlorophyll content and morphological malformations in the freshwater green alga *Pithophora oedogonia* [15]. Decrease in chlorophyll content, viable algal cells, increased reactive oxygen species (ROS) formation, and lipid peroxidation in the freshwater microalga *Chlorella vulgaris* and marine microalga *Dunaliella tertiolecta* were observed after exposure to AgNPs for 24 h [16]. Huang et al. [10] reported that AgNPs at a concentration of 0.5 mg/L caused both significantly induced excess intracellular ROS and

decreased cell viability in the marine diatom *Skeletonema costatum*.

Although the adverse effects of AgNPs on different organisms have been reported, previous studies however focus largely on freshwater environment [6]. There is little understanding about toxic effects of AgNPs on marine species, particularly the ones from tropical region. Therefore, the aims of this study was to investigate the toxicity of AgNPs to different species including the freshwater microalgae, *Scenedesmus* sp. (Chlorophyceae), and the marine diatom, *Thalassiosira* sp. (Bacillariophyceae). The toxic effects were determined by analyzing different end points, such as half maximal effective concentration (EC_{50}), algae growth inhibition, algae cell size, chlorophyll-*a* content, and total lipid production.

2. Materials and Methods

2.1. Silver Nanoparticles. Silver nanoparticles were prepared as previously reported by Becaro et al. [17]. Briefly, stock solution of AgNPs was prepared by dissolving 10 g/L of $AgNO_3$ (Aldrich Chemical Co., MO, USA) in MQ-water and heating at 80°C for 5 min. To this solution, 5 g/L of polyvinyl alcohol (PVA) as a stabilizing agent was added with constant stirring. Ultraviolet-visible (UV-Vis) absorption was monitored from 300 to 600 nm by using a BioThermo spectrophotometer. Diameter of particle size and morphology were characterized by a transmission electron microscope (TEM). Samples were kept in dark at $4.0 \pm 1^\circ C$ and used within 6 months. The physicochemical properties of AgNP were stable under this condition [18].

2.2. Test Species. In this study, the freshwater microalgae *Scenedesmus* sp. isolated from the Saigon River, Ho Chi Minh City, Vietnam, and the marine diatom *Thalassiosira* sp. isolated from coastal waters of the Can Gio Sea, Ho Chi Minh City, Vietnam, were used. The green algae *Scenedesmus* sp. was maintained in COMBO medium (pH: 7.5 ± 0.3) [19], and the diatom *Thalassiosira* sp. was maintained in F/2 medium (pH: 8.0 ± 0.3) enriched with 0.2 μm filtered seawater. Both cultures were grown on a 12 h light:dark cycle at a temperature of $28 \pm 1^\circ C$ under light intensity of 50 μmol photons/ m^2 s provided by cool white fluorescent tubes.

2.3. Algae Growth Inhibition Test. The inhibition of AgNP on growth of *Scenedesmus* sp. and *Thalassiosira* sp. was examined following the OECD 201 guideline methods [20]. Briefly, AgNP at the concentration of 0, 5, 20, 50, 100, and 200 $\mu g/L$ was spiked in Erlenmeyer flasks (500 mL) containing 300 mL culture medium, and living stocks of *Scenedesmus* sp. and *Thalassiosira* sp. were added to the initial concentration of 5×10^4 cell/mL. Samples were prepared in triplicate and incubated at 27°C for 72 h under a 12 h:12 h light-dark cycle. The pH of all test solutions was measured at the beginning and end of the test. After 72 h, subsamples of culture medium

(about 10 mL) were fixed with Lugol's solution and cell density was determined by using a Sedgewick Rafter counting chamber. About 200 mL of culture medium was collected at the end of the test, filtered onto glass fiber filters (GF/C, Whatman, England), dried at 45°C for 48 h, and stored at $-20^\circ C$ prior to total lipid extraction and analysis. The cell size of microalgae was measured directly by using an ocular micrometer. The graduation in arbitrary units is calibrated by using a microscope calibration slide.

The AgNPs concentration that resulted in 50% inhibition growth of algae over 72 h (EC_{50} , 72 h) was calculated by using the specific growth rate (SGR). The SGR for each species was evaluated by the difference cell density after 72 h as follows:

$$\delta_{x-y} = \frac{\ln C_y - \ln C_x}{t_y - t_x}, \quad (1)$$

where δ_{x-y} is the SGR from time x to time y , $t_y - t_x$ is the duration of exposure periods in h , and C_y and C_x are the cell density at times x and y , respectively.

The inhibition growth rate (IGR) of algae was determined as follows:

$$IGR = \frac{\delta_C - \delta_T}{\delta_C} \times 100, \quad (2)$$

where IGR (%) is the inhibition growth rate of each microalgae species, δ_C is the average growth rate of the control, and δ_T is the average growth rate of the exposures.

2.4. Chlorophyll-*a* Determination. To determine the chlorophyll-*a* fraction, a known volume of culture samples (10 mL) was filtered using filter paper (GF/C, Whatman, England), and then the chlorophyll-*a* was extracted using 80% acetone for overnight in dark (4°C). After centrifugation, the supernatant was used to measure chlorophyll-*a* at 630–750 nm by using a spectrophotometer (UV-VIS, Harch, 500), and the concentration of chlorophyll-*a* (% of control) was calculated according to Metzner et al. [21].

2.5. Total Lipid Extraction and Measurement. The dried biomass was ground into powder; the total lipid in the homogenized cells was extracted according to the method of Bligh and Dyer [22] and analyzed using gravimetric quantification methods according to the procedure of Han et al. [23]. Briefly, about 50 mg dry weight (DW) of algae biomass (M1) was homogenized and digested with 3 mL of 1 mol/L HCl in 50 mL centrifuge tube at 80°C for 30 min. Then, the cell debris was collected after centrifugation. Lipid was then extracted with 3 mL methanol:chloroform (2:1 v/v) for 3 h and mixed well. Lipids settle in the upper phase was collected to a new dish that had been preweighed (M2). The dish was then dried completely and reweighed (M3). Lipid concentration (LC) was determined gravimetrically as follows:

$$LC (\%) = \frac{(M3 - M2)}{M1} \times 100. \quad (3)$$

2.6. Statistical Analysis. The growth inhibition (%) of each species was determined according to the method of OECD [20]. The effective concentration (EC_{50}) values after 72 h for each species were evaluated by using the IGR at 50% by nonlinear regression. The data in tested treatments were presented as the mean \pm SD. One-way analysis of variance (ANOVA) and post hoc Tukey's honestly significant difference (HSD) were applied to identify the significant difference between exposure and control treatments. All data were log-transformed to normalize the distribution before analysis. Significant difference was considered at P values < 0.05 .

3. Results

3.1. Characterization of AgNPs. The morphology, absorbance wavelength, and size distribution of AgNPs are shown in Figure 1. The TEM image of AgNPs is shown in Figure 1(a). The UV-Vis absorbance wavelength showed that the samples of AgNPs generated a single peak with maximum absorbance at 410 nm (Figure 1(b)). The particle size of AgNPs stock solution under TEM measurements indicated the dominant of particles with diameter from 6 to 10 nm (Figure 1(c)).

3.2. Growth Inhibition. The inhibition of AgNPs at the concentration from 5 to 200 $\mu\text{g/L}$ on the *Scenedesmus* sp. and *Thalassiosira* sp. after a 72 h exposure is shown in Figures 2(a) and 2(b). A 72 h exposure of *Scenedesmus* sp. and *Thalassiosira* sp. to sublethal concentrations of AgNPs caused a concentration-dependent inhibition of growth. The 72 h EC_{50} values of AgNPs for the growth inhibition of *Scenedesmus* sp. and *Thalassiosira* sp. were 89.92 ± 9.68 and $107.21 \pm 7.43 \mu\text{g/L}$, respectively. AgNPs from the concentration of 20 $\mu\text{g/L}$ or higher resulted in significant inhibition on the growth of both algae. The freshwater green algal *Scenedesmus* sp. showed greater sensitivity than the marine diatom *Thalassiosira* sp. to AgNPs. Exposure to AgNPs at 200 $\mu\text{g/L}$ inhibited completely the growth of *Scenedesmus* sp., whereas this concentration of AgNPs inhibited almost 100% growth of *Thalassiosira* sp. (Figure 2). The pH value rises slightly from 7.5 ± 0.3 at the beginning of the experiment to 7.8 ± 0.3 at the end in the test with *Scenedesmus* sp. (in COMBO medium), while with *Thalassiosira* sp. (in F/2 medium), the pH value remains at approximately 8.0 ± 0.4 throughout the period of incubation.

3.3. Algal Cell Diameter. Cell diameter of the green algal *Scenedesmus* sp. was $4.31 \pm 0.15 \mu\text{m}$. There was no difference in cell diameter of the *Scenedesmus* sp. between the control and treatments after 72 h exposure to AgNPs (Figure 3(a)). In the case of the marine diatom *Thalassiosira* sp., the cell diameter was not different from the control after 72 h exposure to AgNPs with concentration of 5, 20, and 50 $\mu\text{g/L}$, but AgNPs with concentration of 100 and 200 $\mu\text{g/L}$ caused significant increase in cell diameter with respect to the control. The control treatment had an average cell diameter of $8.98 \pm 0.17 \mu\text{m}$, while the cell diameter increased up to

$9.12 \pm 0.31\%$ and $8.05 \pm 0.39\%$ in the exposures with 100 and 200 $\mu\text{g/L}$ of AgNPs, respectively (Figure 3(b)).

3.4. Chlorophyll-*a* Content. Results of chlorophyll-*a* contents in *Scenedesmus* sp. and *Thalassiosira* sp. were changed significantly upon exposure to AgNPs. In the freshwater green algal *Scenedesmus* sp., exposure to AgNPs at the concentration of 5 and 20 $\mu\text{g/L}$ was not different with the control, but exposure to AgNPs at the concentration of 50, 100, and 200 $\mu\text{g/L}$ resulted in significant decrease in chlorophyll-*a* content (the highest decrease of 21.5% in the treatment with 200 $\mu\text{g/L}$ of AgNPs, with respect to the control) (Figure 4(a)). Chlorophyll-*a* content varied almost the same trend in the marine diatom *Thalassiosira* sp. The chlorophyll-*a* content in the lowest treatment of AgNPs (5 $\mu\text{g/L}$) was not different from the control but the treatments with AgNPs from 20 to 200 $\mu\text{g/L}$ resulted in significant decrease in chlorophyll-*a* contents. The lowest level of chlorophyll-*a* (14.5%) was found in the treatment with 200 $\mu\text{g/L}$ (Figure 4(b)).

3.5. Lipid Accumulation. Silver nanoparticles had great influence on the lipid production of *Scenedesmus* sp. and *Thalassiosira* sp. AgNPs at the concentration of 5 and 20 $\mu\text{g/L}$ led to a significant increase in total lipid production in *Scenedesmus* sp., with the maximum total lipid increase of 8.1% and 7.6%, compared with the control, respectively. In contrast, AgNPs at higher concentration (100 and 200 $\mu\text{g/L}$) resulted in significant decrease in total lipid production. The highest concentration of AgNPs (200 $\mu\text{g/L}$) resulted in the lowest total lipid production (Figure 5(a)). In the marine diatom exposed to AgNPs, total lipid production was significantly increased (from 11.6 to 17.4%, compared with the control) in all treatment with AgNPs. The highest increase of total lipid production (17.4%) was found in the treatment with 100 $\mu\text{g/L}$ (Figure 5(b)).

4. Discussion

In aquatic environment, green algae and diatom are not only the primary producers for higher tropic levels but also play an important role for the normal functioning of aquatic ecosystems [10]. Numerous studies have demonstrated that NPs generated adverse effects on freshwater and marine microalgae species [3, 24–26]. NPs are well known for their involvement of ROS in both animal and plant cells, causing oxidative stress and cellular damage [27, 28]. Zhang et al. [29] demonstrated the mechanism of the photosynthetic toxicity against the green algae *Scenedesmus obliquus* by using silver nanoclusters (AgNCs). The authors found that the photosynthetic toxicity of AgNCs was largely attributed to the “joint-toxicity” effect of particulate form of AgNCs and their released Ag^+ which resulted in the disruption of the electron transport chain of light reaction and affected the content of main enzymes of the Calvin cycle of algae cells. Other toxicity mechanisms of NPs in algae cells are the interaction with the algae cell wall or binding to the cell surface that resulted in the formation of large aggregates

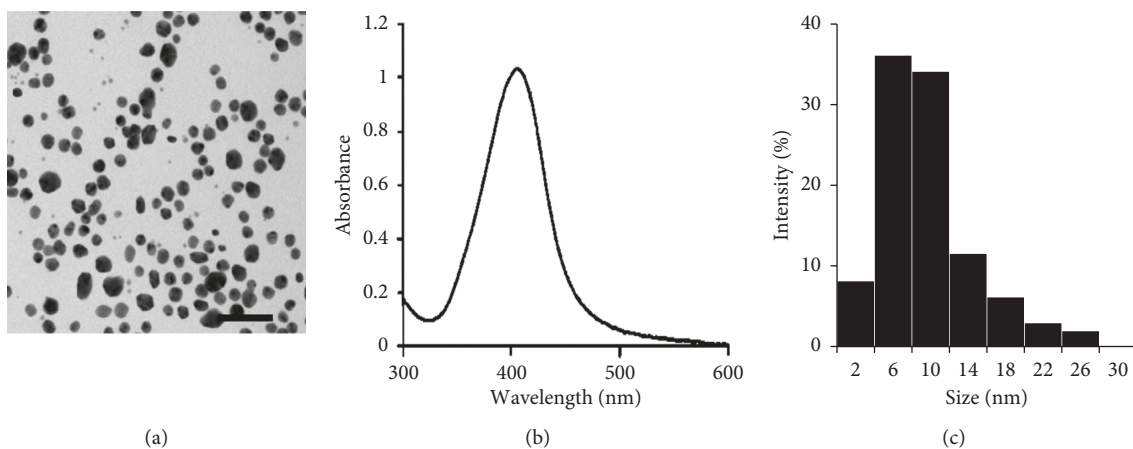


FIGURE 1: Morphology (a), absorbance wavelength (b), and size intensity (c) of silver nanoparticles (AgNPs) (scale bar: 50 nm).

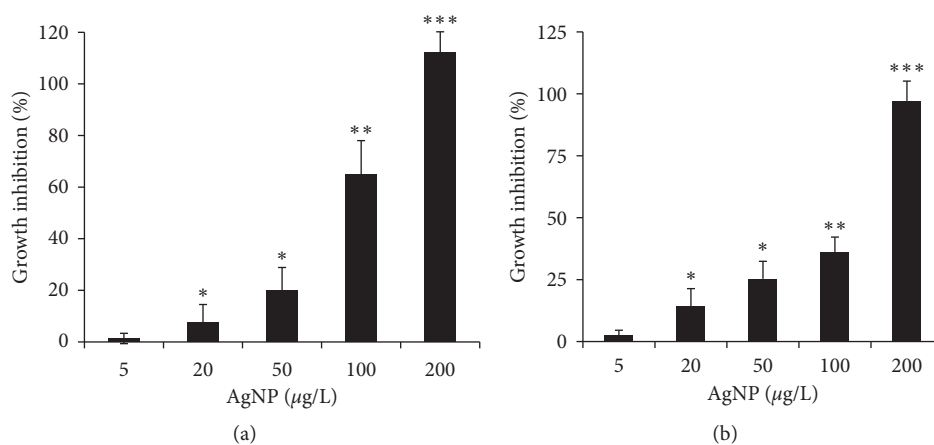


FIGURE 2: Effect of silver nanoparticles on growth of (a) *Scenedesmus* sp. and (b) *Thalassiosira* sp. Asterisks show significant differences compared with the control (* $P < 0.05$; ** $P < 0.01$; *** $P < 0.001$).

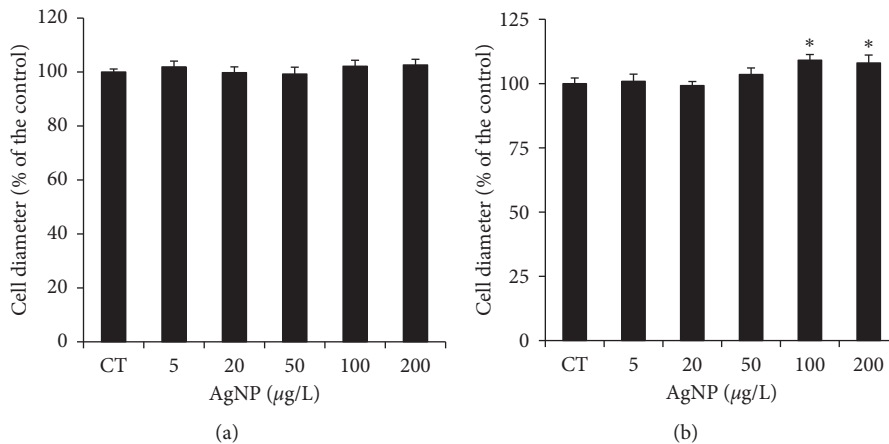


FIGURE 3: Algal cell diameter (μm) of (a) *Scenedesmus* sp. and (b) *Thalassiosira* sp. upon exposure to silver nanoparticles. Asterisks indicate significant differences compared with the control (* $P < 0.05$).

[16, 30]. The formation of aggregates could entrap algal cells and block cell division with consequent inhibition of cell division [31, 32].

The toxicity of NPs on algae may vary from algae species, exposure duration and dose, coating, and size [11, 24, 26, 33]. Sendra et al. [25] indicated that AgNPs have

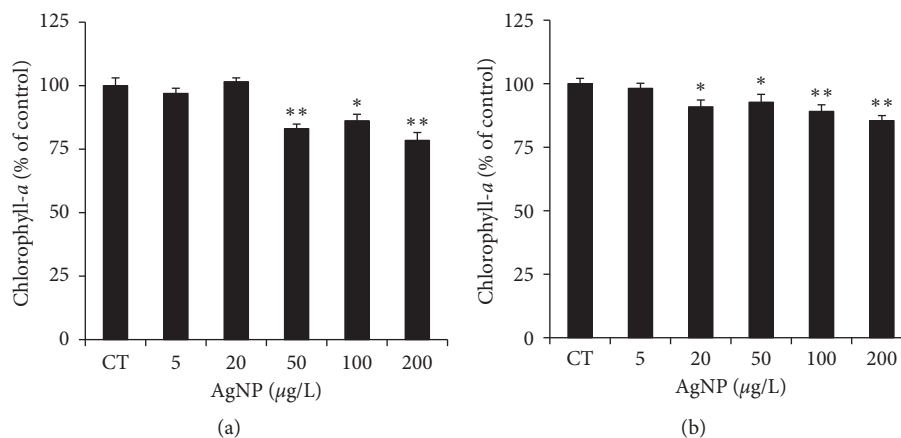


FIGURE 4: Chlorophyll-*a* content of (a) *Scenedesmus sp.* and (b) *Thalassiosira sp.* upon exposure to silver nanoparticles. Asterisks indicate significant differences compared with the control (* $P < 0.05$; ** $P < 0.01$).

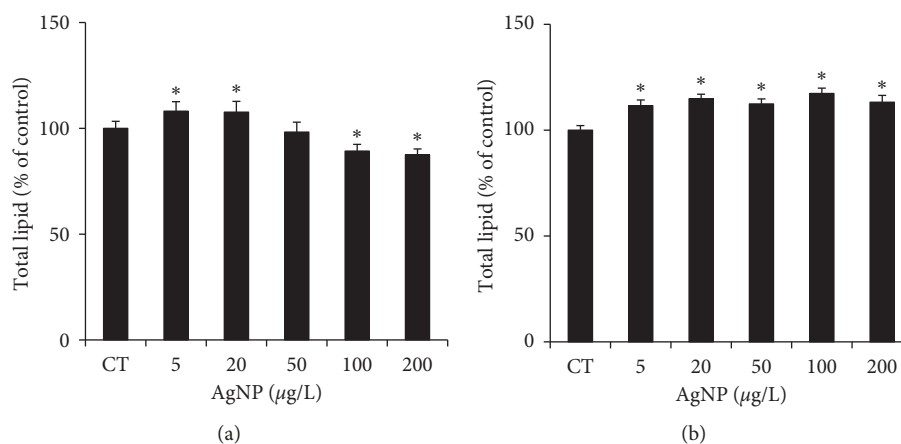


FIGURE 5: Total lipid content of (a) *Scenedesmus sp.* and (b) *Thalassiosira sp.* upon exposure to silver nanoparticles. Asterisks indicate significant differences compared with the control (* $P < 0.05$).

generated direct and indirect deleterious impacts on algae in different exposure environment. Generally, AgNPs tend to dissolve to Ag^+ under the presence of oxygen in aqueous environment [34]. Thus, both AgNPs and Ag^+ are present in the environment and hazardous effects of AgNPs to algae cells were contributed from the effect of AgNPs and their released Ag^+ . In freshwater algae, the toxic effect of Ag^+ was the main mechanism, while under marine condition with the present of high chloride ions (Cl^-), large amount of AgNPs are oxidatively dissolved and generate Ag/AgCl-NPs and $\text{AgCl}_x^{(x-1)-}$ compound. The formation of silver/silver chloride nanoparticles decreases the toxic effect of AgNPs to organisms [25, 26, 34, 35]. In addition, the toxic effects of NPs may depend on various factors such as exposure duration, dose of exposure, and environmental conditions [29]. When exposing the marine algae *Dunaliella tertiolecta* to both ZnO NPs and the bulk ZnO, Manzo et al. [33] reported that the toxic effects of ZnO NPs on the tested algae were stronger than of the bulk ZnO, and the toxicity mechanisms of bulk ZnO may not relate to the ion of zinc. In addition, when using different marine and freshwater species for the toxicity test, Aravantinou et al. [24] found

that toxic effects of ZnNPs obviously depended on the microalgae species as well as the exposure duration and dose. Results of the present study agree well with Sendra et al. [25] that AgNPs is more toxic in freshwater than in marine environment. Probably, the high generation of the dissolved ion Ag^+ in freshwater media resulted in higher toxicity of AgNPs in freshwater microalgae [25, 29].

Previous studies often used physiological alterations as indicators for assessment toxicity of NPs in microalgae [10, 25, 35]. Chlorophyll-*a* content is commonly used to indicate the photosynthesis efficiency or the cell division of algal species [10, 36]. Exposure of microalgae to NPs has resulted in the reduction of chlorophyll-*a* content due to the damage in the pigment of the exposed cells or reduction of the pigment-protein complexes [10, 36]. The decrease in chlorophyll-*a* content in both tested algae upon exposure to AgNPs may be a result of accelerating the activity of the chlorophyllase or stimulating ROS production [10]. Results of the present study are in agreement with the observations of Wei et al. [36] and Huang et al. [10] that AgNPs has induced a physiological response in the freshwater and marine algae through reduction of chlorophyll-*a* content [10]. Under stress condition, living cells have the ability to

generate enzymatic and nonenzymatic antioxidants to regulate ROS adverse effects. Thus, intracellular ROS have been commonly used as biomarkers to quantify the toxic effects of pollutants [10, 25, 35]. In addition, morphological characteristics such as cell size, cell teratology, or deformity have been used as bioindicators for evaluating toxicity of hazardous substances [37]. In this study, exposure to a specific concentration of AgNPs resulted in elevation in cell size of the marine diatom *Thalassiosira* sp. as well as depletion in chlorophyll-*a* content. These results indicated chlorophyll-*a* content and the morphological response in diatom frustule can be used to monitor hazardous substances in water environment.

Green algae and diatoms are known for storing lipid level up to 50% as a reserve food material under stress condition [28, 38]. Higher lipid contents in green algae and diatoms under heavy metals or nanoparticles stress have been reported [28, 38]. Under stress condition, algal cells tend to adjust the cellular metabolism and store more large molecules such as proteins and lipid [10]. Algae can tolerate toxic effects typically at lower doses of toxicants [28]. In this study, the lipid content in the green algae *Scenedesmus* sp. increased significantly at low dose of AgNPs, but decreased as higher dose of AgNPs could be reflected from the above mechanisms. He et al. [28] demonstrated that a specific concentration of NPs could promote neutral lipids accumulation in the green algae *S. obliquus*, but further increase of NPs has resulted in the inhibition of cell growth and reduction of lipid production. Results of this study were also in agreement with observations of Huang et al. [10] that there is a reduction in the chlorophyll-*a* content but an elevation in lipid contents in a dose-dependent manner upon exposure the marine diatom *S. costatum* to AgNPs. Further studies are needed to determine the optimum growth rates as well as for lipid production in the tested species, which could be used to make biodiesel in tropical regions.

5. Conclusions

By using two tropical microalgae species including the freshwater *Scenedesmus* sp. and the marine diatom *Thalassiosira* sp., the present study demonstrated the different toxic effects of AgNPs in freshwater and marine environments. The present results indicated the toxic effects of AgNPs may vary in different aquatic environments. Results indicated that AgNPs are more toxic in freshwater than in marine environment. AgNPs at a certain concentration have resulted in change in cell diameter, reduction in chlorophyll-*a* content, and stimulation of the total lipid production in the tested microalgae. Thus, morphological characteristic of microalgae can be used as an effective tool for monitoring nanoparticles in water.

Data Availability

The data used to support the findings of this study are included within the article.

Conflicts of Interest

The author declares that there are no conflicts of interest regarding the publication of this paper.

Acknowledgments

This study was supported by the Ton Duc Thang University under grant number PTL-HDLV-2019.

References

- [1] M. Ahamed, M. S. AlSalhi, and M. K. J. Siddiqui, "Silver nanoparticle applications and human health," *Clinica Chimica Acta*, vol. 411, no. 23-24, pp. 1841-1848, 2010.
- [2] C. Zhang, Z. Hu, and B. Deng, "Silver nanoparticles in aquatic environments: physicochemical behavior and antimicrobial mechanisms," *Water Research*, vol. 88, pp. 403-427, 2016.
- [3] I. Moreno-Garrido, S. Pérez, and J. Blasco, "Toxicity of silver and gold nanoparticles on marine microalgae," *Marine Environmental Research*, vol. 111, pp. 60-73, 2015.
- [4] Woodrow Wilson Database, *Nanotechnology Consumer Product Inventory*, Wilson Center, Washington, DC, USA, 2011, http://www.nanotechproject.org/inventories/consumer/analysis_draft/.
- [5] M. E. Vance, T. Kuiken, E. P. Vejerano et al., "Nanotechnology in the real world: redeveloping the nanomaterial consumer products inventory," *Beilstein Journal of Nanotechnology*, vol. 6, pp. 1769-1780, 2015.
- [6] C. Gambardella, E. Costa, V. Piazza et al., "Effect of silver nanoparticles on marine organisms belonging to different trophic levels," *Marine Environmental Research*, vol. 111, pp. 41-49, 2015.
- [7] D. Dewez and A. Oukarroum, "Silver nanoparticles toxicity effect on photosystem II photochemistry of the green alga *Chlamydomonas reinhardtii* treated in light and dark conditions," *Toxicological & Environmental Chemistry*, vol. 94, no. 8, pp. 1536-1546, 2012.
- [8] E. McGillicuddy, I. Murray, S. Kavanagh et al., "Silver nanoparticles in the environment: sources, detection and ecotoxicology," *Science of the Total Environment*, vol. 575, pp. 231-246, 2017.
- [9] D. Shevlin, N. O'Brien, and E. Cummins, "Silver engineered nanoparticles in freshwater systems—likely fate and behaviour through natural attenuation processes," *Science of the Total Environment*, vol. 621, pp. 1033-1046, 2018.
- [10] J. Huang, J. Cheng, and J. Yi, "Impact of silver nanoparticles on marine diatom *Skeletonema costatum*," *Journal of Applied Toxicology*, vol. 36, no. 10, pp. 1343-1354, 2016.
- [11] K. Miazek, W. Iwanek, C. Remacle, A. Richel, and D. Goffin, "Effect of metals, metalloids and metallic nanoparticles on microalgae growth and industrial product biosynthesis: a review," *International Journal of Molecular Sciences*, vol. 16, no. 10, pp. 23929-23969, 2015.
- [12] F. Ribeiro, J. A. Gallego-Urrea, K. Jurkschat et al., "Silver nanoparticles and silver nitrate induce high toxicity to *Pseudokirchneriella subcapitata*, *Daphnia magna* and *Danio rerio*," *Science of the Total Environment*, vol. 466-467, pp. 232-241, 2014.
- [13] E. Navarro, B. Wagner, N. Odzak, L. Sigg, and R. Behra, "Effects of differently coated silver nanoparticles on the photosynthesis of *Chlamydomonas reinhardtii*," *Environmental Science & Technology*, vol. 49, no. 13, pp. 8041-8047, 2015.

- [14] D. He, J. J. Dorantes-Aranda, and T. D. Waite, "Silver nanoparticle—algae interactions: oxidative, dissolution, reactive oxygen species generation and synergistic toxic effects," *Environmental Science & Technology*, vol. 46, no. 16, pp. 8731–8738, 2012.
- [15] A. Dash, A. P. Singh, B. R. Chaudhary, S. K. Singh, and D. Dash, "Effect of silver nanoparticles on growth of eukaryotic green algae," *Nano-Micro Letters*, vol. 4, no. 3, pp. 158–165, 2012.
- [16] A. Oukarroum, S. Bras, F. Perreault, and R. Popovic, "Inhibitory effects of silver nanoparticles in two green algae, *Chlorella vulgaris* and *Dunaliella tertiolecta*," *Ecotoxicology and Environmental Safety*, vol. 78, pp. 80–85, 2012.
- [17] A. A. Becaro, C. M. Jonsson, F. C. Puti et al., "Toxicity of PVA-stabilized silver nanoparticles to algae and microcrustaceans," *Environmental Nanotechnology, Monitoring & Management*, vol. 3, pp. 22–29, 2015.
- [18] V. V. Pinto, M. J. Ferreira, R. Silva, H. A. Santos, F. Silva, and C. M. Pereira, "Long time effect on the stability of silver nanoparticles in aqueous medium: effect of the synthesis and storage conditions," *Colloids and Surfaces A: Physicochemical and Engineering Aspects*, vol. 364, no. 1–3, pp. 19–25, 2010.
- [19] S. S. Kilham, D. A. Kreeger, S. G. Lynn, C. E. Goulden, and L. Herrera, "COMBO: a defined freshwater culture medium for algae and zooplankton," *Hydrobiologia*, vol. 377, no. 1–3, pp. 147–159, 1998.
- [20] OECD, *OECD Guidelines for Testing of Chemicals. Guideline 201: Freshwater Alga and Cyanobacteria, Growth Inhibition Test*, Organisation for Economic Co-operation and Development, Paris, France, 2006.
- [21] H. Metzner, H. Rau, and H. Senger, "Untersuchungen zur synchronisierbarkeit einzelner pigmentmangel-Mutanten von *Chlorella*," *Planta*, vol. 65, no. 2, pp. 186–194, 1965.
- [22] E. G. Bligh and W. J. Dyer, "A rapid method of total lipid extraction and purification," *Canadian Journal of Biochemistry and Physiology*, vol. 37, no. 8, pp. 911–917, 1959.
- [23] Y. Han, Q. Wen, Z. Chen, and P. Li, "Review of methods used for microalgal lipid-content analysis," *Energy Procedia*, vol. 12, pp. 944–950, 2011.
- [24] A. F. Aravantinou, V. Tsarpali, S. Dailianis, and I. D. Manariotis, "Effect of cultivation media on toxicity of ZnO nanoparticles to freshwater and marine microalgae," *Ecotoxicology and Environmental Safety*, vol. 114, pp. 109–116, 2015.
- [25] M. Sendra, M. P. Yeste, J. M. Gatica, I. Moreno-Garrido, and J. Blasco, "Direct and indirect effects of silver nanoparticles on freshwater and marine microalgae (*Chlamydomonas reinhardtii* and *Phaeodactylum tricorutum*)," *Chemosphere*, vol. 179, pp. 279–289, 2017.
- [26] T. L. Pham, "Toxicity of silver nanoparticles to tropical microalgae *Scenedesmus acuminatus*, *Chaetoceros gracilis* and crustacean *Daphnia lumholtzi*," *Turkish Journal of Fisheries and Aquatic Sciences*, vol. 19, no. 12, 2018.
- [27] A. Manke, L. Wang, and Y. Rojanasakul, "Mechanisms of nanoparticle-induced oxidative stress and toxicity," *BioMed Research International*, vol. 2013, Article ID 942916, 15 pages, 2013.
- [28] M. He, Y. Yan, F. Pei et al., "Improvement on lipid production by *Scenedesmus obliquus* triggered by low dose exposure to nanoparticles," *Scientific Reports*, vol. 7, no. 1, article 15526, 2017.
- [29] L. Zhang, N. Goswami, J. Xie, B. Zhang, and Y. He, "Unraveling the molecular mechanism of photosynthetic toxicity of highly fluorescent silver nanoclusters to *Scenedesmus obliquus*," *Scientific Report*, vol. 7, no. 1, article 16432, 2017.
- [30] R. D. Handy, G. Cornelis, T. Fernandes et al., "Ecotoxicity test methods for engineered nanomaterials: practical experiences and recommendations from the bench," *Environmental Toxicology and Chemistry*, vol. 31, no. 1, pp. 15–31, 2012.
- [31] V. Aruoja, H.-C. Dubourguier, K. Kasemets, and A. Kahru, "Toxicity of nanoparticles of CuO, ZnO and TiO₂ to microalgae *Pseudokirchneriella subcapitata*," *Science of the Total Environment*, vol. 407, no. 4, pp. 1461–1468, 2009.
- [32] J. Ji, Z. Long, and D. Lin, "Toxicity of oxide nanoparticles to the green algae *Chlorella* sp.," *Chemical Engineering Journal*, vol. 170, no. 2–3, pp. 525–530, 2011.
- [33] S. Manzo, M. L. Miglietta, G. Rametta, S. Buono, and G. Di Francia, "Toxic effects of ZnO nanoparticles towards marine algae *Dunaliella tertiolecta*," *Science of the Total Environment*, vol. 445–446, pp. 371–376, 2013.
- [34] W. Zhang, B. Xiao, and T. Fang, "Chemical transformation of silver nanoparticles in aquatic environments: mechanism, morphology and toxicity," *Chemosphere*, vol. 191, pp. 324–334, 2018.
- [35] B. Xia, B. Chen, X. Sun, K. Qu, F. Ma, and M. Du, "Interaction of TiO₂ nanoparticles with the marine microalga *Nitzschia closterium*: growth inhibition, oxidative stress and internalization," *Science of the Total Environment*, vol. 508, pp. 525–533, 2015.
- [36] C. Wei, Y. Zhang, J. Guo, B. Han, X. Yang, and J. Yuan, "Effects of silica nanoparticles on growth and photosynthetic pigment contents of *Scenedesmus obliquus*," *Journal of Environmental Sciences*, vol. 22, no. 1, pp. 155–160, 2010.
- [37] I. Lavoie, P. B. Hamilton, S. Morin et al., "Diatom teratologies as biomarkers of contamination: are all deformities ecologically meaningful?," *Ecological Indicators*, vol. 82, pp. 539–550, 2017.
- [38] S. Gautam, L. K. Pandey, V. Vinayak, and A. Arya, "Morphological and physiological alterations in the diatom *Gomphonema pseudoaugur* due to heavy metal stress," *Ecological Indicators*, vol. 72, pp. 67–76, 2017.

Research Article

Synthesis of Magnesium Oxide Nanoplates and Their Application in Nitrogen Dioxide and Sulfur Dioxide Adsorption

Thi Hai Yen Duong,¹ Thanh Nhan Nguyen¹, Ho Thi Oanh^{1,2}, Tuyet Anh Dang Thi,^{1,2} Le Nhat Thuy Giang,^{1,2} Hoang Thi Phuong,¹ Nguyen Tuan Anh¹, Ba Manh Nguyen¹, Vinh Tran Quang^{1,2}, Giang Truong Le,^{1,2} and Tuyen Van Nguyen^{1,2}

¹Institute of Chemistry, Vietnam Academy of Science and Technology, 18 Hoang Quoc Viet, Cau Giay, Hanoi, Vietnam

²Graduate University of Science and Technology, Vietnam Academy of Science and Technology, 18 Hoang Quoc Viet, Cau Giay, Hanoi, Vietnam

Correspondence should be addressed to Tuyen Van Nguyen; ngvtuyen@hotmail.com

Received 15 March 2019; Revised 20 April 2019; Accepted 22 April 2019; Published 26 May 2019

Guest Editor: Thanh-Dong Pham

Copyright © 2019 Thi Hai Yen Duong et al. This is an open access article distributed under the Creative Commons Attribution License, which permits unrestricted use, distribution, and reproduction in any medium, provided the original work is properly cited.

In this research, nanostructured magnesium oxide was synthesized through the sol-gel calcination or hydrothermal calcination method using various surfactants. The X-ray diffraction pattern of the materials confirmed that all the prepared magnesium oxide samples were single phase without any impurity. The scanning electron microscopy images and specific surface area values showed that sodium dodecyl sulfate was the most suitable surfactant for the synthesis of magnesium oxide nanoplates with the diameter of 40–60 nm, the average thickness of 5 nm, and a specific surface area of 126 m²/g. This material was utilized for nitrogen dioxide and sulfur dioxide adsorption under ambient condition. The saturated adsorption capacities of magnesium oxide were 174 mg/g for nitrogen dioxide and 160 mg/g for sulfur dioxide, making the magnesium oxide nanoplates a promising candidate for toxic gas treatment.

1. Introduction

Nowadays, air pollution caused by the emission of toxic gases from human and industrial activities poses not only tremendous threats to human health but also the destructive effects to the ecosystem. Nitrogen dioxide (NO₂) and sulfur dioxide (SO₂) are criteria pollutants that have adverse impacts on the environment. Both of NO₂ and SO₂ are released from natural and anthropological sources including forest fires, volcanic eruptions, transportation systems, and the combustion process. While NO₂ gas could be harmful to human due to cardiovascular damage and respiratory pathway [1, 2], SO₂ gas can affect the human health with breathing problems, cardiovascular complications, bronchitis, and eyes irritation [3, 4]. Some studies show that for every 10 ppb increase in SO₂ concentration, the risk of death increased by 0.2–2% [5]. This increasing risk requires feasible solutions to deal with. Various methods have been developed by scientists and experts

including molecular sieves, membrane separation, adsorption, and catalyst [6–9]. Among them, adsorption is one of the most effective methods for toxic gas treatment owing to simple processing and regeneration at low cost. Several materials such as activated carbon, hydroxide, metal oxide, sepiolite, and metal organic frameworks (MOFs) have been widely used as effective adsorbents [10–13].

During the development of nanoscience and nanotechnology, the application of inorganic nanomaterial as toxic gas adsorbents has attracted much attention because of their large specific surface area and high reactivity. Due to the economical and eco-friendly properties, nano-magnesium oxide (MgO) is a potential adsorbent of toxic gas [14–18]. However, to the best of our knowledge, there have been very few reports using MgO for the adsorption of NO₂ and SO₂.

Nanostructured MgO has been synthesized by various physicochemical techniques, such as sol-gel calcination,

chemical precipitation, and hydrothermal and microwave fabrication [19–28]. In this research, we successfully synthesized MgO nanoplates by sol-gel calcination and hydrothermal calcination methods. The influence of surfactant on the morphology of nanostructured MgO was investigated. The MgO nanoplates were used for NO₂ and SO₂ adsorption.

2. Materials and Methods

All chemicals were of analytical grade and directly used without further purification. Magnesium nitrate hexahydrate (Mg(NO₃)₂·6H₂O, 99.9%), sodium hydroxide (NaOH, 99.8%), polyethylene glycol (PEG 6000), cetyltrimethylammonium bromide (CTAB, 98%), sodium dodecyl sulfate (SDS, 98.5%), sulfur dioxide (99.9%), and nitrogen dioxide (99.5%) were purchased from Sigma-Aldrich and used without any further purification.

2.1. Synthesis of Nanostructured MgO. Nanostructured MgO was prepared by the sol-gel calcination or hydrothermal calcination method [29, 30] described as follows.

2.2. Sol-Gel Processing. Typically, 10 mmol Mg(NO₃)₂·6H₂O (2.56 g) was dissolved in 250 ml distilled water, and 0.5 mmol surfactant (3 g PEG 6000, 0.182 g CTAB or 0.144 g SDS) was added into the magnesium nitrate solution. Then, 100 ml NaOH 0.2 M solution was added dropwise into this mixture and stirred vigorously until a relatively high viscosity gel was formed. The gel was stirred gently overnight and then filtered, washed several times with distilled water, and dried at 80°C for 4 hours before calcinating at 500°C for 4 hours to obtain a white solid powder.

2.3. Hydrothermal Processing. The hydrothermal process was performed in a Teflon-lined stainless steel autoclave. 10 mmol Mg(NO₃)₂·6H₂O (2.56 g) was dissolved in 250 ml distilled water, and 0.5 mmol surfactant (3 g PEG 6000, 0.182 g CTAB or 0.144 g SDS) was added into the magnesium nitrate solution. Then, 100 ml NaOH 0.2 M solution was added dropwise into this mixture. Afterward, the resulting mixture was transferred into the autoclave and heated at 100°C for 2 hours. After cooling down to room temperature, the precipitate was collected by vacuum filtration and calcinated at 500°C for 4 hours to obtain a white solid powder.

2.4. Characterization of Materials. All the obtained MgO materials were characterized by different physicochemical techniques. The functional groups on the surface of materials were determined by Fourier-transform infrared spectroscopy (FT-IR, Thermo Fisher, USA). Phase identification was performed by the X-ray diffraction (XRD) technique, using Cu K α ($\lambda = 1.54056 \text{ \AA}$) radiation (D/max Ultima III, Rigaku, Japan). The morphology and particle size were given by scanning electron microscope (SEM, Hitachi, S-4800). The specific surface area was measured from the nitrogen adsorption/desorption at 77 K using the Brunauer–

Ennett–Teller (BET) method (TriStar II Plus, Micromeritics Instrument Corp, USA). The chemical composition of MgO material after adsorption was analyzed with energy-dispersive X-ray spectroscopy (SEM-EDX) (HORIBA-EMAX80; Hitachi High-Technology).

2.5. Adsorption Experiments. The experiments of evaluating the NO₂ and SO₂ adsorption on MgO nanoplates were carried out under ambient temperature. SO₂ or NO₂ gas was mixed with nitrogen carrier gas (5% SO₂ or NO₂ in N₂ atmosphere). A glass tube reactor was loaded with 100 mg of MgO powder with the pretreatment at 200°C for 1 hour. Then, a stream of NO₂ gas or SO₂ gas was supplied with a flow rate of 50 ml/min. The uptake quantities were recorded as a function of time. The adsorption of NO₂ and SO₂ on MgO nanoplates were monitored by FT-IR and EDX. The MgO nanoplates were collected and regenerated by calcination at 500°C for 4 hours. The schematic diagram for NO₂ and SO₂ adsorption experiment is shown in Figure 1.

3. Results and Discussion

3.1. Characterization of Magnesium Oxide Nanoplates. In this study, three different surfactants (PEG, CTAB, and SDS) were utilized for the synthesis of MgO nanocrystals by sol-gel and hydrothermal methods. Their crystalline structures are presented in Figure 2. The most intense peaks in XRD patterns of the synthesized MgO samples were observed at 2θ of 37.16°, 43.12°, and 62.40° which were well-matched with those of JCPDS data file of standard MgO no. 78-0430 [31]. The XRD patterns of MgO synthesized by using different surfactants and synthesis methods were basically similar to the surfactant-free MgO, indicating that the crystal structure of MgO was not affected by surfactants or synthesis methods. Furthermore, both sol-gel and hydrothermal methods produced MgO crystal with single phase.

The morphology of MgO samples is illustrated in Figures 3 and 4. BET specific surface area values of nano-MgO are shown in Table 1. Evidently, surfactant-free MgO samples exhibited undefined morphology and high aggregation.

Among the three surfactants, PEG showed less influence in controlling the size and morphology of MgO nanoplates. In addition, MgO materials synthesized using this surfactant have relatively low surface areas (98 m²/g for the sol-gel method and 110 m²/g for the hydrothermal method). In contrast, SDS was a suitable surfactant for the formation of MgO nanoplates with well-defined morphology and high surface area (115 m²/g for sol-gel method and 126 m²/g for hydrothermal method) (Figure 5). This phenomenon might be explained by the electrostatic interaction between surfactants and MgO surface. The nonionic nature of PEG does not allow effective interaction with positively charged MgO surface while the negatively charged SDS interacts effectively with the surface of MgO. Interestingly, MgO samples synthesized by the hydrothermal method had smaller average size and higher surface area compared with the samples prepared by the sol-gel method. There are two possible

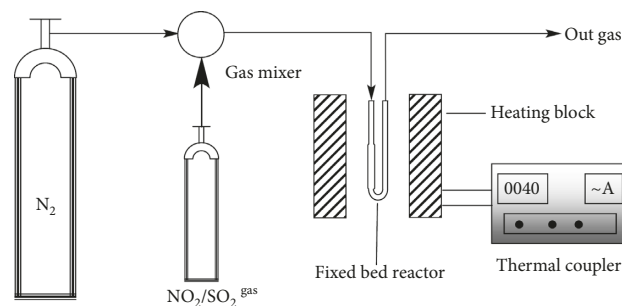


FIGURE 1: Schematic diagram of the experimental setup for NO_2 and SO_2 adsorptions.

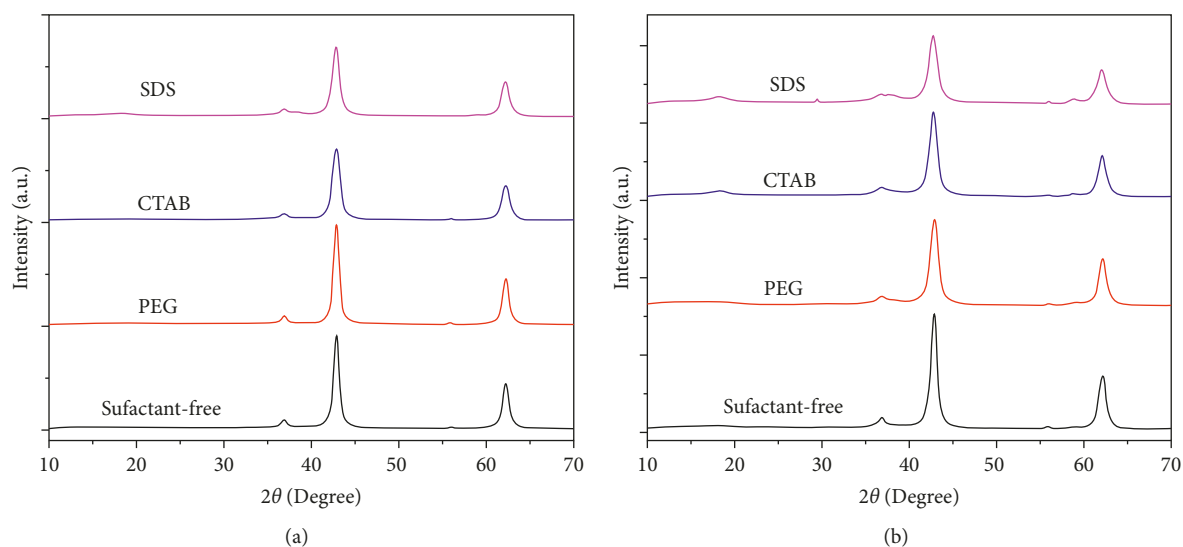


FIGURE 2: XRD patterns of nano-MgO synthesized by (a) the sol-gel method and (b) the hydrothermal method.

reasons for these higher surface areas. Firstly, during the hydrothermal process, the generating and loss of water molecules between adjacent layers of hydroxyl ions create defects, intercrystallite channels, and cracks inside the structure of MgO, which increase the surface area and porosity of the material [30]. Secondly, when increasing temperature suddenly, the formation of nucleations is facilitated which results in the decline of precursor concentration and hence, crystals are formed with smaller size. Due to the highest surface area and good morphology, the MgO nanoplate material synthesized by hydrothermal method using SDS was chosen for the adsorption of NO_2 and SO_2 gases.

3.2. Investigation of Adsorption Ability of the Material. Fourier-transform infrared spectroscopy was employed to determine the presence of NO_2 on the surface of MgO (Figure 6(a)). It was shown that after 10 min of adsorption, a new peak appeared at 1384 cm^{-1} which is assigned for NO_3^- vibration [32]. The appearance of NO_3^- is explained by the interaction between NO_2 and the metal sites of MgO which facilitates the dissociation of NO_2 into NO_3^- and NO [32, 33]:



The intensity of this peak increased with the increase of the adsorption time, indicating higher loading of NO_2 on MgO nanoplates. Figure 6(b) presents the results of the adsorption experiment for NO_2 . The uptake rate increased rapidly during the first 20 min with the adsorbed amount of $111\text{ mg}_{\text{NO}_2}/\text{g}_{\text{MgO}}$. After 60 min of adsorption, the adsorbed NO_2 reached 89% of the maximum capacity (the adsorption equilibrium was achieved after 180 min of adsorption with the uptake value of $174\text{ mg}_{\text{NO}_2}/\text{g}_{\text{MgO}}$). The EDX results (Figure 6(c)) verified the existence of N elements on MgO nanoplates with 4.55 wt.%, corresponding to the NO_2 adsorption of $176\text{ mg}/\text{g}_{\text{MgO}}$, which was in agreement with the adsorption result. The SEM image (inset in Figure 6(c)) illustrated the surface of MgO sample after the adsorption process without any change in comparison with the original sample. In addition, XRD patterns of MgO sample after 180 min of exposure to NO_2 showed no difference with the initial sample (Figure 6(d)).

The results of the SO_2 adsorption on MgO nanoplates are presented in Figure 7. Because of the number of basic sites over MgO, a $\text{SO}_{2,\text{gas}} + \text{MgO} \longrightarrow \text{MgSO}_3$ reaction could be expected [33, 34]. The presence of SO_2 on the MgO surface was affirmed by the broadband at 984 cm^{-1} [35] in the IR spectrum (Figure 7(a)). This band enlarged along the

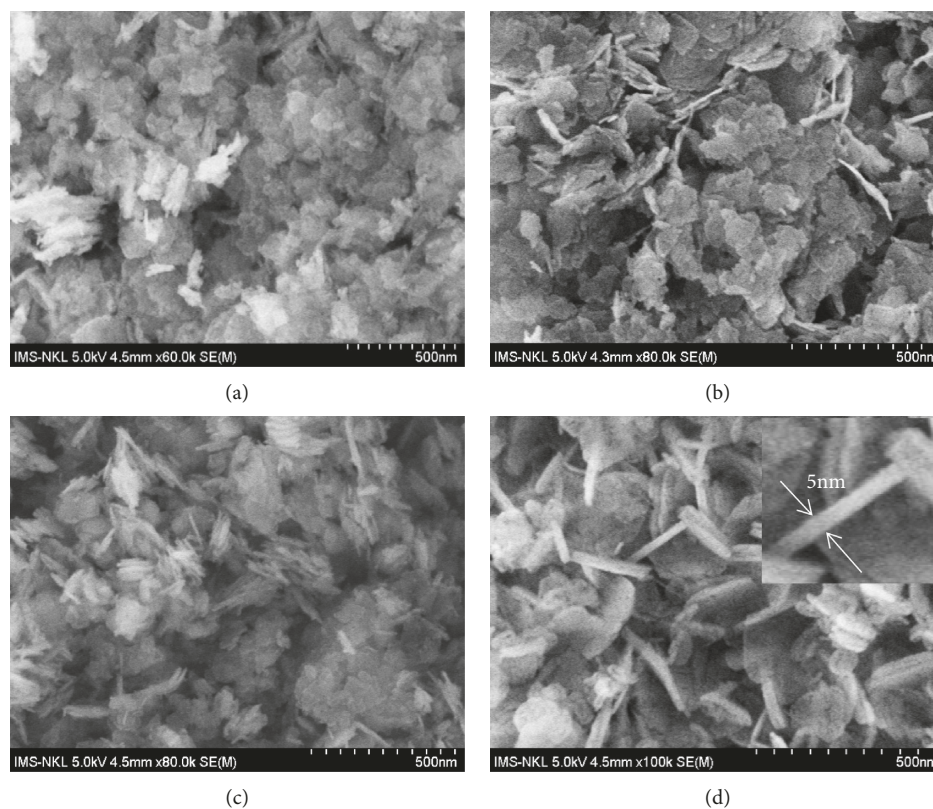


FIGURE 3: SEM images of nano-MgO prepared by the sol-gel method using different surfactants: (a) surfactant-free, (b) PEG, (c) CTAB, and (d) SDS.

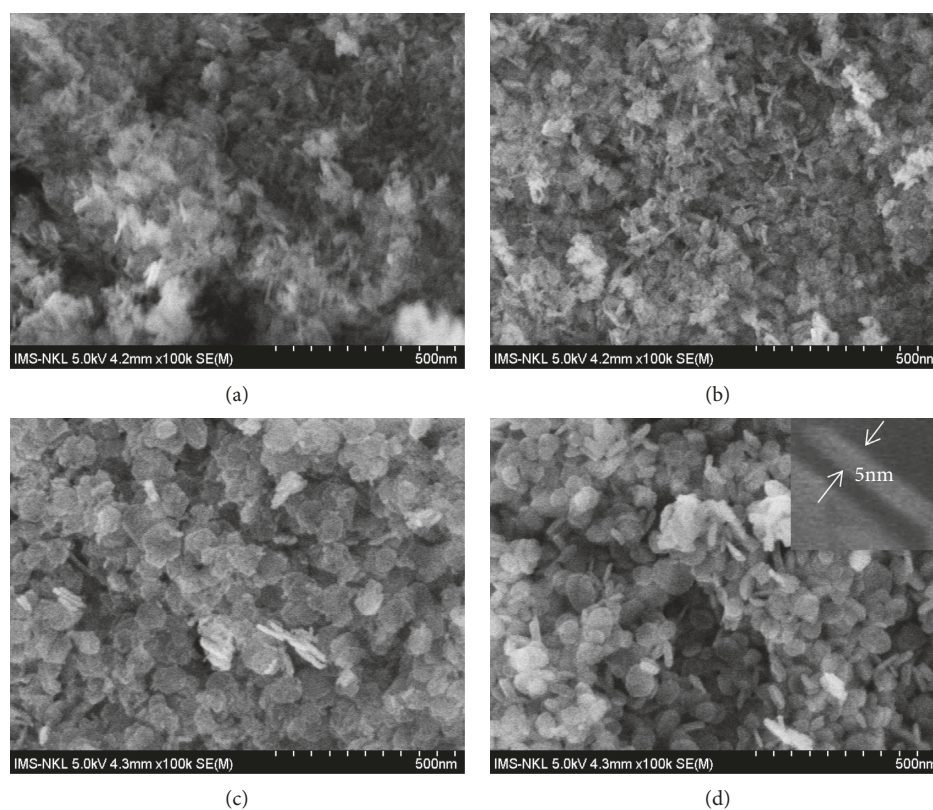


FIGURE 4: SEM images of nano-MgO prepared by the hydrothermal method using different surfactants: (a) surfactant-free, (b) PEG, (c) CTAB, and (d) SDS.

TABLE 1: BET specific surface area values of nano-MgO synthesized by using different surfactants.

	Method	Surfactant-free	PEG	CTAB	SDS
S_{BET} (m^2/g)	Sol-gel	66	98	100	115
	Hydrothermal	88	110	119	126

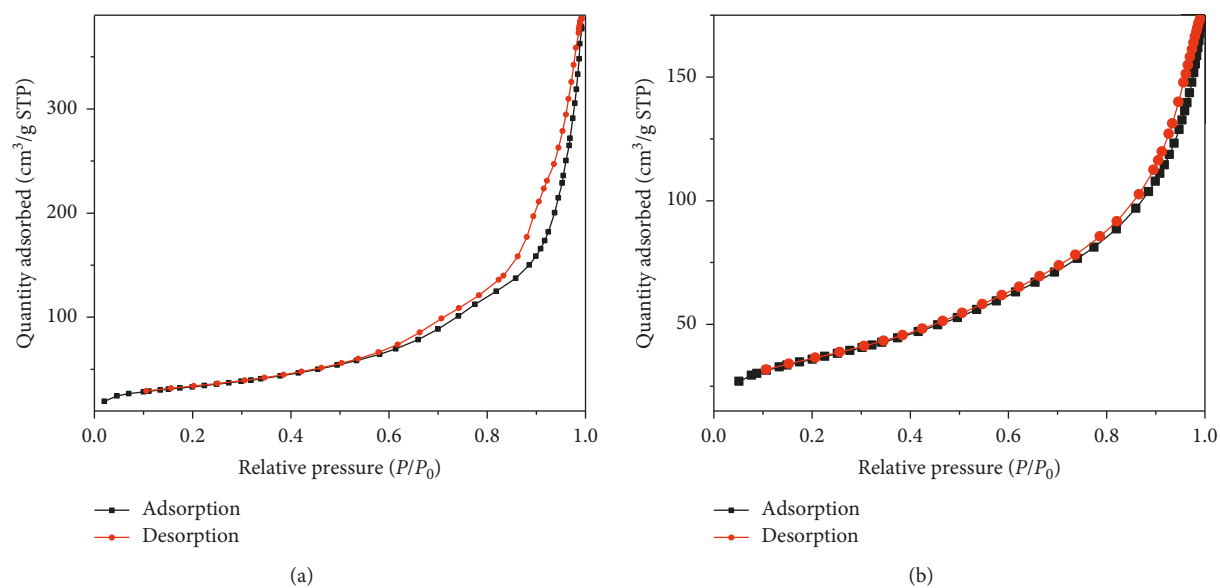
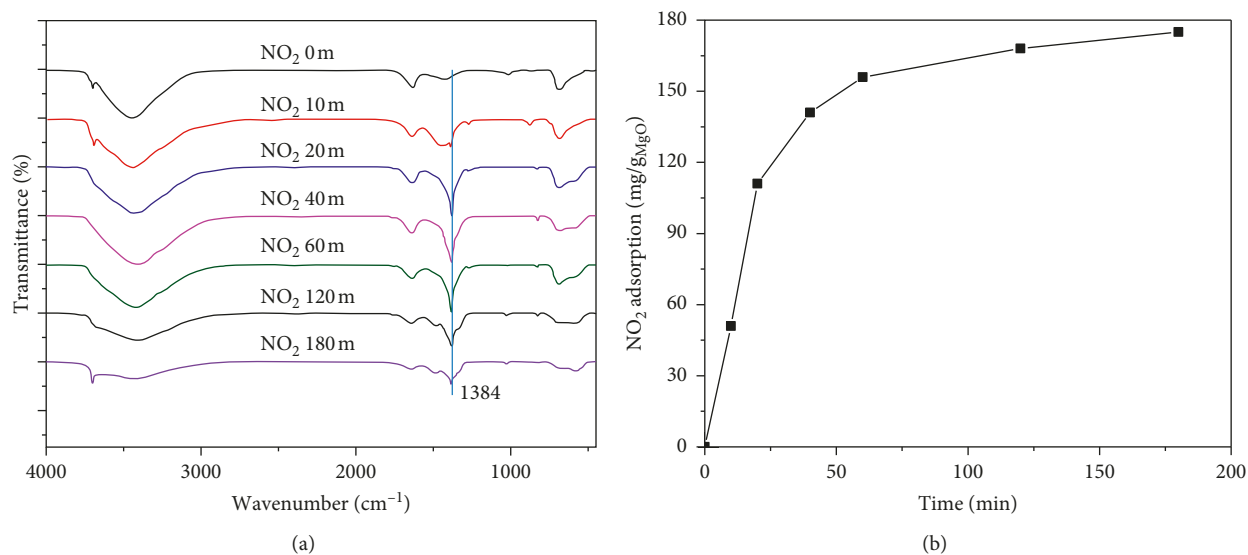
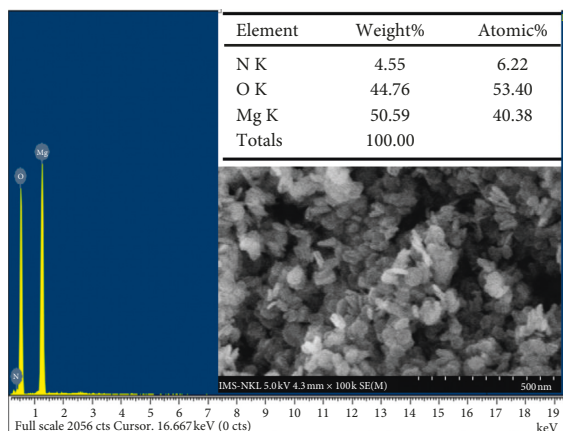
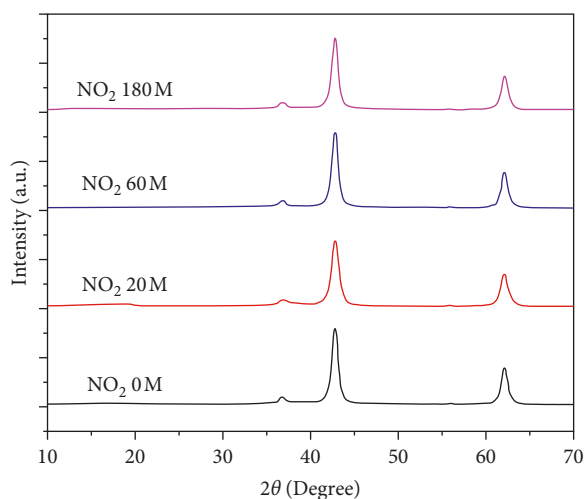
FIGURE 5: N_2 adsorption/desorption isotherms of MgO nanoplates synthesized using SDS by (a) the sol-gel calcination method and (b) the hydrothermal calcination method.

FIGURE 6: Continued.

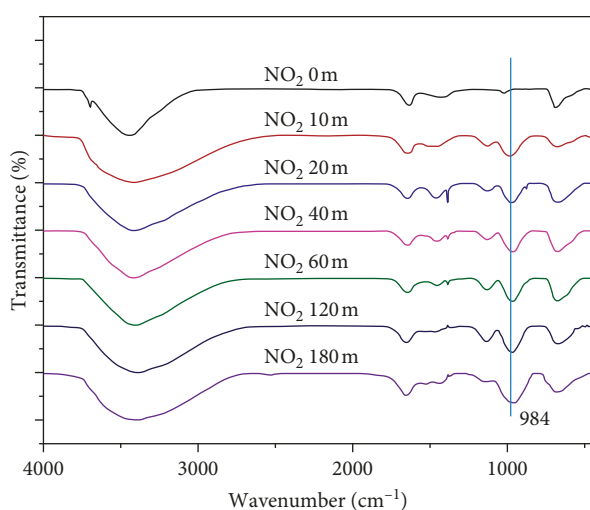


(c)

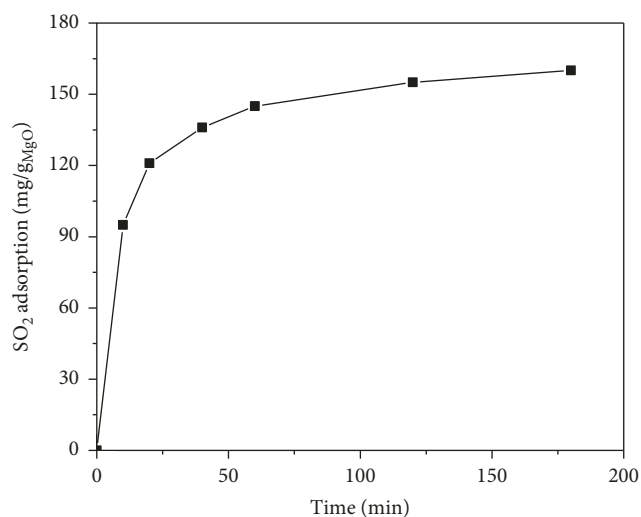


(d)

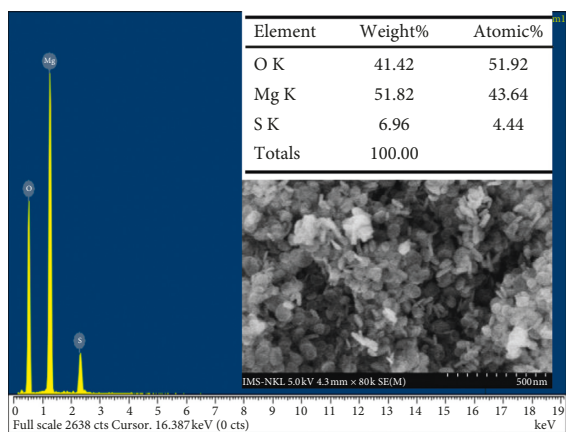
FIGURE 6: (a) FT-IR spectra of MgO samples after different adsorption times; (b) quantity of NO₂ adsorbed on MgO; (c) EDX spectrum and SEM image of MgO after 180 min of adsorption; (d) XRD patterns of MgO samples after different adsorption times.



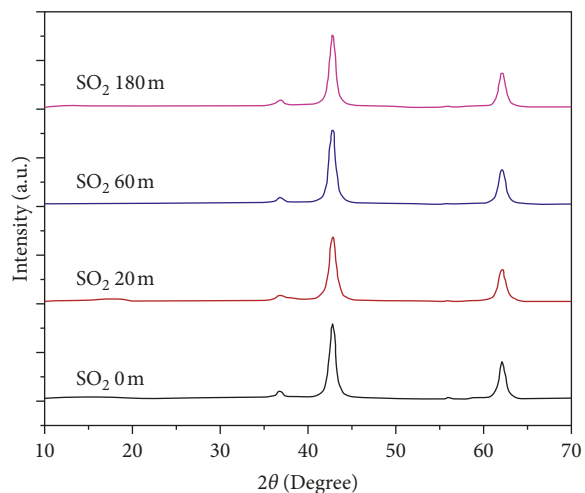
(a)



(b)

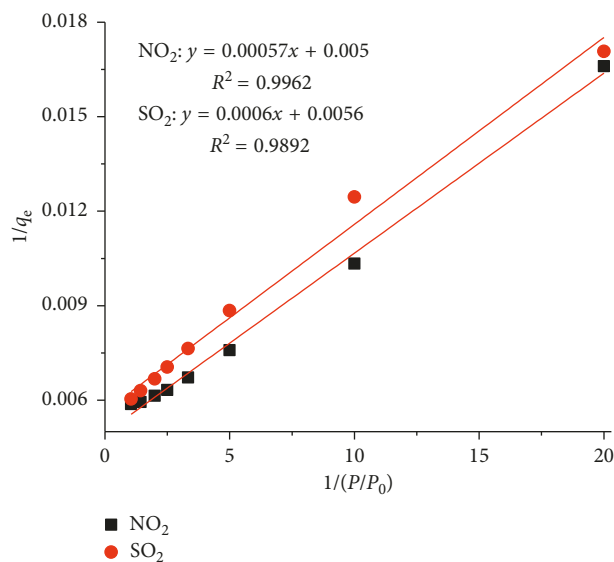


(c)



(d)

FIGURE 7: (a) FT-IR spectra of MgO samples after different adsorption times; (b) quantity of SO₂ adsorbed on MgO; (c) EDX spectrum and SEM image of MgO after 180 min of adsorption; (d) XRD patterns of MgO samples after different adsorption times.

FIGURE 8: Langmuir adsorption isotherm of NO₂ and SO₂ over MgO nanoplates.TABLE 2: NO₂ and SO₂ adsorption capacity of MgO nanoplates compares with well-known adsorbents.

Adsorbent	Experimental condition	Adsorption time (min)	Saturated adsorption capacity (mg/g)		Reference
			NO ₂	SO ₂	
Porous media prepared from sewage sludge ($S_{\text{BET}} = 21.2 \text{ m}^2/\text{g}$)	(i) Concentration: NO ₂ : 70 ppm (0.007%) in nitrogen SO ₂ : 100 ppm (0.01%) in nitrogen	70 (NO ₂); 100 (SO ₂)	1.12	0.98	[36]
	(ii) Moisture: 0%		(0.0244 mmol/g)	(0.0214 mmol/g)	
Zeolite-coated porous media ($S_{\text{BET}} = 13.1 \text{ m}^2/\text{g}$)	(iii) Adsorbent weight: 0.55 g	40 (NO ₂); 65 (SO ₂)	2.08	1.72	[36]
	(iv) Gas flow rate: 17000 ml/min (v) Temperature: 25°C		(0.0451 mmol/g)	(0.0374 mmol/g)	
Activated carbon ($S_{\text{BET}} = 1077 \text{ m}^2/\text{g}$)	(i) Concentration: NO ₂ : 4856 ppm (0.4856%) in nitrogen SO ₂ : 1170 ppm (0.1170%) in nitrogen (relative pressure: 2.47)	60	135.70	42.10 (2.73 wt.%)	[37]
	(ii) Moisture: 0%		(2.95 mmol/g)		
MgO nanoplates ($S_{\text{BET}} = 126 \text{ m}^2/\text{g}$)	(iii) Adsorbent weight: 1.5 g	180	174.00	160.00	This research
	(iv) Gas flow rate: 583 ml/min (v) Temperature: 30°C				
MgO nanoplates ($S_{\text{BET}} = 126 \text{ m}^2/\text{g}$)	(i) Concentration: 5% in nitrogen	180	174.00	160.00	This research
	(ii) Moisture: 0%				
MgO nanoplates ($S_{\text{BET}} = 126 \text{ m}^2/\text{g}$)	(iii) Adsorbent weight: 0.1 g	180	174.00	160.00	This research
	(iv) Gas flow rate: 50 ml/min (v) Temperature: 25°C				

adsorption time. As shown in Figure 7(b), the amount of SO₂ measured after 10 min reached 95 mg/g_{MgO}. After 60 min, the adsorbed SO₂ reached 93% of the maximum capacity (the adsorption equilibrium was achieved after 180 min of adsorption with the uptake value of 160 mg/g_{MgO}). The EDX spectrum (Figure 7(c)) confirmed the presence of S on the MgO surface. The content of S element was 6.96 wt.%, corresponding to 13.92 wt.% SO₂ in the sample after 180 min of exposure. The calculated amount of SO₂ was about 162 mg/g_{MgO}, similar to the obtained SO₂ adsorption of MgO shown in Figure 7(b). The SEM image (inset in Figure 7(c)) and the XRD patterns (Figure 7(d)) show no

change in morphology as well as the crystalline structure after 180 min of SO₂ exposure compared with the original MgO sample, indicating the high stability of MgO nanoplates under the experimental condition.

The Langmuir model was used to evaluate the adsorption of NO₂ and SO₂ over MgO nanoplates. The Langmuir adsorption isotherm plots of NO₂ and SO₂ adsorption over MgO nanoplates are shown in Figure 8. The R^2 values of 0.9892 (in the case of SO₂) and 0.9962 (in the case of NO₂) illustrate the fitness of the Langmuir model for the adsorption. The equilibrium adsorption capacity value (q_e) was calculated with the relative pressure (p/p_0) value of 1. The q_e

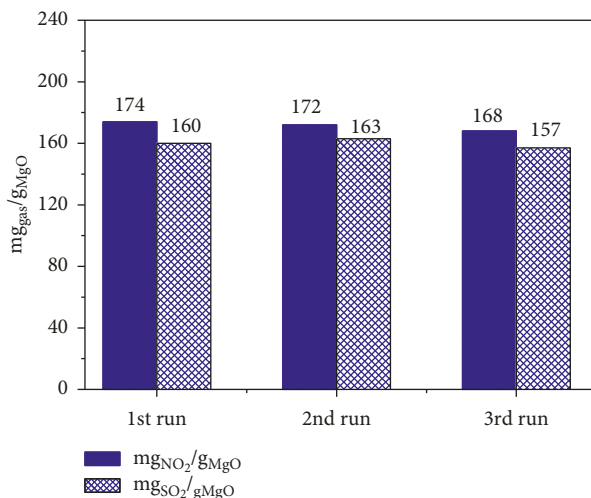


FIGURE 9: Diagram of adsorption capacity of NO₂ and SO₂ over MgO nanoplates after three cycles.

calculated values for the adsorption of NO₂ and SO₂ are 178.52 mg/g and 161.29 mg/g, respectively. These values were similar to the obtained experimental values of 174 mg/g (in the case of NO₂) and 160 mg/g (in the case of SO₂). This result shows the compatibility between experimental and theoretical calculations.

Furthermore, the adsorption capacity of NO₂ and SO₂ over MgO nanoplates was compared with that of reported porous adsorbents. The adsorption capacity and experimental conditions of these materials are summarized in Table 2. Interestingly, the MgO nanoplates exhibited relatively higher adsorption capacity than microporous activated carbon and zeolite [36, 37].

In order to evaluate the recycle of MgO nanoplates, this adsorber was regenerated and reused for NO₂ and SO₂ adsorption. The NO₂ and SO₂ adsorption capacity at the third cycle only decreased 3.45 and 1.87%, respectively (Figure 9). The result further confirmed the potential applicability of MgO nanoplates for the adsorption of NO₂ and SO₂.

4. Conclusions

To summarize, MgO nanoplates were well synthesized by sol-gel and hydrothermal methods using PEG, CTAB, and SDS as the morphology-controlling agents. The MgO nanoplates prepared by the hydrothermal method using SDS surfactant exhibited high specific surface area (126 m²/g) and well-defined morphology of nanoplates with the diameter of 40–60 nm and the average thickness of 5 nm. The adsorption experiments showed high NO₂ and SO₂ uptake values on MgO nanoplates (174 mg/g and 160 mg/g, respectively). Moreover, the MgO samples were highly stable under the exposure of NO₂ and SO₂. These results indicate that MgO is a potential candidate for the adsorption of toxic gases. Further work is ongoing to investigate the adsorption behavior of the material in severe condition. In addition, the kinetic and mechanism of adsorption will be studied for the

future application of MgO nanoplates in toxic gas removal and enhancement of the performance of gas treatment on MgO.

Data Availability

The data used to support the findings of this study are available from the corresponding author upon request.

Conflicts of Interest

The authors declare that there are no conflicts of interest regarding the publication of this paper.

Acknowledgments

This research was funded by the Vietnam Academy of Science and Technology under grant number “TĐPCCC.01/18–20.”

References

- [1] E. Fattore, V. Paiano, A. Borgini et al., “Human health risk in relation to air quality in two municipalities in an industrialized area of northern Italy,” *Environmental Research*, vol. 111, no. 8, pp. 1321–1327, 2011.
- [2] L. Curtis, W. Rea, P. Smith-Willis, E. Fenyves, and Y. Pan, “Adverse health effects of outdoor air pollutants,” *Environment International*, vol. 32, no. 6, pp. 815–830, 2006.
- [3] Y. Omidi, G. Goudarzi, A. M. Heidari, and S. M. Daryanoosh, “Health impact assessment of short-term exposure to NO₂ in Kermanshah, Iran using AirQ mode,” *Environmental Health Engineering and Management*, vol. 3, no. 2, pp. 91–97, 2016.
- [4] M. L. Williams, R. W. Atkinson, H. R. Anderson, and F. J. Kelly, “Associations between daily mortality in London and combined oxidant capacity, ozone and nitrogen dioxide,” *Air Quality, Atmosphere & Health*, vol. 7, no. 4, pp. 407–414, 2014.
- [5] E. Burt, P. Orris, and S. Buchanan, *Scientific Evidence of Health Effects from Coal Use in Energy Generation*, School of Public Health, University of Illinois and Health Care Without Harm, Chicago, IL, USA, 2013.
- [6] D. Plee, “Organic compounds adsorption on molecular sieves in gas phase—a comparison with activated carbons,” *Environmental Science*, vol. 61, pp. 349–357, 1994.
- [7] R. W. Baker and B. T. Low, “Gas separation membrane materials: a perspective,” *Macromolecules*, vol. 47, no. 20, pp. 6999–7013, 2014.
- [8] G. Itskos, N. Koukouzas, C. Vasiliatos, I. Megremi, and A. Moutsatsou, “Comparative uptake of toxic elements from aqueous media by the different particle-size-fractions of fly ash,” *Journal of Hazardous Materials*, vol. 183, no. 1–3, pp. 787–792, 2010.
- [9] H. Yang, Z. Xu, M. Fan et al., “Progress in carbon dioxide separation and capture: a review,” *Journal of Environmental Sciences*, vol. 20, no. 1, pp. 14–27, 2008.
- [10] C. Lu, H. Bai, B. Wu, F. Su, and J. F. Hwang, “Comparative study of CO₂ capture by carbon nanotubes, activated carbons, and zeolites,” *Energy & Fuels*, vol. 22, no. 5, pp. 3050–3056, 2008.
- [11] L. G. Neal, J. L. Haslbeck, and H. P. Tseng, “Sorber for removing nitrogen oxides, sulfur oxides and hydrogen sulfide from gas streams,” U.S. Patent 4, 755, 499, 1988.

- [12] J. A. Delgado, M. A. Uguina, J. L. Sotelo, B. Ruíz, and M. Rosário, "Carbon dioxide/methane separation by adsorption on sepiolite," *Journal of Natural Gas Chemistry*, vol. 16, no. 3, pp. 235–243, 2007.
- [13] I. Ahmed and S. H. Jung, "Composites of metal-organic frameworks: preparation and application in adsorption," *Materials Today*, vol. 17, no. 3, pp. 136–146, 2014.
- [14] C. Liang, T. Sasaki, Y. Shimizu, and N. Koshizaki, "Pulsed-laser ablation of Mg in liquids: surfactant-directing nanoparticle assembly for magnesium hydroxide nanostructures," *Chemical Physics Letters*, vol. 389, no. 1–3, pp. 58–63, 2004.
- [15] Z. Camtakan, S. A. Erenturk, and S. D. Yusan, "Magnesium oxide nanoparticles: preparation, characterization, and uranium sorption properties," *Environmental Progress & Sustainable Energy*, vol. 31, no. 4, pp. 536–543, 2012.
- [16] J. Y. Park, Y. J. Lee, and K. W. Jun, "Chemical synthesis and characterization of highly oil dispersed MgO nanoparticles," *Journal of Industrial and Engineering Chemistry*, vol. 12, pp. 882–887, 2006.
- [17] V. Štengl, S. Bakardjieva, M. Maříková, P. Bezdička, and J. Šubrt, "Magnesium oxide nanoparticles prepared by ultrasound enhanced hydrolysis of Mg-alkoxides," *Materials Letters*, vol. 57, no. 24–25, pp. 3998–4003, 2003.
- [18] J. C. Yu, A. Xu, L. Zhang, R. Song, and L. Wu, "Synthesis and characterization of porous magnesium hydroxide and oxide nanoplates," *Journal of Physical Chemistry B*, vol. 108, no. 1, pp. 64–70, 2004.
- [19] L. Wang, J. Wang, and D. den Engelsen, "Controlled synthesis of magnesium oxide nanoparticles for dye adsorption," *Journal of Nanoelectronics and Optoelectronics*, vol. 12, no. 5, pp. 512–517, 2017.
- [20] G. Yuan, J. Zheng, C. Lin, X. Chang, and H. Jiang, "Electrosynthesis and catalytic properties of magnesium oxide nanocrystals with porous structures," *Materials Chemistry and Physics*, vol. 130, no. 1–2, pp. 387–391, 2011.
- [21] P. Ouraipryvan, T. Sreethawong, and S. Chavadej, "Synthesis of crystalline MgO nanoparticle with mesoporous-assembled structure via a surfactant-modified sol-gel process," *Materials Letters*, vol. 63, no. 21, pp. 1862–1865, 2009.
- [22] M. Rezaei, M. Khajenoori, and B. Nematollahi, "Preparation of nanocrystalline MgO by surfactant assisted precipitation method," *Materials Research Bulletin*, vol. 46, no. 10, pp. 1632–1637, 2011.
- [23] Z. Wei, H. Qi, P. Ma, and J. Bao, "A new route to prepare magnesium oxide whisker," *Inorganic Chemistry Communications*, vol. 5, no. 2, pp. 147–149, 2002.
- [24] L. Yan, J. Zhuang, X. Sun, Z. Deng, and Y. Li, "Formation of rod-like Mg(OH)₂ nanocrystallites under hydrothermal conditions and the conversion to MgO nanorods by thermal dehydration," *Materials Chemistry and Physics*, vol. 76, no. 2, pp. 119–122, 2002.
- [25] Z. Zhao, H. Dai, Y. Du, J. Deng, L. Zhang, and F. Shi, "Solvo- or hydrothermal fabrication and excellent carbon dioxide adsorption behaviors of magnesium oxides with multiple morphologies and porous structures," *Materials Chemistry and Physics*, vol. 128, no. 3, pp. 348–356, 2011.
- [26] L. Kumari, W. Z. Li, C. H. Vannoy, R. M. Leblanc, and D. Z. Wang, "Synthesis, characterization and optical properties of Mg(OH)₂ micro-/nanosstructure and its conversion to MgO," *Ceramics International*, vol. 35, no. 8, pp. 3355–3364, 2009.
- [27] G. Gao and L. Xiang, "Emulsion-phase synthesis of honeycomb-like Mg₅(OH)₂(CO₃)₄·4H₂O micro-spheres and subsequent decomposition to MgO," *Journal of Alloys and Compounds*, vol. 495, no. 1, pp. 242–246, 2010.
- [28] T. X. Phuoc, B. H. Howard, D. V. Martello, Y. Soong, and M. K. Chyu, "Synthesis of Mg(OH)₂, MgO, and Mg nanoparticles using laser ablation of magnesium in water and solvents," *Optics and Lasers in Engineering*, vol. 46, no. 11, pp. 829–834, 2008.
- [29] R. Wahab, S. G. Ansari, M. A. Dar, Y. S. Kim, and H. S. Shin, "Synthesis of magnesium oxide nanoparticles by sol-gel process," *Materials Science Forum*, vol. 558–559, pp. 983–986, 2007.
- [30] Y. Ding, G. Zhang, H. Wu, B. Hai, L. Wang, and Y. Qian, "Nanoscale magnesium hydroxide and magnesium oxide powders: control over size, shape, and structure via hydrothermal synthesis," *Chemistry of Materials*, vol. 13, no. 2, pp. 435–440, 2001.
- [31] M. Badr-Mohammadia, I. Mobasherpoura, E. Marzban Rada, and G. Mortazavic, "Synthesis of cubic MgO nanostructure by an easy hydrothermal-calcinations method," *Journal of Ceramic Processing Research*, vol. 15, no. 2, pp. 88–92, 2014.
- [32] C. Sedlmair, B. Gil, K. Seshan, A. Jentys, and J. A. Lercher, "An in situ IR study of the NO_x adsorption/reduction mechanism on modified Zeolites," *Physical Chemistry Chemical Physics*, vol. 5, no. 9, pp. 1897–1905, 2003.
- [33] J. A. Rodriguez, T. Jirsak, L. González, J. Evans, M. Pérez, and A. Maiti, "Reaction of SO₂ with pure and metal-doped MgO: basic principles for the cleavage of S–O bonds," *Journal of Chemical Physics*, vol. 115, no. 23, pp. 10914–10926, 2001.
- [34] M. Waqif, A. M. Saad, M. Bensitel, J. Bachelier, O. Saur, and J.-C. Lavalley, "Comparative study of SO₂ adsorption on metal oxides," *Journal of the Chemical Society, Faraday Transactions*, vol. 88, no. 19, pp. 2931–2936, 1992.
- [35] F. A. Miller and C. H. Wilkins, "Infrared spectra and characteristic frequencies of inorganic ions," *Analytical Chemistry*, vol. 24, no. 8, pp. 1253–1294, 1952.
- [36] Y. S. Yoo, E. Z. Park, H. J. Ban, and H. J. Chae, "Removal of NO₂ and SO₂ using porous media made from sewage sludge removal," *Materials Science Forum*, vol. 658, pp. 153–156, 2010.
- [37] F. Ahnert and W. Heschel, "Multicomponent adsorption of butane, NO₂ and SO₂ on activated carbon," *Adsorption Science & Technology*, vol. 20, no. 4, pp. 353–370, 2002.

Research Article

Preparation of Graphene Nanoplatelets by Thermal Shock Combined with Ball Milling Methods for Fabricating Flame-Retardant Polymers

Vinh Q. Tran ^{1,2}, Hai T. Doan ¹, Nhiem T. Nguyen ¹ and Cuong V. Do ¹

¹Green Chemistry Department, Institute of Chemistry, Vietnam Academy of Science and Technology, Hanoi 100000, Vietnam

²Graduate University of Science and Technology, Hanoi 100000, Vietnam

Correspondence should be addressed to Vinh Q. Tran; vinhtq79@ich.vast.vn

Received 14 March 2019; Accepted 9 April 2019; Published 28 April 2019

Guest Editor: Ajit Kumar Sharma

Copyright © 2019 Vinh Q. Tran et al. This is an open access article distributed under the Creative Commons Attribution License, which permits unrestricted use, distribution, and reproduction in any medium, provided the original work is properly cited.

Graphene nanoplatelets were successfully prepared from graphite powder by simple and scalable thermal shock combined with ball milling methods. The formation of the graphene nanoplatelets were observed by field-emission scanning electron microscopes and Brunauer–Emmett–Teller methods with the much smaller number of layers and the considerable increase of specific surface area in comparison to the initial expanded graphite material. The other characterizations such as Fourier transform infrared spectroscopy and X-ray powder diffraction methods of graphene nanoplatelets showed unchanged structure. These graphene nanoplatelets were combined with aluminum trihydroxide and zinc borate to prepare flame-retardant polycarbonate plastic and chlorine-sulfonated polyethylene rubber. The prepared composites showed the improvement of flame resistance properties with V0 level according to the UL-94 test method, and the limiting oxygen index value was higher than 27.

1. Introduction

Graphene nanoplatelets (Gnps) and their derivatives are potential flame-retardant additives applied for preparation of flame-retardant polymers [1]. It can be combined with polymer matrix as a nanofiller for the case of plastic [1–4], rubber [5, 6], or coating agent for the case of fabric [7–9]. The flame resistance effect of Gnps depends mainly on their dispersity in polymer matrix. Beside the factor of compatibility between Gnps and polymers, the size and layer number of Gnps also play an important role. Gnps can be prepared by two main methods, the bottom-up and top-down methods [10, 11]. The bottom-up methods, such as chemical vapor deposition and epitaxial growth, are expensive and cannot meet the requirement of big quantitative production of Gnps. On the contrary, the top-down methods are expected to meet large-scale production of graphene with low cost. Graphite material can be cracked and exfoliated using a very useful mechanical method reported by Babak Alinejad et al. [10]. This method simply

used NaCl as an exfoliation agent because this salt is harder than graphite. The mixture of graphite powder and NaCl salt particles were grinded by using a planetary ball mill for 2–5 hours to crack graphite flakes to nanosized pieces. In this paper, we apply another simple method to produce Gnps material by using thermal shock combined with ball milling methods. An expanded graphite (EG) is firstly prepared from graphite powder. Next, a planetary ball milling machine is used for EG exfoliation to form Gnps. The ball milling of the EG instead of graphite powder is expected to improve the exfoliation effectiveness. Properties of the obtained Gnps are characterized by fourier transform infrared the spectroscopy (FTIR), X-ray powder diffraction (XRD), field-emission scanning electron microscope (FE-SEM), and Brunauer–Emmett–Teller (BET) methods. The prepared Gnps are used to fabricate the plastic and rubber flame-retardant materials. The obtained flame-retardant materials are measured the fire resistance property by UL-94 and limiting oxygen index (LOI) methods.

2. Materials and Methods

2.1. Chemicals. Graphite powder (<20 μm , synthetic, Sigma-Aldrich), hydrogen peroxide (H_2O_2 , AR, 30–32%, Xilong Scientific), sulfuric acid (H_2SO_4 , 98%, AR, Xilong Scientific), sodium chloride (NaCl, AR, 99.5%, Xilong Scientific), aluminum trihydroxide (AR, Xilong Scientific), zinc borate (99%, Kayseri, Turkey), polycarbonate plastic (Lotte Chemicals, Korea), and chlorine-sulfonated polyethylene rubber (CSM-3304, KunLun Co. Ltd, China) were used.

2.2. Gnps Preparation. Gnps were prepared from graphite powder via two steps. In the first step, graphite powder was undergone a thermal treatment. Typically, graphite powder was pretreated by being added to the mixture of H_2O_2 (30%): H_2SO_4 (98%) = 1 : 1.5 (v/v) at 20°C for 2 h. The solid was filtered and washed by DI water to have the pH = 7. The obtained solid was dried at 80°C for 24 h. This solid was thermal shocked by using a microwave at 800 W for 60 s. The solid was subjected to the pretreatment and the thermal shock once again by the same procedure described above to obtain EG sample. In the second step, the EG was grinded by using NaCl salt as discussed in [10]. 5 g EG sample was mixed with NaCl salt (EG : NaCl = 3 : 1 in molar ratio). A planetary ball milling machine (Pulverisette 5) with ball to powder weight ratio of 20 : 1 was used to grind the obtained mixture with a rotational speed of 350 rpm for 2 h in argon inert gas medium. NaCl salt was removed from the obtained powder by DI water using an ultrasonic bath. The final sample was centrifuged and dried at 80°C under vacuum to get the final sample.

2.3. Flame-Retardant Polymers Preparation. Gnps were used as nanofiller additive for flame-retardant polycarbonate (PC) plastic and chlorine-sulfonated polyethylene (CSPE) rubber preparation. Typically, a mixture of Gnps, conventional flame-retardant aluminum trihydroxide (ATH), and/or zinc borate (ZB) was melt-compounded with PC plastic or CSPE rubber in a Brabender closed mixing machine. PC plastic or CSPE rubber was melted in the first 4 min with a rotor speed of 50 rpm at 200°C (PC) and 85°C (CSPE). The above mixture with different percentage of Gnps, ATH, and/or ZB was then added to the compound with PC plastic or CSPE rubber for 10 min. The compounded sample was hot-pressed in a Brabender molding machine at 210°C (PC) and 95°C (CSPE) for 7 min to obtain the sample.

2.4. Materials Characterizations. The FTIR spectra were recorded using an IMPACT-410 (Nicolet, Germany) infrared spectrophotometer at room temperature in the range 4000–400 cm^{-1} on thin wafer of KBr in which 1% (w/w) of sample was dispersed. XRD diffraction patterns were recorded on a HUT-PCM-Bruker D8 Advance instrument diffractometer system equipped with Ni-filtered Cu Ka radiation (operating at 40 kV; 40 mA; wavelength $k = 0.154 \text{ nm}$). FE-SEM was carried out using a Jeol JSM-7500F instrument. Sample was dried, mounted on a thin plate, and coated by a thin

gold layer before recording. The BET method was measured by ASAP2010 equipment (Micrometrics-USA). The sample was treated in vacuum of 106 mmHg, at 120°C for 4 h and at 350°C for 9 h.

The fire resistance property of flame-retardant PC plastic and CSPE rubber was tested by the UL-94 method on Atlas Electric HVUL-94 flame test station and LOI analysis on a JF-3 instrument according to GB/T 10707-2008 standard.

3. Results and Discussion

3.1. Characterization of Gnps

3.1.1. FTIR and XRD Methods. The FTIR spectra of the graphite and GNPs samples are shown in Figures 1(a) and 1(b), respectively. Both FTIR spectra show the peaks at about 1635 cm^{-1} and 1450 cm^{-1} assigned to C=C skeletal band of aromatic domains [12] and the peak at 3430 cm^{-1} assigned to OH groups [13]. These OH groups may be corresponded to O–H stretching vibrations of adsorbed water molecules and structural OH groups which do not allow a distinction between C–OH and H_2O peaks. In the FTIR spectrum of Gnps sample, there are more peaks at 2975.09 cm^{-1} assigned to CH_2 (the symmetric and antisymmetric vibrations of methylene) [14] and peaks at 1089.48 and 1048.86 cm^{-1} assigned to OH stretching vibrations [15]. This result shows that by the pretreatment process using H_2O_2 and H_2SO_4 , more OH groups and CH_2 were formed. The intercalation of OH groups may help improve the ball milling effectiveness.

In addition, there is no considerable change between the XRD patterns of graphite and Gnps samples by using XRD method (Figure 2). There is a peak with high intensity at 2-theta of 26.4° assigned to the layer-by-layer structure of both graphite and Gnps samples [10, 12]. This result shows that by using thermal shock and ball milling, the Gnps sample was formed without structural transformation in comparison to the graphite sample.

3.1.2. FE-SEM and BET Methods. The FE-SEM images (Figure 3) show clearly that the structure of Gnps is layer-by-layer assembly. This structure is similar to the initial graphite structure. However, in comparison to the FE-SEM image of the EG sample (Figure 3(a)), the FE-SEM of the Gnps sample (Figures 3(b)–3(d)) shows clearly the exfoliation of EG to obtain Gnps with a monolayer or a few layers in its morphology.

The exfoliation of EG to Gnps is further demonstrated with the increase of specific surface area by BET result that is shown in Figure 4 and Table 1. The similarity of nitrogen adsorption/desorption curves shows the unchanged structure between EG and Gnps samples (Figure 4). The data in Table 1 show that the EG sample obtained by thermal shock has a BET specific surface area of 5.33 m^2/g . After the ball milling process of EG mixed with NaCl salt, BET specific surface area of the obtained GNPs is increased to 638.11 m^2/g (Table 1). It is 130 times higher in comparison to BET specific surface area of the EG sample and also higher than the reported result (524.4 m^2/g) that used virgin graphite powder for the ball milling [10]. In addition, the pore volume of Gnps sample is decreased to 0.02 cm^3/g from 0.04 cm^3/g (the pore

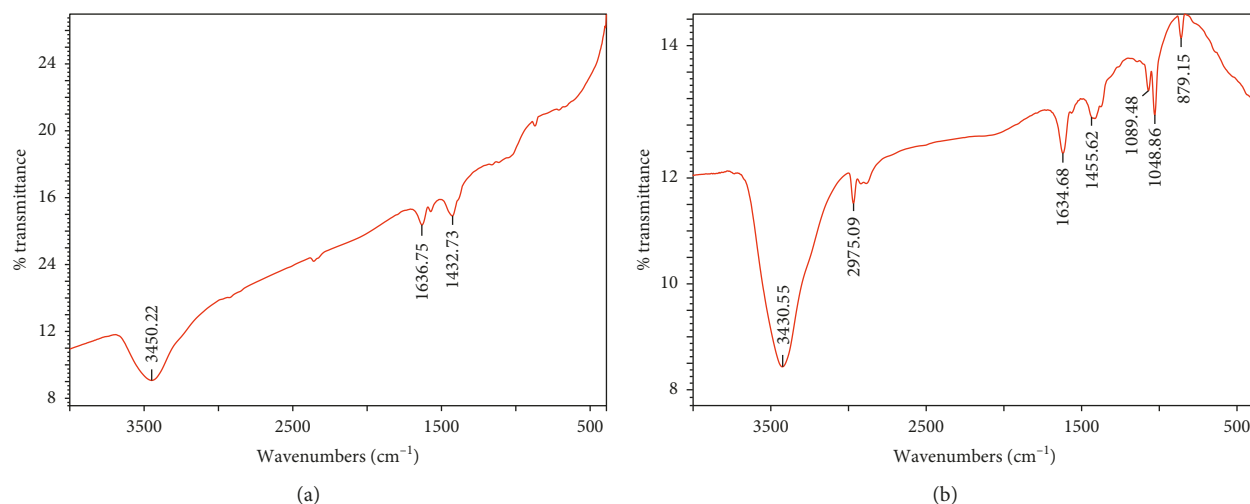


FIGURE 1: FTIR spectra. (a) Graphite sample; (b) Gnps sample.

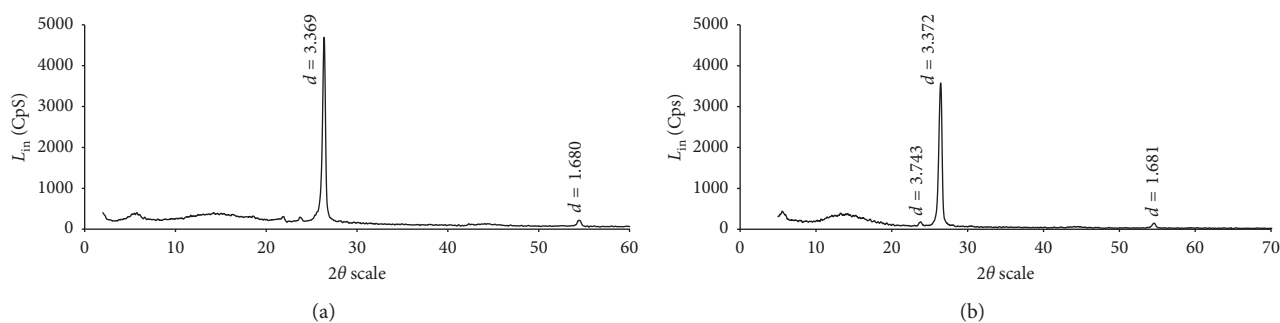


FIGURE 2: XRD patterns. (a) Graphite sample; (b) Gnps sample.

volume of EG sample before the ball milling). This result is in agreement with the FE-SEM result that showed the exfoliation of EG to obtain Gnps material with a few layers.

Gnps have been well known as an effective nanofiller flame-retardant additive with only small amount compounded with polymers (<5 wt.%) [1]. However, to improve the self-extinguishing property of polymers, it is better to use Gnps combined with conventional flame retardants. In this study, the ATH and ZB conventional flame retardants were applied. The compositions of the composite samples are shown in Table 2.

The results in Table 2 show that by using the same content (5 wt.%) of graphite and Gnps as nanofillers to PC material, their flame resistance abilities are UL-94 V2 and V1 levels, respectively. This result shows that the Gnps material is better flame retardant than the graphite material. However, at high content of Gnps, it may result in the agglomeration of Gnps and the decrease of the flame resistance ability. The experiments of decreasing Gnps content have been performed. The observed results show that by decreasing Gnps content to 1.5 and 1.0 wt.%, the UL-94 V0 level is attained. The lower content (0.5 wt.%) of Gnps did not show the good result (UL-94 V2 level).

The self-extinguishing property was improved by combining the Gnps material with the ATH and ZB

conventional flame retardants. The ATH and ZB conventional flame retardants were measured to get the UL-94 V1 level of the PC-ATH and PC-ZB composites. The idea is that by adding more Gnps combined with the PC-ATH and/or PC-ZB composites, the Gnps can help improving PC flame resistance ability to the UL-94 V0 level. The obtained results reach the expectation. By adding Gnps 1.5 wt.% combined with ATH (25 wt.%) or ZB (15 wt.%) to PC, the obtained composites attain the UL-94 V0 level. However, the LOIs of these composite samples are lower than 27% (PC-Gnps-ATH: 22.9%; PC-Gnps-ZB: 24.0%). The LOI of 27% is needed for a flame-retardant composite to become a self-extinguishing material [16]. Thus, the LOI of the composite sample was improved by adding Gnps, ATH, and ZB with the measured optimal contents (1.5 wt.% Gnps, 25 wt.% ATH, and 15 wt.% ZB) to the PC plastic. The result shows that the obtained composite sample (PC-Gnps-ATH-ZB) reaches the UL-94 V0 level and LOI of 29.7%. This shows the role of Gnps to increase the LOI of this sample. Besides the fire resistance measurement, the mechanical property of the samples was also evaluated. The result indicates that the flame-retardant PC (PC-Gnps-ATH-ZB sample) has higher tensile strength (39.5 MPa) in comparison to the virgin PC plastic sample (34 MPa). This shows that adding Gnps can enhance the mechanical property of PC plastic [1].

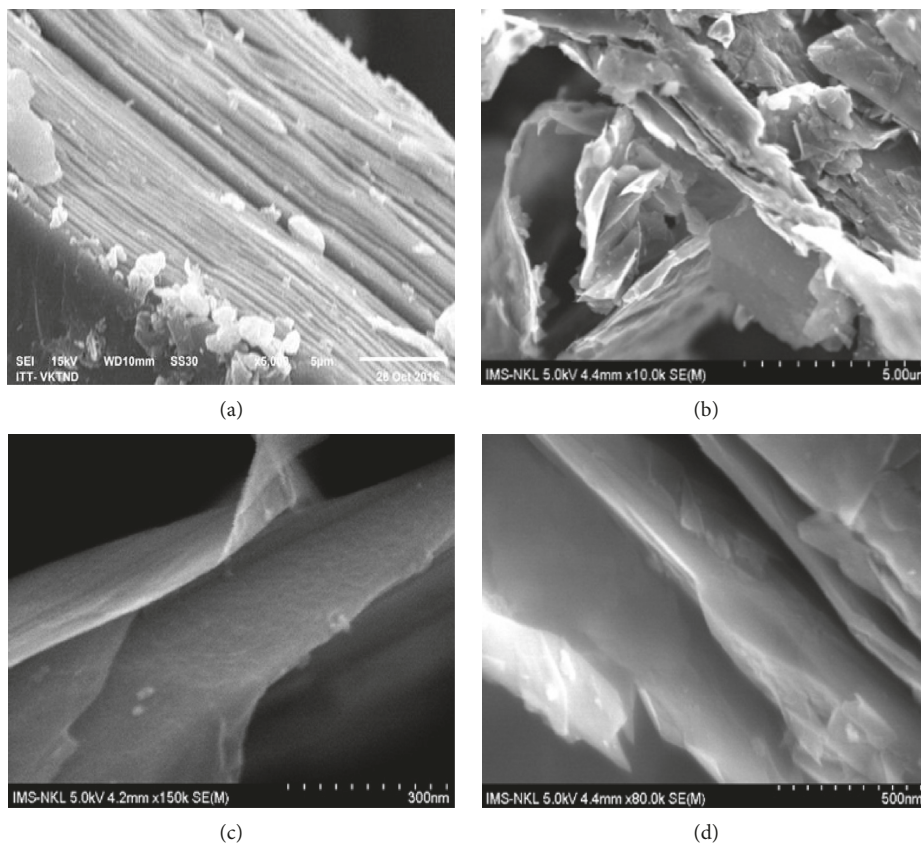


FIGURE 3: FE-SEM images. (a) EG sample; (b–d) Gnps sample.

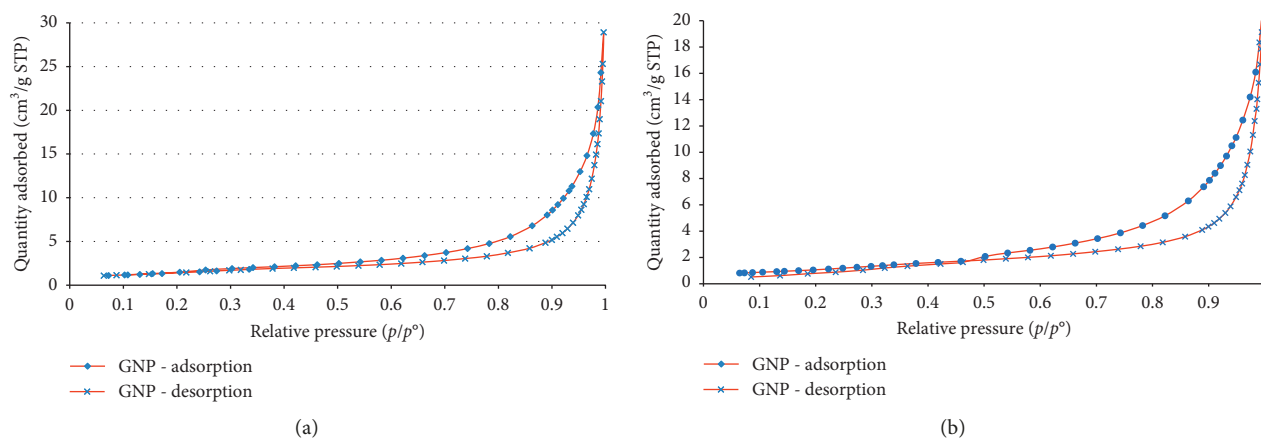


FIGURE 4: Nitrogen adsorption/desorption curves. (a) EG sample; (b) Gnps sample.

TABLE 1: BET data.

Sample	Specific surface area (m^2/g)	Pore volume (cm^3/g)	Pore size (nm)
EG	5.16	0.04	26.58
Gnps	638.11	0.02	27.36

Fire resistance test result of prepared flame-retardant polymers.

Another CSPE rubber polymer was used to illustrate the flame resistance effectiveness of Gnps. ZB has been well known as flame-retardant filler for rubber [17, 18]. The contents

of Gnps (1.0 wt.%) and ZB (15 wt.%) were measured to add to CSPE rubber. The result in Table 2 shows that both the CSPE-Gnps and CSPE-ZB composites attain the UL-94 V1 level. In addition, by combining Gnps and ZB with the contents mentioned above, the CSPE-Gnps-ZB composite (84.0-1.0-15.0 wt.%) sample attains the UL-94 V0 level. However, the LOI of this composite sample attains only 23.1%. This LOI has been improved by increasing Gnps content up to 1.5 wt.%, and the LOI of the CSPE-Gnps-ZB composite (83.5-1.5-15.0 wt.%) reaches the value of 28.6%. This result once again shows that Gnps can be used very effectively as flame-

TABLE 2: Effectiveness of Gnps in combination with the ATH and ZB conventional flame retardants.

Polymer	Filler	Content (wt.%)	UL-94 test	LOI (%)	Tensile strength (MPa)
PC	—	0.0	V2	21.1	34.0
	Graphite	5.0	V2	—	—
		5.0	V1	—	—
		2.0	V1	—	—
	Gnps	1.5	V0	—	—
		1.0	V0	—	—
		0.5	V2	—	—
		25.0	V1	—	—
	ATH	20.0	V2	—	—
		15.0	V2	—	—
		15.0	V1	—	—
	ZB	15.0	V1	—	—
		10.0	V2	—	—
	Gnps-ATH	1.5–25.0	V0	22.9	—
	Gnps-ZB	1.5–15.0	V0	24.0	—
Gnps-ATH-ZB	1.5–25.0–15.0	V0	29.7	39.5	
CSPE	—	0.0	V2	22.1	—
	Gnps	1.0	V1	—	—
	ZB	15.0	V1	—	—
	Gnps-ZB	1.0–15.0	V0	23.1	—
1.5–15.0		V0	28.6	—	

retardant additive, especially for increasing the self-extinguishing property of polymer composite by combining with conventional flame retardants.

4. Conclusions

The Gnps material was successfully prepared with the simple and scalable method of thermal shock combined with ball milling. The characterization methods (FTIR, XRD, FE-SEM, and BET) showed that the initial graphite material was exfoliated to obtain the Gnps material with few layer numbers and unchanged structure. The obtained Gnps material was applied as flame retardant for PC plastic and CSPE rubber. The results obtained by UL-94 and LOI measurement methods showed that by combining the Gnps material with ATH and ZB with suitable content, the PC-Gnps-ATH-ZB and CSPE-Gnps-ZB composite materials can be prepared with highest fire resistance properties (UL-94 V0 level and LOI is higher than 27%). The results also showed that Gnps have important role in improving the LOI of composite material with small added amount (1.5 wt.%).

Data Availability

The data used to support the findings of this study are available from the corresponding author upon request.

Conflicts of Interest

The authors declare that they have no conflicts of interest.

Acknowledgments

This work was funded by a research grant from Vietnam Academy of Science and Technology under the grant number TĐPCCC.03/18–20. The authors would like to thank Prof. Dr. Nguyen Van Tuyen, Director of Chemistry institute, Vietnam Academy of Science and Technology, for the scientific guidance during the research.

References

- [1] B. Sang, Z.-W. Li, X.-H. Li, L.-G. Yu, and Z.-J. Zhang, "Graphene-based flame retardants: a review," *Journal of Materials Science*, vol. 51, no. 18, pp. 8271–8295, 2016.
- [2] S. Park, S. He, J. Wang, A. Stein, and C. W. Macosko, "Graphene-polyethylene nanocomposites: effect of graphene functionalization," *Polymer*, vol. 104, pp. 1–9, 2016.
- [3] A. L. Higginbotham, J. R. Lomeda, A. B. Morgan, and J. M. Tour, "Graphite oxide flame-retardant polymer nanocomposites," *ACS Applied Materials and Interfaces*, vol. 1, no. 10, pp. 2256–2261, 2009.
- [4] B. M. Ganesh, A. M. Isloor, and A. F. Ismail, "Enhanced hydrophilicity and salt rejection study of graphene oxide-polysulfone mixed matrix membrane," *Desalination*, vol. 313, pp. 199–207, 2013.
- [5] N. Wang, M. Zhang, P. Kang, J. Zhang, Q. Fang, and W. Li, "Synergistic effect of graphene oxide and mesoporous structure on flame retardancy of nature rubber/IFR composites," *Materials*, vol. 11, no. 6, p. 1005, 2018.
- [6] K. Y. Chong, C. H. Chia, S. Zakaria, T. H. Pham, D. Lucas, and S. X. Chin, "Puncture resistance and mechanical properties of graphene oxide reinforced natural rubber latex," *Sains Malaysiana*, vol. 47, no. 9, pp. 2171–2178, 2018.
- [7] M. J. Nine, M. A. Cole, D. N. H. Tran, and D. Losic, "Graphene: a multipurpose material for protective coatings," *Journal of Materials Chemistry A*, vol. 3, no. 24, pp. 12580–12602, 2015.
- [8] G. Malucelli, "Surface-engineered fire protective coatings for fabrics through sol-gel and layer-by-layer methods: an overview," *Coatings*, vol. 6, no. 3, p. 33, 2016.
- [9] Y. Ji, Y. Li, G. Chen, and T. Xing, "Fire-resistant and highly electrically conductive silk fabrics fabricated with reduced graphene oxide via dry-coating," *Materials and Design*, vol. 133, pp. 528–535, 2017.
- [10] B. Alinejad and K. Mahmoodi, "Synthesis of graphene nanoflakes by grinding natural graphite together with nacl in a planetary ball mill," *Functional Materials Letters*, vol. 10, no. 4, article 1750047, 2017.
- [11] M. Yi and Z. Shen, "A review on mechanical exfoliation for scalable production of graphene," *Journal of Materials Chemistry A*, vol. 3, no. 22, pp. 11700–11715, 2015.
- [12] S.-H. Liao, P.-L. Liu, M.-C. Hsiao et al., "One-step reduction and functionalization of graphene oxide with phosphorus-based compound to produce flame-retardant epoxy nanocomposite," *Industrial and Engineering Chemistry Research*, vol. 51, no. 12, pp. 4573–4581, 2012.
- [13] K. R. Thilak and S. Umamaheswari, "FTIR, FTR and UV-vis analysis of carbamazepine," *Research Journal of Pharmaceutical, Biological and Chemical Sciences*, vol. 2, no. 4, p. 685, 2011.
- [14] W. Chen, Y. Liu, P. Liu, C. Xu, Y. Liu, and Q. Wang, "The preparation and application of a graphene-based hybrid flame retardant containing a long-chain phosphaphenanthrene," *Scientific Reports*, vol. 7, no. 1, p. 8759, 2017.

- [15] Z. Wang, R. Qi, J. Wang, and S. Qi, "Thermal conductivity improvement of epoxy composite filled with expanded graphite," *Ceramics International*, vol. 41, no. 10, pp. 13541–13546, 2015.
- [16] H. G. Elias, *Macromolecules: Synthesis, Materials and Technology*, Vol. 2, Plenum, New York, NY, USA, 2nd edition, 1984.
- [17] P. Gao and Y. Zhang, "Synthesis and characterization of zinc borate nanowhiskers and their inflaming retarding effect in polystyrene," *Journal of Nanomaterials*, vol. 2015, Article ID 925060, 6 pages, 2015.
- [18] G. S. Jeon, "Adhesion between rubber compounds containing various adhesion promoters and brass-plated steel cords. Part I. Effect of sulfur loading in rubber compounds," *Journal of Adhesion Science and Technology*, vol. 22, no. 12, 2008.

Research Article

A Facile Synthesis, Characterization, and Photocatalytic Activity of Magnesium Ferrite Nanoparticles via the Solution Combustion Method

Loan T. T. Nguyen ¹, Lan T. H. Nguyen,¹ Nhuong Chu Manh,¹ Dung Nguyen Quoc,¹ Hai Nguyen Quang,² Hang T. T. Nguyen,³ Duy Chinh Nguyen ⁴, and Long Giang Bach^{4,5}

¹Faculty of Chemistry, Thai Nguyen University of Education, Thai Nguyen University, Thai Nguyen, Vietnam

²Faculty of Physics, Thai Nguyen University of Education, Thai Nguyen University, Thai Nguyen, Vietnam

³Thai Nguyen University of Technology, Thai Nguyen University, Thai Nguyen, Vietnam

⁴NTT Hi-Tech Institute, Nguyen Tat Thanh University, Ho Chi Minh City, Vietnam

⁵Faculty of Chemical Engineering and Food Technology, Nguyen Tat Thanh University, Ho Chi Minh City, Vietnam

Correspondence should be addressed to Loan T. T. Nguyen; nguyentoloan@dhsptn.edu.vn

Received 27 November 2018; Revised 23 January 2019; Accepted 3 March 2019; Published 25 March 2019

Academic Editor: Darren Sun

Copyright © 2019 Loan T. T. Nguyen et al. This is an open access article distributed under the Creative Commons Attribution License, which permits unrestricted use, distribution, and reproduction in any medium, provided the original work is properly cited.

In this study, we adopted the solution combustion method to synthesize magnesium ferrite (MgFe_2O_4) using urea as the fuel. Various techniques including TGA, XRD, SEM, TEM, FTIR, UV-Vis DRS, and EDS were employed to characterize the synthesized MgFe_2O_4 nanoparticles. The XRD analysis revealed that single-phase MgFe_2O_4 was formed at a calcination temperature of at 500–600°C for 3 hours in the absence of an intermediate phase. TEM analysis also revealed the formation of monodisperse magnesium ferrite nanoparticles, averaged at 30 nm in size. The photocatalytic activity of the synthesized MgFe_2O_4 nanoparticles against methylene blue dye under visible light was investigated, showing the efficiency of 89.73% after 240 minutes of light irradiation with the presence of H_2O_2 .

1. Introduction

Ferrite nanoparticles, MFe_2O_4 where M is any divalent metal ions such as Mg, Mn, Ni, Co, Fe, Cu, etc, find wide applications in several fields [1]. Depending on the area of application, ferrite nanoparticles need to exhibit distinct characteristics. For example, in order to be suitable as an absorbent for decontamination of wastewater, ferrites should have exceptional chemical reactivity, adsorption capacity, and most importantly, reasonable M_s value, which is critical for magnetic recovery of the adsorbent from the aqueous solution [2]. The choice of synthesis method should also be considered when it comes to exploring the mechanism of formation of ferrite properties. To be specific, the distribution of metallic ions among

crystallographic lattice sites, which defines the characteristics of the materials, largely depends on the synthesis method. This effectively makes the method selection crucial when it comes to adapting the materials to the needs of application [1, 3, 4].

Usually, the maximum band gap energy of ferrites is approximately 2 eV, allowing the materials to effectively absorb visible light [5]. Furthermore, advantageous magnetic properties also offer ferrites useful applications [6]. Both forms of ferrites, in individual photocatalysts or in combination with others, are accentuated in literature for being separable and reusable from the reaction mixture [5, 7]. One of the typical uses of ferrites is as visible light photocatalysts for the degradation of pollutants in water and wastewater [7–10]. This capability of ferrite catalysts is

possible due to effective utilization of light energy, which in turn allows formation of e^-/h^+ pairs on the photocatalytic surface. The e^-/h^+ pairs, owing to their susceptibility to oxidation and reduction, play an important role in formation of reactive oxygen species, such as $\cdot\text{OH}$ and $\text{O}_2^{\cdot-}$, consequently promoting the decomposition of pollutants. Previous studies also suggested the addition of oxidants such as H_2O_2 into the reaction to create a Fenton-type system [6, 8, 11, 12] aiding the degradation through formation of hydroxyl radicals.

Among magnetic ferrites, magnesium ferrite (MgFe_2O_4) is a typical inverse spinel, where Fe^{3+} ions are located in the tetrahedral (A) and octahedral (B) sites and Mg^{2+} ions are located in octahedral sites only [13]. The application of magnesium ferrite is diverse ranging from that in high-density recording media [14] to that in the fields of heterogeneous catalysis [7, 15–17], adsorption [18–20], anode material [21], cancer cure [22], and sensors [23]. In addition, the material is also a soft magnetic n-type semiconducting materials with a narrow band gap (1.9 eV) [24].

Methods devised for preparation of magnesium ferrite nanocrystallites included the coprecipitation method [19, 25–28], sol-gel method [20, 29], combustion method [30, 31], hydrothermal method [32], thermal decomposition method [33], and solvothermal method [34]. Among the methods used to synthesize ferrite nanoparticles, the solution combustion synthesis is favored for its simplicity, short reaction time, and low annealing temperature [35]. These advantages have made resulting ferrites to have fine particle size, reduced impurities, and improved physical properties [36]. In the combustion reaction, the fuels play the role of forming complexes with metal cations [35]. Frequently used fuels in previous studies included glycine, urea, citric acid, and EDTA (ethylene diammin tetraacetic acid). In this work, MgFe_2O_4 nanoparticles are prepared by the solution combustion method with urea as fuel. The structural, chemical composition, thermal, morphology, and photocatalytic activity of MgFe_2O_4 nanoparticles are investigated.

2. Materials and Method

2.1. Materials. All chemicals including magnesium nitrate hexahydrate ($\text{Mg}(\text{NO}_3)_2 \cdot 6\text{H}_2\text{O}$), iron nitrate nonahydrate ($\text{Fe}(\text{NO}_3)_3 \cdot 9\text{H}_2\text{O}$), urea ($\text{CH}_4\text{N}_2\text{O}$), and methylene blue ($\text{C}_{16}\text{H}_{18}\text{ClN}_3\text{S}$) were obtained from Merck and used as received.

2.2. Preparation of MgFe_2O_4 Nanoparticles. The combustion preparation of MgFe_2O_4 with urea fuel in this study is described as follows. First, urea was dissolved in water, followed by an appropriate amount of magnesium nitrate hexahydrate and iron nitrate nonahydrate following the mole ratio for $\text{Mg}(\text{II})/\text{Fe}(\text{III})$ of 1 : 2 under vigorous stirring to form a mixed solution. Afterwards, the mixed solution was further stirred for 4 hours until gel was formed. The gel was then dried in an oven at 80°C for 10 hours. Finally, the precipitate was calcined at $500\text{--}800^\circ\text{C}$ for 3 hours with a heating rate of $5^\circ\text{C}\cdot\text{min}^{-1}$ [37].

2.3. Characterizations. The gel precursor was studied for its thermal decomposition behavior through thermogravimetry (TG) and differential thermal analysis (DTA) on a Labsys Evo S60/58988 instrument (Setaram, France) in the temperature range of $30\text{--}800^\circ\text{C}$ with the heating rate of $10^\circ\text{C}\cdot\text{min}^{-1}$. The phase of the obtained powder was characterized by X-ray diffraction (XRD) using a D8 Advance diffractometer (Bruker, Madison, WI, USA) with CuK_α radiation ($\lambda = 1.5406 \text{ \AA}$) in a 2θ angle ranging from 20° to 70° with a step of 0.03° . The crystallite size of spinel (D) was determined by Scherrer formula:

$$D = \frac{k\lambda}{\beta \cos \theta} \quad (1)$$

where λ , k , β , and θ are the X-ray wavelength (0.1504 nm), Scherrer constant (0.89), the full width at half maximum measured in radians, and the angle of diffraction of the (311) peak with the highest intensity, respectively. The morphological properties were analyzed by two techniques including scanning electron microscopy (SEM, Hitachi S-4800, Japan) and transmission electron microscopy (TEM, JEOL-JEM-1010, Japan). For sample composition, energy dispersive X-ray spectroscopy (EDX, JEOL JED 2300 Analysis Station, Japan) was employed. The spinel structure is confirmed for formation by Fourier transform infrared spectroscopy (FTIR Affinity-1S, Shimadzu, Japan). The optical absorption spectra were recorded by UV-Vis absorption spectrometer (U-4100, Hitachi, Japan).

2.4. Photocatalytic Degradation of Methylene Blue. The conditions in which experiments are conducted include room temperature, pH of approximately 7 for methylene blue (MB), and continuous circulation mode. Prior to the photocatalytic reaction, the adsorption/desorption equilibrium of the aqueous solution containing the suspension was achieved by stirring in dark environment for 30 mins. 50 mg of MgFe_2O_4 was dispersed into 100 mL of MB aqueous solution ($10 \text{ mg}\cdot\text{L}^{-1}$). Subsequently, H_2O_2 was introduced and irradiation on the suspension followed immediately using 40 W Compact lamps, Philips. The photocatalytic efficiency of MB (H) was calculated using the following equation:

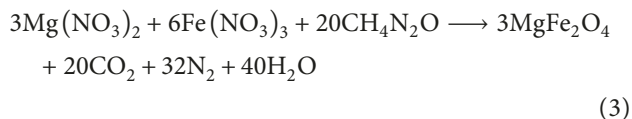
$$H = \frac{C_0 - C_t}{C_0} \times 100\%, \quad (2)$$

where C_0 is the concentration of MB ($\text{mg}\cdot\text{L}^{-1}$). The subscripts 0 and t denote time points where concentration was measured, at initial equilibrium (0) and after t irradiation time, respectively. Concentration was measured by an ultraviolet-visible spectrophotometer (UV-1700 Shimadzu, Japan) with a wavelength of 664 nm.

3. Results and Discussion

3.1. Structural Characterization. In the precursor, urea is not only to provide sufficient heat for the system but also to ensure the formation of stable complexes with the metal ions to increase their solubility and prevent selective precipitation of

metal ions during water removal. The reaction for metal nitrate mixture using urea as the fuel assuming complete combustion can be represented by the following equation [38]:



The TG/DTA of the ferrite precursor are shown in Figure 1(a). It can be observed that there are two exothermal peaks at 137.86°C and 437.04°C. The exothermal peak at 137.86°C has suggested self-combustion, like a process in which the nitrate ions act as an oxidizing agent and urea as fuel. The maximum exothermal peak at 437.04°C could be observed to closely follow a substantial mass loss in the temperature range of 200–450°C, evidencing the occurrence of the decomposition reaction of the ferrite precursor and nitrate. Approximately, the total mass loss that precedes the sharp exothermal reaction is 81.04%, which is consistent with the theoretical result (80.31%). This could be attributable to the relief of gases CO_2 , H_2O , and N_2 from the precursor. At temperature higher than 450°C, the weight of the sample remained almost constant. Therefore, the calcining temperature of the samples was selected in the range from 500 to 800°C.

Figure 1(b) displays the FTIR spectra of the MgFe_2O_4 precursor and two calcined samples at 500 and 600°C relative to the range of 4000–400 cm^{-1} . For the precursor sample, three broad absorption bands were observed at approximately 3446, 1656, and 1384 cm^{-1} , respectively, corresponding to the presence of hydroxyl groups (-OH), the stretching vibration of the carboxyl group, and the presence of NO_3^- ions [29]. In the two spectra of the MgFe_2O_4 calcined at 500–600°C, two bands at 582 and 586 cm^{-1} and two bands at 443 and 445 cm^{-1} could be pairwise indexed to the stretching vibrations of metal-oxygen bonds in tetrahedron sites and in octahedron sites, respectively, suggesting the formation of magnesium ferrite [15, 20]. In addition, the absorption broad bands at 3450 and 3425 cm^{-1} are, respectively, indicative of the stretching mode of H_2O molecules and hydroxyl groups, and in turn, the presence of H_2O molecules on the surface of MgFe_2O_4 nanoparticles [24].

Figure 2 displays different X-ray diffraction patterns of MgFe_2O_4 nanoparticles with temperature varying from 500 to 800°C. The two ferrite samples calcined at 500–600°C were obtained as single spinel phase with peaks at 220, 311, 400, 511, and 440, corresponding to the cubic spinel structure (JCPDS card. no. 01-071-1232) [26]. It is showed that the increase in temperature is associated with the improvement of MgFe_2O_4 powders. However, from 700 to 800°C, new phases of $\alpha\text{-Fe}_2\text{O}_3$ were observed. The spinel phase of MgFe_2O_4 was confirmed by five XRD peaks at 220, 311, 400, 511, and 440 crystal planes. Results reported in Table 1 also indicate that the crystallite size of MgFe_2O_4 was positively associated with the calcination temperature. As temperature moved from 500 to 800°C with 100°C interval, the average crystallite size was expanded from 18 to 61 nm. For the “a” lattice parameter, XRD spectra showed that for MgFe_2O_4 nanoparticles, the value fell in the range of 8.344–8.378 Å.

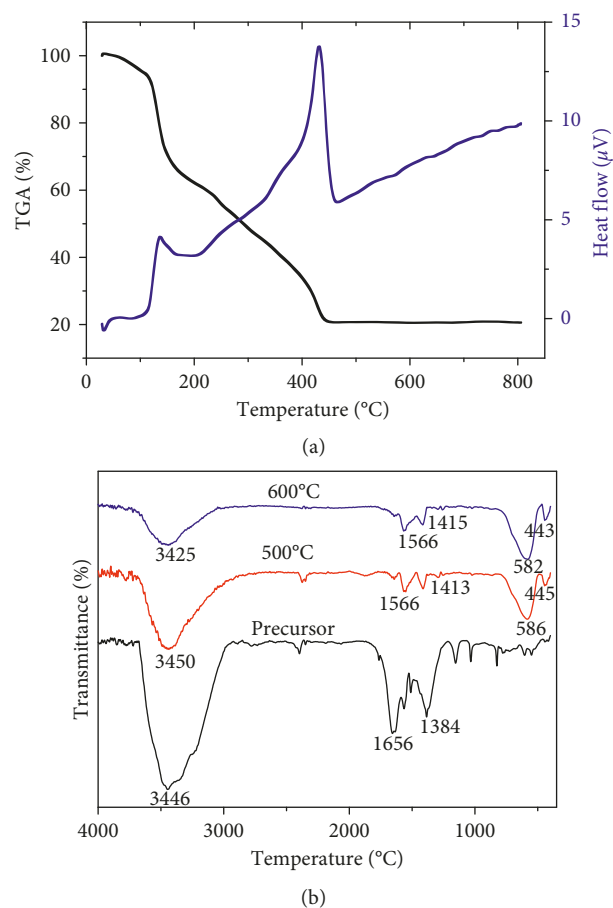


FIGURE 1: TGA/DTA curve of the precursor (a) and FT-IR spectra of the precursor and MgFe_2O_4 calcined samples at 500–600°C (b).

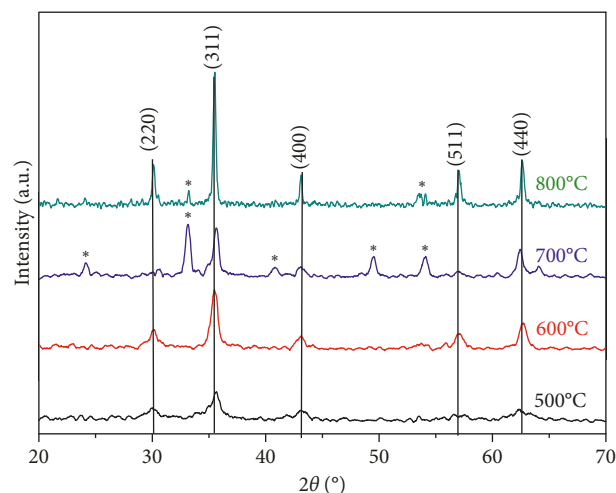
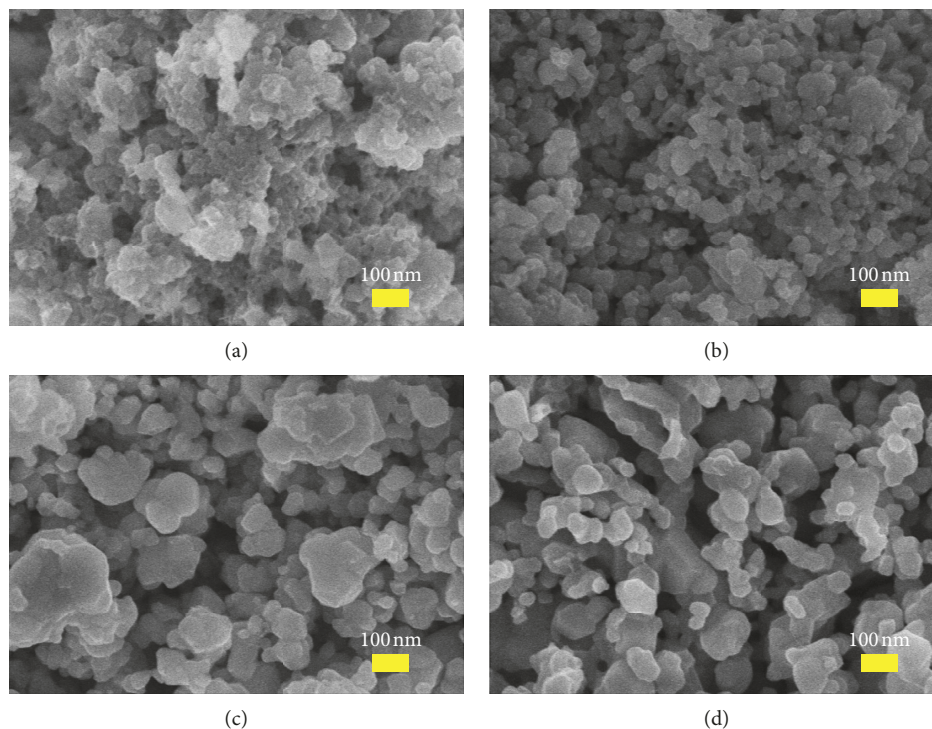


FIGURE 2: X-ray diffraction of MgFe_2O_4 calcined samples from 500°C to 800°C.

The SEM images of different samples of MgFe_2O_4 nanoparticles corresponding to four calcination temperature points of 500°C, 600°C, 700°C, and 800°C are shown in Figures 3(a)–3(d). Visually, the images showed consistent implication with the XRD results. To be specific,

TABLE 1: Average crystallite size, lattice parameter, and unit cell volume of the samples at different calcination temperatures.

t_c (°C)	Average crystallite size (nm)	Lattice constant a (Å)	Cell volume V (Å ³)
500	18	8.348	581.76
600	24	8.378	588.06
700	28	8.344	581.06
800	61	8.367	585.75

FIGURE 3: SEM of MgFe_2O_4 calcined samples at 500°C (a), 600°C (b), 700°C (c), and 800°C (d).

particle size of the prepared samples were found to be proportionally increasing with temperature. This could possibly be due to the aggregation and coalescence during desiccation.

The TEM image of MgFe_2O_4 synthesized at 500°C is presented in Figure 4(a). Evidently, the magnesium ferrite nanoparticles resulted from the solution combustion method were uniform in terms of morphology and crystallite size and reached the particle size of approximately 30 nm.

Figure 4(b) shows chemical purities and elemental composition of the MgFe_2O_4 materials produced by energy dispersive X-ray analysis (EDX). The existence of Mg, O, and Fe was determined by their corresponding peaks and the absence of other characteristic peaks. On the contrary, the synthesized sample was pure and did not contain any other elements.

The UV-Visible absorption spectrum was obtained to investigate the optical properties of magnesium ferrite calcined at 500–600°C as shown in Figure 5. By using the Kubelka–Munk equation, the band gap of MgFe_2O_4 samples was determined from reflectance spectra via conversion to absorbance [39]. The band gap energy E_g

(eV) of the synthesized photocatalyst is calculated by the following equation:

$$E_g = \frac{h \cdot c}{\lambda_{\max}} = \frac{1240}{\lambda_{\max}}, \quad (4)$$

where h , c , and λ_{\max} are the Planck constant ($6.62 \cdot 10^{-34} \text{ J} \cdot \text{s} \cdot \text{photon}^{-1}$), the speed of light ($3 \cdot 10^8 \text{ m} \cdot \text{s}^{-1}$), and the wavelength at the absorption edge (nm), respectively [40]. At wavelengths 500 and 600°C, λ_{\max} of the samples was calculated to be 679 nm and 687 nm, respectively. Therefore, the calculated band gap energy values are 1.83 eV and 1.81 eV for the MgFe_2O_4 samples calcined at 500°C and 600°C, respectively.

3.2. Photocatalytic Activity of Magnesium Ferrite Nanoparticles. Nanoparticles of the MgFe_2O_4 were tested for catalytic activities by performing photo-Fenton-like degradation of MB. Figures 6(a)–6(e) show different UV-Visible spectra of MB with MgFe_2O_4 photocatalyst corresponding to varying conditions including the calcination temperature of the absorbent, availability of H_2O_2 , and presence of light irradiation.

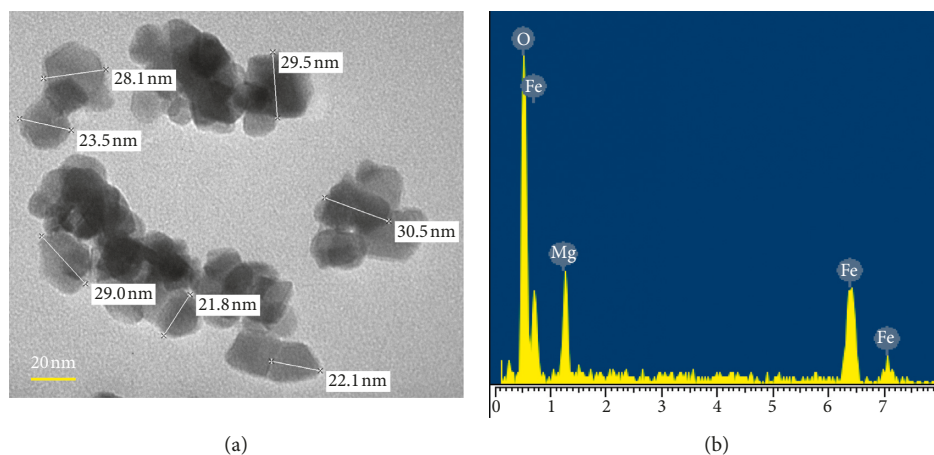


FIGURE 4: TEM and EDS of MgFe_2O_4 calcined sample at 500°C .

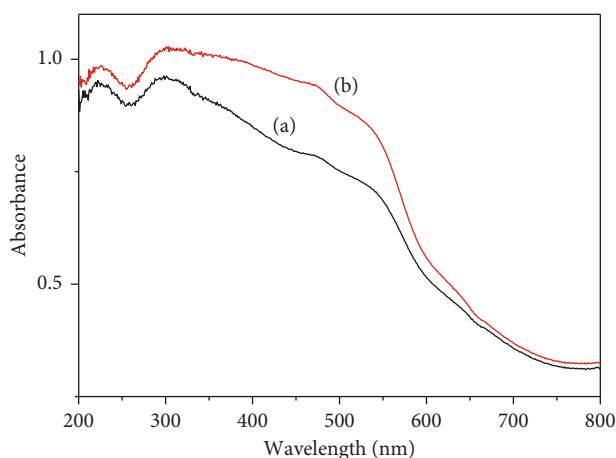


FIGURE 5: The UV-Vis diffuse reflectance spectra of MgFe_2O_4 calcined at $500\text{--}600^\circ\text{C}$.

The presence of methylene blue is indicated by the two absorption peaks at 609 nm and 664 nm [7]. It is visibly observed that the color of the MB solution gradually changed from blue to light blue and finally to colorless, which is presumably due to the estrangement of the chromophoric group. In the first two spectra where H_2O_2 was absent, MB degradation efficiency reached 6.51% (in the dark) and 31.73% (under light irradiation) after 240 minutes, suggesting the positive influence of light on the degradation efficiency. In comparison with the first spectrum, the third spectrum involved the introduction of H_2O_2 , showing a significantly higher efficiency at 35.48%. The last two spectra demonstrated the effect of calcination temperature with the presence of H_2O_2 and light irradiation. The measured efficiencies were 89.73% and 69.17% corresponding to MgFe_2O_4 calcined at 500°C and 600°C , respectively, significant and proportional decline of peak intensity with respect to irradiation time was also recognized in these two spectra. These results suggested that light irradiation, ferrite catalyst, and H_2O_2 were all required for efficient photo-Fenton degradation of MB dye. Similar results have been

reported for NiFe_2O_4 nanoparticles and CuFe_2O_4 spheres by various studies [11, 41].

Thus, it is possible to affirm that the main factors for the photodegradation of methylene blue are the crystallite size and the surface area of the MgFe_2O_4 nanoparticles. The particle size of the calcined sample at 500°C is smaller than that of the calcined sample at 600°C . Therefore, the photocatalytic activity of the sample at 500°C is higher than that of the calcined sample at 600°C . This effect was also observed in the case of the methylene blue degradation in the presence of the copper ferrite nanopowders [42] and in the presence of coating titania-silica on cobalt ferrite nanoparticles [43].

A pseudo-first-order kinetic model was adopted to describe the degradation process in the heterogeneous Fenton/photo-Fenton catalysis system [11, 44, 45]. Figure 6(f) plots $\ln(C_0/C_t)$ versus irradiation time (t) for the MgFe_2O_4 sample, showing an approximated linear relationship between the two variables. This indicates that the photodegradation of MB follows a pseudo-first-order reaction. Calculation of linear slopes revealed that the rate constant

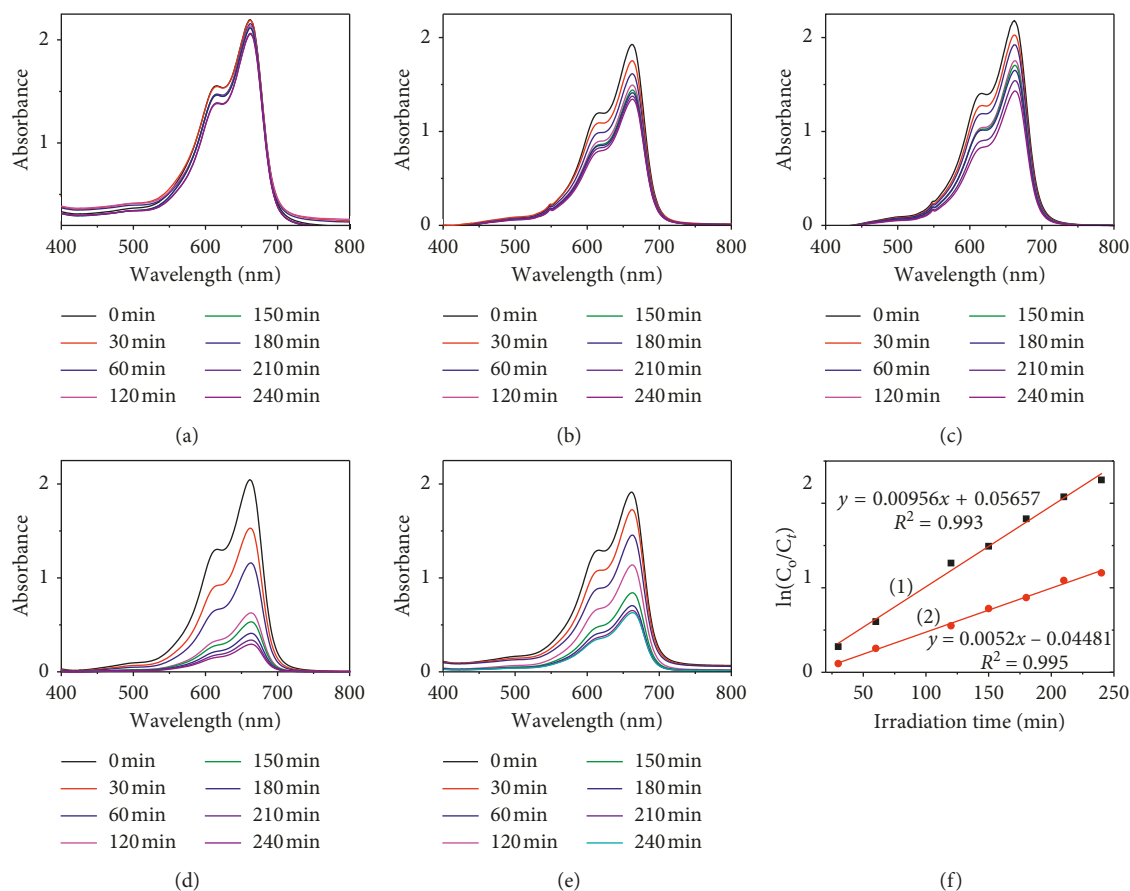


FIGURE 6: UV-Visible spectra of MB in different conditions and calcination temperatures of MgFe_2O_4 catalyst: (a) 500°C + dark, (b) 500°C + light, (c) 500°C + H_2O_2 + dark, (d) 500°C + H_2O_2 + light, (e) 600°C + H_2O_2 + light, and (f) the plots of $\ln(C_0/C_t)$ versus irradiation time (t) in the presence of MgFe_2O_4 calcined samples at 500°C (1) and 600°C (2).

(k) for the MgFe_2O_4 samples calcined at 500°C and 600°C were 0.00956 min^{-1} and 0.0052 min^{-1} , respectively.

4. Conclusions

We have successfully synthesized MgFe_2O_4 nanoparticles using the solution combustion method with urea as fuel. The particle size of prepared samples was shown to be proportional with rising temperature. Phase-pure MgFe_2O_4 nanoparticles were obtained at $500\text{--}600^\circ\text{C}$ for 3 h with the size about 30 nm. UV-Vis also approximated the band gap which ranged from 1.81 to 1.83 eV. The present study also highlighted the role of MgFe_2O_4 in the degradation (89.73% in 240 minutes) of MB dye, suggesting possible applications of the ferrite for photo-Fenton activity in decontamination of wastewater. Kinetics describing the photodegradation process of two samples calcined at 500°C and 600°C also revealed that the reaction adhered to pseudo-first order with a rate constant (k) of 0.00956 min^{-1} and 0.0052 min^{-1} , respectively.

Data Availability

The data used to support the findings of this study are available from the corresponding author upon request.

Conflicts of Interest

The authors declare that they have no conflicts of interest.

References

- [1] Z. Cao, J. Zhang, J. Zhou et al., "Electroplating sludge derived zinc-ferrite catalyst for the efficient photo-Fenton degradation of dye," *Journal of Environmental Management*, vol. 193, pp. 146–153, 2017.
- [2] K. K. Kefeni, B. B. Mamba, and T. A. M. Msagati, "Application of spinel ferrite nanoparticles in water and wastewater treatment: a review," *Separation and Purification Technology*, vol. 188, pp. 399–422, 2017.
- [3] B. Pourgolmohammad, S. M. Masoudpanah, and M. R. Aboutalebi, "Synthesis of CoFe_2O_4 powders with high surface area by solution combustion method: effect of fuel content and cobalt precursor," *Ceramics International*, vol. 43, no. 4, pp. 3797–3803, 2017.
- [4] S. I. Hussein, A. S. Elkady, M. M. Rashad, A. G. Mostafa, and R. M. Megahid, "Structural and magnetic properties of magnesium ferrite nanoparticles prepared via EDTA-based sol-gel reaction," *Journal of Magnetism and Magnetic Materials*, vol. 379, pp. 9–15, 2015.
- [5] E. Casbeer, V. K. Sharma, and X. Z. Li, "Synthesis and photocatalytic activity of ferrites under visible light: a review," *Separation and Purification Technology*, vol. 87, pp. 1–14, 2012.

- [6] P. A. Vinosha, B. Xavier, D. Anceila, and S. J. Das, "Nanocrystalline ferrite (MFe_2O_4 , $M = Ni, Cu, Mn$ and Sr) photocatalysts synthesized by homogeneous Co-precipitation technique," *Optik*, vol. 157, pp. 441–448, 2018.
- [7] M. Shahid, L. Jingling, Z. Ali et al., "Photocatalytic degradation of methylene blue on magnetically separable $MgFe_2O_4$ under visible light irradiation," *Materials Chemistry and Physics*, vol. 139, no. 2-3, pp. 566–571, 2013.
- [8] M. Sundararajan, L. John Kennedy, P. Nithya, J. Judith Vijaya, and M. Bououdina, "Visible light driven photocatalytic degradation of rhodamine B using Mg doped cobalt ferrite spinel nanoparticles synthesized by microwave combustion method," *Journal of Physics and Chemistry of Solids*, vol. 108, pp. 61–75, 2017.
- [9] S. K. Rashmi, H. S. Bhojya Naik, H. Jayadevappa, R. Viswanath, S. B. Patil, and M. Madhukara Naik, "Solar light responsive Sm-Zn ferrite nanoparticle as efficient photocatalyst," *Materials Science and Engineering: B*, vol. 225, pp. 86–97, 2017.
- [10] E. Aghabeikzadeh-Naeini, M. Movahedi, N. Rasouli, and Z. Sadeghi, "Synthesis of $ZnFe_2O_4$ nanoparticles in presence and absence of tween-20: optical property, adsorption and photocatalytic activity," *Materials Science in Semiconductor Processing*, vol. 73, pp. 72–77, 2018.
- [11] X. Guo, K. Wang, D. Li, and J. Qin, "Heterogeneous photo-Fenton processes using graphite carbon coating hollow $CuFe_2O_4$ spheres for the degradation of methylene blue," *Applied Surface Science*, vol. 420, pp. 792–801, 2017.
- [12] S. Q. Liu, L. R. Feng, N. Xu, Z. G. Chen, and X. M. Wang, "Magnetic nickel ferrite as a heterogeneous photo-Fenton catalyst for the degradation of rhodamine B in the presence of oxalic acid," *Chemical Engineering Journal*, vol. 203, pp. 432–439, 2012.
- [13] I. Khishigdemberel, E. Uyanga, H. Hirazawa, and D. Sangaa, "Influence of Cu dope on the structural behavior of $MgFe_2O_4$ at various temperatures," *Physica B: Condensed Matter*, vol. 544, pp. 73–78, 2018.
- [14] Y. Huang, Y. Tang, J. Wang, and Q. Chen, "Synthesis of $MgFe_2O_4$ nanocrystallites under mild conditions," *Materials Chemistry and Physics*, vol. 97, no. 2-3, pp. 394–397, 2006.
- [15] H. Zhou, L. Hu, J. Wan et al., "Microwave-enhanced catalytic degradation of p-nitrophenol in soil using $MgFe_2O_4$," *Chemical Engineering Journal*, vol. 284, pp. 54–60, 2016.
- [16] C. J. Jia, Y. Liu, M. Schwickardi et al., "Small gold particles supported on $MgFe_2O_4$ nanocrystals as novel catalyst for CO oxidation," *Applied Catalysis A: General*, vol. 386, no. 1-2, pp. 94–100, 2010.
- [17] A. G. Abraham, A. Manikandan, E. Manikandan et al., "Enhanced magneto-optical and photo-catalytic properties of transition metal cobalt (Co^{2+} ions) doped spinel $MgFe_2O_4$ ferrite nanocomposites," *Journal of Magnetism and Magnetic Materials*, vol. 452, pp. 380–388, 2018.
- [18] D. Kang, X. Yu, M. Ge, and W. Song, "One-step fabrication and characterization of hierarchical $MgFe_2O_4$ microspheres and their application for lead removal," *Microporous and Mesoporous Materials*, vol. 207, pp. 170–178, 2015.
- [19] V. Srivastava, Y. C. Sharma, and M. Sillanpää, "Application of nano-magneso ferrite ($n-MgFe_2O_4$) for the removal of Co^{2+} ions from synthetic wastewater: kinetic, equilibrium and thermodynamic studies," *Applied Surface Science*, vol. 338, pp. 42–54, 2015.
- [20] M. Kaur, N. Kaur, K. Jeet, and P. Kaur, " $MgFe_2O_4$ nanoparticles loaded on activated charcoal for effective removal of Cr (VI)-a novel approach," *Ceramics International*, vol. 41, no. 10, pp. 13739–13750, 2015.
- [21] N. Sivakumar, S. R. P. Gnanakan, K. Karthikeyan et al., "Nanostructured $MgFe_2O_4$ as anode materials for lithium-ion batteries," *Journal of Alloys and Compounds*, vol. 509, no. 25, pp. 7038–7041, 2011.
- [22] S. Kanagesan, M. Hashim, S. Tamilselvan, N. B. Alitheen, I. Ismail, and G. Bahmanrokh, "Cytotoxic effect of nanocrystalline $MgFe_2O_4$ particles for cancer cure," *Journal of Nanomaterials*, vol. 2013, Article ID 865024, 8 pages, 2013.
- [23] J. Patil, D. Nadargi, I. S. Mulla, and S. S. Suryavanshi, "Spinel $MgFe_2O_4$ thick films: a colloidal approach for developing gas sensors," *Materials Letters*, vol. 213, pp. 27–30, 2018.
- [24] Y. Zu, Y. Zhao, K. Xu, Y. Tong, and F. Zhao, "Preparation and comparison of catalytic performance for nano $MgFe_2O_4$, GO-loaded $MgFe_2O_4$ and GO-coated $MgFe_2O_4$ nanocomposites," *Ceramics International*, vol. 42, no. 16, pp. 18844–18850, 2016.
- [25] M. M. Rashad, "Magnetic properties of nanocrystalline magnesium ferrite by co-precipitation assisted with ultrasound irradiation," *Journal of Materials Science*, vol. 42, no. 13, pp. 5248–5255, 2007.
- [26] S. Ilhan, S. G. Izotova, and A. A. Komlev, "Synthesis and characterization of $MgFe_2O_4$ nanoparticles prepared by hydrothermal decomposition of co-precipitated magnesium and iron hydroxides," *Ceramics International*, vol. 41, no. 1, pp. 577–585, 2014.
- [27] S. Akbari, S. M. Masoudpanah, S. M. Mirkazemi, and N. Aliyan, "PVA assisted coprecipitation synthesis and characterization of $MgFe_2O_4$ nanoparticles," *Ceramics International*, vol. 43, no. 8, pp. 6263–6267, 2017.
- [28] S. Reddy, B. E. Kumara Swamy, U. Chandra, K. R. Mahathesha, T. V. Sathisha, and H. Jayadevappa, "Synthesis of $MgFe_2O_4$ nanoparticles and $MgFe_2O_4$ nanoparticles/CPE for electrochemical investigation of dopamine," *Analytical Methods*, vol. 3, no. 12, pp. 2792–2796, 2011.
- [29] A. Pradeep, P. Priyadharsini, and G. Chandrasekaran, "Sol-gel route of synthesis of nanoparticles of $MgFe_2O_4$ and XRD, FTIR and VSM study," *Journal of Magnetism and Magnetic Materials*, vol. 320, no. 21, pp. 2774–2779, 2008.
- [30] M. Goodarz Naseri, M. H. M. Ara, E. B. Saion, and A. H. Shaari, "Superparamagnetic magnesium ferrite nanoparticles fabricated by a simple, thermal-treatment method," *Journal of Magnetism and Magnetic Materials*, vol. 350, pp. 141–147, 2014.
- [31] Y. Feng, S. Li, Y. Zheng, Z. Yi, Y. He, and Y. Xu, "Preparation and characterization of $MgFe_2O_4$ nanocrystallites via PVA sol-gel route," *Journal of Alloys and Compounds*, vol. 699, pp. 521–525, 2017.
- [32] T. Sasaki, S. Ohara, T. Naka et al., "Continuous synthesis of fine $MgFe_2O_4$ nanoparticles by supercritical hydrothermal reaction," *Journal of Supercritical Fluids*, vol. 53, no. 1–3, pp. 92–94, 2010.
- [33] B. S. Randhawa, H. Kaur, H. S. Dosanjh, and J. Singh, "Precursor route for the synthesis of $MgFe_2O_4$ nanoparticles from the thermolysis of magnesium hexapropionatoferrate(III)," *Ceramics International*, vol. 42, no. 7, pp. 8891–8894, 2016.
- [34] Y. Shen, Y. Wu, X. Li, Q. Zhao, and Y. Hou, "One-pot synthesis of $MgFe_2O_4$ nanospheres by solvothermal method," *Materials Letters*, vol. 96, pp. 85–88, 2013.
- [35] T. Lazarova, M. Georgieva, D. Tzankov et al., "Influence of the type of fuel used for the solution combustion synthesis on the structure, morphology and magnetic properties of nanosized

- NiFe₂O₄,” *Journal of Alloys and Compounds*, vol. 700, pp. 272–283, 2017.
- [36] M. M. Rashad, M. G. El-Shaarawy, N. M. Shash, M. H. Maklad, and F. A. Afifi, “Controlling the composition, microstructure, electrical and magnetic properties of LiFe₅O₈ powders synthesized by sol gel auto-combustion method using urea as a fuel,” *Journal of Magnetism and Magnetic Materials*, vol. 374, pp. 495–501, 2015.
- [37] R. Sen, P. Jain, R. Patidar, S. Srivastava, R. S. Rana, and N. Gupta, “Synthesis and characterization of nickel ferrite (NiFe₂O₄) nanoparticles prepared by sol-gel method,” *Materials Today: Proceedings*, vol. 2, no. 4-5, pp. 3750–3757, 2015.
- [38] K. C. Patil, M. S. Hegde, T. Rattan, and S. T. Aruna, *Chemistry of Nanocrystalline Oxide Materials: Combustion Synthesis, Properties and Applications*, World Scientific, Singapore, 2008.
- [39] P. Lee, E. Saion, N. Al-Hada, and N. Soltani, “A simple up-scalable thermal treatment method for synthesis of ZnO nanoparticles,” *Metals*, vol. 5, no. 4, pp. 2383–2392, 2015.
- [40] R. Lamba, A. Umar, S. K. Mehta, and S. K. Kansal, “CeO₂ZnO hexagonal nanodisks: efficient material for the degradation of direct blue 15 dye and its simulated dye bath effluent under solar light,” *Journal of Alloys and Compounds*, vol. 620, pp. 67–73, 2015.
- [41] P. Annie Vinosha, B. Xavier, A. Ashwini, L. Ansel Mely, and S. Jerome Das, “Tailoring the photo-Fenton activity of nickel ferrite nanoparticles synthesized by low-temperature coprecipitation technique,” *Optik*, vol. 137, pp. 244–253, 2017.
- [42] M. M. Rashad, R. M. Mohamed, M. A. Ibrahim, L. F. M. Ismail, and E. A. Abdel-Aal, “Magnetic and catalytic properties of cubic copper ferrite nanopowders synthesized from secondary resources,” *Advanced Powder Technology*, vol. 23, no. 3, pp. 315–323, 2012.
- [43] F. A. Harraz, R. M. Mohamed, M. M. Rashad, Y. C. Wang, and W. Sigmund, “Magnetic nanocomposite based on titania-silica/cobalt ferrite for photocatalytic degradation of methylene blue dye,” *Ceramics International*, vol. 40, no. 1, pp. 375–384, 2014.
- [44] N. G. Yadav, L. S. Chaudhary, P. A. Sakhare, T. D. Dongale, P. S. Patil, and A. D. Sheikh, “Impact of collected sunlight on ZnFe₂O₄ nanoparticles for photocatalytic application,” *Journal of Colloid and Interface Science*, vol. 527, pp. 289–297, 2018.
- [45] A. Kalam, A. G. Al-Sehemi, M. Assiri et al., “Modified solvothermal synthesis of cobalt ferrite (CoFe₂O₄) magnetic nanoparticles photocatalysts for degradation of methylene blue with H₂O₂/visible light,” *Results in Physics*, vol. 8, pp. 1046–1053, 2018.

Research Article

Novel Removal of Diazinon Pesticide by Adsorption and Photocatalytic Degradation of Visible Light-Driven Fe-TiO₂/Bent-Fe Photocatalyst

Nguyen Minh Phuong ¹, Ngoc Chau Chu,¹ Doan Van Thuan,² Minh Ngoc Ha,¹ Nguyen Thi Hanh,³ Huong Do Thi Viet,¹ Nguyen Thi Minh Thu,¹ Pham Van Quan,⁴ and Nguyen Thi Thanh Truc ⁵

¹Faculty of Chemistry, University of Science, Vietnam National University, 334 Nguyen Trai, Thanh Xuan, Hanoi, Vietnam

²NTT Hi-Tech Institute, Nguyen Tat Thanh University, Ho Chi Minh City 700000, Vietnam

³Faculty of Environmental Science, University of Science, Vietnam National University, 334 Nguyen Trai, Thanh Xuan, Hanoi, Vietnam

⁴Ministry of Industry and Trade, 54 Hai Ba Trung, Hoan Kiem, Hanoi, Vietnam

⁵Faculty of Environment and Labour Safety, Ton Duc Thang University, Ho Chi Minh City, Vietnam

Correspondence should be addressed to Nguyen Minh Phuong; nguyenminhphuong@hus.edu.vn

Received 11 December 2018; Revised 26 January 2019; Accepted 13 February 2019; Published 20 March 2019

Guest Editor: Ajit Kumar Sharma

Copyright © 2019 Nguyen Minh Phuong et al. This is an open access article distributed under the Creative Commons Attribution License, which permits unrestricted use, distribution, and reproduction in any medium, provided the original work is properly cited.

In the study, Fe was used as a dopant to enhance photocatalytic activity of TiO₂. Then, the Fe-doped TiO₂ was deposited on bentonite, which was pillared by Fe. The synthesized materials were characterized by SEM, XRD, UV-Vis, BET, and point of zero charge (pH_{PZC}). Then, the synthesized materials were used for diazinon removal under both dark and visible light conditions to investigate adsorption and photocatalytic degradation abilities of the synthesized materials. The maximum diazinon adsorption capacity of the synthesized Fe-TiO₂/Bent-Fe was 27.03 mg/g. The obtained results indicated that the Fe-TiO₂/Bent-Fe exhibited high photocatalytic degradation activity for removal of diazinon even under visible light. The diazinon removal experiments were also conducted using different photocatalyst dosages, under different pH and light sources to figure the optimal conditions for removal processes. The obtained results indicated that optimal photocatalyst dosage and pH were 0.5 g/L and 4.5, respectively. Finally, the natural light generated from solar could be suitable used for diazinon removal by the synthesized Fe-TiO₂/Bent-Fe.

1. Introduction

Many kinds of pesticides releasing into the environment as a result of runoff from agricultural and urban areas cause pollution of soil, air, surface water, and groundwater and are harmful for the human health [1, 2]. Among them, diazinon (*O*, *O*-diethyl *O*-[6-methyl-2-(1-methylethyl)-4-pyrimidinyl] phosphorothioate), an organophosphorus and highly toxic pesticide, is extensively used to control insects and, just in the USA, 6 million pounds of the pesticide are annually used on farming sites [3]. The diazinon has been classified as moderately hazardous class II chemical to humans, aquatics,

mammals, and other species by the World Health Organization (WHO). Shemer and Linden reported that the fatal human doses of diazinon were in the range from 90 to 444 mg·kg⁻¹ [4]. Kouloumbos et al. reported that toxic effects of the pesticide attributed to its inhibition of the enzyme acetylcholinesterase affecting the nervous system [5]. Therefore, water systems contaminated with diazinon have been treated by various techniques such as adsorption, filtration, membrane separation, biodegradation, oxidation, and chemical coagulation [6]. However, these methods have several certain disadvantages including incomplete removal, high consumption of chemicals, time consuming, and high treatment cost.

Recently, advanced oxidation processes (AOPs), using heterogeneous photocatalysts to produce hydroxyl radicals ($\cdot\text{OH}$), a strong oxidative agent, to totally promote mineralization of organic pollutants into harmless substances such as CO_2 and H_2O , could be a potential technology for removal of diazinon [7–9]. Titanium oxide (TiO_2) is regarded as the most suitable photocatalyst for the degradation of organic pollutants from wastewaters because of its chemical stability, nontoxicity, low cost, and commercial availability [10–12]. However, because of wide band gap of TiO_2 , which is approximately 3.2 eV, the photocatalyst could only be activated by UV irradiation, which only accounts for 3–4% of the solar spectrum [13, 14]. The high-energy consumption and safety issues concerning use of UV irradiation are the main disadvantages of TiO_2 in the practical system. In addition, the fast recombination of the photoexcited electrons and holes is also another disadvantage of the TiO_2 photocatalyst. Hence, numerous studies have been conducted to effectively enhance the photocatalytic activity of TiO_2 and to expand its applications in practical systems using visible light or the solar energy as the excitation source [15–21]. Among these, metals have been used as doping agents to implant or incorporate into the TiO_2 lattice to narrow the band gap of the photocatalyst, thereby enhancing its photocatalytic activity [22–27]. The overlap between d orbital of the substituted metal and d orbital of titanium could narrow band gap or facilitate the visible light absorption of the doped TiO_2 , leading to its photocatalytic enhancement [28]. Therefore, the first aim of the study is to use Fe as dopant to enhance photocatalytic activity of TiO_2 to utilize visible light as excitation sources for its photocatalytic removal of diazinon.

In addition, it is difficult to recover powder photocatalysts after being used in practical system for wastewater treatment. Moreover, the photocatalytic activity of a certain photocatalyst strongly depends on its adsorption capacity [29]. Various materials including activated carbon, glass fiber, polyurethane, silica, alumina, and bentonite have been used as supports to fix photocatalysts to overcome such limitations. In the study, bentonite, which is nontoxic, porous, economical, easily available in our country (Vietnam), and also chemically and mechanically stable, was used as support materials for Fe-doped TiO_2 (Fe-TiO_2). However, the surface area of the natural bentonite is quite small. Many studies reported that the introduction of the inorganic pillars into bentonite could increase its surface area, pore volume, microporosity, and thermal stability [30–32]. Therefore, the study used Fe as a pillar to increase surface area as well as pore volume of the bentonite before being used as support for the Fe-TiO_2 . Thus, the Fe-doped TiO_2 supported on bentonite pillared Fe ($\text{Fe-TiO}_2/\text{Bent-Fe}$) would have high photocatalytic activity and adsorption capacity for removal of diazinon.

2. Experimental

2.1. Material Preparation. First, 10 g bentonite was saturated with Fe^{3+} in 100 mL of 1 M solution of FeCl_3 under constant stirring. The obtained suspension was continuously stirred at

room temperature for 24 h. The resulting product was centrifuged and washed by distilled water until chloride free (tested by AgNO_3). The obtained material was dried at 363 K for 12 h and then milled to get bentonite-pillared Fe (Bent-Fe). Then, the obtained Bent-Fe was swelled in pure ethanol solution with weight ratio of 2%. Second, 6 mL tetra isopropyl orthotitanate (TIOT) was slowly dropped into 34 mL ethanol to get a solution “A” while 48.2 mg $\text{Fe}(\text{NO}_3)_3 \cdot 9\text{H}_2\text{O}$ was diluted in a solution containing 17 mL ethanol, 0.4 mL HNO_3 (68%), and 1.6 mL distilled water to obtain a solution “B”. Then, the solution “A” was slowly dropped into the solution “B” to get sol Fe-TiO_2 . Finally, the obtained sol Fe-TiO_2 was slowly dropped into the swelled Bent-Fe with continuously stirring for 4 h and aging for 24 h. The obtained mixture was changed into a Teflon-lined stainless steel autoclave and then heated under 160°C for 6 h. After the autoclave was cooled to room temperature, the precipitate at the bottom of the autoclave was obtained and washed with ethanol and deionized water several times. The product was dried at 80°C for 24 h to get $\text{Fe-TiO}_2/\text{Bent-Fe}$. The weight ratio of (Fe-TiO_2)/(Bent-Fe) was 3 : 1.

2.2. Photocatalyst Characterization. The surface morphology of the synthesized materials was analyzed using a JED-2300-Analysis Station Plus, JEOL scanning electron microscope (SEM). X-ray diffraction (XRD) spectra of the synthesized TiO_2 , Fe-TiO_2 , $\text{Fe-TiO}_2/\text{Bent}$, Bent-Fe , and $\text{Fe-TiO}_2/\text{Bent-Fe}$ materials were obtained using a D8-Advance 5005 model with $\text{Cu-K}\alpha$ ($\lambda = 1.5406 \text{ \AA}$) radiation over the range $10^\circ < 2\theta < 70^\circ$, at a scanning rate of 0.03°/min. The optical absorption abilities of the synthesized photocatalysts were characterized by an UV 3101PC spectrophotometer, Shimadzu. The point of zero charge (pH_{PZC}) of the synthesized material was determined using the procedure as follows: a 50 mL of 0.01 M NaCl were placed into several closed Erlenmeyer flasks and the pH of each flask was adjusted at 3.0, 4.5, 5.6, and 8.0 by adding HCl (0.01 M) or NaOH (0.01 M). Then, 0.2 g $\text{Fe-TiO}_2/\text{Bent-Fe}$ was added to each flask. The pH_{PZC} is the point where the line of final pH is crossing the line of initial pH.

2.3. Removal Experiments. Experiments were conducted to investigate diazinon removal efficiency by adsorption and photocatalytic degradation of the synthesized materials. In addition, optimal pH, photocatalyst dosage, and light condition were also investigated in the study. In a typical removal experiment, a known dosage of the synthesized photocatalyst (0.25–1 g/L) was transferred to 100 mL of diazinon solution with a distinct concentration (10–50 mg/L) at a certain pH (3–8). The initial pH of solution was adjusted by adding NaOH or HCl (0.1 mol/L) and measured by the pH meter model XT 1200C (Mettler Toledo). After a certain time, the mixture was filtered and the remained diazinon concentrations were measured using a HPLC (Supelco LiChrospher RP-18 column, $250 \times 4.6 \times 5$) coupled to a UV-PDA detector (Shimadzu SPD-M10Avp) at a wavelength of 247 nm. The removal experiment was firstly conducted under dark condition to determine adsorption

capacity of the synthesized material. Then, the visible light was provided to initiate for photocatalytic degradation of diazinon.

3. Results and Discussion

3.1. Material Characteristics

3.1.1. Morphology. Figure 1 shows the SEM images of the synthesized Bent-Fe and Fe-TiO₂/Bent-Fe materials. It can be seen that the synthesized Bent-Fe material existed in form of nanolamella with dominant flake-like morphology and curling edges. The SEM image of the synthesized Fe-TiO₂/Bent-Fe indicated that Fe-TiO₂ particles existed in form of nanospherical particles. The nano-Fe-TiO₂ particles were well-dispersed on the surface of the Bent-Fe layers. This is expected to increase recycling ability of the nano-Fe-TiO₂ photocatalysts after being used for diazinon removal processes. In addition, the deposition of Fe-TiO₂ particles on the surface of the Bent-Fe could increase surface areas of the material, leading to increase in its diazinon removal efficiency. The BET surface area of the synthesized Fe-TiO₂/Bent-Fe (181.13 m²/g) was greatly higher than that of the Bent-Fe (66.22 m²/g).

3.1.2. Crystal Phase Structure. Figure 1 shows the XRD patterns of undoped TiO₂, Fe-TiO₂, and Fe-TiO₂/Bent-Fe materials. It can be seen that the anatase and rutile phases were observed in the XRD pattern of the undoped TiO₂ material (JCPDS card No. 65-5714 for anatase and JCPDS card no. 21-1276 for rutile). However, there was only anatase phase in the XRD pattern of the synthesized Fe-TiO₂ photocatalyst. This could be due to the incorporation of Fe dopant into TiO₂ lattice prevented the formation of the rutile phase [33, 34]. There was no peak corresponding to Fe component in the synthesized Fe-TiO₂ material which confirmed that Fe incorporated in the TiO₂ lattice. Figure 1 also shows that the phase structure of the Fe-TiO₂ photocatalyst unchanged when the material was deposited on the Bent-Fe. In addition, a peak corresponding to the montmorillonite phase of the bentonite was also observed in the XRD pattern of the Fe-TiO₂/Bent-Fe material (JCPDS card No. 03-0014) (Figure 2).

3.1.3. Optical Properties. Figure 3 shows the UV-Vis light absorption of the synthesized TiO₂, Bent-Fe, Fe-TiO₂, and Fe-TiO₂/Bent-Fe materials. The UV-Vis absorption spectrum of TiO₂ exhibited an absorption edge at 390 nm [35]. However, the materials did not exhibit any noticeable absorption in the visible region. Bent-Fe also shows little visible light absorption. As compared to the UV-Vis absorption spectra of the TiO₂ and Bent-Fe, that of the Fe-TiO₂, however, not only showed a red shift of the absorption edge but also exhibited higher adsorption ability in the visible region. The band gap structure of the TiO₂ is comprised of a valence band, which is mainly constructed from an O 2p orbital, and a conduction band, which is mainly constructed from an empty Ti 3d orbital. In the Fe-TiO₂, the 3d orbitals

of Fe dopant not only affected to the top of the valence band and the bottom of the conduction band of the TiO₂ but also inserted into the TiO₂ lattice structure to create a Fe impurity band under the conduction band and upper the valence band of the TiO₂, formed an optical band gap [33, 36]. Therefore, the photoexcited electrons in the TiO₂ valence band could migrate to the Fe impurity band, and then move from the impurity band to the conduction band via next photon absorption. Thus, the Fe dopant led to decrease in the band-gap energy, recombination rate of photo-excited electrons and holes, as well as increase in visible light absorption of the TiO₂. The UV-Vis absorption spectrum of Fe-TiO₂/Bent-Fe shows that the deposition of the Fe-TiO₂ on the surface of the Bent-Fe extended visible light absorption of the Fe-TiO₂. Krishnan and Mahalingam reported that the increase in visible light absorption was due to the interband transitions i.e., charge transfer transition of interlayer tetrahedral and octahedral atoms in the bentonite material [37].

3.2. Diazinon Removal

3.2.1. Adsorption of Diazinon. First, the effect of contact time on the sorption of diazinon was investigated by adding 0.5 g of the synthesized Fe-TiO₂/Bent-Fe material in 100 mL diazinon solution (16.74 mg/L) at pH 5.6 (natural pH without any adjustment) and room temperature of 25°C. The diazinon adsorption capacities by the synthesized Fe-TiO₂/Bent-Fe are shown in Figure 4(a). It can be seen that the diazinon adsorption capacities increased with increase in contact time up to 30 min and then tend to stabilize with further increase in contact time. It means that the diazinon adsorption by the synthesized Fe-TiO₂/Bent-Fe reaches the equilibrium after 30 min. Based on the obtained results, the experiments, which the contact time was fixed (30 min), were conducted to investigate maximum diazinon adsorption capacity of the synthesized Fe-TiO₂/Bent-Fe. The Langmuir model was applied to calculate the maximum adsorption capacities (Figure 4(b)). It can be seen that the adsorption ability is suitable with the Langmuir model, and the maximum diazinon adsorption capacity (q_{max}) by the synthesized Fe-TiO₂/Bent-Fe was 27.03 (mg/g).

3.2.2. Photocatalytic Degradation of Diazinon. In order to investigate photocatalytic degradation of diazinon, 0.5 g Fe-TiO₂/Bent-Fe material was put in 100 mL diazinon solution (25 mg/L). In the condition, the pH of solution was 5.6 (natural pH without any adjustment). Then, the obtained solution was kept in dark condition for 30 min to get adsorption equilibrium, and then the visible light was provided using a 36 W compact bulb, which could provide visible light in range of 400–700 nm. The diazinon removal results are shown in Figure 5. Under dark condition, an approximately 36.18% diazinon was removed by adsorption of Fe-TiO₂/Bent-Fe material. When visible light was provided, the diazinon was continuously removed by photocatalytic degradation. The synthesized Fe-TiO₂/Bent-Fe could absorb significant amount of incident light to generate huge amount

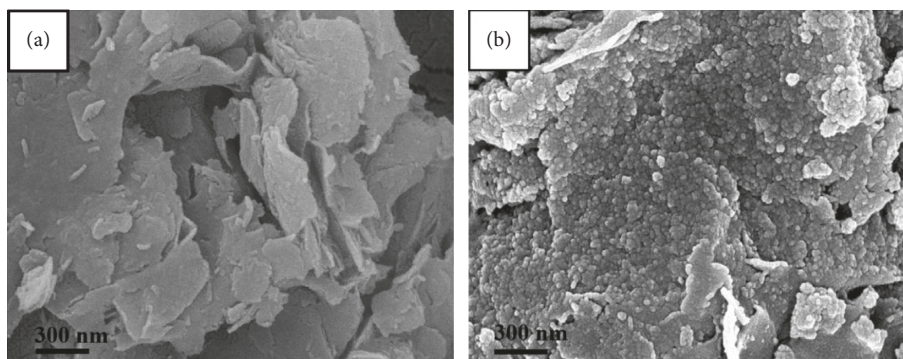


FIGURE 1: SEM images of the synthesized Bent-Fe and Fe-TiO₂/Bent-Fe materials.

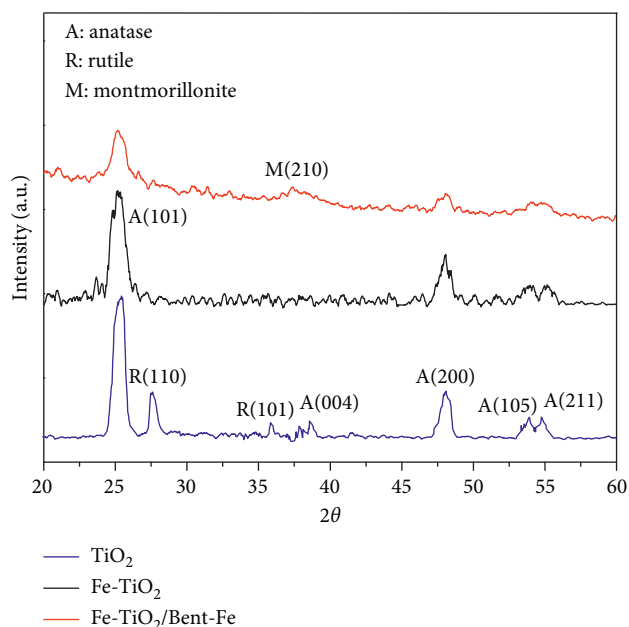


FIGURE 2: XRD patterns of the synthesized TiO₂, Fe-TiO₂, and Fe-TiO₂/Bent-Fe materials.

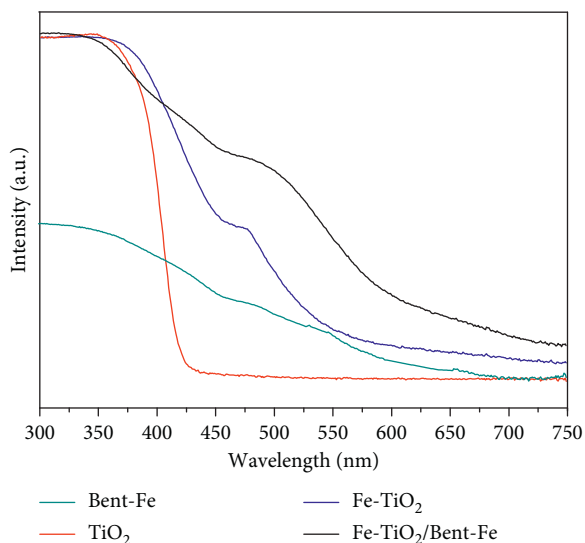


FIGURE 3: UV-Vis absorption spectra of the synthesized TiO₂, Bent-Fe, Fe-TiO₂, and Fe-TiO₂/Bent-Fe materials.

of electrons and holes. Then, the generated electrons and holes could react with H₂O and O₂, respectively, to produce strong oxidative radicals, including hydroxyl and superoxide anion radicals, for degradation of diazinon into harmless inorganic materials [38–40]. The total diazinon removal by both adsorption and photocatalytic degradation was approximately 58.3%.

3.2.3. Optimal Removal Conditions. The effects of photocatalyst dosages on diazinon removal efficiencies are shown in Figure 6(a). When the photocatalyst dosage was 0.25 g/L, the amount of photocatalyst was not enough for the diazinon removal. The diazinon removal efficiencies increased with increase in photocatalyst dosage up to 1.0 g/L. When the photocatalyst dosages increased, the turbidity of the solution increased. An increased level of suspension turbidity resulted from excessive photocatalyst dosage would block the incident visible light required for the photocatalyst activation [41]. Hence, the photocatalytic degradation efficiency decreased. Thus, the optimal photocatalyst dosage for diazinon removal was 0.5 g/L.

The diazinon removal experiments was conducted under different light conditions including artificial light generated from compact bulb and natural light from solar. The intensity of light from the 36 W compact bulb was 190.985 lux and the intensity of solar light, which was measured in 6 hours of the experiment, varied from 32.500 to 65.200 lux. In the experiments, the photocatalytic dosage, pH, and intimal concentration of diazinon were 0.5 g/L, 5.6, and 25 ppm, respectively. The obtained results are shown in Figure 6(b). The diazinon removal efficiency under natural light generated from solar was 53%, which was slightly lower than that under artificial light generated from compact bulb (58.3%). Thus, the natural light could be suitable used for photocatalytic degradation of diazinon by the synthesized Fe-TiO₂/Bent-Fe material.

Finally, the diazinon removal experiments were conducted at different pH (3.0, 4.5, 5.6 and 8.0) to investigate optimal pH for the process. In the experiments, the photocatalytic dosage and intimal concentration of diazinon were 0.5 g/L and 25 ppm, respectively. The diazinon removal efficiencies at different pH are shown in Figure 6(c). First, the pK_a of diazinon is 2.6, thus diazinon is negatively charged at all the selected pH conditions [2]. Point of zero

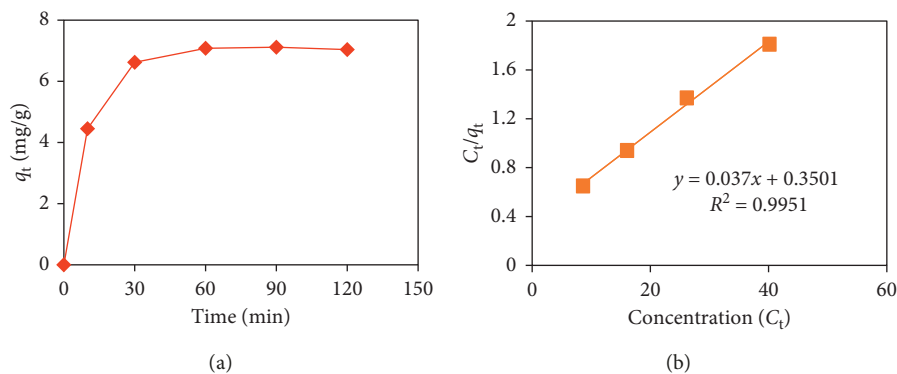


FIGURE 4: Diazinon adsorption capacities by the synthesized Fe-TiO₂/Bent-Fe (a) and Langmuir model (b).

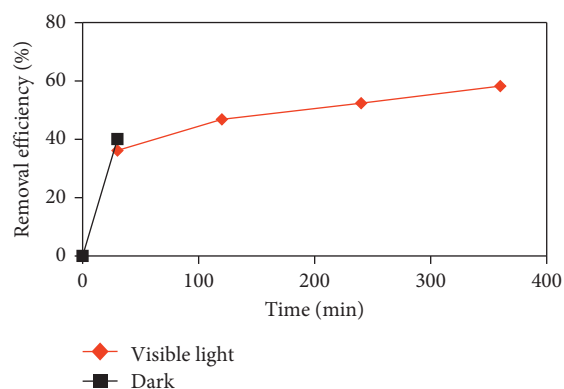


FIGURE 5: Diazinon removal under dark and visible light conditions.

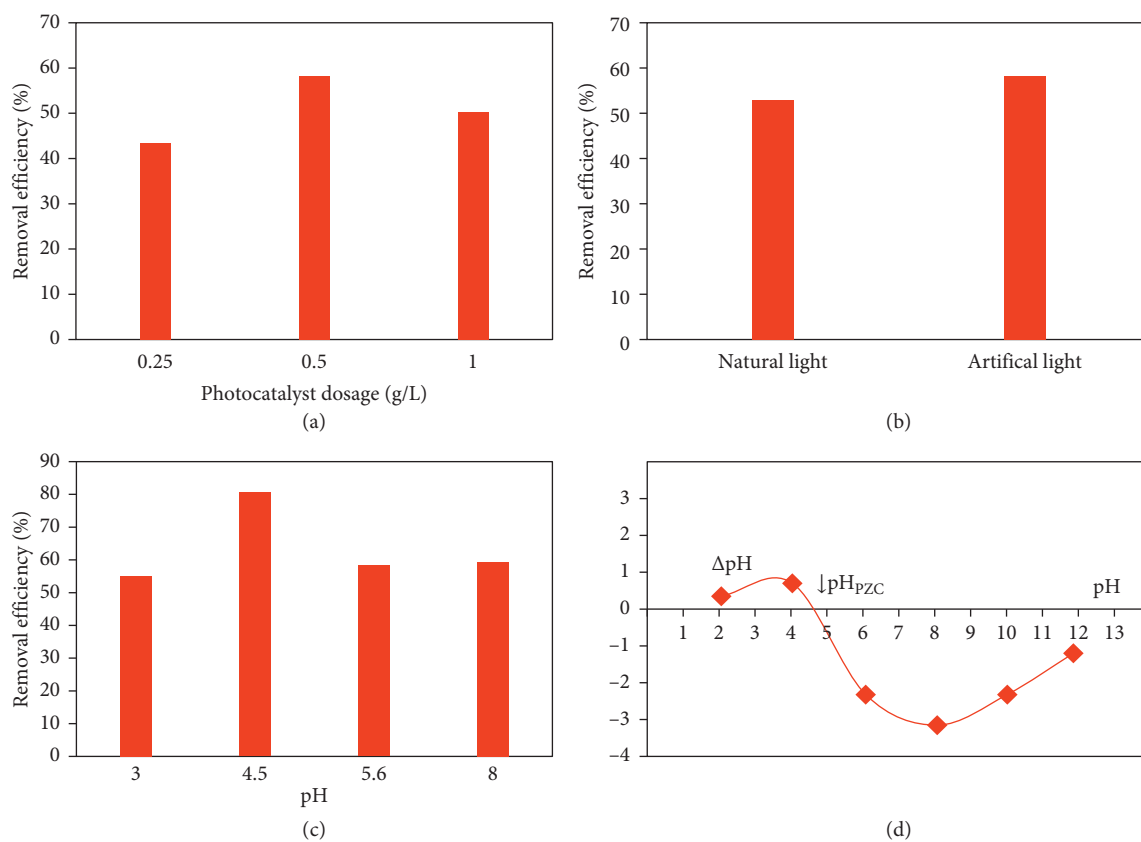


FIGURE 6: Effects of photocatalyst dosage (a), light sources (b), and pH (c) on diazinon removal efficiencies and zeta potential of the synthesized Fe-TiO₂/Bent-Fe (d).

charge of the synthesized Fe-TiO₂/Bent-Fe material was approximately 4.6 (Figure 6(d)). As expected, an optimal condition can be developed in the pH range between pK_a^{diazinon} and $pH_{zpc}^{\text{Fe-TiO}_2/\text{Bent-Fe}}$ at which the positively charged Fe-TiO₂/Bent-Fe material and negatively charged diazinon should readily attract each other. At high pH, both diazinon and Fe-TiO₂/Bent-Fe have negative charges. Therefore, electrostatic repulsion between diazinon and Fe-TiO₂/Bent-Fe causes reduced adsorption of diazinon onto material surface, resulting in decreased photocatalytic removal efficiency. Based on the obtained results of this study, pH 4.5 was identified as an optimum condition for the removal of diazinon using Fe-TiO₂/Bent-Fe material. Under optimal conditions, including dosage (0.5 g/L) and pH (4.5), 80.6% diazinon, which the initial concentration was 25 ppm, has been removed by the synthesized Fe-TiO₂/Bent-Fe.

Recycling experiments were conducted to analyze the stability of the prepared photocatalyst during the diazinon removal processes. After being used for diazinon removal for 360 min, the photocatalysts were collected and vacuum dried for 4 h under the dark condition and then used for the diazinon removal experiment. The diazinon removal efficiency by Fe-TiO₂/Bent-Fe in the first and second time of recycle was 76.8 and 69.3%, respectively. The diazinon removal by Fe-TiO₂/Bent-Fe was not significantly changed after recycling, which demonstrated the stability of the photocatalysts during the removal experiments.

4. Conclusion

We successfully used Fe as a dopant to enhance photocatalytic activity of TiO₂. Then, the Fe doped TiO₂ was deposited on bentonite, which was pillared by Fe, to enhance its adsorption and recycling ability in the practical system. The synthesized material exhibited high adsorption ability to remove diazinon. The maximum diazinon adsorption capacity of the synthesized Fe-TiO₂/Bent-Fe was 27.03 mg/g. Even under visible light, the synthesized Fe-TiO₂/Bent-Fe photocatalyst also exhibited high photocatalytic activity for degradation of diazinon. The optimal photocatalyst dosage for removal of diazinon was 0.5 g/L. The natural light generated from solar could be suitable used for diazinon removal by the synthesized Fe-TiO₂/Bent-Fe. Finally, the optimal pH for diazinon removal was 4.5, which is preferred for adsorption of diazinon by the synthesized Fe-TiO₂/Bent-Fe.

Data Availability

The data used to support the findings of this study are included within the article.

Conflicts of Interest

The authors declare that they have no conflicts of interest.

Acknowledgments

This research was funded by the Vietnam National University, Hanoi (VNU), under project number QG.17.27.

References

- [1] A. F. Hassan, H. Elhadidy, and A. M. Abdel-Mohsen, "Adsorption and photocatalytic detoxification of diazinon using iron and nanotitania modified activated carbons," *Journal of the Taiwan Institute of Chemical Engineers*, vol. 75, pp. 299–306, 2017.
- [2] H. Hossaini, G. Moussavi, and M. Farrokhi, "Oxidation of diazinon in cns-ZnO/LED photocatalytic process: catalyst preparation, photocatalytic examination, and toxicity bio-assay of oxidation by-products," *Separation and Purification Technology*, vol. 174, pp. 320–330, 2017.
- [3] A.-A. Salarian, Z. Hami, N. Mirzaei et al., "N-doped TiO₂ nanosheets for photocatalytic degradation and mineralization of diazinon under simulated solar irradiation: optimization and modeling using a response surface methodology," *Journal of Molecular Liquids*, vol. 220, pp. 183–191, 2016.
- [4] H. Shemer and K. Linden, "Degradation and by-product formation of diazinon in water during UV and UV/H₂O₂ treatment," *Journal of Hazardous Materials*, vol. 136, no. 3, pp. 553–559, 2006.
- [5] V. N. Kouloumbos, D. F. Tsipi, A. E. Hiskia, D. Nikolic, and R. B. Breemen, "Identification of photocatalytic degradation products of diazinon in TiO₂ aqueous suspensions using GC/MS/MS and LC/MS with quadrupole time-of-flight mass spectrometry," *Journal of the American Society for Mass Spectrometry*, vol. 14, no. 8, pp. 803–817, 2003.
- [6] V. N. Nguyen, D. T. Tran, M. T. Nguyen et al., "Enhanced photocatalytic degradation of methyl orange using ZnO/graphene oxide nanocomposites," *Research on Chemical Intermediates*, vol. 44, no. 5, pp. 3081–3095, 2018.
- [7] A. Jonidi-Jafari, M. Shirzad-Siboni, J.-K. Yang, M. Naimi-Joubani, and M. Farrokhi, "Photocatalytic degradation of diazinon with illuminated ZnO-TiO₂ composite," *Journal of the Taiwan Institute of Chemical Engineers*, vol. 50, pp. 100–107, 2015.
- [8] S. R. Mirmasoomi, M. Mehdipour Ghazi, and M. Galedari, "Photocatalytic degradation of diazinon under visible light using TiO₂/Fe₂O₃ nanocomposite synthesized by ultrasonic-assisted impregnation method," *Separation and Purification Technology*, vol. 175, pp. 418–427, 2017.
- [9] M. Shirzad-Siboni, A. Jonidi-Jafari, M. Farzadkia, A. Esrafil, and M. Gholami, "Enhancement of photocatalytic activity of Cu-doped ZnO nanorods for the degradation of an insecticide: kinetics and reaction pathways," *Journal of Environmental Management*, vol. 186, pp. 1–11, 2017.
- [10] E. Rossetto, D. I. Petkowicz, J. H. Z. dos Santos, S. B. C. Pergher, and F. G. Penha, "Bentonites impregnated with TiO₂ for photodegradation of methylene blue," *Applied Clay Science*, vol. 48, no. 4, pp. 602–606, 2010.
- [11] A. T. Kuvarega, R. W. M. Krause, and B. B. Mamba, "Evaluation of the simulated solar light photocatalytic activity of N, Ir co-doped TiO₂ for organic dye removal from water," *Applied Surface Science*, vol. 329, pp. 127–136, 2015.
- [12] T.-D. Pham and B.-K. Lee, "Advanced removal of *C. famata* in bioaerosols by simultaneous adsorption and photocatalytic oxidation of Cu-doped TiO₂/PU under visible irradiation," *Chemical Engineering Journal*, vol. 286, pp. 377–386, 2016.
- [13] N. A. Ramos-Delgado, M. A. Gracia-Pinilla, L. Maya-Treviño, L. Hinojosa-Reyes, J. L. Guzman-Mar, and A. Hernández-Ramírez, "Solar photocatalytic activity of TiO₂ modified with WO₃ on the degradation of an organophosphorus pesticide," *Journal of Hazardous Materials*, vol. 263, pp. 36–44, 2013.

- [14] T.-D. Pham, B.-K. Lee, and D. Pham-Cong, "Advanced removal of toluene in aerosol by adsorption and photocatalytic degradation of silver-doped TiO₂/PU under visible light irradiation," *RSC Advances*, vol. 6, no. 30, pp. 25346–25358, 2016.
- [15] V. Iliev, D. Tomova, L. Bilyarska, A. Eliyas, and L. Petrov, "Photocatalytic properties of TiO₂ modified with platinum and silver nanoparticles in the degradation of oxalic acid in aqueous solution," *Applied Catalysis B: Environmental*, vol. 63, no. 3-4, pp. 266–271, 2006.
- [16] K. Pathakoti, S. Morrow, C. Han et al., "Photoinactivation of *Escherichia coli* by sulfur-doped and nitrogen-fluorine-codoped TiO₂ nanoparticles under solar simulated light and visible light irradiation," *Environmental Science & Technology*, vol. 47, no. 17, pp. 9988–9996, 2013.
- [17] H.-Y. Lin and Y.-S. Chang, "Photocatalytic water splitting for hydrogen production on Au/KTiNbO₅," *International Journal of Hydrogen Energy*, vol. 35, no. 16, pp. 8463–8471, 2010.
- [18] M. Ni, M. K. H. Leung, D. Y. C. Leung, and K. Sumathy, "A review and recent developments in photocatalytic water-splitting using TiO₂ for hydrogen production," *Renewable and Sustainable Energy Reviews*, vol. 11, no. 3, pp. 401–425, 2007.
- [19] X. Chen, S. Shen, L. Guo, and S. S. Mao, "Semiconductor-based photocatalytic hydrogen generation," *Chemical Reviews*, vol. 110, no. 11, pp. 6503–6570, 2010.
- [20] T.-D. Pham and B.-K. Lee, "Novel integrated approach of adsorption and photo-oxidation using Ag-TiO₂/PU for bio-aerosol removal under visible light," *Chemical Engineering Journal*, vol. 275, pp. 357–365, 2015.
- [21] T.-D. Pham and B.-K. Lee, "Cu doped TiO₂/GF for photocatalytic disinfection of *Escherichia coli* in bioaerosols under visible light irradiation: application and mechanism," *Applied Surface Science*, vol. 296, pp. 15–23, 2014.
- [22] H. Yan, S. T. Kochuveedu, L. N. Quan, S. S. Lee, and D. H. Kim, "Enhanced photocatalytic activity of C, F-codoped TiO₂ loaded with AgCl," *Journal of Alloys and Compounds*, vol. 560, pp. 20–26, 2013.
- [23] X. Xu, X. Zhou, L. Zhang et al., "Photoredox degradation of different water pollutants (MO, RhB, MB, and Cr(VI)) using Fe-N-S-tri-doped TiO₂ nanophotocatalyst prepared by novel chemical method," *Materials Research Bulletin*, vol. 70, pp. 106–113, 2015.
- [24] S. M. El-Sheikh, G. Zhang, H. M. El-Hosainy et al., "High performance sulfur, nitrogen and carbon doped mesoporous anatase-brookite TiO₂ photocatalyst for the removal of microcystin-LR under visible light irradiation," *Journal of Hazardous Materials*, vol. 280, pp. 723–733, 2014.
- [25] S. Yu, H. J. Yun, Y. H. Kim, and J. Yi, "Carbon-doped TiO₂ nanoparticles wrapped with nanographene as a high performance photocatalyst for phenol degradation under visible light irradiation," *Applied Catalysis B: Environmental*, vol. 144, pp. 893–899, 2014.
- [26] T.-D. Pham and B.-K. Lee, "Photocatalytic comparison of Cu- and Ag-doped TiO₂/GF for bioaerosol disinfection under visible light," *Journal of Solid State Chemistry*, vol. 232, pp. 256–263, 2015.
- [27] T. D. Pham, B. K. Lee, M. V. Nguyen, and C. H. Lee, "Germicide feasibility of TiO₂/glass fiber and Ag-TiO₂/glass fiber photocatalysts," *Advanced Materials Research*, vol. 864, pp. 518–523, 2012.
- [28] H. Feng, M.-H. Zhang, and L. E. Yu, "Hydrothermal synthesis and photocatalytic performance of metal-ions doped TiO₂," *Applied Catalysis A: General*, vol. 413-414, pp. 238–244, 2012.
- [29] R. Djellabi, M. F. Ghorab, G. Cerrato et al., "Photoactive TiO₂-montmorillonite composite for degradation of organic dyes in water," *Journal of Photochemistry and Photobiology A: Chemistry*, vol. 295, pp. 57–63, 2014.
- [30] L. M. Martínez T, M. I. Domínguez, N. Sanabria et al., "Deposition of Al-Fe pillared bentonites and gold supported Al-Fe pillared bentonites on metallic monoliths for catalytic oxidation reactions," *Applied Catalysis A: General*, vol. 364, no. 1-2, pp. 166–173, 2009.
- [31] M. Yurdakoç, M. Akçay, Y. Tonbul, F. Ok, and K. Yurdakoç, "Preparation and characterization of Cr- and Fe-pillared bentonites by using CrCl₃, FeCl₃, Cr(acac)₃ and Fe(acac)₃ as precursors," *Microporous and Mesoporous Materials*, vol. 111, no. 1–3, pp. 211–218, 2008.
- [32] J. Chen and L. Zhu, "Comparative study of catalytic activity of different Fe-pillared bentonites in the presence of UV light and H₂O₂," *Separation and Purification Technology*, vol. 67, no. 3, pp. 282–288, 2009.
- [33] A. Eshaghi and H. Moradi, "Optical and photocatalytic properties of the Fe-doped TiO₂ nanoparticles loaded on the activated carbon," *Advanced Powder Technology*, vol. 29, no. 8, pp. 1879–1885, 2018.
- [34] G. Wei, L. Wei, Y. Chen et al., "Magnetic coupling and electric transport in Nb, Fe co-doped rutile TiO₂ epitaxial films," *Journal of Alloys and Compounds*, vol. 695, pp. 2261–2265, 2017.
- [35] X. Cao, S. Luo, C. Liu, and J. Chen, "Synthesis of bentonite-supported Fe₂O₃ -Doped TiO₂ superstructures for highly promoted photocatalytic activity and recyclability," *Advanced Powder Technology*, vol. 28, no. 3, pp. 993–999, 2017.
- [36] A. A. Isari, A. Payan, M. Fattahi, S. Jorfi, and B. Kakavandi, "Photocatalytic degradation of rhodamine B and real textile wastewater using Fe-doped TiO₂ anchored on reduced graphene oxide (Fe-TiO₂/rGO): characterization and feasibility, mechanism and pathway studies," *Applied Surface Science*, vol. 462, pp. 549–564, 2018.
- [37] B. Krishnan and S. Mahalingam, "Ag/TiO₂/bentonite nanocomposite for biological applications: synthesis, characterization, antibacterial and cytotoxic investigations," *Advanced Powder Technology*, vol. 28, no. 9, pp. 2265–2280, 2017.
- [38] T.-D. Pham and B.-K. Lee, "Selective removal of polar VOCs by novel photocatalytic activity of metals co-doped TiO₂/PU under visible light," *Chemical Engineering Journal*, vol. 307, pp. 63–73, 2017.
- [39] T.-D. Pham, B.-K. Lee, and C.-H. Lee, "The advanced removal of benzene from aerosols by photocatalytic oxidation and adsorption of Cu-TiO₂/PU under visible light irradiation," *Applied Catalysis B: Environmental*, vol. 182, pp. 172–183, 2016.
- [40] T.-D. Pham and B.-K. Lee, "Novel adsorption and photocatalytic oxidation for removal of gaseous toluene by V-doped TiO₂/PU under visible light," *Journal of Hazardous Materials*, vol. 300, pp. 493–503, 2015.
- [41] D. Kanakaraju and S. P. Wong, "Photocatalytic efficiency of TiO₂-biomass loaded mixture for wastewater treatment," *Journal of Chemistry*, vol. 2018, Article ID 4314969, 14 pages, 2018.

Research Article

A Novel Approach for Fabricating LaMnO_3 Thin Films Using Combined Microwave Combustion and Pulsed Electron Deposition Techniques

Thi Ha Tran,¹ Thi Trung Anh Tang,² Nguyen Hai Pham,² Thanh Cong Bach,² Cong Doanh Sai ,² Quang Hoa Nguyen,² Van Vu Le,² Hoang Nam Nguyen ,² Quoc Khoa Doan,³ Trong Tam Nguyen,⁴ Viet Bau Le,⁵ Khac Hieu Ho,⁶ and Viet Tuyen Nguyen ²

¹Hanoi University of Mining and Geology, Duc Thang, Tu Liem, Hanoi, Vietnam

²VNU University of Science, Vietnam National University, 334 Nguyen Trai, Thanh Xuan, Hanoi, Vietnam

³Quang Tri Teacher Training College, Quang Tri, Vietnam

⁴Department of Physics, Faculty of Basic-Fundamental Sciences, Vietnam Maritime University, 484 Lach Tray, Le Chan, Hai Phong, Vietnam

⁵Hong Duc University, 565 Quang Trung, Dong Ve, Thanh Hoa, Vietnam

⁶Duy Tan University, 03 Quang Trung, Danang, Vietnam

Correspondence should be addressed to Cong Doanh Sai; saidoanh@hus.edu.vn and Viet Tuyen Nguyen; nguyenviettuyen@hus.edu.vn

Received 28 November 2018; Accepted 5 February 2019; Published 4 March 2019

Guest Editor: Ajit Kumar Sharma

Copyright © 2019 Thi Ha Tran et al. This is an open access article distributed under the Creative Commons Attribution License, which permits unrestricted use, distribution, and reproduction in any medium, provided the original work is properly cited.

LaMnO_3 (LMO) nanopowder was synthesized by the microwave combustion method using glycine and nitrate salts of La and Mn as precursors. The as-prepared LMO powder was pressed at high pressure and annealed at 1000°C for 8 hours to make a target for thin film deposition. The structural and elemental analysis was obtained by X-ray diffraction (XRD) and energy dispersive X-ray spectroscopy (EDS). Thin films of LMO were fabricated using pulsed electron deposition (PED) at room temperature. The effects of discharge voltage and oxygen/argon flux ratio on the produced thin films were studied. The study shows that stoichiometry and structure of the target was preserved well in the thin films prepared with a discharge voltage from 14 to 15 kV, while the oxygen/nitrogen flux ratio did not show a clear effect on the quality of thin films.

1. Introduction

Recently, semiconductor magnetic nanomaterials have received much awareness than that of their same bulk materials, due to their size and surface effects, which exhibit unique properties such as photoluminescence, magneto-optical, electrochemical, and photocatalytic activity [1–13]. These unique properties of nanomaterials in turn help to solve a lot of urgent problems related to exhaustion of fossil fuels and environment pollution. In this aspect, production

and application of clean fuels based on nanomaterials become more and more critical for the development of human society [14–17]. In particular, solid oxide fuel cells (SOFCs) have been extensively studied and attracted much attention as a promising way to generate electricity at high efficiency and low cost [18–20]. For such applications, the cathode material must satisfy several criteria such as good electrical conductivity, high porosity to allow gas diffusion, thermal expansion coefficient matching well with that of the solid electrolyte, and chemical stability at a high temperature

[21–23]. Most of the requirements listed above are satisfied by LaMnO_3 perovskites, making it one of the most suitable materials for cathode in SOFCs [24].

Among many effective methods developed to produce nanopowders, microwave-assisted synthesis was first developed in 1985 and has quickly become a major area of study. Since microwave radiations were discovered, these have been widely utilized for synthetic chemistry in order to activate chemical reactions more rapidly and homogeneously [25–29]. Moreover, a self-combustion reaction assisted with microwave is extremely suitable for preparation of perovskite nanomaterials due to notable advantages such as simple and convenient experimental set-up, extremely time, and energy saving, as well as offering homogeneous product [30–32]. These advantages result from a thorough blending among the constituents in an aqueous media under microwave irradiation. Furthermore, an exothermic redox reaction between the fuel and an oxidizer provides a great amount of heat which is necessary for the formation of the perovskite phase [33, 34].

In general, thin films can be manufactured by a variety of methods such as sputtering, thermal evaporation, and molecular-beam epitaxy [35–37]. Pulsed electron deposition (PED) is also a physical thin film deposition technique offering many advantages such as high film homogeneity and low cost. However, this method seems to be not explored for preparation of perovskite thin films even though it is convenient to transfer the target stoichiometry to the deposited films by PED [38].

In this paper, LaMnO_3 (LMO) nanopowder was prepared by microwave combustion where glycine was used as a fuel in a combustion reaction with nitrate salts of lanthanum and manganese. The as-prepared LMO powder was pressed and annealed at 1000°C for 8 hours to make a target for thin film deposition. The fabrication of LMO thin films by PED was investigated in details.

2. Experiment

LaMnO_3 nanopowder was prepared by the microwave combustion method. Analytical grade La_2O_3 (99.99%), $\text{Mn}(\text{NO}_3)_2 \cdot 4\text{H}_2\text{O}$ (99%), and glycine $\text{NH}_2\text{CH}_2\text{COOH}$ (99%) were used as the starting materials. Stoichiometric amount of La_2O_3 was dissolved in HNO_3 to obtain $\text{La}(\text{NO}_3)_3$ solution. Then, $\text{La}(\text{NO}_3)_3$ and $\text{Mn}(\text{NO}_3)_2$ solutions in water at molar ratio of 1 : 1 were mixed well before dropwise addition of glycine.

We first prepared a set of samples with different molar ratios of glycine to the metal ion ($F = 2.5, 3, 3.5, 4, \text{ and } 4.5$) to study the effect of fuel on the nanopowder. After heating on a hot plate at 150°C , the light pink solution evolved into a colorless transparent one and then viscous brown gel. Gel was stored in a glass container covered with an open lid and then quickly transferred to a microwave oven. After a few seconds, the viscous gel bubbled up and autoignited to produce brown fine powder.

The LMO powder was milled, pressed, and annealed at 1000°C for 8 hours to make a target for fabrication of the thin film by pulsed electron deposition system PEBS-20 from

Neocera, Inc. All the LaMnO_3 films were deposited on silicon substrates with the repetition rate of pulses maintained at 5 Hz, pulse width of 100 ns, and 20 000 pulses.

Two sets of thin film samples were prepared to study the effect of discharge voltage (LMO-1) and O_2/N_2 flux ratio (LMO-2). The deposition of the LMO-1 films was carried out at room temperature and at five discharge voltages: 11, 12, 13, 14, and 15 kV. The N_2 gas and O_2 gas were introduced at a pressure of 9×10^{-3} Torr for enhancing the electron beam and stabilizing the beam propagation to the target with a gas flux of 10 sccm and 15 sccm for oxygen and nitrogen, respectively. LMO-2 films were fabricated at 15 kV with various flux ratios of oxygen and nitrogen: 0 : 25; 5 : 20; 10 : 15; 20 : 5; and 25 : 0 sccm. During the deposition process, the pressure was maintained by balancing between the rate of the turbopump and the flow rate of oxygen and nitrogen gas introduced into the chamber. The as-deposited thin films were annealed at 400, 600, and 800°C for 2 h.

The crystallinity of the thin films was characterized by the X-ray diffraction system (Siemens D5005, Bruker, Germany) with $\text{Cu K}_{\alpha 1}$ ($\lambda = 0.154056 \text{ nm}$) radiation. The morphology of the product was investigated by a scanning electron microscope (Nova Nano SEM 450). The composition of the samples was verified by energy dispersive X-ray (EDX) spectrometry (Oxford Isis 300) integrated into the JEOL-JSM 5410 scanning electron microscope.

3. Results and Discussion

Figure 1 shows XRD patterns of LaMnO_3 nanoparticles prepared by the microwave irradiation method when using glycine as fuel in the combustion reaction with the glycine-nitrate molar ratio (G/N) ($F = 2.5, 3, 3.5, 4, \text{ and } 4.5$).

The sample prepared with $F = 2.5$ is amorphous because the released energy is not enough for formation of the perovskite phase. With $F = 3, 3.5, 4, \text{ and } 4.5$, the LaMnO_3 perovskite phase has formed. Sharp and intense XRD peaks of the samples with $F = 3$ suggested that crystal quality of those samples is better. The combustion reaction with a higher value of F liberated more heat. However, gas generated during the reaction can bring out heat from the reaction chamber and reduced the heat used for synthesis of the perovskite material [39]. Heat generated by the reaction might be reduced too much and resulted in an amorphous state of samples with F greater than 4. XRD patterns indicate that LaMnO_3 nanoparticles, prepared with $F = 3; 3.5; \text{ and } 4$, crystallized in a hexagonal structure. Lattice parameters and crystalline size of the samples prepared with different ratios of F are shown in Table 1.

XRD analysis of the LaMnO_3 nanoparticles prepared by combustion assisted with microwave irradiation also shows the presence of both LaMnO_3 and La_2CO_5 . La_2CO_5 is an unwanted phase due to the unavoidable reaction of metal ions with organic precursors.

A pure perovskite is necessary for making cathode of good performance fuel cell. Therefore, such secondary phases need to be removed. As an unsolvable material, La_2CO_5 cannot be washed away using water, so the nanopowder was annealed at 1000°C to convert the remaining

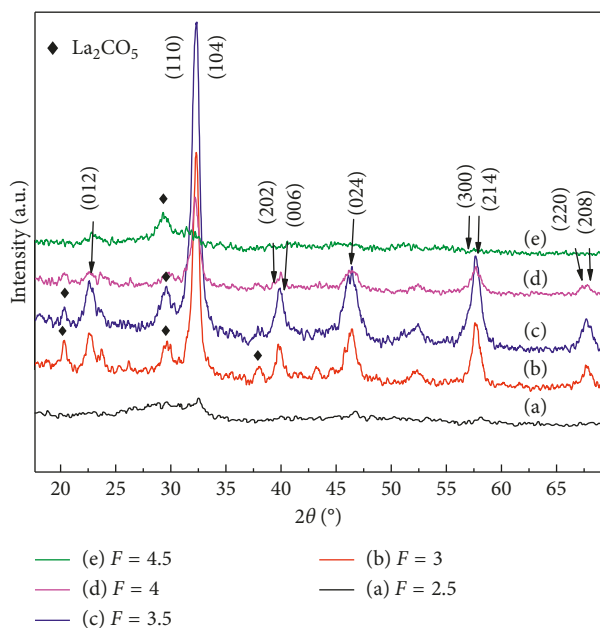


FIGURE 1: XRD patterns of LaMnO_3 nanoparticles with $F=2.5, 3, 3.5, 4,$ and 4.5 .

TABLE 1: The lattice parameters and crystallite size of the LaMnO_3 samples with different ratios of glycine/nitrate molar ($F=3, 3.5,$ and 4).

Sample	a (Å)	b (Å)	c (Å)	\bar{d} (nm)	Volume of unit cell (Å ³)
$F=3$	5.54	5.54	13.46	14.1	357.66
$F=3.5$	5.54	5.54	13.47	10.2	357.62
$F=4$	5.55	5.55	13.45	9.9	358.98

La_2CO_5 into LaMnO_3 . Figure 2 shows the XRD patterns of LaMnO_3 samples with a molar ratio of glycine to metal ion of 3 and 3.5 before and after annealing at 1000°C in 8 h. After annealing, no peak related to La_2CO_5 can be seen in the XRD pattern. The result implies the purity of the final nanopowder. Sharper and stronger diffraction peaks show that crystalline sizes of the LaMnO_3 powder increase clearly after annealing, as expected due to the crystal growth during the annealing process at a high temperature. It should be also noted that, after annealing, a clear peak shift to a higher angle was observed. The reason for lattice expansion in the sample should be taken into account. One possible explanation for lattice expansion in the sample before annealing is small particles size. In other words, in nanomaterials of poor structural order, defect might be introduced at a high concentration, which results in an internal stress in the lattice due to the presence of large La^{3+} at interstitial sites in the lattice. The internal stress is responsible for the lattice expansion, as observed for as-prepared nanopowder samples. The corresponding decrease of the lattice parameter is shown in Table 2.

However, the results show that annealing the samples at 1000°C does not result in transition of the phase structure. Such peak shift to a higher angle, combining with the disappearance of some peaks in the XRD pattern, can be an

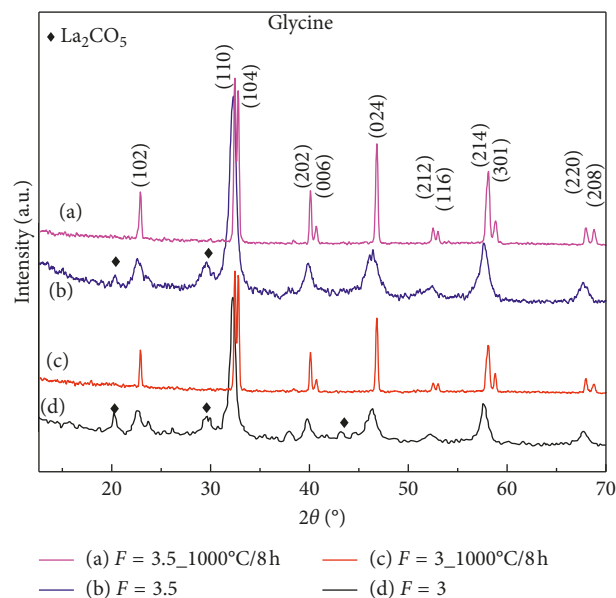


FIGURE 2: XRD patterns of LaMnO_3 samples with $F=3$ and 3.5 before and after annealing at 1000°C in 8 h.

indication of a phase transition. The change in the lattice parameter suggests that annealing phase transition from hexagonal to other structures can occur at a higher temperature or in longer time. However, this is not being mentioned in this paper but would be reported in another study.

The energy dispersive X-ray spectra (Figure 3) of the LaMnO_3 nanopowder with $F=3$ before and after annealing at 1000°C in 8 hours only show the peaks of La, O, and Mn. This result indicates that samples are clean and pure. LaMnO_3 nanopowder prepared with a molar ratio of glycine/nitrate ($F=3$) was used to make a target because the results showed that better crystallinity was achieved for this sample. The as-prepared LMO powder was remilled, pressed at high pressure, and annealed at 1000°C for 8 hours to make a target. The structure and phase purity of the LMO target was examined by XRD measurements, as shown in Figure 4. The XRD patterns reveal that the structure of the LMO target is still hexagonal. The LMO target showed peaks corresponding to reflection from (102), (110), (104), (202), (204), (212), (214), and (220) planes, where (110) and (104) peaks have the strongest intensity clearly demonstrating the preferred crystal growth during the annealing process.

Even though the LMO target can be fabricated by the normal solid-state reaction method from oxides precursors, using nanopowder of LMO to make the target help in reducing the treating temperature to 1000°C , the target prepared by the solid-state reaction normally required a much higher annealing temperature ($1300\text{--}1400^\circ\text{C}$) and longer time (12–24 h).

Figure 5 shows XRD patterns of the LaMnO_3 thin films deposited at 15 kV before and after annealing at different temperatures. It can be seen that the as-deposited films and films annealed at 400°C and 600°C were amorphous because no diffraction peak is observed. As annealing temperature is

TABLE 2: The lattice parameter of the LaMnO_3 samples with different ratios of glycine/nitrate molar ($F = 3$ and 3.5) before and after annealing at 1000°C for 8 h.

Sample	a (\AA)	b (\AA)	c (\AA)	Volume of unit cell (\AA^3)
$F = 3$	5.54	5.54	13.46	357.66
$F = 3$ at 1000°C	5.51	5.51	13.29	349.43
$F = 3.5$	5.54	5.54	13.47	357.62
$F = 3.5$ at 1000°C	5.51	5.51	13.28	351.17

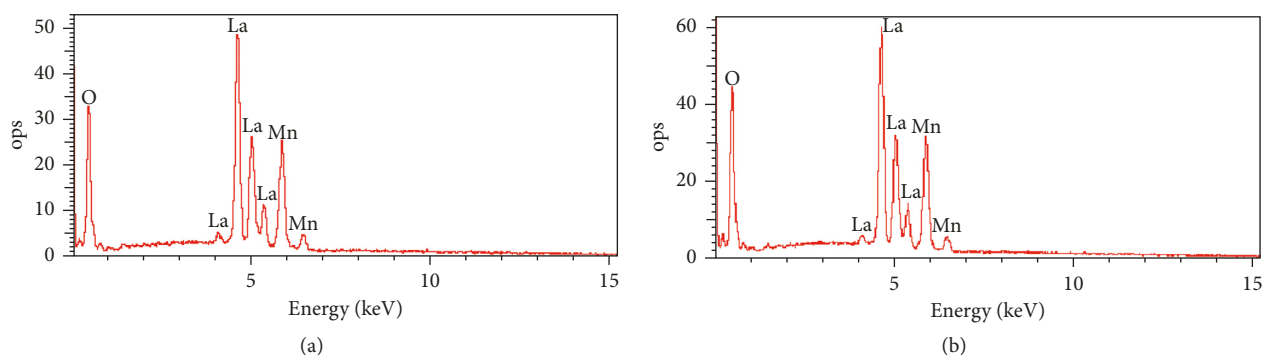


FIGURE 3: EDS spectra of the LaMnO_3 nanopowder with $F = 3$ (a) before and (b) after annealing at 1000°C .

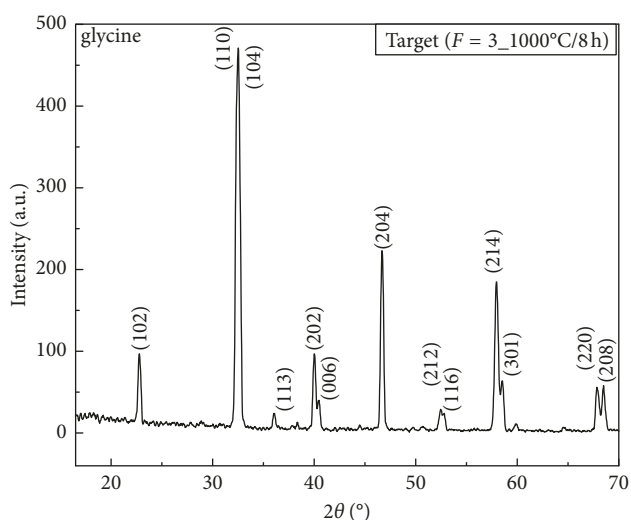


FIGURE 4: XRD pattern of the LaMnO_3 target made of LaMnO_3 nanoparticles prepared by self-combustion assisted with microwave irradiation.

raised up to 800°C , the thin film is crystallized in the hexagonal structure.

Figure 6 shows SEM images of LMO thin films deposited at 15 kV before and after annealing at different temperatures.

SEM images of thin films deposited at 15 kV show that the particle size distribution is quite uniform and post-annealing does not change the morphology of the produced thin films. The film is crack free both before and after being annealed. SEM images also reveal that the films have uniform particulates which are uniformly distributed on the surface.

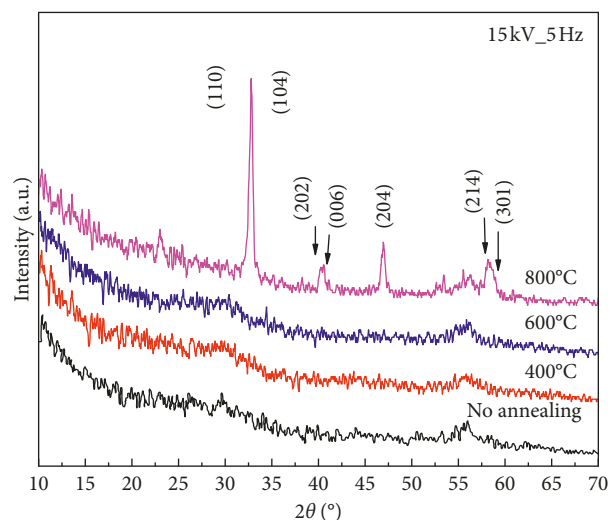


FIGURE 5: XRD patterns of the LaMnO_3 thin films deposited before and after annealing at 400°C , 600°C , and 800°C with a discharging voltage of 15 kV.

XRD analysis (Figure 7) shows that all thin films are amorphous for all discharge voltage. Postannealing at a temperature higher than 800°C is required to obtain crystalline films. However, transition from the amorphous to hexagonal structure occurs only in films deposited at 14 and 15 kV. Other films prepared at voltage lower than 14 kV remains in the amorphous state despite postannealing.

The diffraction peaks were higher at 15 kV which is the maximum voltage available for the used PED system. The above results can be understood that discharge voltage is a critical factor determining the growth of thin films by PED. Voltage higher than 14 kV is required to preserve the

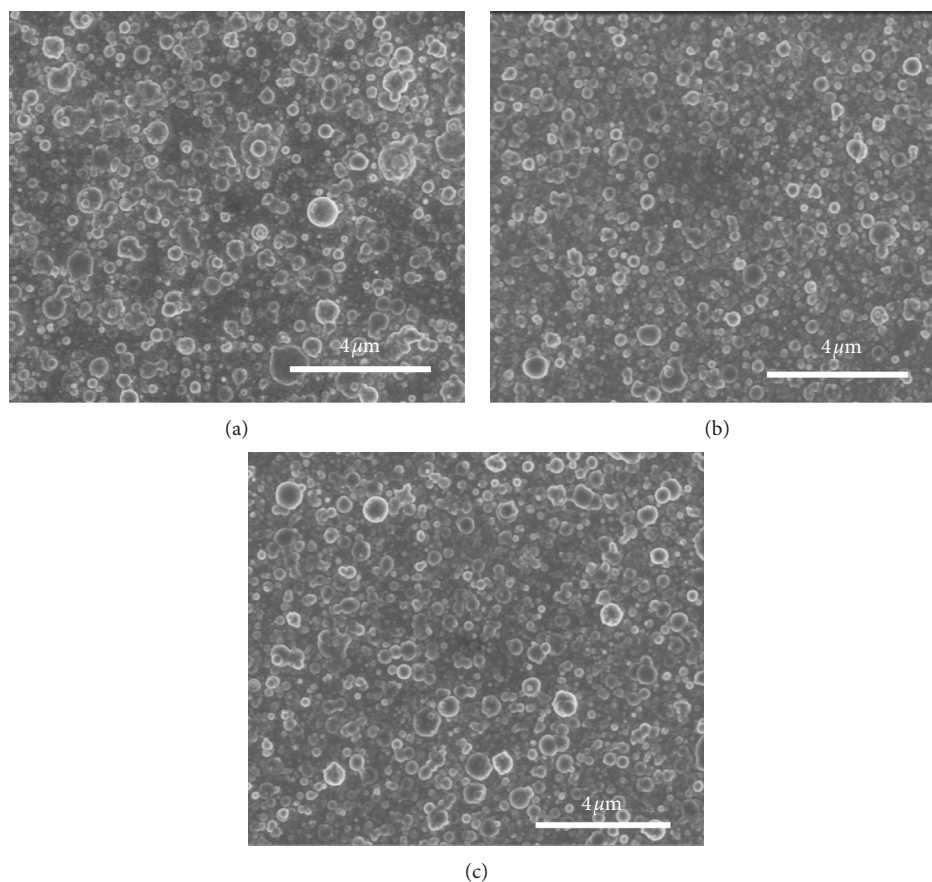


FIGURE 6: SEM images of LMO thin films deposition at 15 kV after annealing at different temperatures (a) as the deposited film; (b) 400°C; (c) 800°C.

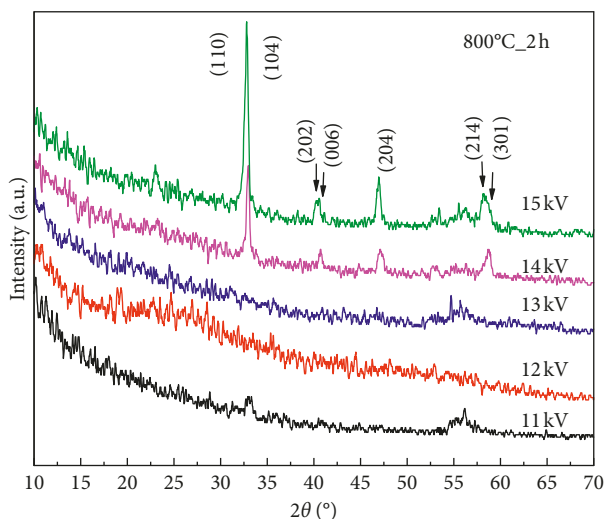


FIGURE 7: XRD patterns of LaMnO_3 thin films deposited at 11, 12, 13, 14, and 15 kV after annealing at 800°C for 2 h.

stoichiometry composition of the target to the thin films. However, the energy transferred by the electron beam is not enough for the atom to arrange on the substrate in a crystalline structure. Hence, postannealing is necessary to activate the crystallization of the thin films. Lattice

parameters of the films prepared at 14 and 15 kV after annealing are shown in Table 3.

In vacuum deposition techniques, gas ambient may also have a great influence on the structure and morphology of the thin films [40]. We also studied the effect of the N_2/O_2 flux ratio on the LMO thin film prepared by pulse electron deposition. Figure 8 shows XRD patterns of the LaMnO_3 thin films deposited at 15 kV and 5 Hz with different ratios of N_2/O_2 flux (25:0, 20:5, 10:15, and 0:25 sccm).

It is clear that the films after postannealing are well crystallized at all different ratios of N_2/O_2 flux. The highest intensity was achieved for film grown at N_2/O_2 flux (10:15 sccm), indicating that partial pressure of oxygen also has a slight effect on the structure of the thin films.

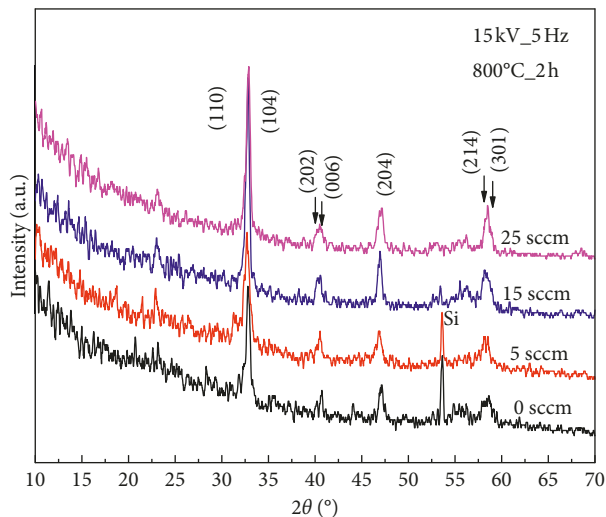
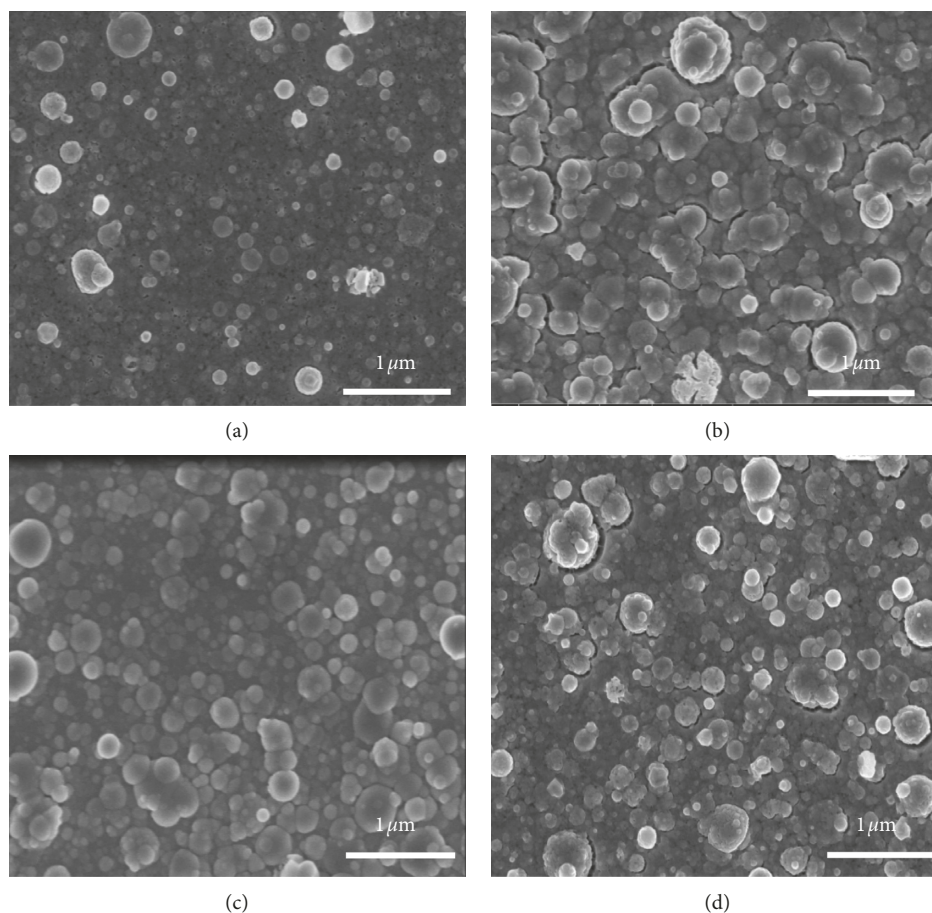
Figure 9 shows SEM images of the LMO-2 films, which were prepared at a different oxygen partial pressure. While the sample prepared in pure nitrogen ambient possesses fine particulates, the samples prepared in oxygen show more particulates. This could be due to the fragmentation of the oxide particulates in the plasma region at higher oxygen partial pressures [41].

4. Conclusion

LaMnO_3 nanopowder was successfully synthesized using combustion assisted with microwave irradiation approach.

TABLE 3: The lattice parameters of the LaMnO₃ thin films deposited at 14 and 15 kV after annealing at 800°C for 2 h.

Sample	Lattice structure	a (Å)	b (Å)	c (Å)	Volume of unit cell (Å ³)
15 kV at 800°C	Hexagonal	5.46	5.46	13.44	358.03
14 kV at 800°C	Hexagonal	5.49	5.49	13.26	346.24

FIGURE 8: XRD patterns of the LaMnO₃ thin films prepared with different O₂ flux at 0, 5, 15, and 25 sccm after annealing at 800°C for 2 h.FIGURE 9: SEM image of LaMnO₃ thin films with different O₂ flux at (a) 0, (b) 5, (c) 15, and (d) 25 sccm after annealing at 800°C for 2 h.

Using nanopowder helps to lower the temperature of heat treatment of the target. Detailed investigation of LaMnO₃ thin films preparation shows that discharge voltage is a critical parameter for film deposition by PED. The obtained films were amorphous but could be converted into the crystalline phase after annealing at relatively a low temperature of 800°C. Suitable ratio of oxygen/nitrogen flux also contributes to better crystal quality of the thin films. The results demonstrate the potential of using PED as a tool for fabrication of perovskite thin films of high quality for various applications in electronic fields.

Data Availability

All data used to support the findings of this study are available from the corresponding author upon request.

Conflicts of Interest

The authors declare that they have no conflicts of interest.

Acknowledgments

The authors would like to thank Faculty of Physics, VNU University of Science, for allowing them to use the equipment. This research was funded by the Vietnam National University (VNU), Hanoi, under project number QG.17.11.

References

- [1] M. Maria Lumina Sonia, S. Anand, S. Blessi, S. Pauline, and A. Manikandan, "Effect of surfactants (PVB/EDTA/CTAB) assisted sol-gel synthesis on structural, magnetic and dielectric properties of NiFe₂O₄ nanoparticles," *Ceramics International*, vol. 44, no. 18, pp. 22068–22079, 2018.
- [2] M. M. L. Sonia, S. Anand, V. M. Vinosel, M. A. Janifer, S. Pauline, and A. Manikandan, "Effect of lattice strain on structure, morphology and magneto-dielectric properties of spinel NiGd_xFe_{2-x}O₄ ferrite nano-crystallites synthesized by sol-gel route," *Journal of Magnetism and Magnetic Materials*, vol. 466, pp. 238–251, 2018.
- [3] S. Asiri, M. Sertkol, H. Güngüneş et al., "The temperature effect on magnetic properties of NiFe₂O₄ nanoparticles," *Journal of Inorganic and Organometallic Polymers and Materials*, vol. 28, no. 4, pp. 1587–1597, 2018.
- [4] A. G. Abraham, A. Manikandan, E. Manikandan, S. K. Jaganathan, A. Baykal, and P. S. Renganathan, "Enhanced opto-magneto properties of Ni_xMg_{1-x}Fe₂O₄ (0.0 < x < 1.0) Ferrites nano-catalysts," *Journal of Nanoelectronics and Optoelectronics*, vol. 12, no. 12, pp. 1326–1333, 2017.
- [5] A. Manikandan, M. Durka, M. Amutha Selvi, and S. Arul Antony, "Sesamum indicum plant extracted microwave combustion synthesis and opto-magnetic properties of spinel Mn_xCo_{1-x}Al₂O₄ nano-catalysts," *Journal of Nanoscience and Nanotechnology*, vol. 16, no. 1, pp. 448–456, 2016.
- [6] H. H. Mai, V. T. Pham, V. T. Nguyen, C. D. Sai, C. H. Hoang, and T. B. Nguyen, "Non-enzymatic fluorescent biosensor for glucose sensing based on ZnO nanorods," *Journal of Electronic Materials*, vol. 46, no. 6, pp. 3714–3719, 2017.
- [7] P. V. Thanh, H. Hanh Mai, N. V. Tuyen, S. C. Doanh, and N. C. Viet, "Zinc oxide nanorods grown on printed circuit board for extended-gate Field-effect transistor pH sensor," *Journal of Electronic Materials*, vol. 46, pp. 3732–3737, 2017.
- [8] T. H. Tran and V. T. Nguyen, "Phase transition of Cu₂O to CuO nanocrystals by selective laser heating," *Materials Science in Semiconductor Processing*, vol. 46, pp. 6–9, 2016.
- [9] T.-D. Pham and B. K. Lee, "Novel capture and photocatalytic conversion of CO₂ into solar fuels by metals co-doped TiO₂ deposited on PU under visible light," *Applied Catalysis A: General*, vol. 529, pp. 40–48, 2017.
- [10] T.-D. Pham and B.-K. Lee, "Novel integrated approach of adsorption and photo-oxidation using Ag-TiO₂/PU for bio-aerosol removal under visible light," *Chemical Engineering Journal*, vol. 275, pp. 357–365, 2015.
- [11] T. D. Pham, B. K. Lee, M. V. Nguyen, and C. H. Lee, "Germicide Feasibility of TiO," *Advanced Materials Research*, vol. 518–523, pp. 864–868, 2012.
- [12] T. D. Pham and B. K. Lee, "Novel integrated approach of adsorption and photo-oxidation using Ag-TiO₂/PU for bioaerosol removal under visible light," *Chemical Engineering Journal*, vol. 275, pp. 357–365, 2015.
- [13] T.-D. Pham and B.-K. Lee, "Photocatalytic comparison of Cu- and Ag-doped TiO₂/GF for bioaerosol disinfection under visible light," *Journal of Solid State Chemistry*, vol. 232, pp. 256–263, 2015.
- [14] E. Hema, A. Manikandan, P. Karthika, M. Durka, S. A. Antony, and B. R. Venkatraman, "Magneto-optical properties of reusable spinel Ni," *Journal of Nanoscience and Nanotechnology*, vol. 16, no. 7, pp. 7325–7336, 2016.
- [15] S. Suguna, S. Shankar, Saravana Kumar Jaganathan, and A. Manikandan, "Novel synthesis of spinel Mn_xCo_{1-x}Al₂O₄ (x = 0.0 to 1.0) nanocatalysts: effect of Mn²⁺ doping on structural, morphological, and opto-magnetic properties," *Journal of Superconductivity and Novel Magnetism*, vol. 30, no. 3, pp. 691–699, 2017.
- [16] V. T. Nguyen, D. Nam, M. Gansukh et al., "Influence of sulfate residue on Cu₂ZnSnS₄ thin films prepared by direct solution method," *Solar Energy Materials and Solar Cells*, vol. 136, pp. 113–119, 2015.
- [17] N. T. T. Truc, N. T. Hanh, M. V. Nguyen et al., "Novel direct Z-scheme Cu₂V₂O₇/g-C₃N₄ for visible light photocatalytic conversion of CO₂ into valuable fuels," *Applied Surface Science*, vol. 457, pp. 968–974, 2018.
- [18] N. Mahato, A. Banerjee, A. Gupta, S. Omar, and K. Balani, "Progress in material selection for solid oxide fuel cell technology: a review," *Progress in Materials Science*, vol. 72, pp. 141–337, 2015.
- [19] W. Wang, C. Su, Y. Wu, R. Ran, and Z. Shao, "Progress in solid oxide fuel cells with nickel-based Anodes operating on methane and related fuels," *Chemical Reviews*, vol. 113, no. 10, pp. 8104–8151, 2013.
- [20] N. Minh, J. Mizusaki, and S. C. Singhal, "Advances in solid oxide fuel cells: review of progress through three decades of the international symposia on solid oxide fuel cells," *ECS Transactions*, vol. 78, no. 3, pp. 63–73, 2017.
- [21] Y. Choi, E. C. Brown, S. M. Haile, and W. Jung, "Electrochemically modified, robust solid oxide fuel cell anode for direct-hydrocarbon utilization," *Nano Energy*, vol. 23, pp. 161–171, 2016.
- [22] C. Yang, J. Li, Y. Lin, J. Liu, F. Chen, and M. Liu, "In situ fabrication of CoFe alloy nanoparticles structured (Pr_{0.4}Sr_{0.6})₃(Fe_{0.85}Nb_{0.15})₂O₇ ceramic anode for direct hydrocarbon solid oxide fuel cells," *Nano Energy*, vol. 11, pp. 704–710, 2015.

- [23] V. A. Sadykov, V. S. Muzykantov, N. F. Yeremeev et al., "Solid oxide fuel cell cathodes: importance of chemical composition and morphology," *Catalysis for Sustainable Energy*, vol. 2, no. 1, pp. 57–70, 2015.
- [24] C. Sun, R. Hui, and J. Roller, "Cathode materials for solid oxide fuel cells: a review," *Journal of Solid State Electrochemistry*, vol. 14, no. 7, pp. 1125–1144, 2010.
- [25] T. Mistumori, K. Sasaki, K. Yano, R. Fujihara, and M. Yoshinaga, "Effects of microwave irradiation heating in the homogeneous precipitation method using the reductant generated by hydrolysis of urea in an autoclave under high pressure," *Journal of the Ceramic Society of Japan*, vol. 123, no. 5, pp. 359–362, 2015.
- [26] T. T. Ha, T. D. Canh, and N. V. Tuyen, "A quick process for synthesis of ZnO nanoparticles with the aid of microwave irradiation," *ISRN Nanotechnology*, vol. 2013, Article ID 497873, 7 pages, 2013, 2013.
- [27] N. V. Tuyen, T. D. Canh, N. N. Long, N. X. Nghia, B. N. Q. Trinh, and Z. Shen, "Synthesis of undoped and M-doped ZnO (M = Co, Mn) nanopowder in water using microwave irradiation," vol. 187, pp. 012020(1)–012020(8).
- [28] T. D. Canh, N. V. Tuyen, and N. N. Long, "Influence of solvents on the growth of zinc oxide nanoparticles fabricated by microwave irradiation," *VNU Journal of Science: Mathematics—Physics*, vol. 25, pp. 71–76, 2009.
- [29] N. V. Tuyen, N. N. Long, and T. D. Canh, "Synthesis and characteristics of single-crystal Ni-doped ZnO nanorods prepared by a microwave irradiation method," *e-Journal of Surface Science and Nanotechnology*, vol. 9, pp. 472–476, 2011.
- [30] E. Hema, A. Manikandan, P. Karthika, S. A. Antony, and B. R. Venkatraman, "A novel synthesis of Zn²⁺-doped CoFe₂O₄ spinel nanoparticles: structural, morphological, opto-magnetic and catalytic properties," *Journal of Superconductivity and Novel Magnetism*, vol. 28, no. 8, pp. 2539–2552, 2015.
- [31] A. Manikandan, M. Durka, and S. A. Antony, "A novel synthesis, structural, morphological, and opto-magnetic characterizations of magnetically separable spinel Co_xMn_{1-x}Fe₂O₄ (0 ≤ x ≤ 1) nano-catalysts," *Journal of Superconductivity and Novel Magnetism*, vol. 27, no. 12, pp. 2841–2857, 2014.
- [32] T. H. Tran, T. C. Bach, N. H. Pham et al., "Phase transition of LaMnO₃ nanoparticles prepared by microwave assisted combustion method," *Materials Science in Semiconductor Processing*, vol. 89, pp. 121–125, 2019.
- [33] A. Manikandan, R. Sridhar, S. Arul Antony, and S. Ramakrishna, "A simple aloe vera plant-extracted microwave and conventional combustion synthesis: morphological, optical, magnetic and catalytic properties of CoFe₂O₄ nanostructures," *Journal of Molecular Structure*, vol. 1076, pp. 188–200, 2014.
- [34] M. Nüchter, B. Ondruschka, W. Bonrath, and A. Gum, "Microwave assisted synthesis—a critical technology overview," *Green Chemistry*, vol. 6, no. 3, pp. 128–141, 2004.
- [35] L. M. Quynh, N. T. Tien, P. V. Thanh et al., "Optical and electrical responses of magnetron-sputtered amorphous Nb-doped TiO₂ thin films annealed at low temperature," *Physica B: Condensed Matter*, vol. 532, pp. 200–203, 2018.
- [36] L. T. Dang, T. H. Dang, T. T. T. Nguyen et al., "Thermoelectric micro-refrigerator based on bismuth/Antimony telluride," *Journal of Electronic Materials*, vol. 46, no. 6, pp. 3660–3666, 2017.
- [37] T. Ginley, Y. Wang, and S. Law, "Topological insulator film growth by molecular beam epitaxy: a review," *Crystals*, vol. 6, no. 11, p. 154, 2016.
- [38] N. D. Sang, P. H. Quang, and D. Q. Ngoc, "Pulsed electron deposition (PED) - a novel tool for growth of thin films," *Communications in Physics*, vol. 22, no. 1, pp. 65–73, 2012.
- [39] X. Pingbo, Z. Weiping, Y. Kuo, J. Long, Z. Weiwei, and X. Shangda, "Size-controllable gly-nitrate low temperature combustion synthesis (LCS) of nanocrystalline La_{1-x}Sr_xMnO₃," *Journal of Alloys and Compounds*, vol. 311, no. 1, pp. 90–92, 2000.
- [40] C. S. Ma, S. K. Hau, K. H. Wong, P. W. Chan, and C. L. Choy, "The role of ambient gas scattering effect and lead oxide formation in pulsed laser deposition of lead-zirconate-titanate thin films," *Applied Physics Letters*, vol. 69, no. 14, pp. 2030–2032, 1996.
- [41] K. Muthukumar, P. Kuppasami, R. Kesavamoorthy et al., "Microstructural studies of bulk and thin film GDC," *Ionic*, vol. 14, no. 2, pp. 165–171, 2008.

Research Article

Metal-Organic Framework MIL-53(Fe) as an Adsorbent for Ibuprofen Drug Removal from Aqueous Solutions: Response Surface Modeling and Optimization

Duyen Thi Cam Nguyen ¹, Hanh Thi Ngoc Le,² Trung Sy Do,³ Van Thinh Pham,⁴ Dai Lam Tran ⁵, Van Thi Thanh Ho ⁶, Thuan Van Tran ⁷, Duy Chinh Nguyen ⁷, Trinh Duy Nguyen ⁷, Long Giang Bach ⁷, Huynh Ky Phuong Ha ⁸, and Van Thuan Doan ⁷

¹Faculty of Pharmacy, Nguyen Tat Thanh University, Ho Chi Minh City, Vietnam

²Institute of Hygiene and Public Health, Ho Chi Minh City, Vietnam

³Institute of Chemistry, Vietnam Academy of Science and Technology, Hanoi, Vietnam

⁴Dong Nai Technology University, Bien Hoa City, Dong Nai Province, Vietnam

⁵Institute for Tropical Technology, Vietnam Academy of Science and Technology, Hanoi, Vietnam

⁶Ho Chi Minh University of Natural Resources and Environment, Ho Chi Minh City, Vietnam

⁷NTT Hi-Tech Institute, Nguyen Tat Thanh University, Ho Chi Minh City, Vietnam

⁸Faculty of Chemical Engineering, Ho Chi Minh City University of Technology, Ho Chi Minh City, Vietnam

Correspondence should be addressed to Van Thuan Doan; doanthuanms@gmail.com

Received 1 December 2018; Revised 21 January 2019; Accepted 3 February 2019; Published 3 March 2019

Guest Editor: Nguayen Van Noi

Copyright © 2019 Duyen Thi Cam Nguyen et al. This is an open access article distributed under the Creative Commons Attribution License, which permits unrestricted use, distribution, and reproduction in any medium, provided the original work is properly cited.

Ibuprofen contamination from water sources has been increasingly alarming due to its environmentally accumulative retention; however, the strategies for ibuprofen-containing water treatment are still an enormous challenge. Herein, we described the utilization of metal-organic frameworks MIL-53(Fe) (MIL = Materials of Institute Lavoisier) for the adsorption of ibuprofen in synthetic solution. Firstly, the MIL-53(Fe) was solvothermally synthesized and then characterized using the X-ray diffraction and Fourier-transform infrared spectroscopy techniques. The optimization of ibuprofen adsorption over MIL-53(Fe) was performed with three independent variables including ibuprofen concentration (1.6–18.4 mg/L), adsorbent dosage (0.16–1.84 g/L), and pH (2.6–9.4) according to the experimental design from response surface methodology. Under the optimized conditions, more than 80% of ibuprofen could be eliminated from water, indicating the promising potential of the MIL-53(Fe) material for treatment of this drug. Kinetic and isotherm models also were used to elucidate the chemisorption and monolayer behavior mechanisms of ibuprofen over MIL-53(Fe).

1. Introduction

Ibuprofen ((±R, S)-2-(4-(2-methylpropyl)phenyl)propanoic acid, IBU), a nonsteroidal anti-inflammatory drugs (NSAIDs), has widely been used for the treatment of bacterial infection-related diseases in many countries (its chemical structure is shown in Figure 1) [1–4]. However, there is a rapid acceleration in IBU contamination due to

the ineffective treatment of wastewater sources, derived from hospitals and pharmaceutical manufacturers [5–7]. According to recent environmental reports, varying amounts of the IBU residue have been detected in some rivers (i.e., Thames River, UK (0.783 μg/L), and Aura River, Finland (20 μg/L)), significantly exceeding the permissible standards for human health [8]. Besides, the accumulation of the IBU pollutant in water may support

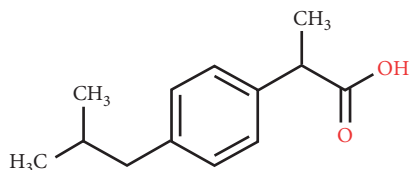


FIGURE 1: 2D structure of the IBU molecule by ChemDraw® ultra 12.0 program.

the antibiotics-resistant bacteria existing in the environment [1, 5, 9]. Therefore, techniques for eliminating this contaminant have received a great attention.

Adsorption is often regarded as a common method for the removal of pollutants in gas and liquid phases [10–15]. Several strong points of this approach include cost-effectiveness and high performance [16, 17]. Thanks to the good reusability of adsorbents, the overall cost can be reduced. Moreover, the adsorption is highly compatible with organic-derived hazardous wastes including IBU contaminant [4]. Therefore, the IBU degradation by the adsorption process has been rapidly developed.

In the adsorption process, solid adsorbents play a decisive role in removing the contaminants [18]. Heterogeneous materials have undergone a long history, especially nanostructured zeolites and mesoporous silica [4, 19–22]. Thanks to the highly porous structure along with open metal sites, these materials have been considered as ideal platforms towards diverse applications in fuel cells, chemical sensing, energy conversion, catalysis, drug delivery, and thin films [23–25]. However, the synthesis strategies for such materials were carried out via many elaborate steps combined with severe condition-controlled reactions, limiting their widespread applications [26]. Several studies reported the use of hazardous and expensive agents (i.e., reversible addition-fragmentation chain transfer (RAFT)) as vital components that control the growing of polymeric organic chains in controlled radical polymerizations, thus imposing the adverse impacts on the environment [26]. It is evident that finding out the greener and sustainable pathways for the fabrication of nanostructured materials is necessary.

Metal-organic frameworks (MOFs) are advanced materials constructed by metal ions or clusters and organic ligands via the coordination bonds [27–30]. Recently, they are considered as remarkable and promising materials because of good crystallinity, complex topologies, high porosity, tunable chemical properties, and large metal cluster density, and thereby, MOFs have attracted much attention in many fields such as drug delivery, catalysis, gas storage, sensor, and adsorption [31]. MIL-53(Fe) or Fe(III)(OH)(1,4-BDC) is a typical class of MOFs generated by a combination between iron(III) cations and 1,4-dicarboxylic acid [32, 33]. This structure consists of FeO_6 hexagonal chains connecting with dicarboxylate anions to form the three-dimensional networks or SBUs (secondary building units) [34–36]. One of the most emergent features of MIL-53(Fe) compared with other MOFs is the “breathing effect,” which experiences a breathing transition in the presence of guest molecules, thus creating the structural flexibility [37]. Moreover, this

material can be easily synthesized via the conventional strategies, such as microwave or solvothermal method [38, 39]. Unlike the other MOFs such as MIL-88B(Cr) or MIL-101(Cr), which also represents the same “breathing effect,” MIL-53(Fe) is chemically stable and constituted of lower toxic metal centers and thus has gained much attention [40].

In this work, we described the MIL-53(Fe) synthesis by the solvothermal method and its application in IBU adsorption. Some techniques including XRD and FT-IR were used to analyze the as-synthesized products. Moreover, the experiments were optimized based on the response surface methodology.

2. Experimental

2.1. Chemicals and Instruments. All chemicals in this study were directly used without any purification. 1,4-Benzenedicarboxylic acid (H_2BDC , 98%) was purchased from Merck. Iron(III) chloride hexahydrate ($\text{FeCl}_3 \cdot 6\text{H}_2\text{O}$, 99.0%), and *N,N*-dimethylformamide (DMF, 99.5%) were purchased from Xilong Chemical, China.

The D8 Advance Bruker powder diffractometer was used to record the X-ray powder diffraction (XRD) profiles using $\text{Cu-K}\alpha$ beams as excitation sources. The FT-IR spectra were recorded on the Nicolet 6700 spectrophotometer to explore the functional groups. The UV-Vis spectrophotometer was used to determine the IBU concentration at wavelength 222 nm. All analytic samples were reactivated at 105°C under nitrogen atmosphere.

2.2. Synthesis of MIL-53(Fe). The MIL-53(Fe) was solvothermally prepared according to a recent study [37]. Firstly, 1.35 g of $\text{FeCl}_3 \cdot 6\text{H}_2\text{O}$ and 0.83 g of H_2BDC were dissolved in 25 mL DMF. The mixture was then transferred into a Teflon-lined autoclave and heated up at 150°C for 6 h. The yellow solid was extracted, refluxed with DMF overnight, washed with $\text{C}_2\text{H}_5\text{OH}$ for three times (3×10 mL), and then dried at 80°C for storage in a desiccator. Figure 2 illustrates the synthesis strategy of MIL-53(Fe).

2.3. Experimental Batches. The stock solutions (20 mg/L) were prepared by dissolving the IBU substrate in distilled water. Various levels of concentration (1.8–18.4 mg/L) for the adsorption were generated by consecutively diluting the initial stock solutions. A series of HCl and KOH solutions was utilized to adjust the pH indexes. Herein, twenty experimental runs were randomly performed at room temperature following the response surface methodology (RSM) [42]. Firstly, MIL-53(Fe) samples (0.16–1.84 g/L) were mixed with 50 mL of ibuprofen solutions (1.8–18.4 mg/L) at various ranges of pH. The flasks were sealed and placed in the shaking tables (200 rpm). After the adsorption process reached the equilibrium state at 120 min, the adsorbent solids were dispensed and separated using the simple centrifugation. The IBU residual concentrations were identified using UV-Vis spectroscopy at the wavelength of

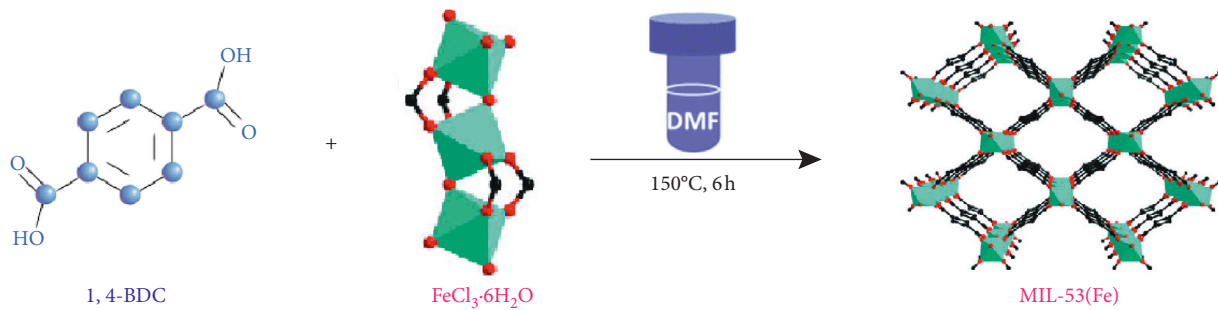


FIGURE 2: Schematic illustration for the synthesis of the MIL-53(Fe). The simulated structure of MIL-53(Fe) and iron(III) clusters was reproduced from [41].

222 nm. The percentage of removal y (%) and adsorption capacity Q (mg/g) can be mathematically defined as follows:

$$y(\%) = \frac{C_0 - C_e}{C_0} \cdot 100,$$

$$Q_t = \frac{C_0 - C_t}{m} \cdot V, \quad (1)$$

$$Q_e = \frac{C_0 - C_e}{m} \cdot V,$$

where C_0 , C_t , and C_e are denoted for the initial concentration, concentration at time t (min), and equilibrium concentrations (mg/L) and m (g) and V (mL) are denoted for adsorbent mass and solution volume, respectively.

2.4. Optimization Model with Response Surface Methodology.

Response surface methodology is the empirically statistical method, which allows optimizing the target (y) or “response” based on the evaluation of chosen variables (x_i) [43]. In this study, three factors as input parameters were selected to investigate including IBU concentration (x_1), MIL-53 dosage (x_2), and pH (x_3). Their random experimental runs were designed according to the guide of the Design-Expert version 10 (DX10) program (Table 1).

The “response” of the model was the removal efficiency (y), and thus, the target of this model is to maximize the “response”; the function of three variables is given by the following equation:

$$y = f(x) = \beta_0 + \sum_{i=1}^k \beta_i x_i + \sum_{i=1}^k \sum_{j=1}^k \beta_{ij} x_i x_j + \sum_{i=1}^k \beta_{ii} x_i^2, \quad (2)$$

where y is the predicted response and x_i and x_j are the independent variables ($i, j = 1, 2, 3, 4, \dots, k$). The parameter β_0 is the offset coefficient, β_i is the linear coefficient, β_{ii} is the second-order coefficient, and β_{ij} is the interaction coefficient [44].

2.5. Error Analysis. In this study, we explored the nonlinear kinetic and isotherm models using error functions, which were fitted by the Origin 9.0 program. Error analysis aims to determine the suitability of any models, and their confidence level could be assessed via commonplace error functions

TABLE 1: List of independent variables and their levels.

Factors	Unit	Code	Levels				
			$-\alpha$	-1	0	$+1$	$+\alpha$
Initial concentration	mg/L	x_1	1.6	5	10	15	18.4
Adsorbent dosage	g/L	x_2	0.16	0.5	1	1.5	1.84
pH	—	x_3	2.6	4	6	8	9.4

[45]. Thus, coefficient of determination (R^2), mean relative error (MRE), and sum square error (SSE) were used, and their mathematical forms were shown in equations (3)–(5). Moreover, $Q_{i,cal}$ and $Q_{i,exp}$ are the respective calculated and experimental adsorption capacity values:

$$R^2 = \frac{\sum_{i=1}^n (Q_{i,exp} - \overline{Q_{i,exp}})^2 - \sum_{i=1}^n (Q_{i,exp} - \overline{Q_{i,cal}})^2}{\sum_{i=1}^n (Q_{i,exp} - \overline{Q_{i,exp}})^2}, \quad (3)$$

$$\text{MRE}(\%) = \frac{100}{n} \sum_{i=1}^n \left| \frac{Q_{i,cal} - Q_{i,exp}}{Q_{i,exp}} \right|, \quad (4)$$

$$\text{SSE} = \sum_{i=1}^n (Q_{i,cal} - Q_{i,exp})^2. \quad (5)$$

3. Results and Discussion

3.1. Structural Characterization of MIL-53(Fe). Figure 3 describes the structural characterization of MIL-53(Fe) using the X-ray diffraction patterns and FT-IR spectra. According to Figure 3(a), several emerging peaks were found at scanning degree of 9.5° (101), 18.6° (002), and 28.2° (302), indicating that the MIL-53(Fe) obtained a crystalline structure. This observation was also commensurate with several previous reports [33, 46, 47], suggesting that the MIL-53(Fe) was solvothermally synthesized.

Moreover, the FT-IR spectrum in Figure 3(b) reveals the collection of functional groups that features the structure of MIL-53(Fe) (Table 2) [48]. In detail, a broad vibration at around 3420 cm^{-1} was ascribed to the presence of O-H groups, which adsorbed water existing in the surface of MIL-53(Fe) [49]. The asymmetric (γ_{as} C-O) and symmetric (γ_s C-O) stretching of dicarboxylate linkers could be verified

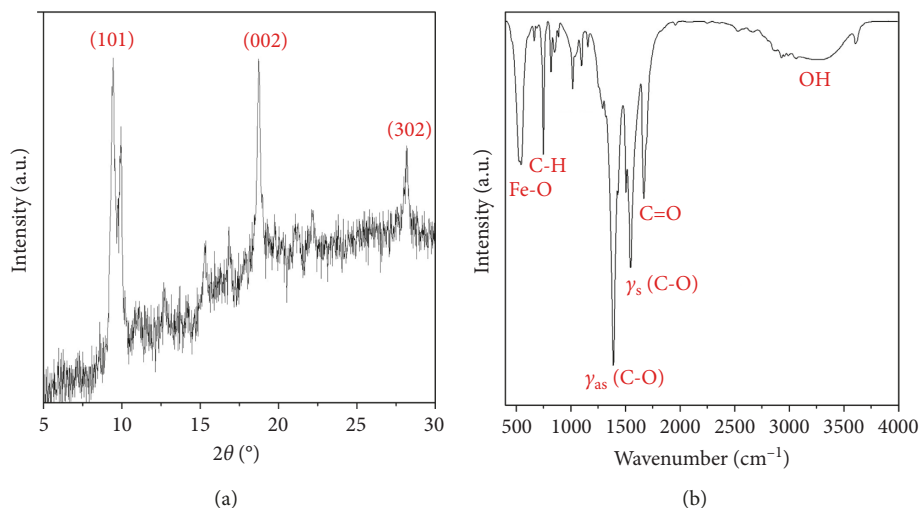


FIGURE 3: X-ray diffraction patterns (a) and FT-IR spectra of MIL-53(Fe) (b).

TABLE 2: The surface functional groups analysis of MIL-53(Fe).

Functional groups	O-H	C=O	γ_{as} (C-O)	γ_s (C-O)	C-H	Fe-O
Wavenumber (cm^{-1})	3420	1678	1550	1390	745	540

by the appearance of sharp vibrations at 1550 cm^{-1} and 1390 cm^{-1} , respectively, [37]. Moreover, the carbonyl groups (C=O) of carboxylate ligand (COO) were visible at 1678 cm^{-1} , whereas a very sharp peak at 745 cm^{-1} was consistently corresponding to Csp²-H bending vibrations, which belong to the aromatic rings of carboxylates [50]. Especially, the characteristic coordination bonds between Fe³⁺ cations and -OOC-C₆H₄-COO- carboxylate anions were observed at the low wavenumber (540 cm^{-1}), revealing the existence of a Fe-oxo bond inherent in the structure of MIL-53(Fe) [51]. Therefore, a combination of two characterization results demonstrates that the crystals of MIL-53(Fe) were successfully fabricated.

The morphological properties of MIL-53(Fe) can be analyzed by the SEM technique. Figure 4 showed the MIL-53(Fe) particles at 100 and $10\text{ }\mu\text{m}$, which generally well-described the polyhedron-like crystalline structure [32]. However, a clear difference of MIL-53(Fe) samples could be observed between before and after purification. Figure 4(b) demonstrated that a certain part of as-synthesized MIL-53(Fe) morphology was not homogeneous, which may be attributable to the residual 1,4-BDC components. A previous study also implied that this precursor may encapsulate the as-synthesized MIL-53(Fe) crystals [52]. Meanwhile, Figure 4(c) showed a relatively smooth surface of refined MIL-53(Fe) along with the complete disappearance of amorphous solid phases, suggesting that the refinement of as-synthesized MIL-53(Fe) was necessary to eliminate the 1,4-BDC trace [52].

Figure 5(a) diagnosed the textual feature of MIL-53(Fe) using the Raman spectrum. Clearly, a shape peak could be observed at the Raman shift of 464 cm^{-1} , revealing the existence of gamma bond of Fe-oxo in the structure of MIL-53(Fe). Also, typical peaks of the aromatic C-H bond were found at 632 and 865 cm^{-1} , while the single peak at

1141 cm^{-1} was ascribed for the bonds between two sp²-hybrid carbon atoms of benzene rings and carboxylate groups. Importantly, the asymmetric (γ_{as} C-O) and symmetric (γ_s C-O) footprints of COO- linkers were again confirmed via a couple of consecutive peaks at 1451 and 1501 cm^{-1} , respectively. Finally, $\nu(\text{C}=\text{C})$ was a kind of typical bond of aromatic cycles, which were emergent at 1616 cm^{-1} .

To gain the insights into the nature of porosity and pore size in MIL-53(Fe), the pore size distribution was measured and shown in Figure 5(b). It is evident that pore diameters of MIL-53(Fe) exhibited a wide range of sizes, revealing the existence of both micropore and macropore in the structure, but macrosized pore (more than 50 nm) was utterly dominant. Notice that there was an infinitesimal amount of micropore, which was less than 2 nm in length. Moreover, the surface area of MIL-53(Fe) was determined by the N₂ adsorption-desorption isotherm at 77 K , which was found to be $5.5\text{ m}^2/\text{g}$. Tuan et al. also reported the very low surface area, at about $14\text{ m}^2/\text{g}$, which may be attributable to the closed pores of MIL-53(Fe) that prevent the arrival of nitrogen molecules [49].

3.2. Optimization of the Ibuprofen Absorbability of MIL-53(Fe) by RSM Tool. Herein, we applied the RSM to optimize the removal of IBU in water using the MIL-53(Fe) as an adsorbent. All experiments were designed and analyzed statistically using the DX10 [11]. In detail, three independent variables including initial IBU concentration, MIL-53(Fe) adsorbent dosage, and pH solution at various five levels were investigated. The relationship between IBU removal efficiency and three independent variables can be described by the following equation:

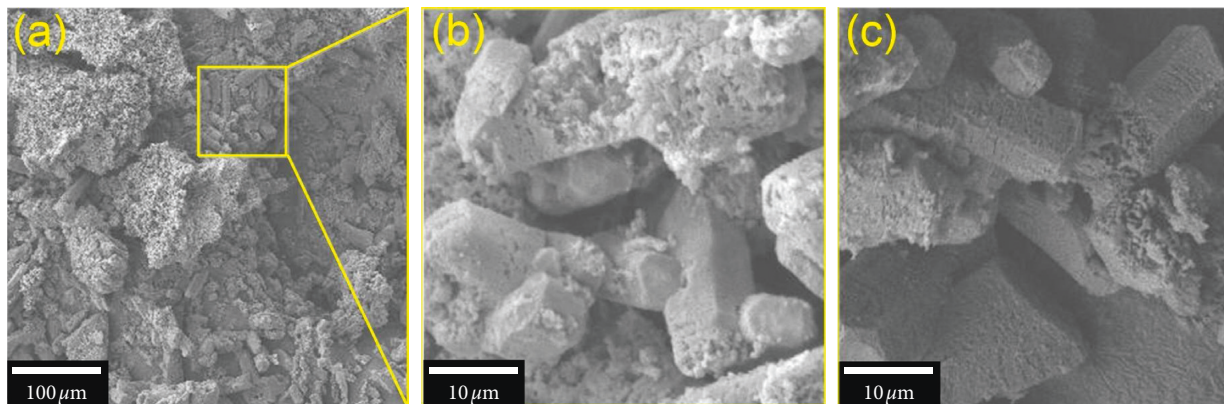


FIGURE 4: SEM images of MIL-53(Fe) before (a), (b) and after refinement (c).

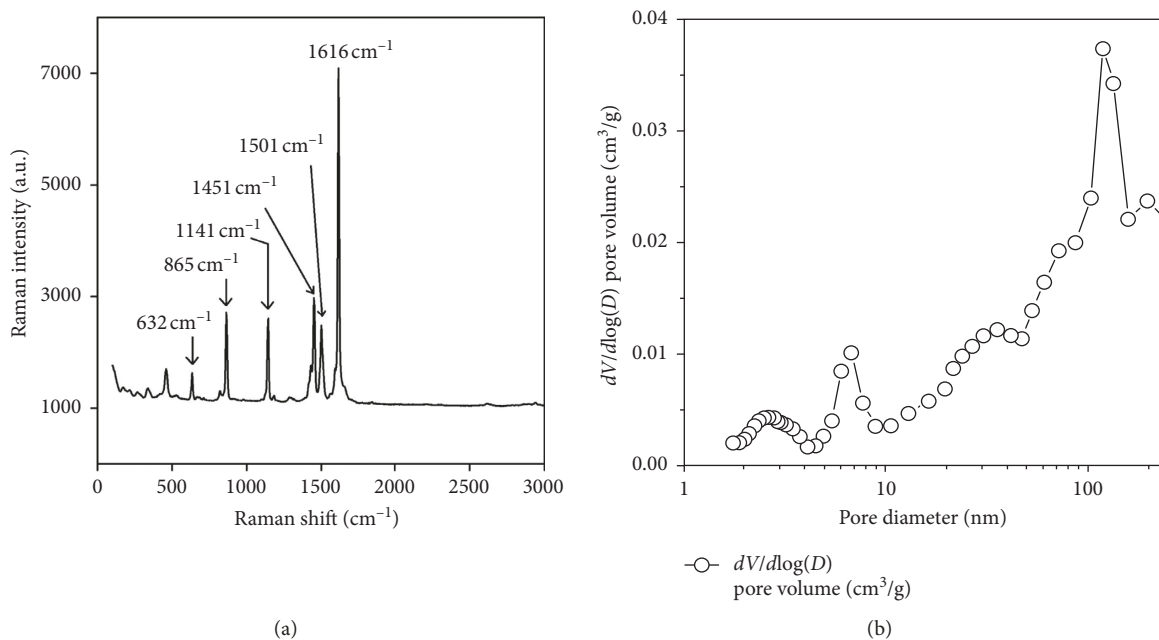


FIGURE 5: Raman spectrum (a) and pore size distribution (b) of MIL-53(Fe).

$$\begin{aligned}
 y(\%) &= 21.56 - 5.21x_1 + 7.15x_2 - 19.58x_3 \\
 &\quad + 6.83x_1x_2 + 0.88x_1x_3 - 4.35x_2x_3 \\
 &\quad + 4.97x_1^2 + 5.69x_2^2 + 11.10x_3^2, \\
 \text{or IBU removal}(\%) &= 21.56 - 5.21(C) + 7.15(\text{dose}) \\
 &\quad - 19.58(\text{pH}) + 6.83(C)(\text{dose}) \\
 &\quad + 0.88(C)(\text{pH}) \\
 &\quad - 4.35(\text{dose})(\text{pH}) + 4.97(C)^2 \\
 &\quad + 5.69(\text{dose})^2 + 11.10(\text{pH})^2.
 \end{aligned}
 \tag{6}$$

The actual and predicted values for the experimental matrix were listed in Table 3. Table 4 illustrates the coefficients of ANOVA data including the sum of squares, degree of freedom, mean square, F value, and Prob. > F [43].

Interestingly, determination coefficients (R^2) and P values of the regression model were found to be 0.9621 and <0.0001 with the confidence level of 95%, respectively. Thus, the proposed quadratic model was statistically significant and could be used to assess the effect of factors (initial IBU concentration, MIL-53(Fe) adsorbent dosage and pH) on the IBU absorbability of MIL-53(Fe) [48]. Figure 6(a) also indicates the high compatibility of experimental and predicted values as their data points were closely distributed to the 45-degree line.

Figures 6(b)–6(d) showing the three-dimensional response surfaces reveal the consistent impacts of three factors on the IBU drug removal efficiencies of MIL-53(Fe). Generally, the removal process of IBU was conducive with an increase in the amount of the MIL-53 adsorbent or a decrease in pH values of IBU solutions. Meanwhile, the initial concentration of IBU solution shows a negligible effect on the IBU removal efficiency.

TABLE 3: Experimental design used for investigation of IBU removal over MIL-53(Fe).

N	Variables			IBU removal efficiency (%)	
	x_1	x_2	x_3	Observed	Predicted
1	5	0.5	4	69.8	64.3
2	15	0.5	4	43.8	38.5
3	5	1.5	4	80	73.7
4	15	1.5	4	78.7	75.1
5	5	0.5	8	35.8	32.1
6	15	0.5	8	10.7	9.8
7	5	1.5	8	26	24.1
8	15	1.5	8	30.8	29.0
9	1.6	1	6	37.5	44.4
10	18.4	1	6	23.5	26.9
11	10	0.16	6	20	25.6
12	10	1.84	6	45.1	49.7
13	10	1	2.6	77.1	85.9
14	10	1	10.4	18.6	20.0
15	10	1	6	22.6	21.6
16	10	1	6	17.7	21.6
17	10	1	6	23.8	21.6
18	10	1	6	25	21.6
19	10	1	6	20	21.6
20	10	1	6	22	21.6

Understandably, the improvement of IBU removal percentage may be ascribed to the presence of “adsorption sites” [53]. When an addition of adsorbent was considerable, “adsorption sites” containing the surface functional groups became more dominant, thus increasing the number of IBU molecules captured [54, 55]. By contrast, a decline in the amount of the MIL-53(Fe) adsorbent may result in the rapid saturation of adsorption sites, possibly rendering the treatment of IBU drug ineffective.

Importantly, the decontamination of the IBU pollutant reached the excellent results in the acidic media, while the figures for the basic/neutral solutions were clearly unfavorable. In detail, Figure 6(d) indicates that nearly 100% of IBU could be removed from water at the very low pH values (i.e., pH = 2.6–4.3) and high adsorbent dosage (1.5–1.84 g/L).

By applying the RSM via model confirmation, several optimal conditions were proposed including the factors along with the predicted response value (Table 5). To test the precision and confidence of proposed optimized conditions, a verification experiment was performed using the above proposed conditions. The observed results were in good agreement with the predicted results because there was an ineligious error between predicted and tested results, and “desirability” values were obtained up to 100%, reflecting the excellent closeness of response (y) to their ideal values [56]. In other words, the model for the optimization of IBU adsorption over MIL-53(Fe) in this study achieved the high compatibility and thus could be used to design and optimize the experimental conditions.

3.3. Adsorption Studies. To gain deeper insights into the adsorption mechanism and behavior of IBU over

MIL-53(Fe), herein, the nonlinear kinetic and isotherm models could be adopted. All experiments were conducted at room temperature, and other experimental conditions were chosen from model optimization (Table 5), at initial concentration (10 mg/L), dosage (1.0 g/L), and pH 2.6. Note that samples were extracted for regular time intervals (0, 10, 20, 40, 60, 80, 100, and 120 min) to investigate the kinetic study, while IBU concentrations were in range from 5 to 20 mg/L. Final IBU content could be measured by using a UV-Vis spectrophotometer at 222 nm.

Any selected model needs to meet the requirements in terms of R^2 , MRE (%), and SSE. A model with a high R^2 value indicates that the predicted data are fitted well with actual data [45]. Meanwhile, lower MRE and SSE values reveal the negligible magnitude of error functions. To assess the models, therefore, terms of R^2 , MRE (%), and SSE were added herein.

For the kinetic models, we optioned four equations including pseudo-first-order, pseudo-second-order, Elovich, and Bangham, which their mathematical forms were illustrated in the equations given in Table 6. Figure 7(a) illustrates the effect of uptake capacity on contact time. It is evident that the adsorption process reached an equilibrium nature after 90 min. According to Table 6, all kinetic models obtained an excellent fitness based on R^2 values (0.981–0.992), indicating the high compatibility between actual and proposed data. Nevertheless, among the models, the pseudo-second-order equation offered the highest degree of suitability because of the highest R^2 , smallest SSE, and very low MRE (%). In fact, Elovich model showed the lowest MRE (3.15%), but its SSE value was so far higher than the pseudo-second-order model, 7.44 compared with 0.39, respectively. Therefore, the pseudo-second-order model could be used to explore the adsorption mechanism of the IBU species onto the adsorbent, which chemisorption plays a crucial role.

For the isotherm models, four equations including Langmuir, Freundlich, Temkin, and Dubinin and Radushkevich (D-R) were applied. Similar to the kinetic models, their mathematical forms were explained in equations given in Table 7. Obviously, the Langmuir demonstrated the most appropriate model via the highest R^2 and lowest MRE and SSE values, suggesting that the monolayer mechanism is more inclining to others. The maximum adsorption capacity (Q_m) obtained from the Langmuir equation was calculated at 10.67 mg/g, revealing the favorable adsorption and good capacity of IBU onto MIL-53(Fe).

4. Conclusion

The MIL-53(Fe) material was successfully synthesized from the precursors including $\text{FeCl}_3 \cdot 6\text{H}_2\text{O}$ and 1,4-BDC via the solvothermal method and structurally characterized using the X-ray diffraction patterns, FT-IR spectra, SEM, pore size distribution, and Raman. The characterization results implied that the MIL-53(Fe) possessed the crystalline structure, along with a low surface area ($5.5 \text{ m}^2/\text{g}$). Moreover, important functional groups were found (Fe-O, COO, C=O, C-O, C-H, and O-H), proving the presence of these chemical bonds in the structure of MIL-53(Fe). For the optimization

TABLE 4: ANOVA data for the IBU removal models.

Source	Sum of squares	Freedom degree	Mean square	F value	Prob. > F	Note
Model	9093.12	9	1010.35	28.18	<0.0001 ^S	
x_1	370.63	1	370.63	10.34	0.0093 ^S	
x_2	697.69	1	697.69	19.46	0.0013 ^S	
x_3	5235.08	1	5235.08	146.00	<0.0001 ^S	
$(x_1)^2$	372.65	1	372.65	10.39	0.0091 ^S	
$(x_2)^2$	6.13	1	6.13	0.1708	0.6881 ^N	^S Significant at $p < 0.05$
$(x_3)^2$	151.38	1	151.38	4.22	0.0670 ^N	^N Nonsignificant at $p > 0.05$
$x_1 \cdot x_2$	356.18	1	356.18	9.93	0.0103 ^S	
$x_1 \cdot x_3$	467.61	1	467.61	13.04	0.0048 ^S	
$x_2 \cdot x_3$	1777.41	1	1777.41	49.57	<0.0001 ^S	

Fit statistics: standard deviations (Std.) = 3.17; mean = 36.43; CV (%) = 16.44; $R^2 = 0.9621$.

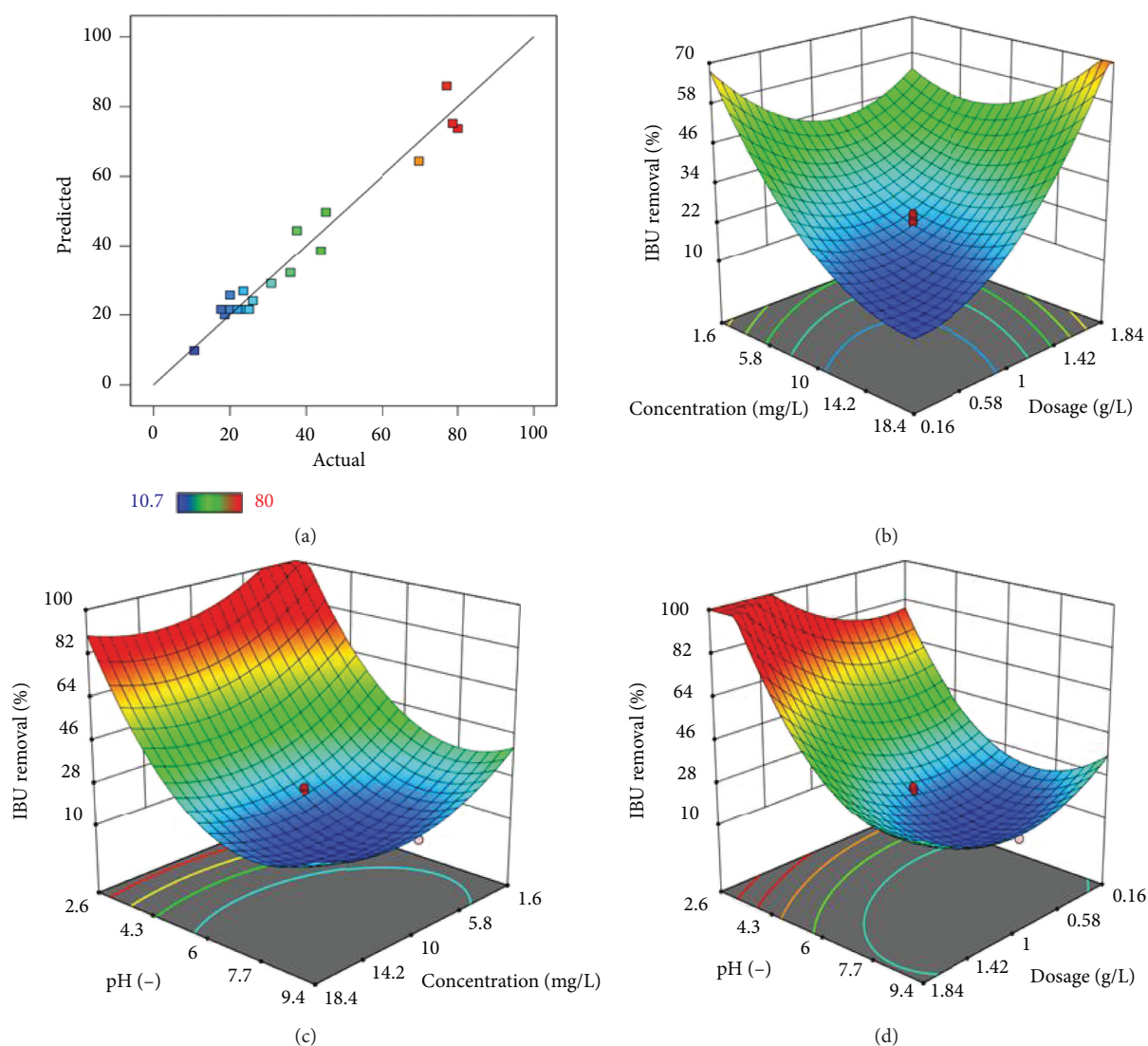


FIGURE 6: Actual versus predicted plots (a) and three-dimensional response surfaces (b)–(d) presenting the effect of factors on the response.

experiment of ibuprofen over MIL-53(Fe), the RSM results indicated that all variables (IBU initial concentration, MIL-53(Fe) dosage, and pH) had a vital impact on the IBU removal efficiency through the very high determination coefficient ($R^2 > 0.9$) and very low P value ($P < 0.0001$). Also,

the proposed model was statistically significant and could be used to find out the optimal conditions. The confirmation tests also proved that the model was highly compatible with experimental data because the observed values were consistent with the predicted values and high removal efficiency

TABLE 5: Optimal conditions and confirmation runs.

Concentration (mg/L)	Dosage (g/L)	pH (-)	IBU removal efficiency (%)			"Desirability"
			Predicted (%)	Tested (%)	Error (%)	
5.47	0.67	3.0	82.3	80.2	-2.55	1.0000
10.00	1.00	2.6	85.9	80.8	-5.94	1.0000
8.11	1.51	3.5	83.2	80.0	-3.73	1.0000

TABLE 6: Nonlinear kinetic constants for the adsorption of IBU over MIL-53(Fe).

Kinetic models	Equation	Parameters	Value
Pseudo-first-order	$Q_t = Q_1 \cdot (1 - \exp(-k_1 t))$	k_1 (min ⁻¹)	0.0496
		Q_1 (mg/g)	7.87
		MRE (%)	5.29
		SSE	0.83
		$(R_{adj})^2$	0.983
Pseudo-second-order	$Q_t = t / ((1/k_2 Q_2^2) + (t/Q_2))$ $H = k_2 \cdot Q_2^2$	k_2 (g/mg·min)	0.0063
		Q_2 (mg/g)	9.28
		H (mg/g·min)	0.543
		MRE (%)	3.67
		SSE	0.39
		$(R_{adj})^2$	0.992
Elovich	$Q_t = (1/\beta)(\ln(1 + \alpha\beta t))$	α (mg/g·min)	1.1
		β (g/mg)	0.5
		MRE (%)	3.15
		SSE	7.44
		$(R_{adj})^2$	0.989
Bangham	$Q_t = k_B \cdot t^{\alpha_B}$	k_B (mL/(g/L))	1.98
		α_B	0.30
		MRE (%)	5.02
		SSE	13.05
		$(R_{adj})^2$	0.981

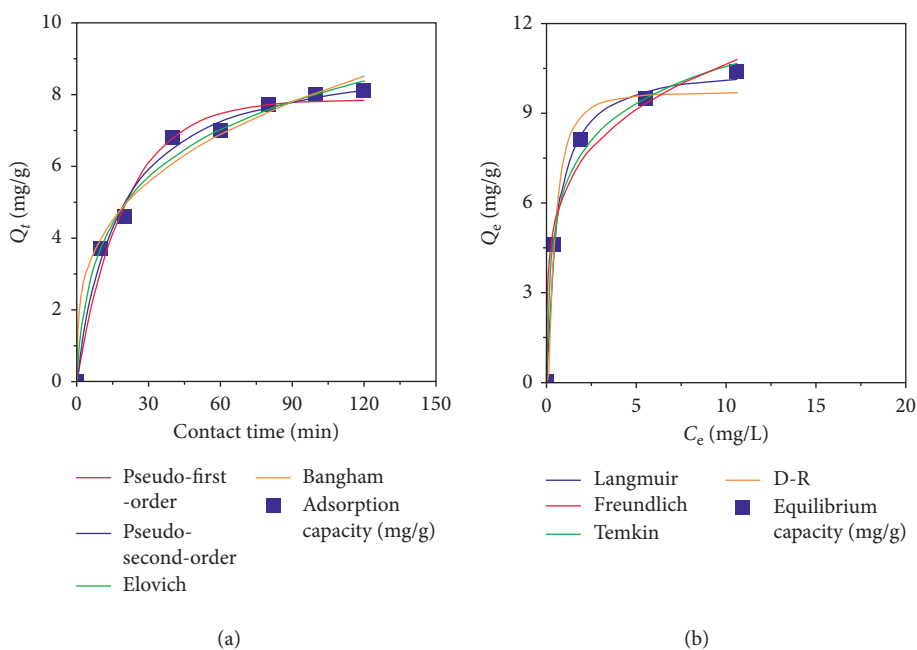


FIGURE 7: Kinetic and isotherm models for adsorption of IBU onto MIL-53(Fe). Experimental conditions consisted of initial concentration (10 mg/L), dosage (1.0 g/L), and pH 2.6 at room temperature.

TABLE 7: Nonlinear isotherm constants for the adsorption of IBU over MIL-53(Fe).

Kinetic models	Equation	Parameters	Value
Langmuir	$Q_e = (Q_m K_L C_e) / (1 + K_L C_e)$ $R_L = 1 / (1 + K_L C_e)$	k_L (L/mg)	1.80
		Q_m (mg/g)	10.67
		R_L	0.03
		MRE (%)	2.46
		SSE	0.18
		$(R_{adj})^2$	0.997
Freundlich	$Q_e = K_F C_e^{1/n}$	k_F (mg/g)/(mg/L) ^{1/n}	6.39
		1/n	0.22
		MRE (%)	6.43
		SSE	0.98
		$(R_{adj})^2$	0.980
		Temkin	$Q_e = B_T \ln(k_T C_e)$ $B_T = (RT)/b$
B_T	1.77		
MRE (%)	3.13		
SSE	0.31		
$(R_{adj})^2$	0.993		
D-R	$Q_e = Q_m \exp(-B\epsilon^2)\epsilon = RT \ln(1 + (1/C_e))$ $E = 1/(\sqrt{2B})$		
		Q_m (mg/g)	9.72
		E (kJ/mol)	2.47
		MRE (%)	5.34
		SSE	1.18
		$(R_{adj})^2$	0.978

obtained (80.0–80.8%). Kinetic and isotherm models also suggested that the adsorption process obeyed the chemisorption and monolayer behavior mechanisms.

Data Availability

No data were used to support this study.

Conflicts of Interest

The authors declare that there are no conflicts of interest.

Acknowledgments

This research was funded by NTTU Foundation for Science & Technology Development (Grant no. 2018.01.15/HĐ-KHCN) and Center of Science and Technology Development for Youth, Ho Chi Minh City Communist Youth Union, Vietnam (no. 06/2018/HĐ-KHCN-VU).

References

- [1] S. Sarre, L. Määttä, T. L. J. Tammela, A. Auvinen, and T. J. Murtola, "Postscreening follow-up of the Finnish prostate cancer screening trial on putative prostate cancer risk factors: vitamin and mineral use, male pattern baldness, pubertal development and non-steroidal anti-inflammatory drug use," *Scandinavian Journal of Urology*, vol. 50, no. 4, pp. 267–273, 2016.
- [2] B. R. da Costa, S. Reichenbach, N. Keller et al., "Effectiveness of non-steroidal anti-inflammatory drugs for the treatment of pain in knee and hip osteoarthritis: a network meta-analysis," *The Lancet*, vol. 390, no. 10090, pp. e21–e33, 2017.
- [3] T.-S. Vo, D.-H. Ngo, L. G. Bach, D.-N. Ngo, and S.-K. Kim, "The free radical scavenging and anti-inflammatory activities of gallate-chitoooligosaccharides in human lung epithelial A549 cells," *Process Biochemistry*, vol. 54, pp. 188–194, 2017.
- [4] A. K. Nguyen, T. H. Nguyen, B. Q. Bao, L. G. Bach, and D. H. Nguyen, "Efficient self-assembly of mPEG end-capped porous silica as a redox-sensitive nanocarrier for controlled doxorubicin delivery," *International Journal of Biomaterials*, vol. 2018, Article ID 1575438, 8 pages, 2018.
- [5] T. D. Březinova, J. Vymazal, M. Koželuh, and L. Kule, "Occurrence and removal of ibuprofen and its metabolites in full-scale constructed wetlands treating municipal wastewater," *Ecological Engineering*, vol. 120, pp. 1–5, 2018.
- [6] S. Adityosulindro, C. Julcour, and L. Barthe, "Heterogeneous Fenton oxidation using Fe-ZSM5 catalyst for removal of ibuprofen in wastewater," *Journal of Environmental Chemical Engineering*, vol. 6, no. 5, pp. 5920–5928, 2018.
- [7] H. A. Hasan, S. R. S. Abdullah, A. W. N. Al-Attabi et al., "Removal of ibuprofen, ketoprofen, COD and nitrogen compounds from pharmaceutical wastewater using aerobic suspension-sequencing batch reactor (ASSBR)," *Separation and Purification Technology*, vol. 157, pp. 215–221, 2016.
- [8] S. Saeid, P. Tolvanen, N. Kumar et al., "Advanced oxidation process for the removal of ibuprofen from aqueous solution: a non-catalytic and catalytic ozonation study in a semi-batch reactor," *Applied Catalysis B: Environmental*, vol. 230, pp. 77–90, 2018.
- [9] Y. Luo, W. Guo, H. H. Ngo et al., "A review on the occurrence of micropollutants in the aquatic environment and their fate and removal during wastewater treatment," *Science of the Total Environment*, vol. 473–474, pp. 619–641, 2014.
- [10] T. Van Thuan, B. T. P. Quynh, T. D. Nguyen, V. T. T. Ho, and L. G. Bach, "Response surface methodology approach for optimization of Cu²⁺, Ni²⁺ and Pb²⁺ adsorption using KOH-activated carbon from banana peel," *Surfaces and Interfaces*, vol. 6, pp. 209–217, 2017.
- [11] T. Van Tran, Q. T. P. Bui, T. D. Nguyen, N. T. H. Le, and L. G. Bach, "A comparative study on the removal efficiency of metal ions (Cu²⁺, Ni²⁺, and Pb²⁺) using sugarcane bagasse-

- derived ZnCl₂-activated carbon by the response surface methodology,” *Adsorption Science & Technology*, vol. 35, no. 1-2, pp. 72–85, 2017.
- [12] T. Van Tran, Q. T. P. Bui, T. D. Nguyen, V. T. T. Ho, and L. G. Bach, “Application of response surface methodology to optimize the fabrication of ZnCl₂-activated carbon from sugarcane bagasse for the removal of Cu²⁺,” *Water Science and Technology*, vol. 75, no. 9, pp. 2047–2055, 2017.
- [13] H. N. Tran, Y.-F. Wang, S.-J. You, and H.-P. Chao, “Insights into the mechanism of cationic dye adsorption on activated charcoal: the importance of π - π interactions,” *Process Safety and Environmental Protection*, vol. 107, pp. 168–180, 2017.
- [14] H. N. Tran, H.-P. Chao, and S.-J. You, “Activated carbons from golden shower upon different chemical activation methods: synthesis and characterizations,” *Adsorption Science & Technology*, vol. 36, no. 1-2, pp. 95–113, 2018.
- [15] S.-A. Sajjadi, A. Mohammadzadeh, H. N. Tran et al., “Efficient mercury removal from wastewater by pistachio wood waste-derived activated carbon prepared by chemical activation using a novel activating agent,” *Journal of Environmental Management*, vol. 223, pp. 1001–1009, 2018.
- [16] T. V. Pham, T. T. Nguyen, D. T. Nguyen et al., “The preparation and characterization of expanded graphite via microwave irradiation and conventional heating for the purification of oil contaminated water,” *Journal of Nanoscience and Nanotechnology*, vol. 19, no. 2, pp. 1122–1125, 2019.
- [17] P. Boakye, H. N. Tran, D. S. Lee, and S. H. Woo, “Effect of water washing pretreatment on property and adsorption capacity of macroalgae-derived biochar,” *Journal of Environmental Management*, vol. 233, pp. 165–174, 2019.
- [18] S. Sabale, V. Jadhav, V. Khot, X. Zhu, M. Xin, and H. Chen, “Superparamagnetic MFe₂O₄ (M=Ni, Co, Zn, Mn) nanoparticles: synthesis, characterization, induction heating and cell viability studies for cancer hyperthermia applications,” *Journal of Materials Science: Materials in Medicine*, vol. 26, no. 3, p. 127, 2015.
- [19] B. Q. Bao, N. H. Le, D. H. T. Nguyen et al., “Evolution and present scenario of multifunctionalized mesoporous nanosilica platform: a mini review,” *Materials Science and Engineering: C*, vol. 91, pp. 912–928, 2018.
- [20] S. Singh, M. B. Bahari, B. Abdullah et al., “Bi-reforming of methane on Ni/SBA-15 catalyst for syngas production: influence of feed composition,” *International Journal of Hydrogen Energy*, vol. 43, no. 36, pp. 17320–17243, 2018.
- [21] S. Zhao, Z. Zhang, G. Sèbe et al., “Multiscale assembly of superinsulating silica aerogels within silylated nanocellulosic scaffolds: improved mechanical properties promoted by nanoscale chemical compatibilization,” *Advanced Functional Materials*, vol. 25, no. 15, pp. 2326–2334, 2015.
- [22] H. Q. Pham, T. T. Huynh, A. Van Nguyen, T. Van Thuan, L. G. Bach, and V. T. Thanh Ho, “Advanced Ti_{0.7}W_{0.3}O₂ nanoparticles prepared via solvothermal process using titanium tetrachloride and tungsten hexachloride as precursors,” *Journal of Nanoscience and Nanotechnology*, vol. 18, no. 10, pp. 7177–7182, 2018.
- [23] D. W. Kim, L. G. Bach, S.-S. Hong, C. Park, and K. T. Lim, “A facile route towards the synthesis of Fe₃O₄/graphene oxide nanocomposites for environmental applications,” *Molecular Crystals and Liquid Crystals*, vol. 599, no. 1, pp. 43–50, 2014.
- [24] Y. V. Kaneti, J. Tang, R. R. Salunkhe et al., “Nanoarchitected design of porous materials and nanocomposites from metal-organic frameworks,” *Advanced Materials*, vol. 29, no. 12, article 1604898, 2017.
- [25] M.-H. Sun, S.-Z. Huang, L.-H. Chen et al., “Applications of hierarchically structured porous materials from energy storage and conversion, catalysis, photocatalysis, adsorption, separation, and sensing to biomedicine,” *Chemical Society Reviews*, vol. 45, no. 12, pp. 3479–3563, 2016.
- [26] L. G. Bach, V. T. T. Ho, B. T. P. Quynh, K. T. Lim, and T. C. Anh, “Synthesis of well-defined amphiphilic diblock copolymer brushes on halloysite nanotubes via surface-initiated reversible addition-fragmentation chain transfer polymerization,” *Journal of Nanoscience and Nanotechnology*, vol. 17, no. 8, pp. 5834–5838, 2017.
- [27] H. V. Dang, Y. T. N. Le, D. T. M. Tran, A. N. Q. Phan, and N. T. S. Phan, “Synthesis of benzo[1,4]thiazines via ring expansion of 2-aminobenzothiazoles with terminal alkynes under metal-organic framework catalysis,” *Catalysis Letters*, vol. 148, no. 5, pp. 1383–1395, 2018.
- [28] V. D. Nguyen, C. K. Nguyen, K. N. Tran et al., “Zeolite imidazolate frameworks in catalysis: synthesis of benzimidazoles via cascade redox condensation using Co-ZIF-67 as an efficient heterogeneous catalyst,” *Applied Catalysis A: General*, vol. 555, pp. 20–26, 2018.
- [29] T. V. Tran, H. T. N. Le, H. Q. Ha et al., “A five coordination Cu(II) cluster-based MOF and its application in the synthesis of pharmaceuticals via sp³ C-H/N-H oxidative coupling,” *Catalysis Science & Technology*, vol. 7, no. 16, pp. 3453–3458, 2017.
- [30] H. T. N. Le, T. V. Tran, N. T. S. Phan, and T. Truong, “Efficient and recyclable Cu₂(BDC)₂(BPY)-catalyzed oxidative amidation of terminal alkynes: role of bipyridine ligand,” *Catalysis Science & Technology*, vol. 5, no. 2, pp. 851–859, 2015.
- [31] Y.-Z. Chen, R. Zhang, L. Jiao, and H.-L. Jiang, “Metal-organic framework-derived porous materials for catalysis,” *Coordination Chemistry Reviews*, vol. 362, pp. 1–23, 2018.
- [32] Z. Yan, W. Zhang, J. Gao et al., “Reverse-phase high performance liquid chromatography separation of positional isomers on a MIL-53(Fe) packed column,” *RSC Advances*, vol. 5, no. 50, pp. 40094–40102, 2015.
- [33] N. D. Trinh and S.-S. Hong, “Photocatalytic decomposition of methylene blue over MIL-53(Fe) prepared using microwave-assisted process under visible light irradiation,” *Journal of Nanoscience and Nanotechnology*, vol. 15, no. 7, pp. 5450–5454, 2015.
- [34] S. H. Doan, K. D. Nguyen, T. T. Nguyen, and N. T. S. Phan, “Direct arylation of benzoazoles with aldehydes utilizing metal-organic framework Fe₃O(BDC)₃ as a recyclable heterogeneous catalyst,” *RSC Advances*, vol. 7, no. 3, pp. 1423–1431, 2017.
- [35] H. L. Nguyen, “The chemistry of titanium-based metal-organic frameworks,” *New Journal of Chemistry*, vol. 41, no. 23, pp. 14030–14043, 2017.
- [36] P. H. Pham, S. H. Doan, H. T. T. Tran et al., “A new transformation of coumarins via direct C-H bond activation utilizing an iron-organic framework as a recyclable catalyst,” *Catalysis Science & Technology*, vol. 8, no. 5, pp. 1267–1271, 2018.
- [37] Y. Zhang, G. Li, H. Lu, Q. Lv, and Z. Sun, “Synthesis, characterization and photocatalytic properties of MIL-53(Fe)-graphene hybrid materials,” *RSC Advances*, vol. 4, no. 15, pp. 7594–7600, 2014.
- [38] T. H. Tu, P. T. N. Cam, L. V. T. Huy, M. T. Phong, H. M. Nam, and N. H. Hieu, “Synthesis and application of graphene oxide aerogel as an adsorbent for removal of dyes from water,” *Materials Letters*, vol. 238, pp. 134–137, 2019.
- [39] T. V. Tran, D. T. C. Nguyen, H. T. N. Le et al., “MIL-53 (Fe)-directed synthesis of hierarchically mesoporous carbon and its

- utilization for ciprofloxacin antibiotic remediation,” *Journal of Environmental Chemical Engineering*, vol. 7, no. 1, article 102881, 2019.
- [40] J.-J. Du, Y.-P. Yuan, J.-X. Sun et al., “New photocatalysts based on MIL-53 metal–organic frameworks for the decolorization of methylene blue dye,” *Journal of Hazardous Materials*, vol. 190, no. 1–3, pp. 945–951, 2011.
- [41] W. Lu, Z. Wei, Z.-Y. Gu et al., “Tuning the structure and function of metal–organic frameworks via linker design,” *Chemical Society Reviews*, vol. 43, no. 16, pp. 5561–5593, 2014.
- [42] V. T. Tran, D. T. Nguyen, V. T. T. Ho, P. Q. H. Hoang, P. Q. Bui, and L. G. Bach, “Efficient removal of Ni₂ ions from aqueous solution using activated carbons fabricated from rice straw and tea waste,” *Journal of Materials and Environmental Science*, vol. 8, pp. 426–437, 2017.
- [43] T. Van Thuan, V. T. T. Ho, N. D. Trinh, N. T. Thuong, B. T. P. Quynh, and L. G. Bach, “Facile one-spot synthesis of highly porous KOH-activated carbon from rice husk: response surface methodology approach,” *Carbon-Science and Technology*, vol. 8, pp. 63–69, 2016.
- [44] P. Samoila, C. Cojocaru, I. Cretescu et al., “Nanosized spinel ferrites synthesized by sol-gel autocombustion for optimized removal of azo dye from aqueous solution,” *Journal of Nanomaterials*, vol. 2015, Article ID 713802, 13 pages, 2015.
- [45] T. V. Tran, V. D. Cao, V. H. Nguyen et al., “MIL-53 (Fe) derived magnetic porous carbon as a robust adsorbent for the removal of phenolic compounds under the optimized conditions,” *Journal of Environmental Chemical Engineering*, vol. 7, article 102902, 2019.
- [46] J. Gordon, H. Kazemian, and S. Rohani, “Rapid and efficient crystallization of MIL-53(Fe) by ultrasound and microwave irradiation,” *Microporous and Mesoporous Materials*, vol. 162, pp. 36–43, 2012.
- [47] P. Horcajada, T. Chalati, C. Serre et al., “Porous metal–organic-framework nanoscale carriers as a potential platform for drug delivery and imaging,” *Nature Materials*, vol. 9, no. 2, pp. 172–178, 2010.
- [48] L. G. Bach, T. Van Tran, T. D. Nguyen, T. Van Pham, and S. T. Do, “Enhanced adsorption of methylene blue onto graphene oxide-doped XFe₂O₄ (X=Co, Mn, Ni) nanocomposites: kinetic, isothermal, thermodynamic and recyclability studies,” *Research on Chemical Intermediates*, vol. 44, no. 3, pp. 1661–1687, 2018.
- [49] T. A. Vu, G. H. Le, C. D. Dao et al., “Arsenic removal from aqueous solutions by adsorption using novel MIL-53(Fe) as a highly efficient adsorbent,” *RSC Advances*, vol. 5, no. 7, pp. 5261–5268, 2015.
- [50] R. Liang, F. Jing, L. Shen, N. Qin, and L. Wu, “MIL-53(Fe) as a highly efficient bifunctional photocatalyst for the simultaneous reduction of Cr(VI) and oxidation of dyes,” *Journal of Hazardous Materials*, vol. 287, pp. 364–372, 2015.
- [51] P. Serra-Crespo, E. Gobechiya, E. V. Ramos-Fernandez et al., “Interplay of metal node and amine functionality in NH₂-MIL-53: modulating breathing behavior through intra-framework interactions,” *Langmuir*, vol. 28, no. 35, pp. 12916–12922, 2012.
- [52] M.-T. H. Nguyen and Q.-T. Nguyen, “Efficient refinement of a metal–organic framework MIL-53(Fe) by UV-vis irradiation in aqueous hydrogen peroxide solution,” *Journal of Photochemistry and Photobiology A: Chemistry*, vol. 288, pp. 55–59, 2014.
- [53] S.-S. Li, W.-Y. Zhou, M. Jiang et al., “Insights into diverse performance for the electroanalysis of Pb(II) on Fe₂O₃ nanorods and hollow nanocubes: toward analysis of adsorption sites,” *Electrochimica Acta*, vol. 288, pp. 42–51, 2018.
- [54] H. N. Tran, C.-C. Lin, S. H. Woo, and H.-P. Chao, “Efficient removal of copper and lead by Mg/Al layered double hydroxides intercalated with organic acid anions: adsorption kinetics, isotherms, and thermodynamics,” *Applied Clay Science*, vol. 154, pp. 17–27, 2018.
- [55] H. N. Tran, P. V. Viet, and H.-P. Chao, “Surfactant modified zeolite as amphiphilic and dual-electronic adsorbent for removal of cationic and oxyanionic metal ions and organic compounds,” *Ecotoxicology and Environmental Safety*, vol. 147, pp. 55–63, 2018.
- [56] M. A. Bezerra, R. E. Santelli, E. P. Oliveira, L. S. Villar, and L. A. Escaleira, “Response surface methodology (RSM) as a tool for optimization in analytical chemistry,” *Talanta*, vol. 76, no. 5, pp. 965–977, 2008.